# Final Report

## Advanced Cathode Catalysts and Supports for PEM Fuel Cells

**Grant No. DE-FC36-07GO17007**

**Submitted to the**

**U. S. Department of Energy, Office of Energy Efficiency and Renewable Energy, Transportation Technologies**

**September 30, 2012**

**by**

**3M Fuel Cell Components Program**
**3M Company, St. Paul, MN 55144**

**Prime Contractor:** 3M Company, St. Paul, MN 55144

**Project Title:** Advanced Cathode Catalysts and Supports for PEM Fuel Cells

**Principal Investigator:** Dr. Mark K. Debe, 3M Fuel Cell Program

**Team Members**: Dalhousie University
Argonne National Laboratory
Jet Propulsion Laboratory

**Key Vendor for Stack Testing:** GM Fuel Cell Activities

(This page left blank intentionally)

## Foreword and Acknowledgements

This report documents the work performed by 3M Company under the Grant No. DE-FC36-07GO17007, “Advanced Cathode Catalysts and Supports for PEM Fuel Cells.” The period of performance for this contract was from April 1, 2007 until June 30, 2012.

The principal objectives of the program were development of a durable, low cost, high performance cathode electrode (catalyst and support), that is fully integrated into a fuel cell membrane electrode assembly with gas diffusion media, fabricated by high volume capable processes, and is able to meet or exceed the 2015 DOE targets.

Work completed in this contract was an extension of the developments under three preceding cooperative agreements/grants Nos. DE-FC-02-97EE50473, DE-FC-99EE50582 and DE-FC36-02AL67621 which investigated catalyzed membrane electrode assemblies for PEM fuel cells based on a fundamentally new, nanostructured thin film catalyst and support system, and demonstrated the feasibility for high volume manufacturability.

All 3M MEA materials and process development were carried out by 3M Co. at its St. Paul, MN, 3M Center campus and its Menomonie, WI, pilot plant. The 3M team included primarily members from the Fuel Cell Components Program, with significant assistance received over varying periods of time from members of 3M’s Corporate Analytical Laboratory, and the Corporate Process Technology Laboratory. The principal technical team included Dr. Mark Debe as the principal investigator and technical team Leader, Mr. Andrew Steinbach as the chief operations specialist and functioning co-PI during the latter half of the contract. Dr. Radoslav Atanasoski was co-PI in the first half of the contract, Mr. Michael Kurkowski and Ms. Susan Hendricks were MEA fabrication and testing specialists, Mr. George Vernstrom was the thin film catalyst deposition specialist, Ms. Amy Hester was the project’s process engineer, and Mr. Paul Kadera the test station and utilities support technologist. Dr. James Larson led the GDL optimization work during the first half of the project before his retirement. The technical team is grateful for the significant help of Dr. Krzysztof Lewinski, Mr. Daniel Pierpont and Dr. Andrew Haug on Tasks 3, 6 and 1.3 respectively, and multiple technical aides and contract employees who assisted throughout the contract, and the invaluable contributions by the fuel cell program’s membrane development group and the manufacturing specialists and engineers at the Menomonie, Wisconsin pilot plant. Mr. Steven Kays of the 3M Government R&D Contracts department was the project’s contract administrator, with assistance from financial, controller, property accounting and sourcing experts Ms. Tara ann Witte, Ms. Anne Ringgenberg, Ms. Debra Budach and Mr. Brian Massel, respectively.

Subcontractors included Dalhousie University, Nova Scotia, Canada; NASA Jet Propulsion Laboratory, Pasadena, California; Argonne National Laboratory, Chicago, Illinois; and for final stack testing, the GM Fuel Cell Activities in Honeoye Falls, N. Y.

From our subcontractors’ organizations we are particularly indebted to Prof. Jeffrey Dahn and Dr. David Stevens of Dalhousie U.; Drs. Nenad Markovic, Vojislav Stamenkovic and Dennis van der Vliet of ANL; Drs. Charles Hays and S. R. Narayanan of JPL, and Eric Thompson of GM.

This work was funded in part by the U. S. DOE, Energy Efficiency and Renewable Energy Office of Transportation Technologies and Advanced Automotive Technologies. DOE technical and administrative oversight of the project was provided by DOE Managers Kathy Epping Martin (HQ) and David Person (GO) of the DOE Hydrogen and Fuel Cells Program, and DOE Technical Advisor Mr. Thomas Benjamin (Argonne National Laboratory).

## Executive Summary

Today the world faces increasingly serious environmental challenges. Solutions to these challenges must come from a proper balance of often conflicting public policy and socio-economic drivers with the availability of appropriate new technology. The development of hydrogen fueled vehicles for transportation is one example of new technology seriously being considered to replace the internal combustion engine (ICE) in order to reduce our dependence on fossil fuels and lower emissions of greenhouse gasses.

The polymer electrolyte membrane fuel cell (PEMFC) is the ultimate electric vehicle drive technology being developed to replace the ICE. By electrochemically combining hydrogen and oxygen from air to produce water, electricity is generated by the fuel cell for powering electric motors that drive the vehicle without pollution and minimal carbon emissions depending on the source of the hydrogen. Although the concept of a fuel cell is well over a century old, only in the last two decades have sufficiently significant advances been made in the PEMFC technology to warrant substantial investments in the development of practical systems. Many materials and process challenges remain to be overcome before cost effective, fuel cell powered vehicles can be successfully commercialized at reasonably high volumes. This report summarizes the work completed over the past five years under a 3M Company/U. S. Department of Energy grant directed specifically at advancing the key fuel cell components most critical for overcoming the PEMFC performance, durability and cost barriers.

The heart of a working PEMFC, where the electrochemical reactions convert the hydrogen and air to electricity, heat and water, is called the membrane electrode assembly, or MEA. At its simplest, the MEA is a multi-layered article comprising two key components: the ion exchange membrane at its center, and the Pt based electrocatalysts on either side of the membrane (see Fig. 1), where $H_2$ is oxidized on the anode and $O_2$ is reduced on the cathode, producing water on the cathode, heat and the desired product electricity flowing through an outside load between the anode and cathode. Fig. 1 illustrates more generally the five principal components forming a three or five layer MEA depending on whether the gas diffusion components are included. The catalyst electrodes can be coated or bonded to the PEM directly, or coated onto the porous carbon gas diffusion media. The MEA components interact strongly and affect the performance and durability of the fully integrated MEA by many complex mechanisms. In practice this necessitates development of the whole MEA package in order to optimize any individual component, particularly the catalysts. The cathode $O_2$ reduction reaction is six or more orders of magnitude slower than the anode $H_2$ oxidation reaction, so most PEM fuel cell research and development focuses on the cathode catalysts and electrodes. The anode electrodes however can have a dramatic influence on the cathode performance through water management effects viz. drying or flooding of the cathode with product water; carbon support corrosion due to cathode voltage excursions from anode $H_2$ starvation or start-up/shut down events; and the PEM lifetime from the anode's role in peroxide production due to cross-over of gases through the PEM, particularly at open circuit potentials. The catalysts and membrane are the most expensive components of the fuel cell for reasons related to the materials necessary to obtain the performance and durability.

Today's commercialized catalysts consist of nanometer sized particles of Pt or Pt alloys dispersed onto carbon black support particles. They are formed into "inks" and applied to the surfaces of the ion exchange membranes or gas diffusion media. However, despite the world's overwhelming research focus on use of carbon black supported nanoparticles for PEM FC catalysts, they have several fundamental limitations. Within the real life automotive fuel cell environment, the carbon support particles can be rapidly corroded at the high potentials seen

during start/stop events, the Pt nano-particles (2-4 nm diameter) have a natural susceptibility to Pt dissolution due to their small radii of curvature, or they tend to surface migrate together, agglomerating or growing by Ostwald ripening and losing effective surface area. The smaller the Pt particles are made in order to increase their surface area, the lower their fundamental activity for reducing oxygen to water, the basic cathode oxygen reduction reaction or ORR. Conversely larger particles have lower surface area. Nano-sized dispersed Pt particles exhibit low specific activity for the primary oxygen reduction reaction compared to extended surface catalysts, and more recently it is found that at ultra-low cathode loadings, the limits of high current density decrease more quickly than expected based on state-of-the-art modeling.

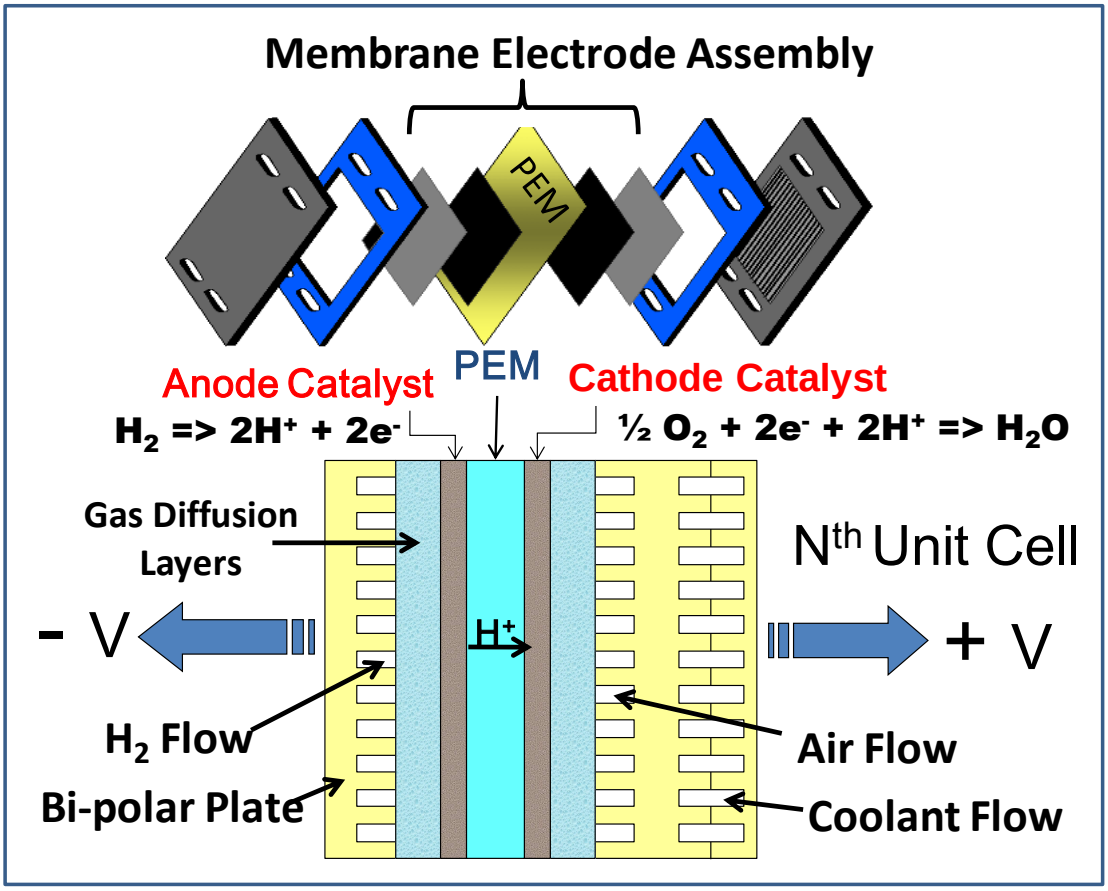


**Fig. 1.** Fuel cell components. Unit cell cross-section of a fuel cell stack showing the components of an expanded MEA.

Higher performing and more durable electrocatalysts at lower loadings must be developed for PEMFCs to meet the power density and lifetime hours required for fuel cell vehicles at acceptable costs. This means the catalyst activities for reducing the oxygen to water must be improved. At the same time the amount of expensive Pt catalyst must be reduced to lower the MEA costs. And while these two properties are met, the catalyst must be made more resistant to multiple degradation mechanisms to reach the necessary operating lifetimes.

In this report, we present a body of work focused on the continued development of a completely new approach to PEMFC electrocatalysts, called nanostructured thin film (NSTF) catalysts that eliminate many of the issues identified above with current catalyst technology. The carbon black supports are eliminated with this new approach and that eliminates the carbon corrosion

issue. The thin film nature of the catalyst significantly improves its robustness against dissolution and grain growth, preserving the surface area. Most important, the fundamental activity of the NSTF Pt catalysts for oxygen reduction is improved by over 500% compared to dispersed Pt catalysts. Finally, the process for fabricating the NSTF catalysts is consistent with high volume roll-good manufacturing, and extremely flexible towards the introduction of new catalyst compositions and structures. In this report we document the progress made developing new multi-element NSTF catalysts with properties that meet or exceed all the DOE Hydrogen Fuel Cells Program's 2015 targets for PEMFC electrocatalysts. The body of work completed advances the fundamental understanding of the NSTF catalyst technology, identifies and develops new NSTF-ternary catalyst materials for higher performance and durability at reduced loadings, and advances the high volume process capabilities for producing the NSTF based MEA's.

## Report Organization

A list of abbreviations and acronyms for the entire report is contained in this introductory section, immediately after the high level table of contents following this introduction. The major body of the report summarizing the accomplishments towards all the project objectives and DOE fuel cell catalyst target metrics has a more detailed table of contents defining its organization, as well as its own list of references. This is followed by a summary of the project technology transfer accomplishments, including publications in technical journals, invited and contributed international presentations, and patent applications resulting from this project.

A Supplementary Section provides more detailed summaries of major aspects of the six specific work Tasks of the project.

The final Appendix reproduces fifteen of the twenty-seven total publications in peer reviewed journals that derived from this project and which we consider to be highly significant outcomes.

## High Level Table of Contents

## List of Abbreviations and Acronyms

| | |
|---|---|
| ADF-STEM | Annular dark field scanning transmission electron microscopy |
| ANL | Argonne National Laboratory |
| AST | Accelerated stress test |
| CCB | Catalyst coated backing |
| CS | Constant stoichiometry |
| CCM | Catalyst coated membrane |
| CV | Cyclic voltammograms |
| DI | Deionized water |
| DOE | Department of Energy |
| DP | Dew point |
| ECSA | Electrochemical surface area |
| EMP | Electron microprobe |
| EW | Equivalent weight, polymer weight per mol of acid groups |
| FC | Fuel cell |
| GDL | Gas diffusion layer |
| HFR | High frequency resistance |
| HOR | Hydrogen oxidation reaction |
| HRTEM | High resolution transmission electron microscopy |
| Hupd | Hydrogen under-potential deposition |
| ICP | Inductively coupled plasma |
| IEC | Ion exchange capacity |
| MEA | Membrane electrode assembly |
| MPL | Microporous layer |
| MYDP | Multi-Year Research, Development and Demonstration Plan |
| NSTF | Nanostructured thin film catalyst |
| NSTFC | Nanostructured thin film catalyst |
| OCV | Open circuit voltage |
| OEM | Original Equipment Manufacturer |
| OER | Oxygen evolution reaction |
| ORR | Oxygen reduction reaction |
| PDS | Potentiodynamic polarization scan |
| PEM | Proton exchange membrane, polymer electrolyte membrane |
| PEMFC | Proton exchange membrane fuel cell |
| PR-149 | Perylene red 149 |
| PGM | Precious group metal |
| PSIG | Pounds per square inch gauge |
| PSS | Potentiostatic scans |
| Pt/C | Pt on carbon catalysts |
| $R^2$ | Least squares fitting parameter |
| R2R | Roll to roll, as in process |
| RDE | Rotating Disc Electrode |
| RH | Relative humidity |
| RHE | Reversible hydrogen electrode |
| RRDE | Rotating ring disc electrode |
| SCCM | Standard cubic centimeter per minute |
| SEF | Surface area enhancement factor |
| SET | Surface energy treatment |
| St. | Stoichiometric |
| $S_{min}$ | Minimum normalized surface area |
| TEM | Transmission electron microscopy |
| TM | Transition metal |
| XRD | X-ray diffraction |
| XRF | X-ray fluorescence |

# Project Overview Table of Contents

## 1. Introduction – Background and Overview of Scope of Work Completed

State-of-the-art proton exchange membrane (PEM) fuel cell electrocatalyst technology utilized in today's prototype fuel cell vehicles reveals limitations with respect to general durability and robustness under start-stop cycling, adequate performance with low PGM loadings, and low-cost manufacturability. To a large degree, these deficiencies are traceable to properties of the conventional carbon supported dispersed Pt catalysts in use today and issues with membrane integration. The research and development of this project were focused on overcoming these three most critical barriers for fuel cell MEA automotive deployment by using an alternative catalyst support and deposition method.

The approach to achieve the above objectives builds on a fifteen-year DOE/3M-funded development of the 3M nanostructured thin film (NSTF) catalyst and MEA technology. The NSTF catalyst is the only practical example of an extended surface catalyst, and thereby fundamentally has higher specific activity for oxygen reduction [1-11], removes all durability issues with carbon supports, demonstrates much lower losses due to Pt dissolution and membrane chemical attack [12-15], and has significant high volume all-dry roll-good manufacturing advantages [16].

The scope of work in the initial three-year 1st budget period included extensive work at 3M to increase the NSTF catalyst support film surface area, fabrication and screening of new alloys in 50 $cm^2$ single cells, and evaluation of multiple deposition parameters to obtain increased catalyst surface area and utilization. Complementary to this work at 3M, collaborative work included high throughput fabrication and characterization of new multi-element Pt alloys (ternaries and quaternaries) with Dalhousie University, fundamental catalyst characterization studies with ANL, and development and evaluation of a pseudo-rotating disk electrode (RDE) catalyst evaluation technique with JPL. Research in the fourth year focused at 3M on continued studies of water management improvements for cool/wet operation via optimization of materials, electrode structure and operating conditions; catalyst fabrication process improvements for increased catalyst performance and production efficiency; in-depth MEA component screening to down-select final configurations for the final short-stack testing; continued accelerated testing to benchmark the NSTF-MEA durability with each generation of MEA components; and initial fabrication of roll-good materials for initial stack testing by the GM fuel cell laboratory.

The final year focus was on a) completing the first year short stack testing to down-select a final MEA type for a 2nd (durability) stack; b) resolving specific production and MEA integration issues related to the final stack MEAs; c) 2nd stack durability protocol development and initial testing; d) extension of the improved, more cost effective P1 deposition process to the as-made NSTF-$Pt_3Ni_7$ catalysts; and e) development of fast roll-to-roll (R2R) capable de-alloying and annealing processes for the next generation NSTF "$Pt_3Ni_7$" catalysts discovered and developed under this project (17-20).

## 2. Project Objectives, Scope and Approach, and Task Definitions

### A. Project Objectives

This project addresses the following technical barriers from the Fuel Cells section of the Fuel Cell Technologies Program Multi-Year Research, Development and Demonstration Plan: (A) Durability, (B) Cost and (C) Performance. The objectives of this project are development of a durable, low cost [both precious group metal (PGM) content and manufacturability], high performance cathode electrode (catalyst and support), which is fully integrated into a proton exchange membrane electrode assembly characterized by: a) total Pt group metal loading per MEA of $\leq$ 0.25 mg/$cm^2$, b) high prospects for 40,000 hours durability under operating conditions for stationary applications, c) short-stack inverse specific power density of < 0.5 g/$kW_{rated}$, d)

durability sufficient to operate at > 80°C for 2000 hours, ≤ 80°C for 5000 hours, with cycling for transportation applications, and e) high volume manufacturability.

**B. Project Scope**

State-of-the-art PEM fuel cell electrocatalyst technology utilized in today's prototype fuel cell vehicles and commercialized stationary systems are demonstrating significant limitations with respect to general durability and robustness under start-stop cycling, adequate performance with low PGM loadings, wide temperature and humidity operating windows, and low cost manufacturability. To a significant degree, these deficiencies are traceable to properties of the conventional cathode catalysts in use today. The focus of this project is development of advanced cathode catalysts and supports based on 3M's nanostructured thin film (NSTF) catalyst technology platform, which has already demonstrated catalyst specific activity and durability significantly higher than conventional carbon supported Pt catalysts. The scope of work includes fundamental catalyst studies, high throughput fabrication and characterization of new multi-element Pt alloys (ternaries and quaternaries), investigation of alternative catalyst support particles, extensive fuel cell testing in 50-$cm^2$ single cells and large area short stacks, and integrated MEA development using advanced 3M membranes and GDL's specific to the new NSTF catalysts.

**C. Task Definitions**

**Task 1.0 Catalyst Activity and Utilization Improvements**

**Subtask 1.1 NSTF surface area optimization**

The purpose of this subtask is to increase the surface area of the NSTF catalysts by increasing the surface area of the catalyst support system. The NSTF catalyst support system consists of a monolayer of oriented, high aspect ratio (length-to-width) crystalline whiskers, ~ 1 micron in length, with area number densities exceeding 3 billion whiskers/$cm^2$. The expected outcome will be an increase in the specific surface area of the NSTF catalysts by a factor of 2x to 3x from the current ~ 10 $m^2$/g-Pt.

**Subtask 1.2 Fundamental studies of NSTF catalysts**

The purpose of this subtask is to obtain a better understanding of the fundamental oxygen reduction reaction pathways on the NSTF ternary catalysts in order to elucidate the source of the well documented 10x gain in specific activity that NSTFC demonstrates over conventional dispersed Pt/Carbon electrocatalysts. An expected outcome of this subtask will be an understanding of the most important material parameters for obtaining further gains in NSTF electrocatalyst specific activity.

**Subtask 1.3 New multi-element catalysts to increase activity and reduce impedance.**

The purpose of this subtask is to obtain further increases in the NSTF catalyst specific activity (A/$cm^2$-Pt) for ORR by fabrication, characterization and screening of new Pt alloys. The approach will use well established methods at 3M and its collaborators for rapid throughput fabrication and characterization of new multi-element alloy catalyst compositions and constructions. An expected outcome of this subtask is a further increase in stable alloy specific activity by 50% or more over the current best PtCoMn ternary.

**Task 2.0 NSTF catalyst stabilization against dissolution**

The purpose of this subtask is to down-select the new catalyst compositions from Task 1 for improved stability against Pt corrosion at high potentials, high temperatures or under conditions of voltage transients or stop/start cycling. The approach will use well-documented methods, by 3M and one of its collaborators, for ex-situ and in-situ evaluation of catalyst

durability and stability. This task includes high throughput fabrication and screening of the new catalyst compositions as well for enhanced grain size stabilization which can maintain surface area. The outcome will be a subset of the higher performing catalysts which demonstrate, using these tests, increased resistance to Pt dissolution over the current PtCoMn state-of-the-art NSTF electrocatalyst.

**Task 3.0 Full Size (> 250 $cm^2$) Single or Multi-Cell Tests**

**Subtask 3.1 Down-selection of cathode catalysts in 50-$cm^2$ cell tests**

The purpose of this subtask is to evaluate MEA's made with subsets of the supports and catalysts down-selected from Tasks 1 and 2, in 50 to 100 $cm^2$ single cells, using well established testing protocols for performance and durability. The approach will consist of performance and durability load-cycle testing under various pressures, temperatures, stoichiometries and relative humidities. Durability testing will include the accelerated testing recommended by DOE in Appendix D of the solicitation, or more rigorous accelerated tests as may be advised at the time. The expected outcome will be the down-selected cathode catalysts which demonstrate the best overall performance and durability when evaluated as 50 to 100 $cm^2$ MEA's that could meet the 5000 hour lifetime targets. Overlaps with down-selection work done under subtasks 5.1 and 5.2

**Subtask 3.2 Large area short stack durability tests**

The purpose of this subtask is to take the down-selected cathode catalysts from Subtask 3.1 and validate with accelerated testing that the same performance and durability is achieved in large area (> 300 $cm^2$) single (or at most several) cells, using existing, proven stack hardware at 3M. The approach may include at least three stack builds. The expected outcome will be validation that under non-accelerated testing the full size MEA's would meet the 5000 hour targets.

**Task 4.0 Alternative Support Structures**

The objective of this task is demonstration of a novel catalyst support which eliminates all carbon corrosion and is optimized for cathode catalyst loadings of $\leq$ 0.2 $mg_{Pt}/cm^2$ so as to enable a cathode catalyst mass activity of ≥ 0.44 $A/mg_{Pt}$ and durability against surface area and activity losses sufficient for 5000 hours operation at ≥ 80°C under cycling conditions for transportation applications or 40,000 hours under operating conditions for stationary applications.

**Subtask 4.1 Durability tests of new NSTF supports**

The purpose of this subtask is to specifically evaluate the stability of the new NSTF based catalyst supports derived from Subtask 1.1. The approach will use accelerated tests to evaluate stability of the catalyst activity and surface areas against corrosion of the support from high voltage cycling, stop/start cycling or fuel starvation. Both high through-put characterization methods as well as 50-$cm^2$ single cell tests will be included in the approach. The expected outcome is a down-selection of the new NSTF catalyst supports from Subtask 1.1 that also meet the durability requirements.

**Task 5.0 Stack Testing and Optimized NSTF MEA**

The objective of this task is development of durable, low cost (PGM content and manufacturability), high volume manufacturable MEA's with optimally integrated components from Tasks 2-4, which demonstrate a stack specific power density of < 0.5 $g/kW_{rated}$, and durability sufficient to operate at $\geq$ 80°C for 5000 hours under cycling operation for transportation applications, while using a total Pt group precious metal loading per MEA of < 0.3 $mg/cm^2$. The approach is to optimize the NSTF catalyst/membrane interface using lower EW

PFSA 3M membranes and GDL media optimized for the unique water management properties of the ultra-thin NSTF electrodes, followed by validation in large area short stacks.

**Subtask 5.1 NSTF catalyst / low EW membrane interface integration**

The purpose of this subtask is to optimize the pilot scale fabrication of catalyst coated membrane (CCM) roll-goods using the advanced cathode catalysts and supports from Tasks 1-4 in combination with new, lower equivalent weight 3M membranes developed (outside of this project) to have enhanced durability and water management properties. There is also a critical stability/durability aspect to this subtask as well due to significant effects of internal and external impurities on the catalyst/membrane interface.

**Subtask 5.2 Optimized MEA components for water management**

The purpose of this subtask is to develop MEA components and their interfaces, e.g. the anode and cathode GDL's, for best overall water management and high current density performance under automotive conditions, including cool/wet operation, in combination with the CCM's from Subtask 5.1. The approach will include evaluating available roll-good fabricated electrode backing materials having various 3M developed water proofing and microporous layer coatings, as well as more novel configurations. The expected outcome is a GDL configuration that best matches the CCM and stack flow field in which the integrated MEA will be tested for performance and durability.

**Subtask 5.3 Short stack testing (> 10 cells, > 250 $cm^2$)**

The purpose of this subtask is the final short-stack testing of large area MEA's developed in Tasks 1 - 5.2. The approach will be to use existing, proven 3M stack hardware and include independent validation at a specified DOE facility. The expected outcome will be a demonstration of advanced MEA's that meet the overall-project's objectives for performance and durability and were fabricated with high-volume capable processes.

**Task 6.0 Reduction of Break-in Conditioning Time**

The purpose of this task is to formally address a critical remaining gap for successful commercialization readiness of the 3M NSTF catalyst based MEA's.

**Subtask 6.1 Break-in conditioning protocol**

The purpose of this subtask is to quantify the effect of test station operating parameters on the time for break-in conditioning of the standard PtCoMn NSTF MEA's in 50 $cm^2$ single cell tests, to determine the best methodology to reach full performance in the shortest time using a facile protocol. The cell operating temperatures, relative humidity or liquid water flow, reactant flow rates, voltage and current density cycling ranges and speeds, will be systematically investigated. The objective is to reduce the time of break-in by a factor of two to four and simplify the protocol over the current NSTF MEA standard "thermal cycling" protocol.

**Subtask 6.2 MEA component factors affecting break-in conditioning time**

The purpose of this subtask is to understand the impact of specific NSTF MEA components on the break-in conditioning time to reach full performance. The current NSTF MEA standard "thermal cycling" protocol will be used for break-in conditioning while specific material changes will be studied for their effect on the break-in time. The focus will be on the catalyst composition and method of preparation, and the membrane and its method of preparation, as these are already observed to have significant impact on the number of thermal cycles required for full break-in. Improved protocols from task 6.1 will be incorporated as they occur. The objective is to reduce the overall time for full break-in conditioning by an order of magnitude.

**Task 7.0 Project Management and Reporting**

This task provided all aspects of the project management, documentation including six DOE Hydrogen Program Annual Merit Review presentations, seven additional annual and Go-No-go reviews requested by DOE managers, four FreedomCAR technical team reviews, twenty-one quarterly reports, five annual reports, and all financial report and documentation requirements including intellectual property development notification.

## 3. Project Timeline and Milestones

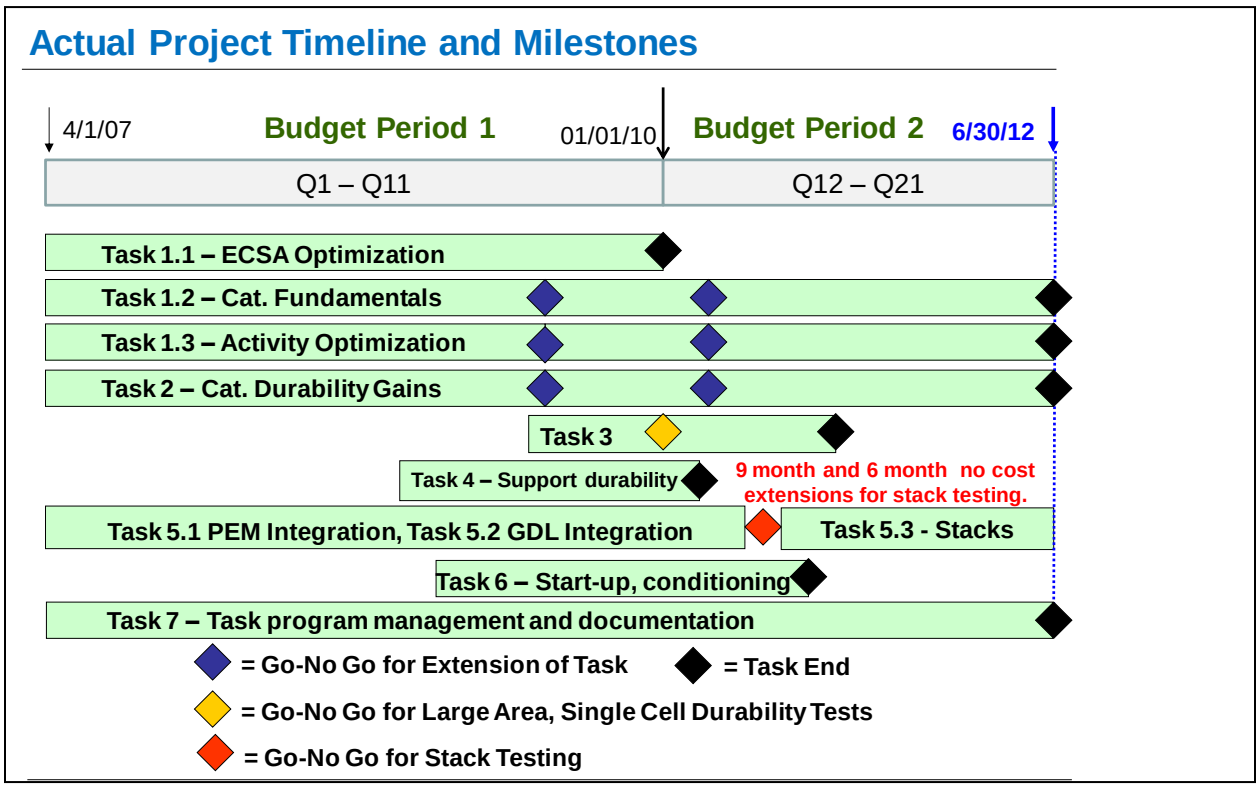


The chart above shows the actual project timeline and milestone dates for the project. The original project performance period was four years. However due to issues with preparation for and execution of the final stack testing, two no-cost extensions were granted for an additional 15 months total.

## 4. Subcontractors, Roles and Other Collaborators

### A. Primary Collaborators by Task

| TASK<br>Collab. | 1.1.1 | 1.1.2 | 1.2 | 1.3 | 2.1 | 2.2 | 3 | 4.1 | 4.2 | 4.3 | 5 | 6 |
|---|---|---|---|---|---|---|---|---|---|---|---|---|
| 3M | X | X | X | X | X | X | X | X | X | X | X | X |
| Dalhousie University | | X | | X | X | X | | X | | | | |
| JPL | | | | X | | X | | | | | | |
| ANL | | | X | | | | | | | | | |
| GM | | | | | | | | | | | X | |

### B. Additional Collaborations (within and outside this contract)

**System Integrators and stack manufacturers (partial list)**

- GM Fuel Cell Activities -Honeoye Falls: Extensive collaboration outside of DOE $H_2$ program with materials generated at 3M under this contract. Multi-year single cell performance and activity validations, stack testing (outside Task 5.3), cold/freeze start and water management evaluations, PEM and GDL integration, durability testing, and modeling studies.
- Nuvera Fuel Cells Corporation. Technology integration project to evaluate for the first time, the combination of the 3M NSTF electrode technology with the Nuvera open flow field bi-polar plate technology.
- Proton OnSite (formerly Proton Energy Systems) – Performance testing of NSTF MEAs in electrolyzers. Ongoing testing of NSTF electrodes in short stacks for both electrolyzer cathodes and anodes.
- Giner EC Systems, LLC – Performance testing of NSTF MEAs in electrolyzers. Testing of NSTF electrodes for both electrolyzer cathodes and anodes.
- DTI, LLC – provided NSTF manufacturing related information for cost analyses.

**National Laboratories**

- LBNL (Weber), LANL– Participating in FFRDC Project on FC Fundamentals at Low and Subzero Temperatures, and ARPA-E funded GRIDS flow battery project.
- ANL (Ahluwalia group) - Extensive Fuel Cell Systems modeling with 3M supplied data for MEA performance under ANL defined conditions.
- ORNL (K. Moore group) – Samples supplied for TEM characterization
- NIST (Eric Stanfield group) – Samples and data supplied to NIST for optical method development under DE-EE0001047 to measure CCM Pt loadings during roll-to-roll fabrication

**Other**

- BASF – provided used NSTF MEA samples for Pt recovery measurements that BASF was carrying out for their own DOE project.

## 5. Definitions and Methodology for ORR Activity Measurements

**Box 1**

**Definitions and activity targets**

- The surface-area enhancement factor is the Pt catalyst surface area, S, measured by the charge generated from an under-potential deposited monolayer of the hydrogen atoms on the Pt catalyst surface divided by the planar area of the sample ($cm^2$ of Pt per planar $cm^2$.)
- Pt loading is the number of mg of Pt per planar $cm^2$ in an MEA electrode layer.
- Absolute ORR kinetic activity is currently defined as the current density measured at 900 mV under one atmosphere of fully saturated pure oxygen, at 80 $^oC$. For an MEA this means 150 kPa absolute pressure due to 50 kPa of water vapor.
- The area-specific activity $A_s$ (amps per $cm^2$ of Pt) is determined by dividing the absolute activity by the surface-area enhancement factor.
- The mass activity $A_m$ (amps per mg of Pt) is determined by dividing the absolute activity by the Pt loading.
- The DOE's 2017 target for $A_m$ is 0.44 A/mg –Pt and its 2015 target for $A_s$ is 0.7 mA per $cm^2$ of Pt.

Reliable measurements of ORR activity depend on generally accepted methods and protocols. Even with these defined "standard operating procedures", laboratory to laboratory variations of 50% are not uncommon in reported ORR activities. Box 1 above gives standard definitions of the meaning of ORR absolute, mass and specific activity and the DOE targets for those quantities.

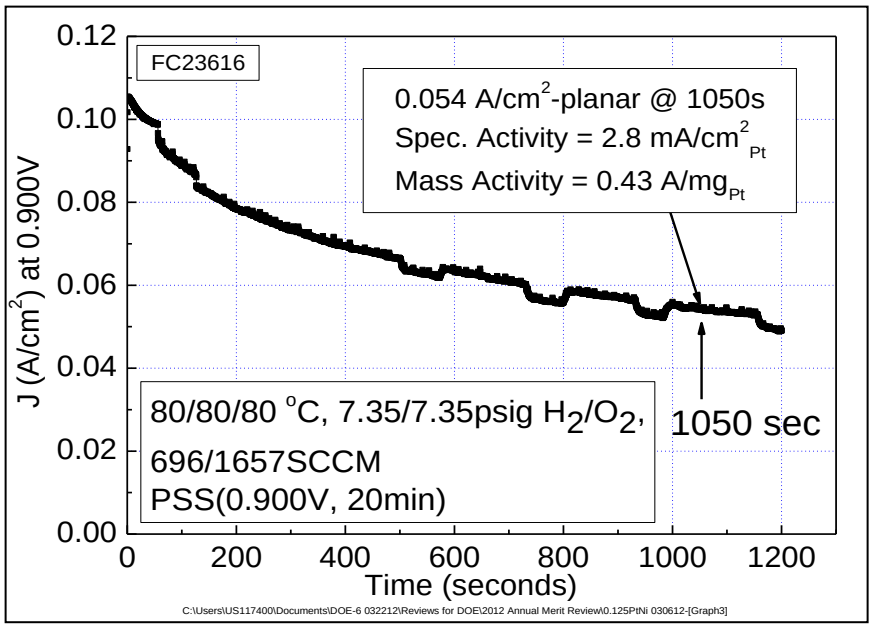


**Fig. 5.1.** Current density vs time trace for an MEA illustrating the protocol for measurement of ORR absolute activity. The MEA in this case is the same as used to generate the polarization curves in Figure 6.3. The current density is corrected for hydrogen cross-over and shorting currents that are measured from cyclic voltammograms taken to obtain the electrochemical surface area of each electrode.

Figure 5.1 illustrates the conditions and protocol used for the ORR measurements in an MEA used in this project; for the MEA ORR activity measurement the total current density is

recorded 1,050 seconds after setting the potential at 900 mV. The current density, in $mA/cm^2_{planar}$, is decreasing as the Pt is oxidizing, so the ORR activity is measured on an oxidized surface in contrast to most RDE measurements in which the current is measured on the "back-scan" from low to high potentials, i.e. from a cleaned surface substantially free of hydroxyls and other anion impurities. Just prior to the start of the time trace in Fig. 5.1, the MEA sat at a cell potential of ~ 0.4 V for 10 minutes. It is possible to obtain good quantitative agreement between the MEA and RDE measurements, as shown in Figs. 5.2 and 5.3, if instead of taking the absolute current at 1050 seconds, one takes it near the start, e.g. at 5 seconds after setting the potential at 900 mV, so the surface is still clean from having operated at near 400 mV just prior to the reset to 900 mV. In this way, the ORR activity of a clean surface is being measured in both cases.

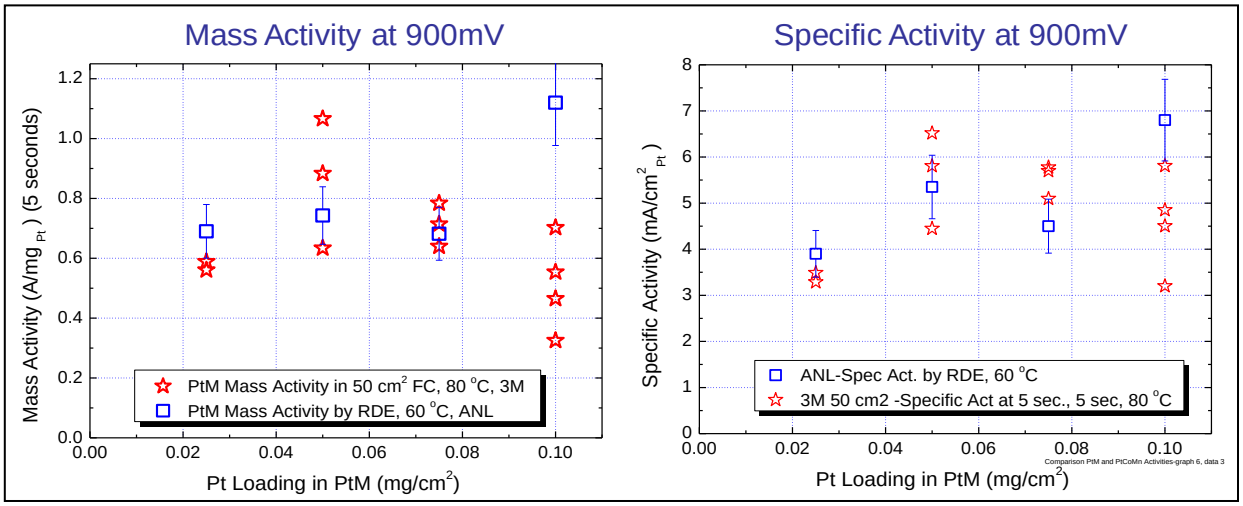


**Fig. 5.2.** Comparison of ORR mass and specific activity measurements at 900 mV by the RDE method at ANL and by the MEA method at 3M when the latter protocol is changed to take the current density at 5 seconds instead of 1050 seconds.

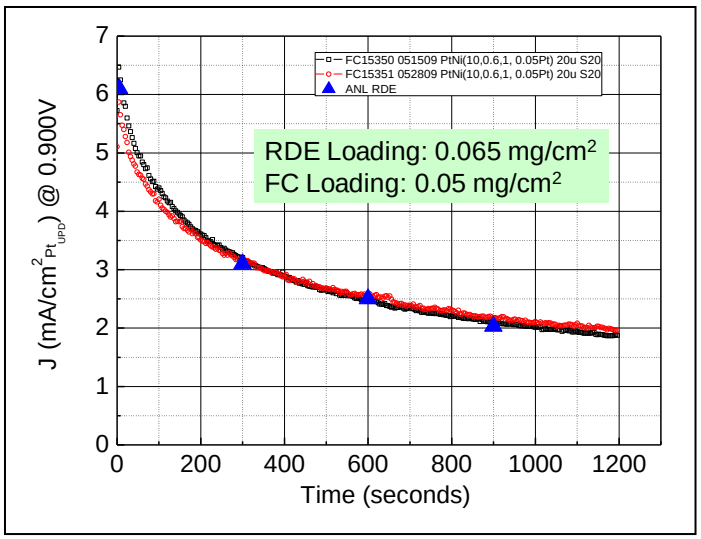


**Fig. 5.3.** Comparison of current versus time decay due to Pt oxidation at 900 mV during an ORR activity measurement for both the ANL RDE protocol and the 3M MEA protocol.

## 6. Summary of Accomplishments

We have chosen in this section to represent the advancements of this project by summarizing our judgment of the outcomes, deliverables, and technology development and transfer activities that have resulted over its 5.25 year period of performance. In addition to the usual reports, presentations and publications, there are important project outcomes we have categorized into three areas of accomplishments. These are:

A. Accomplishments towards 2017 DOE Catalyst and MEA Targets
B. Accomplishments towards Original Project Objectives
C. Accomplishments towards NSTF Technology Development

Table 1 lists the number and type of published documentation provided both as deliverables, execution of Task 7 and general technology transfer and education through publications. More important, it then lists the number (9) of patent applications generated, the number (9) of type A accomplishments meeting the 2017 DOE catalyst and MEA targets, and the number (17) of the type C major technical accomplishments enabling advanced development of the NSTF technology platform.

**Table 1.** Summary of Project Outcomes over the Period of Performance

| Output Number | Outcomes / Technology Transfer Activities / Deliverables |
|---|---|
| 1 | Final Report |
| 4 | FreedomCAR Technical Team Reviews |
| 5 | Annual Reports |
| 6 | DOE Hydrogen Program AMR Presentations |
| 7 | Additional Major Annual Reviews Requested by DOE |
| 21 | Quarterly Reports |
| 22 | Contributed Presentations at International Meetings |
| 26 | Invited Presentations at International Meetings and Institutions |
| 27 | Publications in Peer Reviewed Journals |
| 1 | DOE Hydrogen Program R&D Award |
| **2** | **"Products" Developed** |
| **9** | **Patent Applications** |
| **9** | **Significant Technical Advances Meeting 2017 DOE Catalyst and MEA Targets** |
| **17** | **Major Technical Accomplishments Towards NSTF Technology Development** |
| **2** | **Number of New DOE Projects Spawned** |

Also considered an important outcome is that two other follow-up projects, DE-EE0000456 And DE0005667, have been awarded as an off-shoot or direct follow-on of the work completed in this project. This project received a 2008 DOE Hydrogen Program R&D Award**,** at the DOE Hydrogen Program Annual Merit Review, June 9, 2008. Finally, although no formal 3M products have derived from this project in the sense that anyone can order them, significant quantities of roll good PtCoMn based catalyst coated membranes and as-made catalyst roll-goods of various loadings have been provided to specific automotive OEM customers under blanket purchase agreements. Also full-sized gasketed MEA's with our next generation catalyst "$Pt_3Ni_7$" have been sold for stack testing to a non-automotive customer.

The nine type A, five type B, and seventeen type C accomplishment titles are listed immediately below and then discussed in some depth in the following Sections 7 through 9. Finally in Section 11 we list the publication activities resulting from this project including the 27 publications in peer-reviewed journals, 26 invited presentations at international meetings and institutions, and 22 contributed presentations at international meetings.

**Category A. Accomplishments towards 2017 DOE Catalyst and MEA Targets**

1. Reduction of inverse specific power density, ($g_{PGM}$/kW)
2. ORR kinetic activity (mA/$cm^2_{Pt}$) increase, significantly exceeding 2015 targets
3. ORR mass activity (A/mgPt) increase, meeting 2017 targets
4. Reduction in total MEA loadings, to 0.15 $mg_{PGM}/cm^2$ total per MEA
5. Exceeded durability targets for catalyst support stability for 2017
6. Met durability test targets for catalyst resistance to dissolution and agglomeration under CV cycling to simulate start-stop for 2017.
7. Met durability test targets for MEA durability under OCV hold conditions
8. Demonstrated 9000 hours MEA lifetime under durability load cycling test
9. Demonstrated 0.9 W/$cm^2$ at 600 mV with ~ 0.2 gPt/kW in a GM 29 cell stack

**Category B. Accomplishments towards Original Project Objectives**

1. Total Pt group metal loading per MEA
2. Short stack inverse specific power density
3. Durability sufficient to operate at > 80$^o$C for 2000 hours with cycling for transportation
4. High volume manufacturability.

**Category C. Accomplishments towards NSTF technology development**

1. Discovery of unique NSTF $Pt_3Ni_7$ electrocatalyst
2. Development of roll-to-roll dealloying process
3. Invention and development of SET process for roll-to-roll catalyst annealing
4. Optimization of catalyst deposition process – P1 vs P4
5. Demonstration of first cell reversal tolerant anode catalyst with OER characteristics.
6. Reduction of microstructure feature size of NSTF specific Microstructured Catalyst Transfer Substrate (MCTS)
7. Discovery of the importance of the anode for effective low temperature water management.
8. Determination of how catalyst ECSA depends on NSTF whisker support characteristics
9. Discovery of a new meso-scale fundamental property of extended surface catalysts that enables higher limiting currents due to higher surface area per unit volume in the electrode.
10. Discovery and demonstration of significant effects of flow field types on NSTF MEA high current density performances.
11. First compositional screening of many new catalyst under-layers and over-layers.
12. Development of an experimental path forward to potentially realize the “entitlement” activity of NSTF alloy catalysts.
13. Study of the water and PEM impurity effects on low ECSA catalysts.
14. Discovery of dependence of limiting current on catalyst ECSA.
15. Polarization curve gains over life of contract, Cell voltage vs. A/$mg_{Total\ PGM}$
16. Knowledge and advances in break-in conditioning
17. Support for development of NSTF catalyst and CCM roll-to-roll processes

## 7. Accomplishments towards 2017 DOE Catalyst and MEA Targets

### 7.1. Gains in inverse specific power density, ($g_{PGM}$/kW)

When this project began, the 2005 DOE Fuel Cell Technologies Program Multi-Year Research, Development and Demonstration Plan specified the DOE targets for electrocatalysts for 2010 and 2015. Targets specified for 2010/2015 respectively for PGM total content were 0.3/0.2 $g_{Pt}/kW_e$ rated in a stack (21). This project met those targets as reported at the 2010 DOE Annual Merit Review (AMR) (17). In January 2012, the recommended 2017 targets for PEM fuel cell electrocatalysts were revised for these characteristics and various accelerated stress tests. These new targets (0.125 $g_{Pt}/kW_e$) are given in Table 2, along with the status of the catalysts and MEA's developed under this project. Table 2, presented at the 2012 DOE AMR (19) shows that except for these new 2017 targets for PGM total content and loading, all the targets for ORR mass and specific activity and durability have been met or exceeded in small scale 50 $cm^2$ single cell tests.

**Table 2.** Progress towards Meeting Technical Targets for Electrocatalysts and MEAs for Transportation Applications.

| Characteristic | Units | Targets 2017 | **Status:** Values for roll-good CCM w/ 0.15$mg_{Pt}/cm^2$ per MEA or as stated |
|---|---|---|---|
| **PGM Total Content** | $g_{Pt}/kW_e$ rated in stack | **0.125** | **0.14 - 0.18 $g_{Pt}$/kW for cell 0.6 < V < 0.65** at 80 °C and 150kPaa to 250 kPaa outlet. $Pt_3Ni_7$, 50 $cm^2$ cell w/ 0.15 $mg/cm^2$ total Pt. |
| **PGM Total Loading** | **mg PGM / $cm^2$ total** | **0.125** | **0.15 to 0.20, A+C with PtCoMn alloy**<br>**0.15 A+C with Pt/$Pt_3Ni_7$** |
| **Mass Activity (150kPa $H_2/O_2$ 80°C. 100% RH, 1050 sec)** | **A/mg-Pt @ 900 mV, 150kPa $O_2$** | **0.44** | **0.24 A/mg in 50 $cm^2$ w/ PtCoMn**<br>**0.47 – 0.67 A/mg in 50 $cm^2$ with $Pt_3Ni_7$** |
| **Specific Activity (150 kPa $H_2/O_2$ at 80°C, 100% RH)** | **mA/$cm^2$-Pt @ 900 mV** | **0.720** | **2.1 for PtCoMn, 0.1$mg_{Pt}/cm^2$**<br>**2.7-3.0 for R2R $Pt_3Ni_7$, 0.125 $mg_{Pt}/cm^2$** |
| **Durability: 30,000 cycles 0.6 -1.0V, 50mV/sec,80/80/80°C, 100kPa,$H_2/N_2$** | **- mV at 0.8 A/$cm^2$**<br>**- % ECSA loss**<br>**- % Mass activity** | **< 30mV**<br>**< 40%**<br>**< 40 %** | **10±7mV loss at 0.8 A/$cm^2$**<br>**16±2% loss ECSA, PtCoMn**<br>**37±2% loss mass activity** |
| **Durability: 1.2 V for 400 hrs. at 80°C, $H_2/N_2$, 150kPa, 100% RH** | **- mV at 1.5 A/$cm^2$**<br>**% ECSA loss**<br>**% Mass activity** | **< 30mV**<br>**< 40%**<br>**< 40%** | **10 mV loss at 1.5 A/$cm^2$**<br>**10% loss ECSA**<br>**10 % loss mass activity** |
| **Durability: OCV hold for 500 hrs. 250/200 kPa $H_2$/air, 90°C, 30%RH** | **$H_2$ X-over mA/$cm^2$**<br>**% OCV loss** | **< 20**<br>**< 20 %** | **13 ± 4 mA/$cm^2$ at 500 hrs (5 MEAs)**<br>**12 ± 5 % OCV loss in 500 hrs** |
| **Durability under Load Cycling (membrane lifetime test)** | **Hours, T ≤ 80°C**<br>**Hours, T > 80°C** | **5000**<br>**5000** | **9000 hrs, 3M PEM (20µm, 850 EW w/ stabilizers), 50$cm^2$, 80/64/64 °C**<br>**2000 hrs (OEM short stack,0.1/0.15)** |

### 7.2. ORR mass activity ($A/mg_{Pt}$) increase

The DOE target for ORR mass activity has remained at 0.44 $A/mg_{Pt}$ since first proposed for 2010 in the MY&D plan, with the assumption that the values measured by RDE methods and in an MEA would be similar. We have shown that this is not a valid assumption (9,17) due to the different protocols and state of catalyst surface cleanliness by the two methods. The RDE activities are roughly twice as large as the mass activities measured in a working fuel cell. As indicated in Table 2 and shown specifically in Table 3, we have demonstrated mass activities for our NSTF $Pt_3Ni_7$ catalysts that exceed the target when measured in 50 $cm^2$ fuel cells at both 3M and GM.

**Table 3.** Mass activities measured at GM of 3M CCMs having NSTF $Pt_3Ni_7$, roll-to-roll dealloyed and SET treated cathodes laminated to either cleaned or as-made 3M PEMs. Cathode loadings were 0.121±0.003 mg-Pt/cm$^2$.

| Sample membrane used in CCM | Protocol used for measurement | Standard Treatment (A/mg) | With Additional Pretreatment (A/mg) |
|---|---|---|---|
| As-made PEM | GM | 0.45 | 0.47 |
| As-made PEM | 3M | 0.52 | 0.67 |
| Cleaned PEM #1 | GM | 0.41 | 0.54 |
| Cleaned PEM #1 | 3M | 0.23 | 0.65 |
| Cleaned PEM #2 | GM | 0.41 | 0.58 |
| Cleaned PEM #2 | 3M | 0.21 | 0.62 |

CCMs made with P1 fabricated, roll-to-roll dealloyed and SET treated $Pt_3Ni_7$ alloy cathodes at loadings of 0.121±0.003 mg-Pt/cm$^2$ were tested at GM using both their own and 3M's ORR mass activity protocols. These CCMs were made at 3M with 3M membranes that were either as-made or cleaned using both nitric acid and peroxide baths. Table II summarizes the results from the GM measurements in which the standard treatment refers to the usual NSTF thermal cycling for break-in conditioning. The last column in Table 3 shows that a proprietary GM additional pretreatment process can further substantially increase the apparent mass activities over the standard treatment, which now cover the ranges of 0.47 to 0.58 A/mg by the GM ORR protocol and 0.62 to 0.67 A/mg using the 3M protocol.

Correspondingly, the RDE mass activity values for similar NSTF $Pt_xNi_{1-x}$ catalysts measured at ANL with x ~ 30 % atomic (55% by weight) are on the order of 0.8 A/mg$_{Pt}$ as shown in Fig. 7.1(B) and discussed more completely in reference (6).

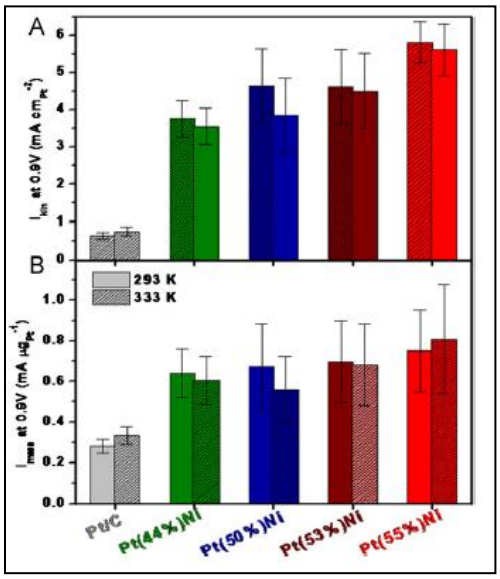


**Fig. 7.1.** Summary of ORR specific (kinetic) and mass activity measurements done on NSTF Pt-Ni alloy catalysts at Argonne National Laboratory using their RDE methodologies.

### 7.3. ORR kinetic activity (mA/cm$^2_{Pt}$) increase

The DOE kinetic or specific activity targets were 0.72 mA/cm$^2_{Pt}$ for ORR catalysts through 2015. This target was apparently dropped for 2017. As shown in Table 2, the NSTF-PtCoMn catalysts are well above these targets as is characteristic of extended surface catalysts compared to Pt/C dispersed nanoparticle catalysts. Table 2 and Fig. 7.1(A) also show that the NSTF $Pt_3Ni_7$ catalysts exceed these targets even further, reaching as high as 3 mA/cm$^2_{Pt}$ in 50 cm$^2$ single cells and over 5.5 mA/cm$^2_{Pt}$ measured by RDE methods.

### 7.4. Reduction in total loadings

When this project began in 2007 the typical NSTF based MEA loadings had 0.2 mg$_{Pt}$/cm$^2$, on each of the anode and cathode. The 2010/2015 DOE targets for PGM total loading per MEA were 0.3/0.2 mg$_{PGM}$/cm$^2$ respectively, and as of January, 2012 the 2017 target was reduced to 0.125 mg$_{PGM}$/cm$^2$. At the end of this project, our 2012 "Best of Class" MEA had 0.03 mg$_{Pt}$/cm$^2$ on

the anode and 0.12 $mg_{Pt}/cm^2$ on the cathode and generated 0.14 – 0.18 $g_{Pt}/kW$ over the 0.6 – 0.65 V range at 80°C and 150 to 200 kPa outlet pressure $H_2$/air, as shown in Fig. 7.2 and summarized in Table 2.

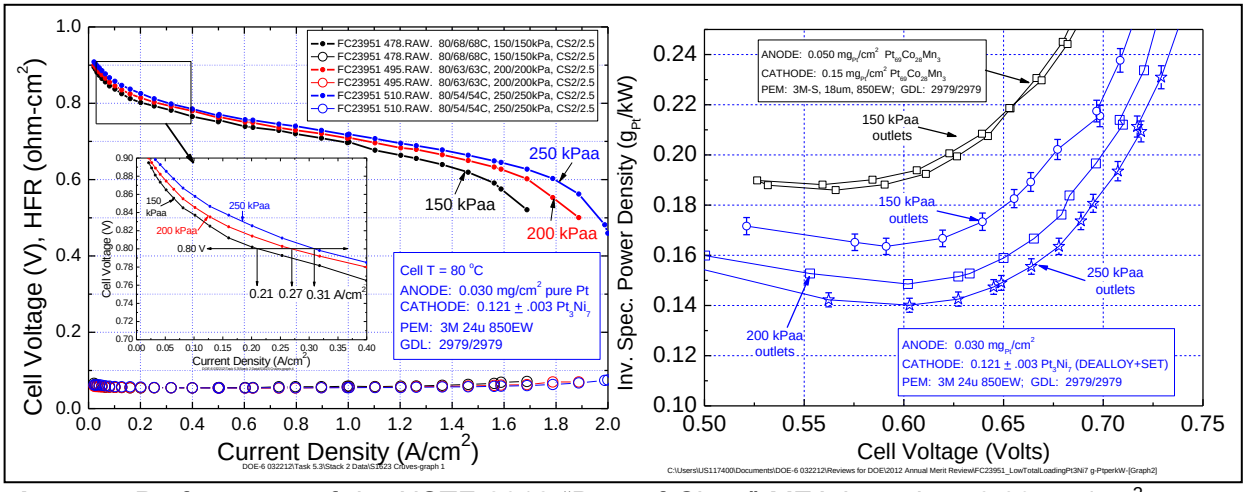


**Fig. 7.2.** Performance of the NSTF 2012 "Best of Class" MEA based on 0.03 mg/cm² pure Pt on the anode and 0.125 $mg_{Pt}/cm^2$ of $Pt_3Ni_7$ (dealloyed and SET processed) on the cathode, a 3M 24 μm thick 850EW PEM, quad-serpentine flow field and 3M 2979 GDL's.

### 7.5. Durability test for catalyst support stability.

Any new electrocatalyst alloy must have the requisite durability and stability, so we continuously tested our new MEA component compositions and process improvements against

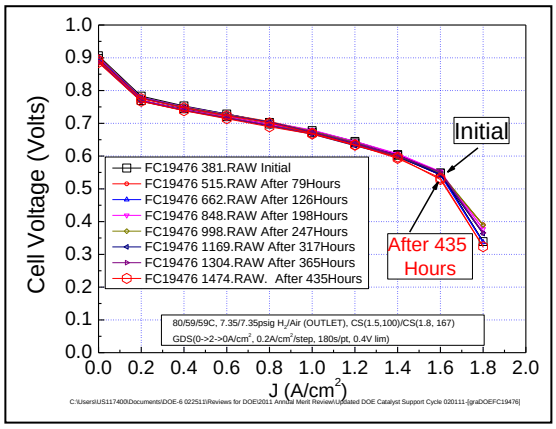


**Fig. 7.3.** Polarization curves versus time during the DOE 1.2 V hold durability test protocol.

the DOE recommended accelerated stress tests. The first of these DOE defined accelerated stress tests (AST), the 1.2 V hold, evaluates the stability of the catalyst support particle against high voltage corrosion. In this test the MEA cathodes are held at 1.2 V vs RHE for nominally 400 hours under 150 kPa $H_2/N_2$ at 80°C. It effectively measures the stability of the catalyst support perylene red whisker against corrosion. The DOE targets are that ORR activity and surface area will each drop ≤ 40%, and the performance at 1.5 A/cm² will drop less than 30 mV from initial levels. Fig. 7.3 shows the series of polarization curves (taken using DOE recommended conditions) measured periodically over a total of 435 hours at 1.2 V, for an MEA having the P1 processed (see Section 9.2) PtCoMn on the anode (0.05 mg/cm²) and cathode (0.15 mg/cm²). The MEA used a 3M made 3M-supported membrane with a chemical additive. It

is apparent that the test had only a small effect on performance. Surface area loss was 10%; specific activity was unchanged, and the performance at 1.5 A/cm$^2$ dropped only 10 mV, so all targets were met and repeated with a second MEA.

### 7.6. Durability test for catalyst resistance to dissolution and agglomeration under CV cycling to simulate start-stop.

The second DOE defined accelerated stress tests (AST) addresses one of the key durability issues facing fuel cell MEAs, namely degradation of the cathode catalysts during start/stop events. These transient events can cause cathode potentials to briefly cycle to 1.5 volts or higher before returning below 1 volt. The subsequent rapid Pt oxidation and reduction can lead to Pt dissolution and agglomeration leading to loss of surface area and Pt catalyst utilization. A recent US Drive FC tech team sanctioned accelerated stress test to evaluate catalyst electrodes for this purpose (21) was used to evaluate the final MEAs developed in this project for the final stack testing at GM, described in more detail under Task 5.3. This test imposed 30,000 cycles of a 50 mV/sec saw-tooth voltage scan on the MEA between 0.60 and 1.0 volts, with 100/100 kPa $H_2/N_2$ flowing at 200/200 sccm on the anode and cathode respectively, at 80$^o$C and 100%RH. The protocol called for periodic measurements of MEA performance and cathode ECSA and ORR activity during the tests. The test target criteria are given in Table 2.

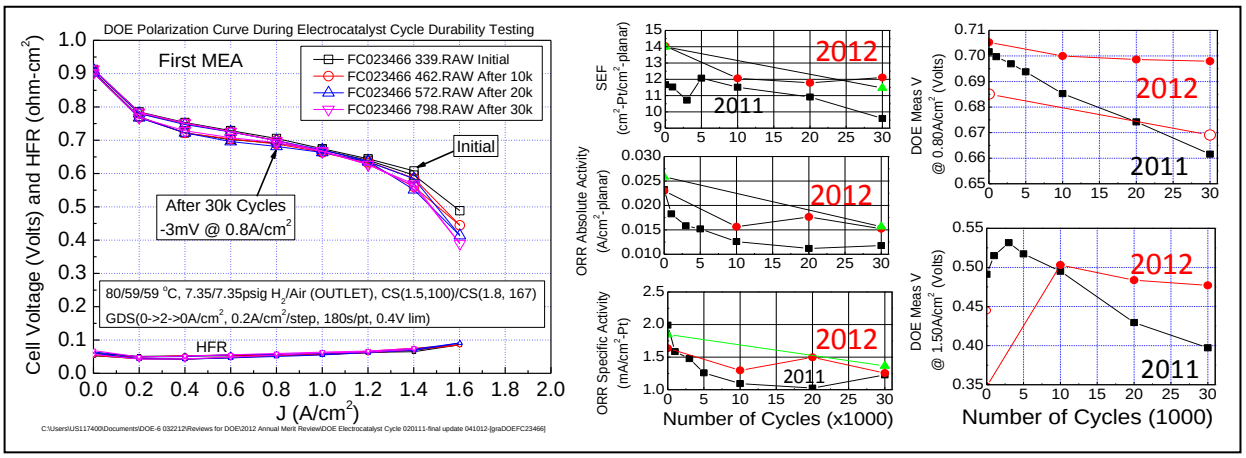


**Fig. 7.4.** Results of US Drive accelerated stress test, applied to NSTF MEA type used for final stack testing, involving 30,000 CV cycles from 0.6 V to 1.0 Volts to simulate start-stop degradation mechanisms that affect catalyst surface area, activity and performance.

Near the end of this project we applied this test procedure to representative MEAs of the same type and from the same lots as were used for final GM stack testing. Two MEA's were tested. These MEAs had anode/cathode loadings of 0.05/0.15 $mg_{Pt}/m^2$ of the NSTF $Pt_{68}Co_{29}Mn_3$ catalysts produced by the P4 deposition process with SET post processing (The P4 and SET processes are discussed in Sections 9.3 and 9.2 respectively). They used an 18 micron thick experimental 3M supported membrane with chemical additives for durability, and 3M standard 2979 GDLs on both the anode and cathode.

Fig. 7.4 (left) compares the first 50 cm$^2$ MEA's fuel cell initial polarization curve with that after 10k, 20k and 30k cycles. It is clear there is very little change due to the voltage cycling. The second MEA was also tested for 30,000 cycles, but only the initial and final performance and catalyst ORR metrics were measured to save time. Fig. 7.4 (right two panels) show the variation of the surface area (SEF), absolute and specific activity and fuel cell performance at 0.8 A/cm$^2$ and 1.5 A/cm$^2$ with number of cycles, for both MEAs, labeled 2012, with our MEA

attempt in 2011 with this test. The 2012 MEA's sustained surface area losses of 14% and 18%, easily meeting the DOE 2017 target of 40% loss. The polarization curve voltage losses at 0.8 A/cm$^2$ of 3mV and 16 mV respectively likewise easily meet the DOE target of 30 mV loss. The mass activity loss of 34% and 39% (same as absolute activity changes) also meet the 2017 target of 40% loss of initial mass activity.

### 7.7. Durability test for MEA durability under OCV hold conditions

The third DOE defined accelerated stress tests (AST), OCV hold, addresses another key durability issues facing fuel cell MEAs, namely degradation of the membrane due to free radical generation when the cell is off or near idle type conditions. The objective of this test is assessment of the whole MEA/membrane durability at OCV at 90$^o$C under 30% RH, 250/200 kPa $H_2$/air. The usual failure mode is perforation of the membrane at some point. The target is 500 hours with less than 20% loss of OCV. Using similar or the same MEA construction as in the 1.2 V hold test above, six MEA's met the 500 hour limit and cross-over targets before stopping the tests. Two MEA's were allowed to go further and exceeded 1400 hours with ~ 12% loss of OCV and acceptable $H_2$ cross-over. Fig. 7.5 shows OCV hold lifetime test summaries for a variety of NSTF MEA constructions. In general, chemical additives are required in order to meet the 500 hour target. For the right graph in Fig. 7.5, lifetime was estimated by visually determining the onset of rapid OCV decay below 800 mV. The PEM chemical additive was used in the 3M 850EW cast membrane. With additive, NSTF $Pt_3Ni_7$ lifetime is slightly better than tht of $Pt_{68}Co_{29}Mn_3$ (698±184 vs 610±40 hrs. at cathode loading of 0.1mg/cm$^2$). With additive and 20 μm PEM, 0.10/0.15 PtCoMn has longer lifetime (1,145±195 hrs) than 0.05/0.10PtCoMn (Av = 610±40 hrs). Thicker membrane and higher loading can meet the target with no additive.

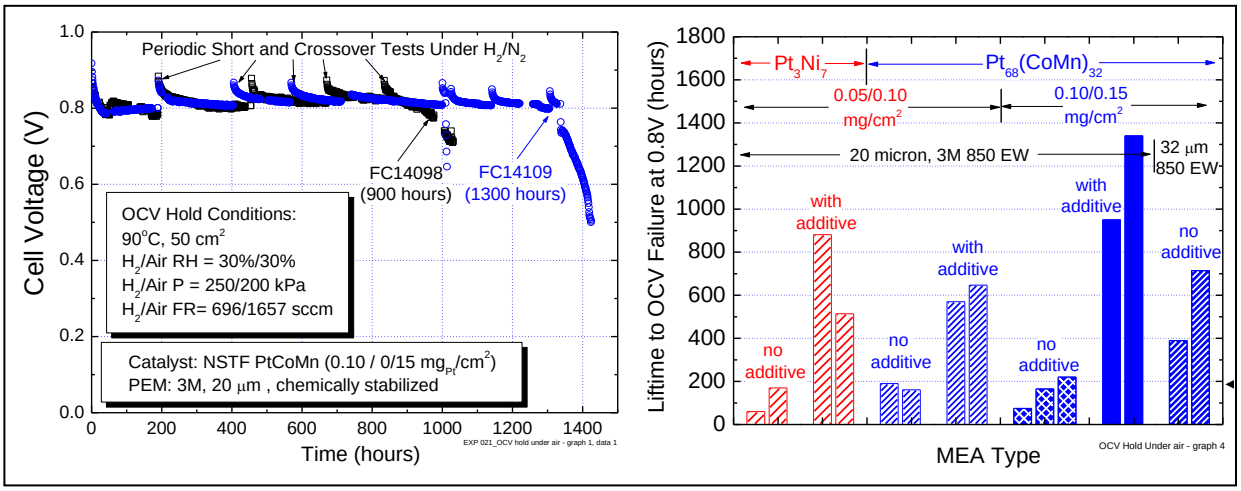


**Fig. 7.5.** (Left) OCV hold test versus time with periodic measurements of crossover and $F^-$ ion release for two NSTF MEAs that contained a chemical stabilizer in the 20 μm 3M PEM. PtCoMn loadings are as stated. (Right) Summary of OCV lifetimes-to-failure at 0.8 V with various MEA constructions, showing the effect of catalyst type, loading, and membrane additives.

It is clear from Fig. 7.5 that many MEA constructions with the NSTF electrodes can meet the DOE OCV hold target at the specified AST conditions.

### 7.8. Durability test under load cycling

A final type of durability test is a lifetime load cycling test completed under a 3M test protocol. This test required long periods of time and as the MEA components have improved, the lifetimes increased substantially. Fig. 7.6 is an update of the load cycling tests under 80 $^{o}$C that we have shown results from over the life of this project. The panel to the right of the graph in Fig. 7.6 illustrates the load cycle protocol. Cell voltages at various current densities are measured versus time under an 80$^{o}$C cell temperature, 64$^{o}$C DP, constant flow load cycling protocol. Open circuit voltages (measured daily) are used to determine end of life in this test (when the OCV falls below 0.8 V). These tests had actually began prior to the start of this contract with the NSTF state-of-the-art MEA's available at that time, with 0.2 mg/cm$^2$ of NSTF PtCoMn on each of the anode and cathode of a 3M 850 EW, 35 micron thick cast membrane made with no support or chemical additives. As shown in Fig. 7.6, four samples of this type dramatically lasted longer than seven conventional MEA's made with dispersed Pt/C electrodes but the same membranes and GDLs. During this project, the first two MEAs were tested with the same catalysts applied to an experimental supported membrane (solid red bars in Fig 7.6). The lifetime had increased to 7000 hours. The next two samples tested obtained ~ 5000 hr lifetimes with the 2009 best of class NSTF CCM with the 0.05/0.10 mg/cm$^2_{Pt}$ loadings on a 3M 850 EW PEM that did not contain any chemical stabilizer or mechanical reinforcement (blue crosshatched bars in Fig. 7.6). The set of black crosshatched bar graphs on the right side of Fig. 7.6 are latest results showing that MEA's with our 2009 best of class CCM, with 0.05/0.1 mg$_{Pt}$/cm$^2$ loadings and a 20 micron 3M PEM with a chemical stabilizer, but still no reinforcement, survived 9000 hours without failure. The NSTF electrodes have been shown to have as little as 1/1000$^{th}$ as much F$^-$ ion release rate as Pt/C electrodes in measurements done at 3M with the same membranes and gas diffusion layers (22).

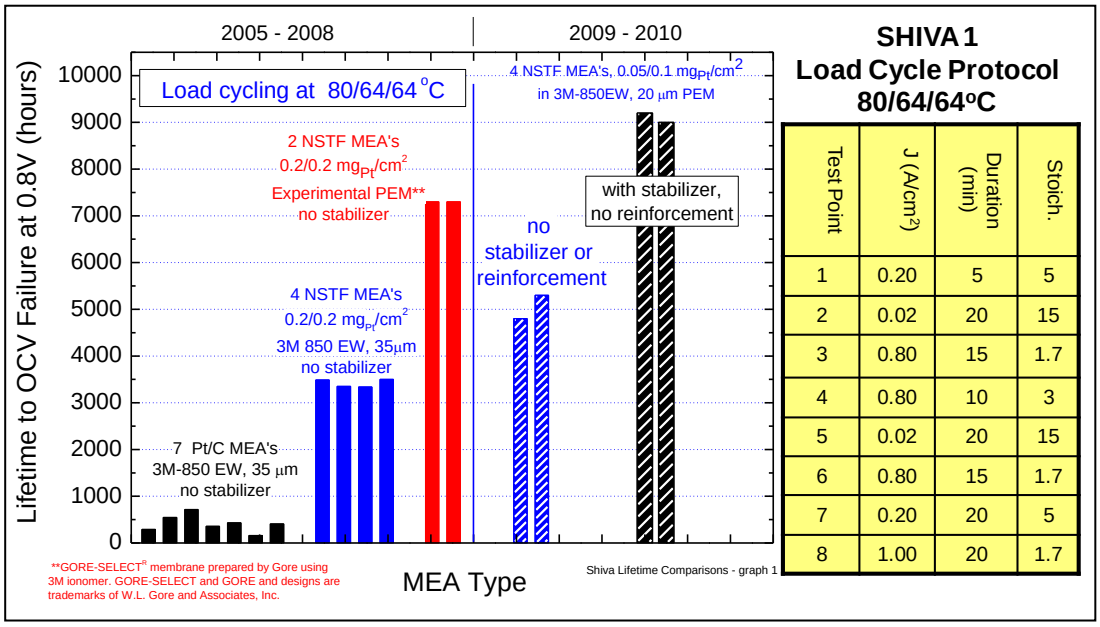


| Test Point | J (A/cm$^2$) | Duration (min) | Stoich. |
|---|---|---|---|
| 1 | 0.20 | 5 | 5 |
| 2 | 0.02 | 20 | 15 |
| 3 | 0.80 | 15 | 1.7 |
| 4 | 0.80 | 10 | 3 |
| 5 | 0.02 | 20 | 15 |
| 6 | 0.80 | 15 | 1.7 |
| 7 | 0.20 | 20 | 5 |
| 8 | 1.00 | 20 | 1.7 |

**Fig. 7.6.** Summary of lifetime versus MEA type measured over a period of 5 years with various NSTF MEA constructions. Chemical stabilizers and membrane reinforcement are important in order to obtain the longest lifetimes. The NSTF electrode based MEA's last much longer than Pt/C electrodes when no chemical additives (stabilizer) or reinforcement are used in the membranes.

A large factor of this is now known to be due to the fundamental properties of the NSTF extended surface catalyst compared to dispersed nanoparticles, as discussed in reference (23). The absence of exposed carbon support, a poor ORR catalyst, and the much higher specific activity of the NSTF catalysts also contribute to lower amounts of $2e^-$ hydrogen peroxide production and subsequent free radicals that attack the membrane.

The load cycling tests in Fig. 7.6 are primarily again an MEA or membrane lifetime test rather than a catalyst durability test. However, since the catalyst is the original source of the peroxide from incomplete oxygen reduction that gives rise to the free radicals that attach the membrane, the nature of the catalyst is important. For the above tests, a limited amount of catalyst activity and surface area measurements during the load cycling were done.

### 7.9. Generation of 0.78 W/cm$^2$ at 650 mV with 0.2 $g_{Pt}$/kW in a GM 29 cell stack.

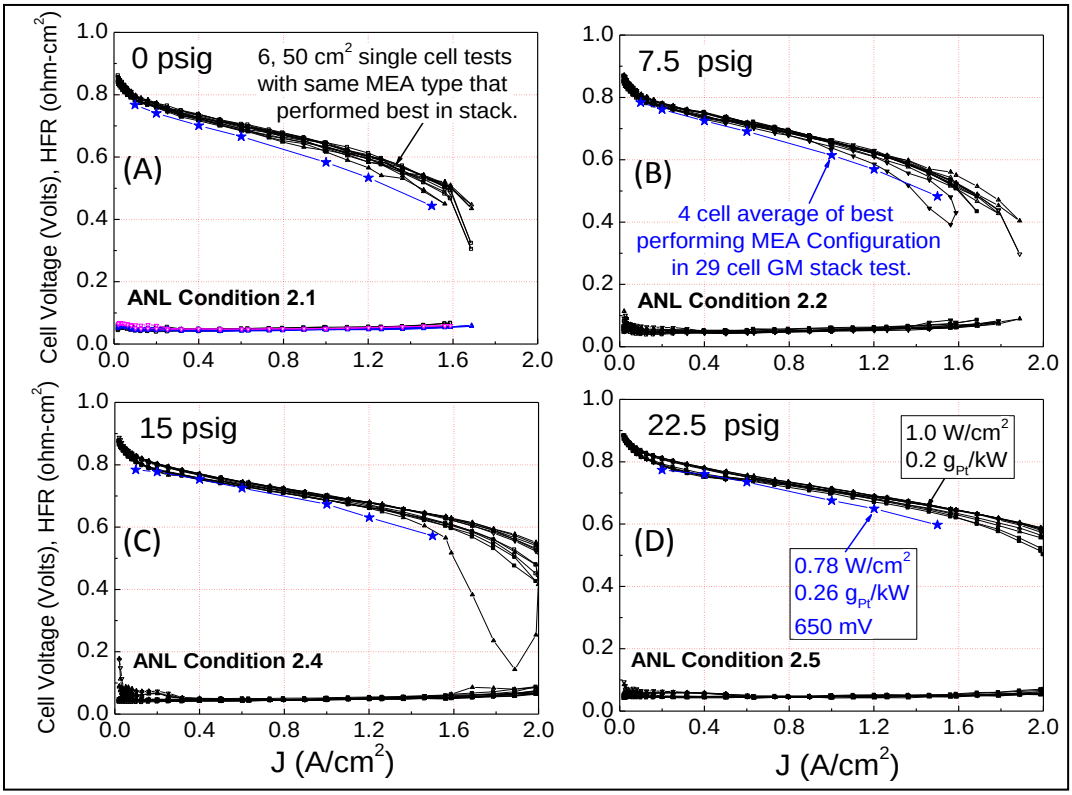


**Fig. 7.7 (a)** GDS polarization curve comparisons at four pressures, of the 4-cell average GM stack 1 performance (configuration-1 MEAs) with six, 50 cm$^2$ single-cell tests (at 3M) having the identical type MEA. GDS polarization scan: 0.02->2->0.02 A/cm$^2$, 10 steps/decade, 120 s/pt, 0.4 V limit, 0.1 max current density step. The test conditions used were those supplied by the systems modeling group at ANL (Ahluwalia et al.) and used by 3M for generating other MEA data requested by that group:

ANL Condition 2.1 = 80/73/73°C, 1/1 atm $H_2$/Air, CS(2,100)/CS(2.0, 200)
ANL Condition 2.2 = 80/70/70°C, 1.25/1.25 atm $H_2$/Air, CS(2,100)/CS(2.0, 200)
ANL Condition 2.4 = 80/56/56°C, 2.0/2.0 atm $H_2$/Air, CS(2,100)/CS(2.0, 200)
ANL Condition 2.5 = 80/40/40°C, 2.5/2.5 atm $H_2$/Air, CS(2,100)/CS(2.0, 200)

There were two stack tests of NSTF MEA's completed at GM at the end of Task 5.3. The first stack's objective was to compare MEA performances of six different types of MEA configurations in a rainbow stack in order to down-select to one MEA configuration for the second and final durability stack test. As explained in detail in the section on Task 5, there were significant issues in both stack tests due primarily to MEA issues we had with bad experimental membrane lots and test station water impurities. It was also not possible to obtain the same peak performance in the stacks as in 50 $cm^2$ single cells with the same MEA lots. This led us to suspect that flow field differences could be partially responsible. Despite these difficulties, the first stack was able to meet its objective of down-selecting to the best performing MEA configuration.

Figure 7.7 shows sets of polarization curves as a function of four different $H_2$/air pressures, all from MEA's assembled with the same roll-to-roll fabricated CCM lot having 0.05/0.15 $mg_{Pt}/cm^2$ total on the anode/cathode respectively. Each panel compares six 50 $cm^2$ single cell polarization curves at a given pressure, with the stack 1 average polarization curve of its four best performing MEA's (all configuration type 1). The test conditions chosen were those specified by the system's modeling group at ANL (Ahluwalia et al.) for other data sets provided to ANL. The MEA performances improve with pressure similarly in single cells and the stack, consistent with mass transport issues. The stack 1, MEA type 1 performance average underperforms the single-cell tests at all conditions, but not by too much as long as the current density is below ~1.5 $A/cm^2$. At higher current densities the stack 1 performance falls considerably short of the small single cells. As indicated in the 22.5 psig panel, despite the underperforming nature of the MEAs, the last two stack average data points at 1.2 and 1.5 $A/cm^2$ and 0.65 and 0.6 volts respectively correspond to 0.78 and 0.9 $W/cm^2$ and 0.26 and 0.22 $g_{Pt}/kW$. This is not as good as the single cells generated but it does exceed our original project goal at the start of the contract, as discussed in B. which follows. Further discussion of the stack 1 performances are given in Task 5 of the Supplementary Section as well as flow field effects discussed immediately below in Section 9.10.

## 8. Accomplishments towards Original Project Objectives

The above summary of accomplishments towards the DOE targets for 2015 and 2017 show that several of the original project objectives specified in section 0.2.A have been exceeded, as summarized in the following Table 4.

**Table 4.** Summary of Accomplishments towards Original Project Objectives

| Project Objective from Slide 4 | Target at Start of Project | Value at End of Project |
|---|---|---|
| Total Pt group metal loading per MEA | $\leq$ 0.25 mg/cm$^2$ | 0.15 mg/cm$^2$ |
| Short stack inverse specific power density | $\leq$ 0.5 g-Pt/kW$_{rated}$ | ▪ 50 cm$^2$ : 0.14 to 0.18 gPt/kW$_{rated}$<br>▪ GM short stack : 0.22 to 0.26 |
| Durability sufficient to operate at > 80°C for 2000 hours with cycling, $\leq$ 80°C for 5000 hours | 2000 hours @ 80°C | $\leq$ 2000 hrs. in OEM stack, testing done outside this project |
| High volume manufacturability | CCM processes not optimized or integrated | Full CCM and components all roll-to-roll fabricated. |
| High prospects for 40,000 hours durability under operating conditions for stationary applications, | N. A. | Not addressed directly, targeted automotive, but 9,000 hours in load cycle tests demonstrated with 50 cm$^2$ MEA's. |

## 9. Accomplishments towards NSTF technology development

A third and very important class of accomplishments are those that refer to advancements in the development of the NSTF electrocatalyst technology itself, whether for materials, processes or cost improvements. In this section we identify and discuss seventeen accomplishments that we believe are significant towards advancing the NSTF catalyst technology platform. These are the ones listed as Category C accomplishments on page 19.

### 9.1. Discovery of unique NSTF $Pt_3Ni_7$ electrocatalyst

Near the beginning of this project, we were still screening simple binary and ternary alloy compositions for increased Pt ORR activity. While testing some $Pt_xNi_y$ compositions at high Ni content we observed an anomalously high ORR activity. Subsequent extensive and careful investigation around this unique x:y feature showed a very novel effect, shown in Fig. 9.1 a, b, in that the ORR activity was sharply peaked at what was gravimetrically determined to be y=0.7, x = 0.3 atomic. Electron microprobe analyses at Dalhousie University determined the peak activity to be at y = 0.76 while X-ray fluorescence analyses at 3M determined the peak activity at y = 0.62. Since neither EMP nor XRF are fundamentally quantitative for mass and subject to matrix effects from the oriented NSTF structure, we have relied on the gravimetrically determined peak position of y = 0.7 for the composition that give the peak ORR activity. Subsequent SEM-EDX analysis at California Institute of Technology through JPL has validated that composition.

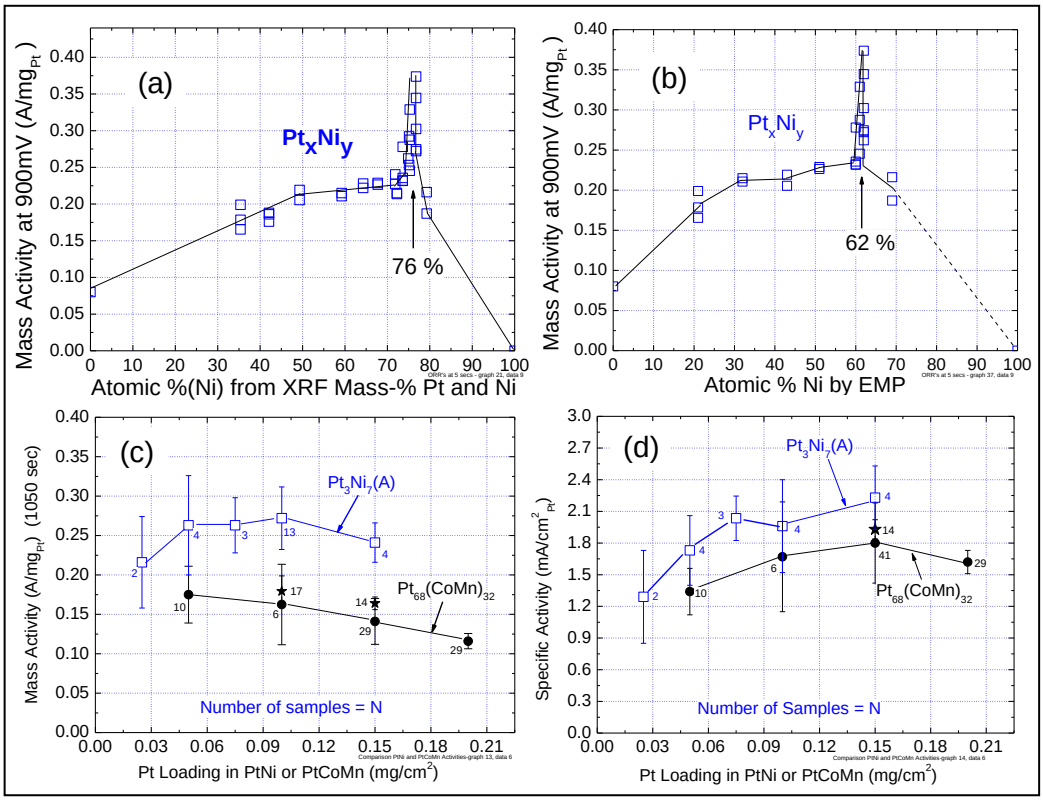


**Fig. 9.1.** Mass and specific activity as a function of Pt composition and loading for as-deposited NSTF PtCoMn and PtNi alloys. (a) and (b) Mass activity versus atomic % Ni measured by XRF and EMP respectively. (c) and (d) Mass and specific activity versus Pt loading for $Pt_3Ni_7$ and $Pt_{68}Co_{29}Mn_3$.

Fig. 9.1(c,d) show the mass activity as a function of Pt loading for these as-deposited $Pt_3Ni_7$ catalysts is substantially higher than our standard PtCoMn. The (A) in $Pt_3Ni_7$(A) in Fig. 9.1 refers to catalyst that has been deposited using our traditional multi-layer P4 process (discussed in Section 9.3 below) and was not further annealed or dealloyed prior to making into CCM's for testing. Further discussion of the unique properties of the $Pt_3Ni_7$ alloy system is given in the key references attached in the appendix that deal specifically with it.

### 9.2. Invention and development of SET process for roll-to-roll catalyst annealing

Most alloy catalysts of any type, including Pt/C, benefit from annealing. Better intermixed alloys and larger crystallite sizes generally result. Work done at ANL by Stamenkovic et al. also indicated that by annealing the NSTF PtM alloys (sent to them as powders) in hydrogen, increased ORR activity could be obtained (24). For powdered, batch processed materials, this is generally straight forward and done in a standard oven with controlled atmosphere. However, the NSTF whiskers are grown on a polyimide film substrate and restricted to temperatures below about 300 $^{o}$C. This prevents use of traditional annealing methods. Since it is also critical that the annealing process be consistent with roll to roll processing at reasonable web speeds, a new approach was needed. Using another important property of the NSTF metal coated whisker films, which is that they appear highly optically black due to strong photon absorption by the whiskers, it was possible to devise a process we call the SET (surface energy treatment) process to pump energy into the catalyst coated whisker film at rapid rates while moving as a

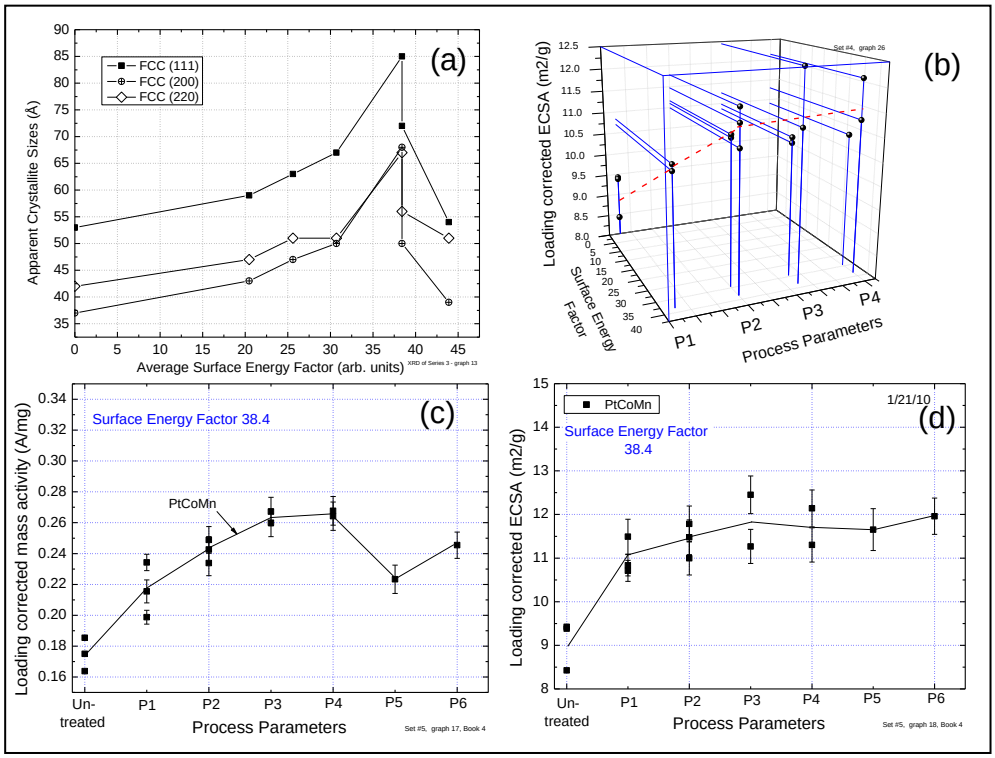


**Fig. 9.2.** Impact of the SET batch process parameters on NSTF PtCoMn crystallite size (a), mass activity (c) and surface area (b,d).

web. Since the NSTF catalyst process takes place in a moderate vacuum, it is also possible to control the atmosphere during the SET "annealing". We first demonstrated the feasibility for this SET process to improve the PtNi ORR activity by designing and building a small batch chamber capable of exposing 50 $cm^2$ sized electrodes.

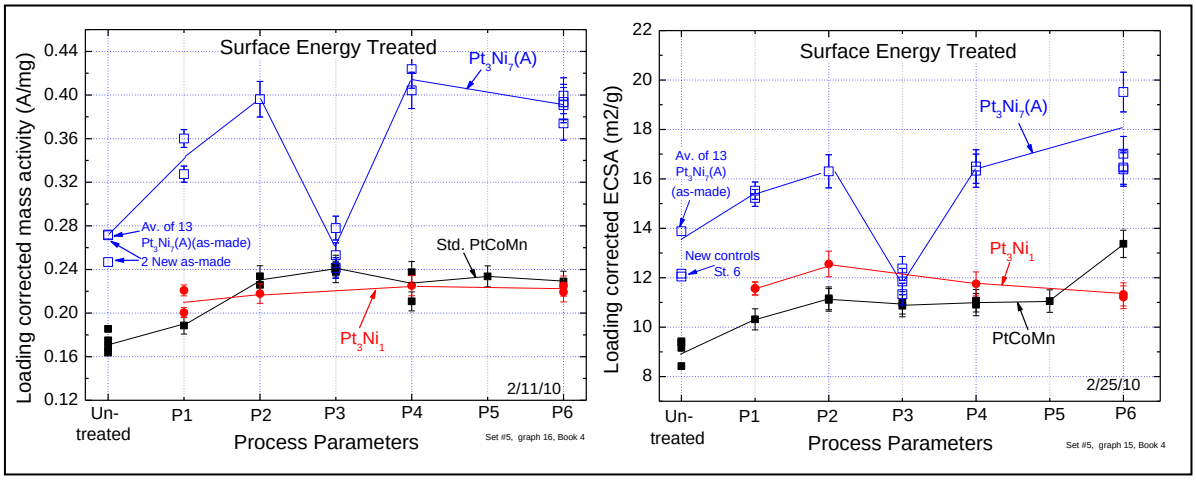


**Fig. 9.3.** Impact of the SET batch process parameters on the NSTF $Pt_xNi_y$ mass activity and ECSA and comparison to the PtCoMn.

Multiple sample series with over a hundred sample exposures enabled us to determine the sensitivity to the incident energy device parameters and the environmental gas compositions and pressures. These results in turn provided the data to design a roll to roll capable SET process. Fig. 9.2 shows examples of the response of the PtCoMn catalysts to different SET batch process conditions. Fig. 9.2(a) illustrates that the XRD measured crystallite size increased dramatically with the SET fluence, while (b) illustrates the effect of both incident energy and the process environmental conditions, P1, P2,….on the catalyst surface area. Figs. 9.2(c, d) show clearly the impact of the process parameters at a fixed surface energy fluence.

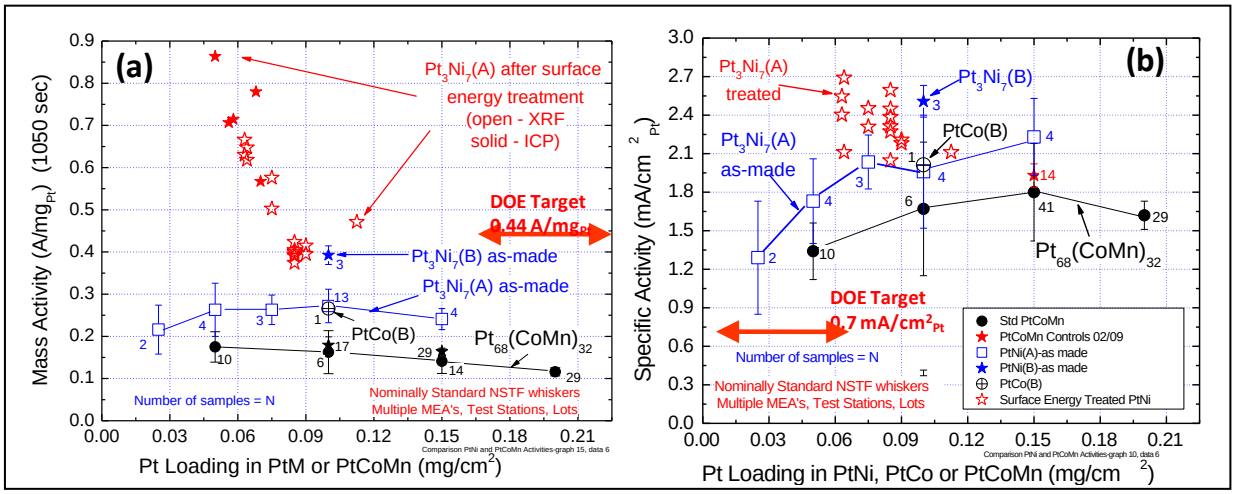


**Fig. 9.4.** Impact of the SET batch process at nominally the best conditions on the $Pt_3Ni_7$ mass (a) and specific (b) activity, as a function of loading. Loading after exposure was corrected for small amounts of Pt loss by both XRF and ICP measurements of the exposed samples.

Similarly, $Pt_xNi_y$ also benefited from the SET process as shown in Fig. 9.3. $Pt_3Ni_7$ mass activity and surface area increased even more than that of PtCoMn, whereas $Pt_3Ni_1$ did not improve with the process parameters explored. Under many conditions used and certainly near

the peak fluence, some of the Pt was vaporized in the batch experiments and hence the loading was measured after SET treatment of each sample and this corrected loading was used for the mass activity values. Finally, in Fig. 9.4 are shown the gains in mass and specific activity when the nominal optimum batch SET process conditions are applied to the as-deposited $Pt_3Ni_7$ NSTF catalysts before they are made into CCM's.

### 9.3. Optimization of catalyst deposition process – P1

Vacuum sputter deposition has as a fundamental advantage for depositing alloys that it is as simple to deposit a mixed composition material as it is a single component material.

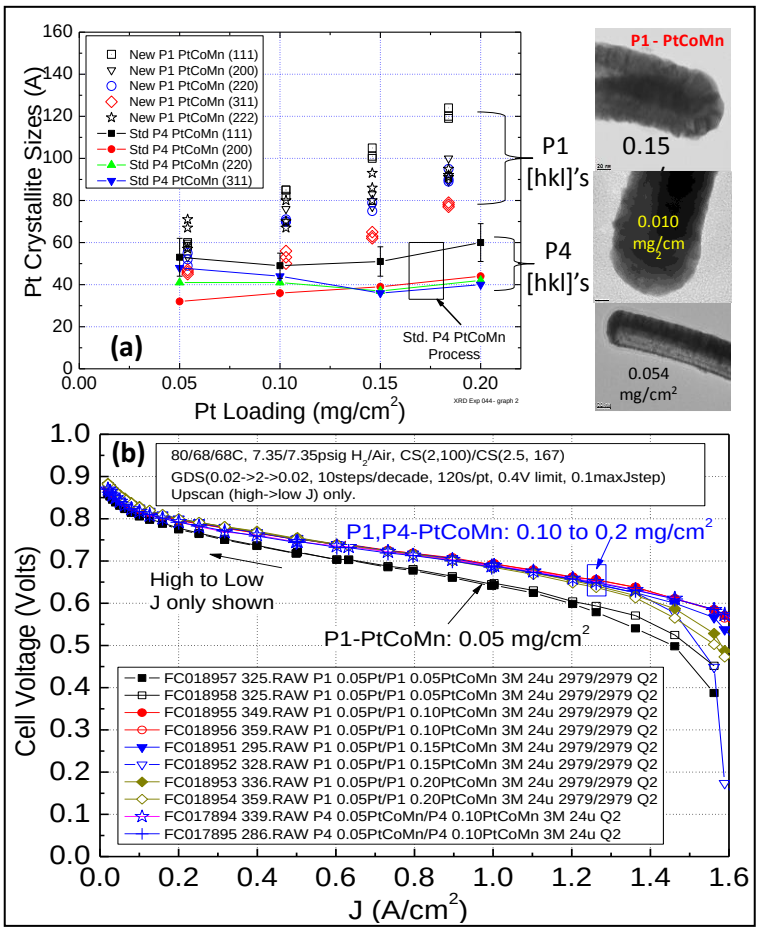


**Fig. 9.5 (a).** Left:PtCoMn fcc[hkl] grain sizes by XRD as a function of Pt loading for catalysts sputter coated by new process P1 versus the standard process P4. Right: TEM images of the PtCoMn coated whiskers using new deposition process P1. At all three loadings the catalyst coating is smoother than by the standard P4 process that produces whiskerettes as discussed in reference (25). **(b)** Polarization curves for PtCoMn deposited by the P1 process at ca. 0.05, 0.10, 0.15 and 0.20 $mg_{Pt}/cm^2$, and the P4 process at 0.10 $mg_{Pt}/cm^2$, under 80 $^oC$ cell temperature, 68$^oC$ dew points and 150 kPa $H_2$/air. 3M-24 μm, 850EW PEM. 3M standard GDL's, all 50 $cm^2$. Actual Pt loadings of the cathodes are 0.054, 0.103, 0.146 and 0.184 $mg_{Pt}/cm^2$.

The differences lie within the details of how one forms the intermixed coating, either in layers from a series of single element targets or a single layer from a mixed element target, or combinations. When exploring new alloy compositions, it is economically sensible to use single element targets so a wide range of compositions can be screened with the same targets. For the NSTF alloy catalysts, all work up to about 2010/11 was done with our so called P4 process in which multiple layers were sequentially deposited from multiple targets. Key process development work completed in this project has focused on improving the NSTF-PtCoMn roll-to-roll process so that the support whiskers and sputter deposited catalyst alloy can be applied simultaneously on the moving substrate web in a single step. This new process, called P1, offers greater simplicity and more cost effective coating than the standard process called P4. It also holds the potential for better alloying due to increased intermixing and self-annealing due to higher heat of condensation with fewer layers. The key is to make sure it does not reduce performance and hopefully improves it. We have demonstrated it with PtCoMn and PtNi

targets. An example of its effectiveness is shown in a series of PtCoMn loadings deposited by the P1 process at 0.054, 0.103, 0.146 and 0.184 $mg_{Pt}/cm^2$. They were coated on production equipment and evaluated for structural differences by X-ray diffraction, SEM/TEM and fuel cell performance. SEM indicated no substantial differences at 40,000 magnification, but the TEM and XRD results showed significant changes. Fig. 9.5(a)(left) shows that whereas the fcc Pt[hkl] grain sizes by the standard process P4 are essentially independent of loading and 4 to 6 nm in size, the P1process produces grain sizes that increase with loading and are larger, 6 to 12 nm. Consistent with this are the TEM images, Fig. 9.5(a) (right), that show the catalyst coatings on the whiskers are smoother than those obtained by the P4 process, which produces highly oriented whiskerettes growing off the sides of the underlying whisker core, as discussed at length in reference (25). This can be understood since aspects of the P1 process provide annealing like conditions.

Fuel cell performance of the P1deposited PtCoMn is also generally the same as with the P4 process, as shown in Fig. 9.5(b). With the conditions shown in the inset of Fig. 9.5(b), in the same 50 $cm^2$ cell with quad-serpentine flow fields, using the same station and production lots of PEM's and GDL's, the P1 processed anodes and cathodes (0.1 to 0.184 $mg_{Pt}/cm^2$ loadings) show very similar performance to each other and to P4 processed 0.10 $mg_{Pt}/cm^2$ PtCoMn cathode. The galvanodynamic scans with the 0.054 $mg/cm^2$ cathodes are substantially lower (black open and closed squares) but at least as good if not better than historical results with P4 cathodes at these loadings. More careful inspection of the curves in Fig. 9.5(b), show the P1 process yields about a 10 mV improvement at 0.32 $A/cm^2$ and 5 mV at 1 $A/cm^2$ over the P4 process, but very similar performance at very low (0.025 $A/cm^2$) and high (1.5 $A/cm^2$) currents. Measurements of the absolute and specific activities at 900 mV under 150 kPa $H_2/O_2$ are very similar for both processes, although the P1 cathodes have slightly higher surface area than the P4 deposited materials. In conclusion, there are slight performance benefits and no penalties for the simpler, faster P1 process for depositing the NSTF alloys.

### 9.4. Development of roll-to-roll dealloying process

Dealloying Pt based transition metal alloy catalysts to increase their ORR mass activity is recognized increasingly in the literature as a potentially important process, particularly for extended surface type catalysts (7). Ex-situ dealloying is particularly relevant for our NSTF $Pt_3Ni_7$ alloy as a way to both increase its ORR activity and remove the excess Ni cations that

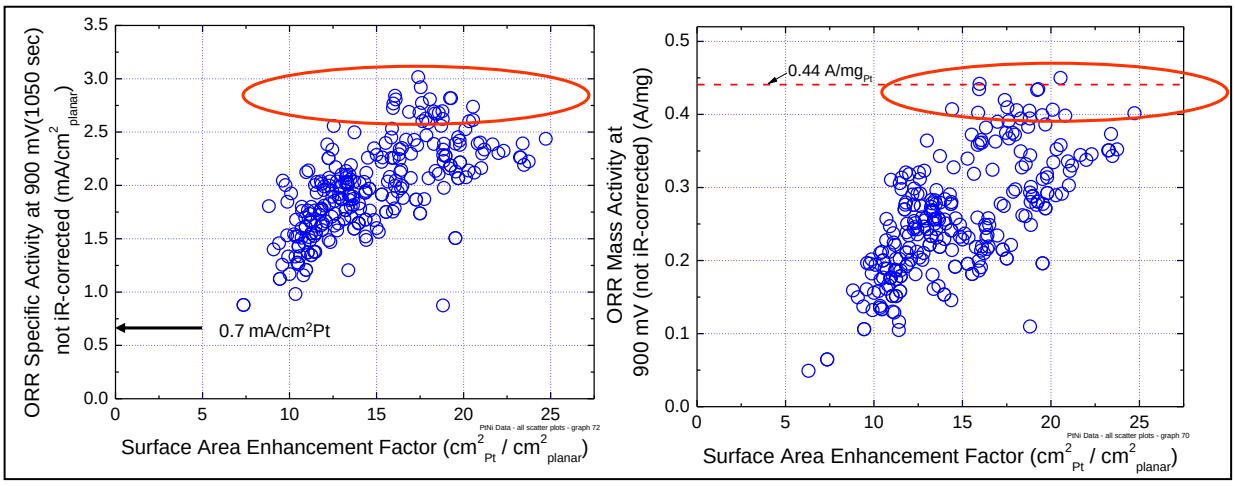


**Fig. 9.6** ORR specific and mass activity as a function of surface area enhancement factor for over 100 different NSTF-PtNi cathodes derived from the as-deposited $Pt_3Ni_7$ catalysts for various loading, dealloying and SET post-process parameters.

will otherwise migrate to the membrane and cause issues with conductivity, water transport and charge transfer impedance, thereby significantly reducing the limiting current density achievable. Typical transition metal dealloying involves acid dissolution of the transition metal. A baseline acid bath for Ni dissolution is nitric acid. To be viable for a roll-to-roll (R2R) catalyst manufacturing process, however, we must also have an effective R2R dealloying process capable of being run at similar web speeds as the catalyst deposition. This required development of new bath chemistries, correlation of batch and R2R process experiments, and finally fuel cell testing to map myriad sample and process parameters with fuel cell performance and ORR activity.

A broad series of batch process experiments were first completed to investigate the effects of both electrochemical and passive chemical dealloying, with acid bath composition, concentrations, time and temperature as parameters. These were applied to various catalyst material factors, including $Pt_3Ni_7$ loading (0.075 to 0.15 mg-Pt/cm$^2$), alloy homogeneity (P1 vs. P4), and the SET annealing process discussed above. The objective was to try and optimize the process both to improve the limiting current density without loss of ORR activity, and to find conditions suitable for roll-to-roll processing at reasonable web speeds. Over 100 different combinations of the acid bath conditions, catalyst fabrication and process parameters were screened and tested in 50 cm$^2$ fuel cells in duplicate. Conditions were found that allowed speeding up the rate of dealloying by a factor of 240 over the baseline nitric acid bath soak. Using existing facilities at 3M, full-width roll-to-roll dealloying was developed with the faster process conditions. Sixteen ORR relevant kinetic and performance metrics were extracted from the fuel cell potentiodynamic and galvanodynamic polarization curves and correlated with materials and proprietary process parameters.

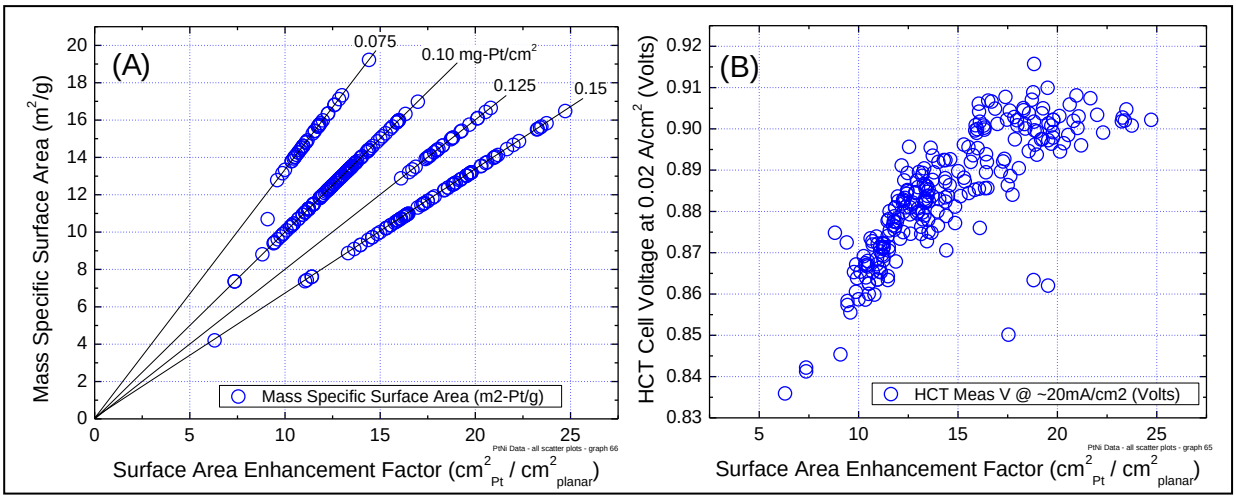


**Fig. 9.7.** (A) Mass specific surface area for different Pt loadings in the $Pt_3Ni_7$ dealloying development experiments plotted versus the surface area enhancement factor. (B) The GDS polarization curve voltage at 20 mA/cm$^2$ plotted versus the surface area enhancement factor.

Without disclosing proprietary process information, a total of 38 global scatter-plots can be generated to illustrate how critical metrics vary with two basic catalyst properties, surface area and loading. Figure 9.6 shows two such global metric plots of ORR specific and mass activity at 900 mV under 150 kPa saturated oxygen, versus the surface area enhancement factor in cm$^2$ of Pt per cm$^2$ of planar surface area. The scatter plot in Figure 9.6 (left) shows the high specific activity of the $Pt_3Ni_7$ derived catalysts, approaching 3 mA/cm$^2$-Pt for some samples, which far exceeds the DOE 2015 targets of 0.7 mA/cm$^2$-Pt. Figure 9.6 (right) is a

similar scatter plot showing that roll-to-roll dealloying and annealing conditions were found which generated mass activities of 0.44 A/mg-Pt using the 3M ORR protocol above, equivalent to the DOE 2017 target. Fig. 9.7(A) plots the electrochemical surface area versus surface enhancement factor for the dealloying sample series. It shows that mass specific surface areas of 15 to 20 $m^2/g$ were common for the dealloyed/SET annealed catalysts with the highest mass activities. These are the highest ECSA values and SEF values we have measured for NSTF catalysts at these loadings. The increased surface area and specific activity both contributed to the improved mass activity. Finally, Fig. 9.7(B) shows the kinetic current density region (0.02 $mA/cm^2$) as a function of the surface area enhancement factor from GDS polarization curves for the ~ 100 samples from the R2R dealloying development and scale-up activities. The kinetic fuel cell performance mirrors the mass activity.

**9.5. Reduction of microstructure feature size of NSTF specific Microstructured Catalyst Transfer Substrate (MCTS) - Task 5.1 – MEA Integration**

The microstructured catalyst transfer substrate (MCTS) web developed for roll to roll vacuum coating of the NSTF whiskers and catalyst over-coating is critical for protecting the whiskers from being brushed off when passing over rollers along the web path. It also provides a square-root-of-two increase in electrochemical Pt surface area. The process for fabricating the MCTS is based on a well established 3M technology platform for manufacture of brightness enhancement film (BEF) for electronic displays. The size of the microstructure feature is different for the NSTF catalysts and the optical film applications. The initial MCTS structure developed for this NSTF fuel cell catalyst application, long before the start of this project, did have feature sizes similar to the larger BEF applications, i.e. $90^o$ peaks, 12 microns tall on a 24 micron pitch. This 90/24 structure was soon reduced to a 90/12 structure, 6 micron tall peaks on a 12 micron pitch to make it more appropriate for thinner membranes. The 90/12 MCTS substrate was the substrate in use prior to the start of this contract. At the beginning of this project we reduced the size of the features with a 90/6 MCTS structure. Here the peak-to-peak distances are only 6 microns and the peak heights only 3 microns. There are twice as many peaks per unit length, but only half as high, so they will penetrate into the membrane only half as deep.

Fig. 9.8 (A) shows SEM cross-sections of a catalyst/whisker coated 90/12 MCTS. Fig. 9.8 (B) shows an SEM cross-section of a fresh CCM made by lamination transfer of such a 90/12 based NSTF catalyst to both sides of a 35 micron thick membrane. Fig. 9.8 (C) shows an SEM cross-section of the CCM after fuel cell testing, illustrating how the GDL compression flattens out the micro-replicated MCTS features in the CCM surface. In so doing, the excess length of catalyst (by a factor of 1.414 ideally) has to go somewhere and is squeezed to form pockets (circled) in which the catalyst is buried as deep as ~ 4 microns into the PEM surface. Fig. 9.8 (D,E) show higher magnifications of these pockets for both a 90/12 and a 90/6 based catalyst/MCTS structure. Although with a 90/6 MCTS structure there will be twice as many such pockets per unit length, they will nominally be only half as deep. Since oxygen permeability will become more and more limited the deeper the catalyst is buried in the PEM surface, shallower pockets might be expected to perform better than the deeper pockets. That is, mass transport overpotential at high current densities would be expected to be improved.

The first 90/6 MCTS substrates were tested by putting on our standard whiskers with 0.1 $mg_{Pt}/cm^2$ of the PtCoMn catalyst on the anode and 0.15 $mg_{Pt}/cm^2$ of PtCoMn on the cathode. (We have shown at the start of this contract as reported at the 2007 DOE annual merit review meeting, that reducing the anode loading from 0.2 to 0.1 $mg/cm^2$ also helped the high current density mass transport.) The PEM used was 35 μm thick 830EW cast 3M. Fig. 9.9 compares the GDS polarization curves at 7.5 psig inlet pressure, from these MEA's with earlier MEA's made with higher anode and cathode PtCoMn loadings (0.2 $mg_{Pt}/cm^2$) on 90/12 MCTS.

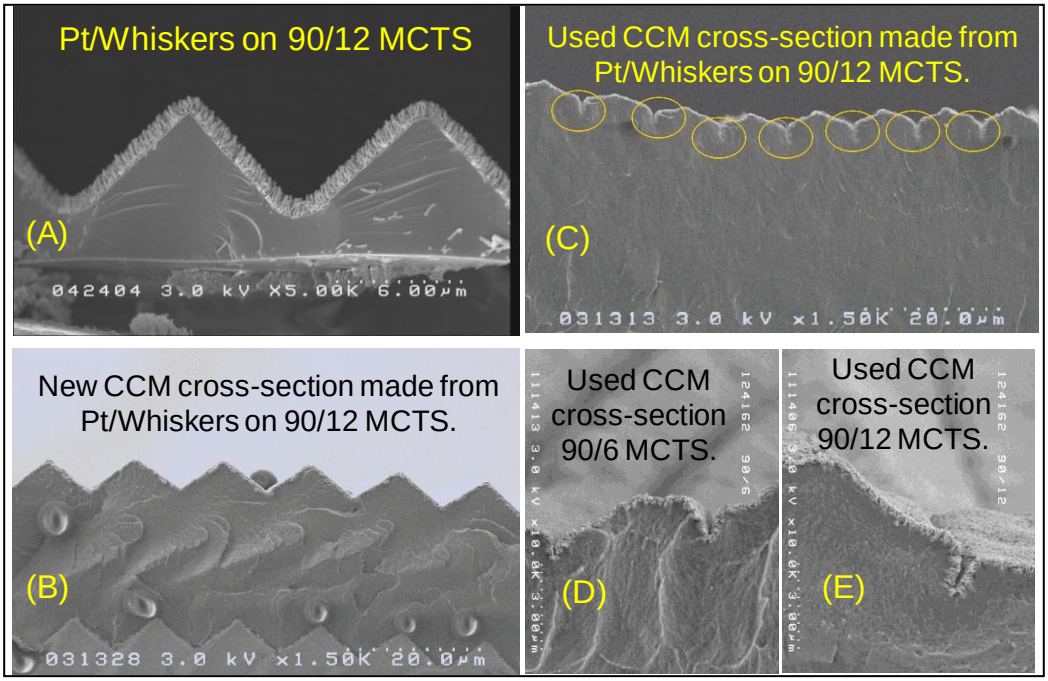


**Fig. 9.8.** SEM cross-sectional images of: (A) catalyst coated whiskers on a 90/12 MCTS, (B) a CCM made with NSTF catalysts formed on a 90/12 MCTS and laminated to an ~ 35 micron thick membrane. The MCTS is micro-replicated on the surface of the PEM. (C) A tested CCM showing how the micro-replicated MCTS structure is flattened out by the GDL compression and how the catalyst coated peaks are buried in the membrane, and (D,E) higher magnification images of the used CCMs made from 90/6 and 90/12 MCTS respectively.

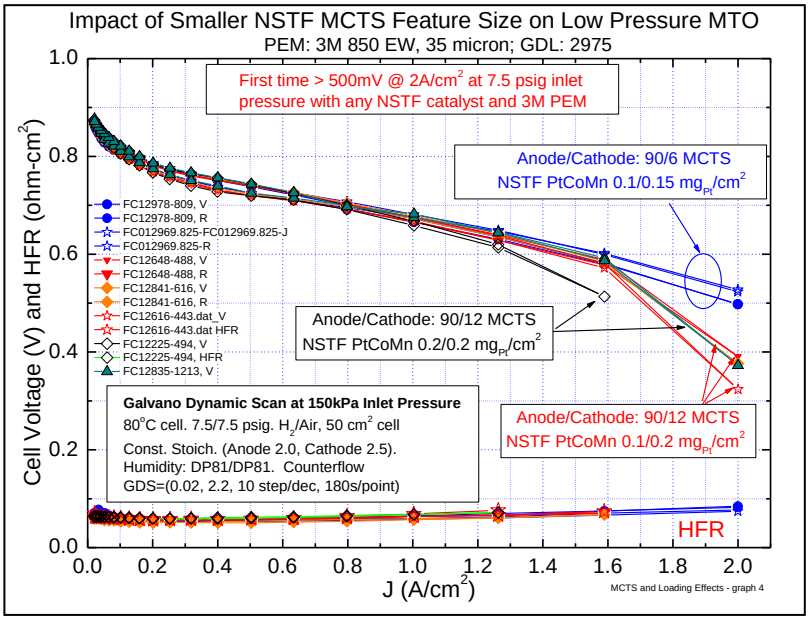


**Fig. 9.9**. GDS polarization curves showing the impact of using smaller 90/6 microstructure features rather than 90/12 features on the MCTS support film when making the NSTF catalyst coated webs and CCM's.

There is a clear boost in performance at high current densities from these first samples made on the 90/6 MCTS compared to the earlier 90/12 based MEAs. This was the first time we had ever obtained over 500mV at 2 A/cm$^2$ with only 7.5 psig inlet pressure. We attribute this benefit to the fact that the catalyst is utilized more effectively since there is in general less mass transfer overpotential with the portion of the NSTF electrode that is squeezed into the shallower pockets.

### 9.6. Demonstration of first cell reversal tolerant anode catalyst with OER characteristics

Start/stop events and other transient phenomena that can momentarily deplete a cell's anode of sufficient hydrogen to support the current demanded by the stack. This may produce local hydrogen starvation. The result is that a current is forced upon the anode electrode at the location of the starvation. The electrode potential quickly rises until potentials are reached where carbon, platinum and water begin to oxidize. Carbon oxidation results in degradation of carbon-supported catalyst layers and the gas diffusion media, leading to increased resistance, reduced catalyst utilization and mass transport losses. Platinum oxidation may result in formation of soluble platinum oxide species, resulting in loss of electrode surface area. In the event of anode starvation, it is preferable that the electrode's water oxidation (oxygen evolution reaction, OER, 2 $H_2O$ -> $O_2$ + $4H^+$ + $4e^-$, E > $E^0$=1.23V.) kinetics are sufficiently fast at relatively low potential, to minimize the carbon (GDL) and platinum oxidation.

In 2008 we carried out the first measurements of the effect of adding sub-monolayer quantities of Ir onto the NSTF PtCoMn anodes to enable the anodes to support OER currents at lower reversed cell potentials, thereby potentially protecting the carbon in the GDL. Ir was sputter deposited at planar equivalent thicknesses of 5, 10, 15, 30 and 60 Angstroms onto the PtCoMn anode catalysts (0.1 $mg_{Pt}/cm^2$) prior to forming the CCM. Due to the approximately factor of ten increase in surface area of the PtCoMn catalyst over the planar surface area, the actual thickness of the Ir deposited once on the PtCoMn was substantially less than the planar equivalent thickness. Fig. 9.10 (A) shows a series of OER polarization curves for these thicknesses compared to the standard anode with no additional Ir. Even the case of just adding 5 Angstroms of Ir substantially increases the OER current over the range of 1.4 to 1.5 volts versus the counter electrode of Pt in 1% $H_2$ in $N_2$. For the specific case of 15 Angstroms of Ir, further analyses were done to show the effectiveness for cell reversal tolerance. First Fig. 9.10 (B) shows that the OER tests did have a small effect on the ECSA and ORR absolute activity of the PtCoMn when used as a cathode, reducing the latter from 14.2 to12.9 $mA/cm^2$-planar. Specific activity remained unchanged at 2.3 $mA/cm^2$-Pt. The small drop in ECSA, 6.3 to 5.7 $cm^2Pt/cm^2_{planar}$, may have been due to the Ir blocking some Pt surface area.

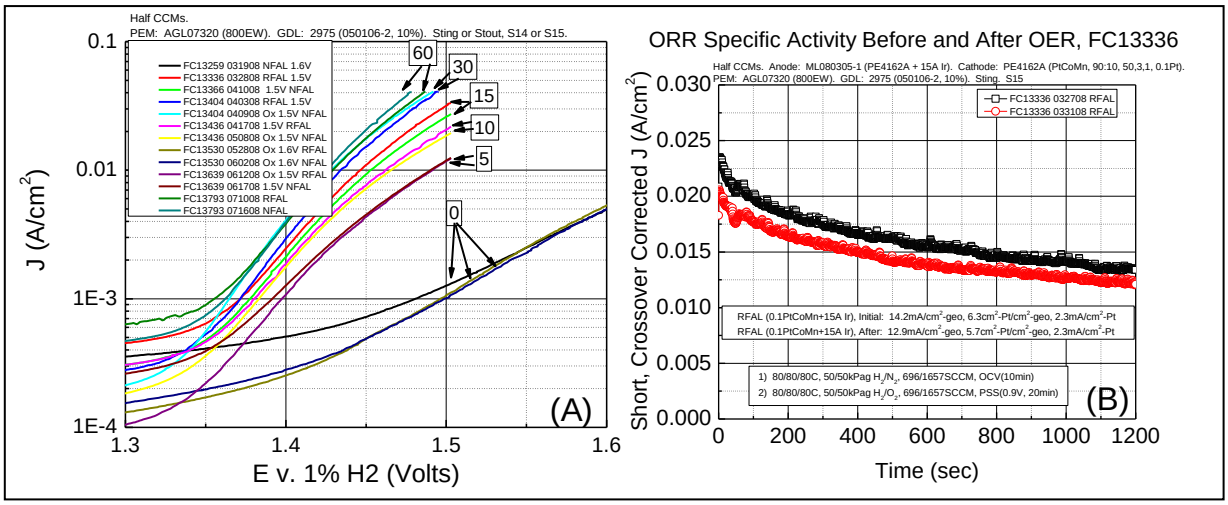


**Fig. 9.10.** (A) Polarization curves of oxygen evolution reaction current density versus electrode potential from a series of MEA's having NSTF PtCoMn anodes with varying amounts of additional Ir sputtered on top of the 0.1$mg_{Pt}/cm^2$ PtCoMn before making the CCM. The amounts shown in the boxes are in Angstroms of Ir. (B) ORR absolute activity current density measurements of the 0.1 $mg_{Pt}/cm^2$ PtCoMn + 15 Å Ir electrodes operated as a cathode, indicating the change caused from OER operation on the anode under a cell reversal test.

For the anode fuel starvation test, four different electrodes were compared, two NSTF and two Pt/carbon. The anode electrode was forced to support a 2mA/cm$^2$ oxidation current in a $N_2$ atmosphere for 5 hrs. All MEAs contained the same PEM and GDLs, and were evaluated with the same test station hardware. Two ½-CCMs were made with two 1.3mil 3M 800EW PEMs to reduce parasitic shorting currents. The baseline NSTF-PtCoMn ternary catalyst (anode loading = 0.1 mg$_{Pt}$/cm$^2$) and a modified version having 15 A of Ir added to the anode catalyst were tested in duplicate. The Pt/Carbon anodes used both 0.2 and 0.4 mg$_{Pt}$/cm$^2$. The test procedure consisted of first measuring the initial baseline performance, then "Corrode" the anode electrode by forcing 2 mA/cm$^2$ oxidation current through anode under $N_2$ for 5 hours, measure post-starvation baseline performance, thermal cycle the cell to recover any reversible losses, and finally measure the post-thermal cycle baseline performance. Fig. 9.11(A) shows the anode starvation voltage versus time profile for the four electrode types. The Pt/C electrodes are initially holding at around 1.35 volts but after a half hour rapidly increase to over 1.75 volts. The higher loading Pt/C electrode appears to hold twice as long as the 0.2 Pt/C before ramping up the electrode voltage. The two NSTF PtCoMn baseline MEA potentials are held to < 1.6 V, better than the Pt/C electrodes. The MEAs with anodes of NSTF-PtCoMn catalyst with the additional 15 Angstroms of Ir show a significant reduction in OER potential to ~ 1.4 V, which is stable for the 5 hours. After longer periods (3-4 hours) the Pt/C and NSTF-PtCoMn approach the potential of the NSTF PtCoMn+Ir, suggesting other avenues of corrosion current are being utilized.

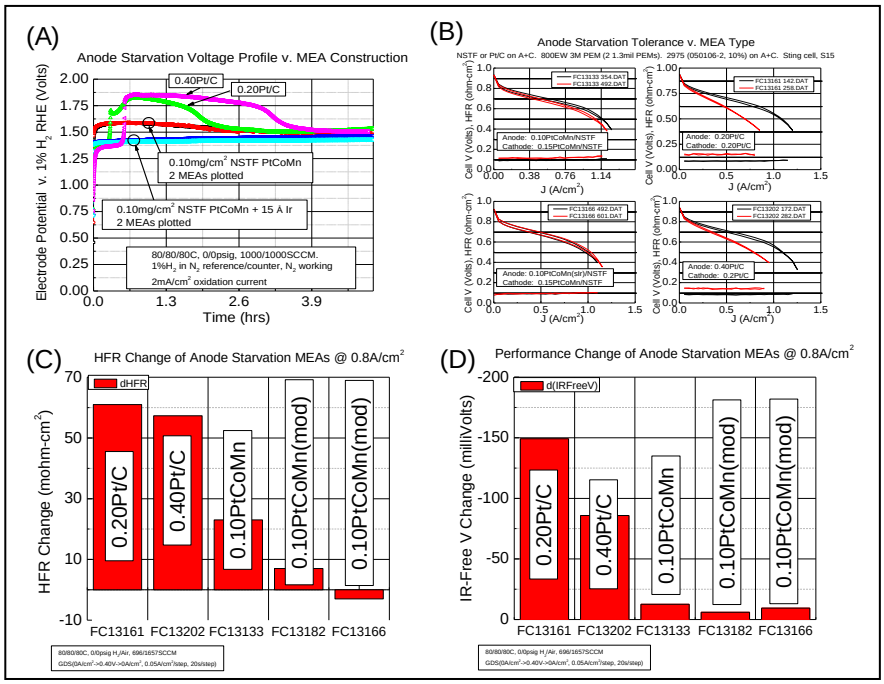


**Fig. 9.11.** Comparison of four types of MEA anode responses to the anode fuel starvation test in which the anodes are driven past the OER equilibrium potential. (A) Electrode potential versus time for four MEA's when forced to pass 2 mA/cm$^2$ for five hours. (B) Initial and post-test $H_2$/air polarization curves for the four types of MEA's in (A). (C) Net changes in high frequency resistance before and after the test for the four types of MEA's. (D) Net changes in iR-free cell voltage after the test for the four MEA's in (A), from polarization curves in (B).

Standard $H_2$/air fuel cell performance is substantially reduced immediately after the anode starvation test for all MEA's, but the extent differs for the different MEA types. Fig. 9.11

(B) compares the initial and recovered performance for the four types of MEA's. The MEAs with 0.20 and 0.40 mg/cm$^2$ Pt/C on the anode showed substantial decreases in performance and increased resistance that could not be recovered. The NSTF MEAs showed much less loss in performance or increase in HFR. These are more specifically plotted in Fig. 9.11(C,D). The 0.4Pt/C anode MEA appeared to suffer slightly less irreversible degradation than the 0.2Pt/C anode MEA. The extent of HFR change appears similar. The irreversible loss of the two NSTF PtCoMn MEA's is much less than the Pt/C's. The modified NSTF PtCoMn anode catalyst with 15 Å Ir shows even less irreversible loss in performance or HFR increase in either MEA tested.

### 9.7. Discovery of the importance of the anode for effective low temperature water management.

Membrane electrode assemblies (MEAs) utilizing the ultra-thin (<1μm) 3M nanostructured thin film catalyst (NSTFC) technology have several demonstrated advantages compared to MEAs comprising conventional, relatively thick (~10μm) carbon-supported catalyst, as noted in the introduction. However, the low temperature (0-50°C) steady state limiting current density of typical NSTFC MEAs with standard GDL's under usual operating conditions is substantially lower than that of many conventional catalyst MEAs (0.3 v. 1.6 A/cm$^2$ at 30°C, air cathode). This reduced low temperature performance can be attributed to the NSTFC's much higher water generation rate per unit catalyst volume or surface area (~ 6x) and to a hydrophilic electrode pore structure that is more susceptible to water condensation. Significant effort was spent studying the low temperature water management aspects of the ultra-thin layer NSTF electrode based MEA's during the first four years of this project under Task 5.2. We developed test protocols for cool start-up and steady state operation, designed and carried out many GDL materials and process design-of-experiments and then used fuel cell test protocols to evaluate the effects of both cathode and anode GDL modifications.

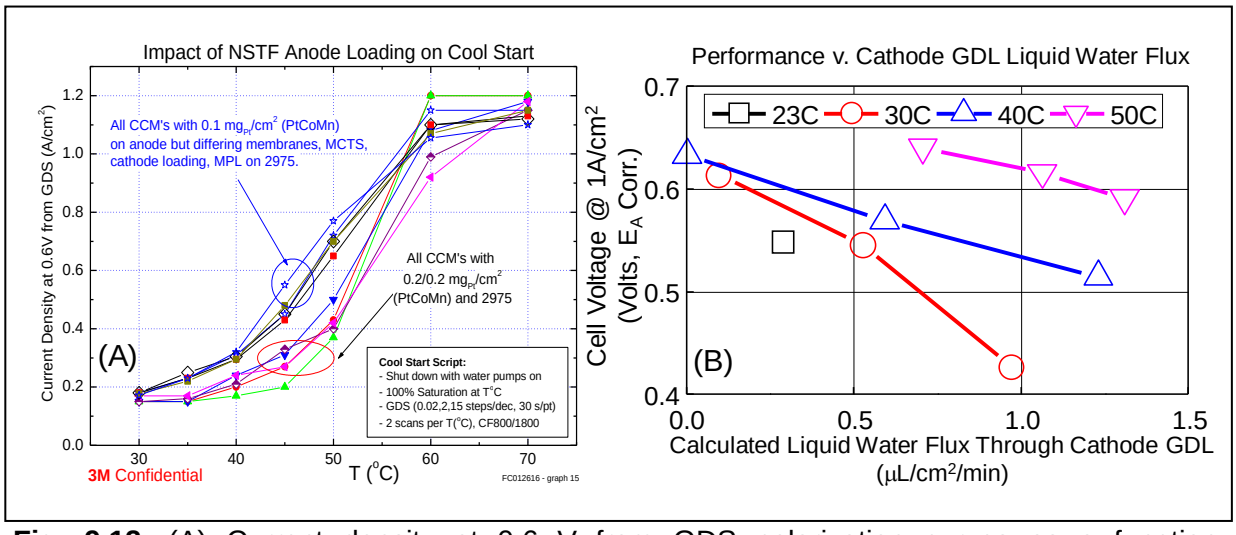


**Fig. 9.12.** (A) Current density at 0.6 V from GDS polarization curves as a function of temperature for two groups of MEA's differing by their anode catalyst loading. (b) Fuel cell performance versus liquid water flux out the cathode based on measurements and calculated fractions of water leaving as vapor versus liquid.

This latter work was a primary effort during the first three years with generally the focus on trying to mitigate flooding at low temperatures by modifying the cathode GDL properties of our baseline EB paper and its MPL coating, although the asymmetric anode/cathode GDLs

combinations were eventually looked at as well. The results were mixed with small improvements in high temp and low temp operation. Other work involved measuring GDL physical properties with a commercial Porotech porosimeter, as well as our own novel GDL liquid water permeation measurements for wide host of carbon paper types, and applied X-ray tomography to characterize GDL's used for above liquid water permeation studies, as discussed in more detail in the section on Task 5.2.

Eventually we began to separately identify the critical anode and cathode factors for controlling water flow and its impact on fuel cell performance. These broadened studies included quantitative water balance measurements of water exiting the anode and cathode vs their inlets; new cathode interfaces between MPL and CCM; modified NSTF (dual) hybrid cathodes; modified anode GDL's (many types of GDL carbon backing papers, hydrophobic coatings, MPL or no MPL); alternative membranes; and variable anode pressure operation. These studies led to significant improvements in low temperature water management, with the overriding result that it was the anode rather than the cathode that was key to demonstrating viable solutions, with the anode operating pressure and the anode GDL backing paper properties the biggest factors.

In retrospect, the first evidence that the anode was potentially more important for low temperature operation than traditionally thought actually came near the start of this project when we determined that reduced anode catalyst loading improved the steady state current density at operating temperatures below 60 $^{o}$C. This is illustrated in Fig. 9.12 (A) which demonstrates that by reducing the anode catalyst loading from 0.2 $mg_{Pt}/cm^2$ (PtCoMn) to 0.1 $mg_{Pt}/cm^2$, the steady state current density was nearly doubled between 40 to 60$^{o}$C cell temperature. Furthermore, the result was not dependent on the membrane, cathode loading, type of MPL or even the MCTS structure of what was tested.

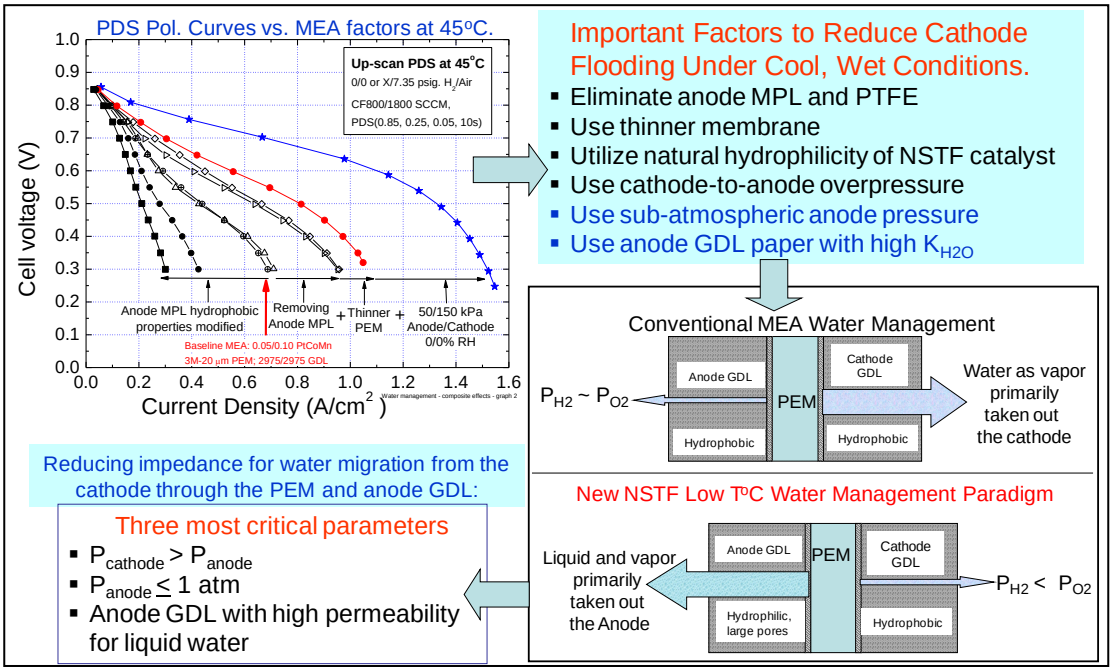


**Fig. 9.13.** Illustration of the new paradigm for minimizing cathode flooding with the NSTF MEAs by increased water removal out the anode. Key material and operating conditions include reduced anode pressure (even subatmospheric), thinner membranes, reduced hydrophobicity of the anode GDL backing layer, elimination of the anode GDL's MPL.

Later studies conducted to better understand water management differences between NSTF and Pt/C electrode MEAs showed that the product water effluent rate out the cathode was highest when evaluated at several conditions where NSTF MEAs typically showed reduced performance (see Fig. 9.12 (B)). By calculating the fraction of water exiting the cathode in the liquid phase and plotting against the performance loss from the 80 $^{o}$C reference performance (all vapor phase water removal), reasonably quantitative agreement is observed for both NSTF and Pt/C electrode MEAs. A primary conclusion from that study was that liquid phase product water removal out the cathode is detrimental to performance for both electrode types, but at a given set of conditions the total water effluent rate out the cathode is less for Pt/C electrodes than NSTF electrodes. It also stresses that taking water out the anode rather than the cathode is a most desirable strategy if possible, since the outgoing water vapor is not interfering with the incoming oxygen, and the cross-over water can keep the membrane humidified. In light of these results, a logical path forward was based upon the premise of minimizing liquid product water removal out the cathode GDL, which is best accomplished by maximizing liquid product water removal out the anode GDL. Fig. 9.13 conceptualizes the key aspects we subsequently determined were most important for improved low temperature water management based on this new paradigm of taking water out the anode. The polarization curves in the top left show the dramatic effects of removing the MPL using a thinner PEM and operating the anode at sub-atmospheric pressure. Low temperature operation is critical for rapid stack start-up from temperatures below 60$^{o}$C. Fig. 9.14(A) shows steady-state current density at 0.4 volts versus absolute anode pressure at 30 $^{o}$C for various combinations of anode GDL, all with no MPL except the baseline GDL (open squares). The anode absolute pressure is seen to be a very effective boundary condition for reducing cathode flooding. The Freudenberg GDL backing layers are much more effective than the baseline MRC type GDL backing layer we standardly use for improving the effectiveness of the sub-atmospheric anode pressure. We started testing the Freudenberg GDL on the anode versus the MRC baseline GDL backing layer since it had a much higher liquid water permeability (6x) from simple liquid water permeability measurements we completed earlier for a whole series of different GDL backing materials (see Task 5.2 section).

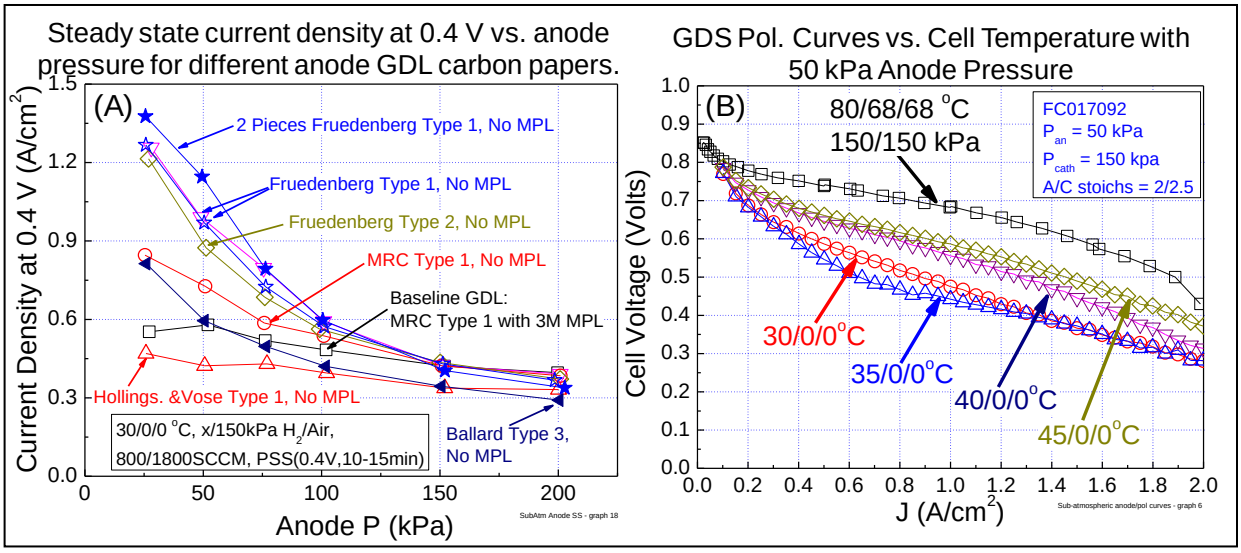


**Fig. 9.14.** (A) Current density at 0.4 volts as a function of absolute anode pressure under steady-state fuel cell operation at 30$^{o}$C, dry inlets and 150kPa $H_2$/air, for various anode GDL types, most without MPL's. (B) GDS polarization scans as a function of temperature and anode pressure for NSTF MEA containing the Freudenberg Type 1 GDL on the anode, 2009 best of class CCM and standard 3M cathode GDL.

Fig. 9.14 (B) shows GDS polarization curves as a function of 50 $cm^2$ cell temperature under 50/150 kPa anode/cathode absolute pressures of $H_2$/air. The MEA uses the 2009 best of class CCM and the as-received Freudenberg GDL backing layer on the anode (no MPL or PTFE treatment). With the proper anode GDL and reduced anode pressure, it is possible to run the cell stably at 2 $A/cm^2$ even at 30 $^oC$. The high temperature curve at 80 $^oC$ and 68 $^oC$ dew points in Fig. 9.14 (B) also shows there is no impact of the anode GDL on standard higher anode pressure/temperature operation. Operating at equal anode/cathode pressures (150kPa) or higher, the same MEA will flood out at a limiting current of < 0.4 $A/cm^2$ at 30$^oC$. But if the cathode pressure exceeds sufficiently the anode pressure, then the cell can hit 2 $A/cm^2$ even with the anode at atmospheric pressure. This is shown in Fig. 9.15(A) for the case of a 2009 best of class CCM (0.05/0.1 $mgPt/cm^2$ of PtCoMn on anode and cathode, 24 micron thick 850 EW 3M PEM) with the anode GDL replaced by Freudenberg backing layer. Similar benefits obtain under transient load conditions as well as steady state. Fig. 9.15 (B) shows the load transient response under cooler, wet conditions as a function of anode pressure under 60$^oC$, 140% RH, of a 2009 best of class NSTF MEA consisting of the CCM and MPL-free anode GDL indicated, and a standard 3M cathode GDL.

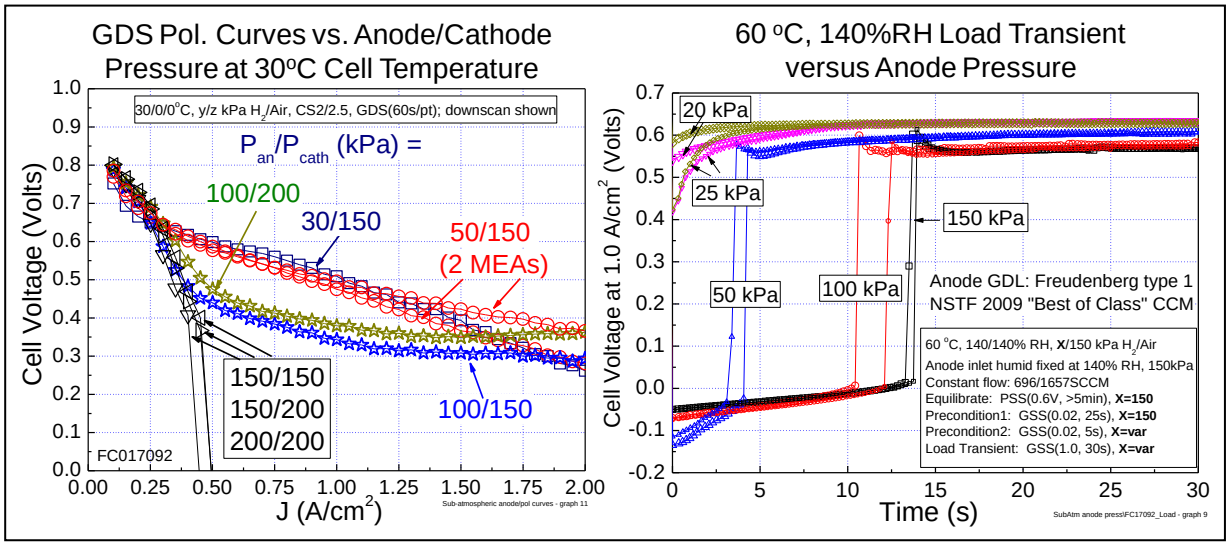


**Fig. 9.15.** (A) GDS polarization curves at 30$^oC$ as a function of anode/cathode pressure ratios. (B) Transient response to a load step from 0.02 to 1 $A/cm^2$ as a function of anode pressure for a 2009 best of class CCM at 60$^oC$, 140% RH, with the MPL-free anode GDL indicated, and a standard 3M cathode GDL (MRC backing paper.)

A less system dependent and probably more practical method for improving the low temperature performance of NSTF MEAs is through materials development. In year four we focused on screening several different vendor supplied *anode* GDL backing to determine their impact on low temperature response. Fig. 9.16 (A) shows results from four tests where the anode GDL backing was varied; all GDLs contained similar hydrophobic treatments and MPLs applied by 3M. Under Test I, the MEAs with GDLs MRC A and Freudenberg A yielded similar performance whereas the MEA with electrode backing paper type MRC C had lower performance at high current density, due to higher HFR. Under Test II, a pseudo-system startup transient, the Freudenberg A GDL provided a short burst of higher performance than MRC A, but the current density dropped to the MRC A level within ~15 sec. MRC C, which had lower performance than the other GDLs under Test I, yielded transient current densities which were 50% higher than Freud A and a steady state current density approximately 3x that of the

other two GDLs. Under Test III, MEAs with either MRC A or Freudenberg A GDL had similarly low performances at 30°C. As the cell was heated, the performance with both GDLs improved, with Freudenberg A having better performance at 40°C than MRC A. MRC C, which performed well under Test II, also performed well at low temperatures under Test III. As the cell temperature exceeded 50°C, all three MEAs performed similarly. Under Test IV, MEAs with either Freudenberg A or MRC C performed similarly as the current density was stepped up from 0.02 to 1A/cm$^2$ when the cell temperature was 70°C, but at 60°C, Freud A was unable to provide a positive cell voltage at 1 A/cm$^2$ whereas MRC C only showed a slight loss relative to 70°C. These results show anode GDL properties are the most promising and effective component variable we have identified for solving low temperature cathode flooding with ultra-thin electrodes. Exactly which properties of the GDL are most critical for this function are still unclear. Measurements of standard physical properties and more involved properties such as the porosity distributions and thermal conductivities done at LBNL and through LANL have not yet been able to identify what makes the MRC type C carbon paper so unique and effective for water transport out the anode. The benefit of selecting the correct anode GDL properties is dramatically illustrated in Fig. 9.16 (b) which is a larger summary of several GDL responses to the pseudo-system startup transient Test II discussed above. It shows results with anode GDL's comprising the MRC C (GDL C in 9.16(b)) with and without MPL's, the Freudenberg A type and 3M standard GDL's. Also shown in Fig. 9.16(b) is the impact of a gradient or hybrid CCB used on the cathode (discussed in the section) with either a standard GDL on the anode or Freudenberg A or MRC C on the anode. The top three response curves in Fig. 9.16(b) are obtained with the MRC C on the anode with or without an MPL and a standard cathode GDL. This combination would seem to be the best solution to the low temperature performance issue with ultra-thin electrodes. In practice, there is still a high temperature issue with the MRC C type which is experimental from the Vendor, due to excessive HFR that remains to be solved as noted in Fig. 9,16 (a) test I. Finally, although removing the MPL from the GDL gives the best transient and steady-state cool temperature response, stray carbon fibers sticking out of the bare carbon backing paper surface plane tend to give increased DC shorting currents through the membrane leading to potentially decreased durability.

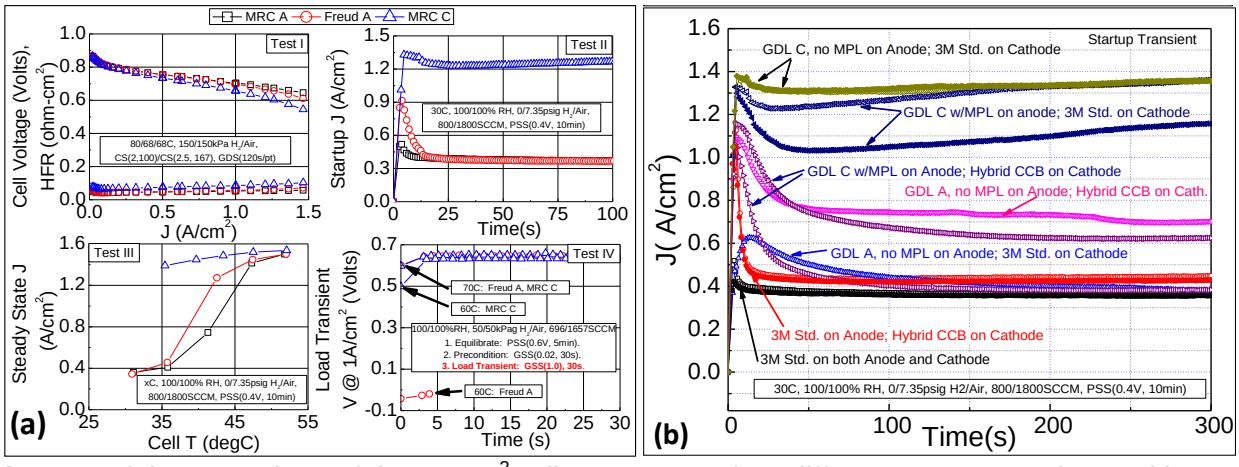


**Fig. 9.16.** (A) Comparison of the 50 cm$^2$ cell response to four different test protocols sensitive to water management: Test I is steady state high temperature performance; Test II is a pseudo-system startup transient at 30 $^o$C; Test III is steady state current density at 0.4 V versus temperature; Test IV is a load transient current density step up from 0.02 to 1A/cm$^2$ at 60 or 70 $^o$C. (B) Comparison of the 50 cm$^2$ cell response to a start-up transient (OCV to 0.4 V) at 30$^o$C and 100% RH for different anode and cathode GDL combinations. $H_2$/air pressures are 100/150 kPa. GDL type C performance with or without an MPL is far superior in transient and steady state operation to the 3M standard GDL.

### 9.8. Determination of how catalyst ECSA depends on NSTF whisker support characteristics

Increasing the electrochemical surface area is one sure way to increase the electrocatalyst mass activity. There are two basic approaches to potentially achieve this. One is to optimize the surface area of the catalyst support whiskers. The second is to increase the surface area of the catalyst coating applied to the whiskers. Both approaches were the key objective of Task 1.1. Subtask 1.1.1 focused on increasing the surface area of the whisker supports. Prior to this project, there had never been an attempt to systematically explore how the whisker geometric parameters and growth conditions affected the surface area of the whiskers or, more importantly, their impact on the subsequent catalyst over coating.

Our approach to do this in this project was to carry out a set of designed experiments on production pilot line web coating equipment at the Menomonie, WI, plant where the NSTF roll to roll catalysts are fabricated. These experiments consisted of a multiple series of designed process experiments, called **Whisker Area Optimization one, two, three, ... or WAO – 1,2,3,4),** in which the whisker production parameters were explored for the optimum whisker number density and dimensions, the most complete conversion of the starting material to the crystalline whiskers, and new aspects of the catalyst deposition parameters.

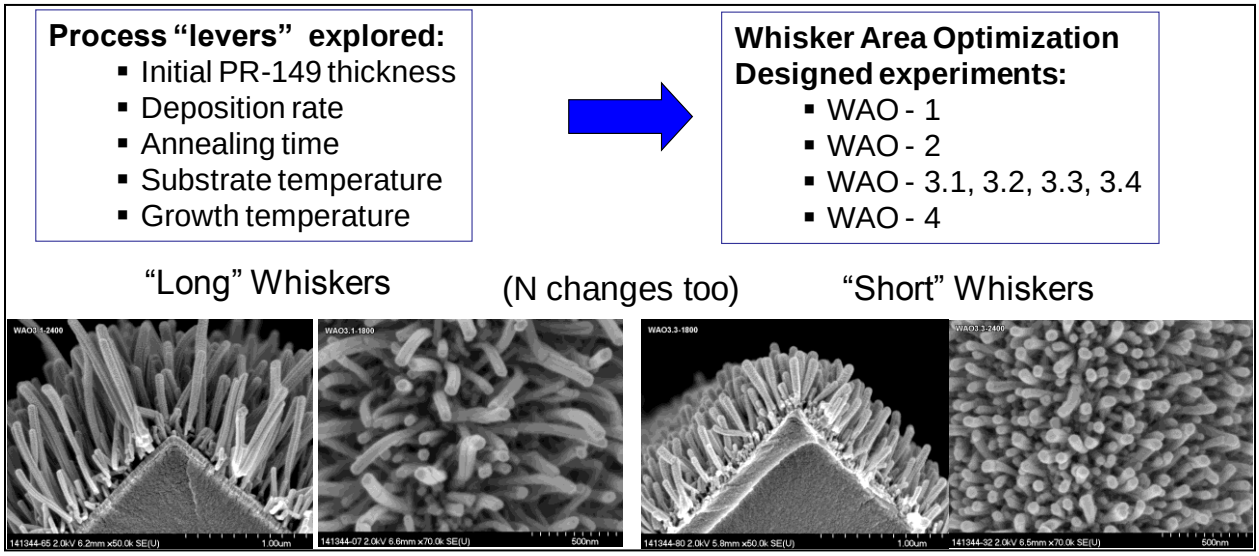


**Fig. 9.17.** Illustration of the whisker growth process parameters explored for their relationship to the whisker physical characteristics and the subsequent catalyst surface area. The SEM images illustrate the range of length and areal number density (number per unit area) of the catalyst coated whiskers explored in the WAO series of experiments.

Fig. 9.17 illustrates the whisker deposition and growth parameters explored in the WAO series of process experiments. A first order approximation of the geometric surface area can be imagined to be given by the simple expression,

$$S_A = 1.414 \times N[\pi d_{av} L + \pi(d_{tip}^2/2)]r_f + 1 . \quad (1)$$

This is the expression that treats the whiskers as an array of right circular cylinders, for which N is the number of whiskers per unit planar area, $d_{av}$ is the average diameter of the coated whiskers, L their mean lengths, $d_{tip}$ their mean diameter at their tops or tips, and $r_f$ is a

roughness factor for the thin film catalyst coating. Good estimates of these factors were measured from many SEM images as illustrated in Fig. 9.18. Although this simple and intuitive expression for estimating the geometric surface area, $S_A$ , of the catalyst coated whiskers is certainly close to what is measured by $H_{upd}$ cyclic voltammetry, it does not sufficiently capture the reality of how the Pt electrochemical surface area and ORR specific activity depend on the underlying bare whisker geometric characteristics.

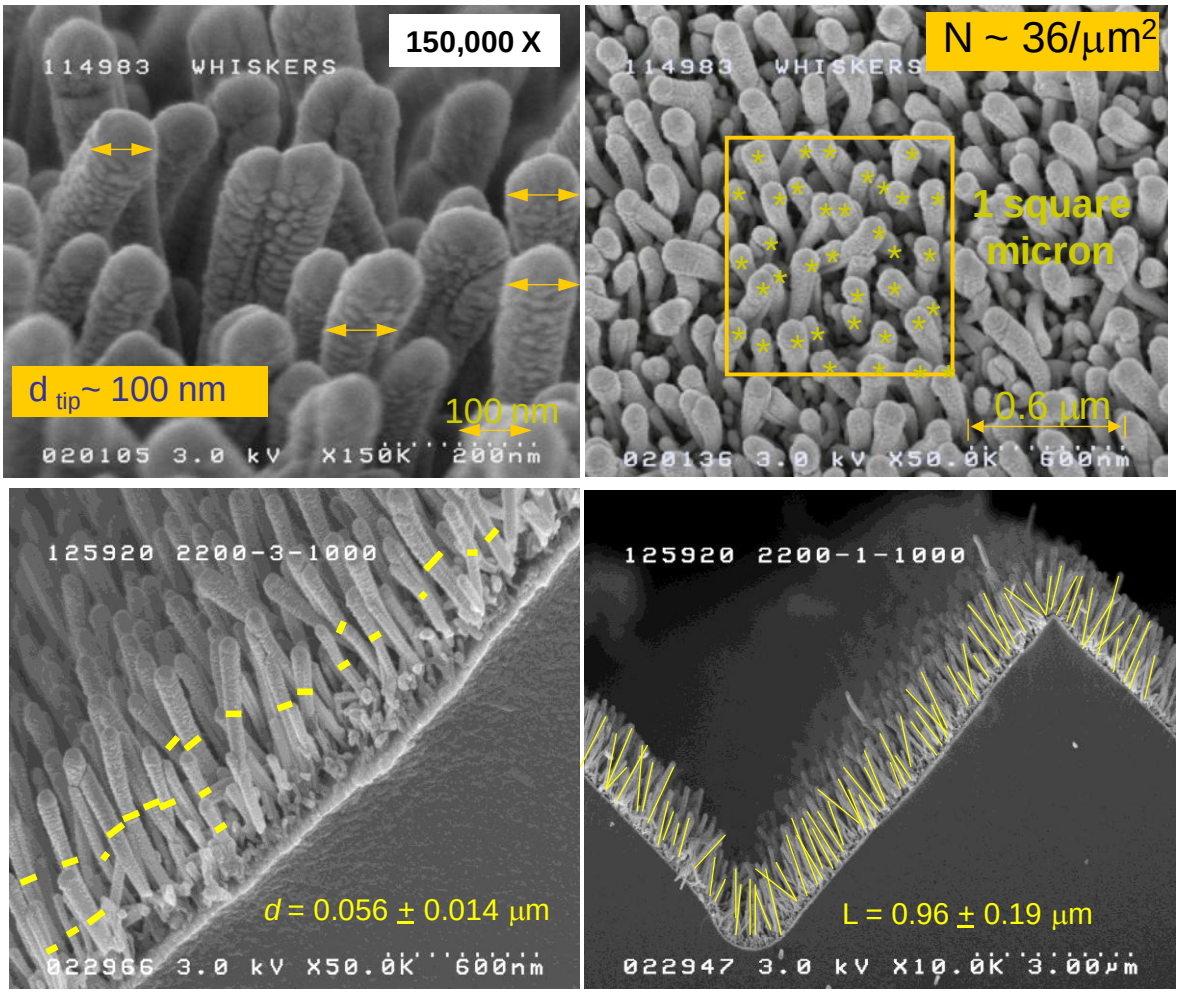


**Fig. 9.18.** Illustration of how distributions of the basic dimensions of the catalyst coated whiskers were determined from SEM images for the WAO-series of experiments.

The **WAO-1** series was the first designed experiment to relate process conditions to whisker geometric parameters. It used three Perylene Red (PR) pigment thicknesses, four whisker growth process conditions, and two catalyst loadings. It was used to develop a more advanced model for how catalyst electrochemical surface area depends on N, L, w, and d, and was the first study to show how catalyst particle structural properties depend on the whisker geometric characteristics.

One of the outcomes from the WAO-1 series was that not all the PR149 was converted to crystalline whiskers in the typical whisker production process. **WAO-2** as the second in the series was done to demonstrate full conversion of PR149 to crystalline whiskers was possible and also determine the potential to generate larger whisker number density and whisker

dimensions. WAO-2 employed two PR149 pigment thicknesses, seven whisker growth process conditions, and multiple catalyst loadings. WAO-1 successfully demonstrated the capability for full conversion of the as-deposited PR149 to the whisker phase, how to get increased values of N*L, but that doing so did not increase the Pt ECSA.

**WAO-3.1 to 3.4** were all part of the third experiments in the WAO series, designed to correlate fuel cell activity metrics with a wider range of whisker growth conditions than considered in WAO 1 or 2. Together they utilized seven PR pigment thicknesses, covering an 18-fold range of values, three whisker growth process conditions, covering a 5-fold range of values, and one value of Pt loading, 0.1 mg/cm$^2$, of standard PtCoMn used on all the different whisker support types generated. They allowed many conclusions to be drawn about the impact of the whisker growth parameter process windows on fuel cell performance.

Finally, the last experiment in the series, **WAO-4**, was designed to correlate various measured ORR activity metrics with the whisker process growth temperatures. The annealing temperatures were increased in $\Delta T = X^oC$ steps from the standard conditions. One PR thickness and one PtCoMn loading were used.

One example (of many) of what was learned from WAO – 1 is the influence of whisker lengths, L, on catalyst particle growth and shape. This is illustrated in Fig. 9.19, which shows

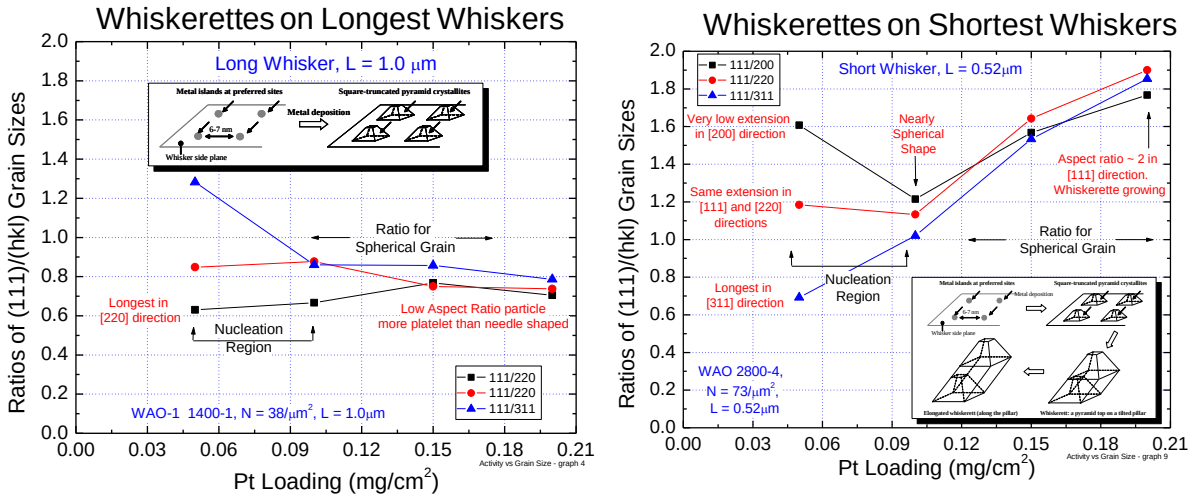


**Fig. 9.19.** X-ray diffraction determined fcc lattice crystallite dimensions in the (hkl) directions ratioed to the fcc(111) dimension, plotted as a function of the catalyst loading on the whiskers for two extreme whisker growth conditions used in WAO-1. The inset figures reflect the catalyst nucleation and growth of the whiskerettes that comprise the thin film coatings of catalyst on the whiskers, as described in reference (25).

X-ray diffraction determined fcc lattice crystallite dimensions in the (hkl) directions ratioed to the fcc(111) dimension, plotted as a function of the catalyst loading on the whiskers for two extreme whisker growth conditions used in WAO-1. The crystallite grains correspond to the whiskerettes that form on the sides of the whiskers, as described in (25). These ratios reflect the degree to which the whiskerette grains are elongated as they loading increases, as shown by the inset figures in each panel of Fig. 9.19. As loading increases on the longer whiskers of the WAO-1 series, how the catalyst crystallite grain morphology changes with loading is dramatically different than it is for the shortest whiskers. Below 0.1 mg/cm$^2$ loading, the grains are still nucleating into low aspect ratio particles, more spherical than elongated. Above 0.1 mg/cm$^2$, on

the longest whiskers, the whiskerettes never seem to get out of the low-aspect ratio regime, and we believe do not develop into proper whiskerettes. On the shortest whiskers, however, above 0.1 mg/cm$^2$, the grains begin to grow into whiskerettes with aspect ratios that increase linearly with loading, approaching 2.

As a second example of what was learned from the WAO – 1 experiment series, we introduce here an advanced model calculation of how the catalyst ECSA depends on the bare whisker geometric factors, i.e. an advanced version of equation (1) above. It assumes a thin shell model, i.e. the catalyst coats uniformly around whisker, but also accounts for Pt deposited on the back plane between the whiskers, as well as the tops and sides of whiskers. It also takes into account how the roughness factor, $r_f$, of catalyst coating on the whisker sides scales with increasing mass loading. The model allows for a two-parameter, $x$ and $f$, fit to data, where $x$ = fraction of catalyst coating on the whisker sides, and $f$ is a scaling parameter for a roughness factor (1+$f$*$d$), where $d$=catalyst thickness. The result is the following expression for $A_{geo}^{Pt}$, the geometric Pt surface area per unit planar surface area: Equation (2)

$$A_{geo}^{Pt} = \sqrt{2}\left[(1-x)+2xNL(w+t)\right]+\left(m/\rho\right)\left\{(1-x)2N(w+t)+\frac{f}{2NL(w+t)}+x\left[\frac{2}{(w+t)}+f\left(1-\frac{1}{2NL(w+t)}\right)\right]\right\}+\left(m/\rho\right)^2\left[(1-x)\frac{f}{\sqrt{2}L}+\frac{\sqrt{2}xf}{NL(w+t)^2}\right]$$

where, $w$ = bare whisker width ( 52.5 nm), $t$ = bare whisker thickness,(27 nm), N = areal number density, L = bare whisker length, m= mass loading, and $\rho$ = alloy density (e.g. 18 g/cm$^3$ for $Pt_{68}Co_{29}Mn_3$). The whisker widths and thickness cross-sections are fixed at values determined by the ratios of the PR149 crystalline side plane surface free energies, as discussed in references (26, 27).

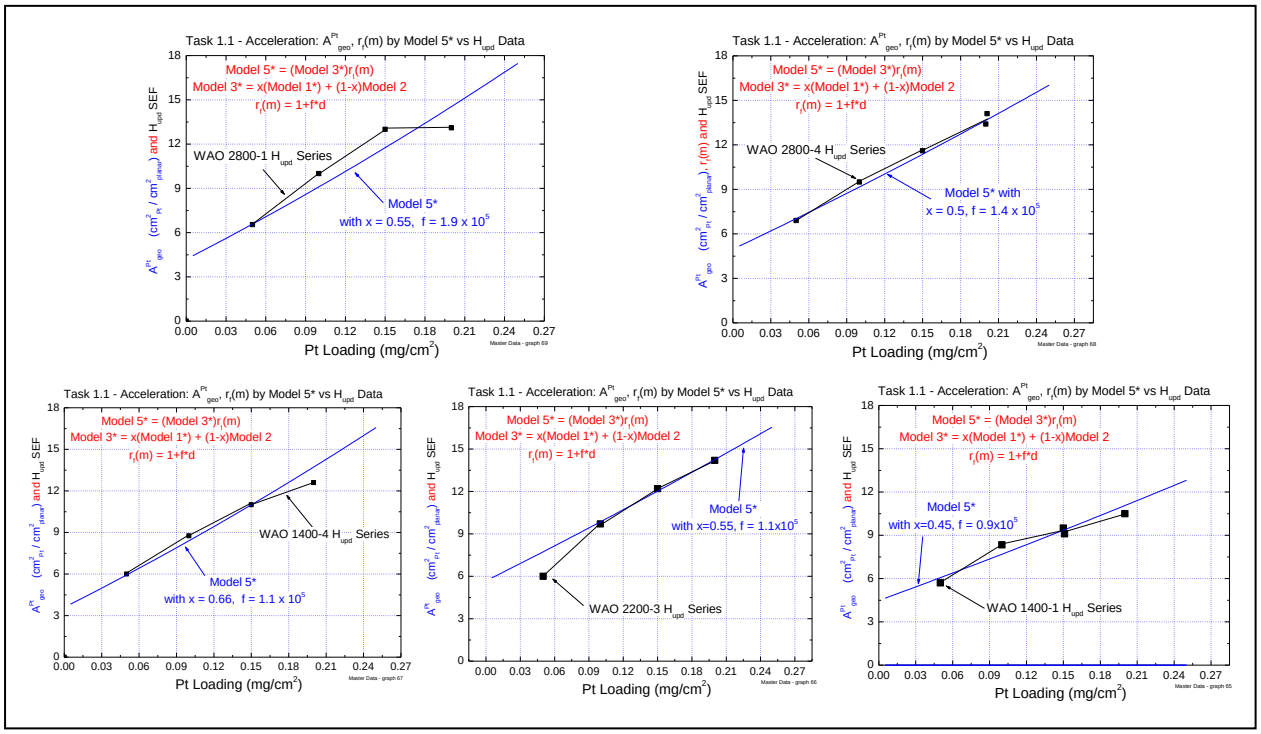


**Fig. 9.20**. Catalyst surface area model equation (2) comparisons to measured Hupd ECSA values versus loading, for five different WAO-1 whisker types, showing good agreement for a common set of fitting parameters ($x$ and $f$).

The above model equation was tested and the two fitting parameters *x* and *f*, determined by fitting calculated surface areas to measured $H_{UPD}$ surface area values from the WAO-1 whisker series. This is shown in Fig. 9.20. The catalyst surface area model equation (2) was able to reasonably fit the measured surface area versus loading for five whisker types in the WAO-1 series, with one set of reasonable values for parameters *x* and *f*. Determined generic values for *f* and *x* from these fits are $x = \sim 0.55$ and $f = 1.1 \times 10^5$ . This value of *x* implies as much as 45% of the Pt catalyst ends up on the back plane between the whiskers and is not used as effectively as it might be. The value of the catalyst coating roughness factor (1+ *fd*) with this *f* gives a reasonable surface roughness for the coating on the whiskers of about 1.28.

With the understanding illustrated in Fig. 9.19 of how the catalyst crystallite size and shape varies with both catalyst loading and the number density and lengths of the support whiskers, combined with the complexity of the electrochemical surface area dependence on the same factors as shown in Fig. 9.20, we began to understand why increasing the Pt mass activity by increasing the support whisker geometric area was not a straightforward process. In short, the ORR specific activity will depend strongly on the distribution of Pt(hkl) surface facets and their sizes, with the Pt(111) being much more active than the others. Those factors in turn depend on the loading and N and L of the support whiskers in complex ways due to how the whiskerette structures vary with loading for a given whisker support type. Simply increasing surface area by increasing the support whisker's values of N and L for a fixed catalyst loading or composition does not lead to proportionate mass activity increases. The WAO-1 series was very successful in revealing these effects as well as correlating the whisker size distributions with the whisker growth parameters and resulting fuel cell performance metrics.

We conclude this NSTF technology accomplishment section 9 with two examples (again of many) of what was learned from the WAO – 3 series of process experiments. Fig. 9.21 (B) illustrates how the Pt surface area (SEF) (solid symbols) and the product N*L of the whisker number density and lengths (open symbols) varied with PR149 thickness. SEF increases linearly with either type of factor up to about 2000 arbitrary units of thickness, but then SEF sharply levels off with thickness even though the N*L product continued to vary with increasing thickness. This again reflects the conclusion above from the WAO-1 series that the simple geometric factors of the whisker supports do not directly determine the Pt ECSA. Fig. 9.21(A) shows that ORR mass activity does vary linearly with the measured ECSA or SEF.

Figs. 9.21(C,D) show how the fuel cell 50 $cm^2$ single cell polarization curves varied for the same PR149 thickness ranges but two different sets of whisker growth parameters. Two things are notable. First there is dramatic variation in fuel cell performance over the whole range of PR149 thicknesses considered, from relative values of 400 to 7200 units. Secondly, there is a relatively broad range of thickness near the peak performance curves for both growth parameter values wherein the polarization curves are independent of thickness, but strongly affected outside this 1200 to 3600 unit window. This means that the process window for the NSTF whiskers is quite broad, which is very important from process and quality control standpoints. A similar set of polarization curves exist for the intermediate set of experiments WAO-3.2 for the whisker growth parameter value 3, with the same conclusion. For the extreme values of thickness (400 and 7200 units) other factors dealing with catalyst transfer issues during the CCM fabrication contribute to the reduced performances.

Other related conclusions from these WAO-3 experiments included the following:

- All fuel cell performance metrics are quite independent of the annealing time.
- GDS voltages at all current densities from 20 $mA/cm^2$ to 1.46 $A/cm^2$ were independent of PR-149 thickness and annealing speed for thicknesses in the range of 1200 to 3600 units.
- Kinetic activity (absolute, mass and voltage at 20 $mA/cm^2$) vary approximately linearly with SEF.

- HFR impedance at low and high current densities are independent of PR-149 thickness, and low in value.
- Pt[111] grain sizes vary significantly with PR thickness for both 3.1 and 3.3, somewhat more for the longer 3.1 series. They decrease as whiskers lengthen (shorter whiskerettes).
- Pt[200] and [220] grain sizes are less dependent on whisker type, but appear to oscillate with increasing PR thickness.
- The grain size ratios, [111]/[hkl] vary strongly as the PR thickness changes, and more uniformly for the longer 3.1 whiskers.
- The grain size ratios, [111]/[hkl] ratios, decrease significantly and fairly uniformly as the whiskers lengthen for the longer 3.1series, but not for the shorter WAO-3.3.

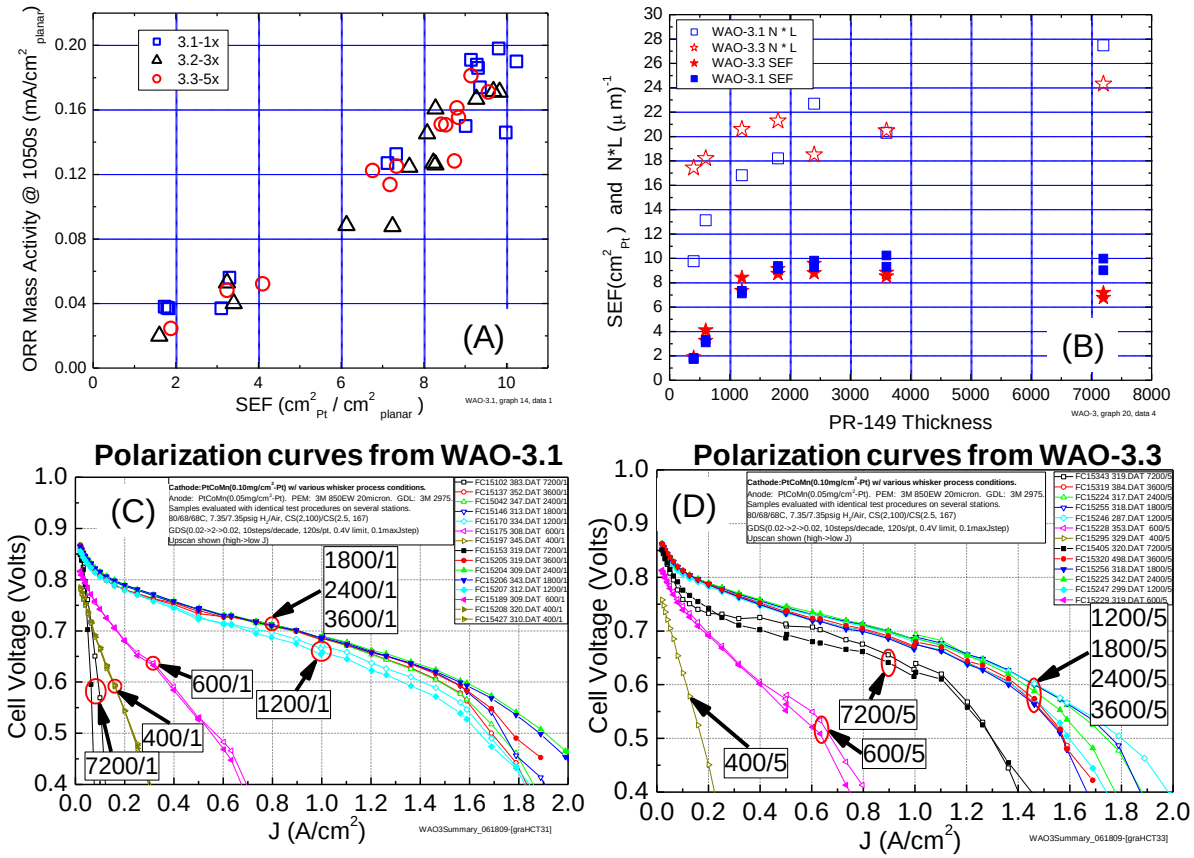


**Fig. 9.21.** (A) ORR mass activity versus the electrochemical Pt surface area enhancement factor (SEF) for the WAO-2.1, 3.2 and 3.3 experiments. (B) SEF and the product N*L as a function of the starting PR149 thickness (arbitrary units). (C) Polarization curves for the WAO-3.1 series of whisker growth for the thickness range of 400 to 7200 units and the growth parameter value number 1. (D) Polarization curves for the WAO-3.3 series of whisker growth for the thickness range of 400 to 7200 units and the growth parameter value number 5.

**9.9. Discovery of a previously unknown fundamental meso-scale property of extended surface catalysts that enables higher limiting currents due to higher surface area per unit volume in the electrode and development of a mathematical model showing it manifested as an additional pre-exponential scaling factor in the Butler-Volmer equation.**

(The accomplishment discussed in this section is discussed in depth in a paper published in the Journal of The Electrochemical Society (23). It is considered one of the key publications resulting from this project and is attached in the Appendix. We try to summarize the results and significance here.)

Commercialization of automotive fuel cells requires current densities of 1.5 A/cm$^2$ above 650 mV with Pt loadings of 0.1 mg$_{Pt}$/cm$^2$ or less. Loss of high current density with cathode loadings below 0.2 mg$_{Pt}$/cm$^2$ in Pt/C electrodes is an issue that current kinetic/transport models are reported inadequate to explain (see references in article attached in the Appendix). In studying these published data for dispersed Pt/C type electrodes, we realized that this effect is much less at a given loading with the NSTF catalyst type electrodes. This is basically because of the fundamentally different geometry of NSTF catalysts and their Pt surface area distribution compared to dispersed carbon supported nanoparticle type catalysts. We were then able to explain these differences using a model based on elementary kinetic gas theory and known molecule/surface interaction mechanisms that take place in the Knudsen regime, i.e. at spatial distances on the order of 80 nm above a catalyst surface within which gas phase collisions are not statistically significant. The oxygen molecule/surface collisions are then the determining factor controlling gas phase trajectories, velocity distributions and chemisorption attempts. The net result of the model is that an additional pre-exponential scaling factor $f(d_s)$ in the Butler-Volmer equation related to a distance metric $d_s$ describing the catalyst surface area distribution:

$$J\left(A/cm^2_{planar}\right) = f(d_s)S\left(cm^2_{Pt}/cm^2_{planar}\right)[i_o(A/cm^2_{Pt})\, p_{O_2}^{\gamma}\,(1-\Theta_{ad})^{x}\exp\left(-\frac{\beta F\eta}{RT}\right)\exp\left(-\frac{\gamma\Delta G_{ad}}{RT}\right)] \qquad (3)$$

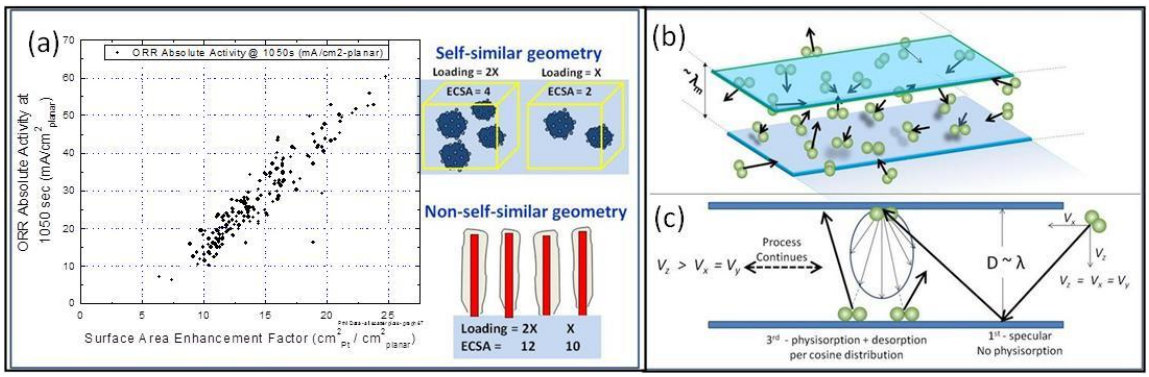


**Figure 9.22.** Two important properties engendered or applicable to the NSTF type geometry. (a) Self- versus non self-similar geometry can impact how the absolute activity varies with surface area. b) and c) Extended surface catalysts can impact the gas velocity distributions in the Knudsen regime within one mean free path of the surface and thereby increase the number of physisorption and chemisorption attempts per unit time (23).

We approximate this distance metric by the inverse of the surface area per unit volume of the electrode and define and test two possible functional forms for $f(d_s)$. The preferred form is able to predict the correct heat of enthalpy for $O_2$ physisorption and the observed ratio of current

densities at V(iR-free) = 0.7 V for NSTF compared to Pt/C dispersed electrodes in the 0.05 to 0.15 $mg_{Pt}/cm^2$ range from published data for eleven different catalyst types and cathode loadings below 0.2 $mg/cm^2$. The model has no adjustable parameters, unlike many more sophisticated MEA models based on CFD and basic transport theory that assume homogeneity down to all levels.

Fig. 9.22(a) illustrates a simple but significant impact of geometry on ORR activity at increasingly reduced loadings. Pt/C dispersed catalysts have self-similar geometries with respect to surface area and loading. That is if the electrode loading in $mg/cm^2$ is changed by a factor of two then the electrochemical surface area is changed by the same factor, all else being the same. NSTF catalysts are not self-similar in this way. If the catalyst loading is changed by a factor of two, resulting in approximately the same change in thickness of the catalyst coating, the surface area is observed to change by a smaller amount that depends on the whisker size and spacing parameters.

In the graph in Fig. 9.22(a) this means the absolute activity change with loading, assuming the specific activity remains unchanged will be a less sensitive function of surface area. As mentioned above the ORR area specific activity is much higher for NSTF catalysts, and this geometric factor contributes as well. The graph in Fig. 9.22(a) illustrates the absolute ORR activity at 900 mV under 1 atmosphere absolute of oxygen as a function of surface area enhancement factor for about 150 NSTF Pt-Ni alloy cathodes, near the unique $Pt_3Ni_7$ composition (30) but differing loadings, degrees and methods of dealloying and post-fabrication annealing. For a doubling in SEF from 10 to 20 $cm^2_{Pt}/cm^2_{planar}$ the absolute activity increases nearly four-fold, from ~ 12 to 48 $mA/cm^2$.

The impact of the higher specific activity is most clearly observed by simply normalizing a fuel cell polarization curve to the Pt electrochemical surface area enhancement factor (SEF). Fig. 9.23 (A) shows this type of plot for a number of NSTF and Pt/C electrode based MEA's as described in detail in (23). The NSTF catalysts appear to be "working much harder" per Pt atom but there is more to the story than just specific activity. We show in (23) that even if the curves in Fig. 9.23 (A) are further normalized to the measured specific activities for the various cathode catalysts, there are still substantial gains from the NSTF electrodes compared to the thicker dispersed electrodes, and these gains increase as the Pt loadings are further reduced.

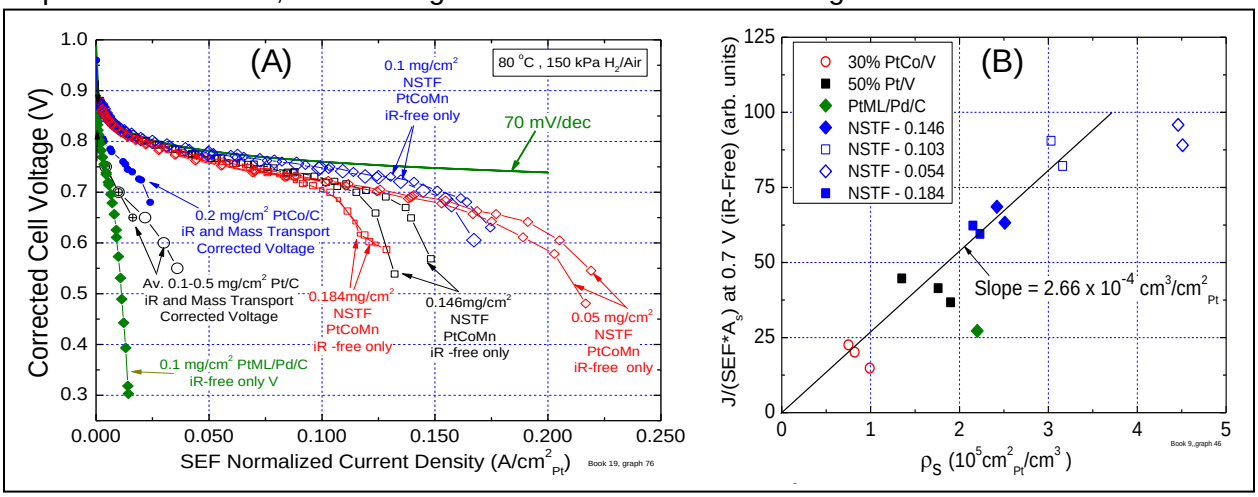


**Figure 9.23.** (A) Galvanodynamic polarization curves of iR-free cell voltage versus current density normalized to the surface area enhancement factor ($cm^2_{Pt}/cm^2_{planar}$) for a series of NSTF and Pt/C based 50 $cm^2$ MEA's with different Pt loadings. The Pt/C cell voltages were also mass transport corrected. (B) Surface area and specific activity normalized current density at 0.7 volts derived from (A), plotted versus the volumetric surface area density, $cm^2$-$Pt/cm^3$ for the seven

types of catalysts, derived from the electrode thickness and the measured or reported surface area enhancement factor values in Table I in reference (23). The least squares fit shown excludes the PtML/Pd/Pt and NSTF-0.054 outliers since the thickness of the former is less accurately known and the iR-free cell voltage for the latter is decreasing due to other factors.

This observation forced us to look for some alternative mechanisms which we attribute to another fundamental geometry difference not previously appreciated before. The mechanisms are dependent on the electrode's surface area per unit volume density ($cm^2_{Pt}/cm^3$) and the ability of the catalyst surfaces' spatial distributions to influence the number of chemisorption attempts per unit time in the Knudsen regime by virtue of their impact on the $O_2$ molecules physisorption precursor events per unit time. The end result is an additional pre-exponential scaling factor in the Butler-Volmer equation that accounts for the impact of those effects on the $O_2$/Pt surface collision frequency. This effect is enhanced by the close-packed nature and parallel orientation of the extended NSTF catalyst surfaces as seen e.g. in Fig. 9.17. These effects combine the statistical physics of ideal gases within one mean free path of the catalyst surface with the impact of Knudsen's cosine law for desorption on their velocity distributions resulting in an enhancement in the collision rate as illustrated in Fig. 9.22 (b,c) for gases between ideal parallel extended surfaces.

Based on these mechanisms we have developed a model to explain the significant difference in current density normalized by both surface area and specific activity, observed between low loaded catalyst electrodes having widely differing volumetric surface area densities, specifically dispersed Pt/C and NSTF electrodes. The model is based on the premises that the average time spent by oxygen molecules in physisorption states plus the mean time in transit between physisorption events determines a surface collision frequency factor that contributes directly to the rate of successful chemisorption and oxygen reduction, and also that the surface area distribution can impact this collision frequency. The rate of physisorption events is related to the gas phase molecular velocities in the Knudsen regime over distances of one mean free path, and a distance metric describing the spatial distance between catalyst surface area sites. Using kinetic gas theory and approximating the distance metric by the inverse volumetric surface area density, we tested two functional forms for a pre-exponential collision scaling factor introduced into the Butler-Volmer equation. The preferred scaling factor is able to satisfy two criteria: i) correct prediction of the desorption heat of 4.77 kCal/mole for $O_2$ from physisorbed states, and ii) prediction of the observed ratio of current densities at 0.7V (iR-free) of published polarization curves from similar MEA's containing eleven Pt/C, PtCo/C and NSTF-PtCoMn cathodes with Pt loadings below 0.2 $mg/cm^2$. The scaling factor was found to have a quadratic dependence on volumetric surface area density and for the fuel cell data used to determine it, numerically ranged from a low of 0.66 to 0.93 for the catalysts having $\rho_s$ in the range of $0.75 \times 10^5$ to $4.5 \times 10^5$ $cm^2_{Pt}/cm^3$. It suggests that electrode surface area densities of at least $3 \times 10^5$ $cm^2_{Pt}/cm^3$ are most desirable to minimize the effect. The enhanced current density for the extended surface area NSTF catalysts is intuitively consistent with the electrode structure's better ability to "entrap" adsorbing oxygen molecules due to the alignment, length to width ratios and spacing of the catalyst coated whiskers in conjunction with Knudsen's cosine law which serves to increase the molecule/surface collision rate per unit time. This concept may not have been considered previously for conventional electrodes and we suggest that a more sophisticated application of the model may be able to partially explain the excessive loss of high current density performance at low loadings seen with conventional Pt/C electrodes.

## 9.10. Discovery and demonstration of significant effects of flow field types on NSTF MEA high current density performances.

The under-performance observed in Task 5.3 of the MEAs in the GM stack compared to the 50 $cm^2$ single cell MEAs suggests there is still a question of the possible impact of flow field differences between the quad-serpentine 50 $cm^2$ cells used at 3M and the flow field design of the GM stack. Flow fields have never before been systematically optimized for the NSTF type ultra-thin electrodes yet can clearly have a strong effect that might not be considered an issue with conventional thick layer electrodes. To establish a baseline of these effects we initiated tests of NSTF MEA's having the same construction as our 2009 best of class in a series of six alternative flow field designs. This was the last major activity of this project. The 50 $cm^2$ flow field graphite blocks were all tested in one set of 3M cell hardware or one set of OEM cell hardware (OEM HW). Figure 9.24 compares the galvanodynamic scan (GDS) polarization curves from six alternative flow fields with the standard quad-serpentine (QS or FF5), completed at the end of this project. As shown there is a large impact of the flow field type on the limiting current density, and several that perform better than our standard quad serpentine. The HFR differences are small and not responsible for the differences when the graphite blocks are all in the same set of 3M Al cell hardware (3M HW). Cathode and anode pressure drops were also measured for the different flow fields, and can explain the high current density performance gain

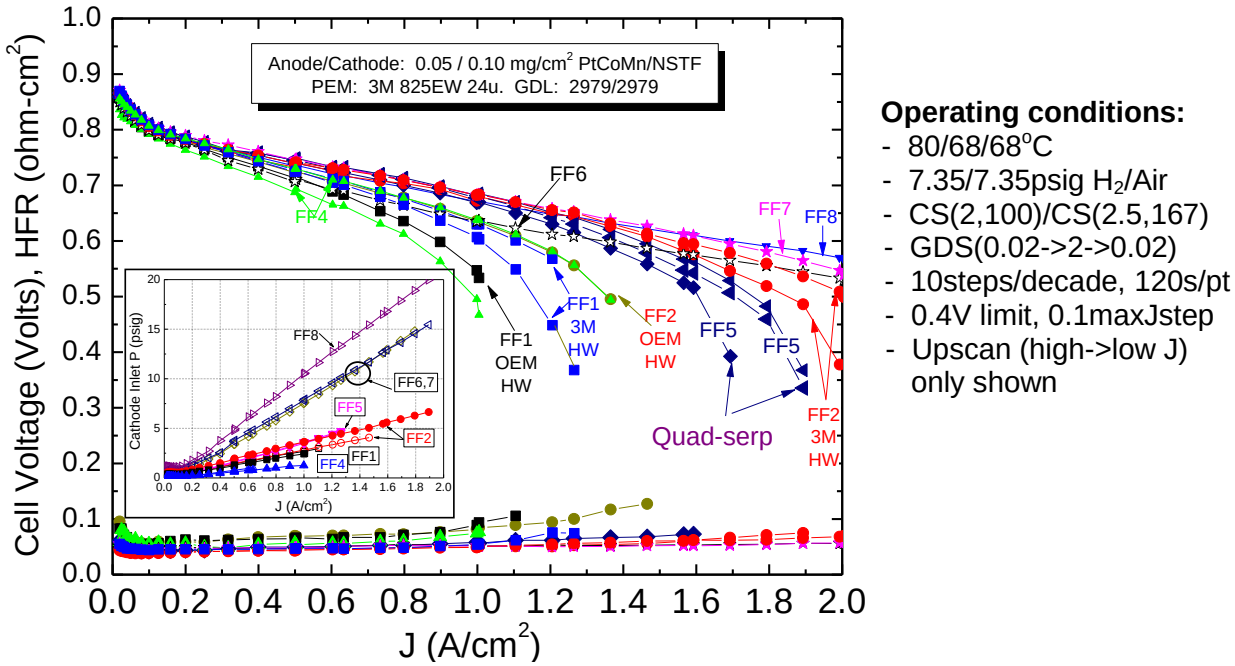


**Fig. 9.24.** Comparison of single cell (50 $cm^2$) GDS polarization curves from the standard quad serpentine flow field (**FF5**) with six alternative flow fields: **FF1** = 6 serpentine channels, 2 loops, 2 mm channel width, 2 mm land width, ~0.3 mm channel depth; **FF2** = 24 serpentine channels, 2 loops, 0.5 mm channel width, 0.5 mm land width, ~0.25 mm channel depth; **FF4** = 9 serpentine channels, 4 loops, 1 mm channel width, 0.6 mm land width, 1 mm channel depth; **FF5** (**quad-serpentine)** = 4 serpentine channels, 10 loops, 0.8 mm channel width, 0.8 mm land width, 1 mm channel depth; **FF6** = single channel 3M Zig-Zag (21); **FF7** = 2 serpentine channels, 21 loops, 1 mm channel width, 1 mm land width, 1 mm channel depth; **FF8** = single serpentine, 43 loops, 0.8 mm channel width, 1.0 mm land width, 1.5 mm channel depth.

with the single channel flow fields FF7 and FF8 relative to the standard FF5. However, the FF2 flow field blocks used in the 3M hardware significantly out-performed the standard FF5 with similar or slightly lower pressure drops. Polarization curves taken using ANL specified test conditions with our 2009 best of class MEA in this FF2 generated 2 A/cm$^2$ at ambient outlet pressure with a stoichiometric flow ratio of two. This is shown in Fig. 9.25. This is a significant result and the first time we have ever obtained 2 A/cm$^2$ at ambient pressure, particularly at a stoichiometric flow ratio of 2 on the cathode. It is notable that the FF2 gain in performance over the QS (FF5) is most dramatic at lower pressures. The three FF types in Fig. 9.25 differ significantly in the number of loops and channels, yet it appears that the land and channel widths are the most significant factor. This suggests that the smaller (0.5 mm) channel and land width dimensions of the FF2 are key to improved performance and a guide to optimizing the flow field for NSTF MEA's.

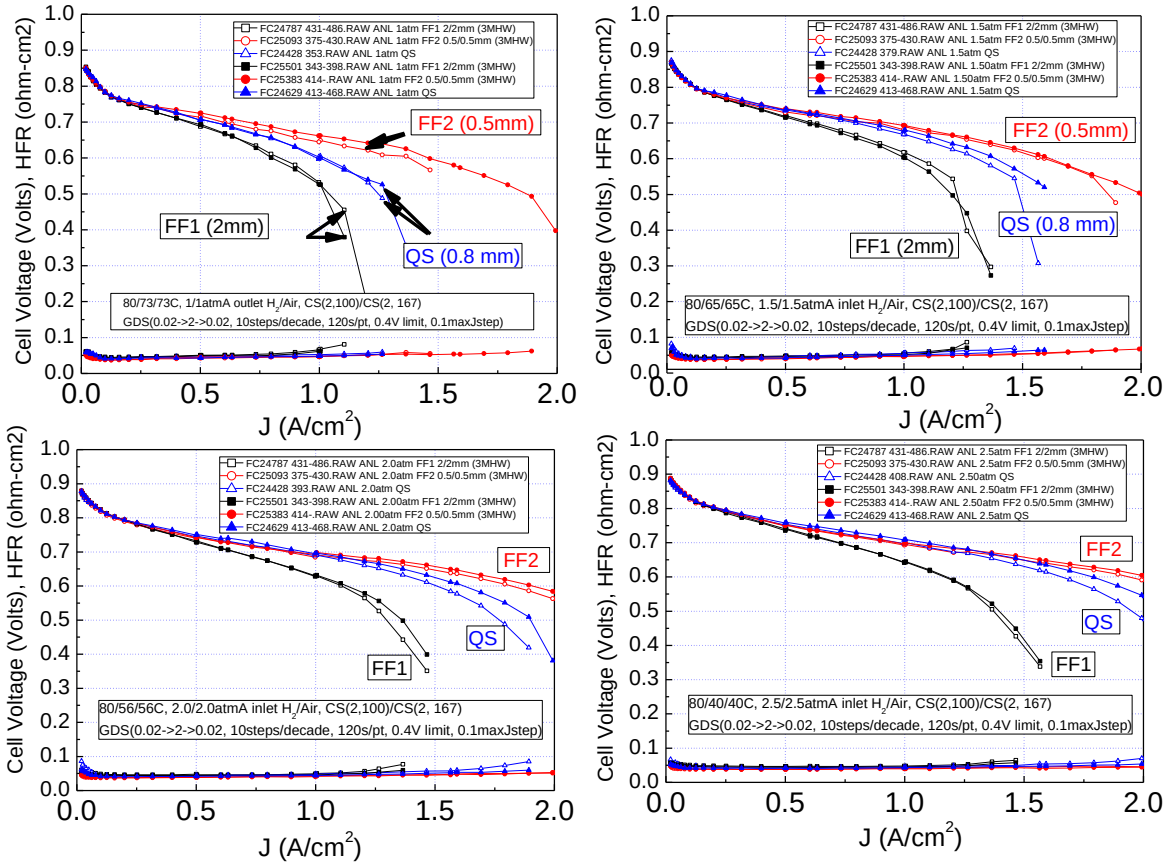


**Fig. 9.25.** Polarization curves under the ANL specified pressure and flow conditions for identical MEA's (2009 NSTF best of class) in three flow fields, showing the effect of pressure and flow field type. QS is the standard quad-serpentine flow field type FF5 in Fig. 6.23.

**9.11. First compositional screening of many new catalyst under-layers and over-layers.**

Dalhousie participated closely with 3M on Tasks 1.1.2, 1.3, 2, and to a smaller degree Task 4, during the first four years of the project. The primary focus was to generate higher activity NSTF catalysts with increased surface area and increased durability. Towards this end they used a unique approach for generating and characterizing new compositional spreads of catalysts in 64 element arrays that could then be electrochemically studied in a 64 channel cell unique to their design (ref.)

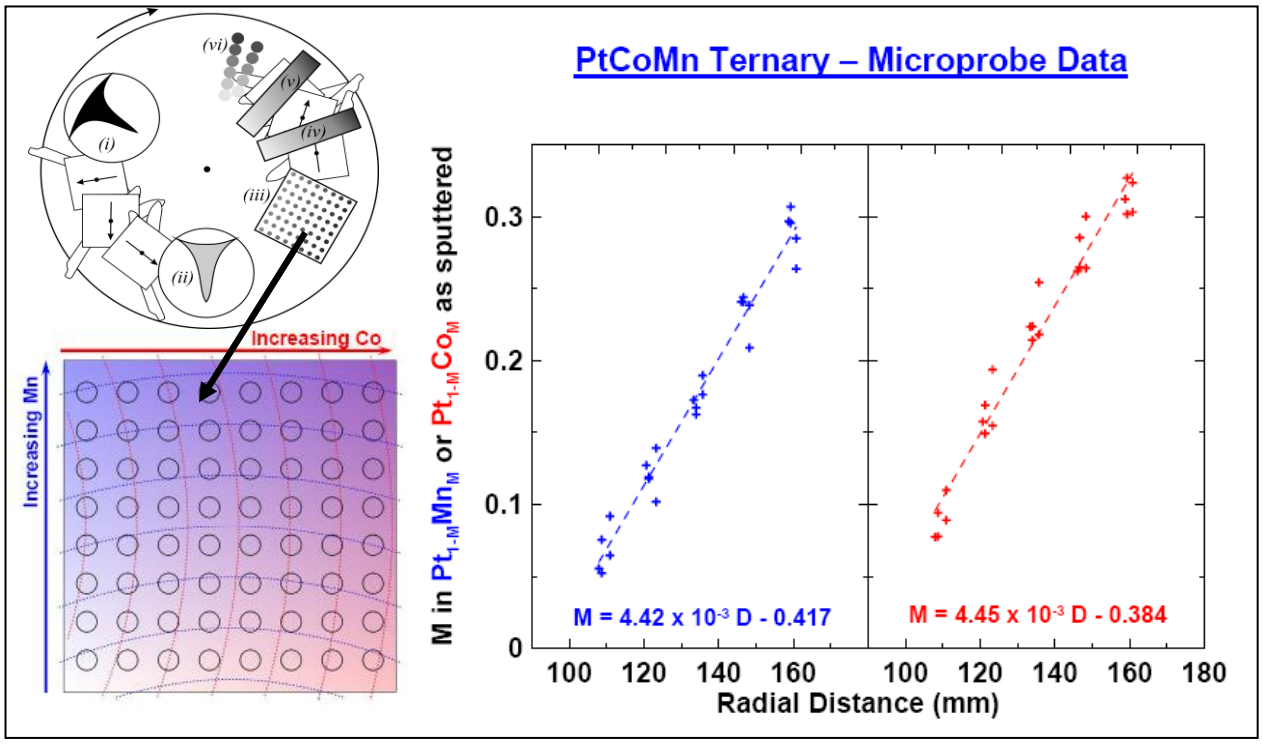


**Fig. 9.26**. (left) Schematic of how Dalhousie coated catalyst compositional spreads of PtM onto 50 $cm^2$ samples of NSTF whiskers provided by 3M. The top diagram shows a plan view of their batch vacuum coater with masks at locations of different sputter target types by which gradient compositions were deposited continuously over the whole sample area. The enlarged array of circles shows positions of electrodes when installed in their 64 channel cell for ECSA and ORR activity measurements. The curved lines represent contours for constant Mn or Co respectively. (Right) Electron microprobe data showing how the atomic percentages of the Mn or Co varied with radial position on the sample array for PtMn (blue) or PtCo (red) binaries.

In our approach, they generated compositional spreads of Pt with various metals and inorganic materials to form new alloys, intermixed layers, inert underlayers, and inert overlayers with the objective to control Pt crystallite grain size, increase surface area, increase specific activity and enhance resistance to Pt corrosion. Key to this approach was that they also used sputter deposition to apply the catalysts to the NSTF whisker supports. 3M supplied rolls of the NSTF standard whisker supports that were then used as substrates for Dalhousie to apply the new catalyst compositional spreads, underlayer and overlayer constructions using the coating methodology illustrated in Fig. 9.26. Multiple sheets of any one type of compositional spread coated onto the whiskers were prepared by Dalhousie at the same time and used for their XRD, electron microprobe and other characterizations. One of each of the compositional gradient spreads of catalyst coated 50 $cm^2$ sheets of NSTF whiskers were then returned to 3M for

transfer to a membrane to form the cathode of a catalyst coated membrane. These CCM's were then returned to Dalhousie for fuel cell testing in their 64 channel cell. This process worked extremely well despite the involved sounding supply chain. For specific compositions chosen for more detailed study at 3M, Dalhousie coated the desired composition onto the entire 50 $cm^2$ area and returned it to 3M where it was made into a CCM for characterization in 3M's single cells. Near the end of the project, 3M also grew whiskers directly onto glassy carbon disks received from Dalhousie, where they were subsequently coated by catalysts and studied by RRDE methods. In total approximately 200 MEA's were made with compositional spreads from Dalhousie and evaluated in their 64 channel cells or in 3M 50 $cm^2$ cells. For each sample array, composition at 64 positions was measured as a function of position by electron microprobe analysis, and crystallite grain sizes by XRD. From the 64 channel cell, cyclic voltammograms as a function of position provided measures of Pt surface area at the beginning of life, stability of the surface area with cyclic voltage cycling accelerated stress tests, and relative measures of fuel cell ORR polarization curves. Extracting ORR activity from the multi-channel cells turned out to be more difficult than first envisioned, in part due to "cross-talk" between adjacent sampling sites from the common anode electrodes.

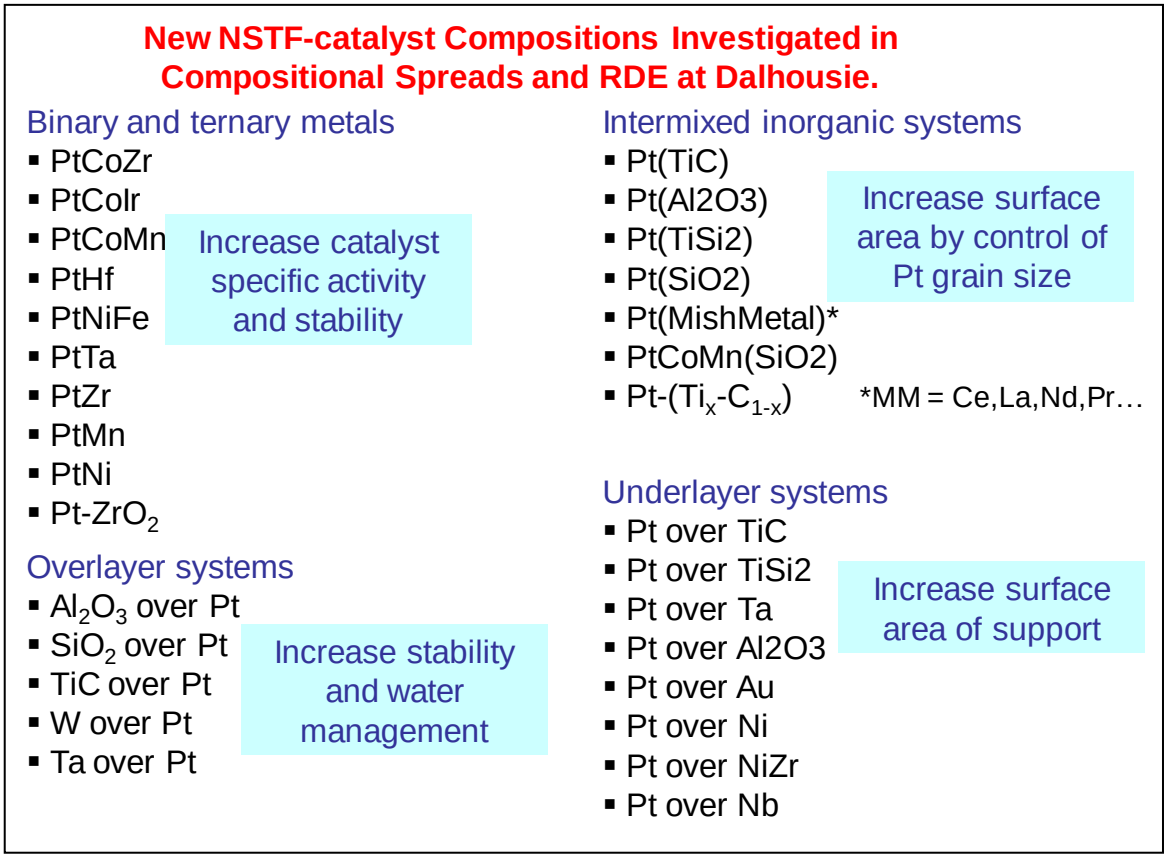


**Fig. 9.27.** New catalyst compositions investigated with Dalhousie, prepared as compositional spread arrays coated onto NSTF whiskers and characterized in their 64 channel cell. For the overlayer systems, the coating was applied after the Pt was sputtered onto the whiskers. The intermixed inorganic systems and the binary and ternary metal alloys were deposited in multi-layer constructions of the component materials. The non-Pt underlayer components were deposited onto the whiskers before the Pt.

Fig. 9.27 lists the new catalyst compositions investigated with Dalhousie, prepared as compositional spread arrays coated onto NSTF whiskers and characterized in their 64 channel cell as described above. Four types of catalyst coating constructions were investigated for different possible end results. Although perhaps counter intuitive, for the overlayer systems, the coating was applied after the Pt was sputtered onto the whiskers, with the objective to look for any increased stability or different water management behavior. The intermixed inorganic systems and the binary and ternary metal alloys were deposited in multi-layer constructions of the component materials with the goal to look carefully for any impact on ORR activity or crystallite grain size stability. The non-Pt underlayer components were deposited onto the whiskers before the Pt with the objective to explore any effect of increased surface area of the support whisker by "fattening" it. In this respect this latter sample category fit the objectives of Task 4. Fig. 9.28 illustrates just some of the data output from the Dalhousie work for one example of the list in Fig. 9.27.

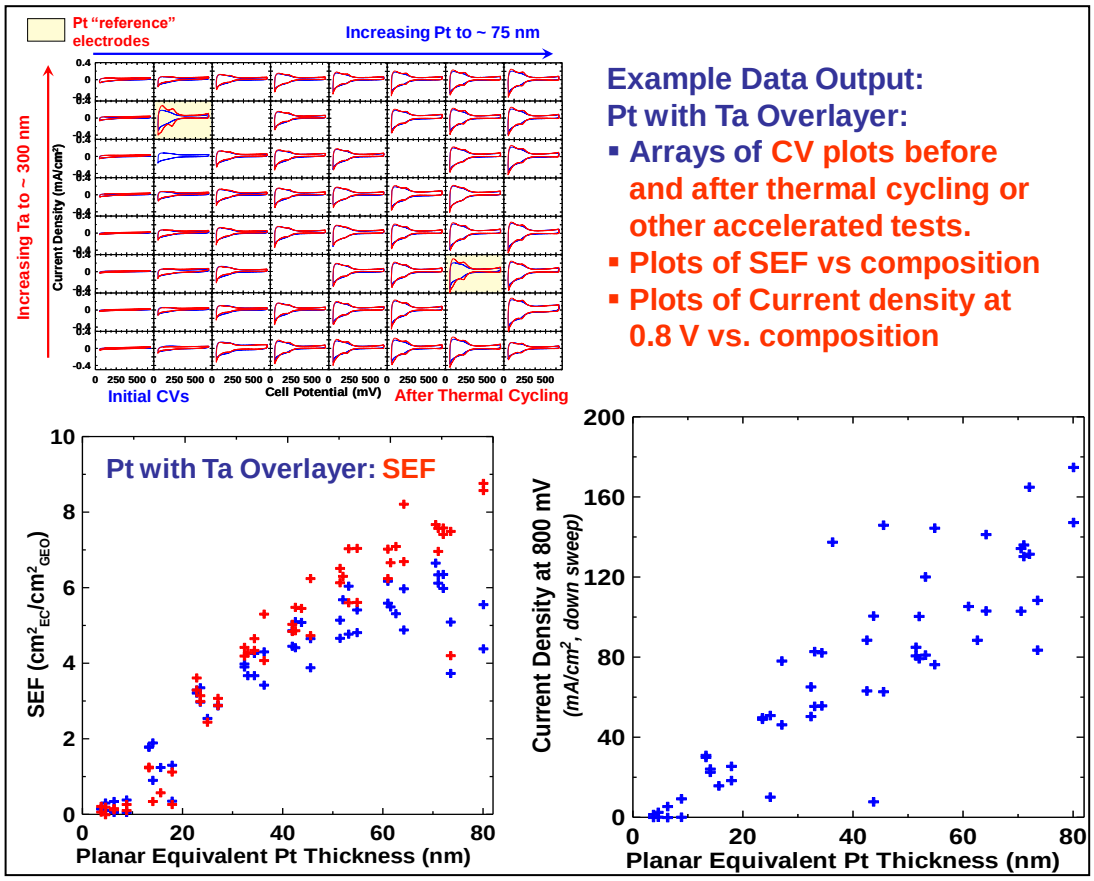


**Fig. 9.28.** Example of data output from the Dalhousie 64 channel cell for a Pt with Ta overlayer spread. Top left shows the array of cyclic voltammograms before and after thermal cycling. Bottom left shows the SEF versus Pt thickness extracted from the CV arrays above it. Bottom right shows the current density at 0.8 V as a function of Pt thickness extracted from polarization curves obtained with each of the 64 channels.

Finally, we conclude with an incomplete summary example in Fig. 9.29, of how the four categories of new catalyst constructions identified in Fig. 9.27 were evaluated with respect to a number of important characteristics relevant to fuel cell performance and durability.

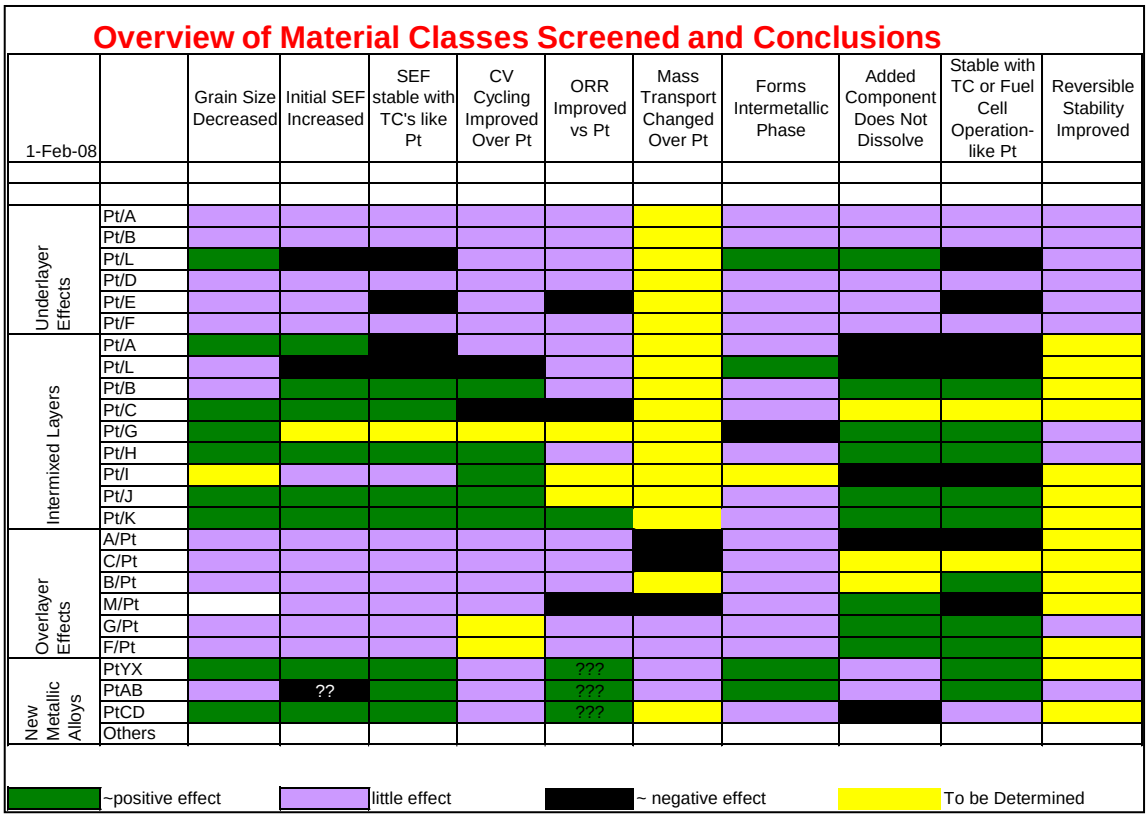


**Fig. 9.29.** Example of relevant fuel cell properties for the four categories of catalyst constructions listed in Fig. 9.27 that were extracted from the 64 channel compositional spread studies done at Dalhousie University.

Much was learned from these in-depth and first of their kind catalyst constructions and analyses, and significant amounts of it has already been published in references (28 - 38). However, no dramatic improvements in catalyst performance was found with the exception of the PtNi series which were done after discovery of and in conjunction with the $Pt_3Ni_7$ alloy work at 3M. Four of the Dalhousie originated journal articles are considered significant and have been included in the Appendix.

**9.12. Development of an experimental path forward to potentially realize the "entitlement" activity of NSTF alloy catalysts.**

Advances in PEM fuel cell electrocatalyst activities have been significant in the past few years. Five key concepts leading to these improvements included use of PtNi alloys; modulated surface composition and lattice strain; extended surface area catalysts; controlled de-alloying; and core-shell catalysts (9). As shown by Stamenkovic et al. (40) of ANL, the $Pt_3Ni_1$ system is unique in showing the highest ultimate potential ORR activity in bulk single crystal RDE measurements, with specific activities that are reported to be 90 times that of state-of-the-art Pt/C catalysts. This is illustrated in the graph portion of Fig. 9.30, a diagram prepared by V. Stamenkovic of ANL to compare their RDE specific activity measurements of various polycrystalline Pt alloys with that of the $Pt_3Ni_1(111)$ single crystals and commercial Pt/C catalysts. Key to this high kinetic activity is the formation of large area flat fcc[111] facets on the surface with a modulated surface composition in the top three surface layers. Also included on the graph are their measured values of the NSTF PtCoMn, NSTF PtNi and hydrogen annealed NSTF PtNi values (red star).

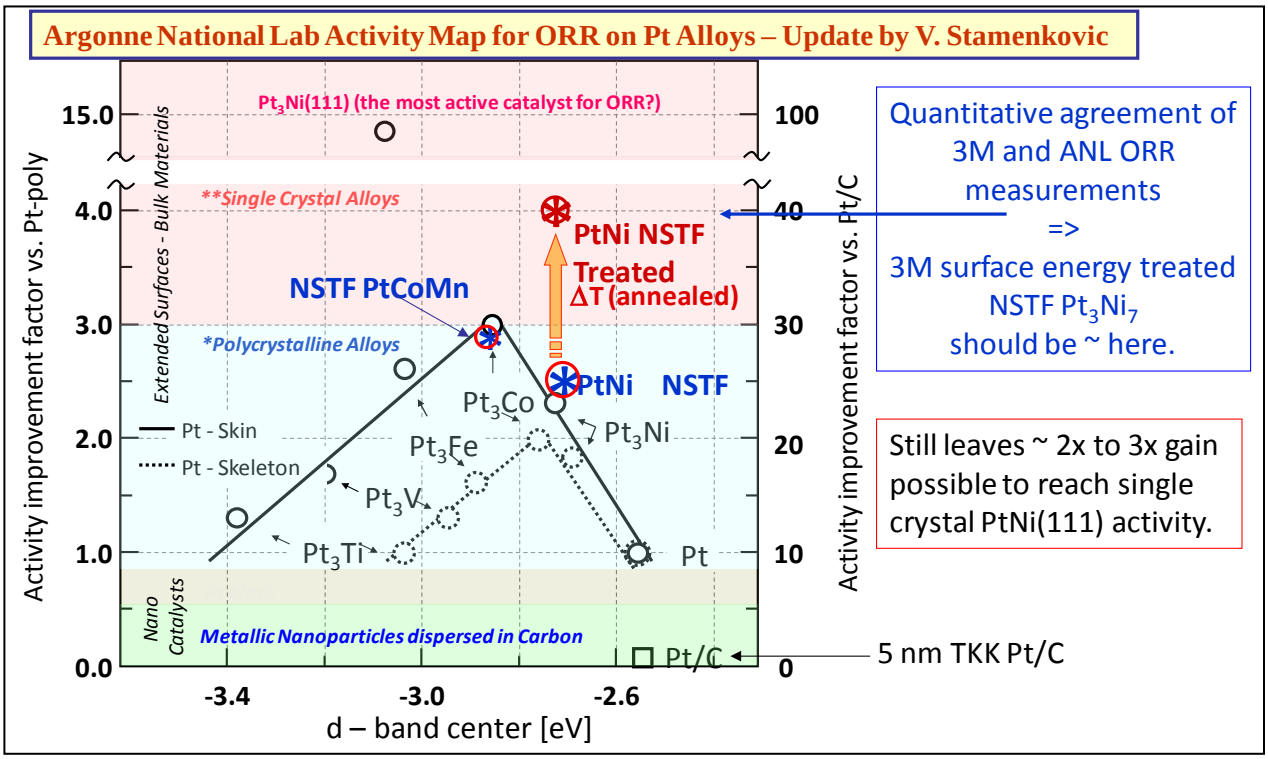


**Fig. 9.30.** Specific activity improvement factors via RDE measurements by ANL of various alloys with Pt skin or Pt skeleton bulk surfaces, over Pt/C catalysts. Also shown are their measured values of the NSTF PtCoMn, NSTF PtNi and hydrogen annealed NSTF PtNi values (red star).

Because of the good quantitative agreement between their RDE and our MEA ORR activity measurements as shown in Fig. 5.2, we have projected that our SET treated and dealloyed $Pt_3Ni_7$ catalysts' activities (see e.g. Fig. 7.1 and Table 3) would also correspond to the level of the arrow shown in Fig. 9.30. This would mean that there could potentially be a factor of 2x to 3x further gain in activity to be realized in the optimum NSTF electrodes in order for their activity to reach that of the bulk single crystal $Pt_3Ni_1(111)$ surface.

How we believe it should be possible to achieve those last remaining gains is illustrated in Fig. 9.31.

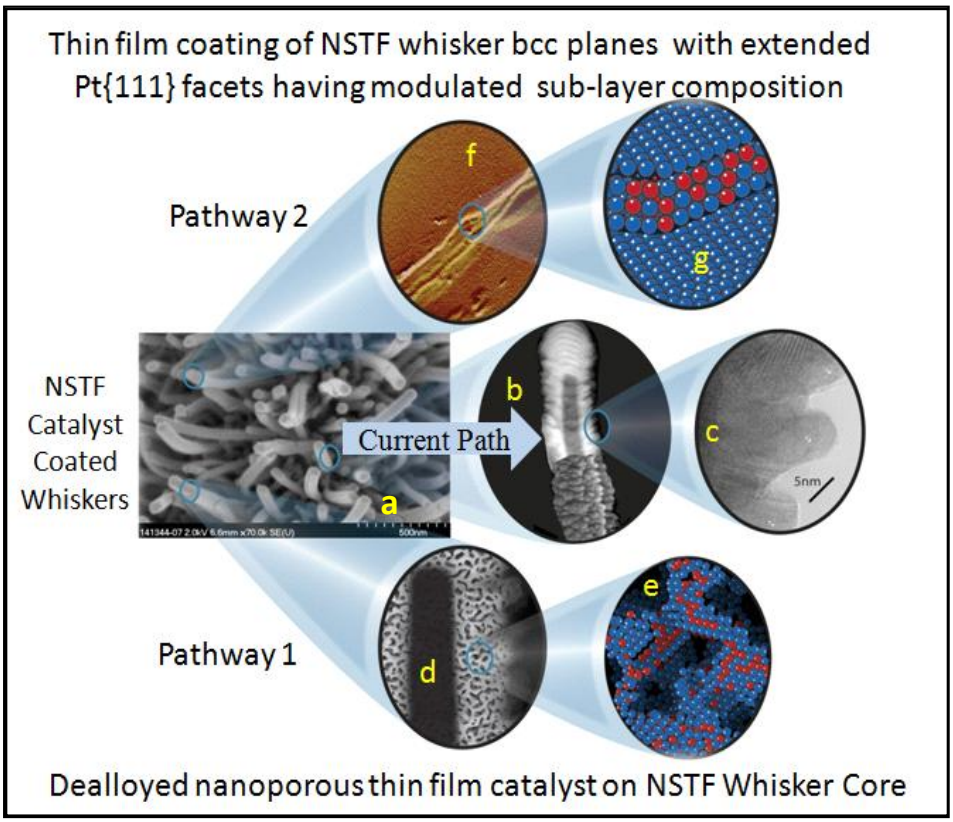


**Fig. 9.31.** Illustration of two NSTF catalyst advancement pathways combining several of the most promising catalyst concepts in practice today; (a, b, c) shows the current status with NSTF as-made whiskerette surface morphology. (d, e) show pathway 1 using optimized *ex-situ* de-alloying to increase the surface area while maintaining alloy activity gains. (f, g) show pathway 2 on which the alloy coating morphology on the body-centered crystalline lattice of the NSTF whisker core is optimized like bulk single crystalline $Pt_3Ni_1$ with modulated surface composition in the outer three layers.

Fig. 9.31 illustrates two possible NSTF advanced pathways for incorporating all five of the electrocatalyst concepts mentioned at the start of this section. The whiskerette structure illustrated in inset (c) of Fig. 9.31, is the result of the current pathway and is probably not the best due to the large number of un-coordinated Pt surface atoms on the small [111] facets.

Pathway 1 in Fig. 9.31 with controlled dealloying of high Ni containing Pt alloys has already been pursued in this project as discussed in Section 9.3, to the point of having successfully developed roll to roll dealloying, with significant gains in activity and surface area of the $Pt_3Ni_7$ alloy. However we do not know that the resulting dealloyed catalyst is optimized as proper *ex-situ* dealloying methods are necessary to obtain the ideal nanoporous structure and composition of the NSTF-PtNi catalyst surface so that it retains the high surface area and develops the modulated composition in the outer surface layers necessary for proper surface lattice strain and d-band structure also believed critical to generating high specific activities (ref (39). Fig. 9.32 shows recent TEM HAADF images obtained by ORNL of samples of the SET and dealloyed NSTF $Pt_3Ni_7$ electrodes from tested CCM's that we provided to them. They show

clearly that the catalyst coatings on the whiskers are highly porous, and no doubt a strong contributor to the large gain in surface area we achieved with this unique alloy.

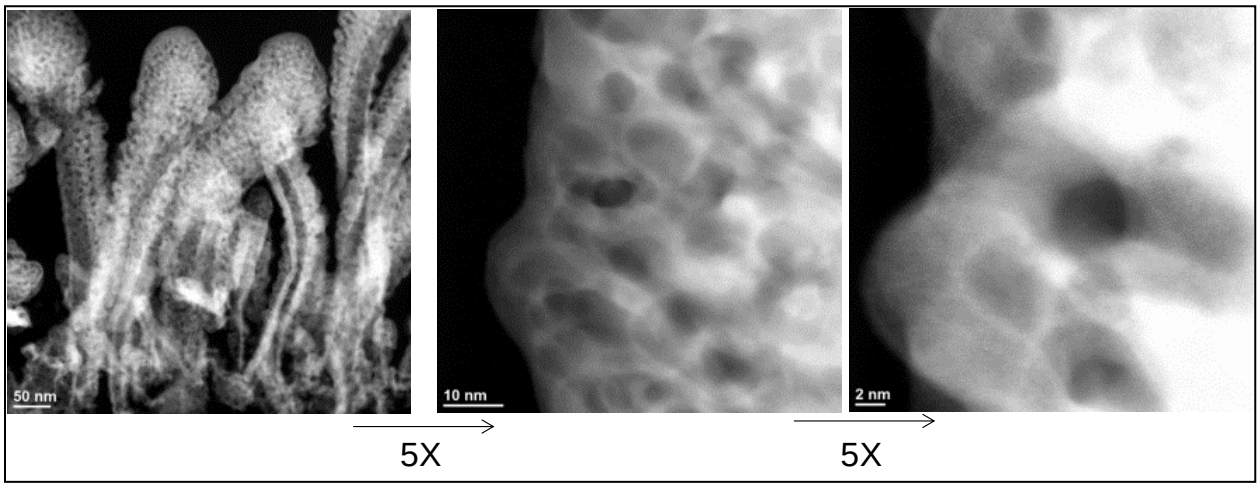


**Fig. 9.32.** TEM HAADF images of whiskers in the cathode of a fuel cell CCM after break-in conditioning. The catalyst coating the whiskers was dealloyed, SET treated NSTF $Pt_3Ni_7$ as discussed in Section 7.4 and Fig. 7.2 The scale of the images increases by 5x from left to right for each pair. (Images courtesy of David Cullen **o**f ORNL)

Surface facets are evident at the 2 nm scale resolution in the right-most image of Fig. 9.32. By EDS the dealloyed composition is ~ $Pt_{62}Ni_{38}$. ORNL also reports that there is evidence of Pt skin seen in the highest magnification TEM images which could account for some of the ORR specific activity gain we measure with this unique $Pt_3Ni_7$ catalyst. It is still not known, however if the surface composition of the topmost layers is modulated as is believed to be important for the ANL $Pt_3Ni_1$(111) single crystal surfaces that set the standard for most active surfaces, or if the dealloying is optimum.

Another, even more intriguing pathway potentially feasible is pathway 2 illustrated in Fig. 9.31 by insets (f, g). Inset (g) is drawn to represent large, flat (111) surface facets on the coatings of $Pt_3Ni_1$ catalyst encapsulating the NSTF whisker cores which have the ideal surface composition modulation like that matching the $Pt_3Ni_1$(111) single crystal results. If the PtNi alloy coating on the NSTF whiskers can be made to model that of the single crystal $Pt_3Ni_1$(111) surfaces, with negligible uncoordinated surface Pt and nearly 100% (111) facets, the activity would presumably be optimum. We do not know if this is possible or not, as the surface energy of Pt is very high, unlike for Au which easily forms large flat facets in vapor deposited films applied to the NSTF whiskers.

## 9.13. Study of the water and PEM impurity effects on low ECSA catalysts

Impurities, from sources either external to the MEA and its catalysts (water, air) or internally generated (PEM decomposition) can seriously affect the MEA performance, usually from direct contamination of the catalyst surface. The first in-depth studies of the effects of externally doped impurities on the NSTF MEA performance (reversible and non-recoverable decay) were completed near the beginning of the project. The standard NSTF MEA at that time had 0.2 mg/cm$^2$ of PtCoMn on both the anode and cathode. These were tested for sensitivity to chloride and sulfide anions at concentrations of tens of micromoles per liter, introduced into the humidification water (supplied as liquid via chromatography pumps.) Desorption of the adsorbed impurities can be generally accomplished by simply thermally cycling the MEA (effectively a cooled shut-down of the cell with flowing clean water moving through the cell and a restart, all repeated three or four times.). This allows cell recovery for the most part, but after multiple such exposures and recoveries, there is some permanent, non-reversible decay observed. Comparative studies were also completed for MEAs having standard Pt/C catalyst electrodes with 0.2 and 0.4 mg$_{Pt}$/cm$^2$ loadings. These studies have been reported in depth in publications in ECS Transactions and are included as numbers four and five included in the Appendix. The following few figures and discussion however illustrate and summarize the main conclusions of this impurity effects study.

Fig. 9.33 illustrates the performance over time of NSTF-PtCoMn (0.2mg$_{Pt}$/cm$^2$), with deionized water (DI) (left column), versus 20 µM HCl (middle column), and 20µM $Na_2S$ (right column) added to the water. The top row shows current density at 0.7 V versus time. The middle row shows the decay and recovery by thermal cycling, and the bottom row shows the initial, poisoned and then recovered polarization curves.

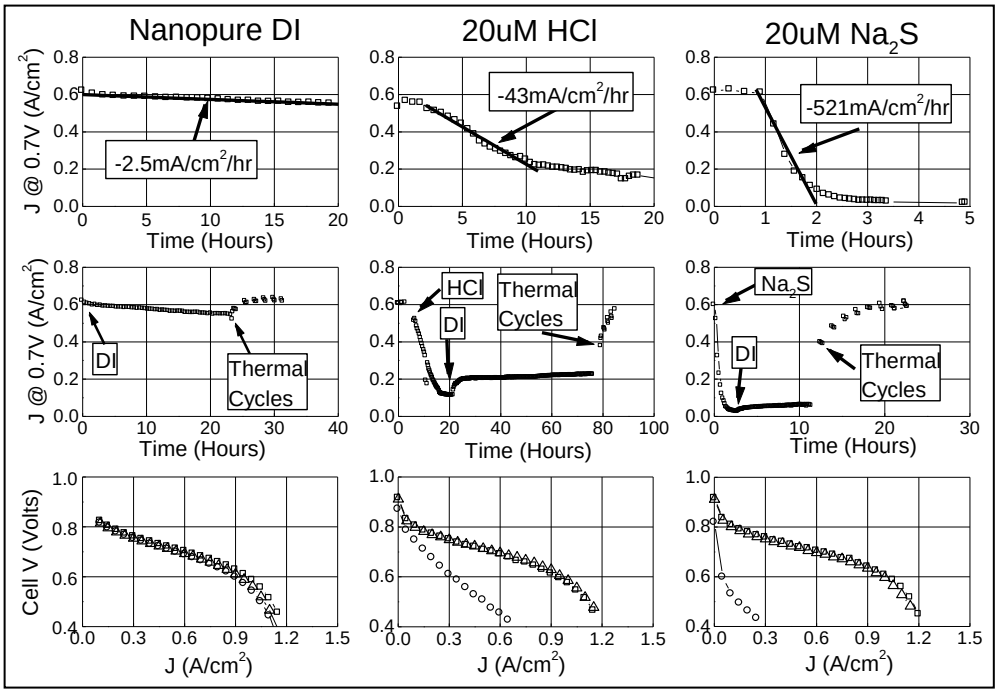


**Fig. 9.33**. Examples of polarization curve performances over time as a result of exposure of the MEA's to HCl and $Na_2S$ added to the inlet humidification water.

In general, the effect of the $Na_2S$ is much worse than the HCl, but complete recovery of the cell performance is possible with the simple thermal cycles.

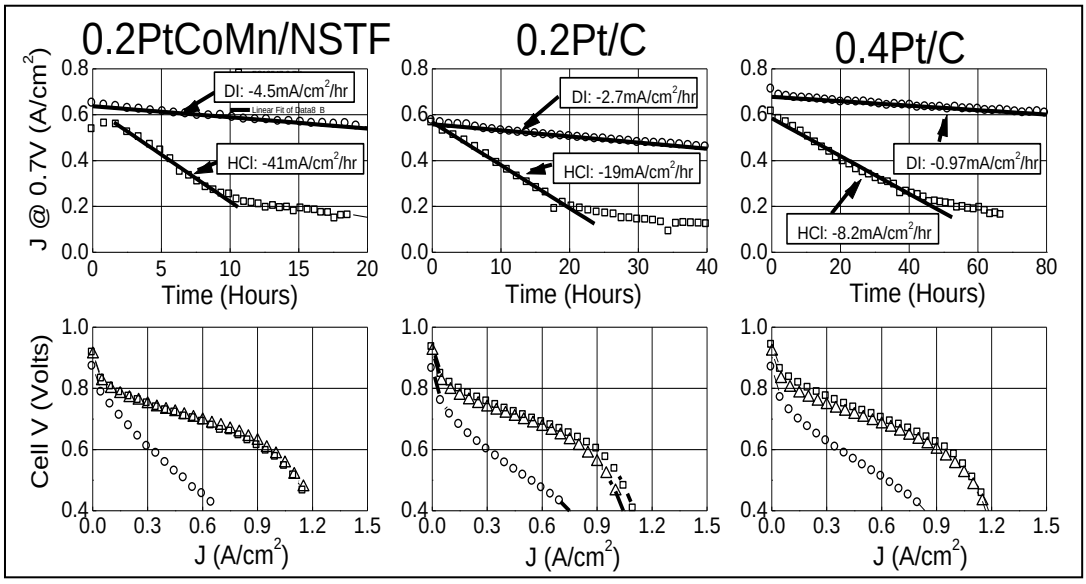


**Fig. 9.34.** Examples of polarization curve performances from Pt/C and NSTF based MEA's over time as a result of exposure of the MEA's to 20 μM HCL added to the inlet humidification water.

Fig. 9.34 compares the effect of 20μM HCl on polarization curve performances from Pt/C and NSTF based MEA's over time. The $Cl^-$ ions cause performance of both catalyst types to rapidly decay. Table IV summarizes the NSTF and carbon supported dispersed Pt (Pt/C) electrodes' current density reversible decay rates due to doping the fuel cell inlet water with 20 μM $Cl^-$ ions. NSTF decays faster than the Pt/C but has many times lower surface area. All decays can be recovered to some extent, but more so for the NSTF MEA's. All MEA's show some reversible decay even on nanopure water.

**Table 4.** Summary of reversible decay rates and initial current density for MEAs operated with either DI or 20μM HCl humidification solution. The number in parentheses indicates the number of MEAs evaluated.

| Catalyst (# of MEAs) | Humid. Solution | Current Decay Rate @ 0.70V ($mA/cm^2/hr$) | Initial J @ 0.70V ($mA/cm^2$) |
|---|---|---|---|
| 0.2Pt/C (5) | DI | -2.0± 0.7 | 597±42 |
| 0.2Pt/C (4) | 20μM HCl | -18±3 | 610 ±23 |
| 0.2PtCoMn/NSTF (12) | DI | -4±2 | 611 ± 27 |
| 0.2PtCoMn/NSTF (5) | 20μM HCl | -63±27 | 596±31 |
| 0.4Pt/C (2) | DI | -0.5 ± 0.1 | 702 ±12 |
| 0.4Pt/C (1) | 18.6μM HCl | -8.96 | 610 |

Table 5 summarizes the effect of exposure and recovery of NSTF and Pt/C MEA surface areas to the 20 μM HCl just discussed. To within statistical variability of surface area measurements, the NSTF surface area loss from chloride (and sulfide) adsorption is essentially

recoverable. The NSTF surface area losses are ~ 0% to 10% respectively. The 0.2 and 0.4 Pt/C cathodes lose ~ 30% and 50% of their surface area respectively. Non-reversible performance loss appears to be primarily due to permanent loss of surface area.

**Table 5.** Variation in cathode Pt Surface area Enhancement Factor (SEF) in initial, poisoned, and recovered state for the 0.2PtCoMn/NSTF, 0.2Pt/C, and 0.4Pt/C MEAs from Fig. 9.34. SEF values are ± 10% or ± 1, whichever is larger.

| **Catalyst** | **Initial SEF ($m^2$-Pt/$m^2$-geo)** | **Poisoned SEF ($m^2$-Pt/$m^2$-geo)** | **Recovered SEF ($m^2$-Pt/$m^2$-geo)** |
|---|---|---|---|
| 0.2PtCoMn/NSTF | 10.6 ± 1.1 | 9.0 ± 1 | 9.8 ± 1 |
| 0.2Pt/C | 75 ± 8 | 44 ± 4 | 51 ± 5 |
| 0.4Pt/C | 150 ± 15 | 63 ± 6 | 70 ±7 |

Following the above studies, the effect of the $Cl^-$ ion concentration was shown to be directly proportional to surface area. Fig. 9.35 (Left) shows the cell current density at 0.7 V response of the 0.2 $mg_{Pt}/cm^2$ Pt/C MEA's to a series of HCl-doped water levels from 0 to over 1000 μM.

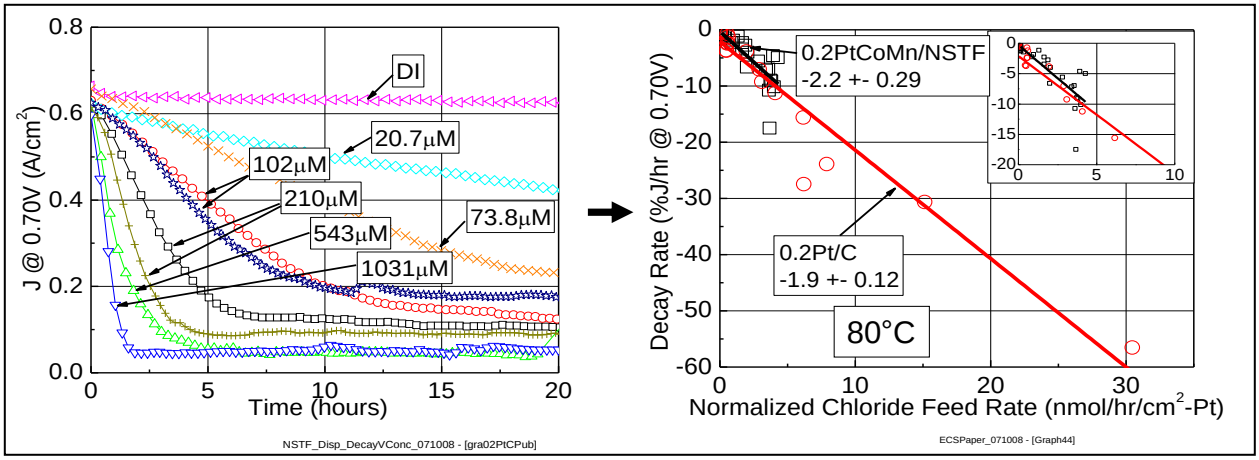


**Fig. 9.35** (Left) Cell response of current density at 0.7 V to the 0.2 $mg_{Pt}/cm^2$ Pt/C based MEAs to a series of HCl-doped water levels. 20 μM = 0.71 ppm. (Right) Decay rates plotted versus the surface-area-normalized chloride ion feed rates.

The graph on the right in Fig. 9.35 plots the decay rate data versus the surface-area normalized chloride ion feed rates, showing a common slope for both types of electrodes. It is apparent that chloride, provided to the fuel cell via the humidification water at micro molar concentration dramatically increased the rate of reversible performance decay for MEAs with 0.2 mg/$cm^2$ Pt/C (above left) electrodes, as it did for the 0.2 $mg_{Pt}/cm^2$ PtCoMn/NSTF electrodes. With identical operating conditions and $Cl^-$ concentration, the reversible decay rate of the Pt/C MEAs decreased **~7x** more slowly than the NSTF MEAs. Fig. 9.36 (right) shows the decay rate in percentage current density loss, extracted from the left figure, plotted versus the surface area-normalized chloride feed rate in nano-Moles per hour per $cm^2$ of Pt surface area. Normalizing to the Pt surface area accounts for the ~7x difference in catalyst surface area between the MEA types, and the reversible performance decay rate increase with SEF-

normalized chloride feed rate was very similar for both the NSTF and Pt/C electrode types. The universal line slope gives a decay rate sensitivity factor of ~2% current density (J) lost per (nmol $Cl^-$ fed per $cm^2$-Pt).

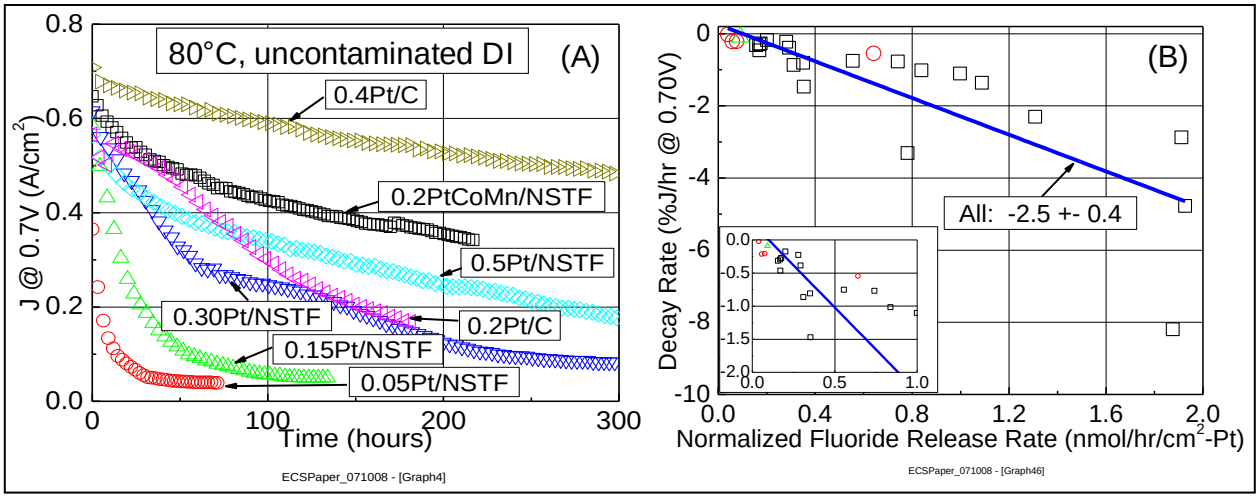


**Fig. 9.36.** (A) Current density at 0.7 volts versus time for various NSTF and Pt/C electrode based MEA's when exposed to just the incoming nominally pure DI water. (B) Decay rates from graph A versus the surface-area-normalized fluoride ion release rates measured in the cell exit water.

So it is very clear that the effect of $Cl^-$ contamination can be simply understood as due to adsorption and poisoning of the Pt surface, regardless of the catalyst type. But even with nominally pure inlet water, there is reversible decay. Fig. 9.36 (A) shows how the current density at 0.7 volts versus time varies for various NSTF and Pt/C electrode based MEA's when exposed to just the incoming nominally pure DI water. The decay rates vary substantially with the catalyst loading and surface area. Again all the data suggest a worsening decay rate with lower surface area for a given catalyst type, even with nominally pure DI. But the performance decay rate data variations between catalysts types cannot be explained by just external low-level residual contaminants, as the variation could not be explained by surface area alone. This is clearly seen in Fig. 9.36 (A) where the MEA with 0.2 mg/$cm^2$ Pt/C electrodes, with 7x higher SEF, decayed faster than 0.2 mg/$cm^2$ PtCoMn/NSTF electrodes. So something internally generated as an adsorption impurity has to be considered. The decay rate data can be explained by normalizing to Pt surface area and the internal production rate of fluoride ions measured in the exit water. The $F^-$ ion rates vary with catalyst surface area, composition, and support type, and can be up to 1000 times less for NSTF vs Pt/C catalysts (22). Fig. 9.36 (B) plots the percent current density (at 0.7 V) decay rates versus the surface-area-normalized fluoride ion release rates measured in the cell exit water. $F^-$ itself is not a contaminant, but rather is a correlated indicator to one or more internally-generated species, such as PEM decomposition products. Different PEMs (e.g. 3M 1000EW v. Nafion™ 112), with all other components fixed, caused the "$F^-$" decay rate sensitivity factor to vary up to 4x, likely due to differences in PEM decomposition (different species produced per unit $F^-$ ratios). Identifying the exact composition(s) and chemical nature of these internally generated (likely membrane decomposition products) is a key need to reduce the reversible decay at low catalyst loadings.

With 0.2 mg/$cm^2$ PtCoMn/NSTF + 3M 1000EW PEM MEA's, the absolute decay rate due to the internally-generated species was measured and found to increase super-linearly with operating temperature, while the $F^-$ production rate also increased. The decay rate temperature sensitivity was found to be linear with temperature, increasing to 0.1% per °C above 62°C and zero below this temperature. Limited data from the earlier $Cl^-$ studies suggested a minimum

sensitivity temperature of ~28°C with 20μM $Cl^-$ and a lower rate of increase with temperature than the internally-generated ($F^-$ ion) species.

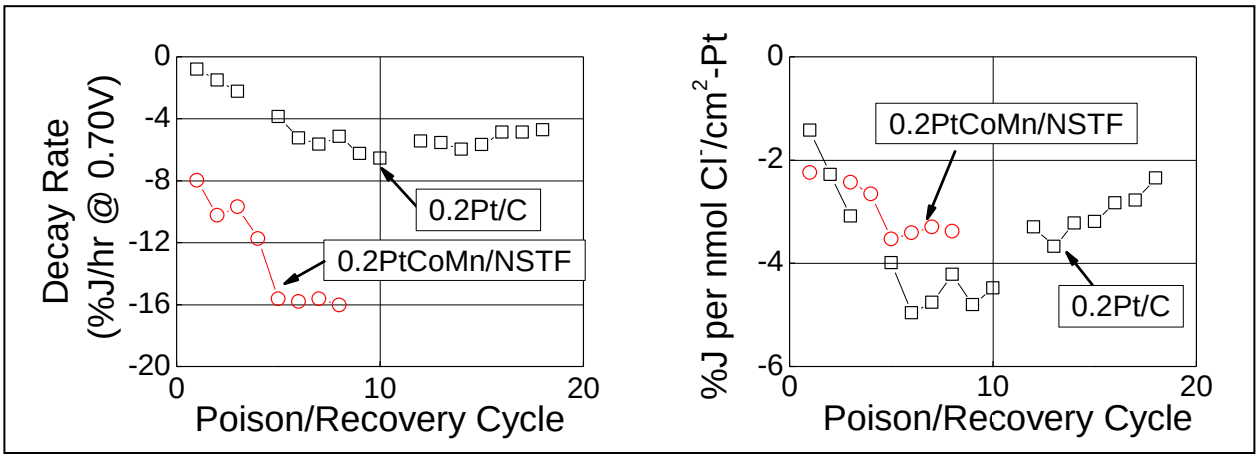


**Fig. 9.37.** Effect of repeated $Cl^-$ ion poisoning and recovery cycles on both Pt/C and PtCoMn/NSTF electrodes at same 0.2 $mg_{Pt}/cm^2$ loading.

Finally, the impact of multiple exposures to poisoning with Cl- ions and subsequent recovery was evaluated. Repeated poison/recovery cycles with 20μM $Cl^-$ caused the absolute decay rates of both 0.2 $mg/cm^2$ PtCoMn/NSTF and 0.2 $mg/cm^2$ Pt/C MEA's to increase, as shown in Fig. 9.37. Both MEAs' decay rate sensitivity factors increased with repeated cycles, but the Pt/C MEAs' rate and extent of sensitivity increase was larger, due to the Pt/C MEAs' 2x and 3x larger rate and extent of surface area loss with poison/recovery cycles. Identical experiments with DI confirmed that 20μM $Cl^-$ did not increase the rate of surface area loss for either MEA.

### 9.14. Dependence of limiting current on ECSA

Traditionally, surface area is only considered to affect the kinetics. In 2010, we identified a correlation between cathode absolute surface area and $H_2$/Air limiting current density for MEA's with Pt/NSTF and PtCoMn/NSTF cathodes. Limiting current density was observed to decrease monotonically with Pt loading and hence surface area, below a certain threshold. This impact on the fuel cell polarization curves is shown in Fig. 9.41. Over time we observed that the trend holds for beginning of life MEA's and for MEA's even after several types of durability tests which led to surface area loss, as shown in the right side plot in Fig. 9.38.

In the plot on the right side of Fig. 9.38, the current density value at 0.5 V (one metric for the limiting current density) appears to stop increasing with the cathode Pt surface area above about 8 or 9 $cm^2_{Pt}/cm^2_{planar}$. This is presumably is because some other factor is limiting this fuel cell performance metric rather than surface area. One example is the type of flow field such as discussed in Section 9.10. The significant gain in high current density provided by the flow field type FF2 in Figs. 9.24 and 9.25 would suggest that with such a flow field, the plot on the right side of Fig. 9.38 would continue to increase with SEF before again flattening out.

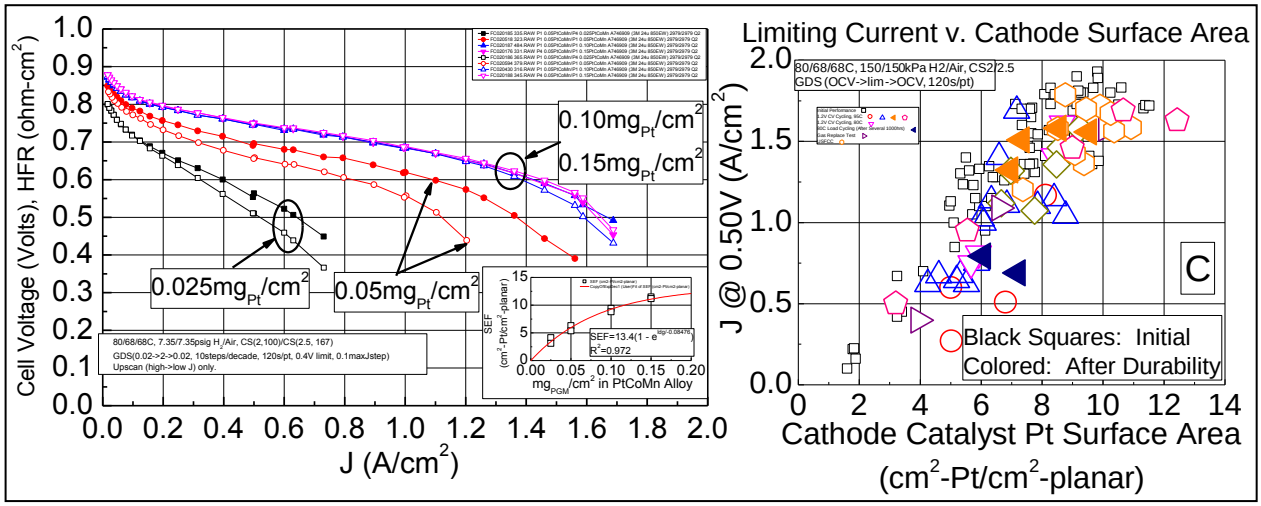


**Fig. 9.38. (Left)** Polarization curves show the effect of reduced Pt loading on the fuel cell and especially the limiting current densities. **(Right)** Cumulative plot over many types of MEA's and cathodes and tests, including durability stress tests and beginning of life tests, showing that the current density at 0.5 V (one metric approximating limiting current) varies linearly with cathode Pt surface area up to a limit that reflects other performance limiting factors.

It remains to be understood what exactly is the cause for this dependence of limiting current density on loading, which is also seen with conventional dispersed Pt/C electrodes as discussed in Section 9.9. The difference is that whereas this increased reduction of high current density with Pt/C electrodes appears to begin at loadings below 0.2 mg/cm$^2$, for the NSTF loadings as Fig. 9.38 shows, do not lose appreciable current density until the loading drops below 0.1 mg/cm$^2$.

### 9.15. Polarization curve gains over life of contract, Cell voltage vs. A/mg$_{\text{Total PGM}}$

As discussed in technology development accomplishment number 11 above, at the end of this project we completed the first systematic study of flow field effects on the NSTF MEA performances. As shown in Fig. 9.24, the land and channel dimensions have a large impact on the high current density performance with the flow field type FF2 having 0.5 mm wide lands and channels giving the best results. When tested with our 2009 best of class (BoC) PtCoMn MEA, having 0.05/0.10 mg$_{Pt}$/cm$^2$ loadings on the anode and cathode, the high current density performance is particularly improved. This coupled with our material improvements since the start of the project give a significant overall improvement in cell voltage versus the Pt loading normalized current, A/mg$_{Pt}$, as shown in Fig. 9.39. Fig. 9.39 (A) compares the polarization curve at 23 psig (2.5 atma) from the 2009 BoC MEA in FF2 under the ANL test conditions shown in Fig. 7.7, with that from our standard PtCoMn NSTF MEA at the start of the project which had 0.2 mg$_{Pt}$/cm$^2$ on both the anode and cathode. The latter polarization curve was shown in slide 8 of this project's presentation given at the 2007 DOE HFCIT Kick-off meeting on Feb. 13-14, 2007, in Washington, D.C. In Fig. 9.39 (B) the current density has been normalized to the MEA total Pt loading. At 0.6 V, we can demonstrate a three-fold gain in A/mg. In addition, the cathode stoichiometry is lower for the end of project data (2.0 vs 2.5) and the test condition drier.

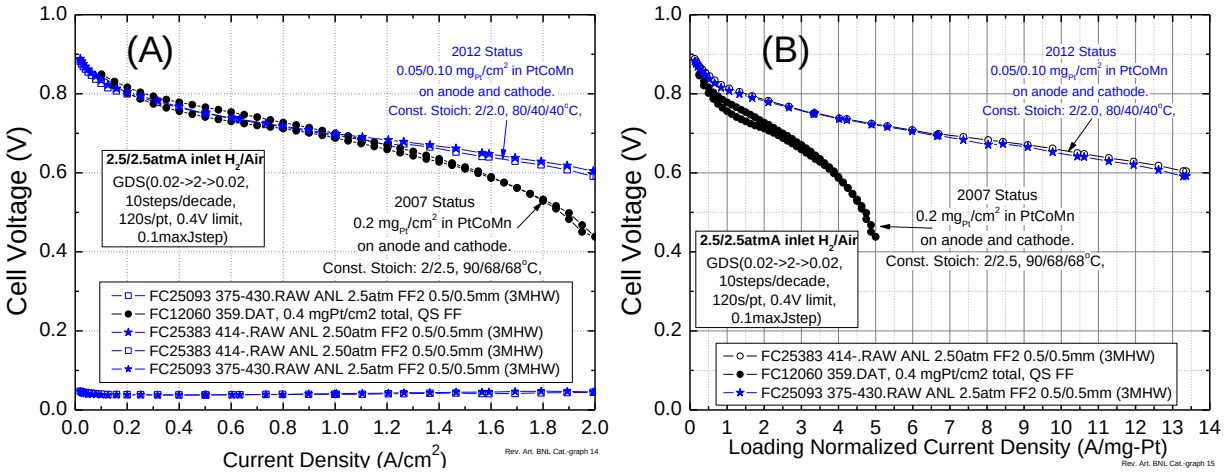


**Fig. 9.39.** (A) Comparison of polarization curves at 23 psig (2.5 atma) from the 2009 BoC MEA in FF2 (blue symbols), taken under the ANL test conditions shown in Fig. 7.7, with that from our standard PtCoMn NSTF MEA at the start of the project which had 0.2 mg$_{Pt}$/cm$^2$ on both the anode and cathode. (B) Polarization curves in A replotted with the current density normalized by the total MEA Pt loading.

## 9.16. Knowledge and advances in break-in conditioning

One of the characteristics determined early in our development of the NSTF electrodes is that the MEA's require very specific break-in conditioning protocols in order to reach full performance. Early studies found that the residual impurities from the membrane casting solvents clearly affected how much conditioning was required. Since then many other factors have been found influential. Around the beginning of this century we devised an effective thermal cycling procedure which allowed dramatic gains in beginning of life performances. The issue was that exceptionally long times for this break-in conditioning, usually 24 – 40 hours, were required for the best performance. This was attributed to the low loading and low surface area of NSTF electrodes. It was believed that the details of the protocol could be very important for accelerating whatever processes were happening to activate the catalysts and clean up the membrane. Many experiments were consistent with the break-in conditioning being tied to removal of residual impurities in the membrane, such as organic anions, that poisoned the catalyst or affected the electrode charge transfer impedance. But one clear observation was that the catalyst kinetics peaked first and relatively quickly, while the remainder of the time was spent to bring up the limiting current density, such as discussed in Section 9.14.

There was a need to find a more effective break-in condition protocol that acted more quickly and was also could be easily implemented in stacks. This activity was incorporated into this project in 2009 as a new Task 6. It consisted of two subtasks focused on test station protocols and materials:

*Subtask 6.1* - Break-in conditioning protocol - quantify the effect of test station operating parameters on the time for break-in conditioning of the standard PtCoMn NSTF MEA's in 50 $cm^2$ single cell tests

*Subtask 6.2* - Component Factors - Identify MEA component factors having greatest effect on break-in conditioning time

Significant work prior to the current project had identified many MEA component materials and their processes, and test station protocols that strongly affect the time for break-in conditioning of new MEA's (see Fig. 9.40).

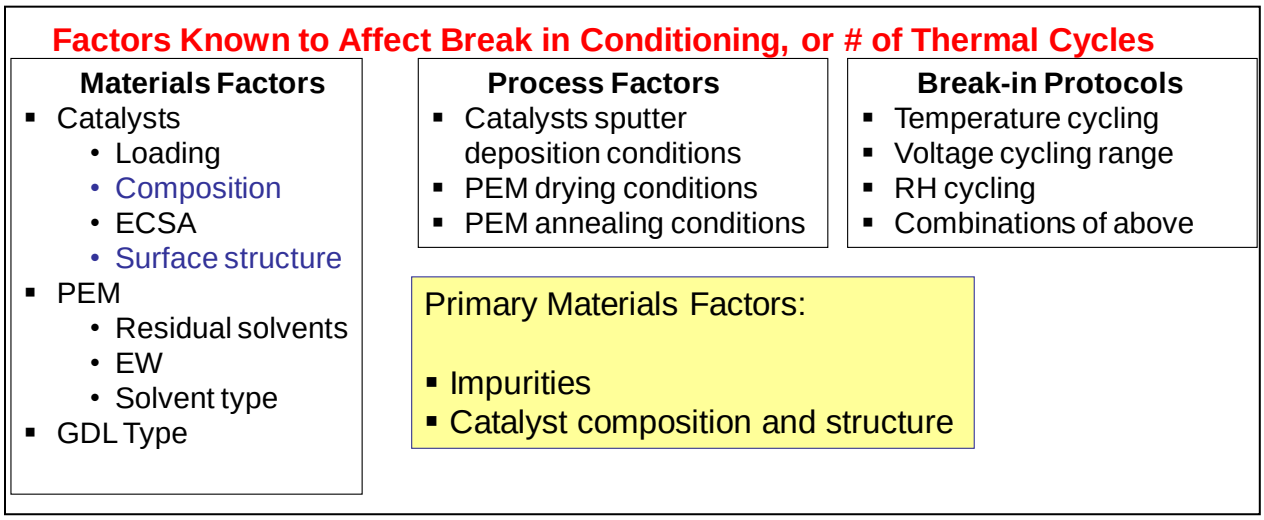


**Fig. 9.40. Factors found to affect break-in conditioning time and effectiveness by the standard thermal cycling protocol.**

These included catalyst composition, surface area, fabrication conditions, membrane processing solvents and drying conditions, and GDL types. Our standard thermal cycling protocol with liquid water injection has been used for years to break-in new NSTF MEA's to obtain full performance. The new task 6 now focused on both materials effects and the protocol effects in order to significantly reduce the time and simplify the procedures for conditioning a new MEA.

***Protocol Effects***

In 2009 new test station protocol work was successful in reducing the conditioning time with our current test stations (i.e. the time to full performance at 0.4 V during GDS polarization scans) from over 24 hours to less than six hours. In the 2009-2010 timeframe protocols were developed that both reduced the time for reaching full power and were more stack friendly to implement. From 2009 to 2010 over 40 new protocols were investigated.

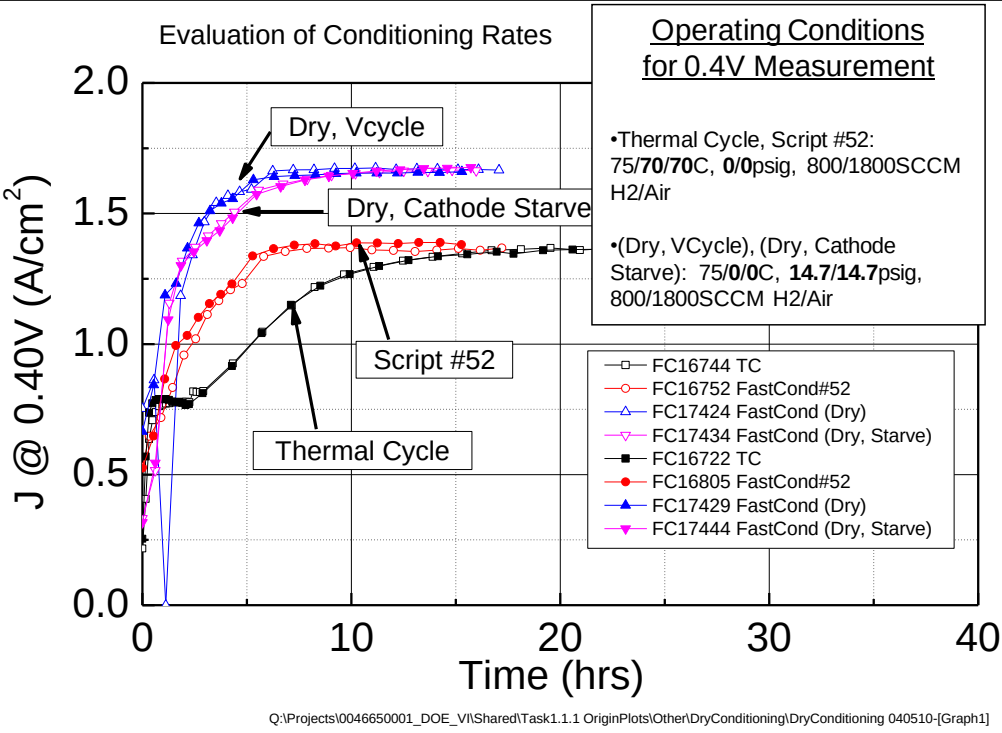


| Script #52 | | |
|---|---|---|
| **Tcycle** | **LoadCycle** | **Duration** |
| {50/45/45C, 800/1800SCCM, 100/100kPa}, {30/60/60C, 200/400SCCM, 100/100kPa} | OCV(2s), 0.5V(2s), 0.25V(10s) 1 PDS Curve per Tcycle (at max T) | 1hr |
| {75/70/70C, 800/1800SCCM, 100/100kPa}, {55/90/90C, 200/400SCCM, 100/100kPa} | OCV(2s), 0.5V(2s), 0.25V(10s) 1 PDS Curve per Tcycle (at max T) | 3hr |
| {75/70/70C, 800/1800SCCM, 100/100kPa}, {30/60/60C, 200/400SCCM, 100/100kPa} | OCV(2s), 0.5V(2s), 0.25V(10s) 1 PDS Curve per Tcycle (at max T) | 16hr |

**Fig. 9.41**. Log plots of current density versus time at 0.4 V as extracted from PDS polarization scans, showing examples of "Stack-Capable" FAST Conditioning Protocol Effects compared to the standard thermal cycling protocol. The table describes the Script 52 protocol.

Examples of this are illustrated in Fig. 9.41, which compares log plots of current density at 0.4 V versus time extracted from potentiodynamic polarization scans taken during the break-in conditioning. The time for the cell current density to reach within 90% of its peak value is much less for the "Script 52" protocol compared to the standard thermal cycling protocol, both of which use ambient pressure outlets. The "dry protocols" in Fig 9.41 (cathode starve and V-cycle) reach higher ultimate performance values due to their higher operating pressure, but they clearly also condition faster, nominally fully conditioned in <8 hours. FAST conditioning has not always achieved performance parity with the slower, historical 3M thermal cycling procedure, and we have seen a test station dependence on their effectiveness that is not understood. Further systematic study is needed to determine how to resolve the performance gaps, but clearly these faster, simpler conditioning protocols are an effective approach.

***Material Factors***

Understanding how the break-in conditioning protocols depend on material factors listed in Fig. 9.40 is also key to finding the complete solution. Both the catalyst composition and the nature of the alloying component can have a large influence on the rate of break-in conditioning.

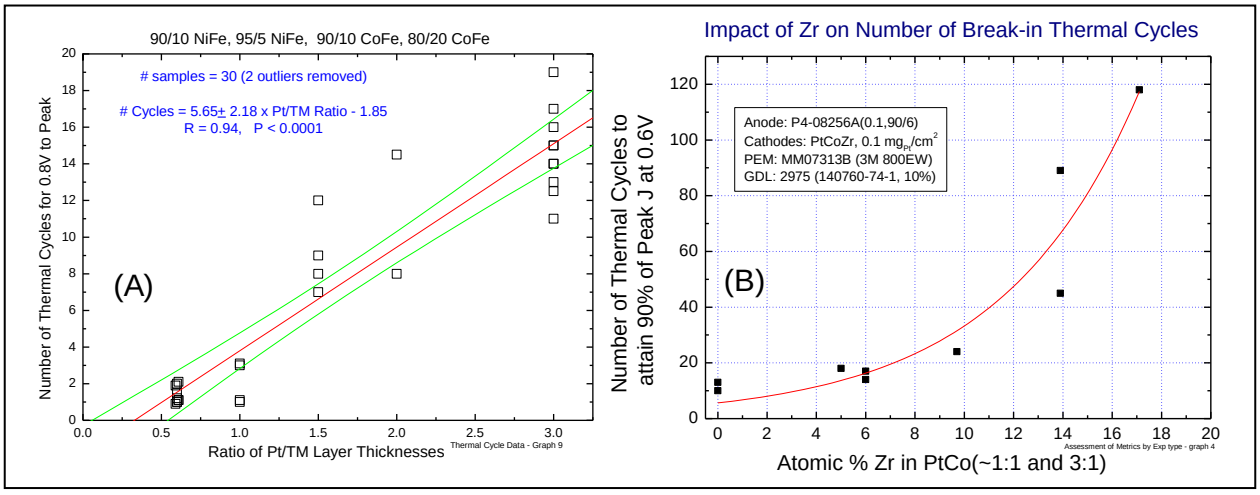


**Fig. 9.42. (A)** Data from the previous 3M/DOE contract preceding the current one, showing how the number of thermal cycles varies as a function of the ratio of the Pt/TM layer thicknesses for a PtCo and PtNiFe alloy series. (B) Impact on the atomic percentage of Zr added to PtCo alloys (PtCo or $Pt_3Co$) on the number of thermal cycles required for break-in conditioning by standard thermal cycles (data from the current project.)

Fig. 9.42(A) shows data from the previous 3M/DOE contract preceding the current one. It shows the number of thermal cycles as a function of the ratio of the Pt/TM layer thicknesses for a PtCo and PtNiFe alloy series. The higher the amount of transition metal, Co or Ni, the faster full kinetic performance was achieved. Fig. 9.42 (B) shows a very surprising result from this project. Small amounts of Zr in two PtCo alloys have an enormous effect on the number of standard thermal cycles required to reach peak performance. As little as 17 at% Zr increased the number of thermal cycles required by an order of magnitude. Surface area and activity were not decreased by the Zr, so clearly some other mechanism is occurring. No other material effect has been seen to be as strong. Equally as interesting is that a post fabrication process

applied to the NSTF PtCoZr has a dramatic impact on the conditioning time of the Zr-containing cathode catalyst. This is illustrated in Fig. 9.43.

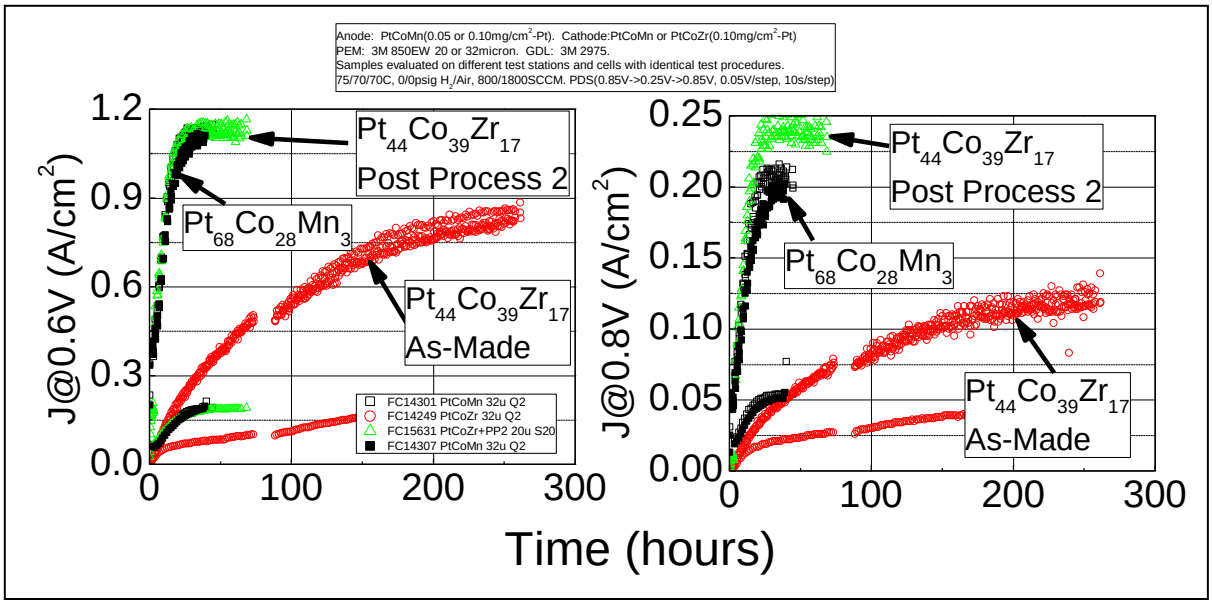


**Fig. 9.43.** Examples of the effect of an electrochemical post-deposition process on start-up performance for NSTF PtCoZr alloys. Current density at 0.6 V (left) and 0.8 V (right) increases with time of thermal cycling in a dramatically different way depending on whether the PtCoZr is as-made or if a post-process was made prior to forming the CCM and fuel cell testing.

As-made, PtCoZr requires significantly longer conditioning time than standard PtCoMn and the ultimate kinetic performance is also suppressed. After application of an electrochemical post process, the conditioning time w/ PtCoZr appears comparable or faster than standard PtCoMn, and may have similar or improved kinetic performance. This illustrates that there is a very rich area of material science process and composition yet to be studied in order to fully understand and thereby achieve the requirements for fast, stack friendly break-in conditioning. At the very least these examples for both protocol effects and material effects shown in Figs. 9.41-9.43 illustrate that there is not likely to be anything fundamentally limiting NSTF electrodes from rapid conditioning, as long as the surface area is sufficiently high.

## 9.17. Support for development of NSTF catalyst and CCM roll-to-roll processes

Process improvements were continuously being implemented for roll-to-roll NSTF catalyst and CCM fabrication, quality and cost. This project was a major driver for these process improvements. Over 260,000 linear ft combined of a) NSTF substrate (MCTS), b) whisker support coated substrates, c) catalyst coated whisker supports, and d) catalyst coated membrane were produced since production tracking started in 2006, for process development, qualification and customer use. Fig. 9.44 shows the yearly increases in the total of a) through d) during the period of this project.

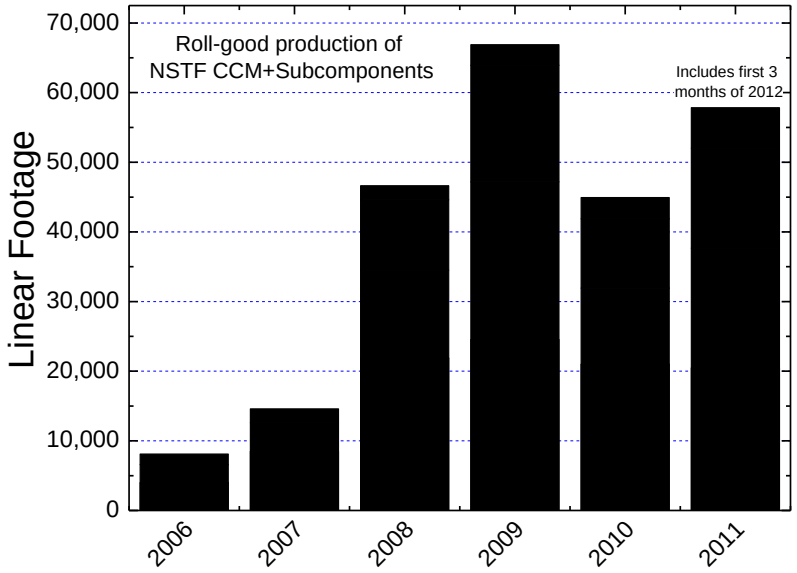


**Fig. 9.44** Summary of the total combined linear footage of NSTF CCM and its components manufactured yearly since production reporting began in 2006. The components refer to the four components of the MCTS substrate, whisker coated substrate, catalyst coated substrate, and CCM.

## 10. References for Sections 1 - 9


1. Arman Bonakdarpour, Krystal Stevens, George D. Vernstrom, Radoslav Atanasoski, Alison K. Schmoeckel, Mark K. Debe, and Jeff R. Dahn, "Oxygen Reduction Activity of Pt and Pt-Mn-Co Electrocatalysts Sputtered on Nanostructured Thin Film Support," Electrochimica Acta **53** (2007) 688-694.
2. D. Van der Vliet, D. Strmcnik, C. Wang, R. Atanasoski, M. Debe. N. Markovic and V. Stamenkovic, "Multimetallic Catalysts for Oxygen Reduction Reaction," 216th ECS Meeting, Vienna, Austria, Oct. 4-9, 2009.
3. K. J. J. Mayrhofer, D. Strmcnik, B. B. Blizanac, V. Stamenkovic, M. Arenz, N. M. Markovic, "Measurement of oxygen reduction activities via the rotating disc electrode method: From Pt model surfaces to carbon-supported high surface area catalysts," *Electrochimica Acta* **53** (2008) 3181-3188.
4. Liu, Gary C-K.; Sanderson, R. J.; Vernstrom, G; Stevens, D. A.; Atanasoski, R. T.; Debe, M. K.; Dahn, J. R., "RDE Measurements of ORR Activity of $Pt_{1-x}$ $Ir_x$ ($0<x<0.3$) on High Surface Area NSTF-Coated Glassy Carbon Disks," *J. Electrochem. Soc.* (2010), **157**(2), B207-B214.
5. Gary Chih-Kang, D. A. Stevens, J. C. Burns, R. J. Sanderson, G. D. Vernstrom, R. T. Atanasoski, M. K. Debe and J. R. Dahn, "Oxygen reduction activity of dealloyed $Pt_{1-x}Ni_x$ catalysts." *J. Electrochem. Soc.* **158**(8) B919-B26 (2011).
6. Dennis van der Vliet, Chao Wang, Mark Debe, Radoslav Atanasoski, Nenad M. Markovic and Vojislav R. Stamenkovic, "Platinum-alloy Nanostructured Thin Film Catalysts for the Oxygen Reduction Reaction," *Electrochimica Acta*. **56** 8695-8699 (2011).
7. A. K. Schmoeckel, G. D. Vernstrom, A. J. Steinbach, S. M. Hendricks, R. T. Atanasoski and M. K. Debe, "Nanostructured Thin Film Ternary Catalyst Activities for Oxygen Reduction," 2006 Fuel Cell Seminar, Honolulu, Hawaii, Nov. 13-17, 2006.
8. M. Debe, A. Steinbach, G. Vernstrom, S. M. Hendricks, M. J. Kurkowski, R. T. Atanasoski, P. Kadera, D. A. Stevens, R. J. Sanderson, E. Marvel and J. R. Dahn, "Extraordinary oxygen reduction activity of $Pt_3Ni_7$," *J. Electrochem. Soc.* **158**(8) B910-B918 (2011).
9. Mark K. Debe, "Electrocatalyst Approaches and Challenges for Automotive Fuel Cells," invited review article, *Nature*, **486**(9401) 43-51(2012).
10. Mark K. Debe, "Nanostructured Thin Film Electrocatalysts for PEM Fuel Cells – A Tutorial on the Fundamental Characteristics and Practical Properties of NSTF Catalysts," *ECS Transactions* **45**, April, 2012.
11. R.K. Ahluwalia, X. Wang, A. Lajunen, A.J. Steinbach, S.M. Hendricks, M.J. Kurkowski, and M.K. Debe, "Kinetics of Oxygen Reduction Reaction on Nanostructured Thin-Film Platinum Alloy Catalyst," *Journal of Power Sources* **215** (2012) 77-88.
12. Debe, M. K.; Schmoeckel, A.; Hendricks, S.; Vernstrom, G.; Haugen, G.; Atanasoski, R., *ECS Transactions* **1**(1), 51 (2006).
13. Debe, M. K.; Schmoeckel, A. K.; Vernstrom, G. D.; Atanasoski, R., *Journal of Power Sources* **161**, 1002 (2006).
14. Steinbach, A.J.; Noda, K.; Debe, M. K., *ECS Transactions* **3**(1) 835 (2006).
15. Bonakdarpour, A.; Lobel, R.; Atanasoski, R. T.; Vernstrom, G. D.; Schmoeckel, A. K.; Debe, M. K.; Dahn, J. R., *Journal of The Electrochemical Society* **153**, A1835 (2006).
16. M. Debe, A. Hester, G. Vernstrom, A. Steinbach, S. Hendricks, A. Schmoeckel, R. Atanasoski, D. McClure and P. Turner , in proceedings of the 50th Annual Technical Conference of the Society of Vacuum Coaters, Louisville, KY, May 1, 2007.
17. Mark K. Debe, Project review at the DOE 2010 Vehicle Technologies and Hydrogen Programs Annual Merit Review, June 8, 2010, Washington, D.C., number FC 001. http://www.hydrogen.energy.gov/pdfs/review10/fc001_debe_2010_o_web.pdf
18. M. K. Debe, A. J. Steinbach, G. D. Vernstrom, S. M. Hendricks, M. J. Kurkowski, R. T. Atanasoski, P. Kadera, D. A. Stevens, R. J. Sanderson, E. Marvel and J. R. Dahn, "Extraordinary oxygen

reduction activity of $Pt_3Ni_7$," *J. Electrochem. Soc.* **158**(8) B910-B918 (2011), and *ECS Trans*., **33** 143 (2010).
19. Mark K. Debe, Project review at the DOE 2012 Vehicle Technologies and Hydrogen Programs Annual Merit Review, May 15, 2012, Washington, D.C., number FC 001. http://www.hydrogen.energy.gov/pdfs/review12/fc001_debe_2012_o.pdf
20. A. Steinbach, M. Debe, M. Pejsa, D. Peppin, A. Haug, M. Kurkowski and S. Maier-Hendricks, "Influence of Anode GDL on PEMFC Ultra-thin Electrode Water Management at Low Temperatures," *ECS Transactions*, **41**(1) 449-457 (2011).
21. Target Tables from the US Drive Fuel Cell Technical Team, Revised January 25, 2012.
22. Greg Haugen, Sara Barta, Mike Emery, Steven Hamrock and Mike Yandrasits, "Open Circuit Voltage Fuel Cell Durability Testing Using Multiple PEM MEA's," in Fuel Cell Chemistry and Operation, eds. Andrew M. Herring, Thomas A. Zawodzinski Jr., and Steven J. Hamrock, *ACS Symposium Series 1040*, page **137** (2010).
23. Mark K. Debe, "Effect of Electrode Structure Surface Area Distribution on High Current Density Performance of PEM Fuel Cells," *J. Electrochemical Society* **159**(1) B54-B67 (2011).
24. Dennis van der Vliet, Chao Wang, Dusan Tripkovic, Dusan Strmcnik, Xiaofeng Zhang, Mark Debe, Radoslav Atanososki, Nenad M. Markovic and Vojislav R. Stamenkovic, "Metallic Nanotubes with Tunable Composition and Structure as Advanced Electrocatalysts," *Nature Materials*, in press (2012).
25. Lajos Gancs, Takeshi Kobayashi, Mark K. Debe, Radoslav Atanasoski, and Andrzej Wieckowski, "Crystallographic Characteristics of Nanostructured Thin Film Fuel Cell Electrocatalysts – A HRTEM Study," *Chemistry of Materials* **20**, 2444-2454 (2008).
26. M. K. Debe, R. J. Poirier, "Post deposition growth of a uniquely nanostructured organic film by vacuum annealing," *J. Vac. Sci. Technol.* **A 12**(4, Pt. 2), 2017-22 (1994).
27. M. K. Debe, A. R. Drube, "Structural characteristics of a uniquely nanostructured organic thin film," *J. Vac. Sci. Technol.* **B 13**(3), 1236-41 (1995).
28. Arnd Garsuch, D. A. Stevens, R. J. Sanderson, S. Wang, R. T. Atanasoski, S. Hendricks, M. K. Debe, and J. R. Dahn, "Alternative Catalyst Supports Deposited on Nanostructured Thin Films for Proton Exchange Membrane Fuel Cells," *J. Electrochemical Society* **157**(2) B187-B194 (2010).
29. D. A. Stevens, J. M. Rouleau, R E. Mar, R. T. Atanasoski, A. K. Schmoeckel, M. K. Debe and J. R. Dahn, "64-Electrode PEM Fuel Cell Studies of CO-Tolerant Hydrogen Oxidation Catalysts," *ECS Transactions* **3**(1) 355-360 (2006).
30. D. A. Stevens, J. M. Rouleau, R. E. Mar, A. Bonakdarpour, R. T. Atanasoski, A. K. Schmoeckel, M. K. Debe, J. R. Dahn, "Characterization and PEMFC Testing of $Pt_{1-x}M_x$ (M=Ru, Mo, Co, Ta, Au, Sn) Anode Electrocatalyst Composition Spreads," *J. of the Electrochem. Soc.* **154**(6), B566-B576 (2007).
31. Arman Bonakdarpour, Krystal Stevens, George D. Vernstrom, Radoslav Atanasoski, Alison K. Schmoeckel, Mark K. Debe, and Jeff R. Dahn, "Oxygen Reduction Activity of Pt and Pt-Mn-Co Electrocatalysts Sputtered on Nanostructured Thin Film Support," *Electrochimica Acta* **53** (2007) 688-694.
32. Arman Bonakdarpour, Tara R. Dahn, Radoslav Atanasoski, Mark K. Debe, and Jeff R. Dahn, "$H_2O_2$ Release During Oxygen Reduction Reaction on Pt Nano Particles," *Electrochemical and Solid-State Letters*, **11,** B208-B211 (2008).
33. Gary C-K. Liu, R. J. Sanderson, G. Vernstrom, D. A. Stevens, R. T. Atanasoski, M. K. Debe, J. R. Dahn, "RRDE Measurements of ORR Activity of $Pt_{1-x}$ $Ir_x$ ($0<x<0.3$) on High Surface Area NSTF-Coated Glassy Carbon Disks," *J. Electrochem. Soc.* **157**(2), B207-B214 (2010).
34. Gary Chih-Kang, D. A. Stevens, J. C. Burns, R. J. Sanderson, G. D. Vernstrom, R. T. Atanasoski, M. K. Debe and J. R. Dahn, "Oxygen reduction activity of dealloyed $Pt_{1-x}Ni_x$ catalysts." *J. Electrochem. Soc.* **158**(8) B919-B26 (2011).
35. D. A. Stevens, R. Mehrotra, R. J. Sanderson, G. D. Vernstrom, R. T. Atanasoski, M. K. Debe and J. R. Dahn, "Dissolution of Ni from high Ni content $Pt_{1-x}Ni_x$ alloys," *J. Electrochem. Soc.* **158**(8) B905-B909 (2011).

36. D. A. Stevens, S. Wang, R. J. Sanderson, G. C. K. Liu, G. D. Vernstrom, R. T. Atanasoski, M. K. Debe and J. R. Dahn, "A combined rotating disk electrode/X-ray diffraction study of Co dissolution from $Pt_{1-x}Co_x$ Alloys," *J. Electrochem. Soc.* **158**(8) B899-B904 (2011).
37. J.E. Harlow, D.A. Steven, R.J. Sanderson, G. C-K Liu, L.B. Lohstreter, G.D. Vernstrom, R.T. Atanasoski, M.K. Debe, and J.R. Dahn, "The oxygen reduction reaction activity of a $Pt_{1-x}Mn_x$ binary composition spread," *J. Electrochemical Society* **159** (6) B670-B676 (2012).
38. D. A. Stevens, S. Wang, R. J. Sanderson, A. Garsuch, M. K. Debe, S. M. Hendricks, R. T. Atanasoski, J. R. Dahn, "Assessing the $Pt_{upd}$ Surface Area Stability of $Pt_{1-x}M_x$ (M=Re, Nb, Bi) Solid Solutions for Proton Exchange Membrane Fuel Cells," *Journal of the Electrochem. Soc.* **157**(5), B737-B743 (2010).
39. P. Strasser, S. Kohr, T. Anniyev, J. Greeley, K. More, C. Yu, Z. Liu, S. Kaya, D. Nordlund, H. Ogasawara, M. Toney and A. Nilsson, "Lattice-strain control of the activity in dealloyed core-shell fuel cell catalysts," Nature Chemistry **2**, 454 (2010).
40. Stamenkovic, V. R. et al., "Improved oxygen reduction activity on $Pt_3Ni(111)$ via increased surface site availability. Science **315**, 493 - 497 (2007)."

## 11. Publication Activities

### 11.1. Publications in peer-reviewed journals


1. A . Bonakdarpour, K. Stevens, G. D. Vernstrom, R. Atanasoski, A. K. Schmoeckel, M. K. Debe, and J. R. Dahn, "Oxygen Reduction Activity of Pt and Pt-Mn-Co Electrocatalysts Sputtered on Nanostructured Thin Film Support," *Electrochimica Acta* **53** (2007) 688-694.
2. K. J. J. Mayrhofer, D. Strmcnik, B. B. Blizanac, V. Stamenkovic, M. Arenz, N. M. Markovic, "Measurement of oxygen reduction activities via the rotating disc electrode method: From Pt model surfaces to carbon-supported high surface area catalysts," *Electrochimica Acta* **53** (2008) 3181-3188.
3. Lajos Gancs, Takeshi Kobayashi, Mark K. Debe, Radoslav Atanasoski, and Andrzej Wieckowski, "Crystallographic Characteristics of Nanostructured Thin Film Fuel Cell Electrocatalysts – A HRTEM Study," *Chemistry of Materials* **20***,* 2444-2454 (2008).
4. Liu, Gary C-K.; Sanderson, R. J.; Vernstrom, G; Stevens, D. A.; Atanasoski, R. T.; Debe, M. K.; Dahn, J. R., "RDE Measurements of ORR Activity of $Pt_{1-x}$ $Ir_x$ (0<x<0.3) on High Surface Area NSTF-Coated Glassy Carbon Disks," *J. Electrochem. Soc.* (2010), **157**(2), B207-B214.
5. Gary Chih-Kang, D. A. Stevens, J. C. Burns, R. J. Sanderson, G. D. Vernstrom, R. T. Atanasoski, M. K. Debe and J. R. Dahn, "Oxygen reduction activity of dealloyed $Pt_{1-x}Ni_x$ catalysts." *J. Electrochem. Soc.* **158**(8) B919-B26 (2011).
6. Dennis van der Vliet, Chao Wang, Mark Debe, Radoslav Atanasoski, Nenad M. Markovic and Vojislav R. Stamenkovic, "Platinum-alloy Nanostructured Thin Film Catalysts for the Oxygen Reduction Reaction," *Electrochimica Acta*. **56** 8695-8699 (2011).
7. Mark K. Debe, "Electrocatalyst Approaches and Challenges for Automotive Fuel Cells," invited review article, *Nature,* **486**(9401) 43-51(2012).
8. Mark K. Debe, "Nanostructured Thin Film Electrocatalysts for PEM Fuel Cells – A Tutorial on the Fundamental Characteristics and Practical Properties of NSTF Catalysts," *ECS Transactions* **45**, April, 2012.
9. R.K. Ahluwalia, X. Wang, A. Lajunen, A.J. Steinbach, S.M. Hendricks, M.J. Kurkowski, and M.K. Debe, "Kinetics of Oxygen Reduction Reaction on Nanostructured Thin-Film Platinum Alloy Catalyst," *Journal of Power Sources* **215** (2012) 77-88*.*
10. M. K. Debe, A. J. Steinbach, G. D. Vernstrom, S. M. Hendricks, M. J. Kurkowski, R. T. Atanasoski, P. Kadera, D. A. Stevens, R. J. Sanderson, E. Marvel and J. R. Dahn, "Extraordinary oxygen reduction activity of $Pt_3Ni_7$," *J. Electrochem. Soc.* **158**(8) B910-B918 (2011), and *ECS Trans*., **33** 143 (2010).
11. M. K. Debe, and A. J. Steinbach, "An empirical model for the flooding behavior of ultra-thin PEM fuel cell electrodes," ECS Transactions 11(1) 659-673 (2007).
12. A. J. Steinbach, M. K. Debe, J. L. Wong, M. J. Kurkowski, A. T. Haug, D. M. Peppin, S. K. Deppe, S. M. Hendricks, and E. M. Fischer, "A New Paradigm for PEMFC Ultra-Thin Electrode Water Management at Low Temperatures," ECS Trans., 33(1), 1179-1188 (2010).
13. A. Steinbach, M. Debe, M. Pejsa, D. Peppin, A. Haug, M. Kurkowski and S. Maier-Hendricks, "Influence of Anode GDL on PEMFC Ultra-thin Electrode Water Management at Low Temperatures," *ECS Transactions*, **41**(1) 449-457 (2011).
14. M. K. Debe, R. T. Atanasoski, and A. J. Steinbach, "Nanostructured Thin Film Electrocatalysts – Current Status and Future Potential, ECS Transactions, 41(1) 937-954 (2011).
15. Mark K. Debe, "Effect of Electrode Structure Surface Area Distribution on High Current Density Performance of PEM Fuel Cells," *J. Electrochemical Society* **159**(1) B54-B67 (2011).

16. Arnd Garsuch, D. A. Stevens, R. J. Sanderson, S. Wang, R. T. Atanasoski, S. Hendricks, M. K. Debe, and J. R. Dahn, “Alternative Catalyst Supports Deposited on Nanostructured Thin Films for Proton Exchange Membrane Fuel Cells,” *J. Electrochemical Society* **157**(2) B187-B194 (2010).
17. D. A. Stevens, J. M. Rouleau, R. E. Mar, A. Bonakdarpour, R. T. Atanasoski, A. K. Schmoeckel, M. K. Debe, J. R. Dahn, “Characterization and PEMFC Testing of $Pt_{1-x}M_x$ (M=Ru, Mo, Co, Ta, Au, Sn) Anode Electrocatalyst Composition Spreads,” *J. Electrochem. Soc.* **154**(6), B566-B576 (2007).
18. Arman Bonakdarpour, Tara R. Dahn, Radoslav Atanasoski, Mark K. Debe, and Jeff R. Dahn, “H2O2 Release During Oxygen Reduction Reaction on Pt Nano Particles,” *Electrochemical and Solid-State Letters*, **11**, B208-B211, 2008.
19. D. A. Stevens, R. Mehrotra, R. J. Sanderson, G. D. Vernstrom, R. T. Atanasoski, M. K. Debe and J. R. Dahn, “Dissolution of Ni from high Ni content Pt1-xNix alloys,” *J. Electrochem. Soc.* **158**(8) B905-B909 (2011).
20. D. A. Stevens, S. Wang, R. J. Sanderson, G. C. K. Liu, G. D. Vernstrom, R. T. Atanasoski, M. K. Debe and J. R. Dahn, “A combined rotating disk electrode/X-ray diffraction study of Co dissolution from Pt1-xCox Alloys,” *J. Electrochem. Soc*. **158(**8) B899-B904 (2011).
21. J.E. Harlow, D.A. Steven, R.J. Sanderson, G. C-K Liu, L.B. Lohstreter, G.D. Vernstrom, R.T. Atanasoski, M.K. Debe, and J.R. Dahn, “The oxygen reduction reaction activity of a $Pt_{1-x}Mn_x$ binary composition spread,” *J. Electrochemical Society* **159** (6) B670-B676 (2012).
22. Dennis van der Vliet, Chao Wang, Dusan Tripkovic, Dusan Strmcnik, Xiaofeng Zhang, Mark Debe, Radoslav Atanasoski, Nenad M. Markovic and Vojislav R. Stamenkovic, “Metallic Nanotubes with Tunable Composition and Structure as Advanced Electrocatalysts,” *Nature Materials*, **in press** (2012).
23. M. K. Debe, A. E. Hester, G. D. Vernstrom, A. J. Steinbach, S. M. Hendricks, A. K. Schmoeckel, R. T. Atanasoski, D. J. McClure, and P. L. Turner, “Nanostructured Thin Film Catalysts for PEM Fuel Cells by Vacuum Web Coating, in proceedings of the 50th Annual Tech. Conference of the Society of Vacuum Coaters, Louisville, KY, May 1, 2007**,** 175-185 ISSN 0737-5921.
24. D. A. Stevens, J. M. Rouleau, R. E. Mar, R. T. Atanasoski, A. K. Schmoeckel, M K. Debe, J. R. Dahn, “Enhanced CO-Tolerance of Pt-Ru-Mo Hydrogen Oxidation Catalysts,” *Journal of the Electrochem. Soc.* **154**(12), B1211-B1219 (2007).
25. A. J. Steinbach, C. V. Hamilton, Jr., and M. K. Debe, “Impact of Micromolar Concentration of Externally-Provided Chloride and Sulfide Contaminants of PEMFC Reversible Stability,” *ECS Transactions* **11**(1) 889-902 (2007).
26. D. A. Stevens, S. Wang, R. J. Sanderson, A. Garsuch, M. K. Debe, S. M. Hendricks, R. T. Atanasoski, J. R. Dahn, “Assessing the $Pt_{upd}$ Surface Area Stability of $Pt_{1-x}M_x$ (M=Re, Nb, Bi) Solid Solutions for Proton Exchange Membrane Fuel Cells,” *Journal of the Electrochem. Soc.* **157**(5), B737-B743 (2010).
27. M. K. Debe, S. M. Hendricks, G. D. Vernstrom, M. Meyers, M. Brostrom, M. Stephens, and Q. Chan, Jason Willey, Monjid Hamden, and Cortney K. Mittelsteadt**,** Christopher B. Capuano, Katherine Ayers and Everett Anderson, “Initial Performance and Durability of Ultra-low Loaded NSTF Electrodes for PEM Electrolyzers,” *J. Electrochem. Soc*., **159**(6) K165-K176 (2012).

### 11.2 Invited presentations at international meetings and institutions

1. M. K. Debe, 2008, and 2009 to 2011 *DOE Hydrogen Program Annual Merit Reviews*, Washington, D.C.
   http://www.hydrogen.energy.gov/pdfs/review09/fc_17_debe.pdf
   http://www.hydrogen.energy.gov/pdfs/review10/fc001_debe_2010_o_web.pdf
   http://www.hydrogen.energy.gov/pdfs/review11/fc001_debe_2011_o.pdf
   http://www.hydrogen.energy.gov/pdfs/review12/fc001_debe_2012_o.pdf
2. M. Debe, A. Hester, G. Vernstrom, A. Steinbach, S. Hendricks, A. Schmoeckel, R. Atanasoski, D. McClure and P. Turner, invited, 50th Annual Technical Conference of the Society of Vacuum Coaters, Louisville, KY, May 1, 2007.
3. M. K. Debe, "Solving Durability and Performance Issues of PEMFC's by Eliminating Carbon Supports and Highly Dispersed Catalysts," Fuel Cells Durability and Performance 2007, Knowledge Foundation's 3rd Annual International Conference, Miami, FL Nov. 15-16, 2007, invited.
4. M. K. Debe, "Meeting Durability, Performance and Cost Targets for Automotive Fuel Cells by using Thin Film Catalysts, Ultra-thin Electrodes and Eliminating Carbon Supports, "NRC Institute for Fuel Cell Innovation, Vancouver, BC, Canada, March 17-18, 2008, invited.
5. M. K. Debe, "Nanostructured Thin Film Electrocatalysts for PEM Fuel Cells - Fundamental Characteristics and Practical Properties to Meet Automotive Requirements," 213th ECS meeting, Phoenix, AZ, May 18-23, 2008, invited.
6. R. Atanasoski, M. Debe, and T. Wood, "High Performance Platinum and Non-precious Metal Catalysts for PEM Fuel Cell Application", Opening key-note presentation at the 7th International Symposium on New Materials and Nano-Materials for Electrochemical Systems, June 24-27, 2008 Montréal, Canada.
7. Radoslav Atanasoski and Mark Debe, "Nano-Structured Thin Film - NSTF Catalysts for PEM Fuel Cells: Fundamentals and Application" ACES Electromaterials Symposium "Nanostructured Electromaterials", University of Wollongong, NSW, Australia, 4-6 February 2009, invited.
8. Radoslav Atanasoski, "Fuel Cell Catalysts of Tomorrow**":** XXth Congress of Chemist and Technologist of Macedonia, Ohrid, Macedonia, September 16–21, 2008, invited.
9. A.J. Steinbach, "Influence of Contaminants, MEA Components, and Temperature on PEM Fuel Cell Stability", Invited, Canada – USA PEM Network Research Workshop, February 16 and 17, 2009, NRC for Fuel Cell Innovation, Vancouver, BC, Canada.
10. D.A. Stevens, R.J. Sanderson, A. Garsuch, S. Wang,R.E. Mar and J.R. Dahn, Invited, "High Throughput Screening of PEM Fuel Cell Catalysts", Canada – USA PEM Network Research Workshop, February 16 and 17, 2009, NRC Institute for Fuel Cell Innovation, Vancouver, BC, Canada.
11. Mark K. Debe, "Ultra-high activity electrocatalysts based on nanostructured organic films and sputtered Pt alloys," Invited, *238th Am. Chem. Soc. Meeting,* Washington, D.C. August 16, 2009.
12. Mark K. Debe, "Update of the activity, performance, durability and water management of the 3M NSTF catalyst based MEA's for PEM fuel cell," Invited, MEA Fuel Cell Modeling and Characterization Workshop, NRC Institute for Fuel Cell Innovation, Vancouver, BC, Canada, Nov. 12-13, 2009.
13. Radoslav Atanasoski and Mark Debe, "Nano-structured thin film-NSTF catalysts for PEM fuel cells: focus on durability," Invited, Ulm Electro Chemical Talks 2010 and 2015 Technologies on Batteries and Fuel Cells, Ulm, Germany, June 16, 2010.
14. D.A. Stevens, T.D. Hatchard, R.J. Sanderson, R.T. Atanasoski, M.K. Debe and J.R. Dahn, (invited), "PEMFC Electrocatalyst Development," 218th ECS meeting.

15. M. K. Debe, "Nanostructured Catalyst Developments," invited, 2nd CARISMA Conference, Montpellier, France, Sept. 2010.
16. M. K. Debe, R. T. Atanasoski and A. J. Steinbach, "Nanostructured Thin Film Electrocatalysts – Current Status and Future Potential," Invited , 220th ECS Meeting, Boston, MA, Oct. 9-14, 2011.
17. Radoslav Atanasoski, "Fundamental and practical aspects of Nano-structured thin film - NSTF catalysts for PEM fuel cells: Durability under Transient Conditions," Invited, 61st ISE – Electrochemical Energy Conversion and Storage, Nice, France, Sept. 2010.
18. M. K. Debe, "NanoStructured Thin Film Catalysts -15 (or is it 28?) Years on an Alternative Path for PEM Fuel Cell Electrocatalysts," Invited, Fuel Cell Seminar and Exposition R&D Award presentation, San Antonio, TX, Oct. 19, 2010.
19. M. K. Debe, "Nanostructured Thin Film Catalysts for PEM Fuel Cells: Status and Path Forward to Meet Performance, Durability and Cost Targets for High Volume Automotive Applications," Invited, Workshop on PEM Fuel Cell Catalyst & MEA Preparation and Characterization, HySA Catalysis Competence Center and University of Cape Town, Cape Town, Rondebosch, South Africa, March 28-29, 2011
20. M. K. Debe, "NSTF Catalyst Technology for Energy Applications," Invited, Northwest University, Potchefstroom, South Africa, March 25, 2011.
21. M. K. Debe,"A General Introduction to Nano-Structured Thin Film Catalyst (NSTFC) Technology for Hydrogen and Fuel Cell Applications," Invited, Council for Scientific and Industrial Research (CSIR) , Pretoria, South Africa, March 24, 2011.
22. Mark K. Debe, "Designing Electrocatalysts for Fuel Cell Vehicles-It's going to Take More than Just High Activity," Invited, Cornell University Annual Energy Materials Symposium, August 12, 2011.
23. M. K. Debe , "PEM Fuel Cell Performance Factors Determined by Electrocatalyst Structure Characteristics," Invited, Zing International Hydrogen and Fuel Cell Conference, Riviera Maya, Mexico, Dec. 1, 2011.
24. Mark K. Debe, "A New Generation of Catalysts and Electrode Designs for PEM Water Electrolysis: Fundamentals and Practical Examples," Invited, Hydrogen Production and Water Electrolysis Short Course, North-West University, Potchefstroom, South Africa, April 18-19, 2012.
25. Mark K. Debe, "Nanostructured Thin Film Electrocatalysts for PEM Fuel Cells – A Tutorial on the Fundamental Characteristics and Practical Properties of NSTF Catalysts," Invited, 221st ECS Meeting, Seattle, Washington, May 8, 2012.
26. Mark K. Debe, "Looking to the Future and Assuming Success – Are current approaches for MEA electrocatalyst and membrane integration on a path to meet cost and high volume manufacturing requirements for automotive PEM fuel cells?," Invited, 6th International Fuel Cell Workshop, Yamanashi University, Kofu, Japan, August 2-3, 2012.

### 11.3 Contributed presentations at international meetings

1. D. Van der Vliet, D. Strmcnik, C. Wang, R. Atanasoski, M. Debe. N. Markovic and V. Stamenkovic, "Multimetallic Catalysts for Oxygen Reduction Reaction," 216th ECS Meeting, Vienna, Austria, Oct. 4-9, 2009.
2. A. K. Schmoeckel, G. D. Vernstrom, A. J. Steinbach, S. M. Hendricks, R. T. Atanasoski and M. K. Debe, "Nanostructured Thin Film Ternary Catalyst Activities for Oxygen Reduction," 2006 Fuel Cell Seminar, Honolulu, Hawaii, Nov. 13-17, 2006.
3. D. Van der Vliet, D. Strmcnik, C. Wang, R. Atanasoski, M. Debe. N. Markovic and V. Stamenkovic, "Catalysts with Multifunctional Active Sites: From well-defined to nanoscale surfaces**,"** 216th ECS Meeting, Vienna, Austria, Oct. 4-9, 2009.
4. A. J. Steinbach, K. Alade-Lambo, H. Le and M. K. Debe, "Investigation of Cation-Induced Performance Losses in PEM Fuel Cells," 2008 Fuel Cell Seminar and Exposition, Phoenix, AZ, Oct. 27, (2008) Extended Abstract GHT35a-22.
5. A. J. Steinbach, C. V. Hamilton, Jr. and M. K. Debe, "Impact of Micro-molar Concentrations of Externally-Provided Chloride and Sulfide Contaminants on PEMFC Reversible Stability," presented at the 212th ECS meeting, Washington, D.C. October 7-12, 2007.
6. M. K. Debe and A. J. Steinbach, "An Empirical Model For The Flooding Behavior Of Ultra-Thin PEM Fuel Cell Electrodes," ECS Transactions 659 (2007), and presented at the 212th ECS meeting, Washington, D.C. Oct. 7-12, 2007.
7. G. Vernstrom, A Schmoeckel, R. Atanasoski, S. Hendricks, A. Steinbach, and M. Debe, "Oxygen Reduction Activities of Nanostructured Thin Film Alloy Electrocatalysts", Fuel Cell Seminar, Oct. 13–17, 2008, Phoenix, Abst. 1365.
8. Gary C-K Liu, R.J. Sanderson, G. Vernstrom, D.A. Stevens, R.T. Atanasoski, M.K. Debe and J.R. Dahn,"RRDE measurements of ORR activity of $Pt_{1-x}Ir_x$($0<x<0.3$) on high surface area NSTF-coated GC disks," 216th ECS Meeting, Vienna, Austria, Oct. 4, 2009.
9. C.C. Hays, J.G. Kulleck, B.E. Haines and S.R. Narayan, "Thin Film Platinum Alloys for Use as Catalyst Materials in Fuel Cells," Abstract for 216th ECS Meeting, Vienna, Austria, Oct. 4, 2009.
10. A.J. Steinbach, H. Le, K Alade-Lambo, C.V. Hamilton Jr., M.J Kurkowski and M.K. Debe, "Reversible Performance Stability of Polymer Electrolyte Membrane Fuel Cells," 238th Am. Chem. Soc. Meeting, Washington, D.C. August 16, 2009.
11. D. Stevens, A. Bonakdarpour, R. Sanderson, S. Wang, R. Atanasoski, M. Debe and J. Dahn, "Development of Multi-component PEM Fuel Cell Catalysts for Enhanced Stop-Start Protection", 217th ECS meeting, Vancouver, BC, Canada, Aril 28, 2010.
12. Gary Chih-Kang Liu, R. Sanderson, D.A. Stevens, G. Vernstrom, R.T. Atanasoski, M.K. Debe and J. R. Dahn, "RRDE measurements of ORR activity of $Pt_{1-x}Ni_x$ ($0 < x < 1$) on high surface area NSTF-coated GC disks," 218th ECS meeting, Las Vegas, NV, Oct. 14, 2010
13. A. J. Steinbach, M. K. Debe, J. L. Wong, M. J. Kurkowski, , A. T. Haug, D. M. Peppin, S. K. Deppe, S. M. Hendricks and E. M. Fischer, "A New Paradigm for PEMFC Ultra-Thin Electrode Water Management at Low Temperatures," 218th ECS meeting, Las Vegas, NV, Oct. 14, 2010.
14. M. K. Debe, A. Steinbach, G. Vernstrom, S. Hendricks, R. Atanasoski, P. Kadera, "Extraordinary ORR activity of Pt3Ni7." 218th ECS meeting, Las Vegas, NV, Oct. 14, 2010.
15. A. Steinbach, M. Debe, M. Pejsa, D. Peppin, A. Haug, M. Kurkowski and S. Maier-Hendricks, "Influence of Anode GDL on PEMFC Ultra-thin Electrode Water Management at Low Temperatures," 220th ECS Meeting, Boston, MA, Oct. 9-14, 2011.

16. Gary Chih-Kang Liu, R.J. Sanderson, D.A. Stevens, G. Vernstrom, R.T. Atanasoski, M.K. Debe and J.R. Dahn, "De-alloying of $Pt_{1-x}M_x$ [M = Ni, Co] (0 < x < 1) catalysts and impact on surface area enhancement, " Presentation at the 218th ECS meeting, Las Vegas, NV, Oct. 12, 2010.
17. D.A. Stevens, S. Wang, R.J. Sanderson, G.C.K. Liu and J.R. Dahn, G. D. Vernstrom, R.T. Atanasoski and M.K. Debe, "A Combined Rotating Disk Electrode/X-Ray Diffraction study of Co Dissolution from $P_{1-x}Co_x$ alloys," Poster paper at the 218th ECS meeting, Las Vegas, NV, Oct. 13, 2010.
18. A. J. Steinbach, M. K. Debe, J. L. Wong, M. J. Kurkowski, A. T. Haug, D. M. Peppin, S. K. Deppe, S. M. Hendricks and E. M. Fischer, "A New Paradigm for PEMFC Ultra-Thin Electrode Water Management at Low Temperatures," Presentation at the 218th ECS meeting, Las Vegas, NV, Oct. 14, 2010.
19. M. Debe, S. M. Hendricks, G. Vernstrom, J. Wiley, M. Hamden, C. Mittelsteadt, C. Capuano, K. Ayers and E. Anderson, "Initial Performance and Durability of Ultra-low Loaded NSTF Electrodes for PEM Electrolyzers," Presentation at the 220Th ECS Meeting, Boston, MA, Oct., 2011.
20. A. Steinbach, M. Debe, M. Pejsa, D. Peppin, A. Haug, M. Kurkowski and S. M. Hendricks, "Influence of Anode GDL on PEMFC Ultra-thin Electrode Water Management at Low Temperatures," Presentation at the 220th ECS Meeting, Boston, MA, Oct. 2011.
21. M. Debe, S. M. Hendricks, G. Vernstrom, J. Wiley, M. Hamden, C. Mittelsteadt, C. Capuano, K. Ayers and E. Anderson, "Initial Performance and Durability of Ultra-low Loaded NSTF Electrodes for PEM Electrolyzers," 220th ECS Meeting, Boston, MA, Oct. 2011.
22. X. Wang, R. K. Ahluwalia, A. J. Steinbach, and M. K. Debe, "Dynamic Performance of Automotive Fuel Cell Systems with Low Platinum Loadings," 220th ECS Meeting, Boston, MA, Oct. 2011.

## 12. Intellectual Property Developments

| Title | Investigators | Date Reported to DOE | Patent Application # |
|---|---|---|---|
| Fuel Cell Nanocatalyst with Voltage Reversal Tolerance | Steinbach, Verstrom, Debe, and Atanasoski | 23-Sep-08 | 12/546775 (61/091643) |
| Catalyst Particle Size Control with Organic Pigments | Debe, Bender, Sowatzke | 1-Oct-09 | 12/766304 (61/172111) |
| Catalyst Property Control with Intermixed Inorganics | Debe, Atanasoski, and Hendricks | 1-Oct-09 | 12/766359 (61/172118) |
| Platinum Nickel Catalyst Alloy | Debe | 18-Apr-11 | US2011/033949 (61/328049) |
| Fuel Cell Electrode with Nanostructured Catalyst and Dispersed Catalyst Sublayer | Haug | 25-May-10 | 12/976168 (61/288882) |
| Membrane Electrode Assemblies including Mixed Carbon Particles | Haug | 25-May-10 | 12/976303 (61/288950) |
| Annealed Nanostructured Thin Film Catalysts | Debe, Smithson, Studiner, Hendricks, Kurkowski, Steinbach, and David Johnson | 18-Apr-11 | US2011/033972 (61/328064) |
| Fuel Cell Electrode Construction with Enhanced Properties | Debe, Hendricks, Vernstrom, Kurkowski. Steinbach, and Hester | | (61/581351) |
| Fuel Cell Water Management via Sub-Atmospheric Anode Reactant Pressure | Steinbach, Debe, Haug, Thomas, Wong and Lee | 18-Apr-11 | US2011/033913 (61/328058) |

## 13. Products developed and advanced under this project

No formal 3M products have derived from this project in the sense that anyone can order them. But significant quantities of roll good PtCoMn based catalyst coated membranes and as-made catalyst roll-goods of various loadings have been provided to automotive OEM customers under blanket purchase agreements. Stack sized gasketed MEA's with dealloyed and SET treated "$Pt_3Ni_7$" have been sold for stack testing to non-automotive customers as well.

## 14. Awards Received

A **2008 DOE Hydrogen Program R&D Award** was received at the DOE Hydrogen Program Annual Merit Review, June 9, 2008, Washington, D.C.

# Supplementary Task Information

## Supplementary Task Information

Over the course of this project the PI and co-PI had the opportunity to prepare and present 1,611 power point slides at 17 requested summary reviews for DOE fuel cell program management, the DOE AMR meetings and the FreedomCAR technical team at USCAR. In addition, at least 400 pages of word documents were provided in the 26 quarterly and annual reports. It is not possible to capture in this final report the extent of the work completed during the 5.25 years that even those reviews were summarizing. In this Section on Supplementary Task Information we provide some additional documentation on specific subjects that either further illustrate the type of work completed, are instructive for understanding the uniqueness of the NSTF electrocatalyst technology, or present what we believe are useful and intriguing results that the PEM fuel cell field as a whole might benefit from knowing.

**Contents** **Page**

# Task 1

# Selected Supplementary Information

## Task 1.1 NSTF surface area increase – NSTF support whisker optimization

*Introduction (see also Section 9.8)*

Despite the higher surface area per unit volume, the thinness of the NSTF catalyst layer prevents the absolute Pt surface area from being nearly as high as that of nanoparticles dispersed on carbon black. The NSTF ECSA is critically dependent on two basic aspects of the electrode structure – the surface area of the underlying layer of PR149 support whiskers, and the roughness factor of the catalyst coating applied to those whiskers. The former in turn will depend on the geometric properties of the PR149 whisker layer, i.e. the number of whiskers per unit area, N and their dimensions, lengths L and cross-sectional dimensions d. The latter will depend on the catalyst layer porosity and any overt crystallite growth structure formed when the catalyst is deposited. In this project we carried out the first systematic attempt to determine how the observed ECSA depends on the whisker support layer geometric properties (and to some extent the process conditions), and catalyst loading for the PtCoMn system. We also correlated these factors to the 50 $cm^2$ fuel cell performance. The net result was a detailed model development with some surprising results of how catalyst ECSA actually depends on the physical properties of the catalyst layer, realization that there are conflicting factors that prevent a simple optimization of surface area by just adjusting the N, L and d of the whiskers, and that the fuel cell performance is very weakly dependent on these and the process parameters for producing the NSTF whisker support layer, i.e. the process windows are wide.

*Approach: Designed experiments on Pilot line web coating equipment in Menomonie, WI*

Because the whisker growth properties are very dependent on the process equipment and parameters used to make them, it was important to do the various experiments on the process line used for roll-good production of the NSTF whisker supports. We defined and executed a series of designed process experiments, called Whisker Area Optimization (WAO – 1,2,3,4), in which the whisker production parameters were explored for the optimum whisker number density and dimensions, the most complete conversion of the starting material to the crystalline whiskers. Fig. 9.17 indicates the high level process parameters that were controlled in defining the WAO experiments.

Various performance metrics were extracted from the fuel cell measurements and correlated with the WAO experimental whisker parameters, as shown in Fig. S1. From these performance metrics and the various whisker parameters, three different plot types could be made, as indicated in Fig**.** S1, viz. global, experiment specific and model comparison plots. Figs. S2 and S3 show two other example plots from an early stage of the WAO series.

In Section 9 we discussed an example of the modeling results. Fig. 9.20 in Section 9 shows an example of the modeling comparison plots for surface area. From such a graph it was apparent the model and experimental fits were fairly good, over the 0.05 to 0.15 mg/$cm^2$ Pt loading range. So the mean or approximate values of *x* and *f* in equation (1) below could be used to explore a general model able to project how the surface area, $A^{Pt}_{geo}$ , would vary with N and L for a given loading.

Equation (1):

$$A_{geo}^{Pt} = \sqrt{2}\left[(1-x)+2xNL(w+t)\right]+\left(m/\rho\right)\left\{(1-x)2N(w+t)+\frac{f}{2NL(w+t)}+x\left[\frac{2}{(w+t)}+f\right]\right\}+\left(m/\rho\right)^2\left[(1-x)\frac{f}{\sqrt{2}L}+\frac{\sqrt{2}xf}{NL(w+t)}\right]$$

To do this the overall expression for $A^{Pt}_{geo}$ in equation (1) was reduced as follows (cont. after Fig. S3):

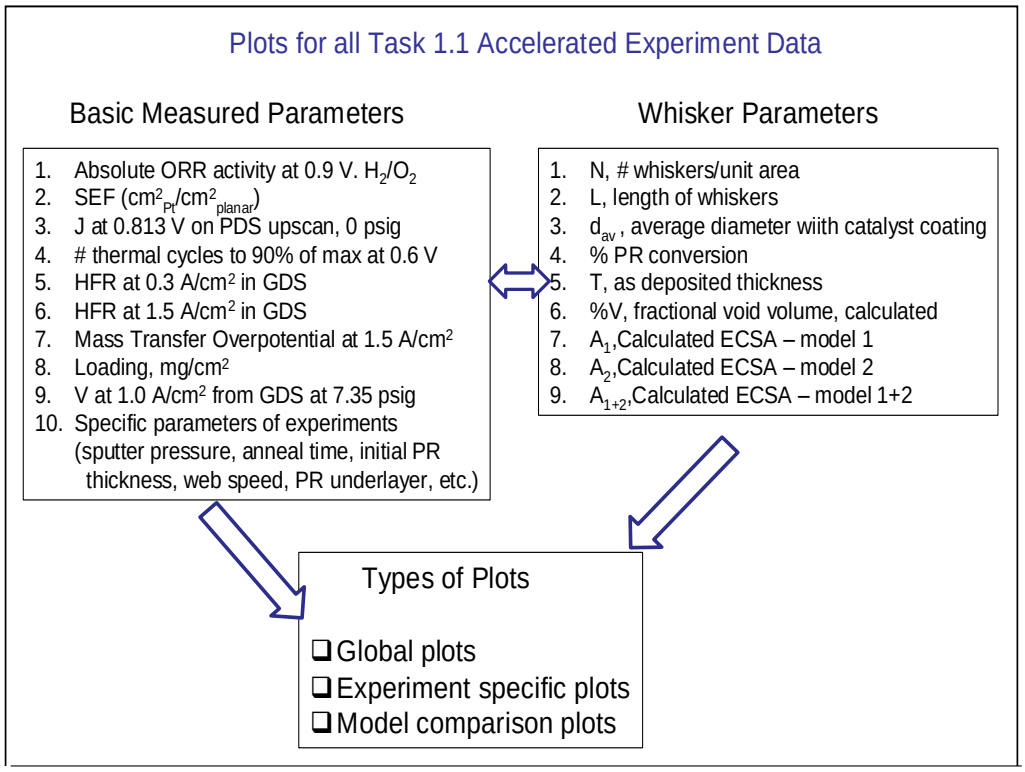


**Fig. S1.** Basic measured parameters, whisker and model parameters investigated in the WAO-series of experiments and the three types of data plots that were used to assess the results.

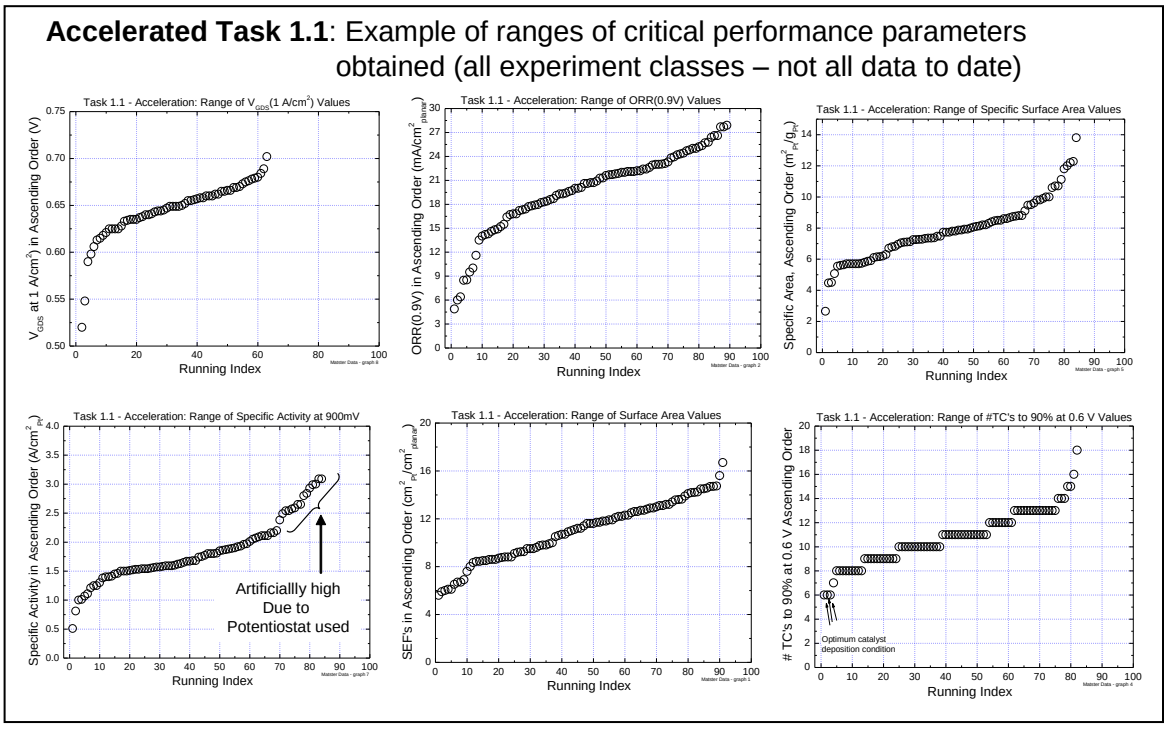


**Fig. S2.** Example of a global plot of various fuel cell performance metrics from the results of 118 MEA's, showing the ranges of the metrics for one material parameters varied.

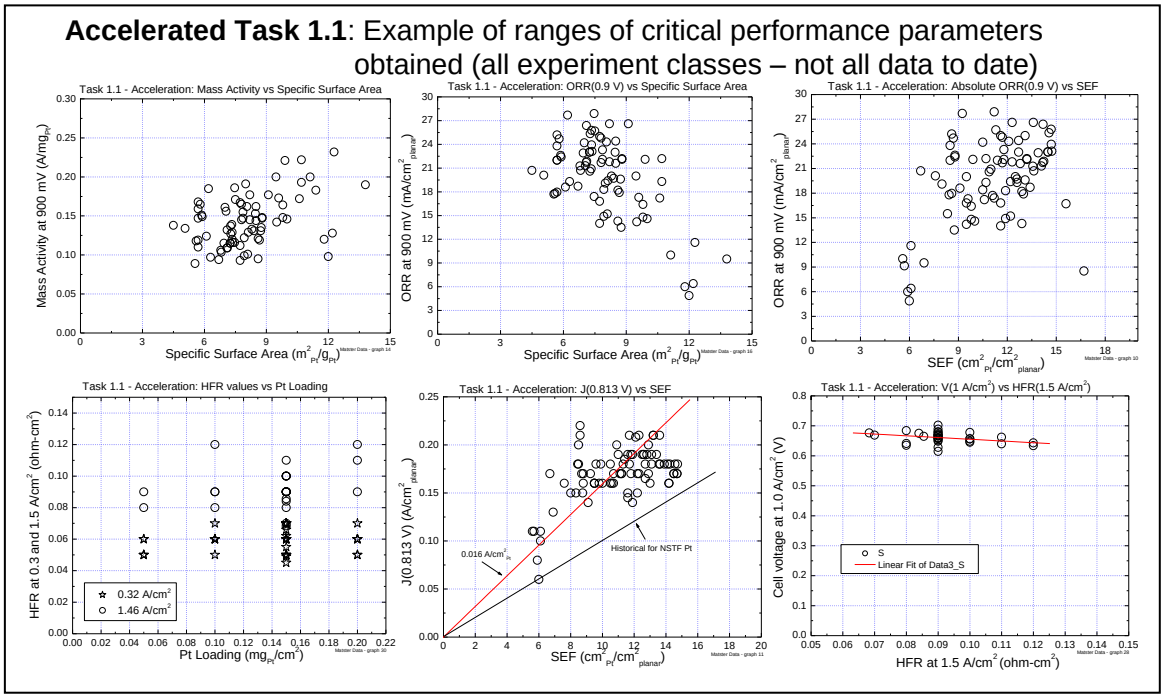


**Fig. S3.** Example of a global plot of various fuel cell performance metrics from the results of 118 MEA's, showing the ranges of the metrics as a function of surface area, Pt loading or HFR.

Using representative values for $f = 3\text{x}10^5$ and $x$=2/3, resulting from the modeling graphs, and known fixed values for w and t of the bare whiskers, $A^{Pt}_{geo}$ can be expressed as a function of N for 10 < N < 50 with L as a parameter in the range of 0.3 < L < 3 microns. Equation 1 then reduces to the following quantitative expression, where N is in units of numbers of whisker per square centimeter and L is in units of centimeters:

(2) $$A^{Pt}_{geo} = 2.52 + 1.067\text{x}10^{-5}\ NL + 2.98\text{x}\ 10^{-11}\ N + 1.05\text{x}10^{5}/NL + 2.2\text{x}10^{-6}\ /\ L$$

This result of $A^{Pt}_{geo}$ can be plotted vs N for various L are shown in Fig. S4. The cross-hatched box indicates the small relative range of N, L parameters screened by the WAO-1 data series. Surprisingly, the predicted surface area is still a monotonically increasing function of N for all L above the smallest values of N and L. Clearly the range of values scanned by WAO-1 is very small, and although not all the ranges of N and L will likely be obtainable, there should be definite benefits to determining the maximum values of N and L likely to be obtainable simultaneously.

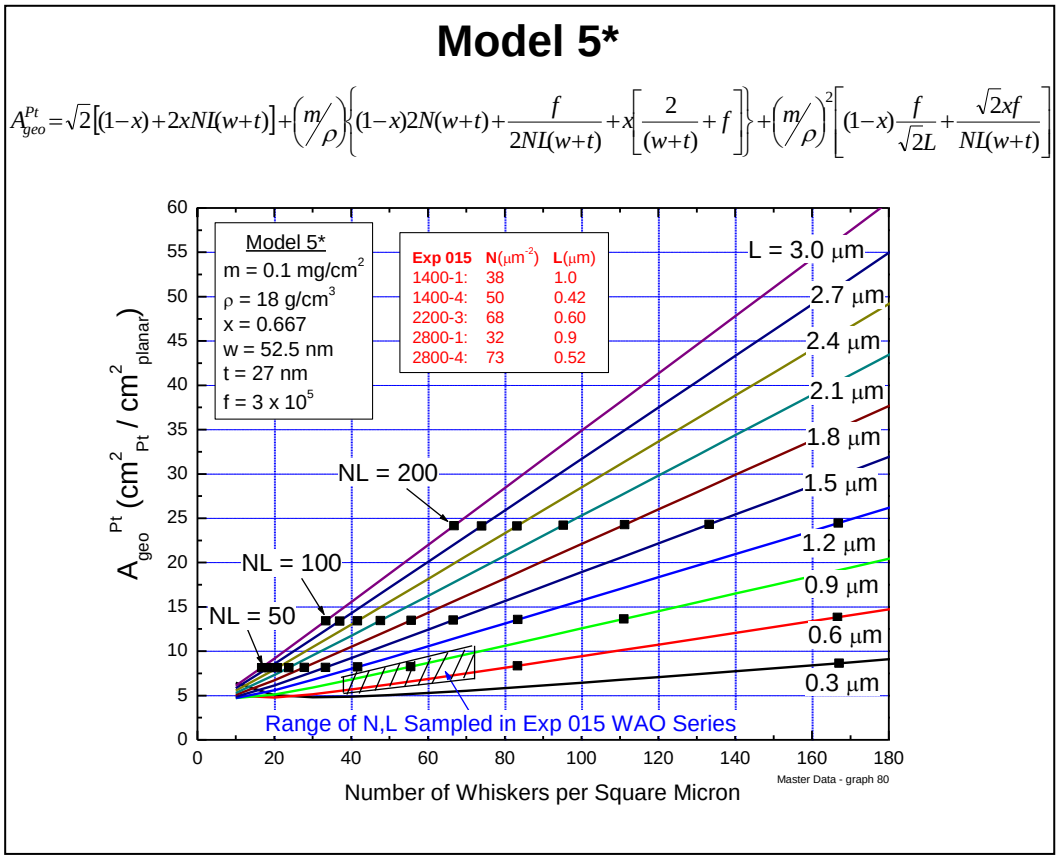


**Fig. S4.** Predicted Model 5* electrochemical Pt surface area from equation (2) based on the parameters in the legend.

# Task 1.2 Fundamentals of NSTF catalytic activity



Task 1.2. Re-assessment of 3M NSTF catalyst entitlement ORR activity

- Measurements of NSTF alloy activities at ANL using RDE methods show significantly higher fundamental activities than state-of-the-art Pt dispersed on carbon, confirming 3M fuel cell measurements.
- ANL data shows also that $H_2$ annealing the NSTF alloys produces similar increases seen with their segregated surface composition profiles produced by $H_2$ annealing bulk polycrystalline and single crystal samples.
- **But are these NSTF activities near the entitlement values?**

Specific Activity Measurements by ANL Rotating Disc Electrode (RDE) System

V. Stamenkovic,
Dennis van der Vliet,
N. Markovic

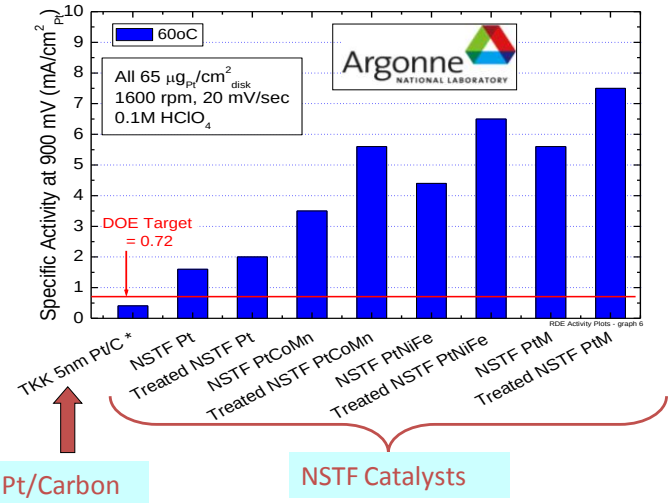


3M Advanced Cathode Catalysts and Supports..... DOE Review, March 16, 2010

Task 1.2. Re-assessment of 3M NSTF catalyst entitlement ORR activity

- Joint ANL/3M presentation at the fall 2009 ECS meeting showed this "Volcano Plot"
- Compares ANL measured NSTF alloy activities and ANL extended surface (bulk) catalyst activities to TKK 5nm Pt/C dispersed catalyst, all measured at ANL.

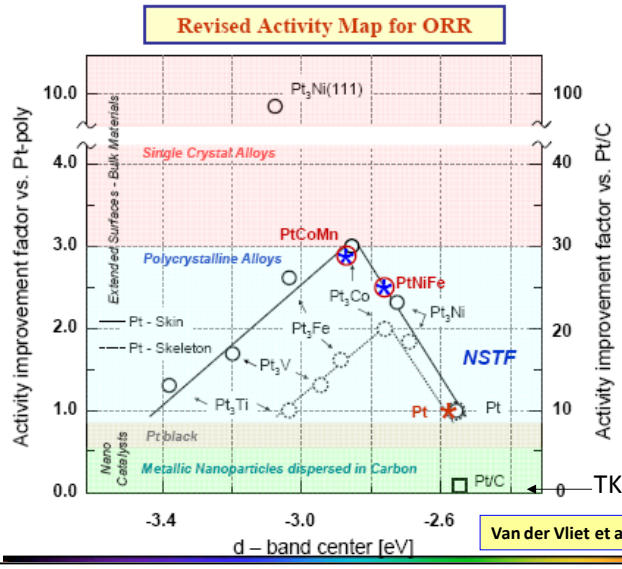


- $Pt_3Ni_1(111)$ single crystal surface activity is ~100 x more active for ORR than the Pt/C by ANL.
- 3M NSTF PtCoMn and PtNiFe appeared to fit their model for polycrystalline alloys
- Still potential for > 3X more to make NSTF equal to single crystal.

Van der Vliet et al., 216th ECS Meeting, Vienna, Oct. 2009

Task 1.2. Re-assessment of 3M NSTF catalyst entitlement ORR activity

## Updated, Revised Activity Map for ORR on Pt Alloys

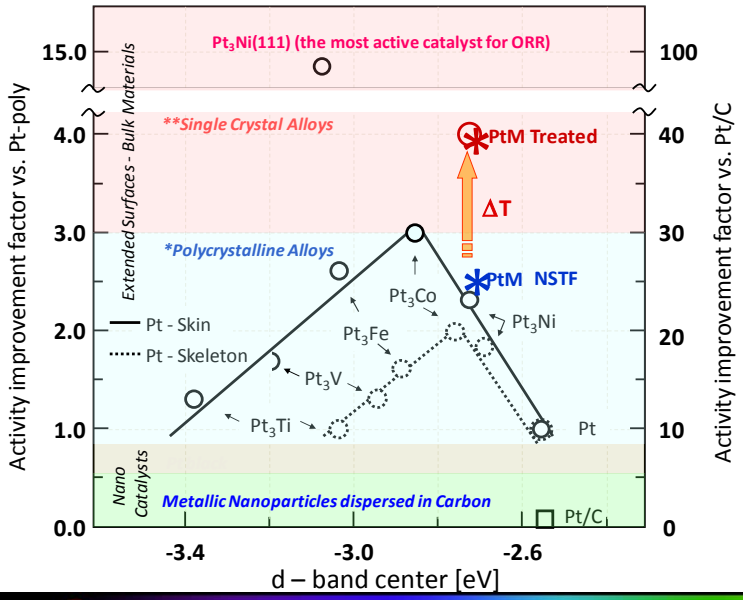


- Recently updated version from Voja of their slide showing the effect of their annealing the NSTF PtM alloys. Now NSTF PtM treated is less than 2.5 X from the bulk $Pt_3Ni(111)$ alloy.
- Is the bulk crystal surface $Pt_3Ni_1[111]$ activity value Nature's fundamental upper limit? Consider the following:

Argonne NATIONAL LABORATORY

*Stamenkovic, Markovic et al., Nature Mat 6(2007) 241

**Stamenkovic, Markovic et al., Science 315(2007) 493

## Nanosegregated Surfaces as Superior Catalysts

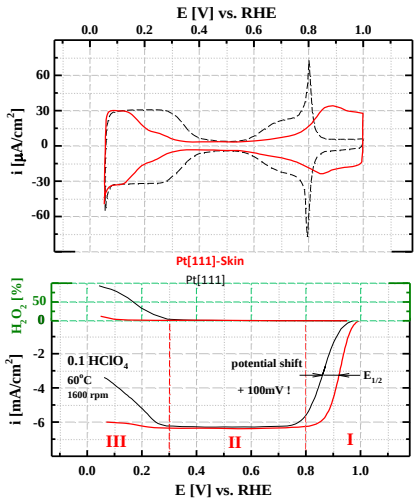


**Pt(111)-Skin** is the most active catalyst for the oxygen reduction reaction, and it is ~100 times more active than the state-of-the-art Pt/C catalysts

Stamenkovic, Markovic et al. Science 315(2007) 493

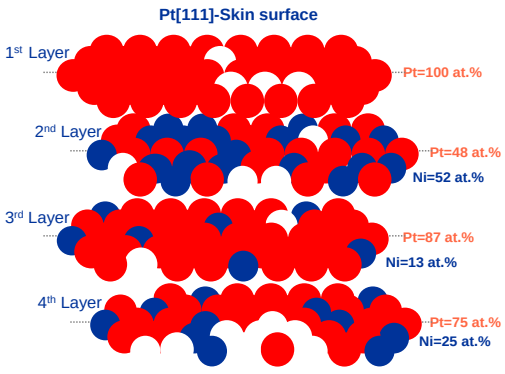


**Nanosegregated Pt[111]-Skin Surface** formed over $Pt_3Ni$ alloy has oscillatory concentration profile in the first four atomic layers, which induces unique electronic and superior catalytic properties.

Argonne NATIONAL LABORATORY

UChicago ▸ Argonne LLC

Office of Science U.S. DEPARTMENT OF ENERGY

Task 1.2. Re-assessment of 3M NSTF catalyst entitlement ORR activity

- Based on ANL work on single crystals, the activity of bulk $Pt_3Ni_1$(111) alloy surfaces is ~ 9 times higher than bulk $Pt_3Ni_1$ (100) and 3.6 times higher than $Pt_3Ni_1$ (110), and many times higher than pure Pt if one has the nano-segregated surface composition profile structure in the top 4 layers.
- Do we have this yet on the NSTF Pt alloy surfaces? Do we even have mainly Pt(111) surface facets?

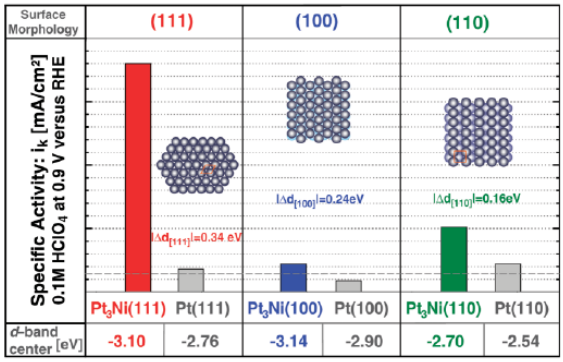


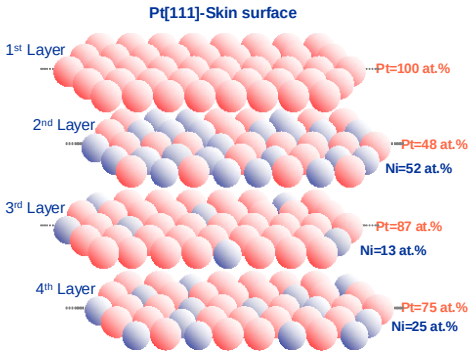


**Stamenkovic et al., Science 315(2007) 493**

3M Advanced Cathode Catalysts and Supports…… DOE Review, March 16, 2010

Task 1.2. Re-assessment of 3M NSTF catalyst entitlement ORR activity

- Stamenkovic et al. have used vicinal single crystal surfaces to study the effect of activity on terrace width. ORR activity drops off if terrace is too small.
- So this is another factor for extended surface area catalysts that is important.

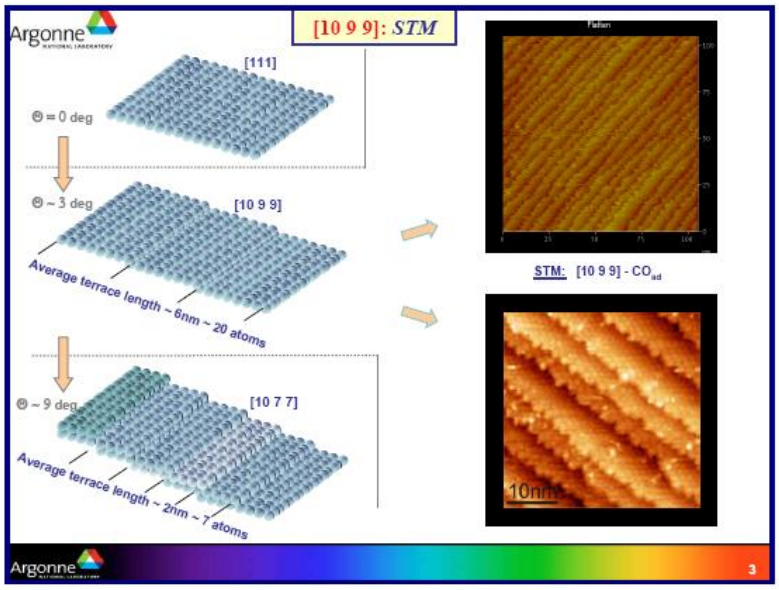

Task 1.2. Re-assessment of 3M NSTF catalyst entitlement ORR activity

Stamenkovic et al. have used vicinal single crystal surfaces to study the effect of activity on terrace width.

**ORR on Pt(hkl) Surfaces**

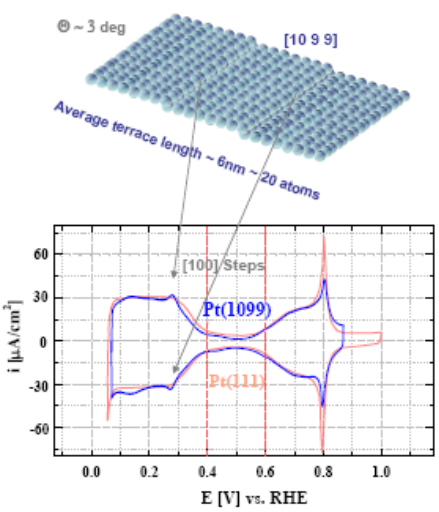


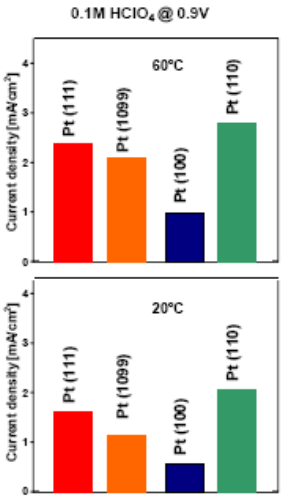


Therefore, 3 things to optimize for NSTF:

- Besides maximizing the proportion of Pt(111) facets, and segrating the surface structure, are those facets large enough is another question:



3M Advanced Cathode Catalysts and Supports..... DOE Review, March 16, 2010

Task 1.2. Re-assessment of 3M NSTF catalyst entitlement ORR activity

TEM studies of NSTF catalysts at 3M suggest current sputtered Pt alloy catalysts have activities that may be far below the entitlement potential.

- Low magnification TEM image of NSTF PtM catalyst coated whiskers, showing metal coating comprises small grains ~ 5-10 nm in size.
- XRD shows apparent crystallite grain sizes in similar range:
  - Pt[111] = 7.7 nm
  - Pt[200] = 5.1 nm
  - Pt[220] = 5.3 nm
  - Pt[311] = 6.3 nm
- Suggests each grain consists primarily of a single crystal.
- Are the grain surface facets the right (preferred) orientation for ORR? Are they large enough? How much of the total whisker surface area is good stuff?

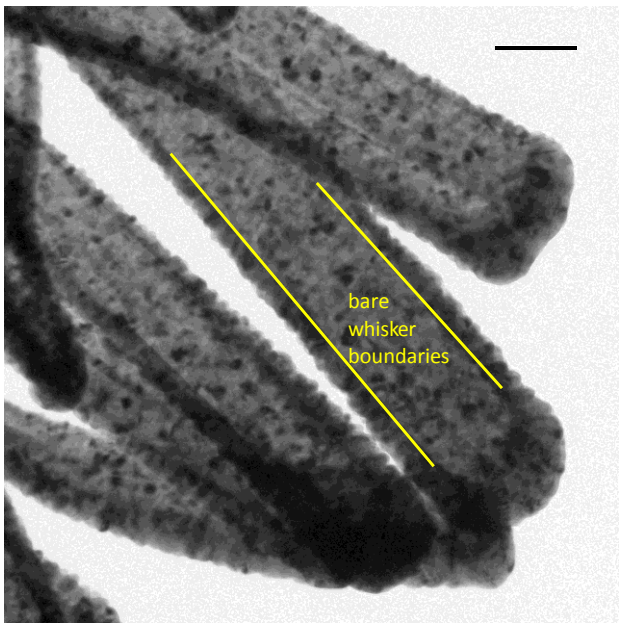

Task 1.2. Re-assessment of 3M NSTF catalyst entitlement ORR activity

Composite TEM images to define terms and elements (not from the same whisker)

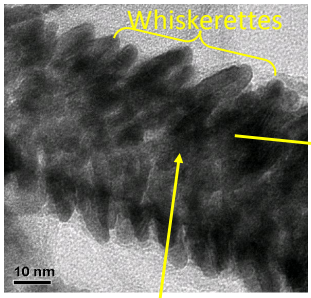


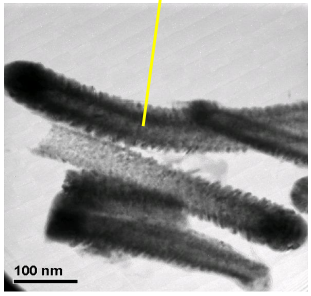


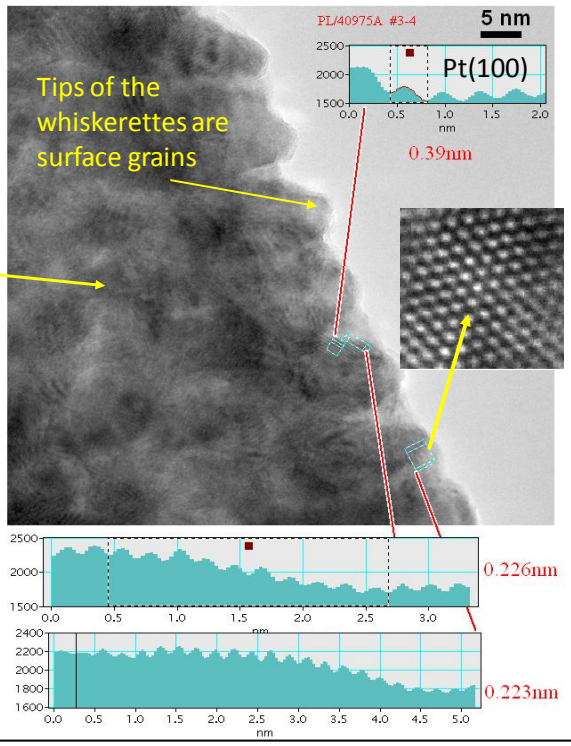




Task 1.2. Re-assessment of 3M NSTF catalyst entitlement ORR activity

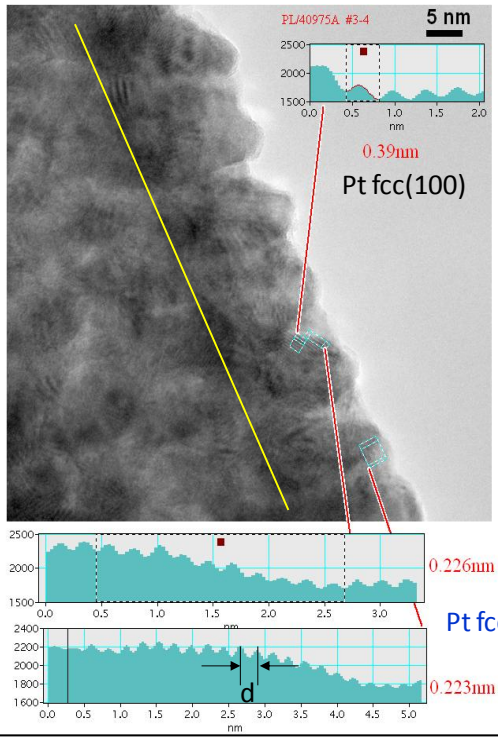


TEM image of one edge of a portion of a standard NSTF catalyst coated whisker of sputter deposited PtCoMn at a loading of 0.1 $mg_{Pt}/cm^2$.

- Surface facets of the grains are mixed, not all the preferred [111].
- Facets are small, ~ 5 nm.
- No large flat terraces apparent.
- Probably a lot of "junk surface" in between the good surface facets.

PtCoMn fcc lattice constant = 3.88 Å:

Pt(111) d = 3.88 / $(3)^{1/2}$ = 2.24 Å

Task 1.2. Re-assessment of 3M NSTF catalyst entitlement ORR activity

TEM image of the tip of a standard NSTF catalyst coated whisker of sputter deposited PtCoMn at a loading of 0.1 $mg_{Pt}/cm^2$.

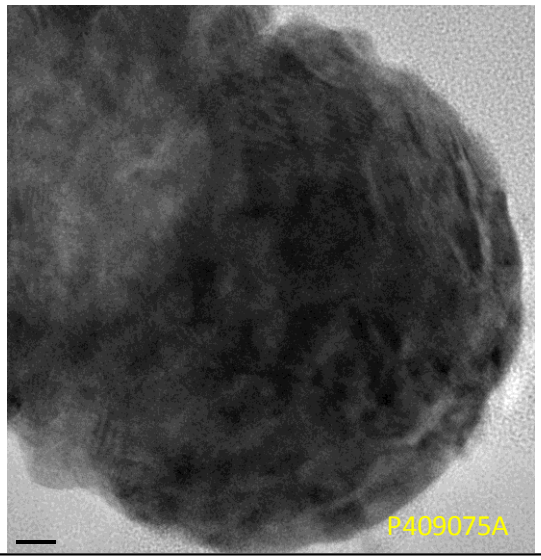


- No clear, well defined facets on the whisker tips.
- Some coarse Moire fringes apparent indicating some overlapping lattice fringes.
- Tips represent a small fraction of the total surface area, but still could be important if it were highly fcc(111) faceted.

3M Advanced Cathode Catalysts and Supports…… DOE Review, March 16, 2010

Task 1.2. Re-assessment of 3M NSTF catalyst entitlement ORR activity

- Vapor deposited Au using e-beam deposition gives very different surface structure.
- There is significant surface coverage of Au(111) terraces.
- Very different from sputter deposited PtCoMn.

- TEM overview of a Au coated whisker end.
- Note smoothness of surface.
- Some grain boundaries are marked in red.

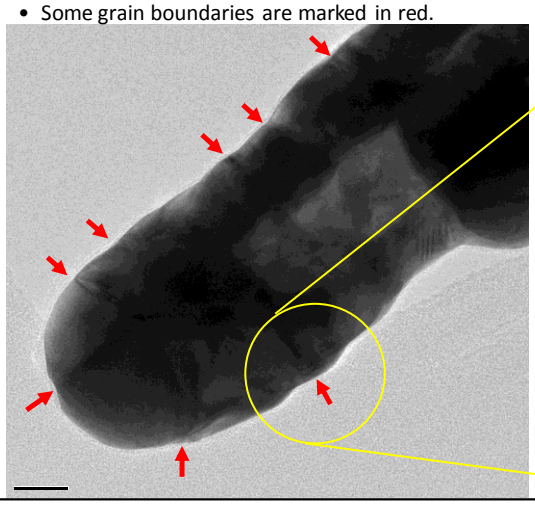

- 3 different gold grains showing 111 lattice fringes in different directions.
- Note the atomically smooth surface, circled.

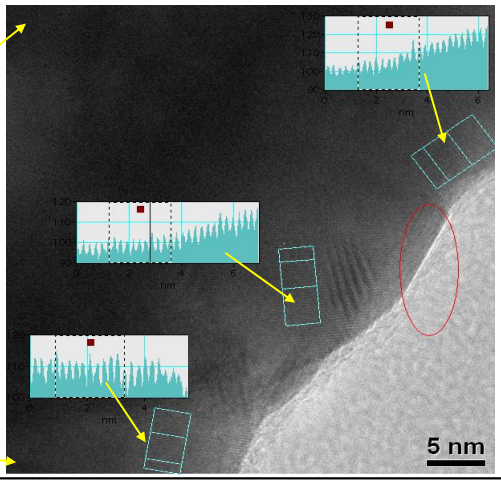

Task 1.2. Re-assessment of 3M NSTF catalyst entitlement ORR activity

- Vapor deposited Au using e-beam deposition gives significant surface coverage of fcc(111) terraces.
- The terraces can be atomically flat over large distances.

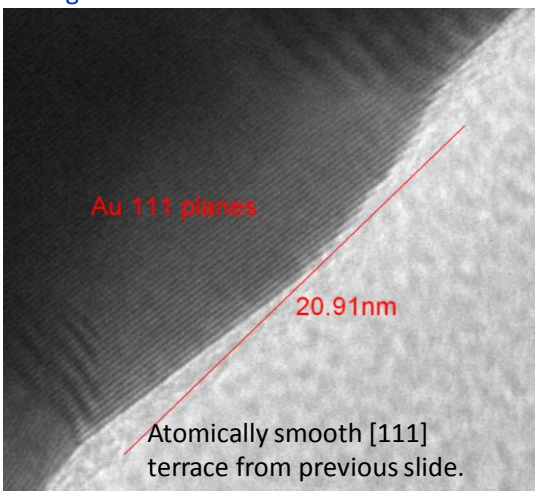


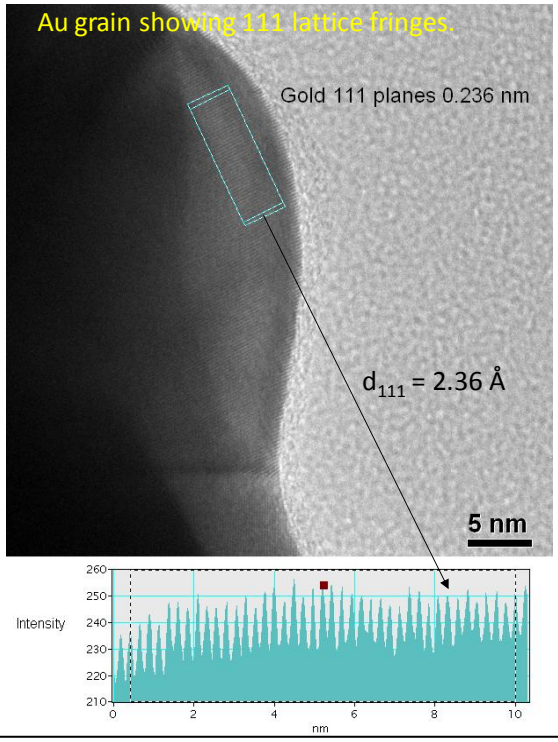




Task 1.2. Re-assessment of 3M NSTF catalyst entitlement ORR activity

- Vapor deposited Pt using e-beam deposition gives very different surface structure again.
- Pt coating consists of a high level of distinct crystalline grains.
- Very different from sputter deposited PtCoMn or vapor coated Au..

0.2 $mg_{Pt}/cm^2$ of pure Pt (images from 2000-2001)

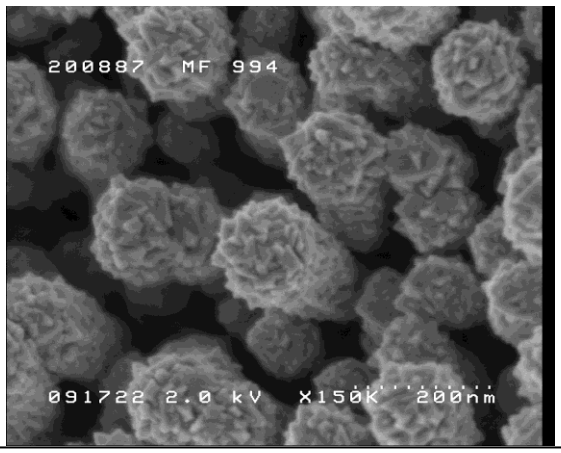


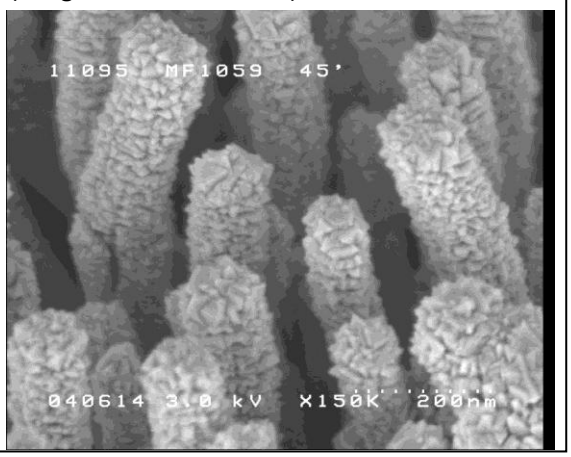

Task 1.2. Re-assessment of 3M NSTF catalyst entitlement ORR activity

## Summary

- We have shown excellent correlation of NSTF fuel cell activity measurements with the fundamental ANL rotating disk electrode measurements.
- The surface morphology of the NSTF catalyst coatings can be dramatically varied depending on the materials used and the deposition process conditions.
- The current standard NSTF Pt and Pt alloy catalyst coatings appear far from ideal based on the fundamental single crystal and polycrystalline surface catalysis and surface structure determination done at ANL by Markovic, Stamenkovic et al.
  - Activity for ORR of bulk $Pt_3Ni_1$[111] surfaces are 9 x larger than $Pt_3Ni_1$[100] and 3.6 x larger than $Pt_3Ni_1$[110] surfaces
  - The [111] terraces must be sufficiently large to realize the full activity potential, > 6 atoms.
  - The nano-segregated bulk Pt[111]-Skin Surface formed over bulk $Pt_3Ni_1$ alloy has an oscillatory concentration profile in the outer four atomic layers, which induces unique electronic and superior catalytic properties. This was obtained at ANL by annealing single crystals of $Pt_3Ni_1$ in hydrogen.
- So there appears to be significant opportunity yet to optimize the NSTF catalysts based on fundamental assessments of extended surface area bulk catalysts.

3M Advanced Cathode Catalysts and Supports…… DOE Review, March 16, 2010

Task 1.2. Re-assessment of 3M NSTF catalyst entitlement ORR activity

How would we measure the amount of NSTF surface area that is in the preferred fcc(111) orientation, vs other fcc(hkl) or garbage surface area?

- TEM – very specific and definitive, but laborious and difficult to get an average ensemble measurement over the whole whisker, or
- ANL's In-situ FTIR rapid scan CO adsorption and oxidation

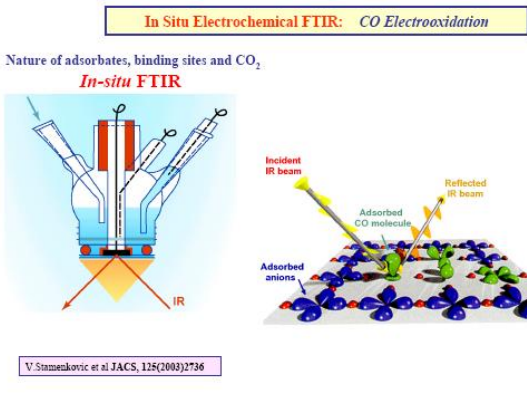


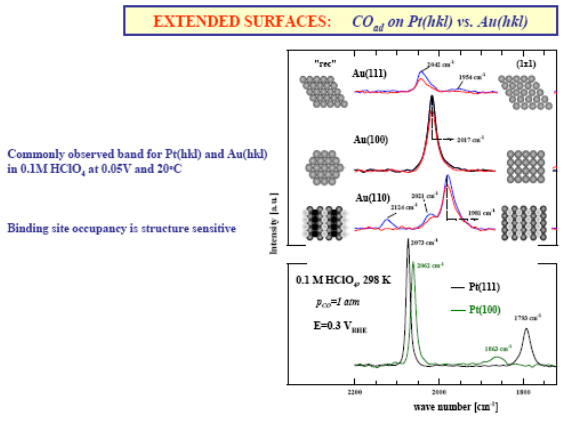

## Pt(hkl) SURFACE MORPHOLOGY: $CO_{ad}$ Oxidation on Pt[hkl] - Rapid In-Situ FTIR

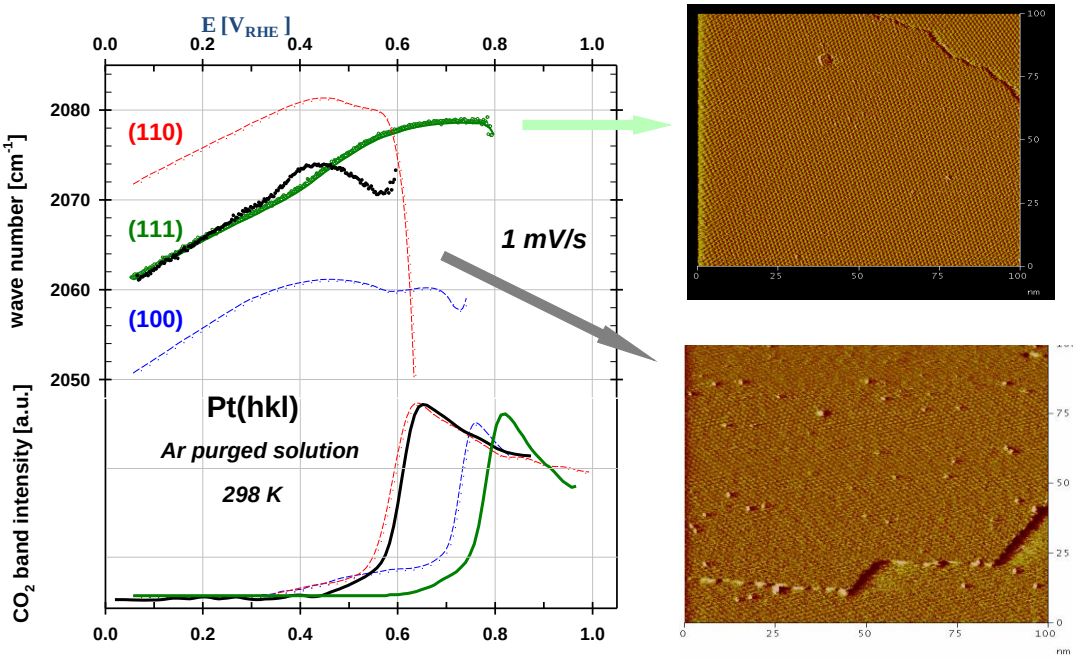


**L-H:** $CO_{ad} + OH_{ad} \rightarrow CO_2 + H^+ + e^-$

Argonne NATIONAL LABORATORY

## Pt-NSTF: Surface Morphology by in-situ FTIR

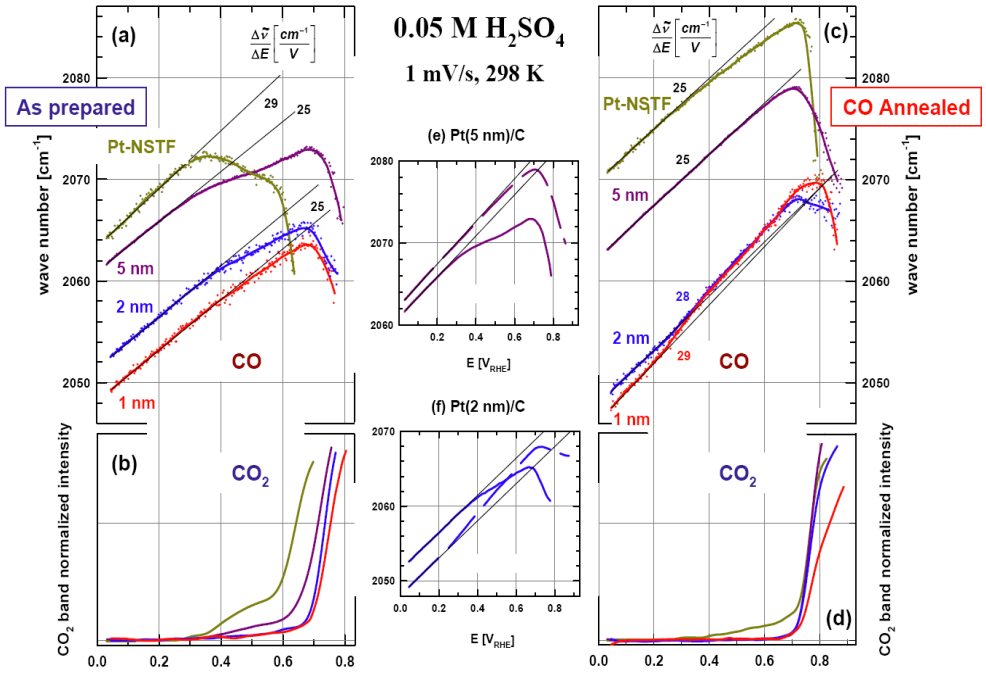


Argonne NATIONAL LABORATORY

ANL, *Unpublished*

Task 1.2. Re-assessment of 3M NSTF catalyst entitlement ORR activity

- ANL's In-situ FTIR studies of the electrochemical oxidation of CO adsorbed on well defined single crystal bulk surfaces and on NSTF-Pt, suggest that NSTF-Pt behaves for CO adsorption like Pt[110].
- This would suggest that a majority of our surface structure is not the preferred Pt[111].

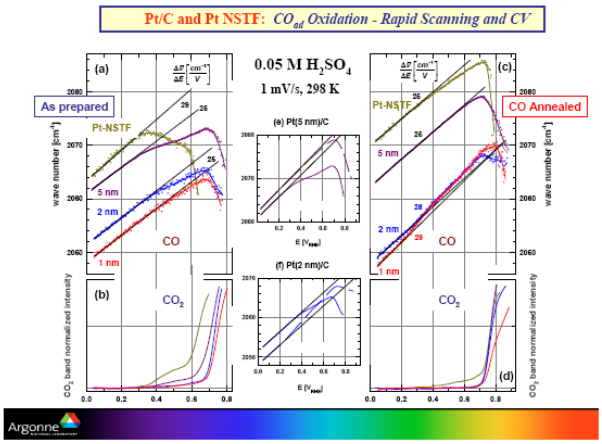


3M Advanced Cathode Catalysts and Supports…… DOE Review, March 16, 2010

Task 1.2. Re-assessment of 3M NSTF catalyst entitlement ORR activity

## Future NSTF Catalyst Development Path

- There appears to be significant opportunity to increase the activity of the NSTF catalysts by maximizing, to the entitlement value:
  1) the fraction of the whisker surface area covered by fcc(111) facets,
  2) forming the fcc(111) facets to be of sufficient size to realize the full activity per unit area seen in single crystal surfaces,
  3) developing the segregated surface composition profile in the outer layers of the Pt alloys.
- Items 1) and 2) will be addressed by modifications to the catalyst deposition process and process parameters, trying to generate a similar surface as e-beam deposited Au. Will require a good metric to assess relative amounts of [hkl] facet areas. TEM is limited. ANL's FTIR–CO fast scan may be better.
- Item 3) may be addressed by roll-good compatible energetic surface treatment processing that simulates the hydrogen annealing of bulk single crystals. As shown on earlier slides we have demonstrated ~ 50% increase in mass activity of the PtM and PtCoMn alloys.

## Task 1.3 New multi-element catalysts to increase activity

### Technical Accomplishments and Progress

Supplemental Slide

**Task 1.** NSTF Catalyst Activity, Surface Area, Fundamentals

- Dalhousie is also capable of excellent RRDE characterization. Now applied to NSTF routinely.
- New aspect is that 3M grows the whiskers directly on the glassy carbon disk.
- Dalhousie applies the catalyst to be studied to the whiskers by sputtering. Then characterizes in multi-RRDE facilities.

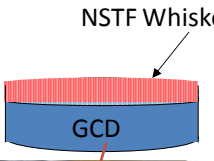


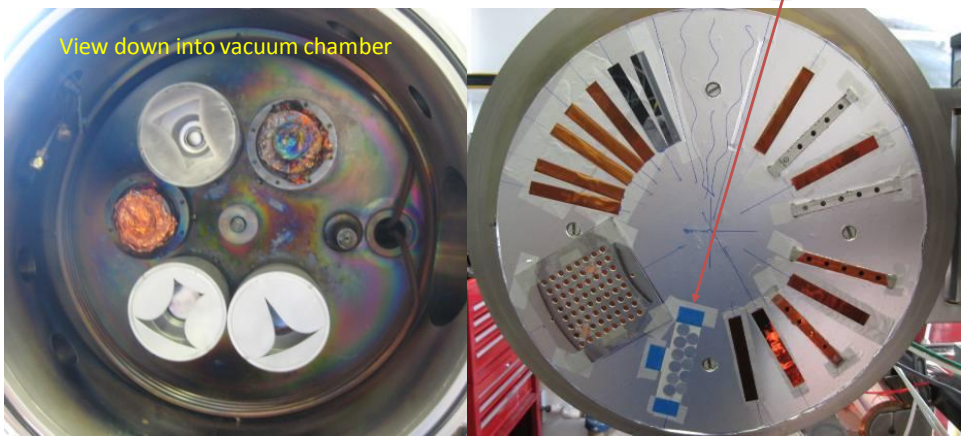






**Task 1.3 – New catalysts for increased ORR activity and stability**

❑ Dalhousie University Activities

2) PtNi dealloying kinetics – Part of Gary C. K. Liu Ph.D thesis, results presented at 218th ECS meeting

Nickel dealloys from the $Pt_3Ni_7$ material at a potential higher than 600 mV .

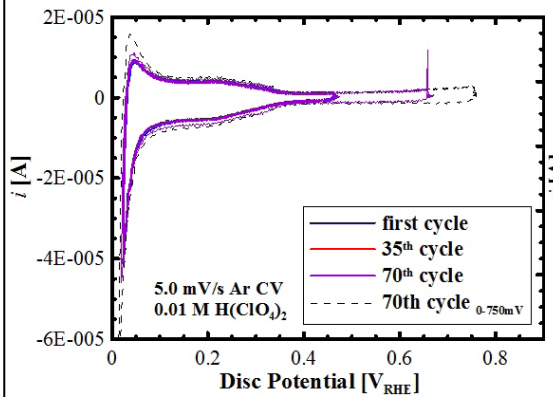


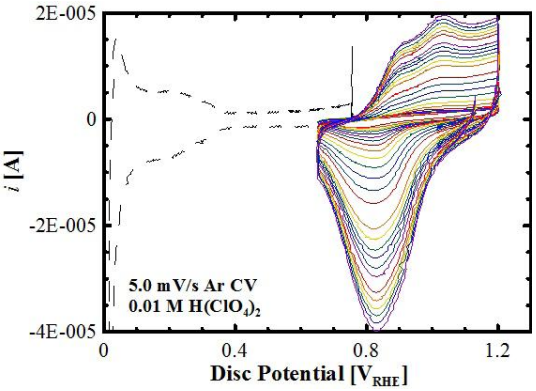


CV of Pt Ni in lower potential regions where pure nickel dissolves fastest. There are no changes to the CV shapes, indicating no dealloying.

CV of Pt Ni in higher potential regions where pure nickel would have already dissolved. There is an apparent increase in the active surface area, indicating dealloying.

## Task 1.3 – New catalysts for increased ORR activity and stability

❑ Dalhousie University Activities – 1) C. K. Liu PtNi on NSTF RDE study

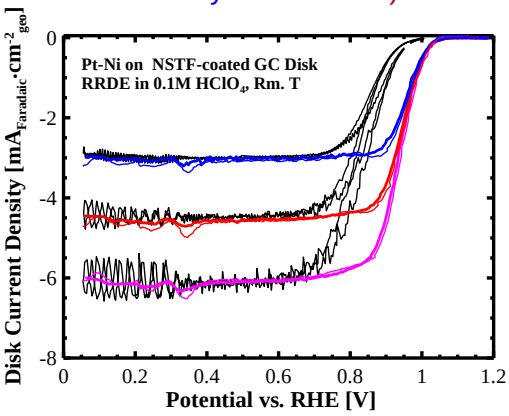


ORR measurements of the sputtered catalysts on different substrates, measured at different rotating rates (400, 1000 and 1600 rpm) at different potential sweep rates (20 and 50 mV/s)

- 400 rpm 20mV/s
- 1000 rpm 20mV/s
- 1600 rpm 20mV/s
- 400 rpm 50mV/s
- 1000 rpm 50mV/s
- 1600 rpm 50mV/s
- $Pt_{poly}$ on mirror-GC

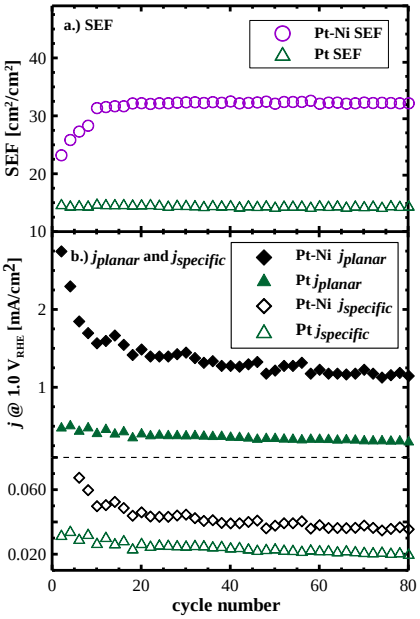


Summary of catalytic activity (SEF, $j_{planar}$ and $j_{specific}$ extracted at 1.0VRHE) of the Pt and Pt-Ni samples measured over 80 potential cycles.

3M Advanced Cathode Catalysts and Supports…… DOE Review, March 16, 2010

## Task 1.3 – New catalysts for increased ORR activity and stability

❑ Dalhousie University Activities

2) PtNi dealloying kinetics – Part of Gary C. K. Liu Ph.D thesis, results presented at 218th ECS meeting

Ni dissolution characterized by CV (A) and electrolysis (potential hold) method (B) shows the Ni dissolution reaction is most active between 200mV and 600 mV .

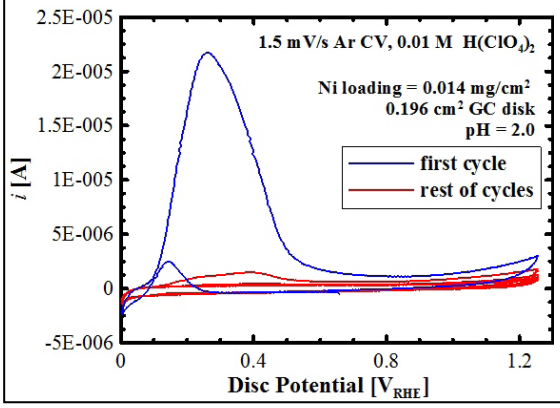


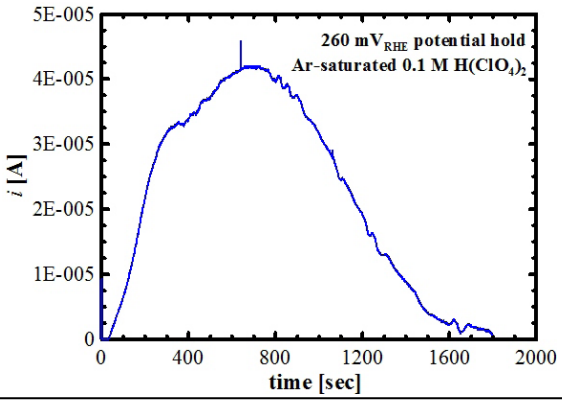

## Task 1.3 – New catalysts for increased activity and stability - hi thru-put studies

**Objective:** Control grain size, lattice spacing, and surface composition to increase activity, catalyst surface area, stability under high voltage cycling,

- We have continued to focus on the binary, ternary and intermixed inorganic materials systems – no further under- or over-layer work.
- There have been no "home runs" resulting yet from the compositional spread, high throughput work at Dalhousie.
- IP has been filed though on systems and methods to control alloy crystalline grain size and lattice parameters.
- Several new material systems have been studied, and also sputtering process parameter effects.
- Most recently, we have asked them to help focus on the PtNi system, as described in Task 1.2.

**New composition spreads studied:**

- Pt-W-C, Pt-Ta-C, Pt-C
- Pt-$TiO_2$, Pt-ZrO, Pt-Re, Pt-Hf, all as intermixes and as 50$cm^2$ for 3M
- PtCoMn sputtered vs pressure
- Pt sputtered in various gases
- Pt-Ni
- Pt-Co
- Pt-Pb
- Pt-Nb

11

The additional compositional spreads listed on this slide are in addition to those listed in Fig. 9.27 in Section 9.

## Task 1.3 – New catalysts for increased activity and stability - cat. deposition

### Background

- STEM work at ORNL during this contract on our standard multi-layer PtCoMn construction showed clearly that the bi-layer Pt/TM thickness of 50 Angstroms was preserved on the whisker tips (very tiny fraction of surface area)
- But layering was still visible on the upper whiskerettes.

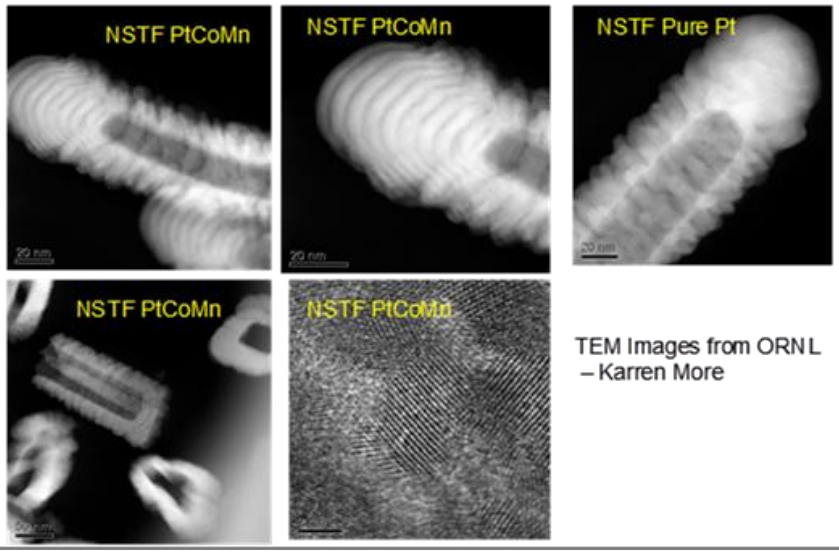


TEM Images from ORNL
– Karren More

## Task 1.3 – New catalysts for increased activity and stability - JPL

### JPL Electrochemical Cell with Rotating Electrolyte (RDE Simulation)

**JPL Original Concept:**

Novel multi-electrode electrochemical cell with rotating electrolyte to simulate rotating disc electrode measurements.

JPL

Charles C. Hays, S. R. Narayanan

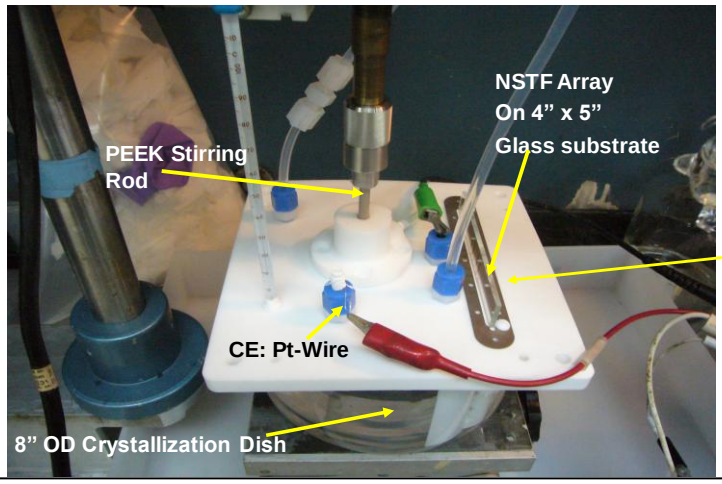


Multi-element sample array

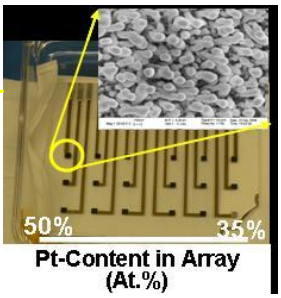


3M Advanced Cathode Catalysts and Supports…… DOE Review, June 30, 2009

Task 1.3 – New catalysts for increased activity and stability - JPL

### JPL Catalyst Array Fabrication

**Co-sputtering of Alloy NSTF**

JPL applies sputtered alloys to 3M NSTF whisker supports in compositional spread over multi-electrode array.

JPL

Charles C. Hays, S. R. Narayanan

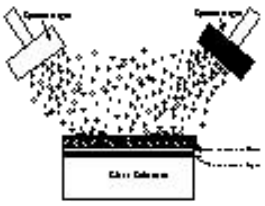

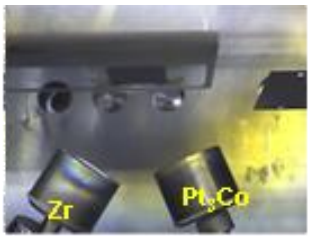


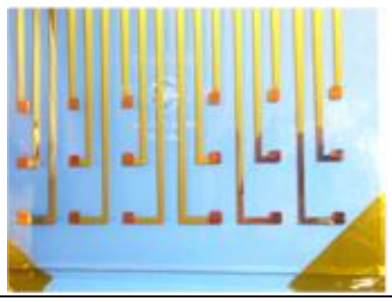

## Task 1.3 – New catalysts for increased activity and stability - JPL

### JPL Catalyst Array Fabrication

JPL

**Approach:**

- JPL sends glass substrate with array of gold-electrodes to 3M
- 3M applies bare NSTF whiskers to JPL substrates
- JPL sputters catalyst onto NSTF whiskers using multiple ion guns
- JPL characterizes the catalysts ex-situ and electrochemically

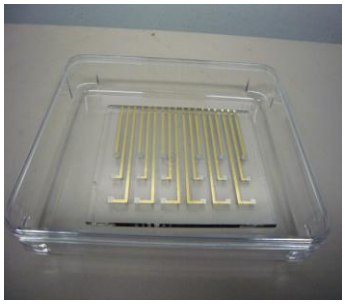

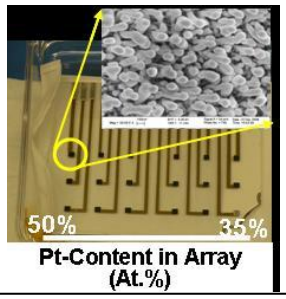


**Characterization by JPL:**

- Ex-situ: XRD, SEM, AFM,
- In-situ electrochemical
  - •Surface area by Hupd
  - •ORR – via Rotating Electrolyte

3M Advanced Cathode Catalysts and Supports…… DOE Review, June 30, 2009

## Task 1.3 – New catalysts for increased activity and stability - JPL

- **Status of thin film synthesis and characterization at end of 2008**
  - – Sputtering Systems: all systems working
  - – Sputtering Process: jig assembly validated
  - – Catalyst synthesis : 4- and 18-electrode substrates demonstrated with Pt, PtCo, PtZr, PtCoZr
  - - Characterization completed: Composition, SEM Images, XRD results, AFM
- **Status of electrochemical testing at end of 2008**
  - – Multi-electrode technique hardware completed
  - – Cyclic voltammetry on multi-electrodes demonstrated
  - – Surface areas by Hupd and ORR scans demonstrated
  - – CV cycling for durability of PtZr completed

**Electrochemical Surface Area**

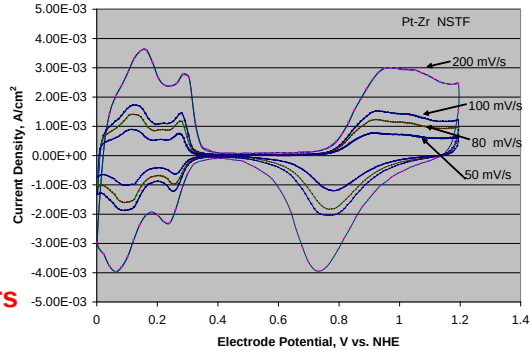


- **Surface area measurements from the novel CV apparatus were as expected.**
- **However, the magnitudes of the ORR currents were anomalously low by orders of magnitude.**

## Task 1.3 – New catalysts for increased activity and stability - JPL

Polarization Curves for ORR with JPL rotating electrolyte apparatus

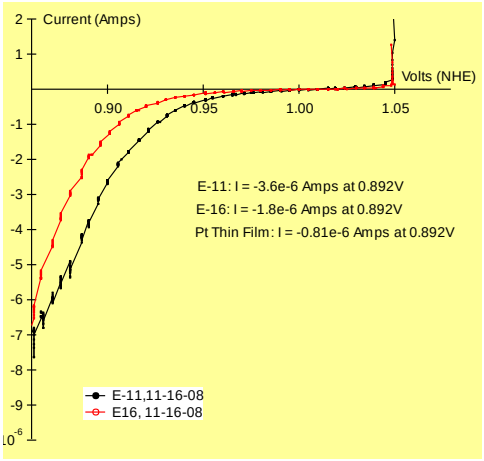


**Limiting currents (not presented) are about three times less than RDE measured at Dalhousie on the same NSTF configuration at 400 rpm.**

Scan Rate Measurements for ORR on PtCoZr NSTF

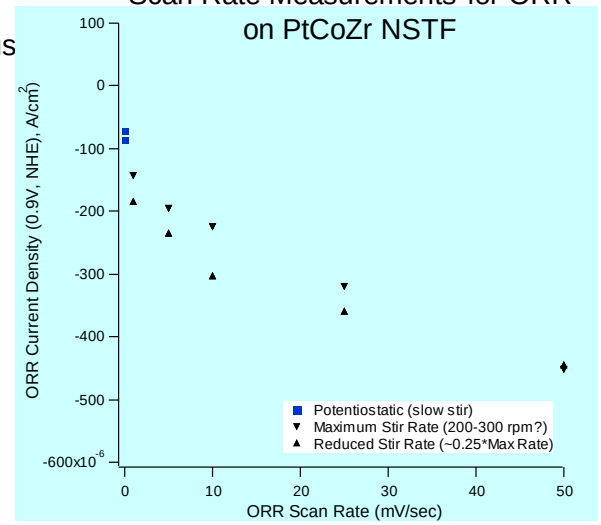


**The current at 0.9 V at 50 mV/s is 3 – 4 times that measured at 1 mV/s.**

3M Advanced Cathode Catalysts and Supports…… DOE Review, June 30, 2009

Task 1.3 – New catalysts for increased activity and stability - JPL

This issue of the JPL device currents caused us to re-examine the fundamentals of the concept approach:

- RRDE measurements of Pt coated GCD's (with and without NSTF whiskers) at Dalhousie were used to estimate the equivalent disk rotation speed of the JPL device's rotating electrolyte (next slide).
- Conclusion was that the equivalent rotation speed of the JPL system is only 10% of the normal RDE system. This meant that the JPL system was dominated by the boundary layer transport properties, not the ORR kinetics of the catalyst surface.
- Further round-robin samples have been made at 3M and Dalhousie for comparison testing at JPL and Dalhousie.

## Task 1.3 – New catalysts for increased activity and stability - JPL

### Estimating Equivalent Rotating Disk Speed of JPL Method

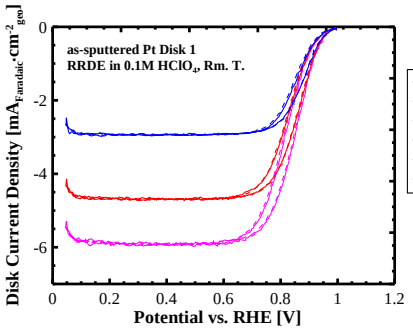


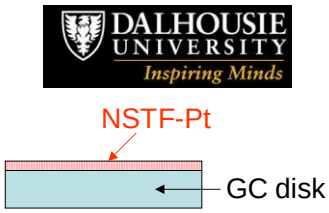


Rotating disk data on smooth Pt and NSTF-Pt coated glassy carbon disks for 1:1 comparison with the JPL rotating electrolyte technique. (from Dalhousie)

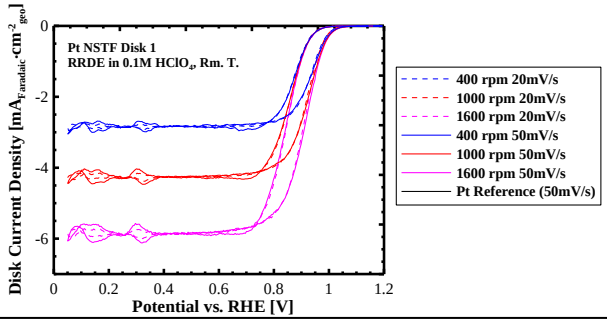


**Based on the values of the limiting currents at 400 rpm, the equivalent rotation rate by JPL method is ~ 44 rpm.**



## Task 1.3 – New catalysts for increased ORR activity and stability

JPL

- JPL/Cal Tech Activities – Charles Hays and Carol Garland (Cal Tech sub.)

### Microstructural Characterization of Note To Date

**Transmission electron microscopy (TEM) Characterization of $Ni_{70}Pt_{30}$ NSTF :**

- Subcontract set up with Caltech for TEM work with Carol Garland
  - Phillips – FEI Technai Field Emission Microscope, Model TF30UT - 300 kV Ultrathin
  - SEM at JPL with Dr. Jim Kulleck, using FEI NOVA Nano SEM 600.

1st Sample Set: $Pt_{30}Ni_{70}$ coated NSTF whiskers from 3M production line process P4.

3M P4 Process Coated $Ni_{70}Pt_{30}$ (At.%) NSTF

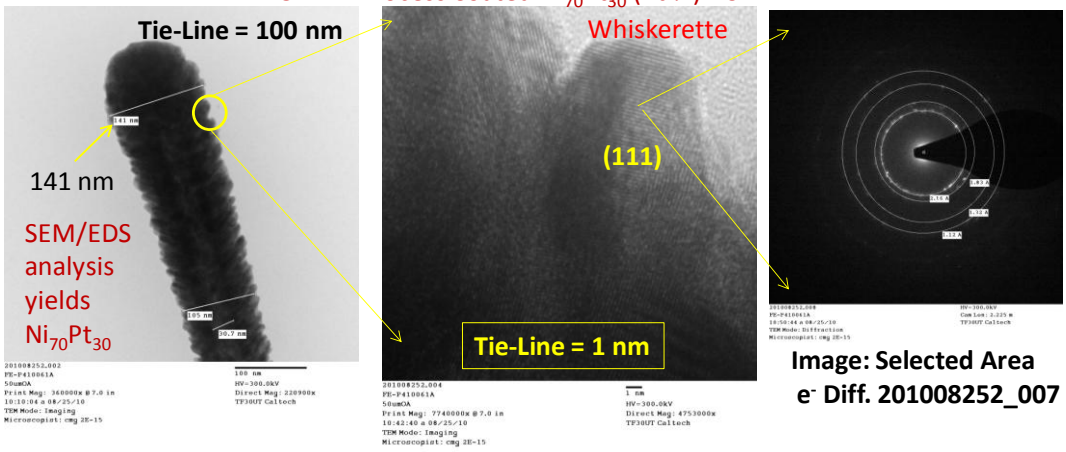

## Task 1.3 – New catalysts for increased ORR activity and stability

- JPL/Cal Tech Activities – Charles Hays and Carol Garland (Cal Tech sub.)

1st Sample Set: $Pt_{30}Ni_{70}$ coated NSTF whiskers from 3M production line process P4.

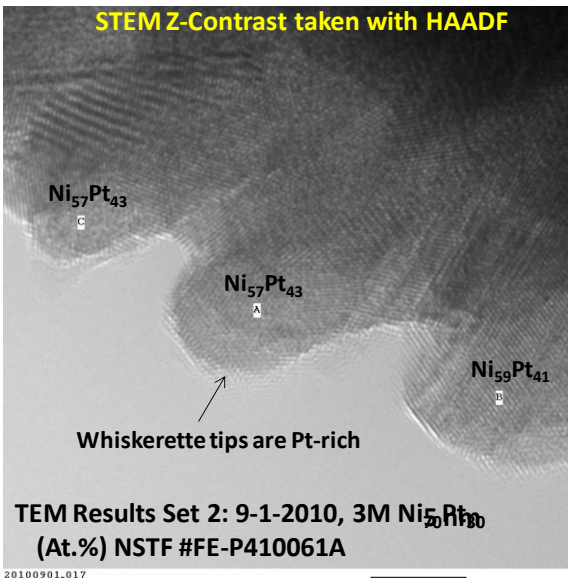


Tips of whiskerettes on sides of whisker are Pt rich vs. the whole whisker coating composition.

Microscopist: CMG ZE-15-A2

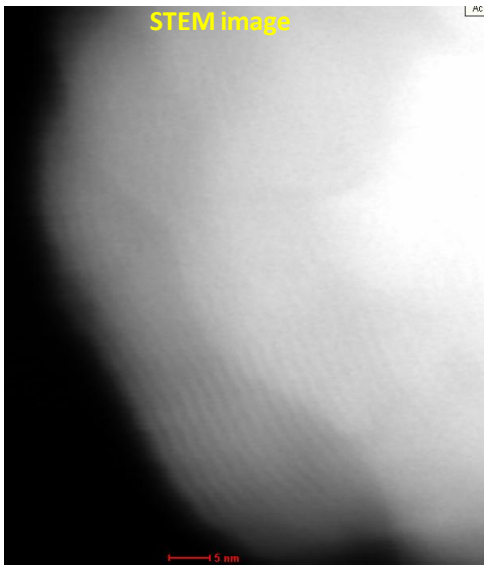


Layering observed at top of whisker from P4 process of sequential deposition.



## Task 1.3 – New catalysts for increased ORR activity and stability

- JPL/Cal Tech Activities – Charles Hays and Carol Garland (Cal Tech sub.)

2nd Sample Set: $Pt_{30}Ni_{70}$ coated NSTF whiskers by JPL co-deposition ion guns.

Strong variation of composition in whiskerettes depending on location on whisker !

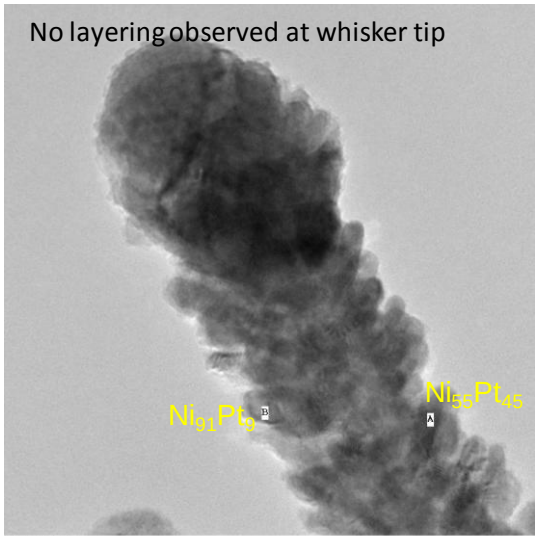


No layering on whisker tip consistent with co-deposition instead of sequential.

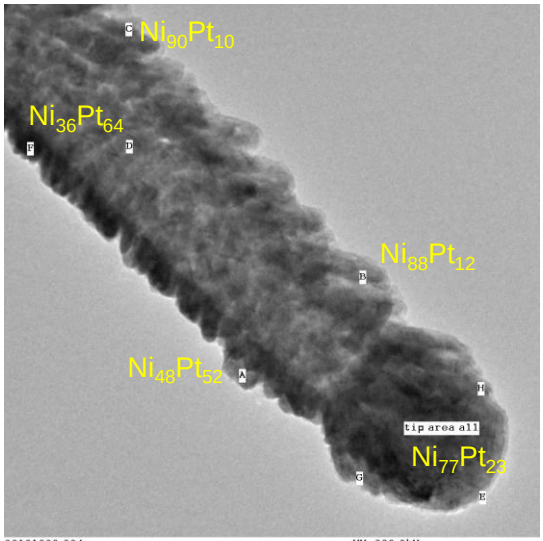


Text boxes denote composition at measurement sites

## Task 1.3 – New catalysts for increased ORR activity and stability

- JPL/Cal Tech Activities – Charles Hays and Carol Garland (Cal Tech sub.)

### Microstructural Characterization Summary

1st Sample Set: $Pt_{30}Ni_{70}$ coated NSTF whiskers from 3M production line process P4.

- Whiskerettes show strong (111) orientation by e-diffraction (same as PtCoMn)
- SEM/EDS analysis of entire whiskerette yields $Ni_{70}Pt_{30}$ composition, right on target
- Tips of whiskers show layering (consistent with sequential deposition) same as we see for PtCoMn)
- Tips of whiskerettes are Pt-rich, but whole whisker composition is 70:30.

2nd Sample Set: $Pt_{30}Ni_{70}$ coated NSTF whiskers by JPL co-deposition ion guns.

JPL coated $Pt_{30}Ni_{70}$ :

- does not show layering on whisker tips as expected.
- shows deposition induced shadowing effects, causing NiPt on one side and $Ni_{90}Pt_{10}$ on the other side (orientation re. Ion guns.)
- NiPt exhibits $L1_0$ Tetragonal superlattice
- $Ni_{70}Pt_{30}$ exhibits $L1_2$ Cubic superlattice

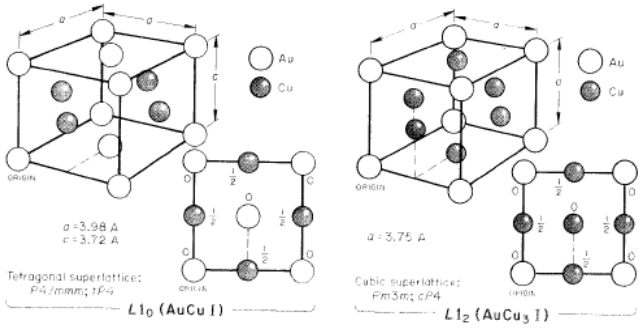

# Task 2

# Selected Supplementary Information

## Task 2 – Voltage Cycling Durability – 4000 cycles, effect of T °C, time

### 50 cm² 2009 Best of Class CCM's

4000 CV cycles, 0.6 – 1.2 V $H_2/N_2$, 20 mv/sec, 1 min./cycle, 80 or 95 °C

- Surface area stability similar with either 80 °C or 95 °C protocol
- Absolute ORR activity losses at 900mV similar for 80 °C or 95 °C protocol
- Production coater catalyst vs ML-2 batch coated catalyst (MT or ST) all similar
- Loss after 4000 minutes at OCV much less than after 4000 minutes of cycling (1 min/cycle)

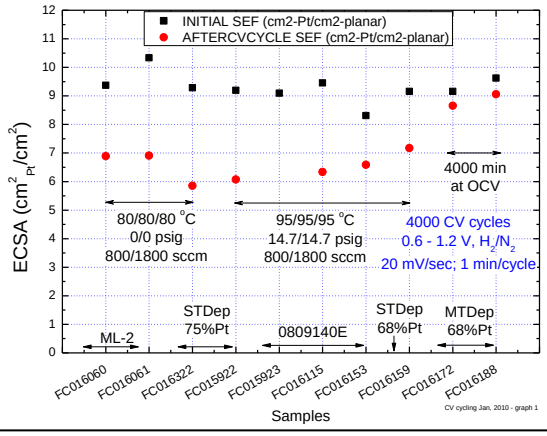


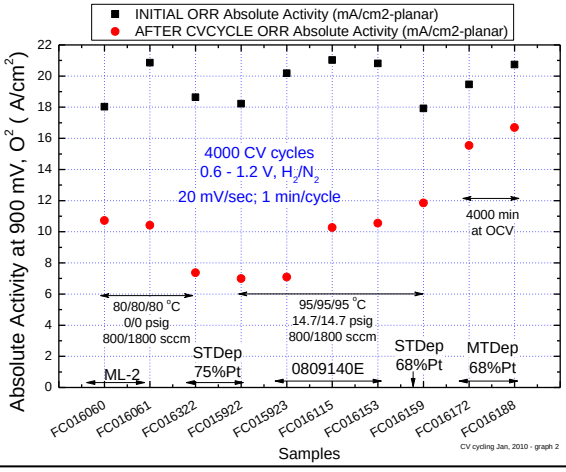


3M Advanced Cathode Catalysts and Supports…… DOE Review, March 16, 2010

Task 2 – Voltage Cycling Durability – 4000 cycles, effect of T °C, time

50 cm² 2009 Best of Class CCM's

4000 CV cycles, 0.6 – 1.2 V $H_2/N_2$, 20 mv/sec, 1 min./cycle, 80 or 95 °C

- Specific activity stability similar with either 80 °C or 95 °C protocol.
- Cell voltage at 0.02 and 1 A/cm² similar for 80 °C or 95 °C protocol
- Production coater catalyst vs ML-2 batch coated catalyst (MT or ST) all similar
- Loss after 4000 minutes at OCV much less than after 4000 minutes of cycling (1 min/cycle)

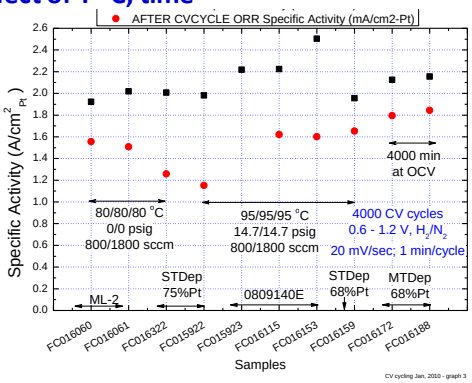


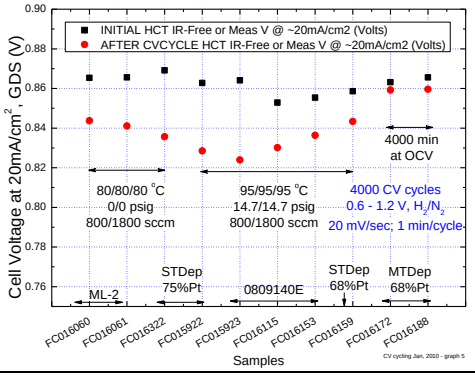


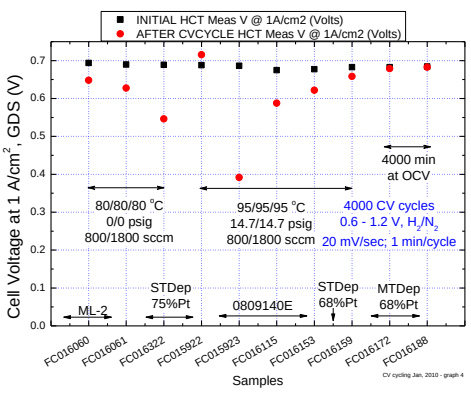

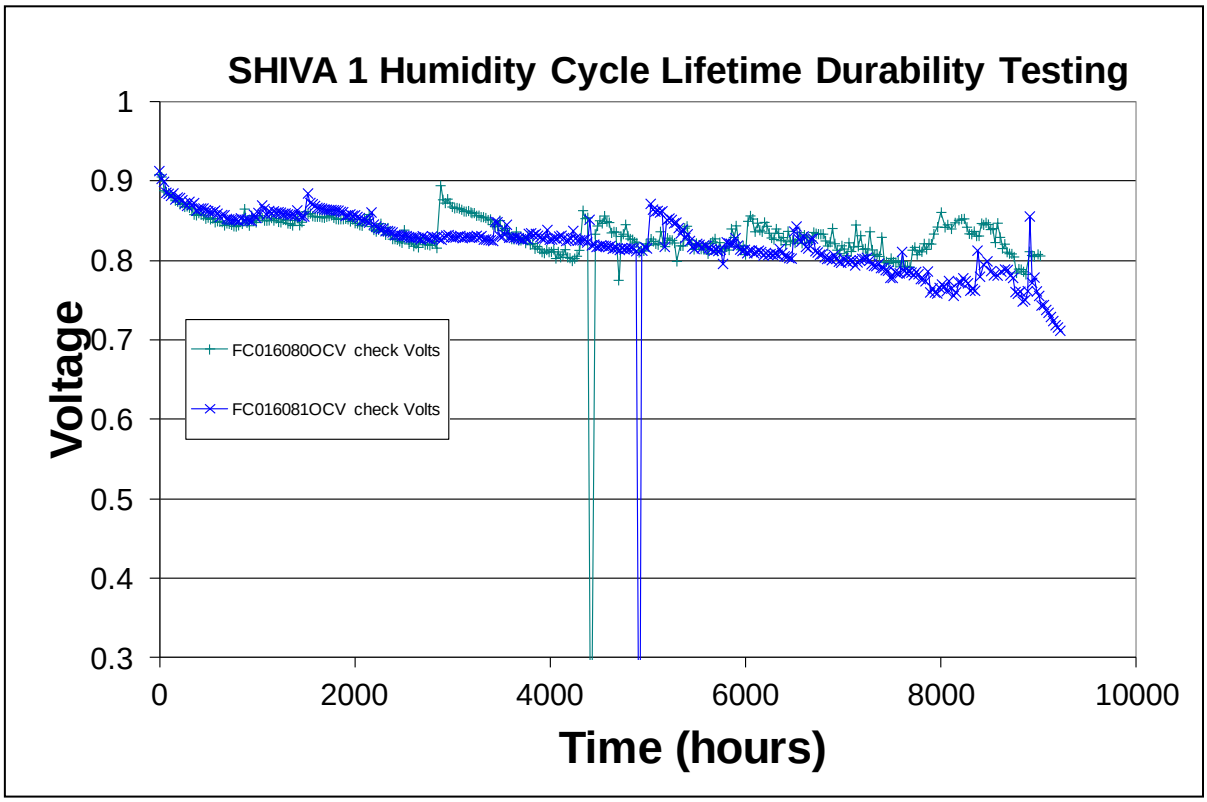


**Fig. S5.** Open circuit voltage versus time under the SHIVA 1 Load Cycling AST shown in Fig. 7.6, for the last two tested MEA's that reached 9000 hours of lifetime as judged by when the OCV fell below 0.8V.

# Task 3

# Selected Supplementary Information

# Task Summary

## Task 3 Full Size (> 250 $cm^2$) Single or Multi-Cell Tests

### Subtask 3.1 Down-selection of cathode catalysts in 50-$cm^2$ cell tests

The purpose of this subtask is to evaluate MEA's made with subsets of the supports and catalysts down-selected from Tasks 1 and 2, in 50 to 100 $cm^2$ single cells, using well established testing protocols for performance and durability. The approach will consist of performance and durability load-cycle testing under various pressures, temperatures, stoichiometries and relative humidities. Durability testing will include the accelerated testing recommended by DOE in Appendix D of the solicitation, or more rigorous accelerated tests as may be advised at the time. The expected outcome will be the down-selected cathode catalysts which demonstrate the best overall performance and durability when evaluated as 50 to 100 $cm^2$ MEA's that could meet the 5000 hour lifetime targets.

### Subtask 3.2 Large area accelerated durability tests

The purpose of this subtask is to take the down-selected cathode catalysts from Subtask 3.1 and validate with accelerated testing that the same performance and durability is achieved in large area (> 300 $cm^2$) single (or at most several) cells, using existing, proven stack hardware at 3M. The approach may include at least three stack builds. The expected outcome will be validation that under non-accelerated testing the full size MEA's would meet the 5000 hour targets.

As in original contract



## Task 3 Full Size (> 250 $cm^2$) Single or Multi-Cell Tests

### Subtask 3.2 Large area short stack durability tests

3M NUVERA FUEL CELLS

Initiated as a technology integration project with Nuvera Fuel Cells

**Driver for a Technology Integration Project between 3M and Nuvera Corp.**

- Key opportunity to evaluate for the first time, the combination of the 3M NSTF electrode technology with the Nuvera open flow field bi-polar plate technology.
- Evaluate the NSTF 2008/9 Best of Class MEA's with Andromeda Stack
- Enables joint assessment of any mutual benefits
- Project began ~ Sept. 2009
- Short stack testing at both 3M and Nuvera now underway:
  - Technical exchange of information
  - Testing facilities upgrades
  - Roll-good parts supplied to Nuvera, gasketed CCM's made by Nuvera
  - Hardware delivery and training at 3M for stack assembly
  - First stack build at 3M on Nov. 17, 2009. Operation tried immediately.
    - 16 cell short stack, Andromeda design
    - used 2008 series of MEA (0.1/0.15 PtCoMn loadings) by default
    - stack operation and conditioning began immediately
      - -- exploring stack cell compression
      - -- stack operating conditions
      - -- feeling the way forward with the new combination
    - NSTF CCMs sent to Nuvera for parallel stack build in late Feb., 2010
      - -- (2009 best-of-class NSTF with 0.05/0.10 PtCoMn loadings)

## Task 3 Full Size (> 250 cm$^2$) Single or Multi-Cell Tests
## Subtask 3.2 Large area accelerated durability tests

To date:

Time Assembled: ~ 2,900 hours

Time Operated: 100 hours

Short stack under test at 3M Menomonie

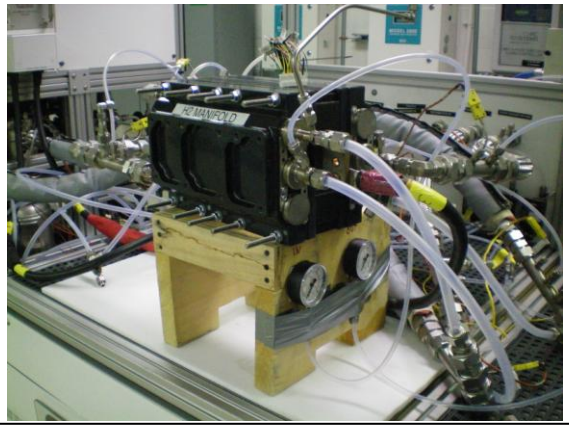

Approximate Event Sequence

Initial Stack Build, 15.5 kgf/cm$^2$ compression
- Stack operation initiated Nov. 17, 2009
- Break-in conditioning for ~ 25 hrs,

Operation at 3 bar, 75/75/75 for initially for station reasons.

Compression increased to 19 kgf/cm$^2$
- Operation at 3 bar, various RH, T
- Single cell tests at similar conditions

Compression increased to 22.5 kgf/cm$^2$
- Operation at various RH, T, P
- Total operating time < 100 hrs to date



## Subtask 3.2 Large area short stack durability tests

Excessive H-pump resistance at 2 A/cm$^2$

Average R ~ 0.096 ohm-cm$^2$ at 22.5 kgf/cm$^2$ and 19 kgf/cm$^2$.

Average R ~ 0.106 ohm-cm$^2$ at 15 kgf/cm$^2$

**Nuvera Stack Tests with NSTF MEAs. $H_2$ Pump Experiment. Individual Cell Resistance Values - All Cells. Test conditions: Pressure 1.0 Bar, Stoichiometry 2.0/2.0 (A/C), Stack Humidification 75/75/75 ºC (A/S/C), Stack Compession 15 kgf/cm$^2$ to 22.5 kgf/cm$^2$.**

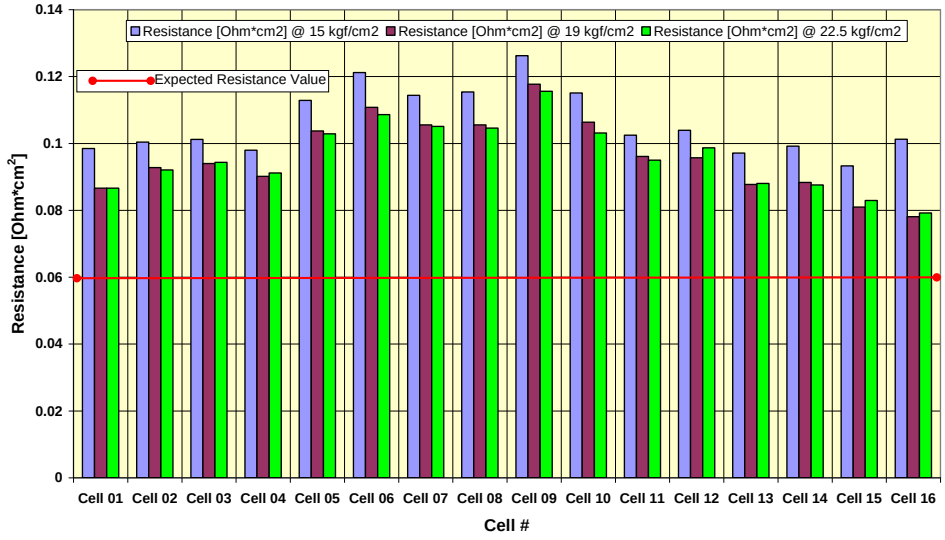

## Subtask 3.2 Large area short stack durability tests

3M NUVERA FUEL CELLS

To date:

- Time Assembled: ~ 2,900 hours
- Time Operated: < 100 hours

General Condition

- Stack cell H-pump impedance ~ 80% high
- Performance stable, appears to have conditioned easily
- Exploring stack compression, operating conditions
- Learning to operate safely, understand effects of operating conditions before any durability starts.

Nuvera Stack Tests with NSTF MEAs - Galvanodynamic Polarization (CV) 0-2.0 A/cm$^2$.
Test conditions: Pressure 3.0 Bar, Stoichiometry 3.0/2.5 (A/C), Stack Humidification 75/75/75ºC (A/S/C), Coolant Flow 25 SLM, Run time 50-75h. Average Cell Voltage Plotted.

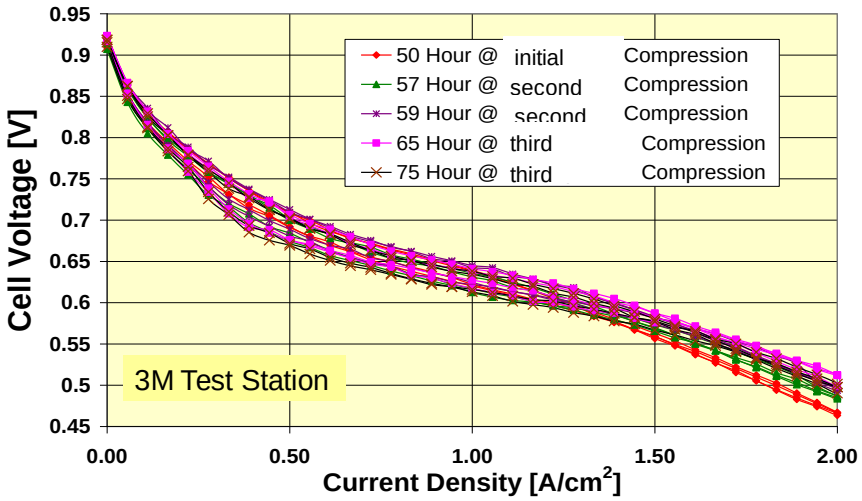




## Subtask 3.2 Large area short stack durability tests

3M NUVERA FUEL CELLS

- RH Sensitivity, Temperature Sensitivity Complete
- Lower pressure operation in progress
- Some durability running, then rebuild w/ 2009 BoC CCM

Nuvera Stack Tests with NSTF MEAs - Galvanodynamic Polarization (CV) 0-2.0 A/cm$^2$.
Test conditions: Pressure 3.0 Bar, Stoichiometry 3.0/2.5 (A/C), Stack Humidification 75/75/75 ºC (A/S/C), Coolant Flow 25 SLM, Third Stack Compession , Run time 75 h.

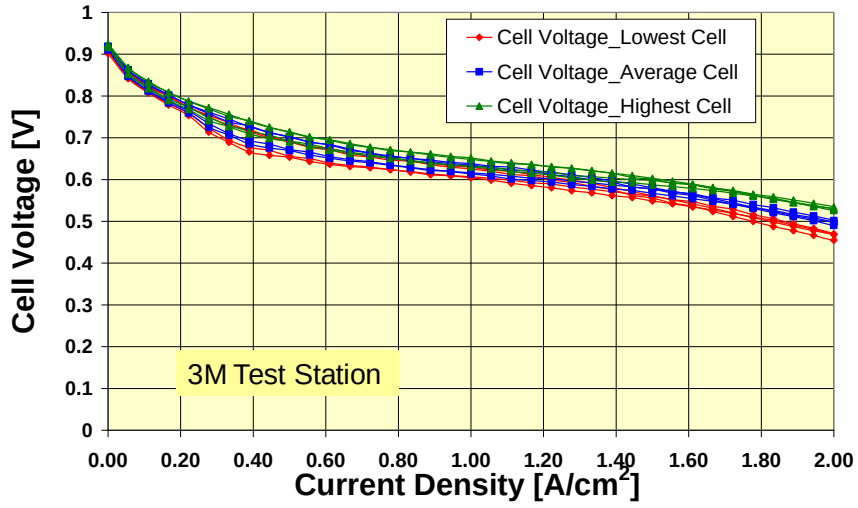

## Subtask 3.2 Large area short stack durability tests

Single cell comparisons to Nuvera stack test conditions

Objectives:

- Assess correlation of stack cell voltage deviations from the average at 2 A/cm$^2$ with H-pump cell resistance deviations:
  - comparison of H-pump resistance sensitivity factors at different compressions,
  - extract estimate of contributions to cell-cell voltage variability from non-resistance factors
- Comparison of best cell performance with 50 cm$^2$ single cell
- Project performance of stack's **best** cell performance if H-pump impedance could be reduced by 0.040 ohm-cm$^2$ to ~ 0.05 ohm-cm$^2$ and compare to single cell performance.

3M Advanced Cathode Catalysts and Supports…… DOE Review, March 16, 2010

## Subtask 3.2 Large area short stack durability tests

### Single Cell Tests to Compare with Current Andromeda-NSTF Stack Build

- Cell: 50 cm$^2$, Quad-Serpentine flow fields
- CCM: NSTF "2009 Best of Class"
- GDL: 3M 2979
- Break-in conditioning: Fast start-up protocol #52, Station 1
- Objective: MEA testing at Nuvera stack operating conditions in order to provide insight on impedances and mass transport over-potentials that may be useful in understanding the stack's MEA conditions.

Reduced anode pressure, some anode RH and lower anode stoich.

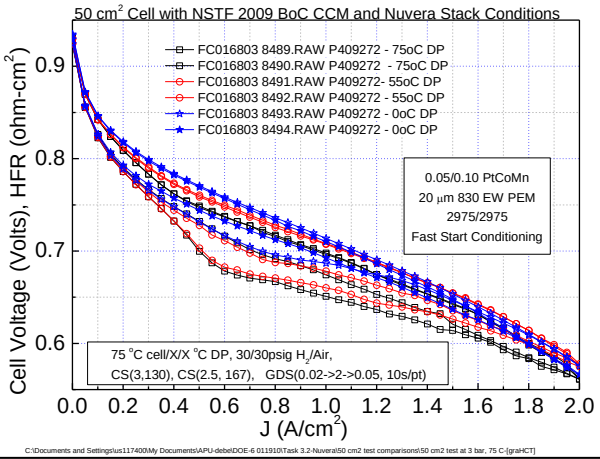


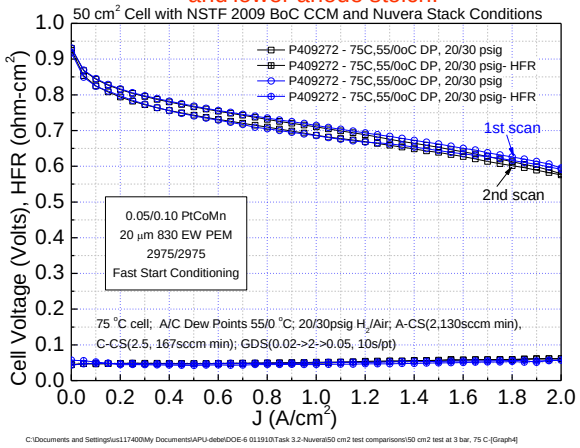

## Subtask 3.2 Large area short stack durability tests

Single cell comparisons to Nuvera stack test conditions

Operating at 20/30 psig and 55/0 °C dew points helped by ~ 15 mV at 2 A/cm$^2$ compared to 30/30 psig and 0/0 °C dew points.

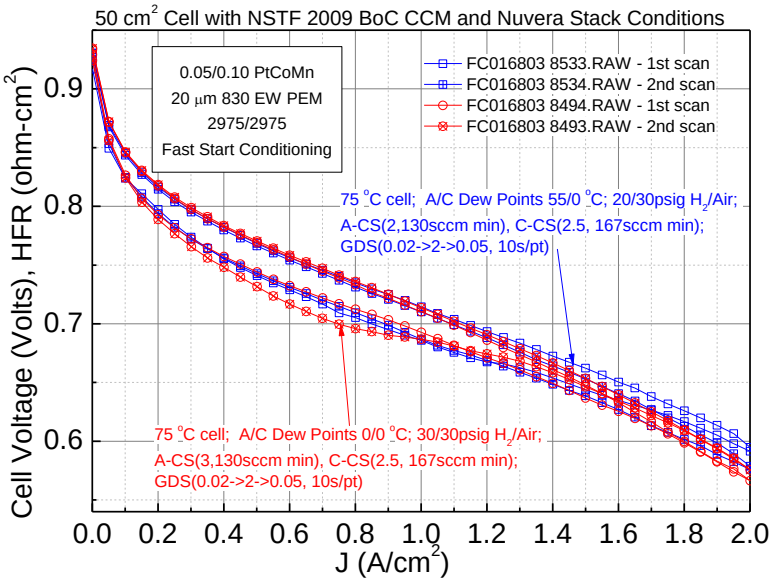


C:\Documents and Settings\us117400\My Documents\APU-debe\DOE-6 011910\Task 3.2-Nuvera\50 cm2 test comparisons\50 cm2 test at 3 bar, 75 C-[Graph6]

From analyses of HFR and IR-corrected ….

To reach 650 mV at 2 A/cm$^2$ :

- Reduce excess HFR by 0.010 ohm-cm$^2$
- Reduce MTO from 60 to ~ 30 mV.

3M Advanced Cathode Catalysts and Supports…… DOE Review, March 16, 2010

## Subtask 3.2 Large area short stack durability tests

Correlation of Cell Voltage at 2 A/cm$^2$ with H-pump resistance

- Higher compression does appear progressively improve average stack cell voltage at current densities above 1 A/cm$^2$. Very clear at 2 A/cm$^2$.
- Some of the improvement may be due to improved performance over time.

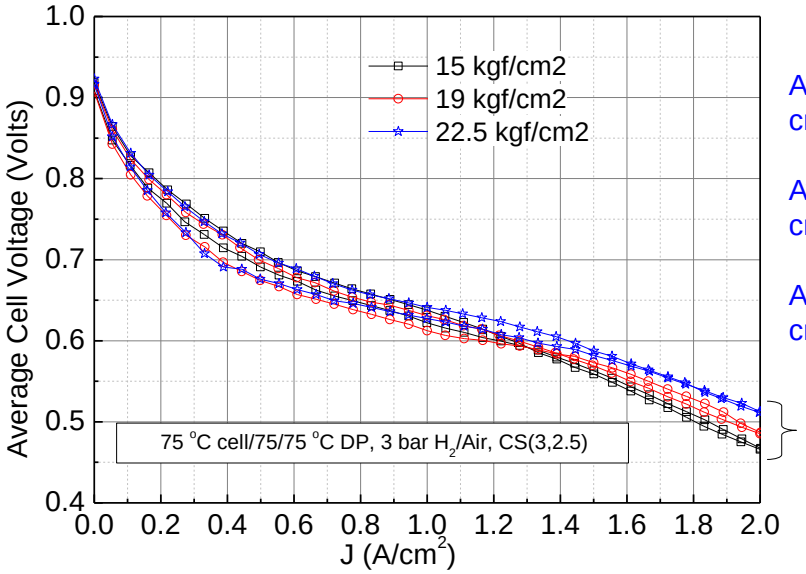


C:\Documents and Settings\us117400\My Documents\APU-debe\DOE-6 011910\Task 3.2-Nuvera\Stack -variable conditions tests\Correlations of R and V-[Graph4]

Average R ~ 0.0959 ohm-cm$^2$ at 22.5 kgf/cm$^2$

Average R ~ 0.0962 ohm-cm$^2$ at 19 kgf/cm$^2$.

Average R ~ 0.106 ohm-cm$^2$ at 15 kgf/cm$^2$

Monotonic increase at 2 A/cm$^2$ not due to just reduction in average R.

## Subtask 3.2 Large area short stack durability tests

Correlation of Cell Voltage at 2 A/cm$^2$ with H-pump resistance

- There appears to be some correlation of cell voltage with H-pump resistance.
- Plot cell voltage difference about average versus cell resistance difference about average: (next slides)

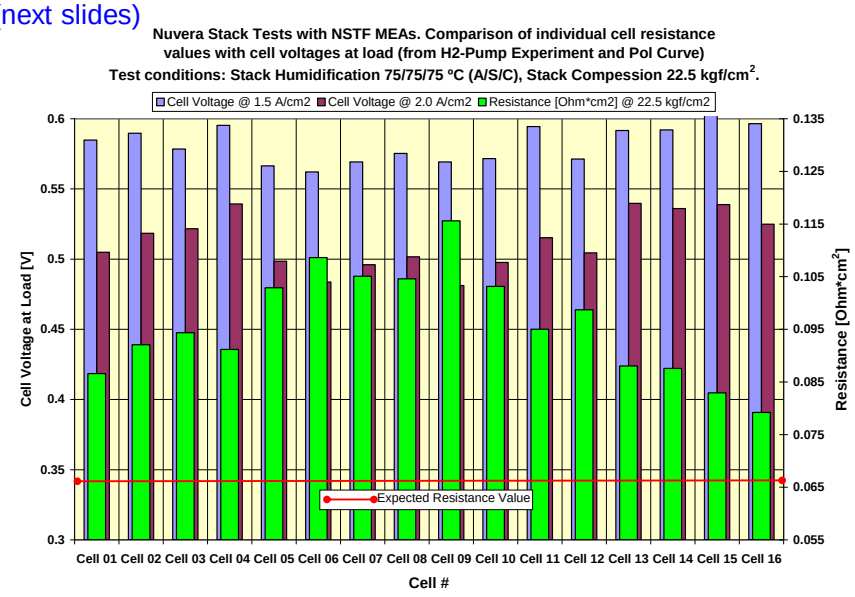


3M Advanced Cathode Catalysts and Supports…… DOE Review, March 16, 2010

## Subtask 3.2 Large area short stack durability tests

Correlation of Cell Voltage at 2 A/cm$^2$ with H-pump resistance

- At 15 kgf/cm$^2$ compression, the variation of cell voltage about the mean at 2 A/cm$^2$ appears to correlate fairly well with the variation in H-pump resistance.
- $R^2$ = only 80.5%, intermediate to the other compression values.

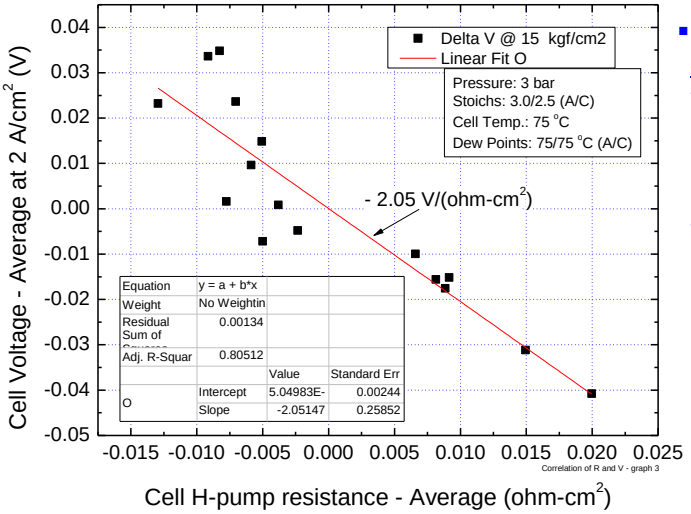


- 1 σ standard deviation of ± 0.26 V/ohm-cm$^2$ implies that for R = ~ 0.1 ohm-cm$^2$ resistance, only ± 26 mV variation is due to non-resistance cell to cell variability factors.

## Subtask 3.2 Large area short stack durability tests

Correlation of Cell Voltage at 2 A/cm$^2$ with H-pump resistance

- At 19 kgf/cm$^2$ compression, the variation of cell voltage about the mean at 2 A/cm$^2$ appears to correlate well with the variation in H-pump resistance.
- $R^2$ = 90.5%, higher than at other compression values.

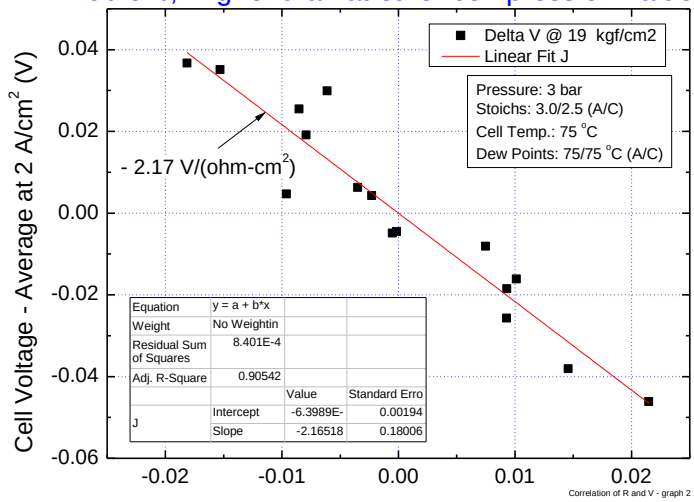


- 1 σ standard deviation of ± 0.18 V/ohm-cm$^2$ implies that for R = ~ 0.09 ohm-cm$^2$ resistance, only ± 16 mV variation is due to non-resistance cell to cell variability factors.



## Subtask 3.2 Large area short stack durability tests

Correlation of Cell Voltage at 2 A/cm$^2$ with H-pump resistance

- At 22.5 kgf/cm$^2$ compression, the variation of cell voltage about the mean at 2 A/cm$^2$ appears to correlate fairly well with the variation in H-pump resistance.
- $R^2$ = only 73%, less than at lower compression values.

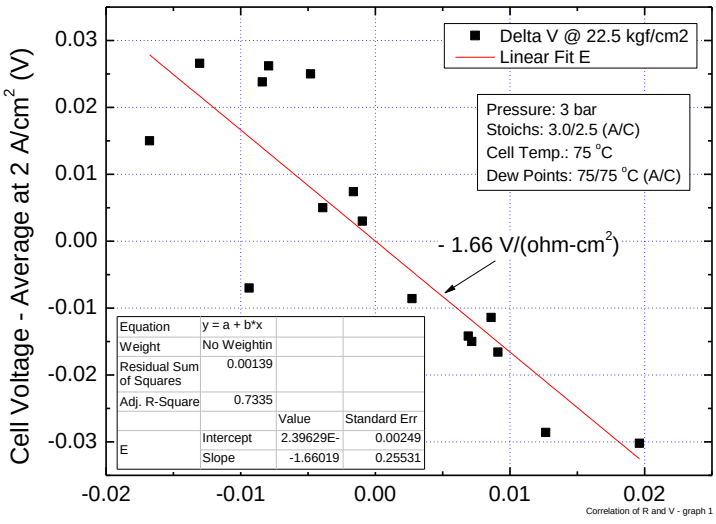


- 1 σ standard deviation of ± 0.26 V/ohm-cm$^2$ implies that for R = ~ 0.09 ohm-cm$^2$ resistance, only ± 23 mV variation is due to non-resistance cell to cell variability factors.
- Sensitivity factor of -1.66 V/ohm-cm$^2$ implies a gain of 83mV at 2 A/cm$^2$ (or 0.0415/(A/cm$^2$)) could result if the H-pump resistance was reduced by 0.040 ohm-cm$^2$.

## Subtask 3.2 Large area short stack durability tests

### Project stack performance at lower H-pump resistance

Use the H-pump resistance sensitivity of -1.6 V/ohm-cm$^2$ at 22.5 kgf/cm$^2$ to project the stack's average cell performance at 75/75/75 $^o$C:

- If H-pump reduced by 0.040 ohm-cm$^2$, stack average cell voltage would exceed the 50 cm$^2$ single cell voltage above 1.2 A/cm$^2$.
- Lower stack voltage below 1.2 A/cm$^2$ reduced by drier or hotter operation as on next slide.

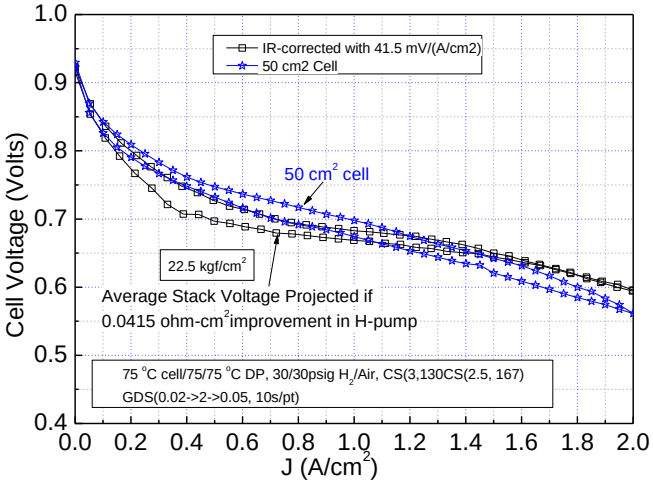


3M Advanced Cathode Catalysts and Supports…… DOE Review, March 16, 2010

## Subtask 3.2 Large area short stack durability tests

### Correlation of Cell Voltage at 2 A/cm$^2$ with H-pump resistance

Conclusions:

- Individual cell voltages at 2 A/cm$^2$ correlate quite well with the H-pump resistances at each compression level for the 75/75/75 $^o$C, 3 bar conditions.
- Non-resistance contribution to cell to cell voltage variability is ~ 25 mV at 2 A/cm$^2$. This suggests mass transport variations are small.
- If the average H-pump resistance could be reduced by 0.04 ohm-cm$^2$, the stack voltage would exceed single cell performance above 1.2 A/cm$^2$.
- The stack's best individual cell performance at 80/80/80 $^o$C is within 50mV of the 50 cm$^2$ cell performance at 75/75/75 $^o$C.

## Subtask 3.2 Large area short stack durability tests

Comparison of stacks best cell performance with single cell performance

Stack's best cell performance at 80/80/80 °C and third compression level is:

- within 50mV of the single cell performance at 75/75/75 °C
- shows less hysteresis than single cell curves.
- improved relative to 75°C stack operation below 1 A/cm$^2$.

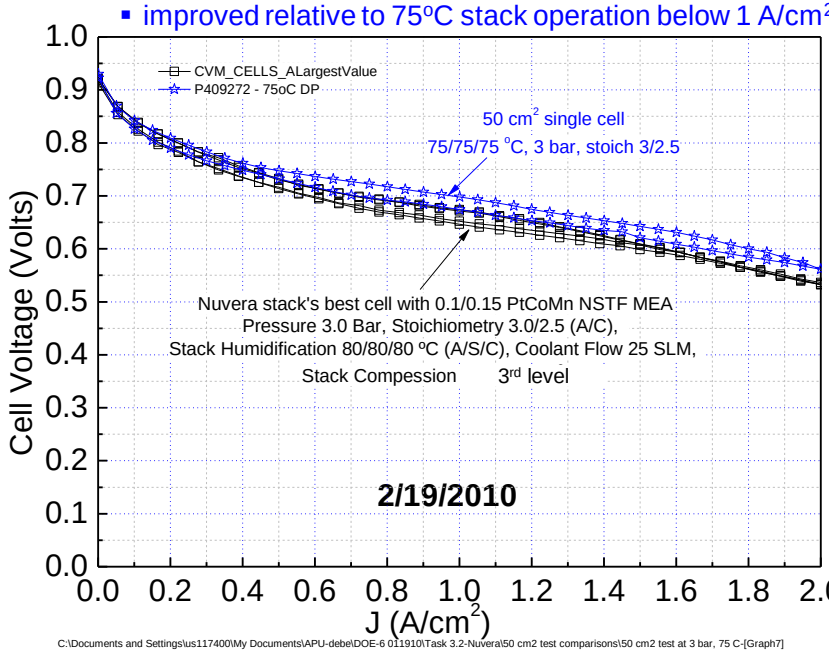


C:\Documents and Settings\us117400\My Documents\APU-debe\DOE-6 011910\Task 3.2-Nuvera\50 cm2 test comparisons\50 cm2 test at 3 bar, 75 C-[Graph7]

Next Steps:

- Lower pressure test series.
- 4th compression level
- Re-build with 2009 BoC CCMs
- Work with Nuvera on their stack testing.

# Task 4

# Selected Supplementary Information

## Subtask 4.1 Durability tests of new NSTF supports

From the statement of work for this project, "the purpose of subtask 4.1 is to specifically evaluate the stability of the new NSTF based catalyst supports derived from Subtask 1.1. The approach will use accelerated tests to evaluate stability of the catalyst activity and surface areas against corrosion of the support from high voltage cycling, stop/start cycling or fuel starvation. Both high through-put characterization methods as well as 50-cm$^2$ single cell tests will be included in the approach. The expected outcome is a down-selection of the new NSTF catalyst supports from Subtask 1.1 that also meet the durability requirements."

The Tasks 1.1 series of experiments, WAO-1, 2, 3 and 4, explored optimization of the NSTF PR-149 whisker support characteristics for best overall fuel cell performance and was highlighted in Section 9.8. Fig. 9.21(A,B) showed ORR mass activity was linearly dependent on the Pt ECSA coating the support whiskers, but was not a discerning function of the PR-149 thickness until it exceeded about 2000 units. Fig. 9.21(C,D) also showed that the polarization curves were not a strong function of the growth parameter in the range of 1 to 5. Fig. S6 below shows similar results for the intermediate growth parameter value of 3. The fuel cell performance is independent of the PR-149 thickness parameter in the range of 1800 to 2400 units.

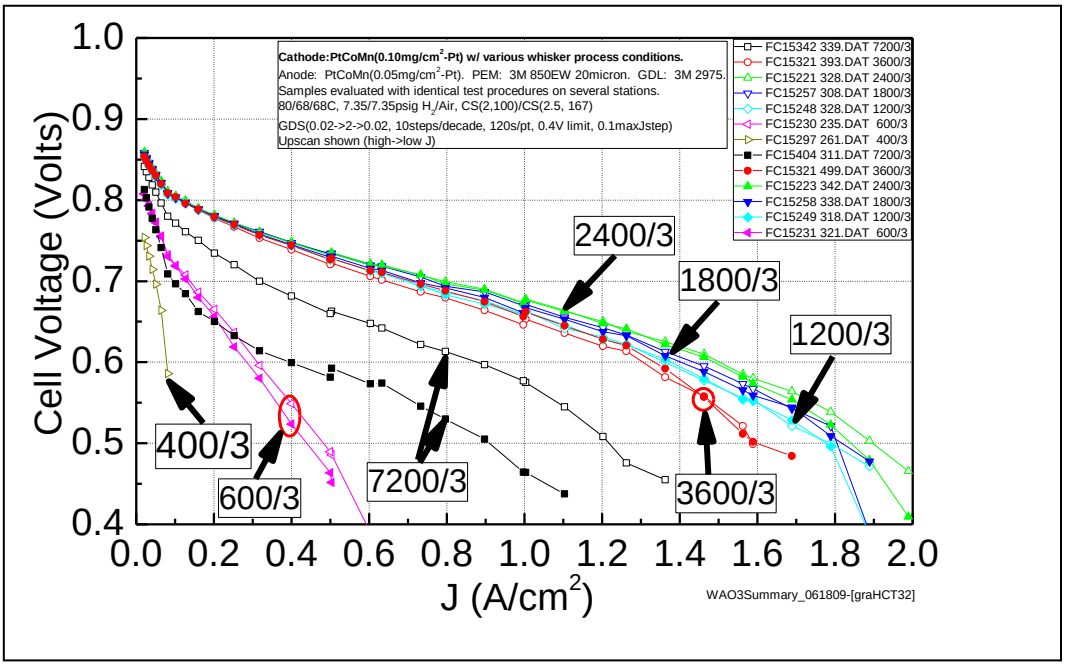


**Fig. S6.** Polarization curves for the WAO-3.2 series of whisker growth for the thickness range of 400 to 7200 units and the growth parameter value number 3.

Since the PR-149 thickness value and the growth parameter value for the "standard" NSTF whiskers were approximately at the 2000/3 values before this project began, a major conclusion of the Task 1.1 experiments is that there was no substantial improvement to be made by changing these whisker growth parameters. This means that all the durability evaluation work done under Task 2, testing new catalyst compositions on standard whiskers in 50 cm$^2$ single cells and as compositional spreads applied by Dalhousie University to the NSTF standard whiskers, met the objectives of subtask 4.1.

# Task 5

# Selected Supplementary Information

## Task 5.0 - Optimized NSTF MEA Roll-good and Stack Testing

### Tasks: 5.1. NSTF catalyst / low EW membrane interface optimization and 5.2. Optimized anode and cathode GDL's

Tasks 5.1 and 5.2 were critical precursors to Task 5.3 since the membrane, catalysts and GDL's can significantly affect one another. However, when doing catalyst development it is necessary to fix the membrane and GDL in order to screen the catalyst parameter one is studying. Ultimately it is necessary to vary the membrane and GDL properties as well since it otherwise can never be known if the three system components are optimized for working together and meeting such diverse requirements as performance, durability, and operational robustness.

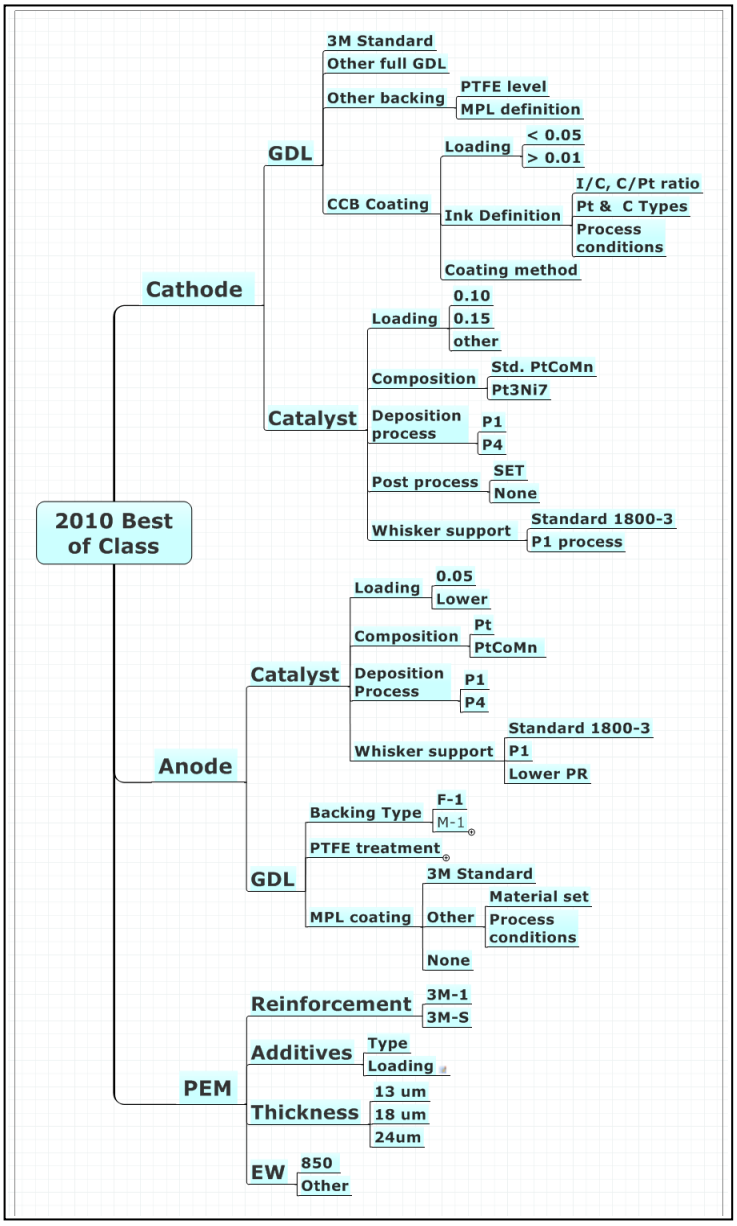


Throughout this project, as improvements were realized in the membranes and GDL's, the new components and a multitude of process and material parameters were evaluated with the continuously improving cathode NSTF catalysts to try and produce the best performing MEA that would go into the final stack testing. The number of variables becomes excessively large, and requires hundreds of different MEA's tested in duplicate at a minimum in order to develop a clear understanding of the component interactions.

In preparation for Task 5.3, the optimization process towards a 2010 best of class MEA went on for over a year as the combinations of material and process decisions illustrated in Fig. S7 below were explored.

**Fig. S7.** Illustration of the process map used in Tasks 5.1 and 5.2 for optimizing the MEA components for down-selection for stack testing in Task 5.3.

## Technical Accomplishments and Progress: GDL Optimization for NSTF CCM

Electrode backing (EB) carbon paper : Designed Experiment

- 7 commercial roll-good papers
  - Variables: wet proofing and MPL coating area weight (necessary due to variable EB)
- 3 commercial fully coated GDLs also evaluated

**Results:** Fuel cell results for all were significantly poorer than 3M baseline GDL

Baseline carbon paper improvement : Designed Experiment

- Variables : wet proofing and MPL area weights
- Seven fuel cell performance metrics

**Results:**

- No single set of GDL parameters were optimum for all seven fuel cell metrics.
- For steady state cool performance, optimal GDL parameters were different for dry conditions (0 % RH) and wet conditions (100 % RH).
- Good second order linear regression fits were obtained for three responses (PDS, cathode stoich. sensitivity, and % RH sensitivity at 90/60/60 °C).

Asymmetric anode/cathode GDLs with baseline EB paper : Designed Experiment

- $2^{4-1}$ factorial with center point replication
- Variables : wet proofing and MPL coating area weight
- **Still in progress -** Largest improvement so far was for extreme difference for anode and cathode GDLs: high wet proofing and MPL weight for cathode and low wet proofing and MPL weight for anode.



## Technical Accomplishments and Progress: GDL Optimization for NSTF CCM

# Best GDL Approaches Identified to Date

| GDL | PDS, 70 C | GDS, 7.35 psig, 80 C | GDS, 14 psig, 85 C | Cathode Stoich Sensitivity | % RH Sens., | Steady State Cool Start amps/cm$^2$ at 0.6 V | | | |
|---|---|---|---|---|---|---|---|---|---|
| | V at J = 1.2 | V at J = 1.5 | V at J = 1.5 | V at 1.4 CS, 80 C | Volts at 90/50/50 C/%RH/%RH | 30 C, 0/0 | 30 C, 100/100 | 40 C, 0/0 | 40 C, 100/100 |
| Baseline GDL | 0.607 | 0.540 | 0.600 | 0.522 | 0.588 | 0.342 | 0.209 | 0.540 | 0.250 |
| GDL A | 0.603 | 0.584 | 0.625 | 0.521 | 0.612 | 0.305 | 0.172 | 0.490 | 0.203 |
| GDL B | 0.623 | 0.591 | 0.628 | 0.531 | 0.536 | 0.295 | 0.120 | 0.514 | 0.169 |
| GDL C | 0.602 | 0.578 | 0.629 | 0.498 | 0.596 | 0.277 | 0.130 | 0.467 | 0.154 |
| GDL D | 0.595 | 0.567 | 0.614 | 0.510 | 0.612 | 0.334 | 0.200 | 0.549 | 0.235 |

- Greatest higher temperature improvements were for GDL Type B (15 mV for PDS and 30 to 50 mV for GDS).
- Generally poorer steady state cool performance results than for baseline GDL.
- Overall best results with minimal impact on steady state cool performance was for GDL D.

3M Advanced Cathode Catalysts ..... 2009 DOE Hydrogen Program Review, May 18 - 22

**Task 5.2 – Optimized anode and cathode GDL's**

**"Fundamental" GDL property characterization**

One of the areas of research undertaken as part of Task 5.2 for optimizing the GDL's for use with the NSTF CCM's was to obtain basic physical and chemical property measurements of the GDL backing layers to develop understanding of the structural characteristics critical for desired water management. This is distinctly different from screening materials and process factors for functional performance trends which was a major activity of the project Task 5.2. Simple to execute, "easy" to interpret liquid water permeability measurements on as-received GDL backing materials from different manufacturers, and PTFE treated GDL's. The approach here was to start with the most basic and elementary measurements of liquid water permeability to try and see what physical characteristics of the GDL media might be most critical. The work began at the start of the project and has mainly been completed except for most important result of extracting those critical properties. A number of intriguing insights have been gained however.

*Water permeability measurements*

The basic premise of the approach was to make liquid water permeation measurements through a wide variety of commercially available GDL media based on primarily capillary flow, as illustrated in Fig. S8.

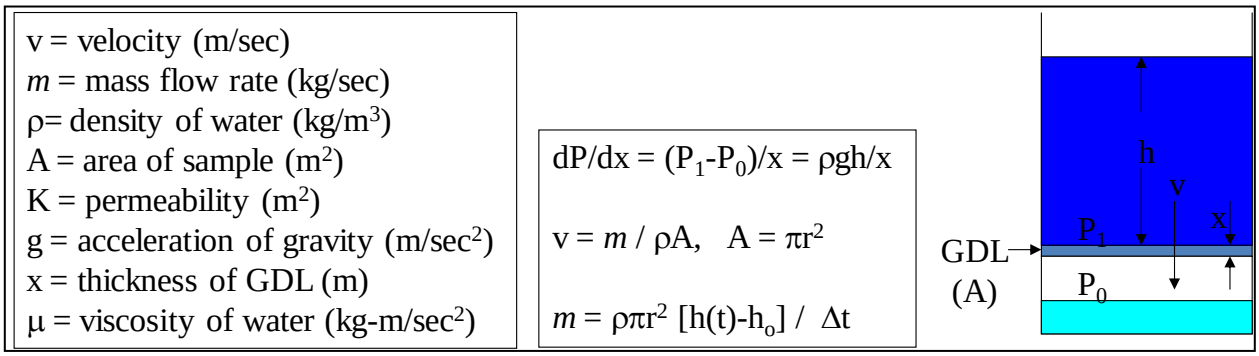


**Fig. S8.** Concept for simple measurement of liquid water permeability, K, through GDL media.

This flow can be characterized by an effective permeability, K, using Darcy's Equation:

(3) $$v(\text{m/sec}) = -(K/m)dP/dx,$$

where the variables are defined in Fig S8. The velocity of a fluid through a porous media is proportional to the pressure gradient in the media and inversely proportional to the liquid viscosity. In practice, this simple approach involved repeated measurements of the mass flow rate, *m*, of water flowing through an area A of the GDL, due to the pressure generated by a standing column of water of height h placed over the area A, without edge leaks. Fig**.** S9 illustrates this. A test method and assembly were worked out with numerous trials and experiments. Very dramatic hysteresis effects and widely ranging rates of water transmission were observed with all the different types of GDL media. The final methodology was very reproducible. It was applied to twelve types of "as-received" GDL electrode backing materials from seven suppliers. Sample pieces were die-punched from four locations on each sample as illustrated in the plan view in Fig. S9. Then six runs with each sample piece were made, recording the time for a certain volume of water to flow through the sample while maintaining a constant water head constant. Another variation practiced, recorded the time for a given volume to flow through the sample from water head $h_1$ to $h_2$.

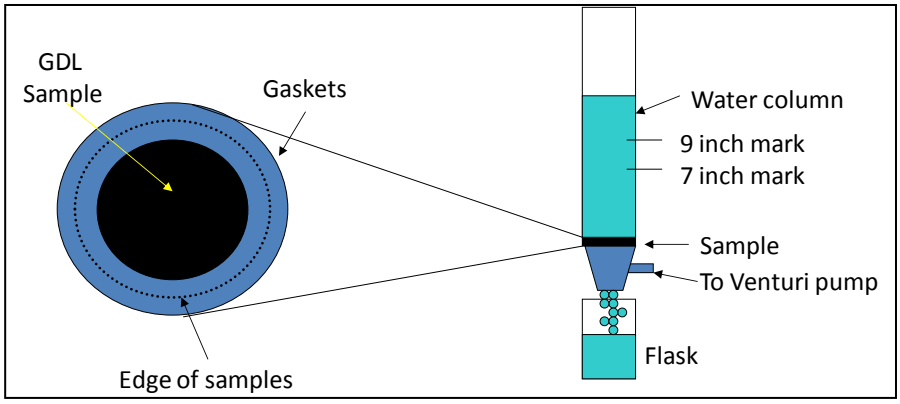


**Fig.** S9**.** Lab set-up for implementing the concept for measuring the liquid water permeability in Fig. S8. The GDL samples' flow-through area were 1 inch in diameter.

Fig. S10 shows the measured water mass flow rates as a function of trial number for ten of the GDL media. All samples were as-received electrode backings with no hydrophobization or microporous layers (MPL's). The error bars reflect the root means squared deviation from 3 to 4 samples of each type. Flow rates were determined from measured time for 175mL flow volume with ± 10mL uncertainty. All measurements were at ambient temperature.

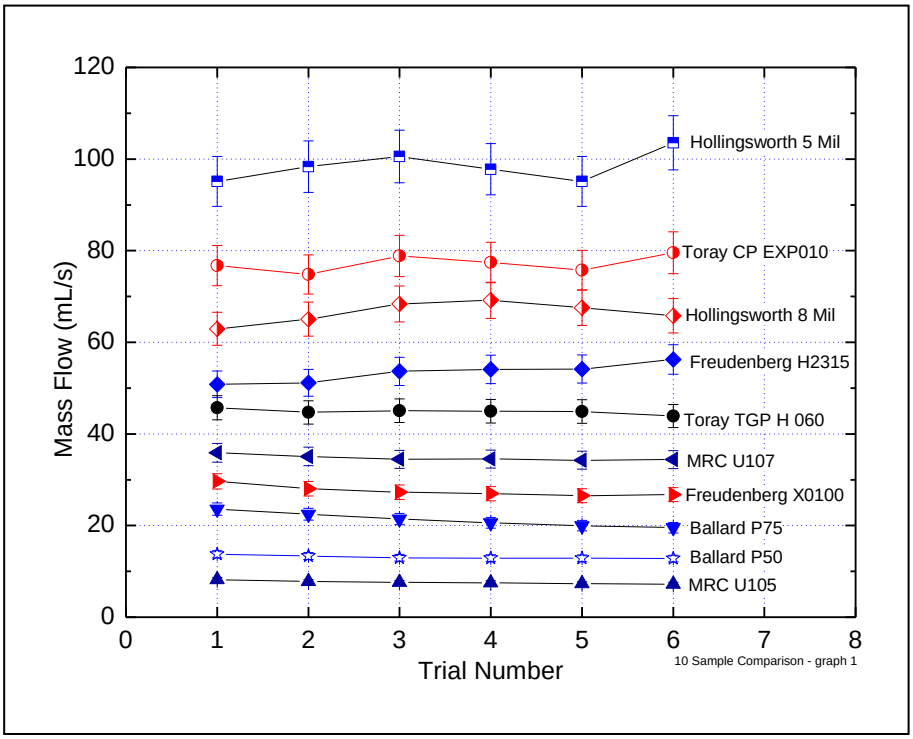


**Fig. S10.** Mass flow rates as a function of trial number for ten different GDL backing media using the approach shown in Figs. S8 and S9.

Fig. S11 shows SEM images of 6 of the GDL material evaluated showing dramatic variations of microstructure, despite most using common sized carbon fibers. The variations are due to the different types of binder material used by the manufacturer. The pore sizes distributions might be expected to be greatly different among them.

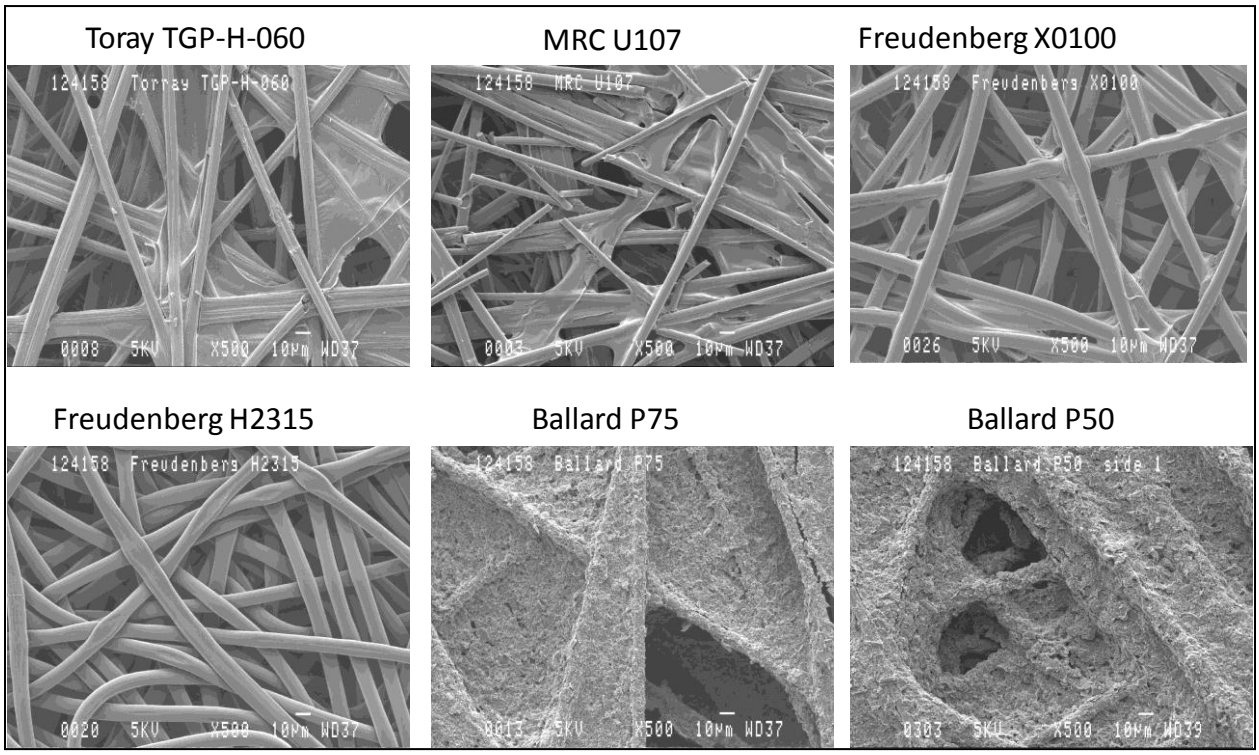


**Fig. S11.** SEM images at 500 X magnification of six of the GDL media evaluated showing dramatic variations of microstructure, despite most using common sized carbon fibers.

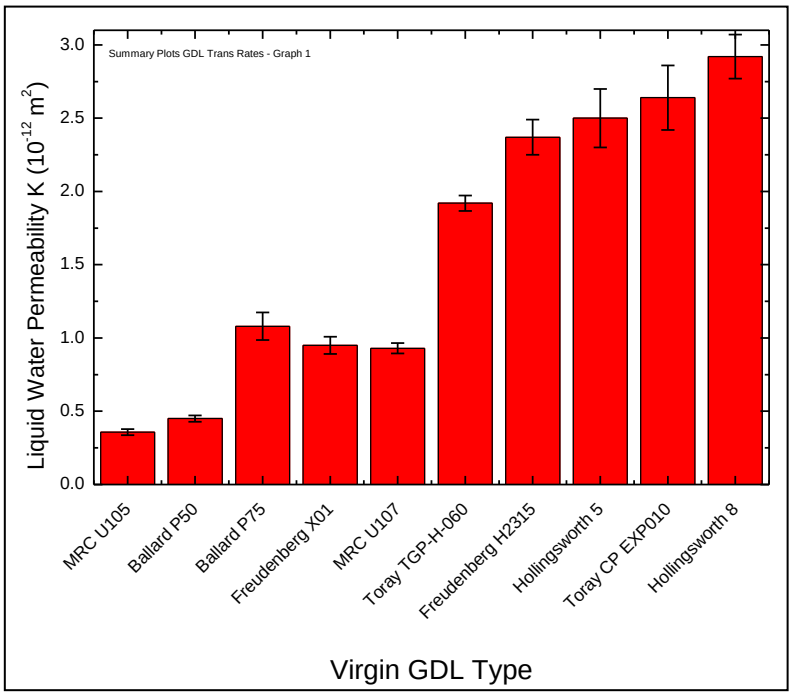


**Fig. S12.** Liquid water permeability values calculated for 10 as-received carbon paper GDL Backing papers from mass flow measurements in Fig. S10 and Darcy's equation (3).

Using the mass flow data in Fig. S10 and Darcy's equation (3), the liquid water permeability, *K*, can be calculated from:

(4) $K = -\mu\, m x / (\rho^2 A g h)$ and $m = \rho\pi r^2 [h(t)-h_o] / \Delta t$

as shown in Fig. S12. The value of *K* appears to vary an order of magnitude among these types.

The next step is to see if this sizeable difference can be attributed to some physical property of the GDL backing layers. This is a difficult task, as there are aspects of the GDL's composition that cannot be obtained from their suppliers. One intriguing model concept we have been pursuing is that the very large pore porosity and possibly the shape of those pores, is a key parameter since the liquid water would most naturally go through the large pores rather than smaller pores, regardless of surface wetting characteristics of the fibers and binder material comprising them. We consider then, as a first approximation, that the GDL media consist of two solid phases, the very dense carbon fibers, and the different binders of varying density. By large pores we mean the large, irregularly shaped, highly angular apertures with dimensions of 10 to 50 microns seen in the SEM images of Fig. S11. The water will flow completely or substantially only through the large pores or apertures defined by the carbon fibers where binder is not present. It will not flow through the very small pores or cracks in the binder phase of the papers. This is because the smaller holes would have a substantially higher pressure drop to pass water than the larger holes, so it would naturally take less energy to flow at a slightly faster rate through any adjacent large aperture or hole

As stated, the water permeability should be a function only of the large holes or pores defined by the non- carbonized binder areas between the fibers. If so, then this large-pore porosity factor, $P_{LP}$, would be the primary factor determining the liquid water permeability, *K*.

To explore this further, let $P_{LP}$ be the porosity of the large pores only, $V_f$ and $m_f$ the volume and mass of the carbon fibers respectively, and $V_b$ and $m_b$ the volume and mass of the binder respectively, where the volume of the micro-pores inside the domain of the binder phase is included in the value of $V_b$. Define also $V_b / V_f = \delta$, and $m_b / m_f = c$, and let *V* = the total sample volume.

Then the measured sample density is $\rho_m = (m_b + m_f) / V = (m_f/V)(1+c)$, and the individual phase densities are $m_f = \rho_f V_f$ , and $m_b = \rho_b V_b$ for the fiber and binder respectively. We can assume that the density of the fibers is that of solid carbon, $\rho_f = 2$ g/cm$^3$. The large pore porosity, $P_{LP}$, is then defined from the void volume as:

5) $P_{LP} \equiv 1 - V_f / V - V_b / V = 1 - (1+\delta)\, V_f / V$ , which can be rewritten as,

(6) $$P_{LP} = 1 - \frac{1+\delta}{\rho_f}\frac{m_f}{V} = 1 - \frac{1+\delta}{\rho_f}\frac{\rho_m}{(1+c)} = 1 - \frac{\rho_m}{h\rho_f}$$ , where

7) $h = (1+c)/(1+\delta) = (1+ m_b/ m_f)/ (1+ V_b/ V_f)$.

So we have a single parameter, *h*, that can be used to adjust the single solid phase porosity, $P_s(\%) = 100\%(1-\rho_m/ \rho_f)$. A plot of the permeability values from Fig. S12 versus the measured density (single solid phase) of the GDL media gives no correlation or apparent functional relationship. But assuming a two-phase (solid) media, of dense fibers and less dense binder, we can pose the question of what value of *h* is required to make all data points for the various carbon papers fall on a single linear function of *K* vs $P_s(\%)$. By inverting (6) and solving for *h* with the definition of $P_s$, it results that

(8) $h = (1- P_s) /(1- P_{LP})$,

where the value of $P_{LP}$ is obtained from the plot of $K$ versus $P_s$.

Fig. S13 shows the resulting plot of permeability versus the large pore porosity, for the values of $h$ used to bring all the measured points coincident with a straight line drawn between the two Freudenberg papers, since they consist of just the single solid phase carbon fibers, i.e. they do not appear to contain any binder phase. Since they have no secondary resin phase carbon, $h$ = 1 is assumed for these two GDL papers. Fig. S13 shows that with very reasonable values of $h$ a remarkable correlation is revealed between $K$ and the large-pore porosity. The insert table in Fig. S13 shows the calculated values of $h$ that collapse all the K vs $P_{LP}$ data onto a single straight line.

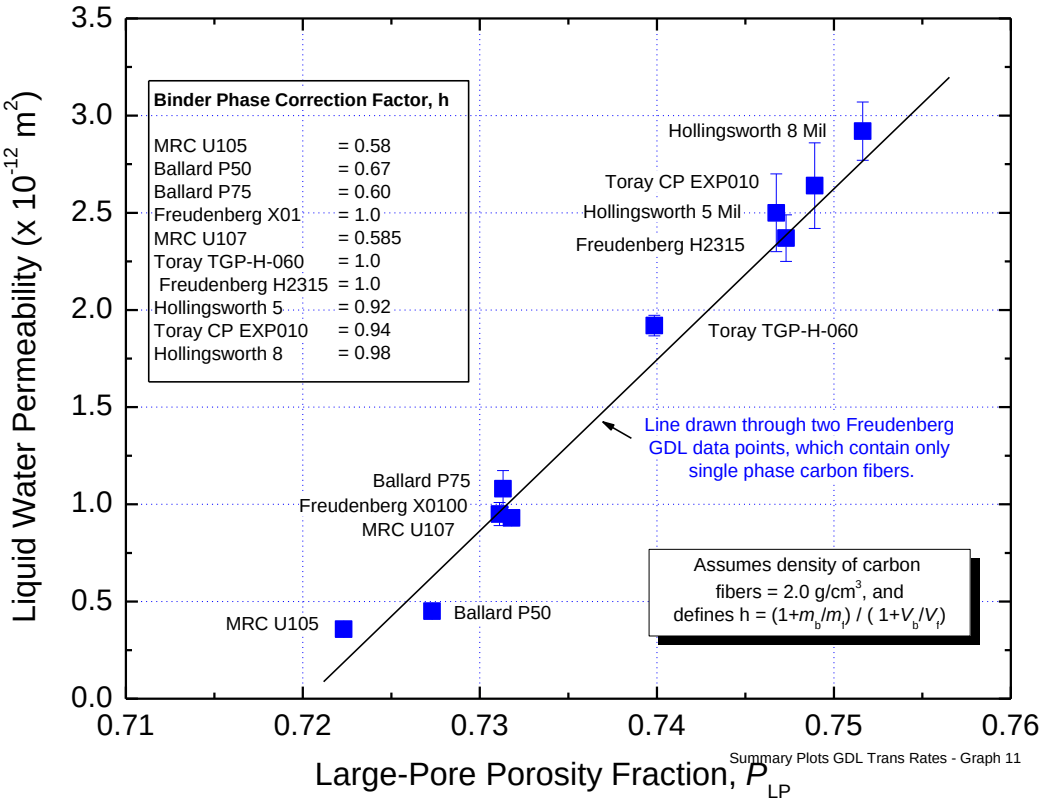


**Fig. S13.** Plot of the GDL liquid water permeability's vs the large-pore porosity calculated from equations (5)-(8) for the "best fit" values of parameter $h$ listed in the inset table.

If we had measured values of $m_b$, $m_f$, and $\rho_b$, then we could determine the values of $h$ from measured quantities using equation (8). (We do not know of any method to do this currently.) Since the density of the binder is less than the solid carbon fibers, the value of $h \leq 1$. The extracted values of $h$ shown in Fig. S13 are consistent with this constraint. Also, it appears reasonable that the more porous the binder phase appears, the larger the value of $h$, as in the MRCU105, and the Ballard P50 and P75 cases. The number of solid carbon fibers per unit volume and their size would also affect the large pore volume, and presumably is the reason for the porosity difference of the Freudenberg H2315 and X0100 samples.

There are several important conclusions that can be drawn from this analysis:

1) The steepness of the slope of *K* versus the large pore porosity shows a very sensitive function of the permeability on the structure and volume of the large pores. This may also explain to the sensitivity to compression for some materials.

2) It appears that there is a large-pore porosity percolation threshold value of ~ 72% below which there is negligible liquid water permeability for the small pressure head used for these measurements.

3) Based on the above analysis, it is remarkable that the water permeability is explainable simply on the basis of physical structure and not surface chemistry. This may be explainable if the large pores are sufficiently sized that water can flow through them with minimal effect from the surface or requirement for surface wetting. Also, it suggests that just the overall, effective porosity is what is important, and not the shapes and sizes or topology of the pores. In a second series of measurements, using twelve GDL types hydrophobically treated with PTFE at levels between 0% to 5 wt %, the presence of the PTFE did not dramatically change or affect the water permeability of most of the GDL types, consistent again with the physical structure being the critical factor for liquid water transport.

We believe these results suggest that some physical property of the GDL papers not presently known is critical for determining their ability to transport liquid water. Our own viewpoint is that classical theories that model transport of liquids through these types of porous media using conventional models for interconnected, round, tubular shaped pores, are not adequate to treat these kind of materials, where the pores appear to be more like stacks of irregularly shaped apertures. In this case, it may be more the energy required to deform a column or “tube” of water as it is forced through the matrix of stacked angular apertures, that determines the effective permeability. This may then depend more on some non-intuitive statistically derived characteristic of the GDL’s apertures or pores, such as might be extracted from mass and pore morphological metrics determined from X-ray CT Images. We have made some effort in this regard, but have not found a unique characteristic yet.

Technical Back-Up Slide

## Task 5.1/5.2/5.3 – MEA Integration for Final Stack Testing

❑ **2010 Best of Class" MEA component down-selection process**

### Example 4: Cathode GDL Options

**Cathode GDL Options:**

- Backing type: Fixed, 3M Standard
- Hydrophobic treatment - % PTFE
- MPL type – probably fixed
- Hybrid vs non-hybrid (Hybrid CCB)
  - Pt/C type and loading, I/C ratio,
  - C diluent fraction
  - Coating chemistry and method

**Deciding Factors:**

- Water management metrics (enhanced water out the cathode)
- ORR metrics
- HCT metrics (Mass transfer overpotential) at high temperature
- Pt loading cost/benefit ratio
- Accelerated stress tests

**Hybrid Type B:** US 6,238,534

- Anode = NSTF Pt, 0.05 mg/cm$^2$
- **Cathode = 3M Gradient** = NSTF + Pt/C (CCB on 3M GDL)
- PEM = 3M 20 µm,
- Anode GDL = MPL-free type A used as-received

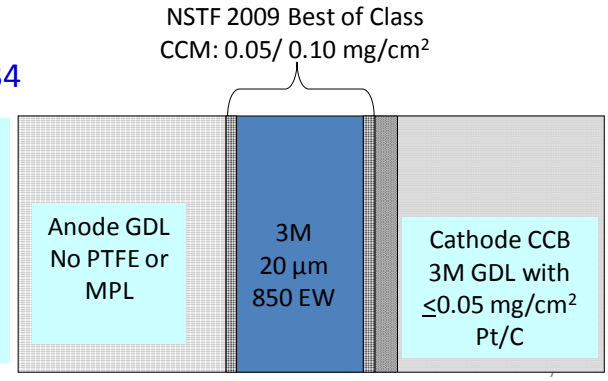






## Task 5.1/5.2/5.3 – MEA Integration for Final Stack Testing

❑ 2010 Best of Class" MEA component down-selection process

### Example 6: Cathode GDL Options

- At 200 and 270 kPa (peak power) Hybrid B performance and HFR are insensitive to temperature and humidity over ranges shown.
- 0.84 V at 0.1 A/cm$^2$ at highest pressure,
- Only ~ 40 mV of MTO ($\eta_{tx}$) at 200 kPa and 90°C at 2 A/cm$^2$.

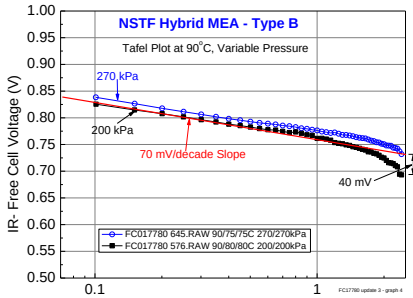


MTO 40 mV @ 2 A/cm$^2$

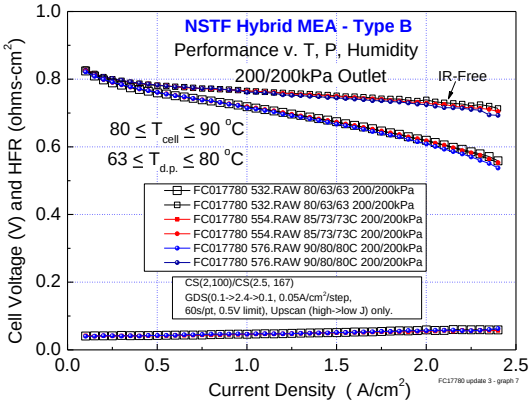


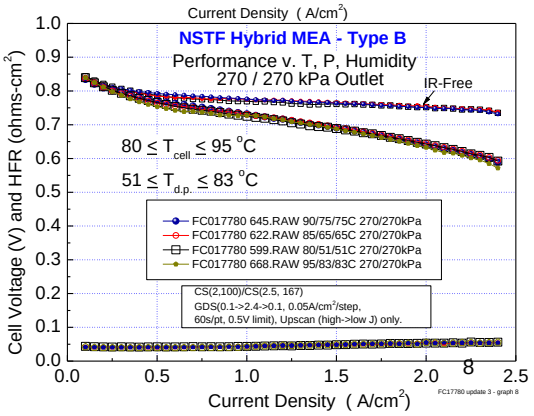

## Task 5.1/5.2/5.3 – MEA Integration for Final Stack Testing

❑ 2010 Best of Class" MEA component down-selection process

**Example 6: Cathode GDL Options**

**Cathode GDL Options:**

- Backing type: Fixed, 3M Standard
- Hydrophobic treatment - % PTFE
- MPL type – probably fixed
- Hybrid vs non-hybrid (Hybrid CCB)
  - Pt/C type and loading, I/C ratio,
  - C diluent fraction
  - Coating chemistry and method

**Deciding Factors:**

- Water management metrics (enhanced water out the cathode)
- ORR metrics
- HCT metrics (Mass transfer overpotential) at high temperature
- Pt loading cost/benefit ratio
- Accelerated stress tests

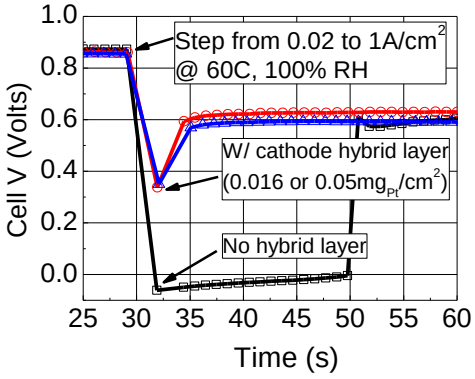


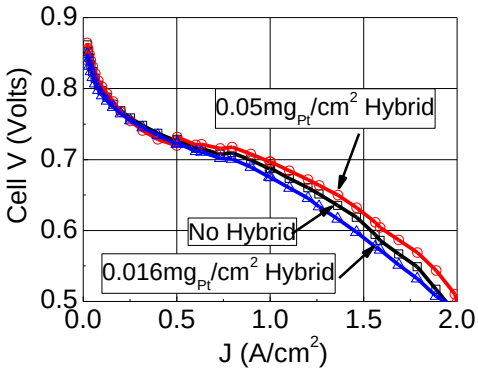




## Task 5.1/5.2/5.3 – MEA Integration for Final Stack Testing

❑ 2010 Best of Class" MEA component down-selection process

**Example 6: Cathode GDL Options: Hybrid B: 30ºC Steady State vs. $P_{Anode}$**

- Hybrid B MEA's show significant low Temperature benefit relative to NSTF CCM-only.
- Water management effects of cathode CCB and Anode GDL, $P_A$ appear primarily additive:
  - CCB helps take water out cathode
  - Anode GDL and low anode pressure help take water out the anode.

Benefit of water out the anode

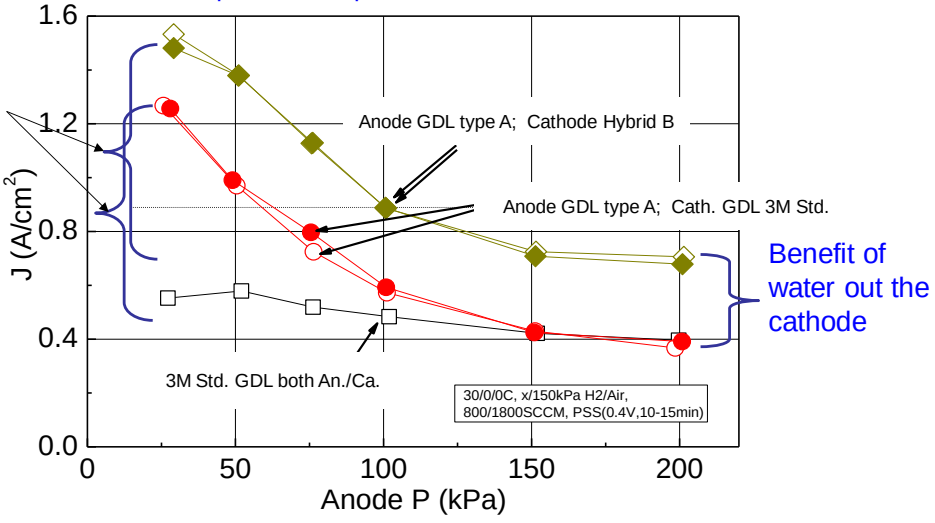


Benefit of water out the cathode

C:\Documents and Settings\us314230\My Documents\publications\2010 ECS\PAPER Water Management - SubAtm Anode SteadyState 020810-[Graph22]

## Task 5.1/5.2/5.3 – MEA Integration for Final Stack Testing

❑ 2010 Best of Class" MEA component down-selection process

**Example 6: Cathode GDL Options**

### Summary - Hybrid B CCB Optimization

- With 0.05Pt/C CCB, Pt in CCB is electrochemically $H_{upd}$ active and measurable by surface area and somewhat by ORR activity. However, no benefit is generally observed under $H_2$/Air pol. curves at low J.
- Presence of CCB improves load transient performance, reversible decay rate, dry performance, cool-dry performance, and high current density-hot performance over non-CCB constructions.
- To date, production CCB's generally have yielded similar or better high J performance than MEAs without CCB, but performance at moderate current densities is suppressed ~10-30 mV.
- Significant performance issues have become evident as the Pt content of the hybrid layer has been reduced to < 0.04 mg/cm$^2$.
- It is not clear yet if a hybrid MEA construction will meet all the necessary conditions for down-selection for the final 2$^{nd}$ stack durability testing.

**Technical Back-Up Slide**

## Task 5.1/5.2/5.3 – MEA Integration for Final Stack Testing

❑ **2010 Best of Class" MEA component down-selection process**

### Low Temperature Water Management Summary

- Strategies to increase the fraction of water moving out the anode and decrease the liquid water moving out the cathode are most effective for increasing cool, wet limiting currents.
  - Natural NSTF hydrophilic property enables this approach
  - Best strategy in principle for any MEA if it can be done – harvests product water to humidify PEM, decreases $O_2$ mass transport impedance on the cathode.
- Novel effect of sub-atmospheric anode pressure ($P_A$) operation demonstrated:
  - Several-fold increase in room temperature limiting current
  - $P_A$ effect sensitive to temperature, anode GDL properties. **Useful for screening GDL's.**
  - Conventional "thick" dispersed electrode MEAs do not show same benefit.
  - Water balance mechanistic study
    - Reduced anode pressure decreases total water flux out cathode.
    - Simple model suggests performance improvement due to decreased *liquid* product water flux through cathode GDL.
- Material Factors
  - **Anode GDL backing layer appears to be most significant component affecting control of water flow from cathode to anode at ambient pressure.**
  - Continuing to screen new vendor supplied GDL backing layers and 3M MPL's for best performance and minimal negative factors such as shorting.

## Task 5.3 – Stack 1

A primary focus of this project during the period 4/2010-3/2011 was the screening process for down-selecting the final MEA component sets for the final stack testing. Much of the GDL development work, P1 vs P4 catalyst deposition and SET process work (see Sections 7 and 9) were all directed at this objective. The MEA component sets investigated in this process included those bulleted items below:

- Cathode catalyst: composition, loading, deposition process, post process
- Anode catalyst: composition and deposition process (finalized)
- PEM: thickness, supported vs un-supported, chemical additive levels, etc.
- Anode GDL: Backing layer type, MPL properties
- Cathode GDL: Backing layer type and MPL properties, interfacial coatings

As illustrated in Fig. S7, the down-selection process itself involved evaluation of hundreds of MEA's in duplicate covering two dozen or more specific component/process parameter experiments. The results are too extensive and proprietary to discuss here but more information and some examples can be found in this project's 2011 presentation at the DOE annual merit review (http://www.hydrogen.energy.gov/pdfs/review11/fc006_atanasoski_2011_o.pdf).

The other major effort over this same time period was to prepare for and then fabricate roll-good CCMs down-selected for stack 1 testing provided by GM's fuel cell facilities at Honeoye Falls, NY. Two stack tests were planned. The first stack was to enable down-selecting to the final MEA type to be tested in a 2nd stack under an accelerated durability protocol. The first stack compared the six MEA configurations shown in Table S.1, consisting of three different membrane options and three cathode catalyst options. Different GDLs were used for the anodes and cathodes, but only one type of each. The anode catalyst was fixed at NSTF-0.05 $mg_{Pt}/cm^2$ of the P1 processed PtCoMn. These six MEA types were fabricated as roll-goods and used to populate Stack 1, a 29 cell "Rainbow" stack, one "color" for each MEA type, for initial beginning of life operation under various automotive relevant test protocols for beginning of life testing to enable further down-selection for a second stack (Stack 2 discussed below) that was directed at longer durability studies.

**Table S.1**. Definition of six MEA configurations evaluated in Stack 1, a 29 cell "rainbow" stack.

| CCM ID | PEM | Anode | Cathode | S1622 Cells |
|---|---|---|---|---|
| Config. 1 | 3M-24um (w/add. 2) | 0.05 P1 PtCoMn | 0.15 P4 PtCoMn + SET | 9-12 |
| | 3M-24um (w/add. 1) | 0.05 P1 PtCoMn | | |
| Config. 2 | 3M-24um (w/add. 2) | 0.05 P1 PtCoMn | 0.10 P1 PtCoMn | 5-8, 22-25 |
| Config. 3 | 3M-S | 0.05 P1 PtCoMn | 0.15 P1 PtCoMn | 13-16 |
| | | 0.05 P1 PtCoMn | | |
| Config. 6 | 3M-X | 0.05 P1 PtCoMn | 0.15 P1 PtCoMn | 17,18 |
| Config. 7 | | 0.05 P1 PtCoMn | 0.10 P1 PtCoMn | 19-21 |
| Config. 8 | 3M-24um (w/add. 1) | 0.05 P1 PtCoMn | 0.15 P1 PtCoMn | 1-4, 26-29 |

The stack 1 performance was a surprise in that it significantly underperformed what we expected based on 50 $cm^2$ single cells. Figure S14(A) compares polarization curves from the four configuration-1 MEAs in stack 1 with what we and GM had previously measured in 50 $cm^2$ single cells for similar MEAs under similar conditions. Significant effort was spent by both 3M and GM to "debug" the low performance over a 2.5 month period. A number of confounding issues contributed, including test station water purity, properties or contamination of the ionomer used for the membrane lots used to fabricate the CCMs, and more effective break-in conditioning that is possible with single cells versus large area stacks. Further tests revealed the catalyst ORR metrics and surface areas were as expected, stack compression was nominal, but 50 $cm^2$ CCMs made in the lab with the same membrane lots as used in roll-to-roll fabrication of the CCM for stack 1 also underperformed what was expected. CCMs from the same roll-to-roll lots were also tested in a 3M short stack (5 cell, 312 $cm^2$) and found to underperform the single cell results at ambient pressure (Fig. S14(B)) but give similar results at 22 psig (Fig. S14(C)), and slightly better than the GM stack at a similar pressure, as shown in Fig. S14( D).

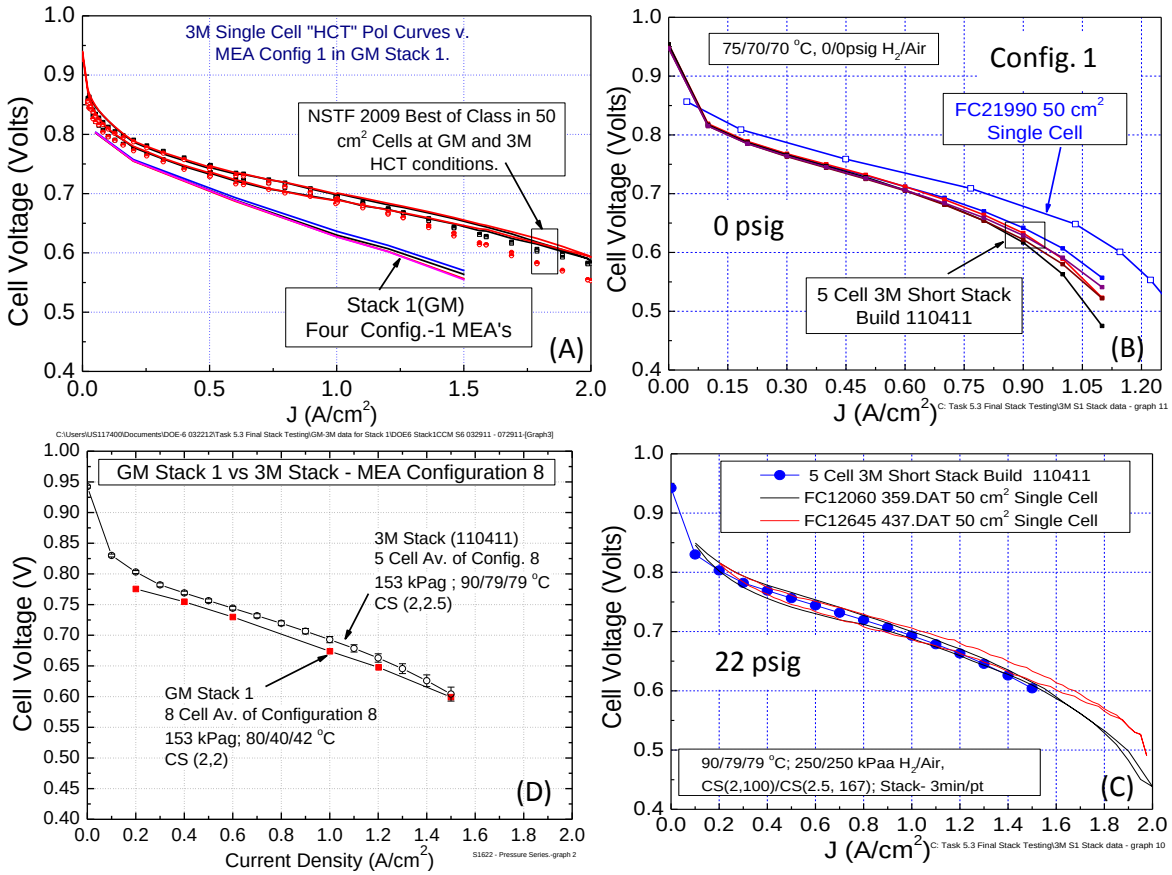


**Fig. S14. (A)** Comparison of the polarization curves obtained from the four configuration 1 MEAs in stack 1, with the expected performance based on 50 $cm^2$ single-cell tests measured both at 3M and GM. **(B)** Comparison of ambient pressure polarization curves from the same MEA configuration (made with the same component lot material inputs as used for the GM stack 1 MEA's), but measured at 3M in a 5 cell 312 $cm^2$ short stack, with the MEA's single cell 50 $cm^2$ performance. **(C)** Same 5 cell 3M stack and single cell MEA tests as in (B) but at 22 psig. **(D)** Polarization curve averages under nearly the same conditions, from the configuration 8 MEA's tested in the GM stack 1 hardware and in the 3M short stack hardware.

Despite these shortcomings, the GM stack 1 tests were successful in clearly being able to delineate the performance order of the six MEA configuration types, with MEA configuration 1 being the best and down-selected MEA for the eventual stack 2 durability testing. This is illustrated in Fig. S15 which compares the various MEA configuration type average cell voltages at 1.2 A/cm$^2$ under one particular test condition in the GM stack during the break-in conditioning period.

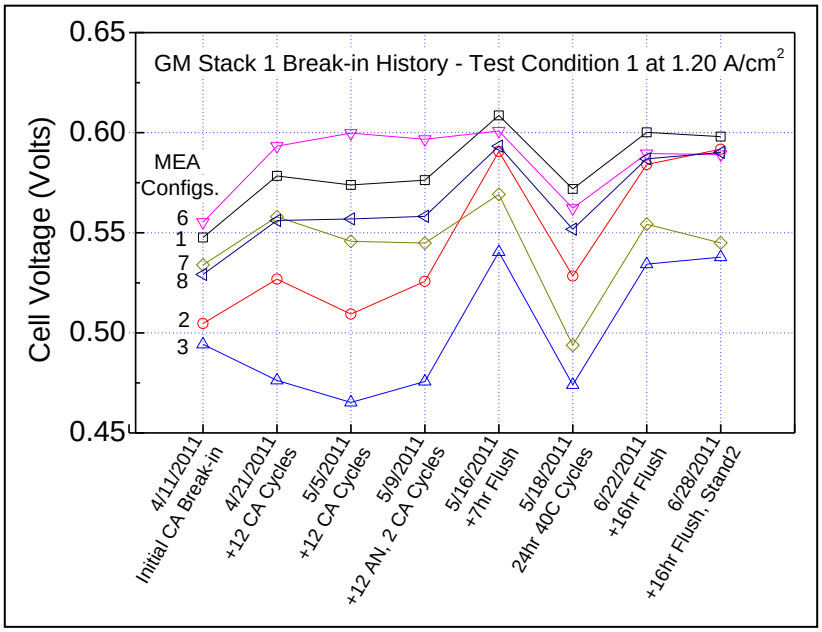


**Fig. S15**. Comaprison of the six MEA configuration types' average cell voltages at 1.2 A/cm$^2$ under one particular test condition in the GM stack during the break-in conditioning period.

Figure 7.7 in Section 7 shows a pressure-series of polarization curves, comparing the 4-cell average stack performance of the configuration-1 MEAs with six, 50 cm$^2$ single-cell tests (done at 3M) having the identical type MEA. (The test conditions used for the data in Fig. 7.7 were those supplied by the systems modeling group at ANL, Ahluwalia et al., and used by 3M for generating other MEA data requested by that group.) Performance improves with pressure similarly in single cells and the stack, consistent with mass transport issues. The stack 1, MEA type 1 performance average underperforms the single-cell tests at all conditions, but not by too much as long as the current density is below ~1.5 A/cm$^2$. At higher current densities the stack 1 performance falls considerably short of the small single cells.

There is still a question of the possible impact of flow field differences between the quad-serpentine 50 cm$^2$ cells used at 3M and the flow field of the GM stack. Flow fields had never been systematically optimized for the NSTF type ultra-thin electrodes but as discussed in Section 9.10, they can clearly have a strong effect that might not be considered an issue with conventional thick layer electrodes. This suggests that the different sized lands and channels of the GM flow fields may be part of the difference seen between the short stack 1 test results and the expected single cell test results.

**Task 5.3 – Stack 2**

The down-selected MEA configuration type 1 in Table S.1 from the stack 1 tests was intended to be the sole MEA type used in the second stack, slated for accelerated durability testing. Due to various issues, this exact MEA configuration 1 did not end up being the final MEA type used in stack 2, as a different membrane was ultimately used. Factoring into the decision were NSTF CCM-production issues with available standard, non-supported PEM lots, which made it attractive to move to the newer generation membrane. This gave the opportunity to switch the membrane type from a standard, non-supported membrane to a new, 3M experimental supported membrane, which previous data had indicated helped improve certain accelerated MEA durability tests. There was risk associated with this decision as these were still

experimental PEMs and optimized integration with the NSTF had not been completed. Work related to resolving these issues required an additional 9 month no-cost extension of the project. The final MEA stack 2 catalysts used were the same as that used in configuration 1 in Table S.1. We subsequently discovered that performance in 50 $cm^2$ single cells was again much worse than expected. Once the final CCM roll-goods were fabricated, and shortly after shipment to GM, the reason for the underperformance was tracked to the inadvertent production release of an experimental PEM lot to make the CCMs that had been put on hold due to suspected contamination of its ionomer. Due to lack of time and funding to make further MEAs, the decision was made to continue with the stack 2 testing with these CCMs.

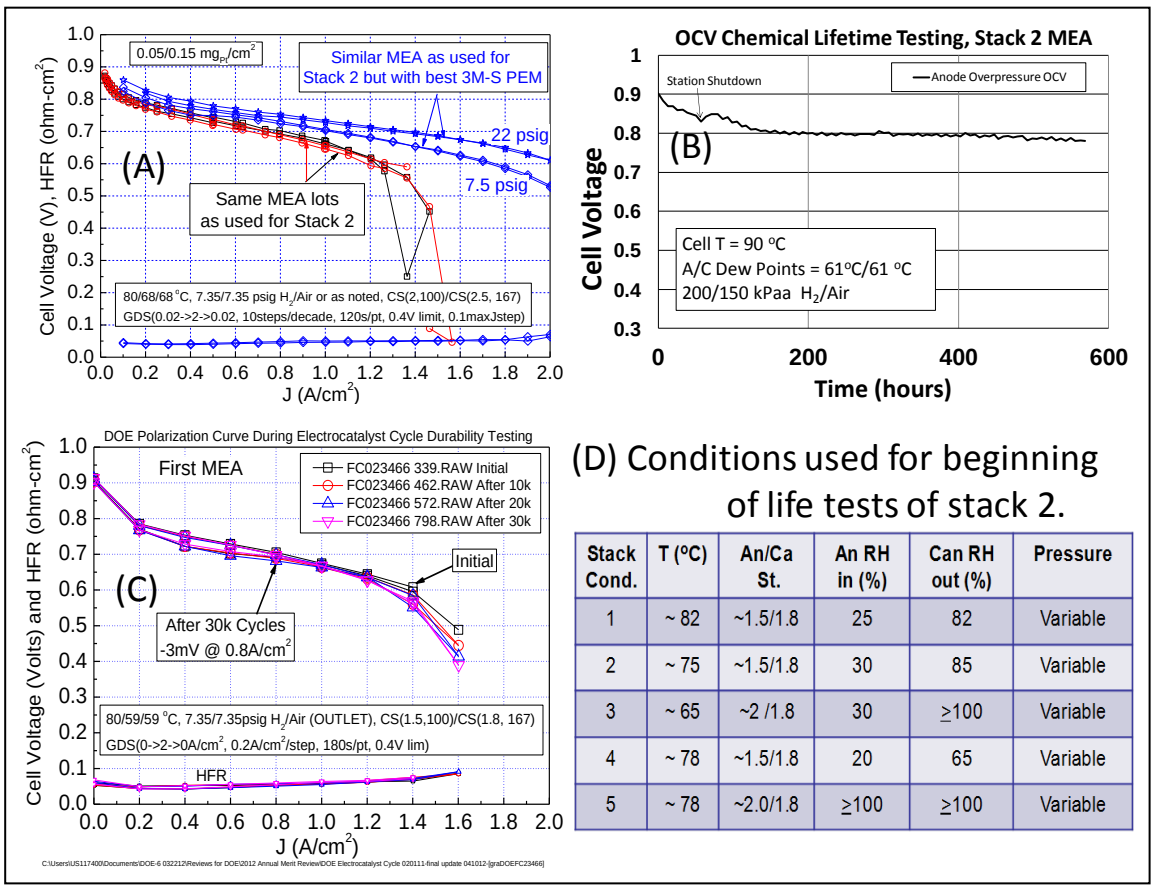


(D) Conditions used for beginning of life tests of stack 2.

| Stack Cond. | T (°C) | An/Ca St. | An RH in (%) | Can RH out (%) | Pressure |
|---|---|---|---|---|---|
| 1 | ~ 82 | ~1.5/1.8 | 25 | 82 | Variable |
| 2 | ~ 75 | ~1.5/1.8 | 30 | 85 | Variable |
| 3 | ~ 65 | ~2 /1.8 | 30 | ≥100 | Variable |
| 4 | ~ 78 | ~1.5/1.8 | 20 | 65 | Variable |
| 5 | ~ 78 | ~2.0/1.8 | ≥100 | ≥100 | Variable |

**Fig. S16. (A)** Single-cell 50 $cm^2$ GDS polarization curves at 7.5 psig from MEAs taken from the same lot as used for stack 2, compared with a similar MEA that used a known non-contaminated 3M-S membrane, at both 7.5 and 22 psig. **(B)** OCV hold versus time durability test for an MEA identical to that used for stack 2. **(C)** GDS polarization curve and HFR impedance for an MEA identical to that used for stack 2 before, during and after 30,000 CV cycles from 0.6 to 1 volt. **(D)** Conditions used for the beginning of life tests in stack 2.

Figure S16A) compares 50 $cm^2$ single cell beginning of life performances at 7.5 psig $H_2$/air from MEAs using the same CCM lots as used in stack 2, with that from MEAs using CCMs made with the same catalyst lots but with normally performing experimental 3M-supported membrane (best 3M-S) at 7.5 and 22 psig $H_2$/air. In addition to the dramatic loss of limiting current density with the contaminated PEM, the ORR activities were slightly depressed, while the catalyst electrochemical surface areas and MEA HFR were normal. Surprisingly however, as the stack 2 type MEA was tested in a single 50 $cm^2$ cell using nominally the same

cycling durability protocol discussed below for stack 2, but with periodic recovery, the MEA performance continuously improved for nearly 400 hours and approached that of the best 3M-S curves shown in Figure S16(A).

Despite these issues with beginning of life performance, Figures S16(B) and S16(C) show that the MEAs using CCMs from the same lots as in the stack 2 MEAs, passed both the DOE OCV hold tests and the CV cycling tests. The objective of the OCV hold test is assessment of the whole MEA/membrane durability at OCV at 90°C under 30% RH, 250/200 kPa $H_2$/air. The target is 500 hours with less than 20% loss of OCV. This MEA went 570 hours with a 13% loss under the 50 kPa $H_2$ overpressure. The CV cycling accelerated stress test characterizes the resistance of the catalyst to dissolution, agglomeration or loss of activity due to high voltage cycling. The protocol involves cycling the cathode between 0.6 and 1.0 volts and back again at 50 mV/sec under 100/100 kPa $H_2/N_2$ at 80°C cell and dew points. The target is to have after 30,000 cycles, less than 40% loss of surface area and ORR mass activity and a polarization curve loss of less than 30 mV at 0.8 A/cm$^2$. The stack 2 lot of MEA's (two were tested) demonstrated a 10±7 mV loss at 0.8 A/cm$^2$, 16±2% loss of surface area, and 37±2% loss of mass activity. This is the first time we have been able to demonstrate meeting all the targets with this accelerated stress test.

The stack 2 beginning of life performance was evaluated under five different sets of operating conditions as in Fig. S16(D). Consistent with the single cell tests, the beginning of life stack 2 MEA performances were much lower than expected and lower than single cell tests with the same MEA lot, but did not vary significantly from the driest to the wettest conditions, as shown in Fig. S17(A). Average cathode surface areas were approximately normal at 8.2 m$^2$/g, while in-stack shorting resistances were lower than the standard GM baseline MEAs used as end-cells in the 29-cell short stack.

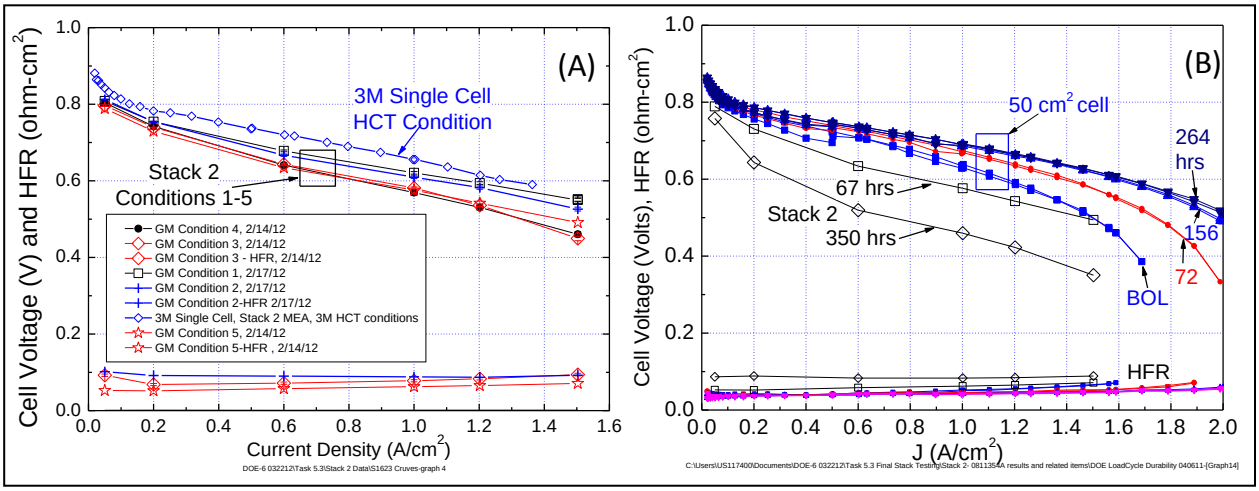


**Fig. S17(A)** Average MEA beginning-of-life performance in stack 2 at the five conditions shown in Fig. S16(D) compared to the 50 cm$^2$ single-cell test under GDS high current test conditions of: 80/68/68°C cell temperature/anode/cathode dew points; 150 kPa $H_2$/air; and anode/cathode stoichiometric flows of 2/2.5. GDS polarization curve conditions are same as in Figure 3.
**(B)** Comparison of stack 2 performance change after 4 sets of 1,500 load cycles (~300 hours) with the performance change of the same MEA type in a 50 cm$^2$ single cell (at 3M) after 200 hours of a similar load cycle, interspersed with periodic recovery shutdowns every 12 or 24 hours. Procedure Loop: 1) 5 thermal cycles, 2) polarization curves, 3) 12- or 24-hr cycling under

The objective of stack 2 was to conduct a load-cycling protocol representative of an accelerated stress test for lifetime durability. The protocol chosen was close to that

recommended by the U.S. Drive Fuel Cell Tech Team with some modifications to adapt it to the under-performing MEA and the slower cool-wet transient behavior of the thin layer NSTF electrodes with the GDLs used (see publication numbers four and five in the Appendix for the impact of the anode GDL type on this behavior). Higher pressure, controlled current ramp rate, and minimum voltage control were the main modifications to the protocol. After four sets of 1,500 cycles, ~350 hours of operation, the following observations were made: two point (beginning and end) performance decay rates were much higher than expected (by factors of 3x to 8x); cross-over leak rates and hydrogen take-over in the cells were high; high frequency resistance increased with time but could not account for the lost performance; there were significant fluctuations in performance between each of the 4-cycle sets. Fig. S17(B) shows the beginning-of-life performance (67 hours, open squares) of the stack and that after 350 hours (open diamonds) of cycling, showing extreme decay. Also shown in Fig. S17(B) are the performances of the same stack 2 type MEA tested in a 50 $cm^2$ single cell at 3M at beginning of life and after 72 hours (red circles), 156 hours (up triangles) and 264 hours (down triangles) with nominally the same load cycling protocol. One key difference in the single cell tests and the stack tests is that the single cell was recovered periodically (12- or 24-hour period) by stopping the load cycling and doing five thermal cycles before resuming the load cycling. Thermal cycling is the typical break-in conditioning protocol used for NSTF MEAs and the large improvement in performance of the single-cell MEA seen with the load cycling is consistent with removal of impurities in the vicinity of the electrodes. The performance of the single cell MEA in Fig. S17(B) continued to improve or stabilized depending on current density for nearly 400 hours, after which its performance started to decay and by 580 hours it had failed due to edge failure of the CCM. This MEA did not have subgasket edge-protection which would be expected to improve lifetime significantly. Low performing cells in the stack 2 prevented going to high current densities and necessitated replacing MEAs and rebuilding the stack on two occasions.

The first rebuild replaced four original NSTF based MEA's with baseline GM MEA's at ~ 330 hours of operation. The second rebuild replaced six more original NSTF stack 2 MEA's with NSTF stack 1 MEA's (which already had ~ 300 Hours on them) at ~ 360 hours of operation. Following the second rebuild, the stack was water-flushed, but another cell failed above 1.2 $A/cm^2$ while several durability cycles were run. Performance started reasonably well but then quickly diminished. It was observed that the shorting resistance for every cell, including all the GM baseline cells, would significantly worsen (drop in value) after each such rebuild. The reason for this was not determined.

The stack sat for 6 weeks after a wet shut down, then polarization curves were re-ran and one further cycling attempt was made on 8/16/12. Only several hours of cycling were completed before the stack 2 forced a test station E-stop. It was eventually determined that further work with the stack would not be instructive and testing was discontinued.

The following three sets of figures show the final polarization curves obtained with the stack 2 during the last trials. They show stack 2's cell by cell plots of three types of polarization curve voltages at 0.2, 0.6 and 1 $A/cm^2$ versus time. The NSTF cells are in blue, the control cells in red. Replacement of failed NSTF cells by the GM baseline cells (red curves) can pull the whole stack averages up. Replacing the bad Stack 2 MEA's with (used) Stack 1 MEA's also improved the average. After 300 hours, there was some indication that all cells were improving even the original bad stack 2 MEA's.

## Task 5.3 Final Stack Testing (cont.)

Example of degradation versus time with polarization curve type A at 0.2, 0.6 and 1 A/cm$^2$.

- Some cells appeared to be recovering slightly at all currents, near the end.
- The stack 1 (Performance stack) MEA's were much better when replacing the failed stack 2 (Durability stack) MEA's.

Polarization Curve Type A, 1.0A/cm$^2$

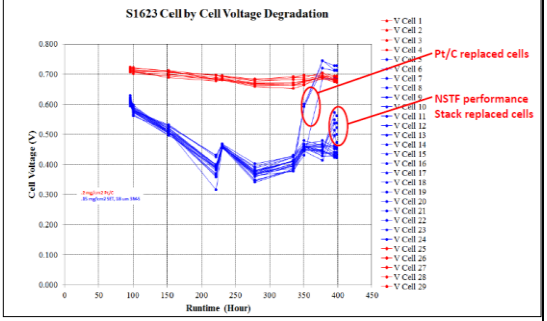


Polarization Curve Type A, 0.2 A/cm$^2$

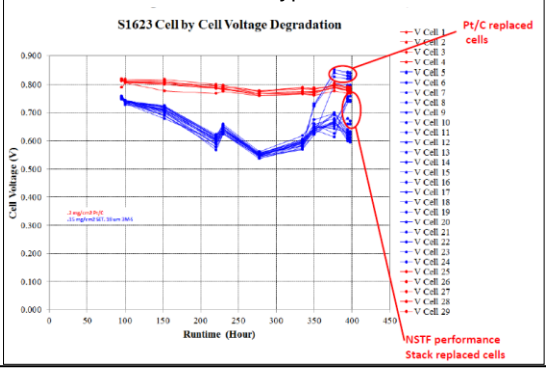


Polarization Curve Type A, 0.6 A/cm$^2$

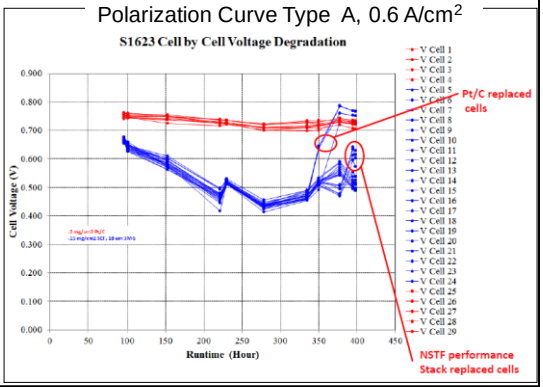


## Task 5.3 Final Stack Testing

Example of degradation versus time with polarization curve type B at 0.2, 0.6 and 1 A/cm$^2$.

- Some cells appeared to be recovering slightly at all currents, near the end.
- The stack 1 (performance) MEA's were much better when replacing the failed stack 2 (durability) MEA's.

Polarization Curve Type B, 1.0 A/cm$^2$

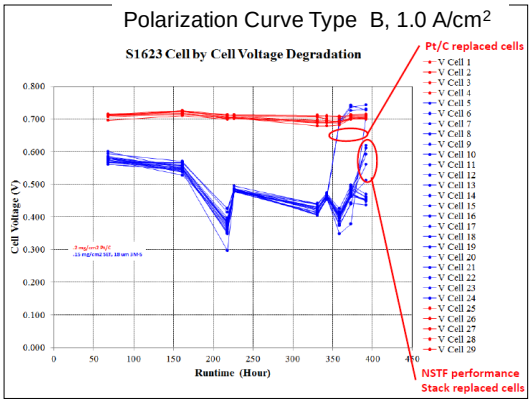


Polarization Curve Type B, 0.2A/cm$^2$

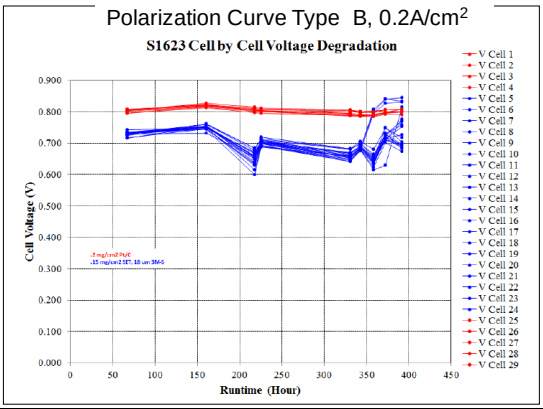


Polarization Curve Type B, 0.6 A/cm$^2$

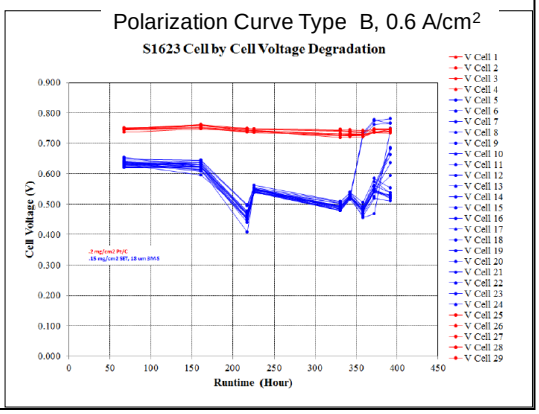

### Task 5.3 Final Stack Testing

Example of degradation versus time with polarization curve type A at 0.2, 0.6 and 1 A/cm$^2$.

- Some cells appeared to be recovering slightly at all currents, near the end.
- The stack 1 (Performance stack) MEA's were much better when replacing the failed stack 2 (Durability stack) MEA's.

Polarization Curve Type C, 1.0 A/cm$^2$

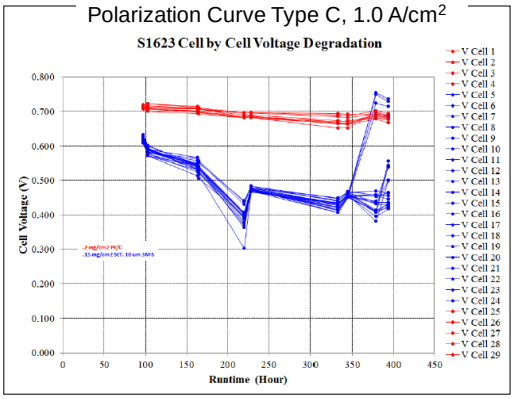


Polarization Curve Type C, 0.2 A/cm$^2$

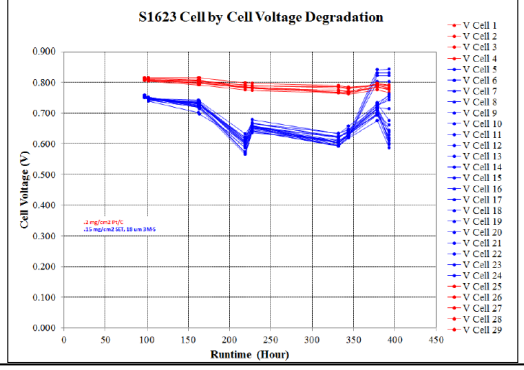


Polarization Curve Type C, 0.6 A/cm$^2$

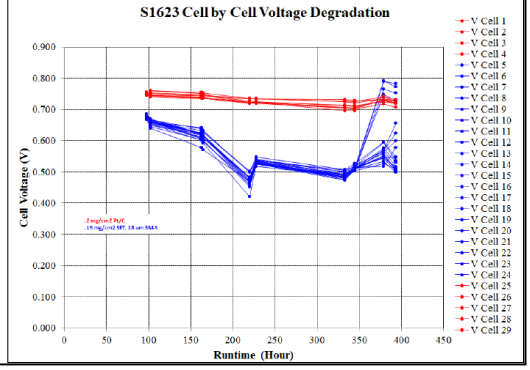


**Stack 2 Testing Conclusions provided by Eric Thompson, GM**
(Comments in parenthesis added by 3M for clarification.)

"Following the last rebuild, durability cycling data was discouraging. The "Durability NSTF cells" (meaning stack 2) degraded quickly. Cell instability in polarization curves was reported by the technician. On the bright side, data following the last rebuild when "Performance Stack NSTF Cells" (i.e. stack 1) were used to replace the troublesome "Durability NSTF cells", those cells displayed a more expected and reasonable behavior for NSTF. Significant separation in performance (was observed) between the two sets of NSTF parts in the durability cycling data. Also, "NSTF performance stack" (stack 1) MEAs performed higher in polarization curve degradation data. This gives some positive indication that with a healthy membrane, the NSTF can perform much better in the (modified) durability cycling protocol.

In hindsight we may have gotten more hours and more useful data doing a full replacement of "Durability NSTF cells" with "Performance NSTF cells" earlier in the process. (We were headed in this direction and debated doing so.) The presence of any contaminated NSTF Durability cells just held back and limited what could be run and observed with Performance Stack NSTF parts (in the Durability stack 2). This exercise has also given learning as a framework of how the DOE durability cycling protocol should be modified to accommodate and align with NSTF attributes: Higher pressure (200 kPa) as opposed to near ambient pressure; Utilize at least a 5 sec ramp-in in load transients, as opposed to direct step transient; Maintain cell voltage above 0.6 V based on Jingxin's study seems beneficial, although we have not fully confirmed this here."

# Task 6

# Selected Supplementary Information

## Task 6.0 - New Task focused on faster/simpler break-in conditioning

### 6.1 Improved break-in protocols and conditions

3M Advanced Cathode Catalysts and Supports…… DOE Review Nov. 9, 2010

**Task 6 MEA break-in conditioning**

**Objective:** Dramatically reduce the time and simplify the process for initial break-in conditioning of NSTF catalyst based MEA's.

- **Issue:** Low loading and low surface area of NSTF electrodes requires unacceptable times, > 24 hours, to reach peak performance under current break-in and conditioning protocols. Water flushing also is used in our standard "thermal cycling" protocol and may not be available for stack conditioning.

- **Two subtasks focusing on test station protocols and materials:**
  - Subtask 6.1. Break-in conditioning protocol - quantify the effect of test station operating parameters on the time for break-in conditioning of the standard PtCoMn NSTF MEA's in 50 $cm^2$ single cell tests
  - Subtask 6.2.Component Factors - Identify MEA component factors having greatest effect on break-in conditioning time

Work this period:
- Limited to evaluating success of "stack capable" start-up protocol to wider array of stations and material component sets.
- Effectiveness for wider array of all MEA performance protocols.

3M Advanced Cathode Catalysts and Supports…… DOE Review Nov. 9, 2010

**Task 6 MEA break-in conditioning**

Development of "Stack-Capable" FAST Conditioning Methodology

- Objective of experiments is to determine if NSTF MEAs can be conditioned using rapid conditioning protocols which should be feasible in stacks
  - Low reactant flows
  - Current rather than voltage control
  - Completely dry inlet gases (simpler conditioning; less expensive conditioning equipment required)

- To allow completely dry operation, water balance calculations suggest that pressurized reactants are required
  - ~200kPa for 70-75C cell with constant stoich 2.0/2.0

- Experiments based on modification of April 2010 baseline "fan-cooling" script, Script #52
  - Script #52: High reactant flows, voltage control, humidified gases

- Tests done with 2009 Best of Class NSTF MEAs (0.05PtCoMn/0.10PtCoMn, 3M 850EW 20u, 2979 GDLs), on single test station (S20).

## Task 6 MEA break-in conditioning

### Development of "Stack-Capable" FAST Conditioning Methodology

### Protocol Definitions

| Script #52 | | |
|---|---|---|
| **Tcycle** | **LoadCycle** | **Duration** |
| {50/45/45C, 800/1800SCCM, 100/100kPa}, {30/60/60C, 200/400SCCM, 100/100kPa} | OCV(2s), 0.5V(2s), 0.25V(10s) 1 PDS Curve per Tcycle (at max T) | 1hr |
| {75/70/70C, 800/1800SCCM, 100/100kPa}, {55/90/90C, 200/400SCCM, 100/100kPa} | OCV(2s), 0.5V(2s), 0.25V(10s) 1 PDS Curve per Tcycle (at max T) | 3hr |
| {75/70/70C, 800/1800SCCM, 100/100kPa}, {30/60/60C, 200/400SCCM, 100/100kPa} | OCV(2s), 0.5V(2s), 0.25V(10s) 1 PDS Curve per Tcycle (at max T) | 16hr |

**April 2010 FAST Baseline**

| Fast Startup (Dry VCycle) | | |
|---|---|---|
| **Tcycle** | **LoadCycle** | **Duration** |
| {50/0/0C, 800/1800SCCM, 200/200kPa}, {30/0/0C, 200/400SCCM, 200/200kPa} | OCV(2s), 0.5V(2s), 0.25V(10s) 1 PSS(0.4V) per Tcycle (at max T) | 1hr |
| {75/0/0C, 800/1800SCCM, 200/200kPa}, {55/0/0C, 200/400SCCM, 200/200kPa} | OCV(2s), 0.5V(2s), 0.25V(10s) 1 PSS(0.4V) per Tcycle (at max T) | 3hr |
| {75/0/0C, 800/1800SCCM, 200/200kPa}, {30/0/0C, 200/400SCCM, 200/200kPa} | OCV(2s), 0.5V(2s), 0.25V(10s) 1 PSS(0.4V) per Tcycle (at max T) | 16hr |

**Differences from #52**
- Dry gases
- 200kPa Pressure
- PDS curves replaced w/ PSS(0.4V, 5min)
  - •avoid dryout at low J portion of test

3M Advanced Cathode Catalysts and Supports…… DOE Review Nov. 9, 2010

Task 6 MEA break-in conditioning

Development of "Stack-Capable" FAST Conditioning Methodology

Protocol Definitions

Script #52

| Tcycle | LoadCycle | Duration |
|---|---|---|
| {50/45/45C, 800/1800SCCM, 100/100kPa}, {30/60/60C, 200/400SCCM, 100/100kPa} | OCV(2s), 0.5V(2s), 0.25V(10s) 1 PDS Curve per Tcycle (at max T) | 1hr |
| {75/70/70C, 800/1800SCCM, 100/100kPa}, {55/90/90C, 200/400SCCM, 100/100kPa} | OCV(2s), 0.5V(2s), 0.25V(10s) 1 PDS Curve per Tcycle (at max T) | 3hr |
| {75/70/70C, 800/1800SCCM, 100/100kPa}, {30/60/60C, 200/400SCCM, 100/100kPa} | OCV(2s), 0.5V(2s), 0.25V(10s) 1 PDS Curve per Tcycle (at max T) | 16hr |

April 2010 FAST Baseline

| Fast Startup (Dry CathodeStarve) | | |
|---|---|---|
| **Tcycle** | **LoadCycle** | **Duration** |
| {50/0/0C, 140/124SCCM, 200/200kPa}, {30/0/0C, 140/124SCCM, 200/200kPa} | OCV(2s), 0.1A/cm2(10s), 0.2A/cm2(3s) 1 PSS(0.4V) per Tcycle (at max T) | 1hr |
| {75/0/0C, 140/124SCCM, 200/200kPa}, {55/0/0C, 140/124SCCM, 200/200kPa} | OCV(2s), 0.1A/cm2(10s), 0.2A/cm2(3s) 1 PSS(0.4V) per Tcycle (at max T) | 3hr |
| {75/0/0C, 140/124SCCM, 200/200kPa}, {30/0/0C, 140/124SCCM, 200/200kPa} | OCV(2s), 0.1A/cm2(10s), 0.2A/cm2(3s) 1 PSS(0.4V) per Tcycle (at max T) | 16hr |

**Differences from #52**
- "Stack capable"
  - •J Control
  - •Low V induced by cathode starvation
- Low J; low reactant flows
- Dry gases
- 200kPa Pressure
- PDS curves replaced w/ PSS(0.4V, 5min)
  - •avoid dryout at low J portion of test

## Task 6 MEA break-in conditioning

### Development of "Stack-Capable" FAST Conditioning Methodology

Evaluation of Conditioning Rates

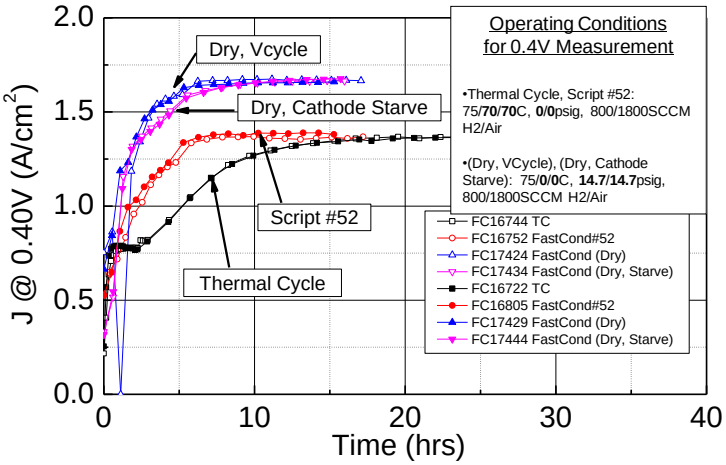


Q:\Projects\0046650001_DOE_VI\Shared\Task1.1.1 OriginPlots\Other\DryConditioning\DryConditioning 040510-[Graph1]

- Startup rates with dry conditioning protocols similar to baseline FAST protocol #52.
- Nominally fully conditioned in <8 hours.
- Absolute performance differences possibly due to different reactant pressures used.

3M Advanced Cathode Catalysts and Supports…… DOE Review Nov. 9, 2010

## Task 6 MEA break-in conditioning

### Development of "Stack-Capable" FAST Conditioning Methodology

80C Polarization Curve Performance

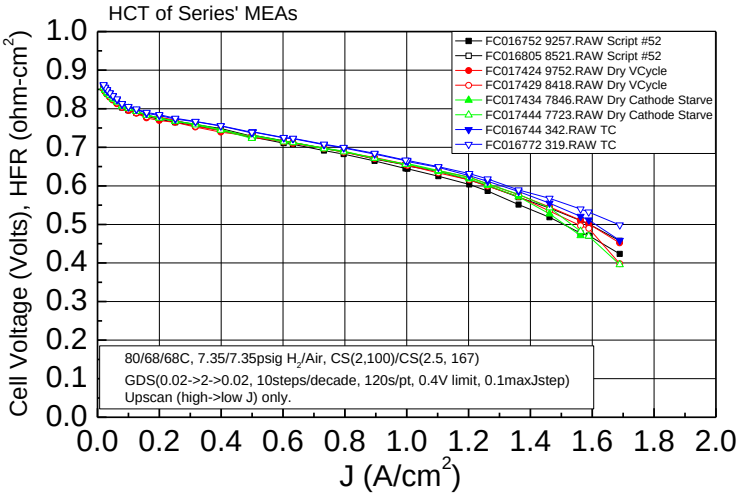


Q:\Projects\0046650001_DOE_VI\Shared\Task1.1.1 OriginPlots\Other\DryConditioning\DryConditioning 040510-[graHCTUS]

- HCT performance at high J slightly lower with FAST than thermal cycle protocol.

## Task 6 MEA break-in conditioning

### Development of "Stack-Capable" FAST Conditioning Methodology

Activity and HCT Relative Metric Values

| Performance Relative to Thermal Cycling (40hrs) | Wet Vcycle (Script #52) | | Dry Vcycle | | Dry CathodeStarve | |
|---|---|---|---|---|---|---|
| | Abs | %Change | Abs | %Change | Abs | %Change |
| PDS 0.813V J (A/cm2-planar) | -0.044 | -22 | -0.032 | -16 | -0.027 | -14 |
| SEF (cm2-Pt/cm2-planar) | -0.314 | -3 | | | | |
| ORR Absolute Activity @ 1050s (mA/cm2-planar) | 0.496 | 3 | -0.394 | -3 | -2.378 | -16 |
| HCT Meas V @ 0.020A/cm2 (Volts) | -0.006 | | -0.009 | | -0.006 | |
| HCT Meas V @ 0.32A/cm2 (Volts) | -0.009 | | -0.013 | | -0.007 | |
| HCT Meas V @ 1.00A/cm2 (Volts) | -0.017 | | -0.011 | | -0.008 | |
| HCT Meas V @ 1.46A/cm2 (Volts) | -0.031 | | -0.021 | | -0.026 | |

- Tabulated metrics indicate that FAST conditioning generally results in modest reductions in performance v. thermal cycling
- Large losses in low J PDS and high J HCT tests.

3M Advanced Cathode Catalysts and Supports…… DOE Review Nov. 9, 2010

## Task 6 MEA break-in conditioning

### Evaluation of FAST Conditioning by All Performance Characteristics

| Sample ID | Short Sample Description | Anode Catalyst ID | Anode GDL ID | Cathode Catalyst ID | Cathode GDL ID | Cathode Pt Loading (mg/cm2-planar) | PEM ID | Start Date | Station ID |
|---|---|---|---|---|---|---|---|---|---|
| FC017092 | 0.05PtCoMn/0.10PtCoMn 3M 20u H2315/2979 TC S14 | P409281B | H2315 | P409272 | 297995007B | 0.1 | MM09168B | 2/26/2010 | 14 |
| FC017228 | 0.05PtCoMn/0.10PtCoMn 3M 20u H2315/2979 TC S14 | P409281B | H2315 | P409272 | 297995007B | 0.1 | MM09168B | 3/12/2010 | 14 |
| FC017910 | 0.05Pt/0.15PtCoMn 3M/G 2979/2979 TC S14 | P1D10145 | 297995007B | P408344A | 297995007B | 0.15 | A747420 | 6/2/2010 | 14 |
| FC018060 | 0.05Pt/0.15PtCoMn 3M/G H2315/2979 FASTCOND S14 | P1D10145 | Freudenberg H2315 | P408344A | 297995007B | 0.15 | A747420 | 6/14/2010 | 14 |
| FC018102 | 0.05Pt/0.15PtCoMn 3M/G H2315/2979 TC S14 | P1D10145 | Freudenberg H2315 | P408344A | 297995007B | 0.15 | A747420 | 6/16/2010 | 14 |
| FC018172 | 0.05Pt/0.15PtCoMn 3M/G 2979/2979 FASTCOND S14 | P1D10145 | 297995007B | P408344A | 297995007B | 0.15 | A747420 | 6/24/2010 | 14 |
| FC018197 | 0.05Pt/0.15PtCoMn 3M/G H2315/2979 FASTCOND S14 | P1D10145 | Freudenberg H2315 | P408344A | 297995007B | 0.15 | A747420 | 6/29/2010 | 14 |
| FC018224 | 0.05Pt/0.15PtCoMn 3M/G H2315/2979 FASTCOND S14 | P1D10145 | Freudenberg H2315 | P408344A | 297995007B | 0.15 | A747420 | 7/6/2010 | 14 |
| FC018235 | 0.05Pt/0.15PtCoMn 3M/G H2315/2979 TC S14 | P1D10145 | Freudenberg H2315 | P408344A | 297995007B | 0.15 | A747420 | 7/8/2010 | 14 |

- During FAST conditioning protocol development, only typically evaluated high T performance.
- Here, evaluating activity, low and high T water management, performance stability, activities and surface areas.
- Note different material set than protocol development study – 0.05Pt/0.15PtCoMn, 3MG, H2315/2979 – and different test station.

## Task 6 MEA break-in conditioning

### Evaluation of FAST Conditioning by All Performance Characteristics

80 °C Polarization Curve Performance

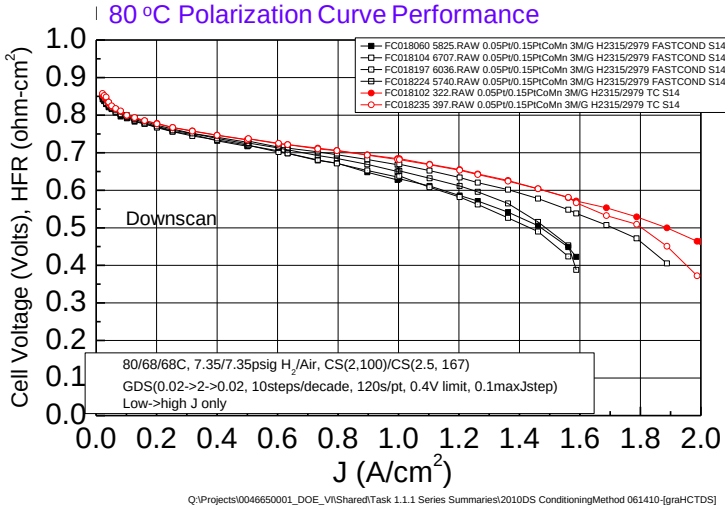


- FAST conditioned samples had significantly reduced limiting current than thermal cycled MEAs.
- Much larger gap than expected based on previous protocol development study
  - Materials?
  - Station?

3M Advanced Cathode Catalysts and Supports…… DOE Review Nov. 9, 2010

## Task 6 MEA break-in conditioning

### Evaluation of FAST Conditioning by All Performance Characteristics

80C Polarization Curve Metrics

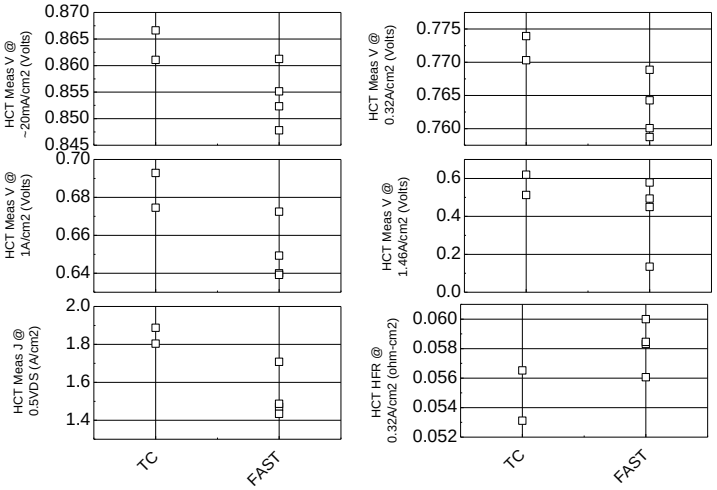


- FAST COND MEAs had lower performance overall.
- HFR was slightly higher with FAST COND MEAs @ 0.32A/cm2 (not enough to explain performance difference)

## Task 6 MEA break-in conditioning

### Evaluation of FAST Conditioning by All Performance Characteristics

Activity Metrics

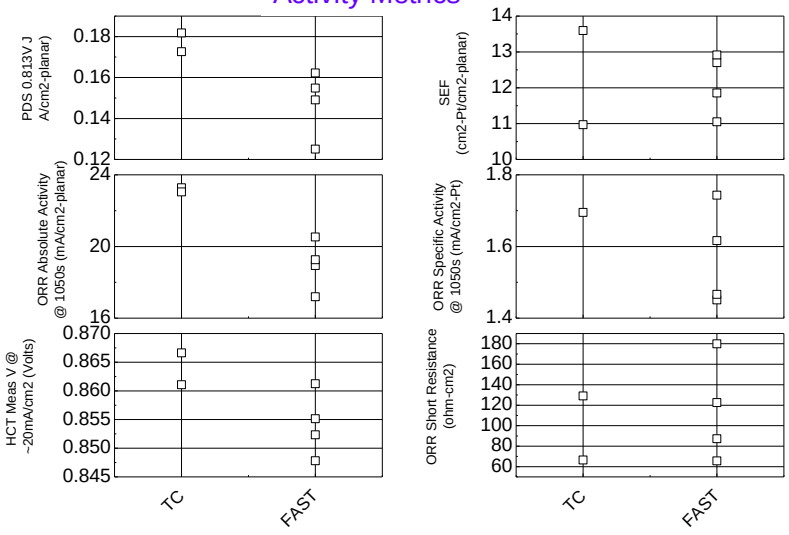


- FAST MEAs typically had lower absolute kinetic performance



## Task 6 MEA break-in conditioning

### Evaluation of FAST Conditioning by All Performance Characteristics

30 °C Steady State Performance

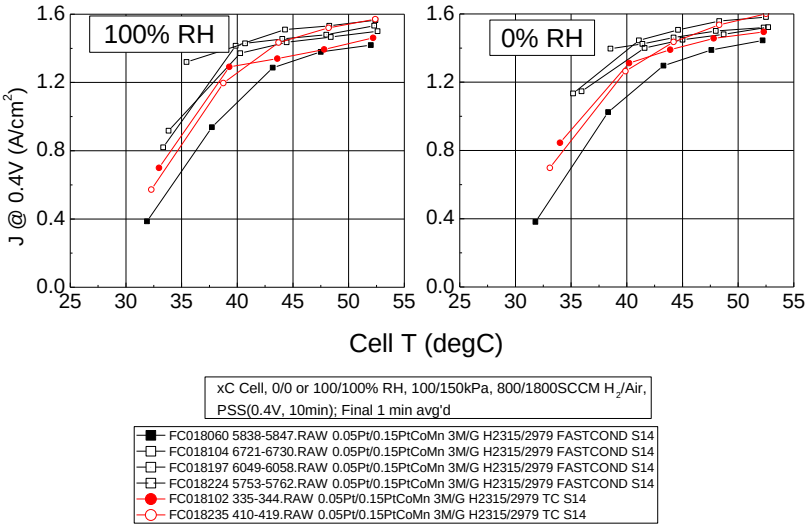


- FAST Conditioned MEAs generally had similar or higher cool PSS performance than MEAs that were conditioned by the standard thermal cycling protocol.

## Task 6 MEA break-in conditioning

### Evaluation of FAST Conditioning by All Performance Characteristics

30C Startup Transient Performance

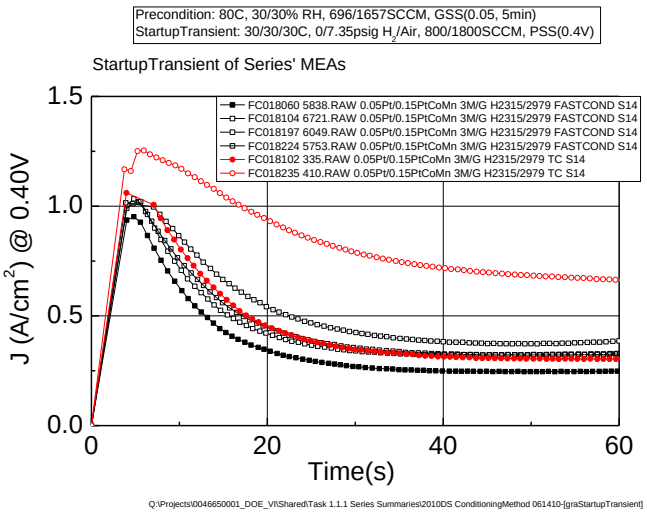


- Other than one thermal-cycled MEA, all MEAs generally had similar startup transients.

3M Advanced Cathode Catalysts and Supports…… DOE Review Nov. 9, 2010

## Task 6 MEA break-in conditioning

### Evaluation of FAST Conditioning by All Performance Characteristics

Hot and Dry Performance of Series' MEAs

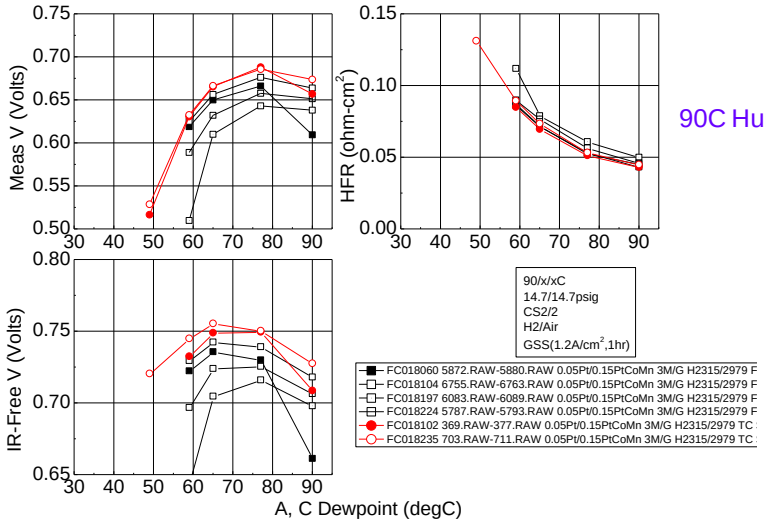


90C Humidification Sensitivity

- FAST COND MEAs generally had worse performance than TCd MEAs, especially at lower RH
- FAST COND MEAs generally had slightly high HFR at all humidities
- Many FAST Conditioned MEAs died during the driest part of this test.

## Task 6 MEA break-in conditioning

# FAST Conditioning Summary

- Systematic studies of the factors important for FAST conditioning were conducted. Critical factors included rapid and numerous voltage cycles over a sufficiently large range and sufficiently large temperature cycles.
- FAST conditioning methods were further developed which enabled achievement of nominally peak performance in < 8 hours via nominally stack-capable methods.
- However, FAST conditioning does not always achieve performance parity with the slower, historical 3M thermal cycle conditioning procedure. Small but significant reductions in cathode kinetic metrics occur, and depending upon the material set, significant reductions in the high current density performance are observed.
- Further systematic study is needed to determine if the performance gaps can be resolved.

## Task 6. MEA break-in conditioning

# Protocols

- Protocols' primary repeat sections are shown.
- Protocols are repeated until stable performance is achieved.
- Reactant flows shown for 50cm$^2$ cell.

### Standard Thermal Cycle

```
//WARMUP WITH POL. CURVES AND V HOLDS//
SET_CELL_TEMPERATURE (75C)
SET_ANODE_FLOW (800SCCM)
SET_CATHODE_FLOW (1800SCCM)
SET_ANODE_HUMIDIFICATION (70C)
SET_CATHODE_HUMIDIFICATION (70C)
SET_ANODE_PRESSURE (0 psig)
SET_CATHODE_PRESSURE (0 psig)
COUNT= (0); WHILE_COUNT_< (4)
   COUNT+1 ()
   POL. CURVE (0.85V->0.25V->0.85V, 0.05V/STEP, 10S/STEP)
   V=0.4V,5min
END_WHILE_COUNT ()
//COOL TO ROOM T, GASES OFF, LIQ WATER INJECT//
SET_CELL_TEMPERATURE (25C)
SET_ANODE_FLOW (0SCCM)
SET_CATHODE_FLOW (0SCCM)
SET_ANODE_HUMIDIFICATION (0.26CC/MIN)
SET_CATHODE_HUMIDIFICATION (0.40CC/MIN)
J=0A/cm2, 45min
```

### Fast Condition (Dry, Starve)

```
//WARMUP WITH J (CURRENT DENSITY) CYCLE//
SET_CELL_TEMPERATURE (75C)
SET_ANODE_FLOW (140SCCM)
SET_CATHODE_FLOW (124SCCM)
SET_ANODE_HUMIDIFICATION (DRY)
SET_CATHODE_HUMIDIFICATION (DRY)
SET_ANODE_PRESSURE (14.7 psig)
SET_CATHODE_PRESSURE (14.7 psig)
COUNT= (0); WHILE_COUNT_< (22)
   COUNT+1 ()
   J=0A/cm2, 2s
   J=0.1A/cm2, 10s
   J=0.2A/cm2, 3s
END_WHILE_COUNT ()
//PERFORMANCE CHECK//
SET_ANODE_FLOW ( 800SCCM)
SET_CATHODE_FLOW (1800SCCM)
V=0.4V, 5min
//MORE J CYCLE AT 75C//
SET_ANODE_FLOW (140SCCM)
SET_CATHODE_FLOW (124SCCM)
COUNT= (0); WHILE_COUNT_< (22)
   COUNT+1 ()
   J=0A/cm2, 2s
   J=0.1A/cm2, 10s
   J=0.2A/cm2, 3s
END_WHILE_COUNT ()
//COOL CELL TO 55C WITH J CYCLE//
SET_CELL_TEMPERATURE (55C)
COUNT= (0); WHILE_COUNT_< (44)
   COUNT+1 ()
   J=0A/cm2, 2s
   J=0.1A/cm2, 10s
   J=0.2A/cm2, 3s
END_WHILE_COUNT ()
```

# Appendix

# Appendix

## Reproduction of Key Publications Resulting from this Project

Fifteen of the twenty-seven publications resulting from this project are considered sufficiently important to be included in this final report because they provide concise and complete summaries of the progress made in several of the key accomplishment areas discussed in sections 7 and 9 of the project overview. The first one, a tutorial on the NSTF technology, provides all background information necessary to understand the results discussed in the main body of this report. Several in the list below, including numbers 1, 2, 7, and 8, provide a broader perspective of how the NSTF electrocatalyst technology and materials generated in this project compare with the broader field of ORR electrocatalysts for fuel cells, and also opportunities for OER applications on fuel cell anodes and water electrolysis.

### A.1 Key 3M Publications

1. Updated version of: Mark K. Debe, "Nanostructured Thin Film Electrocatalysts for PEM Fuel Cells – A Tutorial on the Fundamental Characteristics and Practical Properties of NSTF Catalysts," *ECS Transactions* **45** (2) 47-68 (2012). Prepared for submission to The *JES*.
2. M. K. Debe, R. T. Atanasoski, and A. J. Steinbach, "Nanostructured Thin Film Electrocatalysts – Current Status and Future Potential, *ECS Transactions*, **41**(1) 937-954 (2011).
3. M. K. Debe, A. J. Steinbach, G. D. Vernstrom, S. M. Hendricks, M. J. Kurkowski, R. T. Atanasoski, P. Kadera, D. A. Stevens, R. J. Sanderson, E. Marvel and J. R. Dahn, "Extraordinary oxygen reduction activity of $Pt_3Ni_7$," *J. Electrochem. Soc.* **158**(8) B910-B918 (2011), and *ECS Trans*., **33** 143 (2010).
4. A. J. Steinbach, M. K. Debe, J. L. Wong, M. J. Kurkowski, A. T. Haug, D. M. Peppin, S. K. Deppe, S. M. Hendricks, and E. M. Fischer, "A New Paradigm for PEMFC Ultra-Thin Electrode Water Management at Low Temperatures," *ECS Trans.*, **33**(1), 1179-1188 (2010).
5. A. Steinbach, M. Debe, M. Pejsa, D. Peppin, A. Haug, M. Kurkowski and S. Maier-Hendricks, "Influence of Anode GDL on PEMFC Ultra-thin Electrode Water Management at Low Temperatures," *ECS Transactions*, **41**(1) 449-457 (2011).
6. Mark K. Debe, "Effect of Electrode Structure Surface Area Distribution on High Current Density Performance of PEM Fuel Cells," *J. Electrochemical Society* **159**(1) B54-B67 (2011).
7. M. K. Debe, S. M. Hendricks, G. D. Vernstrom, M. Meyers, M. Brostrom, M. Stephens, and Q. Chan, Jason Willey, Monjid Hamden, and Cortney K. Mittelsteadt**,** Christopher B. Capuano, Katherine Ayers and Everett Anderson, "Initial Performance and Durability of Ultra-low Loaded NSTF Electrodes for PEM Electrolyzers," *J. Electrochem. Soc.,* **159**(6) K165-K176 (2012).
8. Mark K. Debe, "Electrocatalyst Approaches and Challenges for Automotive Fuel Cells," invited review article, *Nature,* **486**(9401) 43-51(2012).

### A.2 Key Dalhousie Publications

9. Gary Chih-Kang, D. A. Stevens, J. C. Burns, R. J. Sanderson, G. D. Vernstrom, R. T. Atanasoski, M. K. Debe and J. R. Dahn, "Oxygen reduction activity of dealloyed $Pt_{1-x}Ni_x$ catalysts." *J. Electrochem. Soc.* **158**(8) B919-B26 (2011).
10. Arnd Garsuch, D. A. Stevens, R. J. Sanderson, S. Wang, R. T. Atanasoski, S. Hendricks, M. K. Debe, and J. R. Dahn, "Alternative Catalyst Supports Deposited on Nanostructured Thin Films for Proton Exchange Membrane Fuel Cells," *J. Electrochemical Society* **157**(2) B187-B194 (2010).

11. Arman Bonakdarpour, Tara R. Dahn, Radoslav Atanasoski, Mark K. Debe, and Jeff R. Dahn, "$H_2O_2$ Release During Oxygen Reduction Reaction on Pt Nano Particles," *Electrochemical and Solid-State Letters*, **11**, B208-B211, 2008.
12. D. A. Stevens, R. Mehrotra, R. J. Sanderson, G. D. Vernstrom, R. T. Atanasoski, M. K. Debe and J. R. Dahn, "Dissolution of Ni from high Ni content $Pt_{1-x}Ni_x$ alloys," *J. Electrochem. Soc.* **158**(8) B905-B909 (2011).

### A.3 Key ANL Publications

13. Dennis van der Vliet, Chao Wang, Mark Debe, Radoslav Atanasoski, Nenad M. Markovic and Vojislav R. Stamenkovic, "Platinum-alloy Nanostructured Thin Film Catalysts for the Oxygen Reduction Reaction," *Electrochimica Acta*. **56** 8695-8699 (2011).
14. R.K. Ahluwalia, X. Wang, A. Lajunen, A.J. Steinbach, S.M. Hendricks, M.J. Kurkowski, and M.K. Debe, "Kinetics of Oxygen Reduction Reaction on Nanostructured Thin-Film Platinum Alloy Catalyst," *Journal of Power Sources* **215** (2012) 77-88.
15. Dennis van der Vliet, Chao Wang, Dusan Tripkovic, Dusan Strmcnik, Xiaofeng Zhang, Mark Debe, Radoslav Atanasoski, Nenad M. Markovic and Vojislav R. Stamenkovic, "Metallic Nanotubes with Tunable Composition and Structure as Advanced Electrocatalysts," *Nature Materials*, **in press** (2012).

# Tutorial on the Fundamental Characteristics and Practical Properties of Nanostructured Thin Film (NSTF) Catalysts

Mark K. Debe

3M Fuel Cell Components Program, 3M Company
201-2N-19, 3M Center, St. Paul, MN 55144, USA

This tutorial reviews the key aspects and literature to date around the nanostructured thin film (NSTF) electrocatalyst technology platform for PEM fuel cells and electrolyzers. The NSTF technology is to date the only practical example of an extended surface area catalyst shown to effectively address several of the performance, cost and durability barriers facing cathode and anode catalysts for fuel cell vehicles. The unique physical characteristics of these ultra-thin, low Pt-loaded electrodes also require alternative solutions for water management and impurity tolerance. We present an overview of the NSTF electrocatalysts' four primary differentiating features, to show how their material and basic geometric and material characteristics translate to functional performance factors. We conclude by briefly recounting the historical origins of the NSTF material with the recommendation that the field of ordered organic molecular solids represents a large opportunity for developing tailored support materials for heterogeneous catalysis.

## Introduction

Performance, cost and durability targets for automotive fuel cell vehicles translate into stringent performance, durability and cost requirements for the membrane electrode assemblies (MEA's) and their electrocatalysts: a) high mass activity (A/mg-Pt); b) high current density capability at ultra-low catalyst loadings; c) durability to withstand high electrochemical potentials, high temperatures, and tens of thousands of stop/start cycles with minimal corrosion; d) robustness for operations from very dry to very wet conditions; e) adequate cool start, cold (freeze) start and freeze tolerance; f) impurity tolerance; g) cell reversal tolerance; h) minimal $H_2O_2$ production to minimize radicals that degrade the ion exchange membrane; and i) ultimate rates of MEA fabrication on the order of a second or less (1-8). Finding simultaneous solutions for all these requirements requires looking deeply at all aspects of the oxygen reduction (ORR) and hydrogen oxygen (HOR) reactions and how they depend on the electrocatalyst structures, compositions, supports and fabrication processes. The type of heterogeneous electrocatalysts utilized almost exclusively to date for PEM fuel cells are Pt nanoparticles dispersed onto the surfaces of larger carbon black particles, Pt/C. This structural form of high surface area catalyst has multiple proven properties well suited for meeting many of the above automotive requirements, key among them being very high surface areas and widespread commercial availability which has led to their exclusive use to date for current generation vehicles. There are also well documented durability and high current density challenges remaining to be met at the ultra-low loadings believed necessary for

high volume commercialization (1-7). These needs have spawned research and some development of alternative electrocatalyst forms and this tutorial recounts the properties and progress of one of the more promising ones based on 3M's nanostructured thin film (NSTF) catalyst technology platform (8-12). The NSTF catalyst approach is to date the only practical example of an extended surface area catalyst with the potential to eliminate or significantly reduce many of the above performance, cost and durability barriers standing in the way of cathodes and anodes for $H_2$/air PEM fuel cells for vehicles. It's potential benefits as well as its specific challenges are slowly being revealed as is use in realistic automotive stack environments is explored. The NSTF catalyst structure, support particle and fabrication processes are completely different from those of Pt/C and although to date a fair amount of published research summarized here has documented the consequences of those differences, this tutorial format offers the chance to expand on the broader nature of this new class of catalyst supports and ramifications of its fundamentally different geometry. One of the most significant advantages of Pt/C is the widespread availability and low cost of its effective support particle, carbon black, in its various forms. From a different point of view this ready availability may turn out to be one of its deficiencies also, as this low "activation" barrier to generating an effective catalyst has meant an almost total focus world-wide on Pt/C at the exclusion of research and development activity towards defining what could be referred to as the optimum catalyst and support system. A major message this author hopes to convey in this tutorial is that the class of extended surface catalyst support particles for which NSTF is the first "poster child" but just one of myriad possibilities, offers a far broader range of material possibilities than perhaps the whole universe of carbon does for Pt/C. It is our hope that interested researchers might strive to work outside-the-box and begin to explore this rich topical area of ordered heterocyclic organic molecular solids as new catalyst supports for any heterogeneous catalysis application.

## Organization of the NSTF literature

There is of course a broad based NSTF patent literature, but sticking with convention we summarize here the journal literature that we and our collaborators have published to date, organized by their relevance to basic electrocatalyst characteristics, properties and functionality. References (8-14) provide a more general background on the NSTF technology as applied to PEM fuel cells. The next category, (15-19), focuses on the NSTF catalyst support particle, its characterization and processing. The third category (20-23), pertains most closely to the nature of the NSTF catalyst structure. The largest group of publications, (24-38) is related to the NSTF catalyst electrochemical characteristics, from fundamental RDE measurements of unique alloys and compositional spreads, to activity and surface area characterizations in 50 $cm^2$ MEA fuel cells. References (39-40) relate to the vacuum coating processes for NSTF fabrication. The next section, (41-54) include all the papers discussing electrode and MEA durability tests. References (55-62) are focused on a relatively new area of NSTF electrode modeling, and (63-68) on characterization of water management and operational robustness issues. References (69-77) are specific to oxygen evolution reaction (OER) forms of NSTF catalysts for applications on fuel cell anodes for cell reversal tolerance and $H_2/O_2$ electrolyzers. Finally, references (78-86) are specific to showing the NSTF origins out of the field of self-organizing organic thin films and the potential for catalyst supports remaining to be explored in this broad class of materials.

## Four Primary Differentiating Characteristics of NSTF Catalysts

There are four principle characteristics of the NSTF catalyst technology that most clearly differentiate it from the conventional Pt/C dispersed catalysts or the older precious group metal blacks. An appreciation of these differences is the best way to understand the NSTF catalyst material and electrochemical properties and how those relate to the observed functional performance metrics for use in PEM fuel cells. These four primary differentiating characteristics are the natures of the 1) support particle, 2) catalyst structure, 3) fabrication process, and 4) NSTF electrodes.

### Nature of the Support Particle

The first of four primary aspects of the NSTF catalysts that differentiate them from Pt/C or PGM blacks is that the catalyst support particle is a pure, organic molecular solid in the form of a crystalline whisker (see Figs. 1 and 2 and Table I). The chemical compound is a perylene based heterocyclic organic solid used commercially in high volumes for its colorant/pigment qualities. The specific molecule, N,N-di(3,5,xylyl) perylene-3,4:9,10bis(dicarboximide), (or PR-149 see Table I), is extremely UV, thermally and electrochemically stable; non-toxic; used primarily as an insoluble organic pigment. It has good vapor pressure above 450$^{o}$C without significant decomposition or melting so sublimation vapor deposition is a very effective high volume coating process for forming thin films. As a thin film it undergoes an extraordinary and rapid disorder-order transition above 250$^{o}$C with zero supersaturation ratio to form a monolayer of highly oriented, densely packed single crystalline whiskers. The whiskers are lath-shaped with nanometer dimensions, body centered cubic lattice, 4 molecules per unit cell and areal number densities of 3 to 5 billion/cm$^{2}$. The single crystalline nature of the whiskers assures highly reproducible and uniform surface properties for subsequent coating with catalysts or other materials. The crystallinity of the whisker can also influence the nucleation, growth and thin film morphology of an over-coated material such as a catalyst applied by the preferred methods of physical vapor deposition. The perylene compound is a p-type organic photoconductor with a large "band-gap" and resistivity that prevents electrochemical corrosion to RHE potentials above 2 volts. This means that as a support for a Pt catalyst, there is no electrochemical corrosion as is typical with a conductive carbon black support particle. The whisker lengths grow in proportion to the initial PR-149 film thickness, while the cross-sectional dimensions are fixed by the ratio of the surface free energies of the bcc (22$\underline{2}$) and (01$\underline{1}$) side facets (Wulff's theorem). The high aspect ratio (length to width) of the whiskers and areal number density determines the surface area per unit planar area of the substrate and a large factor (~ 8x) of the ultimate Pt surface area. Table I summarizes these and other support characteristics.

### Nature of the catalyst structure

The second primary differentiating aspect is the nature of catalyst coating applied to the whiskers (Figs. 2-4). It is a polycrystalline thin film, rather than a distribution of discrete and isolated nanoparticles. One significant consequence of this factor is that the specific activity for oxygen reduction is 5 to 10 times higher than for 2-3 nm diameter particles, in line with the kinetic activity of polycrystalline single crystal bulk surfaces. This compensates for the relatively low absolute surface area of the electrode. A second

significant consequence is that the catalyst is already highly agglomerated and less susceptible to loss of surface area by that mechanism.

Similarly the larger radii of curvature of the metal coated whiskers compared to nano-particles makes the Pt less susceptible to dissolution under periodic oxidation and reduction from voltage cycling above 1 volt. Both effects make the Pt catalyst surface more robust to start-stop or cell reversal events.

The catalyst coating can be deposited as a single or multiple layers (Fig. 3(a)) as an alloy or intermixed material. The degree of crystallinity and size of the surface facets will depend on details of the catalyst deposition process conditions and the materials' surface energies. The surface roughness factor of the catalyst coating on the whiskers contributes to the electro-chemically active Pt surface area measured in the electrode. For most Pt alloys examined, the thin film catalyst coating morphology consists of fairly uniform sized crystallites, called "whiskerettes", oriented at an angle of about $70^{o}$ w.r.t. the whisker axis (Figs. 3, 4 and reference (23)). Post-fabrication annealing or dealloying processes are also practiced and roll-good compatible (10(2011)).

**Nature of the Process**

The third primary differentiating aspect is the nature of the process for generating the whiskers and forming a perfect, oriented monolayer. The process is vacuum based roll to roll coating and thereby completely dry and high volume capable. Conventional dispersed Pt/C catalysts are coated from solvents and require the three primary ingredients and high level process steps shown in Fig. 5 for a decal transfer electrode formation process. The NSTF catalyst process requires the same basic types of ingredients, a source of Pt, a source of powdered support material and a substrate on which to coat them. The similarities end there. The NSTF catalyst source is simply a bulk metallic sputtering target made by metallurgical methods. The PR-149 powder is commercially manufactured at high volumes and available in tank-car size volumes for its major applications such as adding colorants to polyolefins. The NSTF substrate is specialized and unique to 3M, called a microstructured catalyst transfer substrate (MCTS), shown in cross-section in Fig. 2 with properties that facilitate roll to roll coating and increase the electrode surface area by a square root of two. Whereas the major Pt/C electrode formation steps have to be done in serial fashion, the NSTF and catalyst coating processes can all be done in one continuous process step within the vacuum roll-coater: the PR-149 pigment is sublimed onto the MCTS web, annealed to convert the perylene layer to the single monolayer of oriented whiskers, then sputter coated with catalyst.

The whisker coating and growth steps and catalyst coating step are often separated for R&D purposes, but the ability to do it all in one step is critical for high volume scale-up to the quantities and speeds that will be required for fuel cell vehicle commercialization. This uniqueness of the NSTFC process is a direct result of the whisker growth itself, enabling the instantaneous distribution of Pt alloys from a bulk metal target into atomic layers uniformly coated onto a perfect monolayer of high aspect ratio oriented crystalline supports – in a single solvent free step. Finally, with either type of catalyst approach, using a decal process to form the catalyst coated membrane (CCM) requires a lamination transfer step as shown in Fig. 5 to form the roll of CCM shown in the photograph.

Although the NSTFC process is not yet scaled to the kinds of volumes that would be needed for producing say 0.5 million vehicles per year, on the order of 90,000 linear meters combined of the MCTS, whisker and catalyst coated MCTS, and CCM have been produced for process development and customer needs since production reporting began in 2006. For those readers unfamiliar with high volume vacuum coating by physical vapor deposition, it is important to appreciate how mature and extensively commercialized these processes are. Just one example serves to illustrate this, the coating of low-emissivity, semi-precious metal and inorganic multi-layers by cylindrical magnetron sputter deposition onto twelve foot wide sheets of glass for 80% of the worlds market for architectural and residential window glass. We choose that since it is applying complex inorganic multi-layers with high quality and yield requirements. Already in 2005, 250 million square meters of low-E glass were fabricated with obviously adequate costs, quality and yields (40). Such a volume if it had been making fuel cell electrodes would be sufficient for 25 million vehicles, a number that will not probably be reached until long after 2040 worldwide. Such deposition processes are already established world-wide for many high volume products, so the infrastructure to support such technology (equipment design and manufacturing houses, sputtering target suppliers) exists. Finally we note, that many significant technologies that currently are based on such thin film vacuum coating processes, and we include here electronic data storage technology, all began product development and commercialization using media produced by wet chemical dispersion and solvent drying processes. But as the material property requirements, throughputs, yields and quality demands all increased and the cost demands decreased, the process technology of choice moved from wet chemical to vacuum thin film coating. We believe the same transition may have to happen in fuel cell electrodes.

## Nature of the electrode

The fourth set of primary differentiating aspects has to do with the NSTF catalyst electrode. As shown in Fig. 6 it is 20 to 30 times thinner than a conventional Pt/C electrode. The reason for this thinness is the absence of carbon black which in a Pt/C electrode is there to provide electrical conductivity to and from the catalyst particles.

In the NSTF catalyst electrode this function is provided by the polycrystalline catalyst thin film itself and the close packed spacing of the catalyst coated whiskers in the electrode. Their spacings are only tens of nanometers in the as-made film before transfer to the membrane (see Fig. 2) while after transfer, they are packed even closer which generally enables whisker to whisker contact (see Fig. 6 (c, d)). It is not necessary to add additional ionomer to the catalyst layer, and multiple attempts to do so only resulted in added mass transport impedance to the catalyst surface. The extreme thinness of the NSTF catalyst layer enables minimum $O_2$ mass transport impedance at standard operating temperatures so higher current densities are possible meaning the whole electrode can be accessed at all current densities. The CCM catalyst transfer step micro-replicates the MCTS structure into the PEM surface (Fig. 6(a)). The catalyst coated whiskers end-up partially embedded in the PEM surface into which they were transferred by heat and pressure during the lamination step. This means a very short proton pathway from the

catalyst surface to the membrane ionomer, on the order of a few tens of nanometers around the circumference of the catalyst coated whiskers at most.

Although there are competing views for the means of ionic transport in the NSTF electrode, as discussed later, we believe that proton conduction as hydronium ions moving over the Pt surface typically covered with hydroxyl species plays a large part of the mechanism. Table I summarizes the critical characteristics of the NSTF electrodes, specifically for the alloys, loadings and PEM properties shown. The $H_{upd}$ surface area (ECSA) is in the range of 10 to 25 $m^2/g$, and small compared to high surface area Pt/C catalysts. But the 5 to 10 fold gain in specific activity noted earlier enables gains in absolute and mass activity, the product of specific activity with the surface area enhancement factor or ECSA.

The other very major consequence of the extreme thinness of the NSTF catalyst layer is its propensity to flood under cool, wet operating conditions. At a given current density, the water generation rate per unit thickness on the cathode is 20 to 30 times higher for an electrode proportionately thinner. This requires different water management strategies and MEA GDL properties as discussed later to meet challenging transient cool start requirements.

Table II summarizes the MEA and short stack performance and durability specifications against, for the most part, the DOE Hydrogen and Fuel Cells program targets (1). Most of the 2015 DOE targets have been met, but other requirements for actual stack operation remain to be demonstrated. Before turning to a brief discussion of performance and durability tests, we end this section with a final consideration of two more fundamental ways in which the geometric differences of the NSTF catalysts and electrodes contribute to their differentiating properties.

## Significance of Geometry

Fig. 7(a) illustrates a simple but significant impact of geometry on ORR activity at increasingly reduced loadings. Pt/C dispersed catalysts have self-similar geometries with respect to surface area and loading. That is if the electrode loading in $mg/cm^2$ is changed by a factor of two then the electrochemical surface area is changed by the same factor, all else being the same. NSTF catalysts are not self-similar in this way. If the catalyst loading is changed by a factor of two, resulting in approximately the same change in thickness of the catalyst coating, the surface area is observed to change by a smaller amount that depends on the whisker size and spacing parameters.

In the graph in Fig. 7(a) this means the absolute activity change with loading, assuming the specific activity remains unchanged will be a less sensitive function of surface area. As mentioned above the ORR area specific activity is much higher for NSTF catalysts, and this geometric factor contributes as well. The graph in Fig. 7(a) illustrates the absolute ORR activity at 900 mV under 1 atmosphere absolute of oxygen as a function of surface area enhancement factor for about 150 NSTF Pt-Ni alloy cathodes, near the unique $Pt_3Ni_7$ composition (32) but differing loadings, degrees and methods of dealloying and post-fabrication annealing. For a doubling in SEF from 10 to 20 $cm^2_{Pt}/cm^2_{planar}$ the absolute activity increases nearly four-fold, from ~ 12 to 48 $mA/cm^2$.

The impact of the higher specific activity is most clearly observed by simply normalizing a fuel cell polarization curve to the Pt electrochemical surface area enhancement factor (SEF). Fig. 8 shows this type of plot for a number of NSTF and Pt/C electrode based MEA's as described in detail in (13). The NSTF catalysts appear to be "working much harder" per Pt atom but there is more to the story than just specific activity. We show in (13) that even if the curves in Fig. 8 are further normalized to the measured specific activities for the various cathode catalysts, there are still substantial gains from the NSTF electrodes compared to the thicker dispersed electrodes, and these gains increase as the Pt loadings are further reduced. This observation forced us to look for some alternative mechanisms which we describe in reference (13) as due to another fundamental geometry difference not previously appreciated before. The mechanisms are dependent on the electrode's surface area per unit volume density ($cm^2_{Pt}/cm^3$) and the ability of the catalyst surfaces' spatial distributions to influence the number of chemisorption attempts per unit time in the Knudsen regime by virtue of their impact on the $O_2$ molecules' number of precursor physisorption events per unit time. The end result is an additional pre-exponential scaling factor in the Butler-Volmer equation that accounts for the impact of those effects on the $O_2$/Pt surface collision frequency. This effect is enhanced by the close-packed nature and parallel orientation of the extended NSTF catalyst surfaces as seen e.g. in Fig. 6(c). These effects combine the statistical physics of ideal gases within one mean free path of the catalyst surface, with the impact of Knudsen's cosine law for desorption on their velocity distributions. This results in an enhancement in the collision rate as illustrated in Fig. 7 (b,c) for gases between ideal parallel extended surfaces.

## Performance and Durability

### Selected Performance Examples

There are many publications documenting the high area and mass specific ORR activities of NSTF Pt alloys (2-38), in both RDE and MEA fuel cell configurations. A particularly recent and relevant set of measurements by the ANL group of Stamenkovic et al. (36) is shown in Fig. 9, which compares these RDE activities from a series of NSTF catalyst alloys all prepared via roll-to-roll processing, with their TKK Pt/C baselines. The NSTF Ni rich Pt alloys significantly exceed the kinetic and mass activities of the latter.

The mass activities of this new NSTF-"$Pt_3Ni_7$" (quotation marks signify as-made composition) are similarly high when measured in 50 $cm^2$ MEA's. Table III summarizes mass activities measured at GM using both GM's and 3M's ORR mass activity protocols. These CCMs were made at 3M with 3M membranes that were either as-made or cleaned using both nitric acid and peroxide baths. The "$Pt_3Ni_7$" cathodes were roll-to-roll dealloyed and surface energy treated (annealed) prior to lamination at 3M to either cleaned or as-made 3M PEMs. In Table III the standard treatment refers to the usual NSTF thermal cycling for break-in conditioning. The last column in Table III shows that a proprietary GM additional pretreatment process can further substantially increase the apparent mass activities over the standard treatment, which now cover the ranges of 0.47 to 0.58 A/mg by the GM ORR protocol and 0.62 to 0.67 A/mg using the 3M protocol (10(2012)).

The NSTF–$Pt_{68}Co_{29}Mn_3$ catalyst has been the workhorse cathode and anode of choice for a number of years. The peak NSTF polarization curve performance examples are illustrated in Fig. 10 at 150kPa $H_2$/air and 80°C from what we call the 2009 best of class MEA, based on the $Pt_{68}Co_{29}Mn_3$ catalysts. They demonstrate < 0.18 $g_{Pt}$/kW peak inverse power density and only 43 mV of mass transport overpotential at 2 A/cm$^2$ using a total of 0.15 $mg_{Pt}$/cm$^2$ per MEA (10(2009)). The higher mass active NSTF-PtNi catalysts allow further improvements, even though its membrane integration is not yet optimized. To test the best overall performance possible with these roll-to-roll dealloyed/annealed Pt/Ni cathode catalysts, 50 cm$^2$ CCMs were prepared with $Pt_3Ni_7$ cathode loadings of 0.121±0.003 mg-Pt/cm$^2$, pure NSTF-Pt anodes with 0.030 mg/cm$^2$, and 3M 24 micron, 850 equivalent weight non-supported membrane, as-made. Figure 11(A) shows GDS polarization curves at three pressures and the conditions indicated in the legend. The inset graph shows that the higher kinetic performance expected from the high mass activity is realized in the MEAs at 0.8 V (quarter peak power point), with 0.21 to 0.31 A/cm$^2$ at 0.8 V obtained over a 150 to 250 kPaa outlet pressure. Even though the limiting current densities are still not as high as they should be, there is a substantial improvement over that obtained without first dealloying the "$Pt_3Ni_7$" catalysts (about 0.8 A/cm$^2$, as shown in [10(2011)] and reasonable current densities are being realized at 650 mV. Figure 11(B) shows the inverse specific power density plots for the three polarization curves shown in Figure 11(A). These advanced PtNi cathodes with the lower anode loading on a 24-micron thick membrane exhibit values of 0.14 to 0.18 g-Pt/kW over 0.6 to 0.65 V and the 150 to 250 kPaa operating range at 80°C. There is little temperature sensitivity over the 80 to 95°C range (see slide 34 in reference 10(2012). Further improvements in understanding and controlling the dealloying and SET treatment processes are required to take advantage of thinner membranes which should further improve their performance towards the 0.125 g-Pt/kW target for 2017.

Finally, the most recent advance in understanding how to reach the NSTF MEA entitlement performance has come from the first systematic assessment of the effect of flow fields (10(2012)). We traditionally only test with one type of flow-field, a quad-serpentine with 0.8 mm wide channels and lands. To establish a baseline of these effects we initiated tests of identical NSTF 2009 best of class MEA's in a series of alternative flow field designs. The 50 cm$^2$ flow field graphite blocks were all tested in one set of 3M cell hardware or one set of OEM cell hardware (OEM HW). Figure 12 compares the galvanodynamic scan (GDS) polarization curves from six alternative flow fields with the standard quad-serpentine (FF5). As shown there is a huge impact of the flow field type on the limiting current density, and several that perform better than our standard quad serpentine. The HFR differences are small and not responsible for the differences when the graphite blocks are all in the same set of 3M aluminum cell hardware (3M HW). Cathode pressure drop was also measured for the different flow fields, and can explain the high current density performance gain with the single channel flow fields FF7 and FF8 relative to the standard FF5. However, the FF2 flow field blocks used in the 3M hardware significantly out-performed the standard with similar or slightly lower pressure drops. This suggests that the smaller (0.5 mm) channel and land width dimensions of the FF2 are key to improved performance and a guide to optimizing the flow field for NSTF MEA's.

## Accelerated Durability Examples

The NSTF's absence of corrodible carbon and its thin film catalyst morphology that is less susceptible to agglomeration and corrosion were discussed earlier as key differentiating characteristics. Many different types of accelerated durability tests have been done in the past few years to illustrate these features. Four of these types of tests are shown in Figure 13. The much longer lifetimes and reduced fluoride ion release rates observed at 120$^{o}$C in Fig. 13(c) in NSTF MEA's compared to otherwise identical Pt/C MEA's, all made with membranes having no chemical additives, are also seen in OCV hold tests under $H_2/O_2$, where the rates are 1000 times less for the NSTF MEA's as shown in reference (50). This enhanced reduction of $F^-$ ions is due in part to better scavenging of free radicals and peroxides within the catalyst layer facilitated by the close-packed nature of the NSTF extended surfaces as discussed above in reference (13) and shown experimentally in RRDE measurements (29). TEM studies of the NSTF catalyst surfaces after 30,000 CV cycles by 3M, GM and ORNL are consistent in showing that the whiskerettes (see Figs. 3 and 4) have been considerably smoothed (54), and is likely a major reason for the approximately 15% reduction in surface area.

## Water Management

The extreme thinness of the NSTF electrode provides both advantages and disadvantages as noted earlier. The key issue is water management at low temperatures which means the cathode can easily flood, causing a severely reduced limiting current, if conventional "out the cathode" water removal methods are used. For thin electrodes like NSTF a better water management strategy is to take the cathode water out the anode, Fig. 14(a), which keeps the membrane better humidified and reduces the impact of outgoing cathode water vapor on incoming oxygen flux. The thin and hydrophilic NSTF electrodes easily pass water, so the key is to select the other parts of the MEA to do so also. Figs. 14(b, c) show the impact on low temperature polarization curves when a thinner membrane, and improved anode GDL are used. Using differential pressures (cathode ~ 5 psig higher) also facilitates liquid water movement out the anode and NSTF electrodes have demonstrated 2 A/cm$^2$ steady state current density at 30$^{o}$C with this approach (64, 65). Fig. 15 shows that the anode GDL is also the most dramatic component for effecting adequate load transient response.

## OER Catalyst Applications

The intrinsically higher NSTF ORR activity also appears to apply to OER as well. For applications where electrode potentials above 1.2 volts are the norm, the absence of any carbon based support material is also a significant advantage. The anodes of $H_2/O_2$ electrolyzers is one such example. Working with two electrolyzer manufacturers over a three year period, we have found that the NSTF OER catalysts can give equivalent or better performance in their equipment than their baseline Pt alloy blacks while using 90% less PGM's on either the anode or cathode, Fig. 16 (69-72). Durability of the same MEA's was also tested extensively with stable performance on the cathode for 4600 hours of test and up to 2000 hours on the anode above 2.2 volts the whole time, without failure (72).

More recently this excellent OER behavior with very low PGM loadings has been adapted for automotive fuel cells (51-53, 73-77). This ability to oxidize water to effectively clamp the electrode potentials from going so high that other cell or GDL materials could be damaged during off-nominal events is a key solution approach to prevent cell component damage during cell reversal from fuel starvation, or start-up/shut-down (SU/SD) events. Figs. 17 (A,B) shows two examples of where adding as little as 10 $\mu g/cm^2$ of an OER catalyst to the NSTF anode, for a total anode loading of 0.06 $mg_{PGM}/cm^2$ effectively prolongs the life of the electrode under test protocols designed to simulate cell reversal from such fuel starvation events. Even more encouraging, AFCC has found through more than 10 short stack tests involving over 80 full scale MEA's containing the OER-Pt/NSTF catalysts on the anode and their Pt/C cathodes, promising results demonstrating performance, CO tolerance, freeze tolerance, SU/SD benefits and reversal tolerance. In Fig. 17(D) the AFCC data shows the OER-Pt/NSTF anode consistently outperformed dispersed baselines with higher loadings. Even more interesting, Fig. 17(C) shows that the same OER-Pt/NSTF catalyst protects the dispersed cathode against performance losses from SU/SD better than the baseline dispersed anode catalysts. This has been shown to be due to the poorer ORR of the OER-Pt/NSTF that keeps the anode potential lower, and hence the cathode potential, as the $H_2$/air wave moves through the flow field during SU or SD.

## Issues Needing Development

The above synopsis shows that the key differentiating characteristics of the NSTF supports, catalysts and electrodes translates into many performance and durability advantages for automotive fuel cells. There are still several key issues that need to be worked for overall general acceptance. It may never be possible to have the same "drop-in replacement" characteristics in the NSTF MEA's as currently seen with thick, dispersed electrodes. However it should be appreciated that as the conventional electrodes move towards the ultimate target catalyst loadings of 0.125 $mg/cm^2$ total per MEA, with barely adequate support durability of graphitized carbon, the electrode layer thickness and its surface area will approach those now being realized by the NSTF electrodes at those loadings. So many of the issues facing the NSTF electrode development will face conventional electrodes at the commercialization relevant durability and cost targets. These key issues include development of a commercially available anode GDL that provides the water management demonstrated in Figs. 14 and 15 without worsening MEA shorting or high frequency impedance. Two other key issues with the NSTF electrodes relate to the low surface area and subsequent sensitivity to impurities for both break-in conditioning and reversible performance loss. Currently we use "thermal cycling" protocols to evolve away the effects of such impurities as they build up from various sources or are in the membrane from its processing solvents. These conditioning or recovery protocols have to be acceptable to automotive stack operation, but are significantly helped by minimizing the sources of the impurities in the first place. Non-recoverable decay processes are also observed over long periods of time, as in stacks. We believe these processes have their origins in impurities, particularly membrane degradation products, as well as in catalyst alloy surface structure changes. In either case, further optimization of the catalyst surface structure and electrode/PEM integration will help significantly (12).

## Origins of NSTF Technology in Self Organizing Organic Thin Films

We conclude this tutorial with a brief recounting of how the NSTF technology came to be discovered and applied to PEM fuel cells as we think it is instructive for future areas of investigation. Although the initial application of the NSTF electrocatalysts to PEM fuel cells in 1995 was deliberate and stemmed from their earlier application to electrochemical gas sensors, the discovery of the unique NSTF perylene red whiskered thin films in 1982 was completely serendipitous. Our early work in applying optical probes to study and extract structural information on organic thin films and their interfaces led to the realization that vapor deposited heterocyclic planar molecules would often preferentially self assemble into highly ordered and oriented films (78-86). We also observed that such organic molecular solid thin films would undergo further extreme order-disorder transitions when heated *in-vacuuo* (15-18, 78-80). It was only upon SEM observation of those annealed films, PR-149 being the first, to try and explain the extraordinary amount of molecular reorganization observed optically, that the monolayer of oriented crystalline whiskers was first seen. Two points must be made. First the PR-149 is but one of hundreds of similar members of a very broad class of heterocyclic ("van der Waal solids") substantially planar molecules for which multiple crystalline polymorphs and bulk whisker growth are common place, highly thermally stable, non-toxic and inert. The second point is that relatively minor changes in molecular structure of these molecules can result in significant changes in their vapor pressures, critical substrate temperature behavior, crystalline lattice structures, and processability. Given what we have learned about the way these organic crystalline materials can influence the subsequent growth and properties of catalyst particles and films coated onto them, we believe they represent a rich class of potential catalyst supports, with a broad set of properties that remains completely open yet to investigation.

## Acknowledgments

We gratefully acknowledge the extraordinary dedication and effort over the past 15 years by all members of the 3M Fuel Cell Components program members, and especially the NSTF development team. With great thanks we acknowledge our collaborators at Dalhousie University, Argonne National Laboratory and the critical role of our OEM customers. We strongly acknowledge the financial support and guidance by the Office of Energy Efficiency and Renewable Energy in the US Department of Energy, especially for Grants DE-FC-02-97EE50473, DE-FC02-99EE50582, DE-FC36-02AL67621, and DE-FG36-07GO17007.

## References


General Literature

1. DOE Website http://www.eere.energy.gov/hydrogenandfuelcells/mypp/pdfs/fuel_cells.pdf. and U.S. DRIVE Fuel Cell Technical Team Technology Roadmap Revised January 25, 2012, www.uscar.org/guest/teams/17/Fuel-Cell-Tech-Team.
2. H. Gasteiger, S. Kocha, B. Sompalli, and F. Wagner, "Activity benchmarks and requirements for Pt, Pt-alloy, and non-Pt oxygen reduction catalysts for PEMFC's," *Appl. Catal.* B **56**, 9-35 (2005).
3. F. T. Wagner, H. A. Gasteiger, R. Makharia, K. C. Neyerlin, E. L. Thompson, and S. G. Yan, *ECS Transactions* **3**(2006) 19.
4. Frederick T. Wagner, "Automotive Challenges and Opportunities for Oxygen Reduction Catalysts," 1st CARISMA International Conf., La Grande Motte, France, Sept. 23, 2008.
5. F. T. Wagner, B. Lakshmanan and M. F. Mathias, "Electrochemistry and the Future of the Automobile," *J. of Physical Chemistry Lett*. **2010**, 1, 2204-2219.
6. P. Y. Abel Chuang, "Fuel Cell Vehicle Commercial Applications and Challenges in Stack Research and Development," 2010 Fuel Cell Seminar and Exposition, San Antonio, TX, Oct. 19, 2010.
7. Chen, S., Gasteiger, H. A., Hayakawa, K., Tada, T., Shao-Horn, Y., "Platinum-Alloy Cathode Catalyst Degradation in Proton Exchange Membrane Fuel Cells: Nanometer-Scale Compositional and Morphological Changes," *J. Electrochem. Soc.* **157**(1) A82-97 (2010).

General NSTF Technology Related

8. Mark K. Debe, "Electrocatalyst Approaches and Challenges for Automotive Fuel Cells," invited review article, *Nature*, **486**(9401) 43-51(2012).
9. M. K. Debe, "Novel catalysts, catalyst support and catalyst coated membrane methods," in Handbook of Fuel Cells – Fundamentals, Technology and Applications, W. Vielstich, A. Lamm, H. A. Gasteiger, Editors, Ch. 45, John Wiley & Sons (2003).
10. M. K. Debe, 2009 to 2011 *DOE Hydrogen Program Annual Merit Reviews*, Washington, D.C. http://www.hydrogen.energy.gov/pdfs/review09/fc_17_debe.pdf http://www.hydrogen.energy.gov/pdfs/review10/fc001_debe_2010_o_web.pdf http://www.hydrogen.energy.gov/pdfs/review11/fc001_debe_2011_o.pdf http://www.hydrogen.energy.gov/pdfs/review12/fc001_debe_2012_o.pdf
11. Mark K. Debe et al., "Advanced Cathode Catalysts and Supports for PEM Fuel Cells," DOE Hydrogen and Fuel Cells Program, FY 2010 Annual Progress Report, V.E.1 pp 1-9; FY 2011 Annual Progress Report, V.D.1 pp 697-705; FY 2012 Annual Progress Report, V.D.1 *in press*.
12. M. K. Debe, R. T. Atanasoski, and A. J. Steinbach, "Nanostructured Thin Film Electrocatalysts – Current Status and Future Potential, *ECS Transactions*, **41**(1) 937-954 (2011).
13. Mark K. Debe, "Effect of Electrode Structure Surface Area Distribution on High Current Density Performance of PEM Fuel Cells," *J. Electrochemical Society* **159**(1) B54-B67 (2011).
14. Mark K. Debe, "Nanostructured Thin Film Electrocatalysts for PEM Fuel Cells – A Tutorial on the Fundamental Characteristics and Practical Properties of NSTF Catalysts," *ECS Transactions* **45**, (2) 47-68 (2012).

Support Particle Characterization and Processing

15. K. K. Kam, M. K. Debe, R. J. Poirier, and A. R. Drube, "Dramatic variation of the physical microstructure of a vapor deposited organic thin film," *J. Vac. Sci. Technol.* **A 5**(4),1914-1916 (1987).
16. M. K. Debe, K. K. Kam, J. C. Liu and R. J. Poirier, "Vacuum vapor deposited thin films of a perylene dicarboximide derivative: microstructure versus deposition parameters," *J. Vac. Sci. Technol.* **A 6**(3), 1907-11 (1988).
17. M. K. Debe, R. J. Poirier, "Post deposition growth of a uniquely nanostructured organic film by vacuum annealing," *J. Vac. Sci. Technol.* **A 12**(4, Pt. 2), 2017-22 (1994).
18. M. K. Debe, A. R. Drube, "Structural characteristics of a uniquely nanostructured organic thin film," *J. Vac. Sci. Technol.* **B 13**(3), 1236-41 (1995).
19. Arnd Garsuch, D. A. Stevens, R. J. Sanderson, S. Wang, R. T. Atanasoski, S. Hendricks, M. K. Debe, and J. R. Dahn, "Alternative Catalyst Supports Deposited on Nanostructured Thin Films for Proton Exchange Membrane Fuel Cells," *J. Electrochemical Society* **157**(2) B187-B194 (2010).

Catalyst Structure Related

20. Matthias Arenz, Karl J. J. Mayrhofer, Vojislav Stamenkovic, Berislav B. Blizanac, Tada Tomoyuki, Phil N. Ross and Nenad M. Markovic, "The Effect of the Particle Size on the Kinetics of CO Electrooxidation on High Surface Area Pt Catalysts," *J. AM. CHEM. SOC.* (2005), **127**, 6819-6829.
21. K. J. J. Mayrhofer, M. Arens, B. B. Blizanac, V. Stamenkovic, P. N. Ross and N.M. Markovic, "CO surface electrochemistry on Pt-nanoparticles: A selective review," *Electrochimica Acta* **50** (2005) 5144-5154.
22. J. McBreen, M. Balasubramanian, W.-S. Yooon, K. Y. Chung, H. S. Lee, X. Q. Yang, R. T. Atanasoski, A. K. Schmoeckel, g. D. Vernstrom and M. K. Debe, "PEM Fuel Cells: Material Issues," *ECS Transactions* **1**(16) 149-160 (2006).
23. Lajos Gancs, Takeshi Kobayashi, Mark K. Debe, Radoslav Atanasoski, and Andrzej Wieckowski, "Crystallographic Characteristics of Nanostructured Thin Film Fuel Cell Electrocatalysts – A HRTEM Study," *Chemistry of Materials* **20**, 2444-2454 (2008).

Catalyst Electrochemical Characteristics

24. A. K. Schmoeckel, G. D. Vernstrom, A. J. Steinbach, S. M. Hendricks, R. T. Atanasoski and M. K. Debe, "Nanostructured Thin Film Ternary Catalyst Activities for Oxygen Reduction," 2006 Fuel Cell Seminar, Honolulu, Hawaii, Nov. 13-17, 2006.
25. D. A. Stevens, J. M. Rouleau, R E. Mar, R. T. Atanasoski, A. K. Schmoeckel, M. K. Debe and J. R. Dahn, "64-Electrode PEM Fuel Cell Studies of CO-Tolerant Hydrogen Oxidation Catalysts," *ECS Transactions* **3**(1) 355-360 (2006).
26. D. A. Stevens, J. M. Rouleau, R. E. Mar, A. Bonakdarpour, R. T. Atanasoski, A. K. Schmoeckel, M. K. Debe, J. R. Dahn, "Characterization and PEMFC Testing of $Pt_{1-x}M_x$ (M=Ru, Mo, Co, Ta, Au, Sn) Anode Electrocatalyst Composition Spreads," *J. of the Electrochem. Soc.* **154**(6), B566-B576 (2007).
27. Arman Bonakdarpour, Krystal Stevens, George D. Vernstrom, Radoslav Atanasoski, Alison K. Schmoeckel, Mark K. Debe, and Jeff R. Dahn, "Oxygen Reduction Activity of Pt and Pt-Mn-Co Electrocatalysts Sputtered on Nanostructured Thin Film Support," *Electrochimica Acta* **53** (2007) 688-694.
28. K. J. J. Mayrhofer, D. Strmcnik, B. B. Blizanac, V. Stamenkovic, M. Arenz, N. M. Markovic, "Measurement of oxygen reduction activities via the rotating disc electrode method: From Pt model surfaces to carbon-supported high surface area catalysts," *Electrochimica Acta* **53,** 3181-3188 (2008).
29. Arman Bonakdarpour, Tara R. Dahn, Radoslav Atanasoski, Mark K. Debe, and Jeff R. Dahn, "$H_2O_2$ Release During Oxygen Reduction Reaction on Pt Nano Particles," *Electrochemical and Solid-State Letters*, **11,** B208-B211, 2008.
30. D. Van der Vliet, D. Strmcnik, C. Wang, R. Atanasoski, M. Debe. N. Markovic and V. Stamenkovic, "Multimetallic Catalysts for Oxygen Reduction Reaction," 216$^{th}$ ECS Meeting, Vienna, Austria, Oct. 4-9, 2009.
31. Gary C-K. Liu, R. J. Sanderson, G. Vernstrom, D. A. Stevens, R. T. Atanasoski, M. K. Debe, J. R. Dahn, "RRDE Measurements of ORR Activity of $Pt_{1-x}$ $Ir_x$ ($0<x<0.3$) on High Surface Area NSTF-Coated Glassy Carbon Disks," *J. Electrochem. Soc.* **157**(2), B207-B214 (2010).
32. M. Debe, A. Steinbach, G. Vernstrom, S. M. Hendricks, M. J. Kurkowski, R. T. Atanasoski, P. Kadera, D. A. Stevens, R. J. Sanderson, E. Marvel and J. R. Dahn, "Extraordinary oxygen reduction activity of $Pt_3Ni_7$," *J. Electrochem. Soc.* **158**(8) B910-B918 (2011).
33. Gary Chih-Kang, D. A. Stevens, J. C. Burns, R. J. Sanderson, G. D. Vernstrom, R. T. Atanasoski, M. K. Debe and J. R. Dahn, "Oxygen reduction activity of dealloyed $Pt_{1-x}Ni_x$ catalysts." *J. Electrochem. Soc.* **158**(8) B919-B26 (2011).
34. D. A. Stevens, R. Mehrotra, R. J. Sanderson, G. D. Vernstrom, R. T. Atanasoski, M. K. Debe and J. R. Dahn, "Dissolution of Ni from high Ni content $Pt_{1-x}Ni_x$ alloys," *J. Electrochem. Soc.* **158**(8) B905-B909 (2011).
35. D. A. Stevens, S. Wang, R. J. Sanderson, G. C. K. Liu, G. D. Vernstrom, R. T. Atanasoski, M. K. Debe and J. R. Dahn, "A combined rotating disk electrode/X-ray diffraction study of Co dissolution from $Pt_{1-x}Co_x$ Alloys," *J. Electrochem. Soc.* **158**(8) B899-B904 (2011).
36. Dennis van der Vliet, Chao Wang, Mark Debe, Radoslav Atanasoski, Nenad M. Markovic and Vojislav R. Stamenkovic, "Platinum-alloy Nanostructured Thin Film Catalysts for the Oxygen Reduction Reaction," *Electrochimica Acta*. **56** 8695-8699 (2011).

37. J.E. Harlow, D.A. Steven, R.J. Sanderson, G. C-K Liu, L.B. Lohstreter, G.D. Vernstrom, R.T. Atanasoski, M.K. Debe, and J.R. Dahn, "The oxygen reduction reaction activity of a $Pt_{1-x}Mn_x$ binary composition spread," *J. Electrochemical Society* **159** (6) B670-B676 (2012).
38. Dennis van der Vliet, Chao Wang, Dusan Tripkovic, Dusan Strmcnik, Xiaofeng Zhang, Mark Debe, Radoslav Atanososki, Nenad M. Markovic and Vojislav R. Stamenkovic, "Metallic Nanotubes with Tunable Composition and Structure as Advanced Electrocatalysts," *Nature Materials*, in press (2012).

Catalyst Coating Process

39. M. K. Debe, A. E. Hester, G. D. Vernstrom, A. J. Steinbach, S. M. Hendricks, A. K. Schmoeckel, R. T. Atanasoski, D. J. McClure, and P. L. Turner, "Nanostructured Thin Film Catalysts for PEM Fuel Cells by Vacuum Web Coating, in proceedings of the 50th Annual Tech. Conference of the Society of Vacuum Coaters, Louisville, KY, May 1, 2007**,** 175-185 ISSN 0737-5921.
40. Global and China Low-E Glass Industry Report, November, 2010, at http://pressexposure.com/Global_and_China_Low-E_Glass_Industry_Report,_2010_-_Published_by_ResearchInChina-205310.html

Electrode and MEA Durability Tests

41. A. Bonakdarpour, J. Wenzel, D. A. Stevens, S. Sheng, T. L. Monchesky, R. Lobel, R. T. Atanasoski, A. K. Schmoeckel, G. D. Vernstrom, M. K. Debe, J. R. Dahn, "Studies of Transition Metal Dissolution from Combinatorially Sputtered, Nanostructured $Pt_{1-x}$ $M_x$ (M = Fe, Ni; $0<x<1$) Electrocatalysts for PEM Fuel Cell," *Journal of the Electrochem. Soc.* **152**(1), A61-A72 (2005).
42. A. Bonakdarpour, R. Lobel, R. T. Atanasoski, G. D. Vernstrom, A. K. Schmoeckel, M. K. Debe, J. R. Dahn, "Dissolution of transition metals in combinatorially sputtered $Pt_{1-x-y}M_xM'_y$ (M, M' = Co, Ni, Mn, Fe) PEMFC electrocatalysts," *J. of the Electrochem. Soc.* **153**(10), A1835-A1846 (2006).
43. M. Debe, A. Schmoeckel, S. Hendricks, G. Vernstrom, G. Haugen, R. Atanasoski, "Durability Aspects of Nanostructured Thin film Catalysts for PEM Fuel Cells," *ECS Transactions* **1**(8) 51-66 (2006).
44. M. K. Debe, A. K. Schmoeckel, G. D. Vernstrom, R. T. Atanasoski, "High voltage stability of nanostructured thin film catalysts for PEM fuel cells," *Journal of Power Sources* **161**, 1002 (2006).
45. A. J. Steinbach, K. Noda and M. K. Debe, "Stop-Start and High-Current Durability Testing of Nanostructured Thin film Catalysts for PEM Fuel Cells," *ECS Transactions* **3**(1) 835-853 (2006).
46. D. A. Stevens, J. M. Rouleau, R. E. Mar, R. T. Atanasoski, A. K. Schmoeckel, M K. Debe, J. R. Dahn, "Enhanced CO-Tolerance of Pt-Ru-Mo Hydrogen Oxidation Catalysts," *Journal of the Electrochem. Soc.* **154**(12), B1211-B1219 (2007).
47. A. J. Steinbach, C. V. Hamilton, Jr., and M. K. Debe, "Impact of Micromolar Concentration of Externally-Provided Chloride and Sulfide Contaminants of PEMFC Reversible Stability," *ECS Transactions* **11**(1) 889-902 (2007).
48. A. J. Steinbach, K. Alade-Lambo, H. Le and M. K. Debe, "Investigation of Cation-Induced Performance Losses in PEM Fuel Cells," 2008 Fuel Cell Seminar and Exposition, Phoenix, AZ, Oct. 27, (2008) Extended Abstract GHT35a-22.
49. D. A. Stevens, S. Wang, R. J. Sanderson, A. Garsuch, M. K. Debe, S. M. Hendricks, R. T. Atanasoski, J. R. Dahn, "Assessing the $Pt_{upd}$ Surface Area Stability of $Pt_{1-x}M_x$ (M=Re, Nb, Bi) Solid Solutions for Proton Exchange Membrane Fuel Cells," *Journal of the Electrochem. Soc.* **157**(5), B737-B743 (2010).
50. Greg Haugen, Sara Barta, Mike Emery, Steven Hamrock and Mike Yandrasits, "Open Circuit Voltage Fuel Cell Durability Testing Using Multiple PEM <MEA's, in Fuel Cell Chemistry and Operation, eds. Andrew M. Herring, Thomas A. Zawodzinski Jr., and Steven J. Hamrock, *ACS Symposium Series 1040*, page **137** (2010).
51. D. A. Cullen, K. L. More, K. S. Reeves, G. D. Vernstrom, L. L. Atanasoska, G. M. Haugen and R. T. Atanasoski, "Characterization of durable nanostructured thin film catalysts tested under transient conditions using analytical aberration-corrected electron microscopy," Abstract and Presentation #1201, 220th ECS Meeting, Boston, MA, Oct. 9-14, 2011.
52. R. T. Atanasoski, *DOE Hydrogen Program Annual Merit Reviews*, for 2010, 2011, and 2012, Washington, D.C.:
http://www.hydrogen.energy.gov/pdfs/review10/fc006_atanasoski_2010_o_web.pdf
http://www.hydrogen.energy.gov/pdfs/review11/fc006_atanasoski_2011_o.pdf
http://www.hydrogen.energy.gov/pdfs/review12/fc006_atanasoski_2012_o.pdf

53. L.L. Atanasoska, G. D. Vernstrom, G. M. Haugen, and R. T. Atanasoski, "Catalyst Durability for Fuel Cells under Start-up and Shutdown Conditions: Evaluation of Ru and Ir Sputter-Deposited Films on Platinum in PEM Environment," *ECS Transactions* **41**(1) 785-795 (2011).
54. Anusorn Kongkanand, Zhongi Liu, Indrajit Dutta and Frederick T. Wagner, "Electrochemical and Microstructural Evaluation of Aged Nanostructured thin Film Fuel Cell Electrocatalyst," *Journal of the Electrochem. Soc.* **158**(11), B1286-B1291 (2011).

Modeling of NSTF Properties

55. Mark K. Debe and Thomas Herdtle, "Design and development of a novel flow field for PEM fuel cells to obtain uniform flow distributions," *ECS Transactions* **1**(6) 581-604 (2006).
56. Q. Wang, M. Eikerling, D. Song, and Z. S. Liu, *J. Electrochem. Soc.* **154**, F95 (2007).
57. K. Chan and M. Eikerling, *J. Electrochem. Soc.*, **158**, B18 (2011).
58. A. Kongkanand and P. K. Sinha, *J. Electrochem. Soc.*, **158**, B703 (2011).
59. P. K. Sinha, W. Gu, A. Kongkanand, and E. Thompson, *J. Electrochem. Soc.* **158**, B831 (2011).
60. K. Chan and M. Eikerling, *J. Electrochem. Soc.* **159**, B155 (2012).
61. R.K. Ahluwalia, X. Wang, A. Lajunen, A.J. Steinbach, S.M. Hendricks, M.J. Kurkowski, and M.K. Debe, "Kinetics of Oxygen Reduction Reaction on Nanostructured Thin-Film Platinum Alloy Catalyst," *Journal of Power Sources* **215** (2012) 77-88.
62. Ryan J. Balliet and John Newman, "Cold-Start Modeling of a Polymer-Electrolyte Fuel Cell Containing an Ultrathin Cathode," *J. Electrochem. Soc.* **158**(9), B1142-B1149 (2011).

Water Management and Operational Robustness

63. M. K. Debe, and A. J. Steinbach, "An empirical model for the flooding behavior of ultra-thin PEM fuel cell electrodes," *ECS Transactions* **11**(1) 659-673 (2007).
64. A. J. Steinbach, M. K. Debe, J. L. Wong, M. J. Kurkowski, A. T. Haug, D. M. Peppin, S. K. Deppe, S. M. Hendricks, and E. M. Fischer, "A New Paradigm for PEMFC Ultra-Thin Electrode Water Management at Low Temperatures," *ECS Trans*., **33**(1), 1179-1188 (2010).
65. A. Steinbach, M. Debe, M. Pejsa, D. Peppin, A. Haug, M. Kurkowski and S. Maier-Hendricks, "Influence of Anode GDL on PEMFC Ultra-thin Electrode Water Management at Low Temperatures," *ECS Transactions*, **41**(1) 449-457 (2011).
66. Adam Weber, 2012 *DOE Hydrogen Program Annual Merit Reviews*, "Fuel Cell Fundamentals at Low and Subzero Temperatures," "http://www.hydrogen.energy.gov/pdfs/review11/fc026_weber_2011_o.pdf.
67. Anusorn Kongkanand, Matthew Dioguardi, Chunxin Ji and Eric L. Thompson, "Improving Operational Robustness of NSTF Electrodes in PEM Fuel Cells," *J. Electrochem. Soc.*, **159** (8) F405-F411 (2012).
68. Anusorn Kongkanand, Jeanette E. Owejan, Scott Moose, Matthew Dioguardi, Mahesh Biradar, and Rohit Makharia, "Development of Dispersed-Catalyst/NSTF Hybrid Electrode," *J. Electrochem. Soc.*, **159** (11) F676-F682 (2012).

OER Catalysis Applications

69. K. E. Ayers, E. B. Anderson, C. B. Capuano, B. D. Carter, L. T. Dalton, G. Hanlon, *ECS Transactions* **33**(1) 3-15 (2010).
70. Monjid Hamden, 2011 *DOE Hydrogen Program Review*, PD030 May, 2011, Washington, D.C. http://www.hydrogen.energy.gov/pdfs/review11/pd030_hamdan_o_web.pdf
71. M. Debe, S. M. Hendricks, G. Vernstrom, J. Wiley, M. Hamden, C. Mittelsteadt, C. Capuano, K. Ayers and E. Anderson, "Initial Performance and Durability of Ultra-low Loaded NSTF Electrodes for PEM Electrolyzers," Abs. #694, 220$^{Th}$ ECS Meeting, Boston, MA, Oct., 2011.
72. M. K. Debe, S. M. Hendricks, G. D. Vernstrom, M. Meyers, M. Brostrom, M. Stephens, and Q. Chan, Jason Willey, Monjid Hamden, and Cortney K. Mittelsteadt**,** Christopher B. Capuano, Katherine Ayers and Everett Anderson, "Initial Performance and Durability of Ultra-low Loaded NSTF Electrodes for PEM Electrolyzers," *J. Electrochem. Soc*., **159**(6) K165-K176 (2012).
73. D. A. Cullen, K. L. More, K. S. Reeves, G. D. Vernstrom, L. L. Atanasoska, G. M. Haugen, and R. T. Atanasoski: "Characterization of durable nanostructured thin film catalysts tested under transient conditions using analytical aberration-corrected electron microscopy," *ECS Transactions*, **41** (1) 1099-1103 (2011).

74. L.L. Atanasoska, G. D. Vernstrom, G. M. Haugen, and R. T. Atanasoski: "Catalyst Durability for Fuel Cells under Start-up and Shutdown Conditions: Evaluation of Ru and Ir Sputter-Deposited Films on Platinum in PEM Environment," *ECS Transactions*, **41** (1) 785-795 (2011).
75. R.T. Atanasoski, L.L. Atanasoska, D.A. Cullen, G.M. Haugen, K.L. More, G.D. Vernstrom. "Fuel Cell Catalyst for Start-up and Shutdown Conditions: Electrochemical, XPS, and TEM Evaluation of Sputter-Deposited Ru, Ir, and Ti on Pt-Nano-Structured Thin Film (NSTF) Support," in press, *Electrocatalysis*, (DOI 10.1007/s12678-012-0092-3).
76. R.T. Atanasoski, L.L. Atanasoska, D.A. Cullen, G.M. Haugen, K.L. More, and G.D. Vernstrom, "Fuel Cells Catalyst for Start-up and Shutdown Conditions: Electrochemical, XPS, and TEM Evaluation of Sputter-Deposited Ru, Ir, and Ti on Pt-Nano-Structured Thin Film (NSTF) Support," *Electrocatalysis*, DOI 10.1007/s12678-012-0092-3.
77. Radoslav T. Atanasoski, Ljiljana L. Atanasoska**,** and David A. Cullen, "Efficient Oxygen Evolution Reaction Catalysts for Cell Reversal and Start/Stop Tolerance," in M. Shao ed. Electrocatalysis in Fuel Cells: A Non and Low Platinum Approach**,** Chapter 23, Springer, 2013.

Origins of NSTF in Self Organizing Organic Thin Films

78. M. K. Debe, "The interface orientation of perylene red and phthalocyanine molecules vapor-deposited on aluminum," *Journal of Vacuum Science and Technology* **21**(1), 74-9 (1982).
79. M. K. Debe, "Organic/metal interface studies with reflection-absorption infrared spectroscopy: photomasked surfactants and organic photoconductors on aluminum," *Applications of Surface Science* **14**(1), 1-40 (1982).
80. M. K. Debe, "Extracting physical structure information from thin organic films with reflection absorption infrared spectroscopy," *Journal of Applied Physics* **55**(9), 3354-66 (1984), and Erratum in J. Appl. Physics **62**(4), 1546 (1987).
81. M. K. Debe, "Optical probes of organic thin films: photons-in and photons-out," Monograph in *Progress in Surface Science* **24**(1-4), 1-282 (1987).
82. M. K. Debe and R. J. Poirier, "Effect of gravity on copper phthalocyanine thin films. III. Microstructure comparisons of copper phthalocyanine thin films grown in microgravity and unit gravity," *Thin Solid Films* **186**(2), 327-47 (1990).
83. M. K. Debe, R. J. Poirier, and K. K. Kam,"Organic-thin-film-induced molecular epitaxy from the vapor phase," *Thin Solid Films* **197**(1-2), 335-47(1991).
84. M. K. Debe, D. R. Field, "Variable angle spectroscopic ellipsometry studies of oriented phthalocyanine films," *Journal of Vacuum Science & Technology* A **9**(3), 1265-71(1991).
85. M. K. Debe, "Variable angle spectroscopic ellipsometry studies of oriented phthalocyanine films. II. Copper phthalocyanine, "*Journal of Vacuum Science & Technology*, A **10**(4), 2816-2821 (1992).
86. C. J. Liu, M. K. Debe, P. C. Leung, C. V. Francis, "Highly ordered films of para-chlorophenylurea by vapor deposition," *Applied Physics Communications* **11**(2-3), 151-64 (1992).

**Table I.** Summary of NSTF support, catalyst coated supports and electrode properties.

| NSTF Catalyst | | Characteristic | Value | References |
|---|---|---|---|---|
| Catalyst Support Particle | Chemical Composition | Pure Organic Molecular Solid – C. I. Pigment Red 149 | N,N-di(3,5,xylyl) perylene-3,4:9,10bis(dicarboximide) | CI No. 71137 |
| | Morphology | Body centered cubic, lath-shaped crystalline whisker | 14.5 Å lattice constant | 16, 17 |
| | | | (01$\underline{1}$), ($\underline{2}$22) side facets | |
| | Growth Mechanism – vacuum annealing vapor deposited thin film of perylene red. | Zero supersaturation ratio surface diffusion to screw dislocation on tip of whisker | [211] screw axis growth tip, $\Delta E_{diff}$ = 18 kCal/mole $D_{surf}$(475K) = 2 x $10^{-12}$ $cm^2/s$ | |
| | | Growth Temperature | > 250°C under < 1Torr | |
| | | Width in [01$\underline{1}$] direction | 550 $\pm$ 120 Å | |
| | Physical, Chemical Characteristics | Thickness in [111] direction | 270 $\pm$ 75 Å | |
| | | Ratio of whisker thickness/width | ~0.5 | |
| | | Length (controllable) | 0.5 to > 2 microns | 9 |
| | | Oriented Monolayer | Growth direction normal to substrate | 16, 17 |
| | | Areal Number Density | 3 to 5 billion/$cm^2$ | 9, 17 |
| | | Electrical conductivity | p-type organic photo-conductor, > 2 V "bandgap", | Field of organic photoconductors |
| | | Solubility in common solvents, acids or bases. | Extremely low, forms dispersions | 9 |
| | | EC oxidation (deduced from OER) | ~ 0 to E = 2.3 Volts RHE | 71 |
| | | Surface area enhancement | ~ 8 $cm^2/cm^2_{planar}$ | 9 |
| | Substrate for growing whiskers | Any material stable to 300°C using PR-149 to grow whiskers. | Microstructured for roll to roll manufacturing preferred. | 9 |
| **Method for applying catalyst coating over the whiskers** | | Any Suitable Vapor Coating Process: PVD, CVD, ALD. All dry. | Magnetron sputter deposition, e-beam preferred | 39 |
| | | Catalyst layer construction | Multi, single, or mixed | Historical, 3M |
| | | Overlayer Compositions | Pt combined with any metals, alloys, inorganics or organics. | |
| NSTF Electrode | Preferred electrode fabrication method | Decal transfer by roll to roll lamination to the PEM. Conditions dependent on many factors. Ionomer free. | | |
| | Electrochemical properties for Pt transition metal alloys with cathode loadings in the range of 0.05 to 0.15 mg-Pt/$cm^2$. | Range of $H_{upd}$ ECSA's | 5-17 ($m^2/g$) | |
| | | $H_{upd}$ surface area enhancement factor (SEF) | 10 to 25 $cm^2_{Pt}/cm^2_{planar}$ | |
| | | ORR activities at 900 mV, 100 kPa saturated $O_2$: Kinetic improvement versus Pt-poly by RDE | 2 to 8 depending on alloy and annealing | 36, 38 |
| | | ORR activities at 900 mV, 100 kPa saturated $O_2$: Specific activity, MEA's | 2.1 to 2.5 mA/$cm^2_{Pt}$ | 8, 10 - 12 |
| | | ORR activities at 900 mV, 100 kPa saturated $O_2$: Specific activity by RDE | 2 to 5.5 mA/cm2 | 8, 36 |
| | | ORR activities at 900 mV, 100 kPa saturated $O_2$: Mass activity by RDE | 0.2 to 0.8 A/mg-Pt | 36 |
| | | ORR activities at 900 mV, 100 kPa saturated $O_2$: Mass activity in MEA's | 0.24 to > 0.5 A/mg-Pt | 8, 10, 11 |
| | | Proton charge transport mechanisms proposed | $H^+$ surface migration over Pt-OH, $H_2O$ diffusion | 56 - 60 |
| | | OER anode cell reversal tolerance durability test: -0.2 A/$cm^2$ | Cell V remained below - 2 V for 20 hrs with 0.06 mg/$cm^2$ | 52(2011), 74, 76, 77 |
| | | Typical double layer capacitance | 0.181 $\pm$ 0.03 μF/unit SEF | Historical, 3M |
| | | MEA Observed Tafel Slopes | 65 - 70 mV/decade | |
| | Physical Properties | Electrode thickness range | 0.2 to 0.6 microns | 9 |
| | | Thickness vs loading ($Pt_{68}Co_{28}Mn_3$) | 3.3 microns/mg-Pt | 13 |
| | | Surface area volumetric density | 2 to 4 x $10^5$ $cm^2_{Pt}/cm^3$ | 13 |

**Table II.** Property Summary of NSTF CCM's and MEA's.

| NSTF Catalyst | | Characteristic | Value | Refs. |
|---|---|---|---|---|
| **Full CCM / MEA Properties** | Sat. 20 μm, 850 EW PFSA PEM. | HFR (8 – 10 kHz), 0 to 2 A/cm$^2$ | 0.05 to ~ 0.08 ohm – cm$^2$ | Historical 3M |
| | Short Stack Peak Inverse Specific Power Density | GM 400 cm$^2$ cell size, 0.05 / 0.10 mg-Pt/cm$^2$ PtCoMn | 0.19 g-Pt/kWe | 10 (2010) |
| | $F^-$ ion release, 60 μm Nafion™ 1000 | 90$^o$C $H_2/O_2$, 30 % RH, 0 psig, OCV, 0.15 mg/cm$^2$ pure Pt | 1 μg/day-cm$^2$ | 10, 50 |
| | $F^-$ ion release, 24 μm PFSA PEM, no additives | 120$^o$C, $H_2$/air, 0.4 A/cm$^2$, PtCoMn 0.1 mg/cm$^2$ on anode and cathode | < 0.6 μg/day-cm$^2$ average over 1080 hrs | |
| | Durability by Cyclic Voltammetry | 30,000 cycles, 0.6 – 1.0 V, 50 mV/sec, 100 Kpa $H_2/N_2$ 80/80/80$^o$C | - 3 mV loss at 0.8 A/cm$^2$ | 10(2012) |
| | | | - 14% loss of ECSA | |
| | | | - 34% loss mass activity | |
| | Durability, 1.2 V hold for 400 hours | 150 / 150 kPa $H_2/N_2$ 80$^o$C, 100 % RH | - 10 mV loss at 1.5 A/cm$^2$ | 10 (2011) |
| | | | - 10% loss of ECSA | |
| | | | - 10 % loss mass activity | |
| | Durability, OCV hold for 500 hours | 250 / 200 kPa $H_2$/Air 90$^o$C, 30% RH | 13 $\pm$ 4 mA/cm$^2$ $H_2$ X-over | |
| | | | - 12 $\pm$ 5% OCV loss | |
| | Durability as $H_2/O_2$ electrolyzer anode | 0.15 mg/cm$^2$ PtIr | Stable for 2000 hours at 80$^o$C, 2.23 volts,1.5 A/cm$^2$ | 72 |
| | Performance $H_2/O_2$ electrolyzer | 0.15 mg/cm$^2$ PtIr alloys | 2.2V Cell Voltage at 3.5 A/cm$^2$ | |
| | Lifetime under load cycling: 80/64/64 $^o$C, 0.02 to 1 A/cm$^2$ | 50 cm$^2$ single cell, 3M load cycle protocol. 20 μm 850 EW PEM with stabilizers, no support; 0.05/0.10 mg/cm$^2$ PtCoMn | 9000 hours, two samples | 10 (2011) |
| | Short Stack AOEM Freeze Start, -20$^o$C | High flow rate 60%RH purge before -20$^o$C idle at 0.1 A/cm$^2$. | Full power reached in 30 seconds. | 10 (2011) |

**Table III.** Mass activities measured at GM of 3M CCMs having NSTF $Pt_3Ni_7$, roll-to-roll dealloyed and SET treated cathodes laminated to either cleaned or as-made 3M PEMs. Cathode loadings were $0.121 \pm 0.003$ mg-Pt/cm$^2$.

| Sample membrane used in CCM | Protocol used for measurement | Standard Treatment (A/mg) | With Additional Pretreatment (A/mg) |
|---|---|---|---|
| As-made PEM | GM | 0.45 | 0.47 |
| As-made PEM | 3M | 0.52 | 0.67 |
| Cleaned PEM #1 | GM | 0.41 | 0.54 |
| Cleaned PEM #1 | 3M | 0.23 | 0.65 |
| Cleaned PEM #2 | GM | 0.41 | 0.58 |
| Cleaned PEM #2 | 3M | 0.21 | 0.62 |

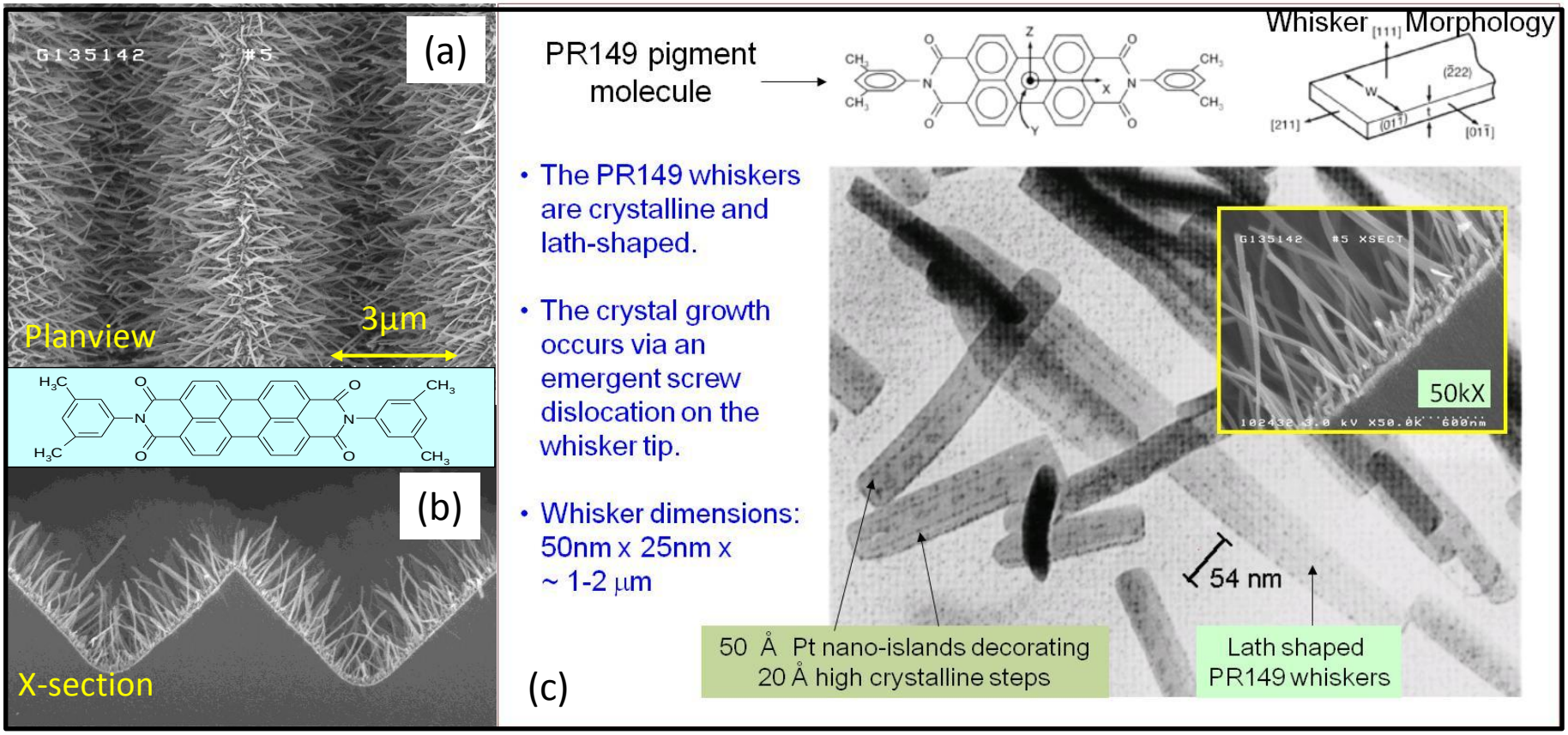


**Figure 1.** SEM and TEM images of the perylene red NSTF catalyst support whiskers: a) and b) as a monolayer of oriented whiskers on a microstructured substrate web, and c) decorated with Pt nano-islands for TEM imaging.

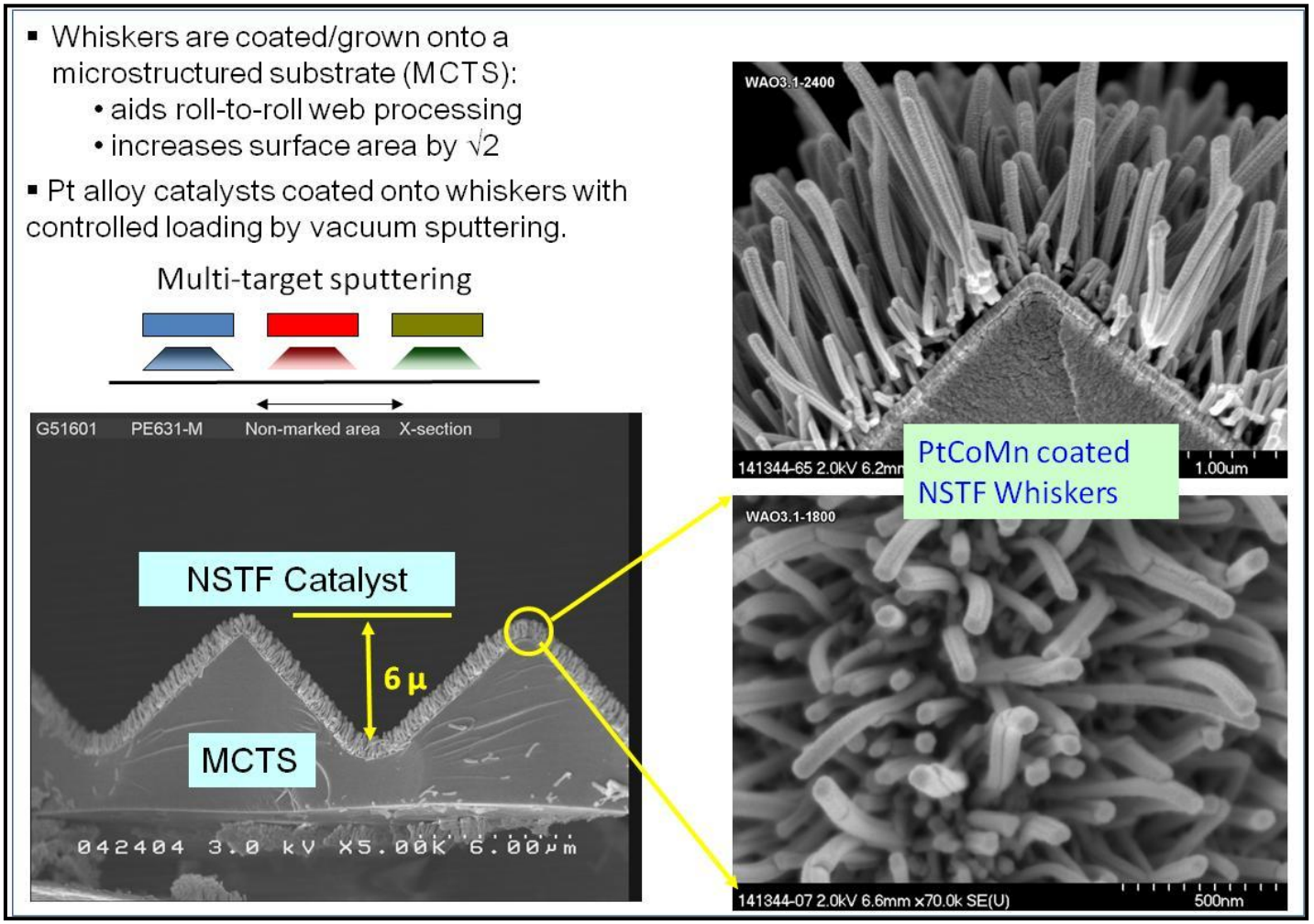


**Figure 2.** SEM views of the catalyst coated whiskers on a microstructured substrate after sputter coating with a PtCoMn alloy.

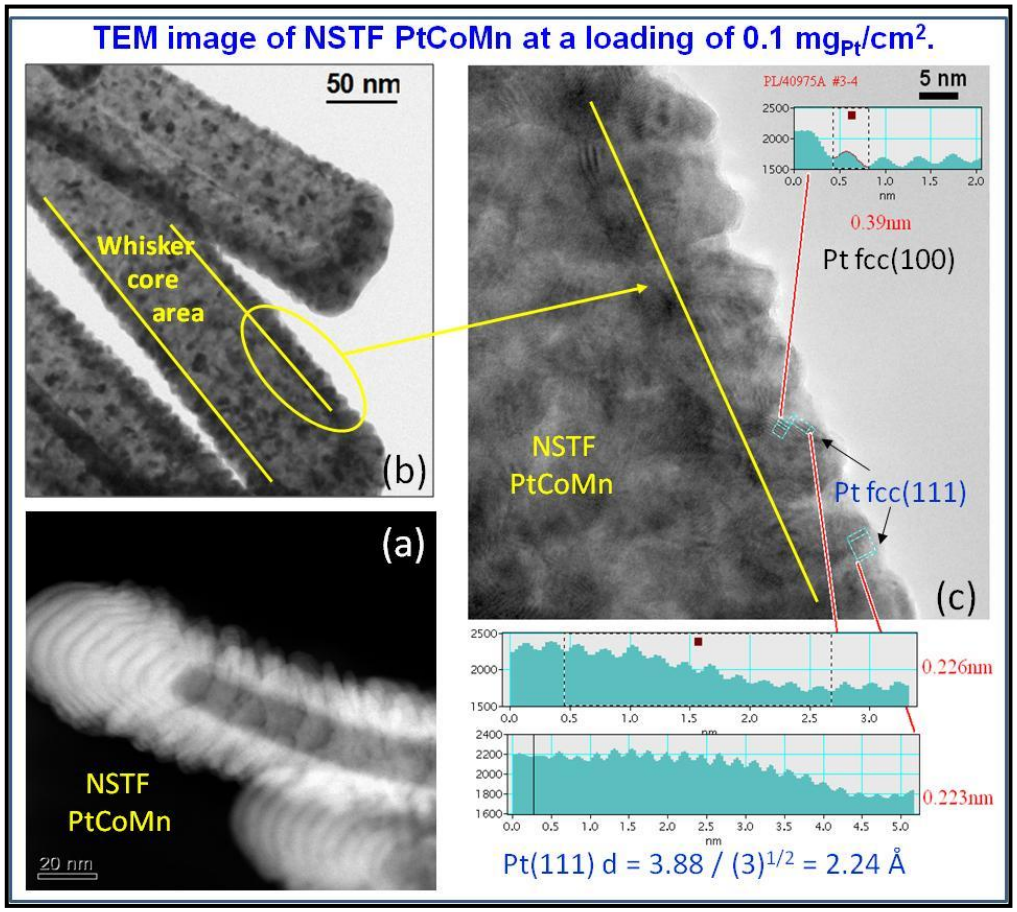


**Figure 3.** TEM images of NSTF whiskers with (a) multilayered PtCoMn grains that are oriented with mixed surface faceting (b,c).

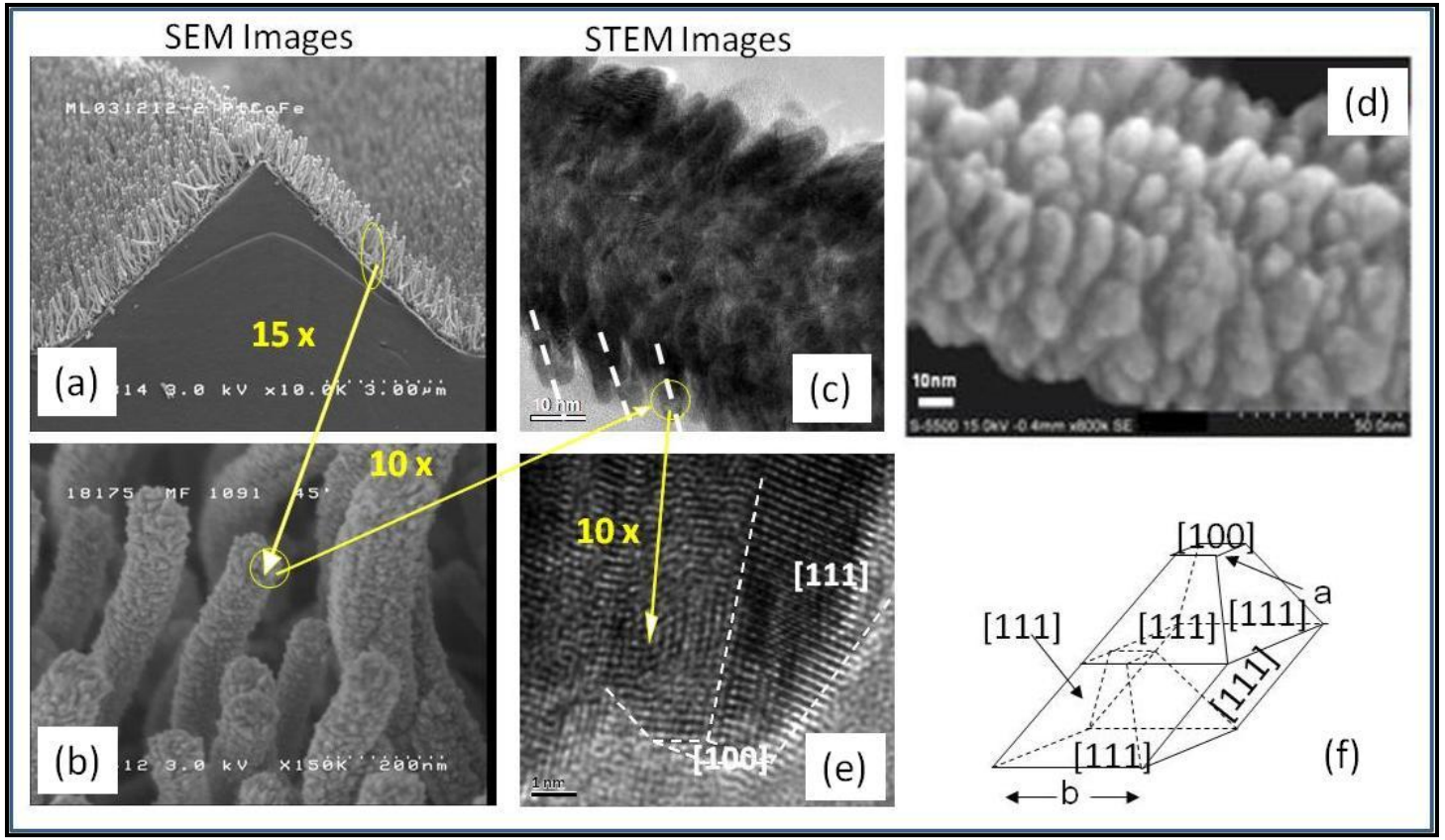


**Figure 4.** SEM (a,b) and STEM images of the "whiskerette" grains forming the catalyst coating that encapsulates the NSTF whisker core. The grain's axes are oriented at an angle of 70$^{o}$ w.r.t. the whisker axis, equal to the angle between (111) planes in a cubic system, suggesting an influence of the whisker's bcc(111) side facets on the Pt fcc(111) growth planes. The Pt alloy whiskerette grains have tip shapes shown in (e) and (f) (23). The STEM images shown were not taken from the same whisker but are representative.

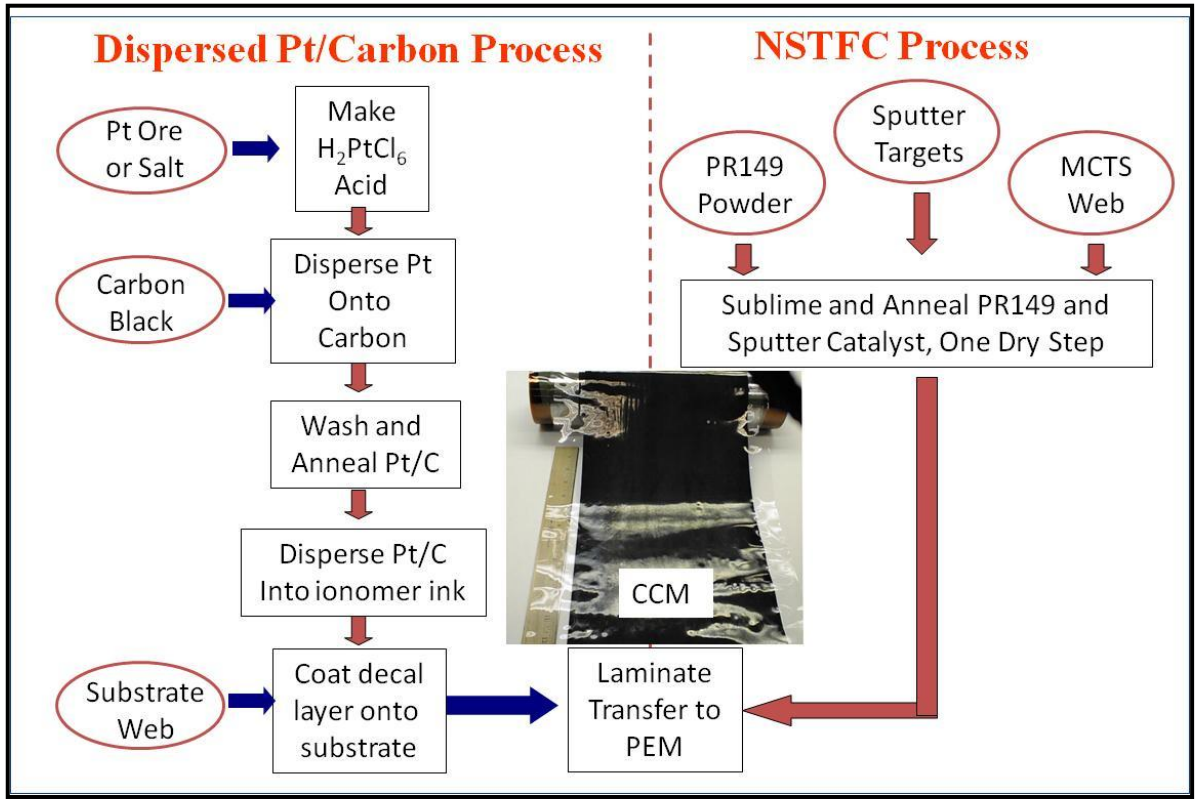


**Figure 5.** Schematic comparison of the high level processing steps required to fabricate Pt/C and NSTF based CCM's.

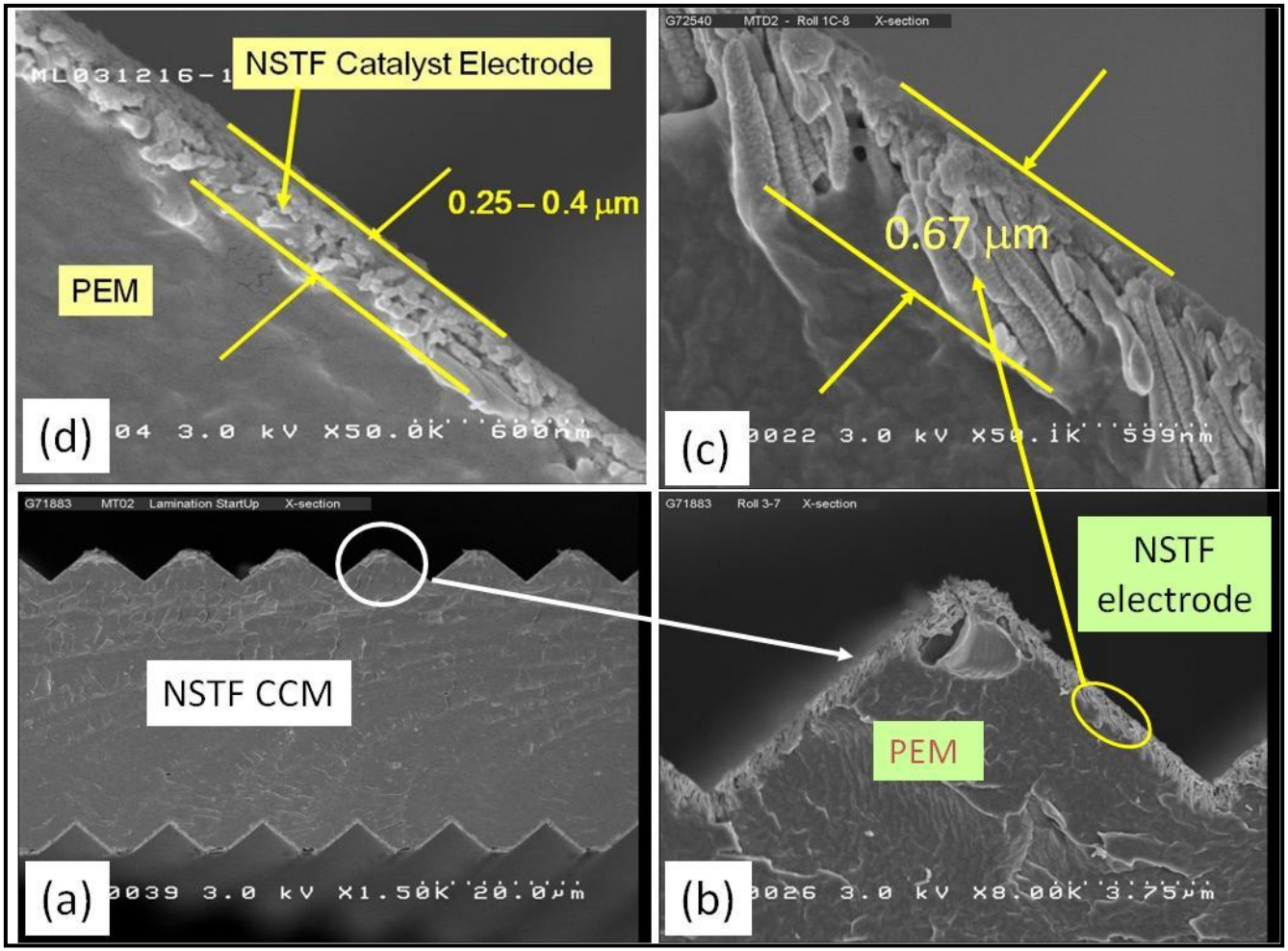


**Figure 6.** SEM cross-sections of NSTF electrodes: (a) the whole CCM, b) expanded view of one of the MCTS peaks embossed in the PEM, c) expanded view of the catalyst electrode showing the reduced thickness and whisker orientation is maintained for a higher loading of catalyst, and d) a lower loading of catalyst.

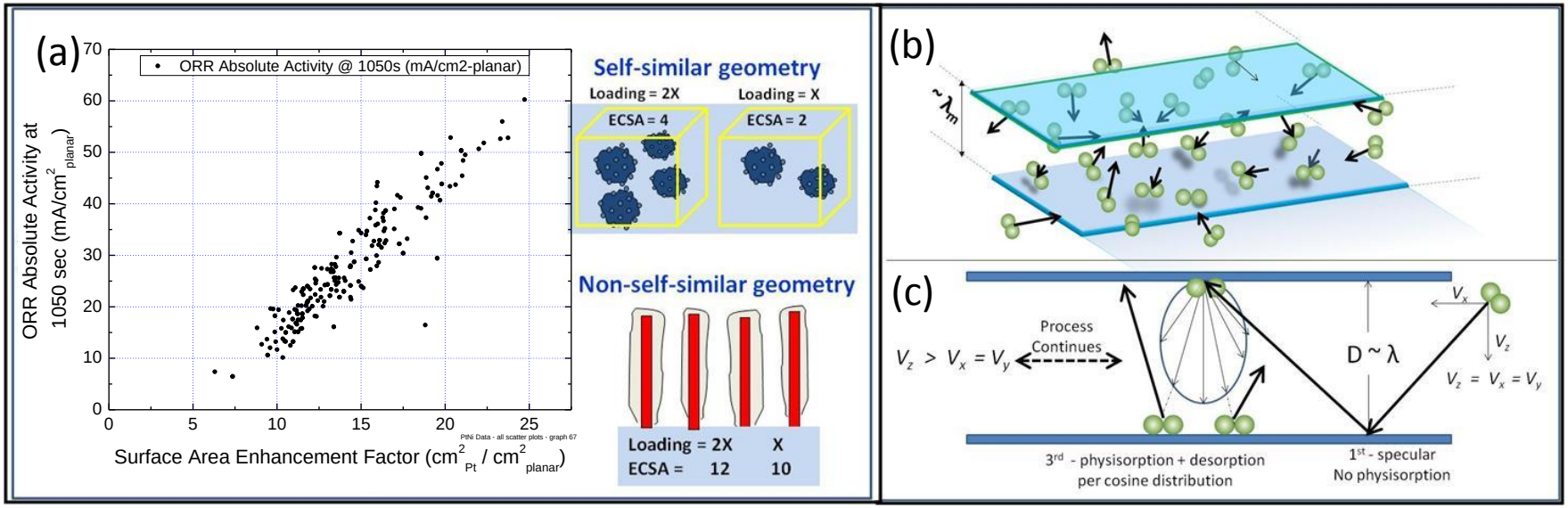


**Figure 7.** Two important properties engendered or applicable to the NSTF type geometry. (a) Self- versus non self-similar geometry can impact how the absolute activity varies with surface area. b) and c) Extended surface catalysts can impact the gas velocity distributions in the Knudsen regime within one mean free path of the surface and thereby increase the number of physisorption and chemisorption attempts per unit time (13).

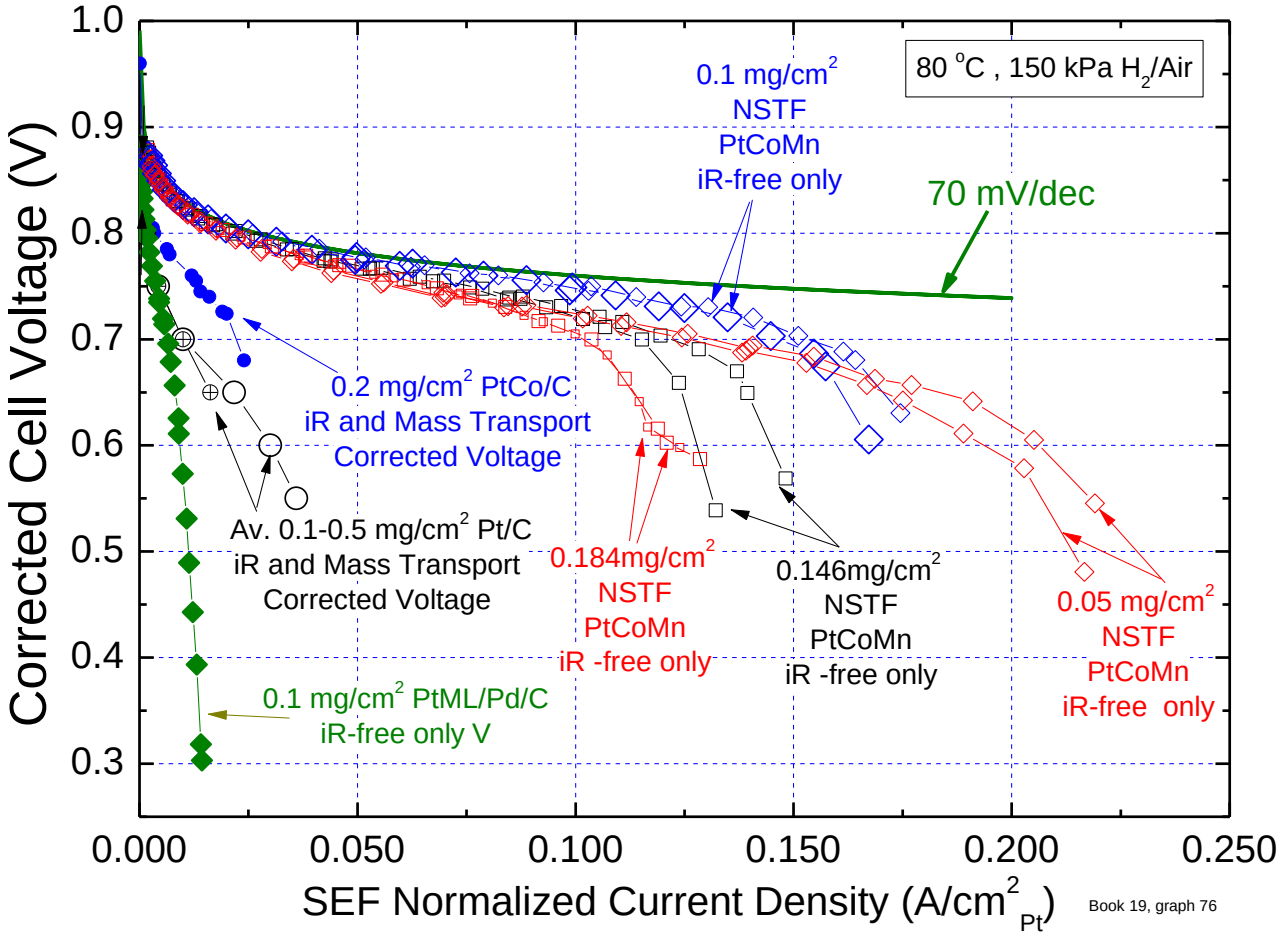


**Figure 8.** Galvanodynamic polarization curves of iR-free cell voltage versus current density normalized to the surface area enhancement factor ($cm^2_{Pt}/cm^2_{planar}$) for a series of NSTF and Pt/C based 50 $cm^2$ MEA's with different Pt loadings. The Pt/C cell voltages were also mass transport corrected. From reference (12).

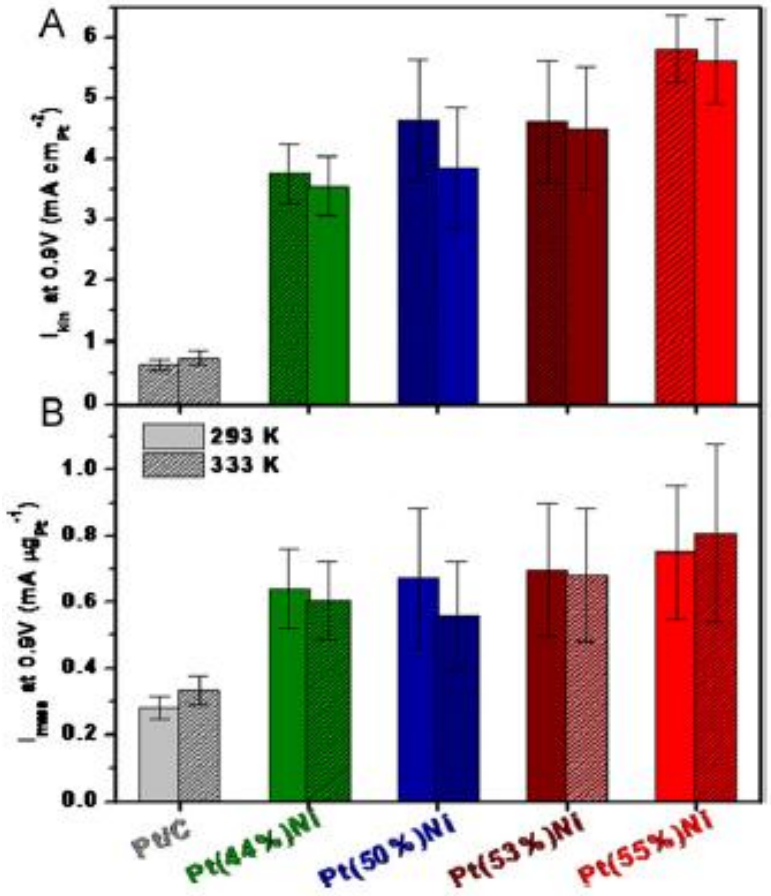


Fig. 9. Bar graphs of the ORR and on NSTF PtNi catalysts with different wt% Pt content compared to the Pt/C baseline catalyst. A) Specific and (B) mass activities at 0.9 V. The solid color bars represent the values at 293 K, the accented bars the values at 333K. From reference ( ).

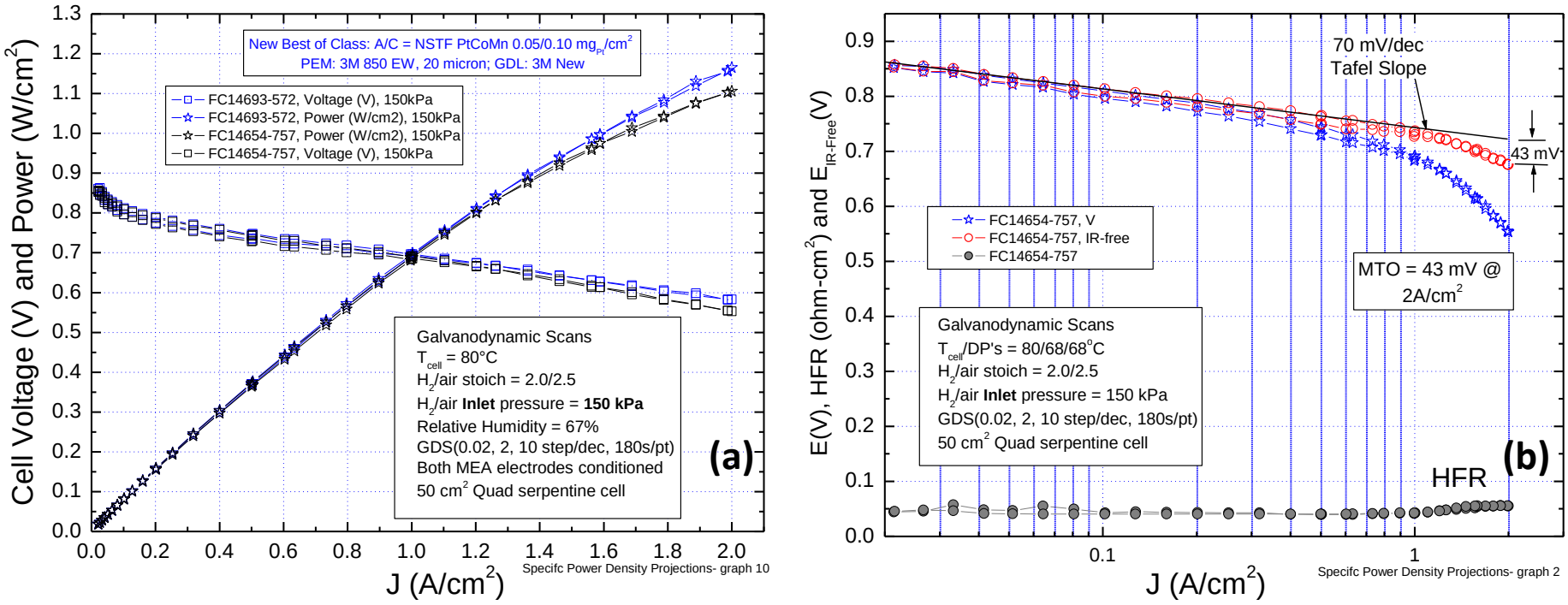


**Figure 10.** (a) Galvanodynamic polarization and power density curves at the conditions shown in the legend, for the NSTF 2009 best of class MEA's having $Pt_{68}Co_{29}Mn_3$ on the anodes and cathodes with Pt loadings of 0.05 and 0.10 $mg_{Pt}/cm^2$ respectively. (b) Same polarization curves as in (a) but plotted as a Tafel plot, from reference 10(2009).

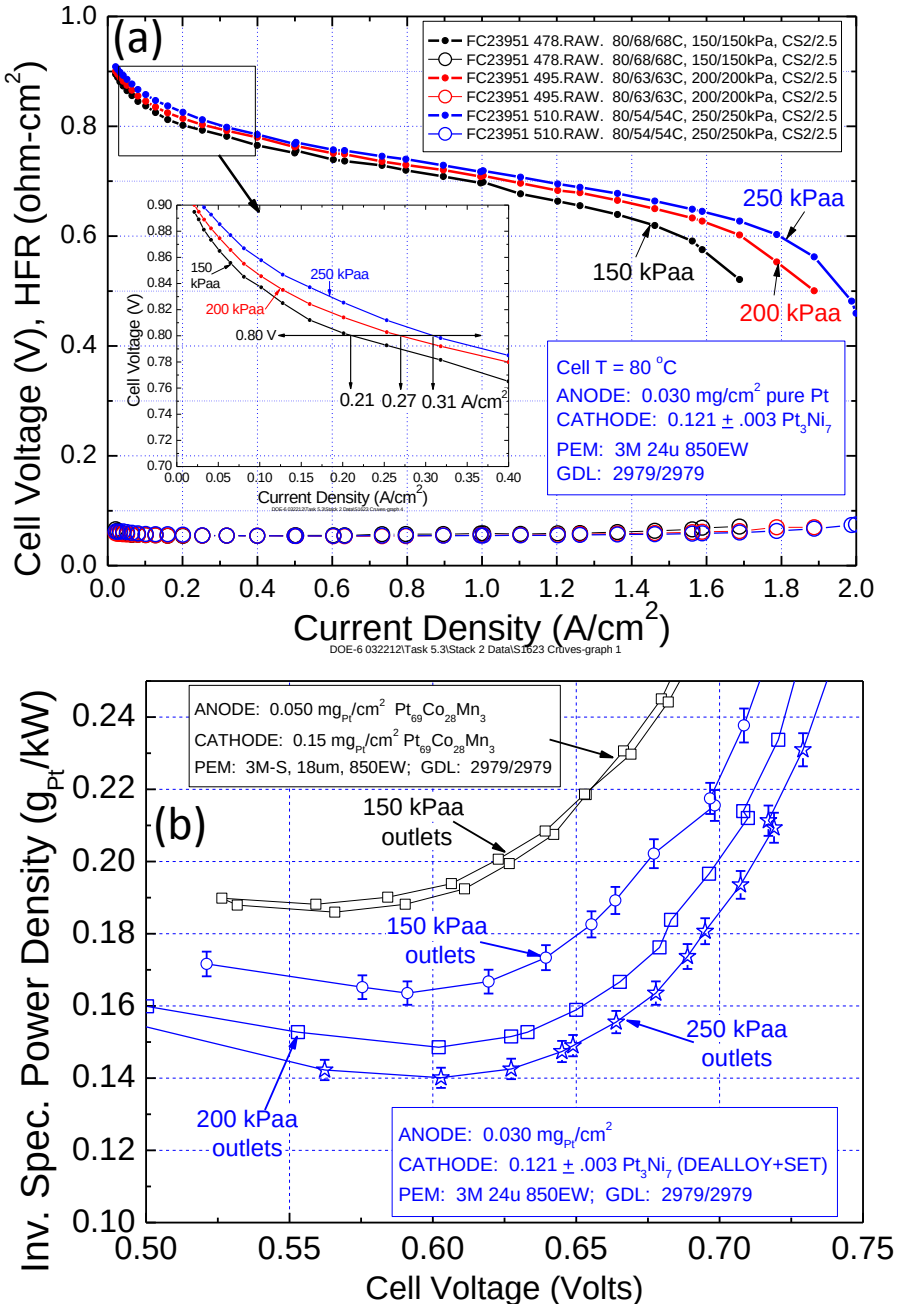





**Figure 11**. **(A)** GDS polarization curve performances for the 2012 "best of class" MEA based on the roll-to-roll dealloyed and SET "annealed" NSTF-$Pt_3Ni_7$ cathodes. The MEA contained a total PGM loading of 0.15 mg-Pt/cm$^2$. **(B)** Inverse specific power density versus cell voltage for the three GDS polarization curves shown in (A).

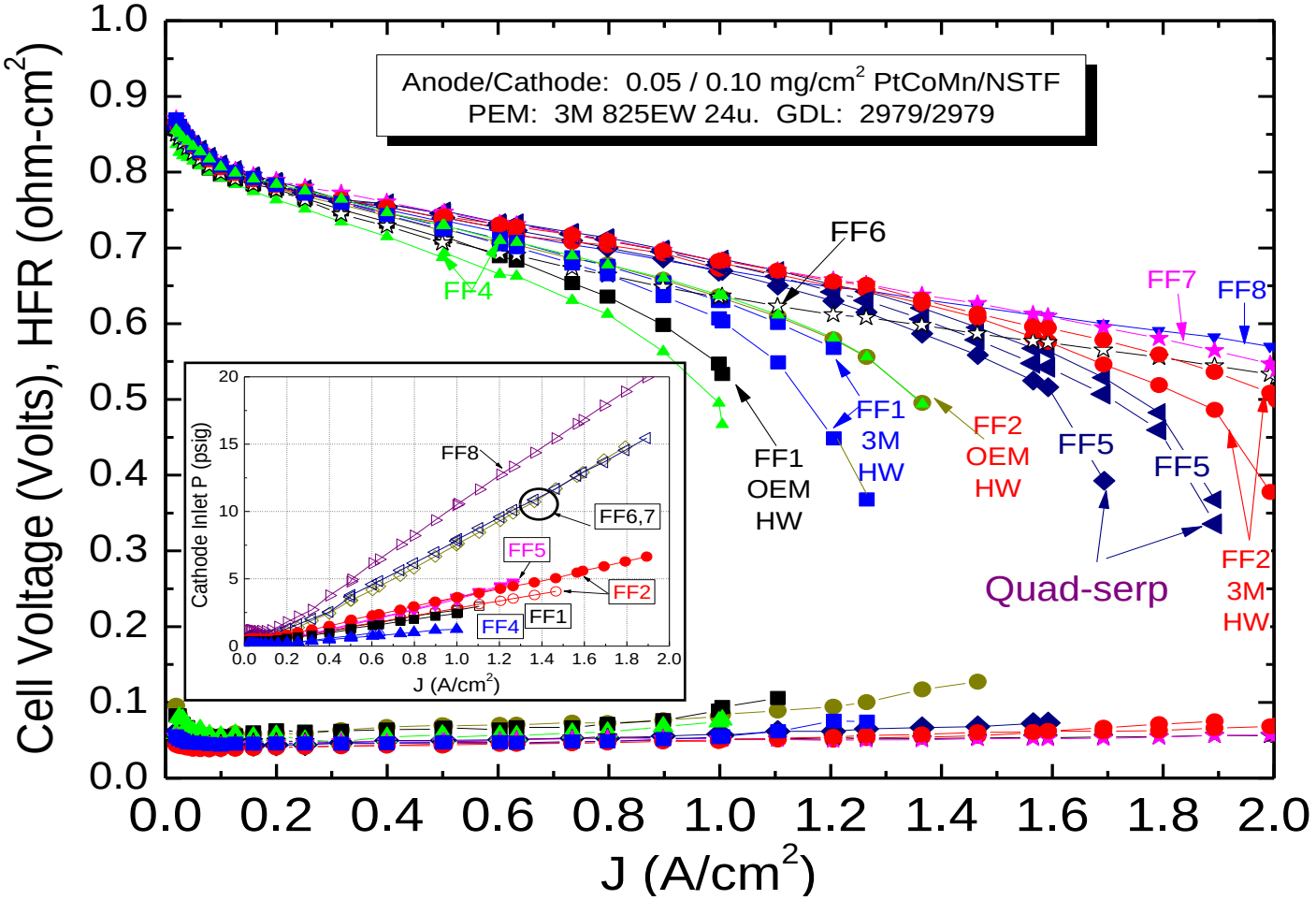


**Figure 12.** Comparison of single cell (50 $cm^2$) GDS polarization curves from the standard quad serpentine flow field (**FF5**) with seven alternative flow fields: **FF1** = 6 serpentine channels, 2 loops, 2 mm channel width, 2 mm land width, ~0.3 mm channel depth; **FF2** = 24 serpentine channels, 2 loops, 0.5 mm channel width, 0.5 mm land width, ~0.25 mm channel depth; **FF4** = 9 serpentine channels, 4 loops, 1 mm channel width, 0.6 mm land width, 1 mm channel depth; **FF5** (**quad-serpentine)** = 4 serpentine channels, 10 loops, 0.8 mm channel width, 0.8 mm land width, 1 mm channel depth; **FF6** = single channel 3M Zig-Zag (21); **FF7** = 2 serpentine channels, 21 loops, 1 mm channel width, 1 mm land width, 1 mm channel depth; **FF8** = single serpentine, 43 loops, 0.8 mm channel width, 1.0 mm land width, 1.5 mm channel depth; **FF9** = 19 full parallel channels, 1.95 mm channel width, 1.75 mm land width, 2 mm channel depth.

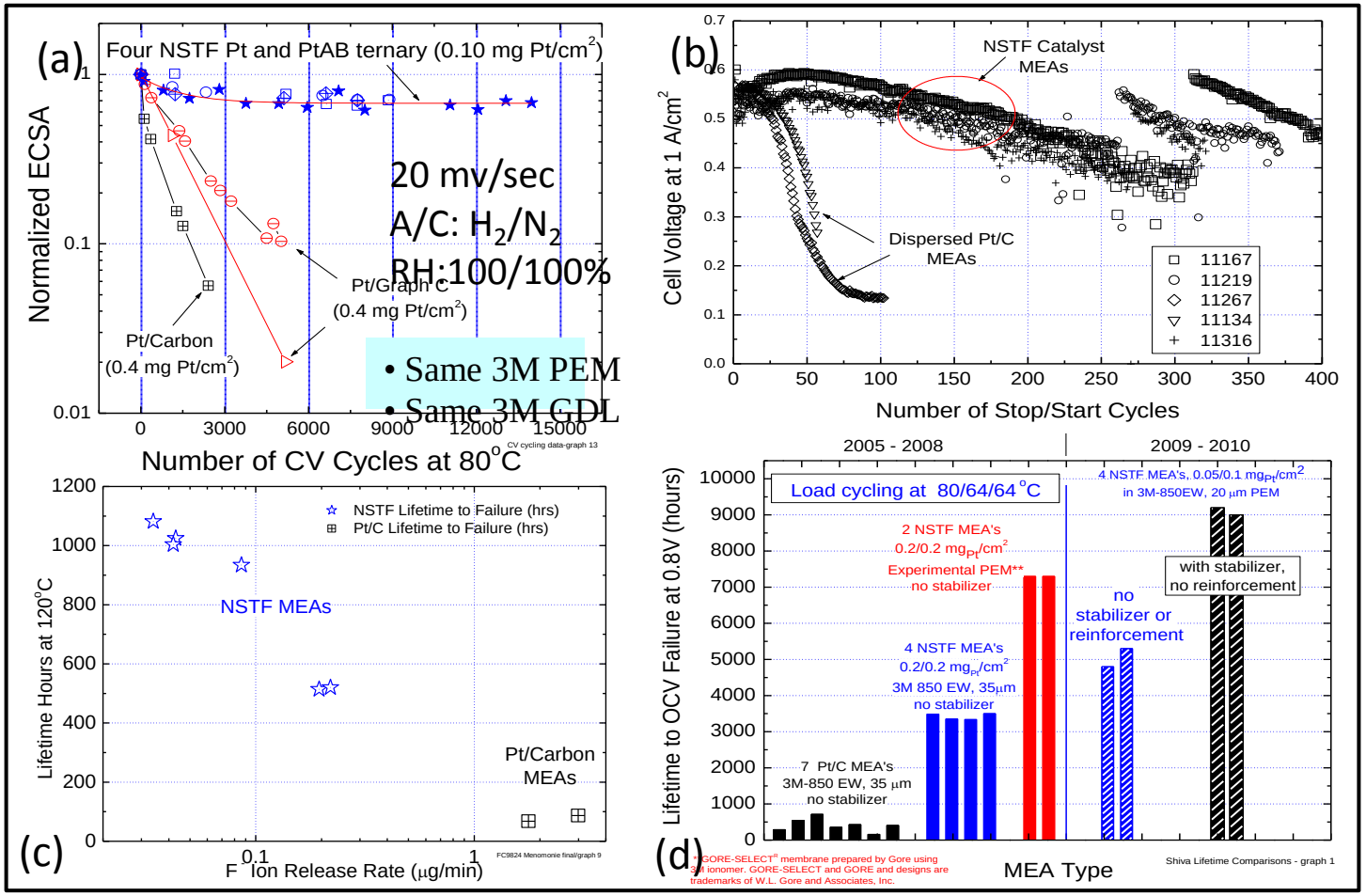


**Figure 13.** Examples of four accelerated durability tests comparing NSTF and Pt/C electrodes: (a) surface area stability versus number of CV cycles under $H_2/N_2$ from 0.6 to 1.2 V at 20 mV/sec. (43); (b) Cell voltage at 1 A/cm$^2$ versus number of automotive stop-start cycles for five NSTF MEA's and two Pt/C based MEA's (44);(c) Lifetime hours operating at 120$^o$C versus average daily fluoride ion release rate for six NSTF MEA's and two Pt/C based MEA's; (d) MEA lifetime hours under a load cycling protocol for different NSTF MEA types between 2005 and 2010, from reference 10(2011).

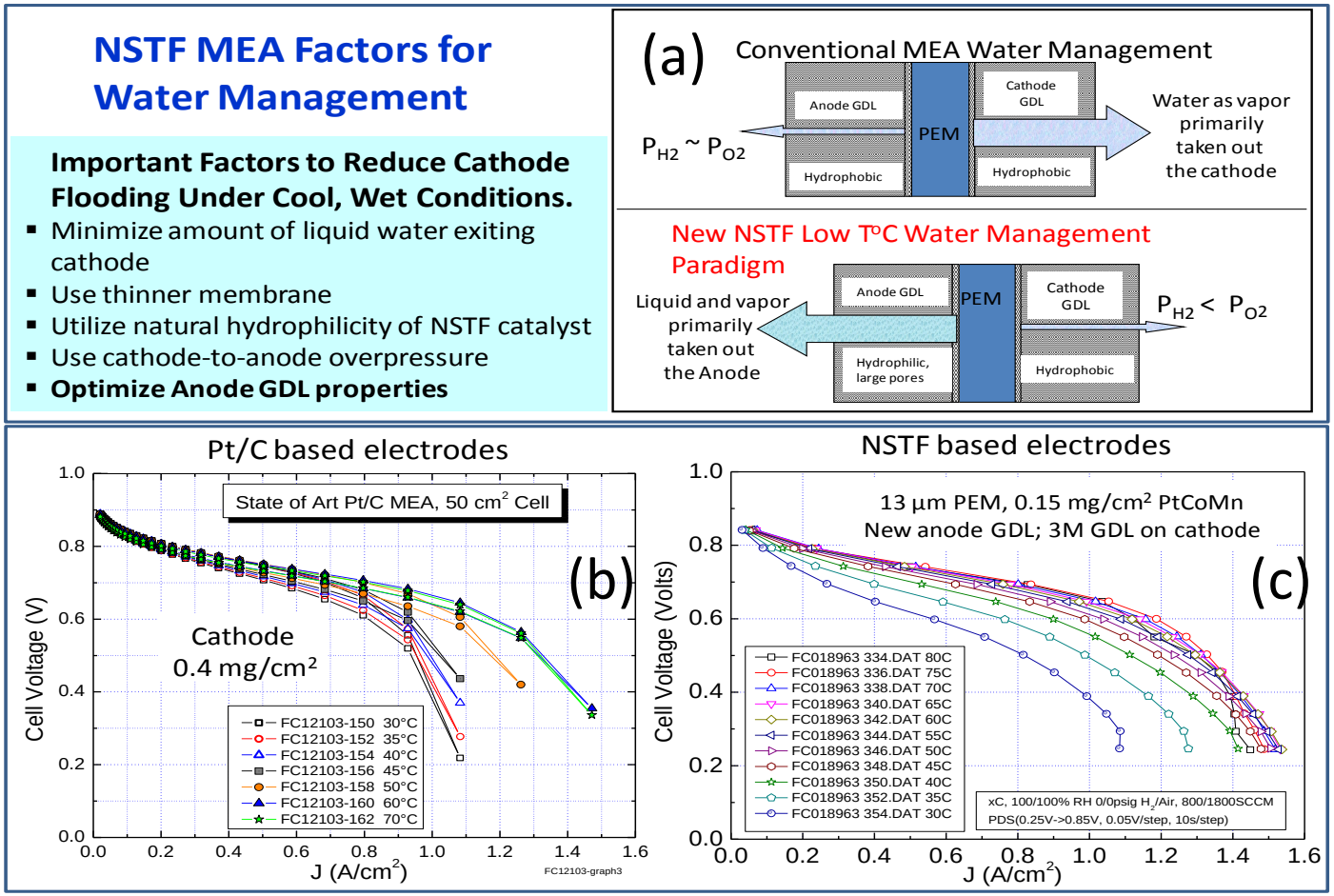


**Figure 14.** Water management strategy for ultra-thin NSTF type electrodes (a). Potentiodynamic polarization curves over the temperature range of 30°C to 80°C from two types of NSTF MEA's for which a) the MEA construction is not optimized, and b) the anode GDL and membrane thickness are better optimized for reduced cathode flooding at low temperatures.

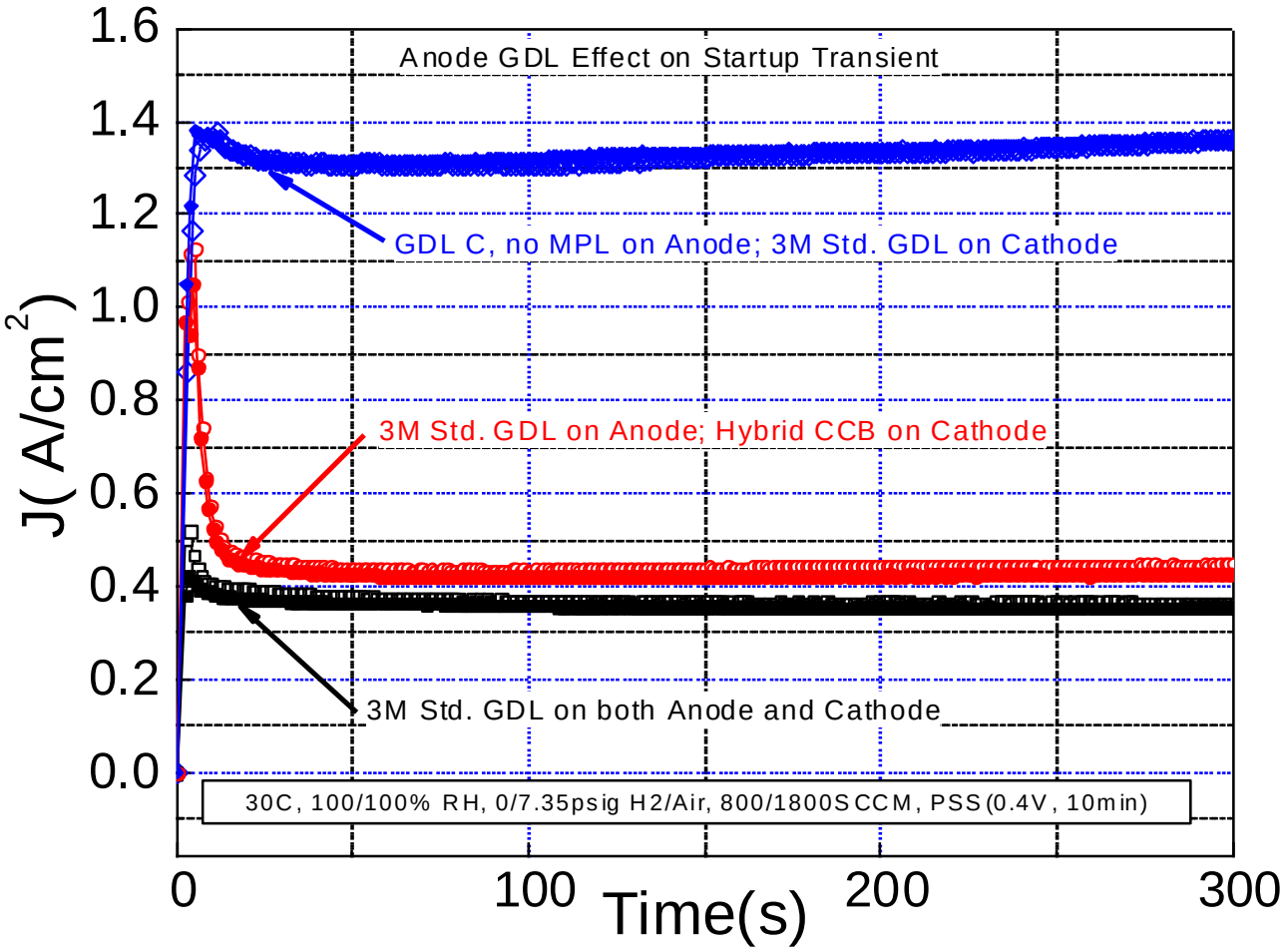


**Figure 15.** Current density versus time during a transient start-up protocol at 30°C for identical NSTF CCM's having the same cathode GDL but different anode GDL's. GDL type C with no microporous layer (MPL) is able to reach full current at 0.4 volts from an "off" state (0 A/cm$^2$) as fast as the current can ramp up and maintains it in steady state, from reference (65).

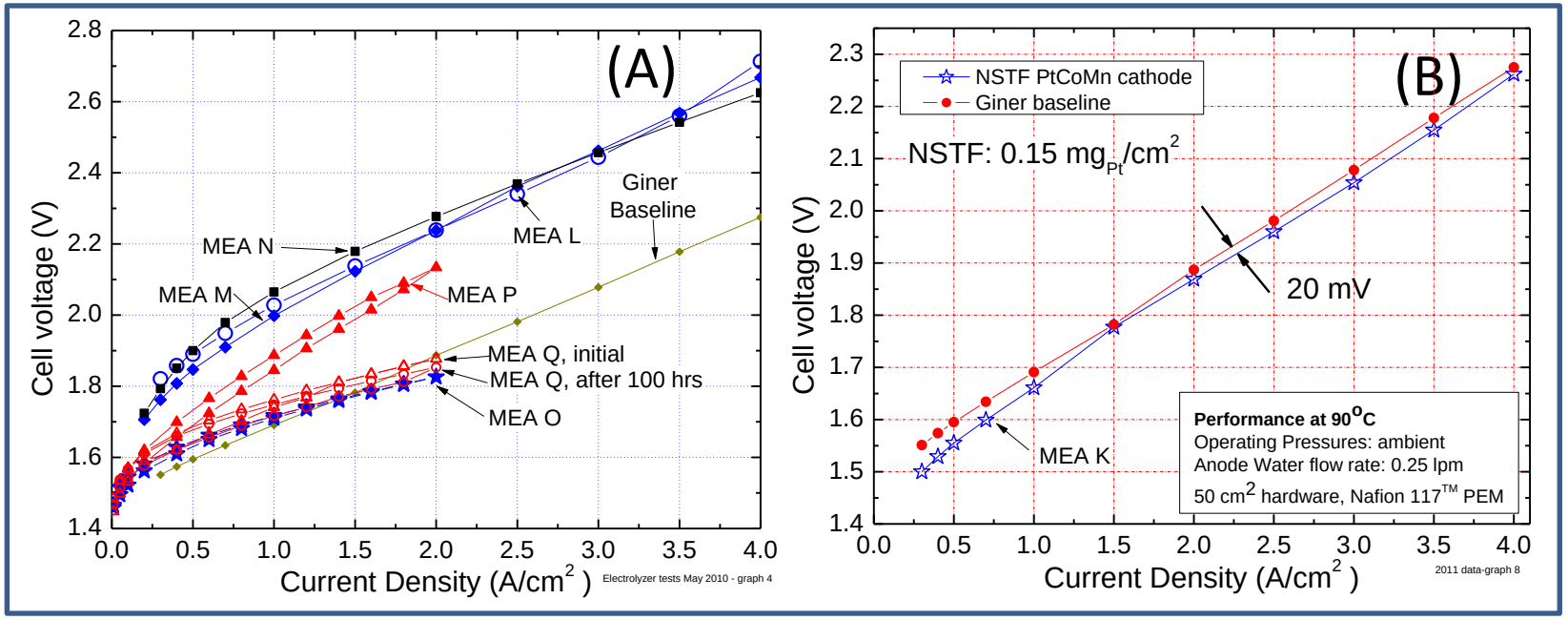


**Figure 16.** $H_2/O_2$ electrolyzer polarization curves, measured in Giner Electrochemical Systems cells, from a series of NSTF catalyst based MEA's having less than 10% of the of the PGM loading as the Giner baseline MEA on (a) the anode and (b) the cathode, from reference (72).

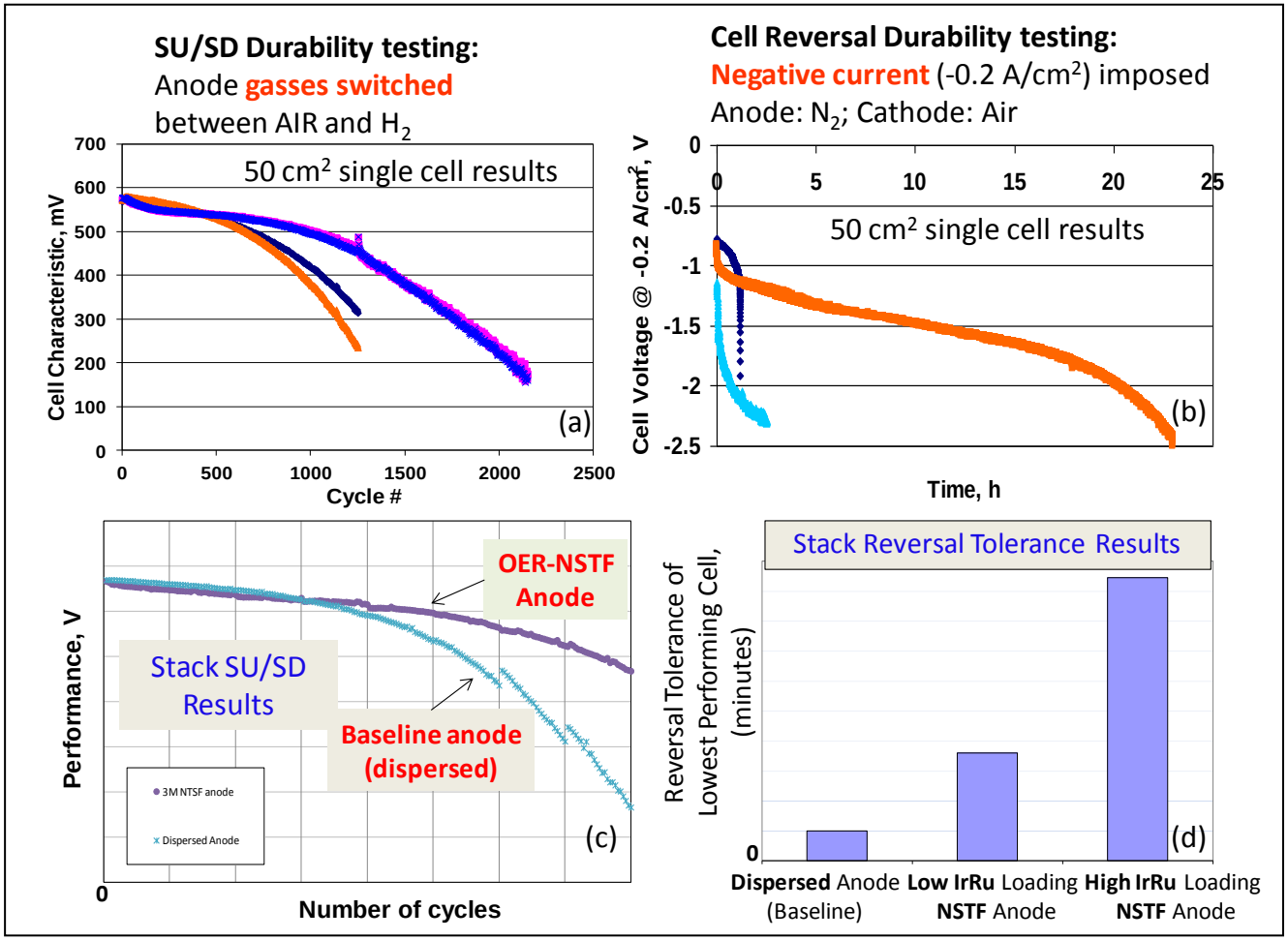


**Figure 17.** Accelerated durability tests for start-up/shut-down and cell reversal in single cells and AFCC short stacks using MEA's having NSTF OER catalysts on the anode versus commercial Pt/C + OER catalysts on the anode: 0.06 mg/cm$^2$ PGM/NSTF vs. 0.05 mg/cm$^2$ commercial Pt/C+ OER, and 0.05 mg/cm$^2$ Pt/NSTF tested for comparison, from references 52 (2011 and 2012). (A) Single cell start-up and shut down test protocol; (B) single cell, cell reversal test protocol; (C) AFCC short stack SU/SD results showing the NSTF OER anode can protect the Pt/C cathode; (D) AFCC short stack cell reversal tolerance results.

ECS Transactions, 41 (1) 937-954 (2011)
10.1149/1.3635628 ©The Electrochemical Society

# Nanostructured Thin Film Electrocatalysts – Current Status and Future Potential

M. K. Debe, R. T. Atanasoski, A. J. Steinbach
3M Fuel Cell Components, 3M Company, St. Paul, MN

3M's nanostructured thin film (NSTF) catalyst technology platform is the only practical example of an extended surface area catalyst which significantly reduces many performance, cost and durability barriers facing electrodes for $H_2$/air PEM fuel cells for vehicles. In this paper we first discuss the recent gains in NSTF alloy ORR activities from both materials and process improvements, followed by accelerated durability tests of MEA's with these catalyst improvements. Next we discuss recent progress in tailoring NSTF anode catalysts with ultra-low precious group metal oxygen evolution reaction (OER) catalysts for high tolerance to automotive start up/shut down and cell reversal events. We follow with our progress in developing strategies and anode GDL's for optimized fuel cell water management for automotive low temperature operation. Finally we discuss a path forward to achieve the entitlement NSTF activity and comment on critical durability issues intrinsic to ultra-low loading catalysts.

## Introduction

In the overall field of heterogeneous electrocatalysts, extended surface area catalysts demonstrate the highest overall potential specific activity for the oxygen reduction reaction (ORR). 3M's nanostructured thin film (NSTF) catalyst technology platform (1-5) is to date the only practical example of an extended surface area catalyst and has been shown to eliminate or significantly reduce many of the performance, cost and durability barriers standing in the way of cathodes and anodes for $H_2$/air PEM fuel cells for vehicles. The NSTF catalysts are formed by high volume capable vacuum sputter-deposition of polycrystalline thin film catalyst alloys onto a supported monolayer of oriented crystalline organic-pigment whiskers. The whisker support particles are immune to corrosion and eliminate the high voltage corrosion plaguing carbon supports. This makes them particularly useful for high voltage applications, such as in electrolyzers and fuel cell MEA anodes where high tolerance to anode fuel starvation events and cell reversal tolerance are required. Besides the catalyst thin film nature, coating method and support characteristics, the other dominant differentiator of the NSTF catalyst from dispersed carbon supported nanoparticles is the electrode thickness. The NSTF electrode thickness is 20 to 30 times thinner and this has both advantages for reduced mass transport losses at high current densities with very low loadings, and complications for cathode water removal for operation at low temperatures.

NSTF catalyst ORR activities have been widely reported on using both RDE methods (6-14) and in fuel cell MEA's (15-18). Accelerated durability stress tests for support corrosion, start/stop, high voltage cycling, OCV and high voltage hold, impurity effects and MEA lifetime load cycling have all been reported as well (16, 19-28). More recent reports of oxygen evolution catalysts applied to the NSTF anodes and cathodes for fuel cell, cell reversal tolerance and electrolyzer applications are also starting to appear (29-34). Finally strategies and approaches to resolve low temperature water management issues characteristic of ultra-thin electrodes have been reported (16, 35-37). In the following we update various fuel cell performance and durability metrics including new

applications for cell reversal tolerant anode catalysts and gas diffusion layers for water management. Key issues remaining for achieving long term durability and reaching the ultimate NSTF ORR activity potential are discussed as well.

## Performance Characteristics

The NSTF – $Pt_{68}Co_{29}Mn_3$ catalyst has been the workhorse cathode and anode of choice for a number of years. With it we have been able to exceed the previous DOE 2015 target of 0.2 g-Pt/kW in a full size short stack with 0.05 mg/cm$^2$ of PGM on the anode and 0.1 mg/cm$^2$ on the cathode (16). More recent work has focused on improving the NSTF-PtCoMn roll-to-roll process so that the support whiskers and sputter deposited catalyst alloy can be applied simultaneously on the moving substrate web in a single step. This new process, called P1, offers greater simplicity and more cost effective coating than the standard process called P4. The key is to make sure it does not reduce performance and hopefully improves it. A series of PtCoMn loadings by the P1 process at 0.054, 0.103, 0.146 and 0.184 mg$_{Pt}$/cm$^2$ were coated in the production equipment and evaluated for structural differences by X-ray diffraction, SEM/TEM and fuel cell performance. SEM indicated no substantial differences at 40,000 magnification, but the TEM and XRD results showed significant changes. Fig. 1 shows that whereas the fcc

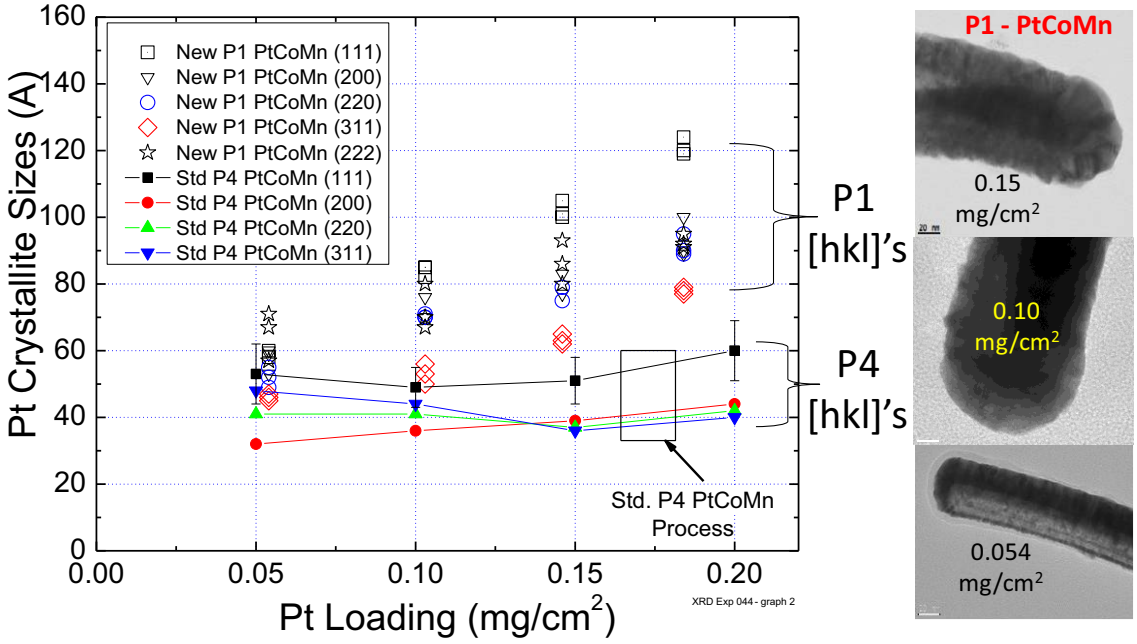


Figure 1. Left: PtCoMn fcc[hkl] grain sizes by XRD as a function of Pt loading for catalysts sputter coated by new process P1 versus the standard process P4. Right: TEM images of the PtCoMn coated whiskers using new deposition process P1. At all three loadings the catalyst coating is smoother than by the standard P4 process that produces whiskerettes as in Fig. 4 and reference (4).

Pt[hkl] grain sizes by the standard process P4 are essentially independent of loading and 4 – 6 nm in size, the P1process produces grain sizes that increase with loading and are larger, 6 – 12 nm. Consistent with this are the TEM images that show the catalyst

coatings on the whiskers are smoother than those obtained by the P4 process, which produces highly oriented whiskerettes growing off the sides of the underlying whisker core, as shown in Fig. 4 and discussed at length in reference (4). This can be understood since aspects of the P1 process provide annealing like conditions.

Fuel cell performance of the P1deposited PtCoMn is also generally the same as with the P4 process, as shown in Fig. 2.

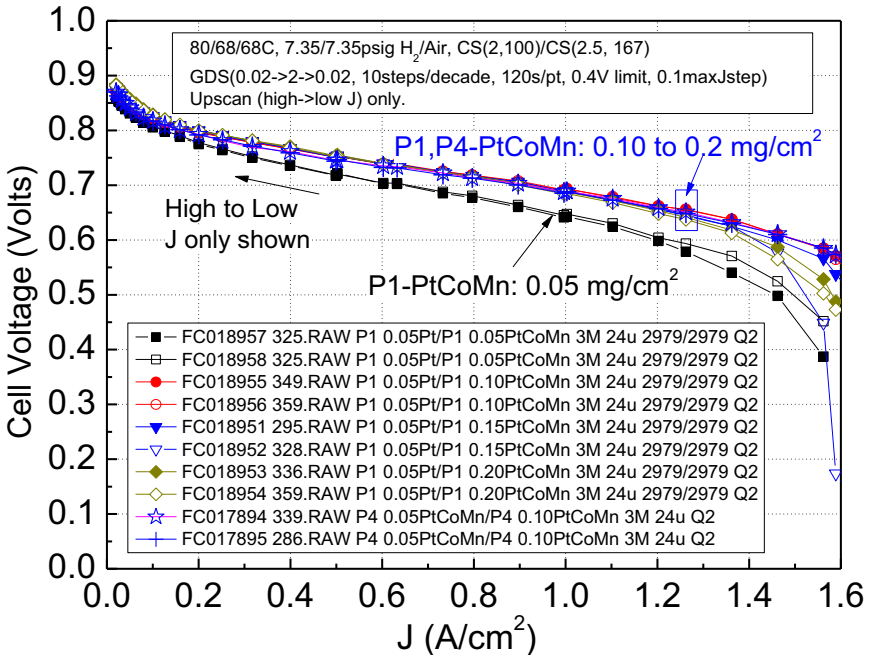


Figure 2. Polarization curves for PtCoMn deposited by the P1 process at 0.05, 0.10, 0.15 and 0.20 $mg_{Pt}/cm^2$, and the P4 process at 0.10 $mg_{Pt}/cm^2$, 80 °C cell temperature, 68°C dew points and 150 kPa $H_2$/air. 3M-24 μm, 850EW PEM. 3M standard GDL's, all 50 $cm^2$. Actual Pt loadings of the cathodes are 0.054, 0.103, 0.146 and 0.184 $mg_{Pt}/cm^2$.

With the conditions shown in the inset of Fig. 2, in the same 50 $cm^2$ cell with quad-serpentine flow fields, using the same station and lots of PEM's and GDL's, the P1 processed anodes and cathodes (0.1 to 0.184 loadings) show very similar performance to each other and to P4 processed 0.10 $mg_Pt/cm^2$ PtCoMn cathode. The galvanodynamic scans with the 0.054 $mg/cm^2$ cathodes are substantially lower (black open and closed squares) but at least as good if not better than historical results with P4 cathodes at these loadings. More careful inspection of the curves in Fig. 2 show the P1 process yields about a 10 mV improvement at 0.32 $A/cm^2$ and 5 mV at 1 $A/cm^2$ over the P4 process, but very similar performance at very low (0.025 $A/cm^2$) and high (1.5 $A/cm^2$) currents. Measurements of the absolute and specific activities at 900 mV under 150 kPa $H_2/O_2$ are very similar for both processes, although the P1 cathodes have slightly higher surface area than the P4 deposited materials, despite the smoother coatings on the whiskers as in Fig. 1. We suspect this may be due to increased nanoporosity of the catalyst surface from improved dealloying resulting from better intermixing of the alloy elements by the P1 process' annealing like conditions. This increased nanoporosity of the flat surface is believed to more than compensate for the reduced roughness factor of the smoothed whiskerettes. In conclusion, there are slight performance benefits and no penalties for the simpler, faster P1 process for depositing the NSTF alloys.

The recently revised 2015 DOE target of 0.125 g-Pt/kW (down from 0.2 g-Pt/kW for 2015) with a total of 0.125 mg/cm$^2$ of PGM per cm$^2$ of MEA will require further work and probably a new NSTF alloy material. This will likely be based on a $Pt_xNi_y$ alloy. As discussed in detail in reference (18) this alloy shows a remarkable dependence of activity on Ni alloy content near a gravimetrically determined as-made composition of 70% Ni.

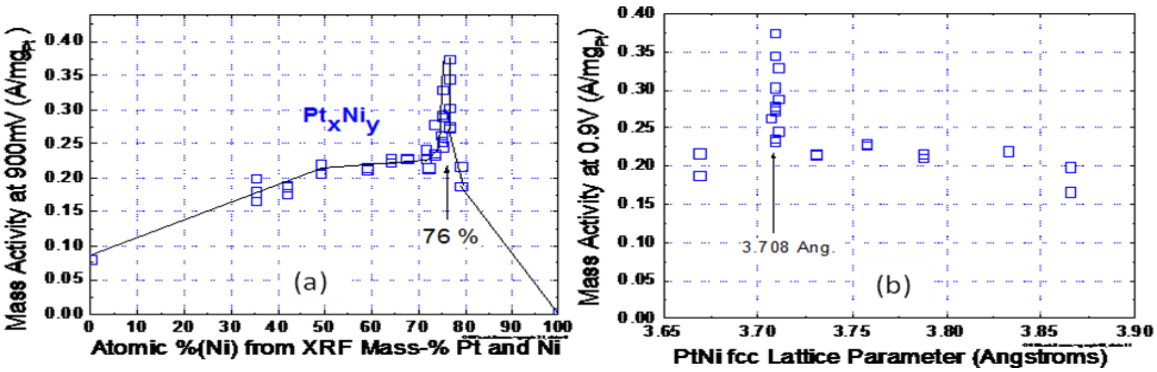


Figure 3. (a) Mass activity of NSTF $Pt_xNi_y$ versus the atomic % Ni measured by XRF. (b) Mass activity as a function of the fcc lattice parameter from X-ray diffraction measurements of the samples in (a). Reproduced from reference (18).

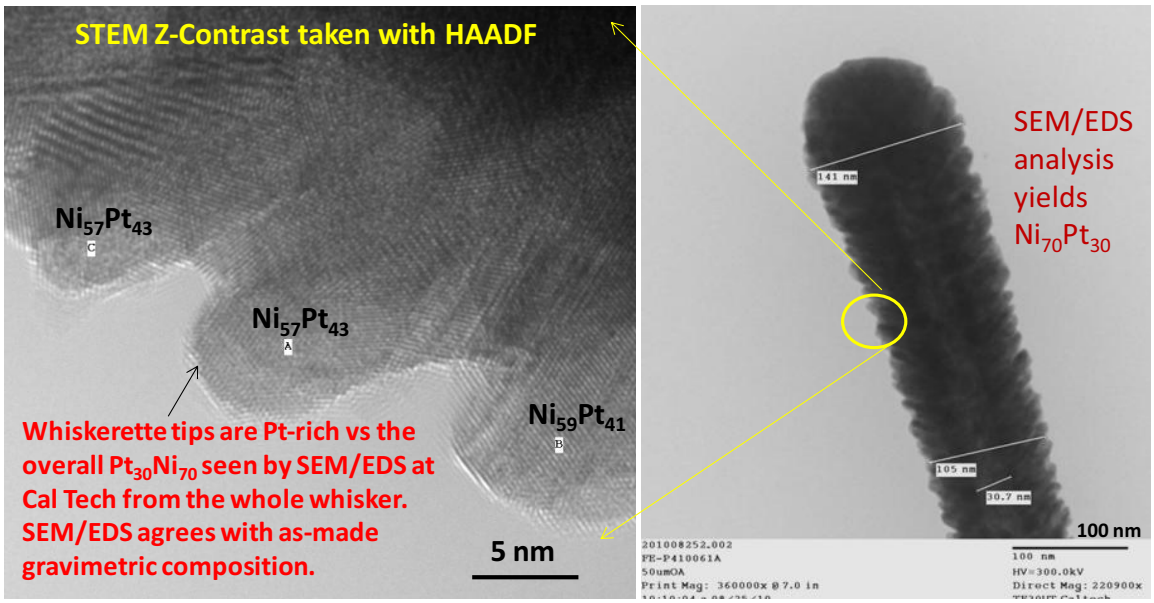


Figure 4. TEM images of roll-good fabricated $Pt_3Ni_7$ alloy coated NSTF whiskers showing the composition of the whiskerettes on the sides of the whiskers have a composition that is Pt-rich versus the overall as-made composition and composition determined from EDS of the whole whisker. Images provided by Carol Garland (Cal Tech) and Charles Hays (JPL).

Fig. 3 reproduces mass activity as a function of at% Ni and lattice parameter. The peak appears to occur at 76 at% by XRF and 62 at% by EMP due to influences of the nanostructure, so we take the gravimetrically determined value of 70 at% Ni as representative of the as-deposited composition. This value has been confirmed on P4 - production coated $Pt_3Ni_7$ catalyst as shown in Fig. 4. Notable in Fig. 4 is that the composition by STEM of the whiskerettes that grow off the sides of the internal crystalline whisker are Pt rich compared to the overall average composition, being closer to $Pt_{43}Ni_{57}$. Since most of the surface area is on the sides of the whiskers, this may better reflect the actual as-made composition of the working surface. Once the catalyst coated whiskers are embedded in the surface of the PEM to make the CCM, the surface composition quickly changes as the PtNi dealloys. This causes both the surface area and specific activity to increase so that the as-made $Pt_3Ni_7$ alloys made by the P4 process produce mass activities in MEA's that are 50% higher than the standard NSTF-PtCoMn. Much higher activities are possible, however, by post-processing the as-made $Pt_3Ni_7$ using another process improvement developed over the past few years. This process we refer to as a surface energy treatment (SET) process that effectively anneals the as-made NSTF catalyst layers prior to their incorporation into a CCM. It is fully roll-to-roll capable and we discuss its effect on the PtNi system next.

## NSTF ORR Specific and Mass Activities

Fig. 5 summarizes the ORR mass and specific activities measured in 50 $cm^2$ MEA's for both the PtCoMn and PtNi systems. The blue squares show the improvement of the as-made $Pt_3Ni_7$ alloy over the $Pt_{68}Co_{29}Mn_3$ alloy. The SET process improves the activities of both the PtCoMn and the PtNi systems, but the latter benefits much more.

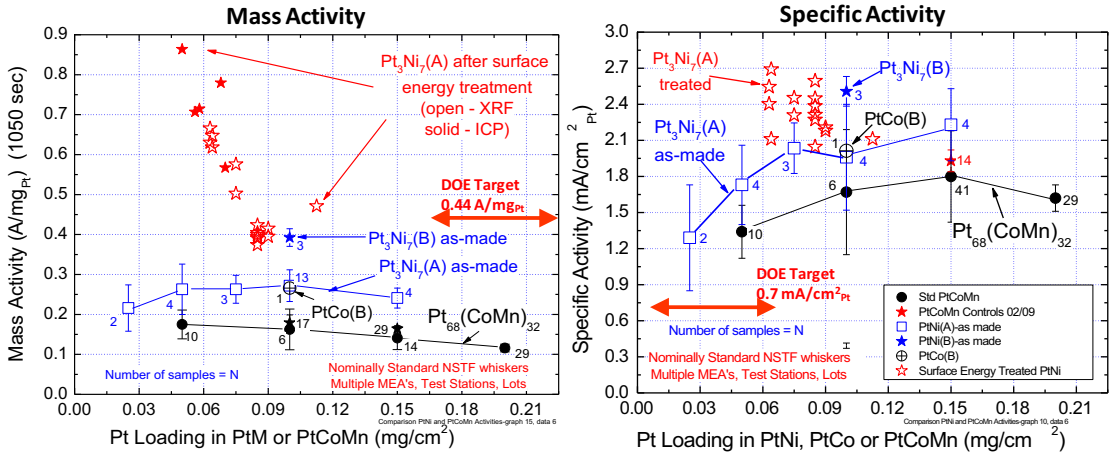


Figure 5. Summary of NSTF alloy ORR mass and specific activity as a function of Pt loading, comparing PtCoMn and $Pt_3Ni_7$ as-made and after surface energy treatment. $Pt_3Ni_7$ (A) was roll-good production fabricated at 3M. $Pt_3Ni_7$ (B) was lab coated at Dalhousie University with extremely thin alternating layers compared to (A).

SET treated production fabricated $Pt_3Ni_7$ (type A) cathodes are shown by the red stars in Fig. 5 and show there is a dramatic improvement of the measured activities. The examples in Fig. 5 were batch processed and it was necessary to re-measure the loading of the catalysts after the SET treatment in order to get accurate mass activities, as there was some loss of catalyst from the 0.1 mg/$cm^2$ as-made loadings. This was done by both

XRF and ICP as indicated by the solid and open red stars in Fig. 5. These values now indicate the promise for significantly exceeding the nominal 2015 DOE electrocatalyst target for mass activity at 900 mV of 0.44 A/mg. To further validate the SET treated $Pt_3Ni_7$ activities, a multi-sample set of 50 $cm^2$ MEA's were produced and measured at both 3M and GM using slightly different ORR activity protocols inherent to each lab. The mass loadings were also measured independently by both labs. Table I summarizes the results which range from 0.35 to 0.59 A/mg depending on the protocols used and confirm that the activity values are very near the DOE targets.

**TABLE I.** Mass activities of surface energy treated $Pt_3Ni_7$ NSTF alloys measured at 3M and GM using independently measured loadings and ORR activity protocols. 50 $cm^2$ MEA's. Lab refers to the place of measurement. ORR protocol refers to the source of the protocol.

| Loading Measurement Method | Lab/ORR Protocol | Mass Activity (A/mg-Pt) at 900 mV |
|---|---|---|
| 3M XRF/ICP | 3M/3M | $0.59 \pm 0.08$ |
| 3M XRF/ICP | GM/3M | $0.51 \pm 0.06$ |
| 3M XRF/ICP | GM/GM | $0.43 \pm 0.06$ |
| GM ICP | GM/3M | $0.42 \pm 0.08$ |
| GM ICP | GM/GM | $0.35 \pm 0.06$ |

Fuel cell performance under $H_2$/air in the kinetic region with the $Pt_3Ni_7$ alloy mirrors the gain in mass activity. However a major issue with the current constructs is that the dealloying of the excess Ni into the membrane severely attenuates the high current density performance above about 0.8 A/$cm^2$, as shown in reference (16, 2011). Proper *ex-situ* dealloying methods are being investigated but ultimately, the structure and composition of the catalyst surface as it actually ends up in the working electrode is what we must make initially to mitigate any complex processing requirements.

## Durability Characteristics

Any new electrocatalyst alloy must have the requisite durability and stability, so we continuously test our new compositions and process improvements against the DOE recommended accelerated stress tests. Most such tests are directed at the cathode, but new advances and strategies for cell reversal tolerant anodes, specifically using NSTF anodes, are also under development (30). We consider both of these in this section.

### Cathode Accelerated Stress Test Status

1.2 V hold. In this test the MEA cathodes are held at 1.2 V vs RHE for nominally 400 hours under 150 kPa $H_2/N_2$ at 80°C. It effectively measures the stability of the catalyst support particle against corrosion. The targets are that ORR activity and surface area will each drop $\leq$ 40%, and the performance at 1.5 A/$cm^2$ will drop less than 30 mV from initial levels. Fig. 6 (left) shows the series of polarization curves (DOE conditions) measured periodically over a total of 435 hours at 1.2 V, for an MEA having the P1 processed PtCoMn on the anode (0.05 mg/$cm^2$) and cathode (0.15 mg/$cm^2$). The MEA used a 3M-supported membrane with a chemical additive. It is apparent that the performance is little affected by the test. Surface area loss was 10%, specific activity was unchanged and the performance at 1.5 A/$cm^2$ dropped only 10 mV, so all targets were met and repeated with a second MEA. These results were expected due to the absence of

corrosion of the NSTF perylene red pigment core whisker at voltages as high as 2.2 V for hundreds of hours as an electrolyzer anode (34).

OCV hold. The objective of this test is assessment of the whole MEA/membrane durability at OCV at 90°C under 30% RH, 250/200 kPa $H_2$/air. The target is 500 hours with less than 20% loss of OCV. Using similar or the same MEA construction as in the 1.2 V hold, six MEA's met the 500 hour limit and cross-over targets before stopping the tests. Two MEA's were allowed to go further and have exceeded 1400 hours with ~ 12% loss of OCV and acceptable $H_2$ cross-over.

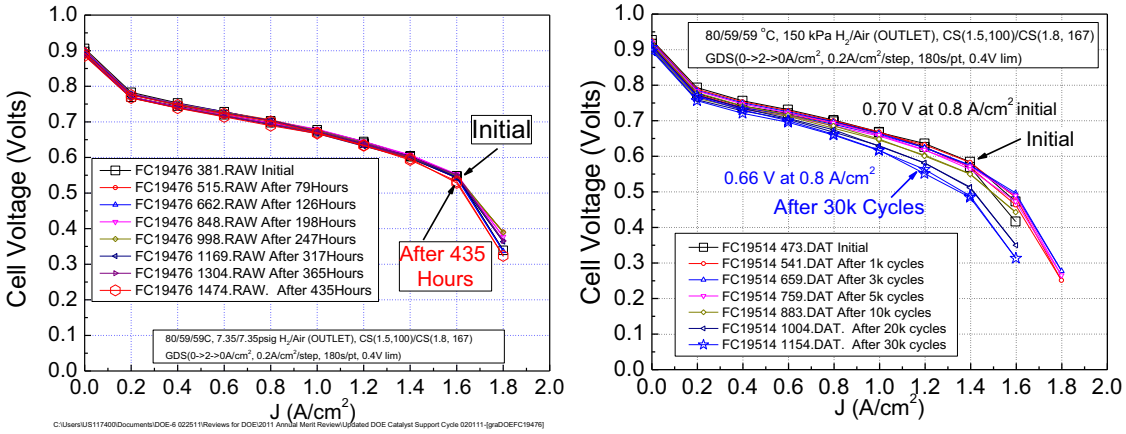


Figure 6. Left: Polarization curves versus time during the DOE 1.2 V hold durability test protocol. Right: Polarization curves versus time during the DOE CV cycling durability test protocol, 0.6 - 1.0 - 0.6 V, 50 mV/sec under 100/100 kPa $H_2/N_2$. Anode /cathode catalysts were all PtCoMn made by the P1 process at 0.05/0.15 $mg_{Pt}/cm^2$ loadings; 3M-supported PEM with additive; standard 3M GDL's.

CV Cycling. This accelerated stress test (AST) characterizes the resistance of the catalyst to dissolution, agglomeration or loss of activity due to high voltage cycling. The protocol involves cycling the cathode between 0.6 and 1.0 volts and back again at 50 mV/sec under 100/100 kPa $H_2/N_2$ at 80 °C cell and dew points. The target is to have after 30,000 cycles, less than 40% loss of surface area and ORR activity and a polarization curve loss of less than 30 mV at 0.8 $A/cm^2$. This test was applied to the same MEA type as used for the previous two AST's. The surface area loss of 18% met and exceeded the DOE target. The mass activity loss was 48% and therefore did not quite meet the target of $\leq$ 40%. Fig. 6 (right) shows the polarization curves before and after 30,000 cycles. The loss of cell voltage at 0.8 $A/cm^2$ was 40 mV and therefore also did not meet the 30 mV target. Further results are given in reference (16), but improvements in stability under this test are required.

## Efficient OER Catalysts for Cell Reversal and Start/Stop Tolerance

One of the key FC durability issues is failure of the catalyst and the other thermodynamically unstable MEA components during start-up/shut-down (SU/SD) and local fuel starvation events at the anode that can lead to cell reversal. During these periods the electrodes can reach potentials up to 2 V. One way to minimize the damage from such transient events is to minimize the potential seen by the electrodes. At lower positive potentials, increased stability of the catalysts themselves and reduced

degradation of the other MEA components is expected. In order to alleviate the damaging effects during transient conditions *from within* the fuel cells, we have modified both the anode and the cathode catalysts to favor the oxidation of water over carbon corrosion by maintaining the cathode potential close to the thermodynamic potential for water oxidation (30). The addition of a small amount of a highly active OER catalyst onto the existing catalyst reduces the overpotential for a given current demand thus reducing the driving force for carbon and platinum dissolution.

In our approach, the key requirements for mitigating both SU/SD and cell reversal events are similar: incorporate an effective OER catalyst with negligible inhibition of the ORR/HOR on the existing cathode/anode NSTF catalyst using minimal amounts of PGM. This is accomplished by sputter depositing the OER catalyst as a separate, discontinuous phase of nanoparticles onto the base of NSTF anode or cathode catalyst coated whiskers. The inherent corrosion resistance of the NSTF support at high potentials makes this a logical choice as a support for the added OER catalyst (19-21). In addition, the NSTF fabrication process of physical vapor deposition via sputtering in vacuum allows for a wide range of OER materials in a variety of compositions to be easily synthesized.

We have shown that the oxides of ruthenium and iridium known to have the best catalytic properties for OER in aqueous solutions, exhibit an excellent activity as tested in fuel cell MEAs under oxygen. For the tests described below, the NSTF Pt loadings of the anode were 0.05 mg/cm$^2$ and the cathode Pt loadings were 0.15 mg/cm$^2$. For SU/SD accelerated stress tests, an additional 1 to 10 μg/cm$^2$ of $Ru_{0.1}Ir_{0.9}$ were added to the cathode and for cell reversal tolerance the OER was added to the anode (30, 2011).

Tests of NSTF-OER Catalysts to Mitigate SU/SD Corrosion. The electrochemical test protocols were designed to mimic a series of real SU/SD events. The electrochemical testing simulating the SU/SD is described as follows. After conditioning and initial electrochemical surface area measurement of the 50 cm$^2$ MEA, the electrode of interest was subjected to a series of pulses during which the potential was ramped at 250 mV/sec from 0.95 to 1.45 volts, held at 1.4 volts until a charge of 5 mC/cm$^2$ was accumulated, then ramped back to 0.95 V and held for 10 seconds until the next pulse. The charge is to mimic the consumption of a substantial amount of the oxygen left in a cathode GDL upon shut-down. This cycle was repeated 10 times, followed by a stay at 0.9 V for 10 seconds. After the 50$^{th}$ such cycle, the cell was held at 0.7 volts for 50 seconds, then returned to 0.9 V briefly before starting another block of 50 cycles. After each block of 1000 such OER pulses, the electrochemical surface area was remeasured as an indication of Pt dissolution. Fig. 7 shows the Pt ECSA versus number of cycles for 6 different samples with 2 and 10 μg/cm$^2$ of OER catalyst. (*No comparative data for pure Pt are available since pure Pt without the additional OER cannot meet the test requirements*). After 10,000 cycles the OER modified Pt/NSTF loses approximately 30 % of its original activity (see inset) towards OER. However, the OER nanoparticle coating protects the Pt catalyst, which loses only 20 % of the initial Pt surface area.

NSTF-OER Catalysts for Cell Reversal Tolerance. From an electrochemical standpoint, the requirements for cell reversal are equivalent to testing the OER activity of the anode at high positive potentials and relatively higher current densities. For this test the protocol consists of ECSA measurements under 1% $H_2$, followed by 20 pulses to 12 mA/cm$^2$ for 60 s, then 20 pulses to 44 mA/cm$^2$ for 30 seconds after which the ECSA is

remeasured. This is then followed by 100 pulses at 200 mA/cm$^2$ for 15 seconds under 100% $H_2$. During each pulse, the cell voltage after t =15 seconds is recorded. Fig. 8 summarizes these voltages at 15 seconds as a function of the three current densities for three loadings of NSTF-Pt with and without the additional OER catalyst. Fig. 8 (left) shows that the OER activity is independent of the underlying Pt loading and with just 10 µg/cm$^2$ of the OER catalyst is able to maintain the voltage below 1.6 V at 0.2 A/cm$^2$.

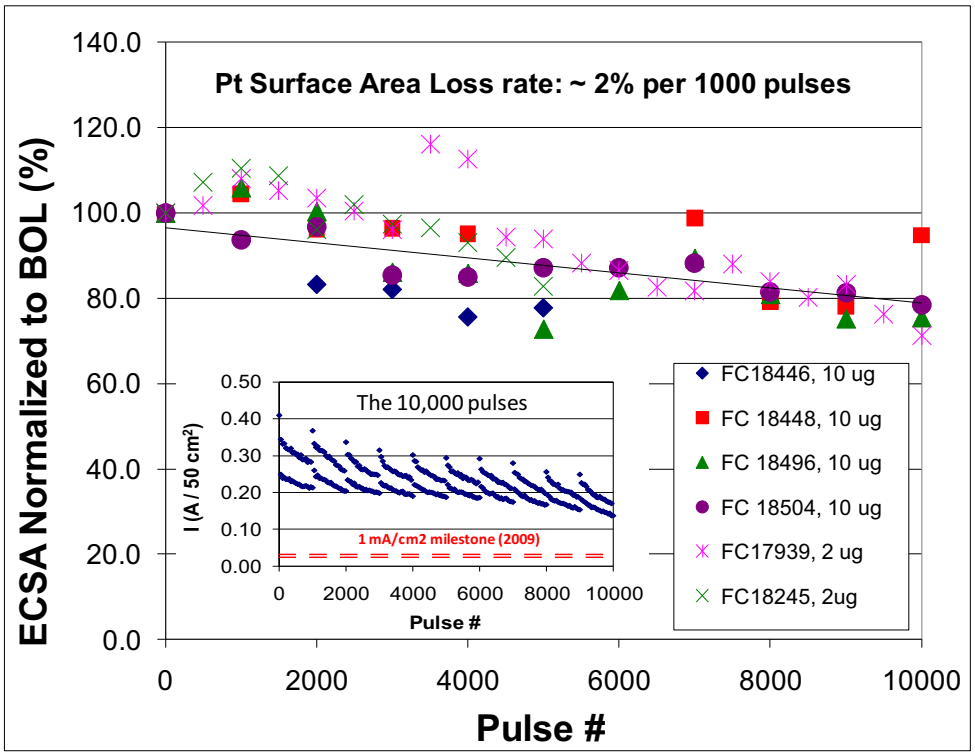


Figure 7. Pt ECSA versus pulse number for 6 different samples with 2 or 10 µg/cm$^2$ of OER catalyst applied to 0.05 mg/cm$^2$ of NSTF-Pt. After 10,000 pulses the OER modified 0.05-Pt/NSTF loses approximately 30 % of its original OER activity (see inset). However, it protects the Pt catalyst, which loses only 20 % of the initial ECSA. The Pt without any OER catalyst does not survive the test.

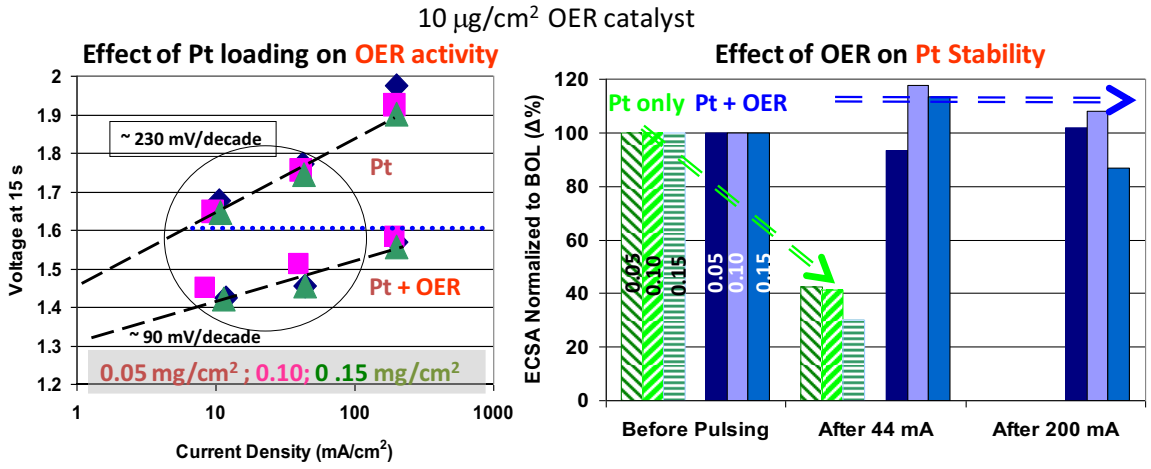

Figure 8. Left: Impact of OER activity on cell reversal current with just 10 μg/cm$^2$ of OER catalyst sputtered onto the NSTF-Pt coated whiskers at 0.05(diamonds), 0.10 (squares) and 0.15(triangles) mg$_{Pt}$/cm$^2$. The voltage is measured at 15 seconds after the start of each pulse to 12, 44 or 200 mA/cm$^2$. The OER activity is independent of Pt loading. Right: ECSA area loss of NSTF-Pt with (solid shaded bars) and without (cross-hatched) the additional OER catalyst after the 10,000 pulses. The presence of the 10 μg/cm$^2$ of OER catalyst protects the underlying Pt at all currents and voltages.

Fig. 8 (right) shows that addition of the 10 μg/cm$^2$ of $Ru_{0.1}Ir_{0.9}$ OER catalyst completely protects the surface area of the underlying Pt by keeping the Pt voltage below 1.6 V, which appears to be the stability limit for the NSTF-Pt by this test.

## Strategies for Water Management at Low Temperatures

Membrane electrode assemblies (MEAs) utilizing the ultra-thin (<1μm) 3M nanostructured thin film catalyst (NSTFC) technology have several demonstrated advantages compared to MEAs comprising conventional, relatively thick (~10μm) carbon-supported catalyst, as noted in the introduction. However, the low temperature (0-50°C) steady state limiting current density of typical NSTFC MEAs under usual operating conditions is substantially lower than that of many conventional catalyst MEAs (0.3 v. 1.6 A/cm$^2$ at 30°C, air cathode, Fig. 9 left). This reduced low temperature performance can be attributed to the NSTFC's much higher water generation rate per unit catalyst volume and to an electrode pore structure that is more susceptible to water condensation. The consequences of this lower performance in the 0-50°C cell temperature regime are primarily related to automotive system startup, where the fuel cell stack has cooled from its normal operating regime (e.g. 60-80°C) and is expected to provide substantial fractions of system rated power shortly after system startup. While system level methods can be employed to reduce the time to reasonable power levels in typical cases, improvements in materials to improve the low temperature performance are likely necessary to minimize system complexity, parasitic power loss from dry-out preconditioning prior to shutdown, and to maximize system robustness to handle atypical startups and freeze-starts from -40°C.

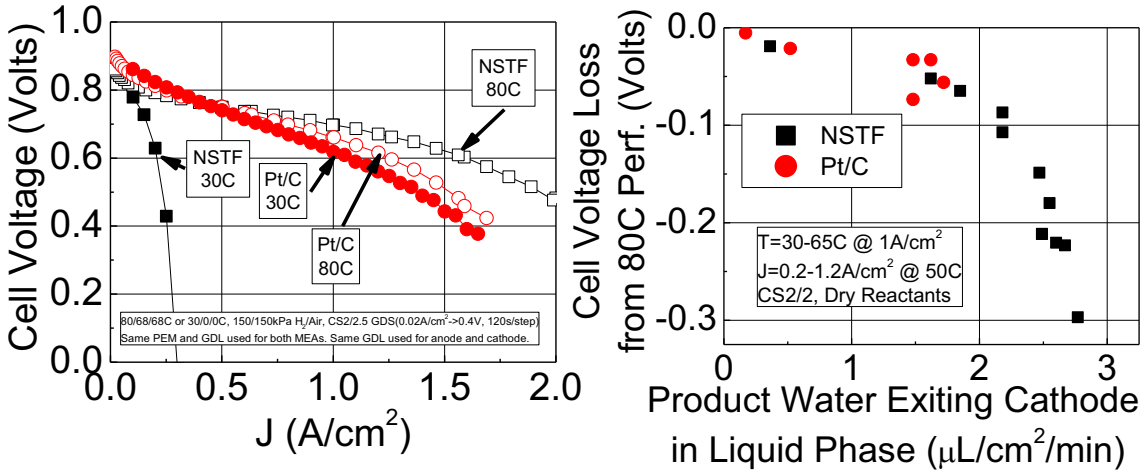


Figure 9. Temperature sensitivity and product water effluent rates of NSTF and Pt/C electrode MEAs.

Recent studies have been conducted to better understand water management differences between NSTF and Pt/C electrode MEAs. In one study, the product water effluent rate out the cathode was evaluated at several conditions where NSTF MEAs typically show reduced performance due to flooding. By calculating the fraction of water exiting the cathode in the liquid phase, using a simple analysis reported previously (37), and plotting against the performance loss from 80 °C reference performance, reasonably quantitative agreement is observed for both NSTF and Pt/C electrode MEAs (Fig. 9 right). A primary conclusion from this study is that liquid phase product water removal out the cathode is detrimental to performance for both electrode types, but at a given set of conditions the total water effluent rate out the cathode is less for Pt/C electrodes than NSTF electrodes.

In light of these results, a logical path forward is based upon the premise of minimizing liquid product water removal out the cathode GDL, which is accomplished by maximizing liquid product water removal out the anode GDL. One such method found to be effective towards this premise is decreasing the total anode pressure to enable both enhanced liquid and vapor phase product water removal out the anode GDL. Fig. 2 shows examples of this method, previously shown by us (37). In Fig. 10 (left), decreasing the anode pressure from 200 to 25kPa resulted in nearly a three-fold gain in the current density at 30°C cell temperature. Fig. 10 (right) shows that the limiting current density increased from 0.4 to over 2A/cm$^2$ as the anode pressure was reduced from 150 to 50kPa at 30 °C.

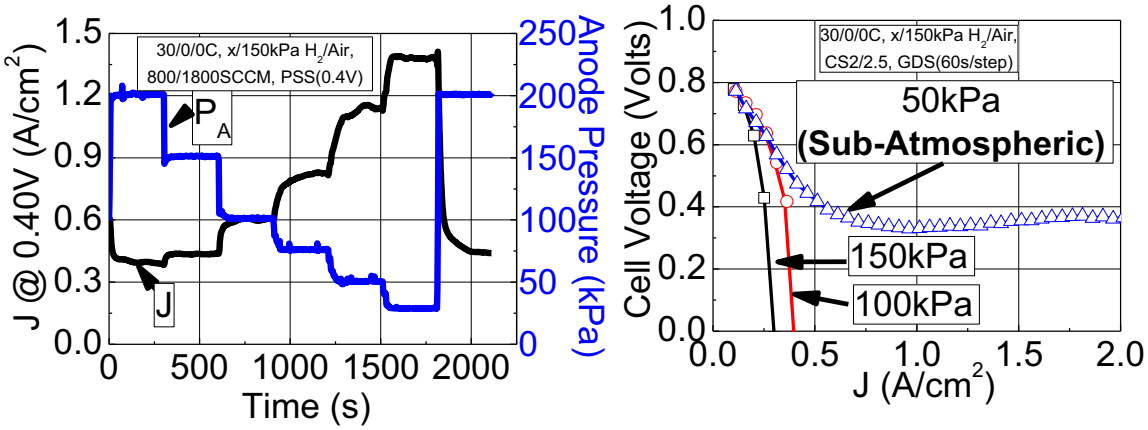


Figure 10. Impact of reduced anode pressure on 30°C steady state and polarization curve performance w/ NSTF MEAs having standard 3M GDL's on both electrodes.

Fig. 11 (left) shows an analysis of the product water effluent removal out the cathode as a function of temperature and reduced anode pressure, which confirmed that performance was maximized as the calculated liquid water flux out the cathode GDL was minimized. Analysis suggested that reduction of the anode pressure enhanced both liquid and vapor phase removal out through the anode GDL, schematically represented in Fig. 11 (right).

In addition to the reduced anode pressure system-level method for improving the low temperature performance of NSTF MEAs, materials development was also found to be a useful and probably more practical solution. Led by the idea of minimizing the product

liquid water removal out the cathode GDL, several different *anode* GDL backings were evaluated to determine their impact on low temperature response. Fig. 12 shows results from four tests where the anode GDL backing was varied; all GDLs contained similar hydrophobic treatments and MPLs applied by 3M. Other examples are in reference (16).

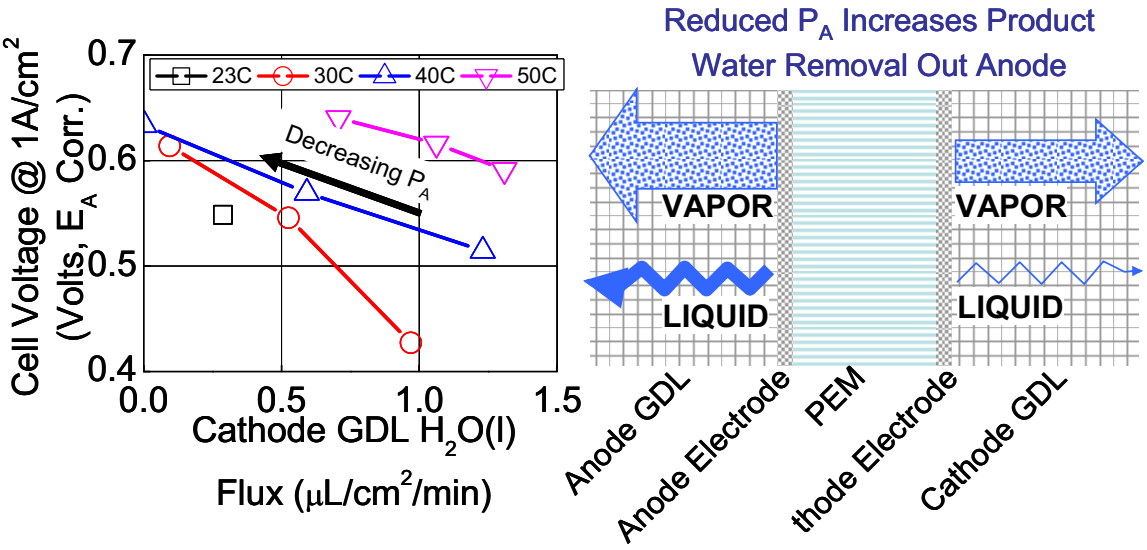


Figure 11. Left: Cell voltage at several cell temperatures and anode pressures v. calculated product water flux out the cathode GDL. Right: Schematic of product water distribution via four generic pathways.

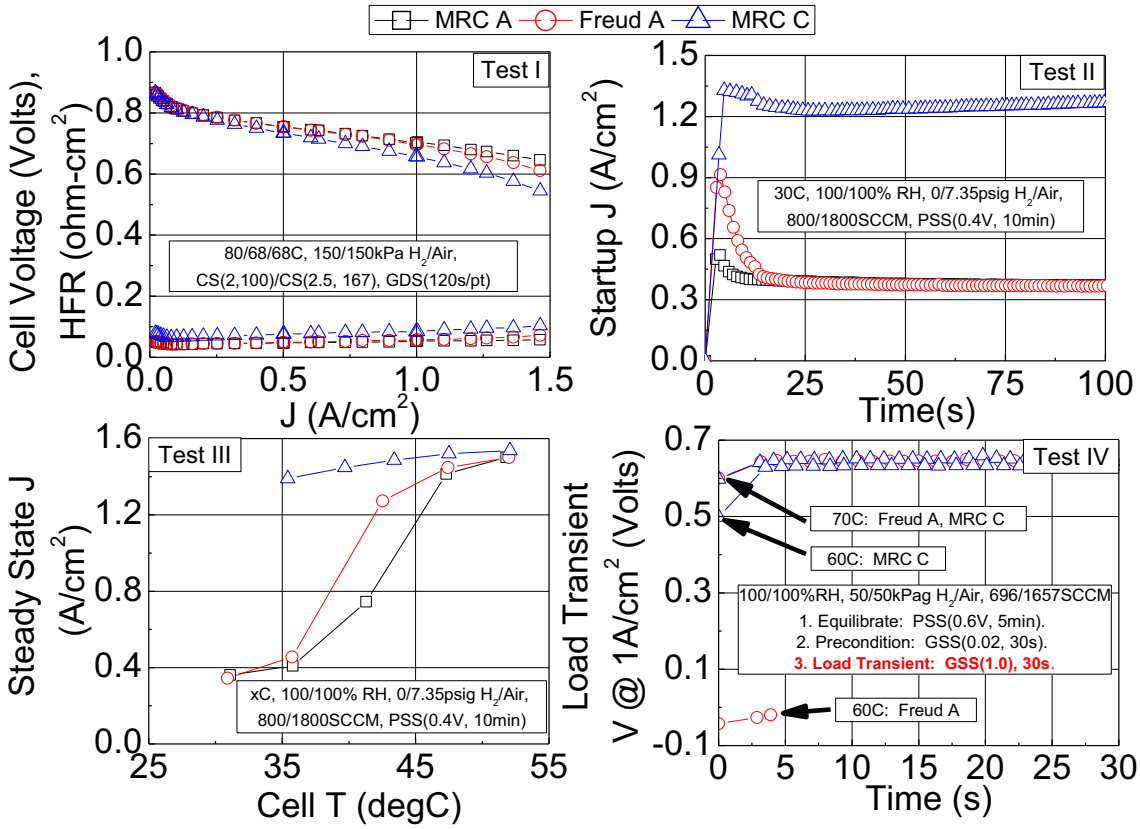


Figure 12. Influence of anode GDL backing on 80°C polarization curve (I), coolstart Transient (II), coolstart steady state (III), and load transient performance (IV).

Under Test I, the MEAs with GDLs MRC A and Freud A yielded similar performance whereas the MEA with MRC C had lower performance at high current density, due to higher HFR. Under Test II, a pseudo-system startup transient, Freud A GDL provided a short burst of higher performance than MRC A, but the current density dropped to the MRC A level within ~15s. MRC C, which had lower performance than the other GDLs under Test I, yielded transient current densities which were 50% higher than Freud A and a steady state current density approximately 3x than of the other two GDLs. Under Test III, MEAs with either MRC A or Freud A GDL had similarly low performances at 30°C. As the cell was heated, the performance with both GDLs improved, with Freud A having better performance at 40°C than MRC A. MRC C, which performed well under Test II, also performed well at low temperatures. As the cell temperature exceeded 50°C, all three MEAs performed similarly. Under Test IV, MEAs with either Freud A or MRC C performed similarly as the current density was stepped up from 0.02 to 1A/cm$^2$ when the cell temperature was 70°C, but at 60°C, Freud A was unable to provide a positive cell voltage at 1A/cm$^2$ whereas MRC C only showed a slight loss relative to 70°C.

The anode GDL properties are the most promising and effective component variable we have identified for solving low temperature cathode flooding with ultra-thin electrodes. Exactly which properties of the GDL are most critical for this function are still unclear and something we are trying to determine. We have also explored gradient cathode electrode options that can also provide some benefit, using hybrid combinations of NSTF and thin Pt/C dispersed layers (16, 2011), but the ratio of benefits to added Pt loading and processing costs are not nearly as favorable as with just anode GDL optimization.

Non-Recoverable Performance Decay Issues for 5000 hour MEA Lifetimes

Achieving the end-of-life performance and lifetimes required for automotive applications at the Pt loadings projected to be required for real commercialization of 8 – 10 g of PGM per vehicle will be a challenge. This translates to about 0.125 mg$_{PGM}$/cm$^2$ total of MEA and rated power levels of over 600 mV at 1.5 A/cm$^2$ minimum. To date, the highest performing conventional dispersed alloy electrodes show unexpected performance losses as the loading is decreased below 0.2 mgPt/cm$^2$ on the cathode (38-41) and hence even beginning of life performances at these lower target loadings are well below the mark. This issue is not as severe with the NSTF electrodes as the fall-off of performance begins at lower loading values. However, all the lifetime degrading issues become much worse at lower loadings, as surface areas are lower so the impact of adsorbing impurities and the general stresses from heat and current density per unit volume of electrode can be much worse. Even with the advanced PtNi NSTF electrodes, the surface areas will be limited to about 30 m$^2$/g and graphitized carbon supported dispersed Pt alloys will not likely be much better (42). With a low surface area NSTF PtCoMn alloy, at 0.2 mg/cm$^2$ we observe single cell reversible decay rates under repetitive galvanodynamic polarization operation that can amount to -4 $\pm$ 2 mA/cm$^2$/hr at 0.7 V, vs -2.0 $\pm$ 0.7 mA/cm$^2$/hr of a high surface area Pt/C at the same loading (22). At lower loadings the decay rates are strongly dependent on loading and are also dependent on the type of membrane. These reversible decays are recoverable by shutting down the

cell and restarting a number of times, in so-called thermal cycles. But some small fraction of the reversible decay is often not recoverable and over time accumulates to a significant non-recoverable performance loss that determines end of life. We do not understand the nature of this non-recoverable loss with very low loaded cathodes but believe that the losses of surface area and specific activity is related to ppb levels of impurities, such as some type of organic anions generated as the membrane is attacked and slowly degrades. This we believe is one of the key issues to understand and resolve at the performance and Pt loadings required for realistic automotive applications.

## Strategies for Reaching Entitlement Performance

Advances in PEM fuel cell electrocatalyst activities have been significant in the past few years. Five key concepts leading to these improvements included use of PtNi alloys; modulated surface composition and lattice strain; extended surface area catalysts; controlled de-alloying; and core-shell catalysts. As shown by Stamenkovic et al. (43) of ANL, the $Pt_3Ni_1$ system is unique in showing the highest ultimate potential ORR activity

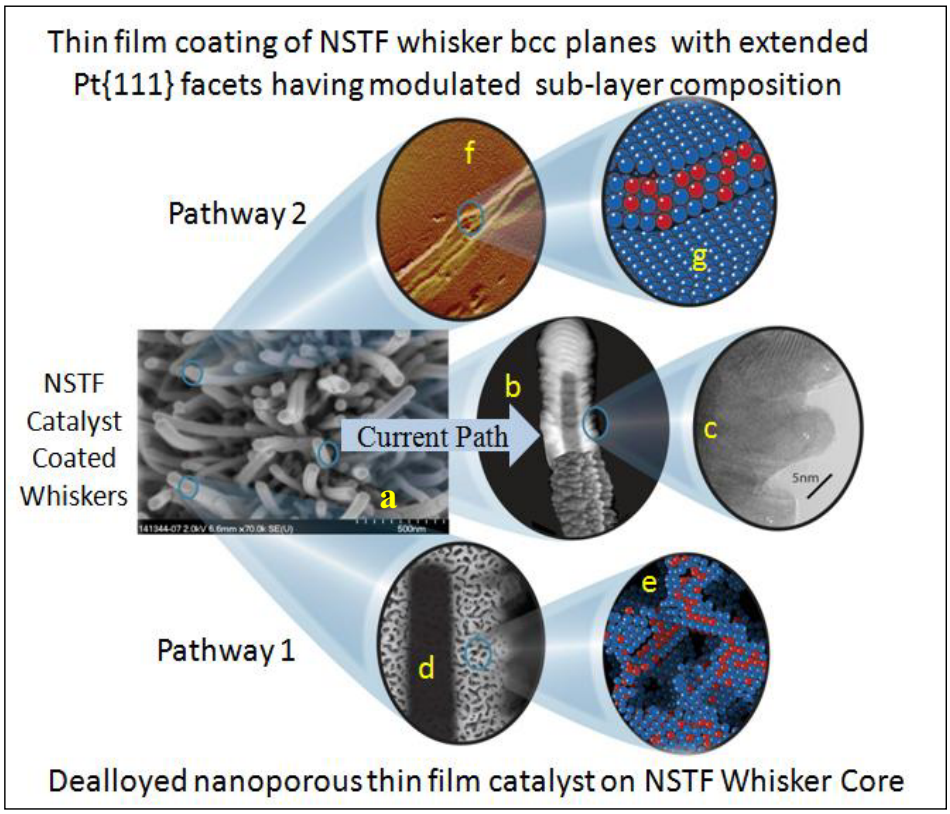


Figure 13. Illustration of two NSTF catalyst advancement pathways combining several of the most promising catalyst concepts in practice today; (a,b,c) show the current status with NSTF as-made whiskerette surface morphology as in Fig. 4. (d,e) show pathway 1 using optimized *ex-situ* de-alloying to increase the surface area while maintaining alloy activity gains. (f,g) show pathway 2 on which the alloy coating morphology on the body-centered crystalline lattice of the NSTF whisker core is optimized like bulk single crystalline $Pt_3Ni_1$ with modulated surface composition in the outer three layers.

in bulk single crystal RDE measurements, with specific activities that are reported to be 90 times that of typical Pt/C catalysts. Key to this high kinetic activity is the formation of large area flat Pt[111] facets on the surface with a modulated surface composition in the top four layers. NSTF PtCoMn polycrystalline film catalysts measured by the same ANL group show RDE activities that are within a factor of about three of their single crystal results with excellent quantitative agreement of the ANL RDE and 3M 50 $cm^2$ fuel cell activities (7). The SET treated $Pt_3Ni_7$ alloys show further improvement by a factor of about two as discussed above with Fig. 5. This suggests there are still further gains to be reached with the NSTF alloys by better control of the catalyst coating morphology on the whiskers.

Fig. 13 illustrates two possible NSTF advanced pathways for incorporating all five of the electrocatalyst concepts mentioned at the start of this paragraph. The whiskerette structure in Fig. 4, the current pathway in Fig. 13(a,b,c) is probably not the best due to the large number of un-coordinated Pt surface atoms on the small [111] facets. Pathway 2 results in a structure such as that illustrated in Fig. 13(f,g). It should be able to match the single crystal results. Another possible approach is suggested by the results of Erlebacher's group with controlled dealloying of high Ni containing Pt alloys (44). As discussed in connection with Table I, proper *ex-situ* dealloying methods are necessary to obtain the ideal nanoporous structure and composition of the NSTF-PtNi catalyst surface so that it retains the high surface area and develops the modulated composition in the outer surface layers necessary for proper surface lattice strain and d-band structure also believed critical to generating high specific activities (45). This pathway is illustrated in Fig. 13(d,e). For both of these approaches, the advantages of the roll-to-roll P1 and SET catalyst deposition and surface energy treatment processes will be utilized.

## Conclusion

In summary, the NSTF type anode and cathode electrocatalysts continue to offer solutions for a number of the barriers facing the longer term needs for fuel cell vehicle commercialization. There are many requirements beyond those reported on here that need to be met, all simultaneously and at economically viable PGM loadings. This is a major challenge for any catalyst approach. For any catalyst type, as the loadings are reduced, issues with durability and sensitivity to nominal as well as off-nominal operating conditions can be expected to worsen. Effects of the other MEA components on the catalyst layers become more pronounced at loadings. Many of these requirements can only properly be judged in short-stack operation, which is clearly more expensive and time consuming, but assures one is working on the right problem, or by long term single cell testing which is also expensive and time consuming. We anticipate that the NSTF PtNi alloys will meet and exceed the beginning of life performance requirements at the 0.125 $mg_{PGM}/cm^2$ total required to match current ICE vehicle PGM content. Demonstrating 5000 hour durability targets in operating stacks will likely take longer due to the complexity of programs necessary to do this. Water management for low temperature transient operation with the ultra-low loaded electrodes should also be possible by some of the approaches discussed here. Freeze tolerance has yet to be seriously characterized but might be expected to be at least as good if not better with the NSTF electrode design. The NSTF anode OER catalysts are perhaps the most likely to be qualified for automotive use first, since there appear to be no negative consequences and

only benefits of adding the minute amounts of OER catalysts. Of course, one never really knows until long term short stack testing is completed.

## Acknowledgments

The Hydrogen, Fuel Cells and Infrastructure Technology Program [in the Office of Energy Efficiency and Renewable Energy] at the US Department of Energy, specifically for Grants DE-FG36-07GO17007 and DE-EE0000456. We also gratefully acknowledge the dedication and efforts of the 3M fuel cell components program members, especially the NSTF development team.

## References

1. Debe, M. K.; Drube, A. R., "Structural characteristics of a uniquely nanostructured organic thin film," *Journal of Vacuum Science & Technology* B: Microelectronics and Nanometer Structures **13**(3), 1236-41 (1995).
2. Debe, M. K.; Poirier, R. J., "Post deposition growth of a uniquely nanostructured organic film by vacuum annealing," *Journal of Vacuum Science & Technology*, A: Vacuum, Surfaces, and Films **12**(4, Pt. 2), 2017-22 (1994).
3. M. K. Debe, in Handbook of Fuel Cells – Fundamentals, Technology and Applications, W. Vielstich, A. Lamm, H. A. Gasteiger, Editors, Ch. 45, John Wiley & Sons (2003).
4. Lajos Gancs, Takeshi Kobayashi, Mark K. Debe, Radoslav Atanasoski, and Andrzej Wieckowski, "Crystallographic Characteristics of Nanostructured Thin Film Fuel Cell Electrocatalysts – A HRTEM Study," Chemistry of Materials **20**, 2444-2454 (2008).
5. M. K. Debe, A. E. Hester, G. D. Vernstrom, A. J. Steinbach, S. M. Hendricks, A. K. Schmoeckel, R. T. Atanasoski, D. J. McClure, and P. L. Turner, "Nanostructured Thin Film Catalysts for PEM Fuel Cells by Vacuum Web Coating, in proceedings of the 50th Annual Tech. Conference of the Society of Vacuum Coaters, Louisville, KY, May 1, 2007**,** 175-185.
6. Arman Bonakdarpour, Krystal Stevens, George D. Vernstrom, Radoslav Atanasoski, Alison K. Schmoeckel, Mark K. Debe, and Jeff R. Dahn, "Oxygen Reduction Activity of Pt and Pt-Mn-Co Electrocatalysts Sputtered on Nanostructured Thin Film Support," Electrochimica Acta **53** (2007) 688-694.
7. D. Van der Vliet, D. Strmcnik, C. Wang, R. Atanasoski, M. Debe. N. Markovic and V. Stamenkovic, "Multimetallic Catalysts for Oxygen Reduction Reaction," 216th ECS Meeting, Vienna, Austria, Oct. 4-9, 2009.
8. K. J. J. Mayrhofer, D. Strmcnik, B. B. Blizanac, V. Stamenkovic, M. Arenz, N. M. Markovic, "Measurement of oxygen reduction activities via the rotating disc electrode method: From Pt model surfaces to carbon-supported high surface area catalysts," *Electrochimica Acta* **53** (2008) 3181-3188.
9. Arman Bonakdarpour, Tara R. Dahn, Radoslav Atanasoski, Mark K. Debe, and Jeff R. Dahn, "$H_2O_2$ Release During Oxygen Reduction Reaction on Pt Nano Particles," *Electrochemical and Solid-State Letters*, **11,** B208-B211, 2008.
10. D. A. Stevens, S. Wang, R. J. Sanderson, G. C. K. Liu, G. D. Vernstrom, R. T. Atanasoski, M. K. Debe and J. R. Dahn, "A combined rotating disk electrode/X-ray diffraction study of Co dissolution from $Pt_{1-x}Co_x$ Alloys," *J. Electrochem. Soc.* **158**(8) B899-B904 (2011).
11. Liu, Gary C-K.; Sanderson, R. J.; Vernstrom, G; Stevens, D. A.; Atanasoski, R. T.; Debe, M. K.; Dahn, J. R., "RDE Measurements of ORR Activity of $Pt_{1-x}$ $Ir_x$ ($0<x<0.3$) on High Surface Area NSTF-Coated Glassy Carbon Disks," *J. Electrochem. Soc.* (2010), **157**(2), B207-B214.
12. Gary Chih-Kang, D. A. Stevens, J. C. Burns, R. J. Sanderson, G. D. Vernstrom, R. T. Atanasoski, M. K. Debe and J. R. Dahn, "Oxygen reduction activity of dealloyed $Pt_{1-x}Ni_x$ catalysts." *J. Electrochem. Soc.* **158**(8) B919-B26 (2011).

13. D. A. Stevens, R. Mehrotra, R. J. Sanderson, G. D. Vernstrom, R. T. Atanasoski, M. K. Debe and J. R. Dahn, "Dissolution of Ni from high Ni content $Pt_{1-x}Ni_x$ alloys," *J. Electrochem. Soc.* **158**(8) B905-B909 (2011).
14. Dennis van der Vliet, Chao Wang, Mark Debe, Radoslav Atanasoski, Nenad M. Markovic and Vojislav R. Stamenkovic, "Platinum-alloy Nanostructured Thin Film Catalysts for the Oxygen Reduction Reaction," submitted to *Electrochimica Acta*.
15. Stevens, D. A.; Rouleau, J. M.; Mar, R. E.; Bonakdarpour, A.; Atanasoski, R. T.; Schmoeckel, A. K.; Debe, M. K.; Dahn, J. R., "Characterization and PEMFC Testing of $Pt_{1-x}M_x$ (M=Ru, Mo, Co, Ta, Au, Sn) Anode Electrocatalyst Composition Spreads," *J. of the Electrochemical Society* (2007), **154**(6), B566-B576.
16. M. K. Debe, 2009 to 2011 *DOE Hydrogen Program Reviews*, Washington, D.C. 2009:http://www.hydrogen.energy.gov/pdfs/review09/fc_17_debe.pdf 2010:http://www.hydrogen.energy.gov/pdfs/review10/fc001_debe_2010_o_web.pdf, 2011:http://www.hydrogen.energy.gov/pdfs/review11/fc001_debe_2011_o.pdf
17. A. K. Schmoeckel, G. D. Vernstrom, A. J. Steinbach, S. M. Hendricks, R. T. Atanasoski and M. K. Debe, "Nanostructured Thin Film Ternary Catalyst Activities for Oxygen Reduction," 2006 Fuel Cell Seminar, Honolulu, Hawaii, Nov. 13-17, 2006.
18. M. Debe, A. Steinbach, G. Vernstrom, S. M. Hendricks, M. J. Kurkowski, R. T. Atanasoski, P. Kadera, D. A. Stevens, R. J. Sanderson, E. Marvel and J. R. Dahn, "Extraordinary oxygen reduction activity of $Pt_3Ni_7$," *J. Electrochem. Soc.* **158**(8) B910-B918 (2011).
19. Debe, M. K.; Schmoeckel, A.; Hendricks, S.; Vernstrom, G.; Haugen, G.; Atanasoski, R., "Durability Aspects of Nanostructured Thin film Catalysts for PEM Fuel Cells," *ECS Transactions* **1**(8) 51-66 (2006).
20. Debe, M. K.; Schmoeckel, A. K.; Vernstrom, G. D.; Atanasoski, R., "High voltage stability of nanostructured thin film catalysts for PEM fuel cells," *Journal of Power Sources* **161**, 1002 (2006).
21. A. J. Steinbach, K. Noda and M. K. Debe, "Stop-Start and High-Current Durability Testing of Nanostructured Thin film Catalysts for PEM Fuel Cells," *ECS Trans.* **3**(1) 835-853, 2006.
22. A. J. Steinbach, C. V. Hamilton, Jr., and M. K. Debe, "Impact of Micromolar Concentration of Externally-Provided Chloride and Sulfide Contaminants of PEMFC Reversible Stability," *ECS Trans.* **11**(1) 889-902 (2007).
23. A. J. Steinbach, K. Alade-Lambo, H. Le and M. K. Debe, "Investigation of Cation-Induced Performance Losses in PEM Fuel Cells," 2008 Fuel Cell Seminar and Exposition, Phoenix, AZ, Oct. 27, (2008) Ext. Abstract GHT35a-22.
24. Stevens, D. A.; Wang, S.; Sanderson, R. J.; Garsuch, A.; Debe, M.K.; Hendricks, S. M.; Atanasoski, R. T.; Dahn, J. R., "Assessing the $Pt_{upd}$ Surface Area Stability of $Pt_{1-x}M_x$ (M=Re, Nb, Bi) Solid Solutions for Proton Exchange Membrane Fuel Cells," *Journal of the Electrochemical Society* (2010), **157**(5), B737-B743.
25. Garsuch, Arnd; Stevens, D. A.; Sanderson, R. J.; Wang, S.; Atanasoski, R.T.; Hendricks, S.; Debe, M. K.; Dahn, J. R., "Alternative Catalyst Supports Deposited on Nanostructured Thin Films for Proton Exchange Membrane Fuel Cells," *Journal of the Electrochemical Society* (2010), **157**(2), B187-B194.
26. Stevens, D. A.; Rouleau, J. M.; Mar, R. E.; Atanasoski, R. T.; Schmoeckel, A. K.; Debe, M. K.; Dahn, J. R., "Enhanced CO-Tolerance of Pt-Ru-Mo Hydrogen Oxidation Catalysts," *Journal of the Electrochemical Society* **154**(12), B1211-B1219 (2007).
27. Bonakdarpour, A.; Lobel, R.; Atanasoski, R. T.; Vernstrom, G. D.; Schmoeckel, A. K.; Debe, M. K.; Dahn, J. R., "Dissolution of transition metals in combinatorially sputtered $Pt_{1-x-y}M_xM'_y$ (M, M' = Co, Ni, Mn, Fe) PEMFC electrocatalysts," *J. of the Electrochemical Society* (2006), **153**(10), A1835-A1846.
28. Bonakdarpour, A.; Wenzel, J.; Stevens, D. A.; Sheng, S.; Monchesky, T. L.; Lobel, R.; Atanasoski, R. T.; Schmoeckel, A. K.; Vernstrom, G. D.; Debe, M. K.; Dahn, J. R., "Studies of Transition Metal Dissolution from Combinatorially Sputtered, Nanostructured $Pt_{1-x}$ $M_x$ (M

= Fe, Ni; 0<x<1) Electrocatalysts for PEM Fuel Cell," *Journal of the Electrochemical Society* **152**(1), A61-A72 (2005).
29. D. A. Cullen, K. L. More, K. S. Reeves, G. D. Vernstrom, L. L. Atanasoska, G. M. Haugen and R. T. Atanasoski, "Characterization of durable nanostructured thin film catalysts tested under transient conditions using analytical aberration-corrected electron microscopy," Abstract #1201, 220th ECS Meeting, Boston, MA, Oct. 9-14, 2011.
30. R. T. Atanasoski, 2011 *DOE Hydrogen Program Review*, FC006, May 9-13, 2011, and FC006, June 8, 2010, Washington, D.C. http://www.hydrogen.energy.gov/pdfs/review11/fc006_atanasoski_o_web.pdf http://www.hydrogen.energy.gov/pdfs/review10/fc006_atanasoski_o_web.pdf
31. G. D. Vernstrom, L. L. Atanasoska, G. M. Haugen and R. T. Atanasoski, "Catalyst durability for fuel cells under start-up and shutdown conditions: Evaluation of Ru and Ir sputter deposited on platinum in PEM environment," Abstract #1106, 220th ECS Meeting, Boston, MA, Oct. 9-14, 2011.
32. K. E. Ayers, E. B. Anderson, C. B. Capuano, B. D. Carter, L. T. Dalton, G. Hanlon, *ECS Transactions* **33**(1) 3-15 (2010)
33. Monjid Hamden, 2011 *DOE Hydrogen Program Review*, PD030 May 11, Washington, D.C. http://www.hydrogen.energy.gov/pdfs/review11/pd030_hamdan_o_web.pdf
34. M. Debe, S. M. Hendricks, G. Vernstrom, J. Wiley, M. Hamden, C. Mittelsteadt, C. Capuano, K. Ayers and E. Anderson, "Initial Performance and Durability of Ultra-low Loaded NSTF Electrodes for PEM Electrolyzers," Abs. #694, 220Th ECS Meeting, Boston, MA, Oct., 2011.
35. A. Steinbach, M. Debe, M. Pejsa, D. Peppin, A. Haug, M. Kurkowski and S. Maier-Hendricks, "Influence of Anode GDL on PEMFC Ultra-thin Electrode Water Management at Low Temperatures," Abstract #781, 220th ECS Meeting, Boston, MA, Oct. 9-14, 2011.
36. Debe, M. K. and Steinbach, A. J., "An empirical model for the flooding behavior of ultra-thin PEM fuel cell electrodes," *ECS Transactions* **11**(1) 659-673 (2007).
37. A. J. Steinbach, M. K. Debe, J. L. Wong, M. J. Kurkowski, A. T. Haug, D. M. Peppin, S. K. Deppe, S. M. Hendricks, and E. M. Fischer, "A New Paradigm for PEMFC Ultra-Thin Electrode Water Management at Low Temperatures," *ECS Trans*., **33(1)**, 1179-1188 (2010).
38. F. T. Wagner, B. Lakshmanan and M. F. Mathias, "Electrochemistry and the Future of the Automobile," J. of Physical Chemistry Lett. **2010**, 1, 2204-2219.
39. T. Greszler, S. Kumaraguru, N. Subramanian, B. Litteer, Z. Liu and R. Makharia, "Hydrogen-Air Performance of Carbon –Supported Pt-alloy Catalyst Measured at High Current Density in Proton Exchange Membrane (PEM) Fuel Cells," 2008 Fuel Cell Seminar, Phoenix, AZ, Oct. 28, 2008. http://www.fuelcellseminar.com/assets/pdf/2008/wednesdayPM/GHT33-2_SKumaraguru.ppt.pd
40. K. Sakai, K. Sato, T. Mashio, A. Ohma, K. Yamaguchi, and K. Shinohara, "Analysis of Reactant Gas Transport in Catalyst Layers: Effect of Pt-Loadings," ECS Transactions 25(1) 1193-1201 (2009).
41. P. Y. Abel Chuang, "Fuel Cell Vehicle Commercial Applications and Challenges in Stack Research and Development," 2010 Fuel Cell Seminar and Exposition, San Antonio, TX, Oct. 19, 2010.
42. Frederick T. Wagner, "Automotive Challenges and Opportunities for Oxygen Reduction Catalysts," 1st CARISMA International Conf., La Grande Motte, France, Sept. 23, 2008.
43. V.R. Stamenkovic, B. Fowler, B.S. Mun, G. Wang, P.N. Ross, C.A. Lucas, N.M. Markovic,"Improved Oxygen Reduction Activity on $Pt_3Ni(111)$ via Increased Surface Site Availability," *Science*, **(2007)**, 315, 493-497.
44. J. Snyder, T. Fujita, M. W. Chen and J. Erlebacher, "Oxygen reduction in nanoporous metal-ionic liquid composite electrocatalysts," Nature Materials 9 (2010) 904-907.
45. P. Strasser, S. Kohr, T. Anniyev, J. Greeley, K. More, C. Yu, Z. Liu, S. Kaya, D. Nordlund, H. Ogasawara, M. Toney and A. Nilsson, "Lattice-strain control of the activity in dealloyed core-shell fuel cell catalysts," Nature Chemistry **2**, 454 (2010).

*Journal of The Electrochemical Society*, **158** (8) B910-B918 (2011)
0013-4651/2011/158(8)/B910/9/$28.00 © The Electrochemical Society

# Extraordinary Oxygen Reduction Activity of $Pt_3Ni_7$

**M. K. Debe,[a,*,z] A. J. Steinbach,[a,*] G. D. Vernstrom,[a,*] S. M. Hendricks,[a] M. J. Kurkowski,[a] R. T. Atanasoski,[a,*] P. Kadera,[a] D. A. Stevens,[b,*] R. J. Sanderson,[b] E. Marvel,[b] and J. R. Dahn[b,*]**

[a]*Fuel Cell Components Program, 3M Co. 201-2N-19, 3M Center, St. Paul, Minnesota 55144-1000*
[b]*Departments of Physics and Chemistry, Dalhousie University, Halifax, Nova Scotia, Canada B3H 3JS*

Nanostructured thin film catalysts (NSTF) with widely varying compositions of $Pt_xM_y$ and $Pt_xM_yN_z$ (M, N = Ni, Co, Zr, Hf, Fe, Mn) have been evaluated for $0 \leq x, y, z < 1$. The catalysts' activity for oxygen reduction (ORR) was measured in 50 $cm^2$ fuel cell membrane electrode assemblies. $Pt_{1-x}Ni_x$ was found to be unique in showing an extraordinarily sharp peak in ORR activity as a function of the as-made composition around $x = 0.69 \pm 0.02$ determined gravimetrically. This composition gave a corresponding fcc lattice parameter of 3.71 Angstroms and a grain size of 7.5 nm. Both surface area and specific activity increases contribute to the increased mass activity of the resultant dealloyed films. The ORR mass activity of the $Pt_3Ni_7$ is 60% higher than for the NSTF standard $Pt_{68}Co_{29}Mn_3$ alloy. Rotating disk electrode measurements of a $Pt_{1-x}Ni_x$ series on NSTF coated glassy carbon disks show a similar large and sharp peak in activity. In contrast, PtCo shows a diminished but still sharply peaked mass activity in 50 $cm^2$ tests near $x = 0.62$ by electron microprobe over the $0 < x < 0.7$ range examined.
 [DOI: 10.1149/1.3595748] 

Manuscript submitted January 25, 2011; revised manuscript received April 11, 2011. Published June 8, 2011. This was Paper 689 presented at the Las Vegas, Nevada, Meeting of the Society, October 10–15, 2010.

Proton exchange membrane fuel cell systems must meet demanding performance, durability, and cost targets simultaneously if commercialization for automotive applications is to be successful.[1] The MEA (membrane electrode assembly) at the heart of the fuel cell must also pass challenging performance, durability, quality and cost targets. To a significant degree, deficiencies in state of the art MEAs are traceable to properties of the Pt based cathode catalysts in use today, with mass activity, rated specific power density ($kW/g_{Pt}$), resistance to Pt dissolution and agglomeration, and stability of oxygen reduction activity among the most critical. 3M's nanostructured thin film (NSTF) catalyst technology platform[2,3] has been shown to eliminate or significantly reduce many of these issues. Catalyst specific activity[4–6] and durability[7–9] can be significantly higher than conventional carbon supported Pt catalysts. Currently the NSTF based MEA designated as "2009 best of class," with $Pt_{68}Co_{29}Mn_3$ alloy catalysts at 0.15 $mg_{Pt}/cm^2$ total loading per MEA has met all but one of the currently specified DOE 2015 targets for performance and durability under designated testing protocols, including specific power density (g-Pt/kW) in a short stack, total PGM loading, and various accelerated stress tests such as OCV hold, 5000 h load cycling, high voltage cycling and long duration holds.[10] The remaining mass activity target of 0.44 $A/mg_{Pt}$ is met with the PtCoMn catalyst in rotating disk electrode measurements but the latter falls about 40% short of the target in standardized 50 $cm^2$ fuel cell measurements at 900 mV and 150 kPa of saturated $O_2$.[10,11] The NSTF catalyst fabrication processes are highly facile for rapid preparation and screening of new alloy compositions. Over ninety $Pt_xM_yN_z$ (M, N transition metals, TM) ternary compositions were investigated under a previous DOE/3M cooperative agreement,[12] with M, N = Co, Ni, Fe, Mn. Most Pt/TM ratios were between 0.5 and 3.0 in that study. More recently we have continued to explore these common Pt/transition metal (TM) binary materials but over a broader range of atomic %TM:Pt ratios, and with a much finer mesh. We have discovered NSTF-$Pt_{1-x}Ni_x$ to be unique in showing an extraordinarily sharp and high peak in activity as a function of composition gravimetrically determined around $x = 0.7$, or $Pt_3Ni_7$, correlating to an fcc lattice parameter of 3.71 Angstroms and 7.5 nm grain size. The value of the as-made composition at the peak ORR activity varies to some extent, depending on the technique used to measure it. Both surface area and specific activity increases contribute to the increased mass activity of the in-situ dealloyed electrodes. The ORR mass activity of the as-made $Pt_3Ni_7$ is 60% higher than for the NSTF standard $Pt_{68}Co_{29}Mn_3$ alloy, but suffers from lower values of limiting currents due to dealloying and subsequent dissolution of the excess Ni into the membrane and its effect on water management. Rotating disc electrode (RDE) measurements of a compositional spread of $Pt_{1-x}Ni_x$ for $(0.2 < x < 0.84)$ sputter-deposited onto NSTF whisker coated glassy carbon disks show a similar behavior to the fuel cell measurements. A similar series of $Pt_{1-x}Co_x$ 50 $cm^2$ fuel cell measurements also show a peak in activity at $x = \sim 0.62$ determined by EMP, but its width and amplitude are broader and smaller than that seen with $Pt_{1-x}Ni_x$. A literature summary of recent high Ni or Co loaded PtM binary electrocatalyst studies show similar increased activities at high values of Ni but do not report the strong response of ORR activity dependence on composition nor its correlation with grain size and lattice parameter concluded here.

## Experimental

*Catalyst preparation and evaluation.*—The NSTF binary and ternary catalysts were formed by vacuum sputter-deposition of metal multi-layers onto a supported monolayer of oriented crystalline organic-pigment whiskers.[3] The process for fabricating the crystalline whisker support film and subsequent over coating with catalyst is scaled-up as a roll-to-roll web coating process.[13] For all of the catalyst compositions studied in this work in 50 $cm^2$ cells, the NSTF whisker support films used were roll-good fabricated. For the majority of the catalyst alloys coated onto those whisker supports, the catalysts were sputter deposited in a batch loaded vacuum chamber with multiple sputtering targets chosen for the particular alloy composition to be made, as described in detail in section 2.1.3 of Ref. 12. For several of the $Pt_3Ni_7$ MEA's, the catalysts were also fabricated using the 3M roll-to-roll sputtering process (process A). For all these, the Pt and transition metal alloy loadings are controlled by gravimetric calibration of the sputter deposition rates and known to be accurate to ±5% both cross-web and down-web.

Several samples of $Pt_3Ni_7$ and a $Pt_{1-x}Co_x$ series were also sputter coated from separate Pt, Ni and Co targets onto 50 $cm^2$ sized areas of the NSTF whisker support films in a batch sputter coater at Dalhousie University (process B) for testing at 3M in 50 $cm^2$ fuel cells. The details of this sputter deposition chamber and methodology for producing compositional spreads have been described previously.[14,15] One key difference between process A and process B is the effective thickness of the sputtered layers per pass of the sample by the source targets, which is much less than a monolayer for process B but controlled for process A to values generally greater than 20 Å. A more

* Electrochemical Society Active Member.
z E-mail: mkdebe1@mmm.com

extensive report on the results of an RDE investigation of the $Pt_{1-x}Co_x$ series is in press.[16] Finally, this same "process B" coater was used to deposit multiple compositional spreads of $Pt_{1-x}Ni_x$ for $(0.2 < x < 0.84)$ onto NSTF whisker coated glassy carbon disks (prepared at 3M) for RDE measurements at Dalhousie University. Coated disks numbering from 1 to 9, each with a different value of x, were coated in seven different runs for the data discussed in Fig. 12.

X-ray fluorescence (XRF) analysis was completed on a subset of the as-made $Pt_{1-x}Ni_x$ alloy compositions made at 3M Co. Electron microprobe (EMP) and XRD measurements were completed on the same subset at Dalhousie University. The EMP measurements were made with a JEOL JXA-8200 Superprobe using an accelerating voltage of 5 kV, with 50 nA current. An electron spot size of 50 $\mu$m was used to average the film composition over a reasonable area. X-ray diffraction (XRD) data were collected with a Bruker D8 discover x-ray system equipped with an x-y-z translation stage, a Cu target x-ray tube, an incident beam monochromator to select Cu K$\alpha$ radiation and an area detector. The incident beam was set at 6° and the detector was placed at 37°. Grain sizes and lattice constants were calculated from Lorentzian peak fits to the strongest diffraction peak. It was assumed that this peak came from (111) planes in an FCC lattice.

*MEA preparation and evaluation.*—NSTF catalyst coated membranes (CCM) were formed by embedding NSTF anode and cathode catalysts into the surfaces of 3M fabricated PFSA proton exchange membranes with ~825 equivalent weight (EW), using a decal-transfer type nip-roll lamination process. The 3M membrane used had thicknesses in the 20–24 $\mu$m range. For all the cathodes evaluated, the anodes used were NSTF-PtCoMn with a Pt loading of 0.05 $mg_{Pt}/cm^2$. CCM's were placed between 3M-coated roll-good gas diffusion layer (GDL) media based on hydrophobically pretreated MRC (Mitsubishi Rayon Co.) carbon paper backing layers. GDL's were not bonded to the CCM's. The MEA-GDL's were compressed ~10% by strain-controlling gaskets in 50 $cm^2$ quad serpentine flow fields purchased from Fuel Cell Technologies, Inc.

Fuel cell break-in conditioning used the standard NSTF thermal cycling discussed in Ref. 8. This conditioning begins with continuous acquisition of alternating galvanodynamic polarization curves (GDS) (0.02 $A/cm^2$ to limiting currents) and potentiostatic holds (0.4 V) at 70°C for several hours. This is followed by a repetitive operation at 75°C, in which three or four such pairs of GDS and potentiodynamic scans (PDS) are obtained, followed by shutting down and cooling the cell to room temperature while continuing to flow liquid water through the cell. This cycle is then repeated for at least 12 h. During this time, the cathode electrodes are significantly dealloyed of the less noble metal.

Electrochemical surface areas of the cathode catalysts were determined from integrated hydrogen adsorption and desorption cyclic voltammograms, corrected for shorting and hydrogen cross-over, and assuming 210 $\mu C/cm^2$ of Pt surface area at saturation coverage.

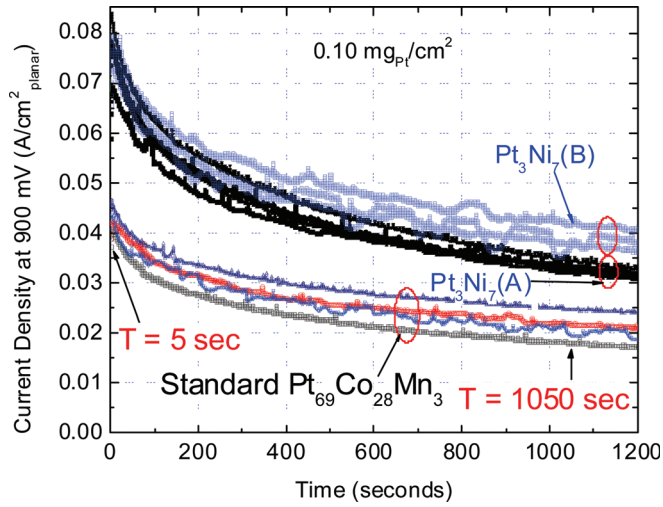


**Figure 1.** (Color online) Illustration of the protocol for 50 $cm^2$ fuel cell ORR activity measurement showing the current density versus time at 900 mV under saturated 150 kPa $H_2/O_2$.

*ORR activity measurement.*—Catalyst activity for ORR was measured in 50 $cm^2$ fuel cells using the following protocol. After fully conditioning the MEAs and acquiring stable ambient pressure potentiodynamic $H_2$/air polarization curves at 75°C, the oxidant gas is switched to $N_2$ with the cell set to OCV, at the same pressures, flow rates and inlet humidity conditions used for the ORR measurement, viz. 150kPa (abs) anode/cathode, 80°C cell temperature, 100% RH and flow rates of 696/1657 $H_2/N_2$. After a short period, the cathode gas is then switched to pure $O_2$, and after ~20 s, the cell voltage is set by the potentiostat to 900 mV. The cell current is tracked for approximately 20 min, corrected for shorting and hydrogen cross-over to obtain corrected current density versus time decay curves as illustrated in Fig. 1. For the absolute activity, by this method, the current density at 1050 s is recorded. This value is divided by the electrochemical surface area measured by traditional $H_{upd}$ adsorption-desorption to calculate the specific activity at 900 mV and by the Pt loading for the mass activity. The 50 $cm^2$ fuel cell current decay with time is due to Pt oxidation and it is worth noting that kinetic current densities recorded at t = 5 s, rather than 1050 s, represent the activity of a clean surface and agree quantitatively with ORR activity values measured by RDE at Argonne National Laboratory by Stamenkovic et al., with the same catalysts applied to glassy carbon disks in 0.1M $HClO_4$.[10,11] All the $Pt_{1-x}Ni_x$ electrodes fabricated at 3M were used as-made, without any further processing. The $Pt_{1-x}Ni_x$ and $Pt_{1-x}Co_x$ material sets that were coated onto 50 $cm^2$ sized NSTF whisker substrate decals in the Dalhousie University batch coater (process B), were acid washed at 3M prior to fabrication into MEAs for testing.

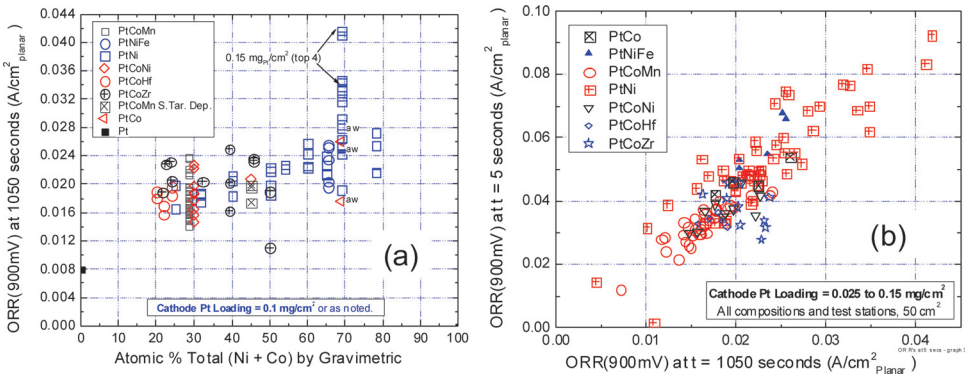


**Figure 2.** (Color online) (a) Absolute activity at 900 mV at t = 1050 s for the series of alloys shown in the inset. (b) ORR activity at 5 s is plotted versus that illustrated in Fig. 1 at 1050 s.

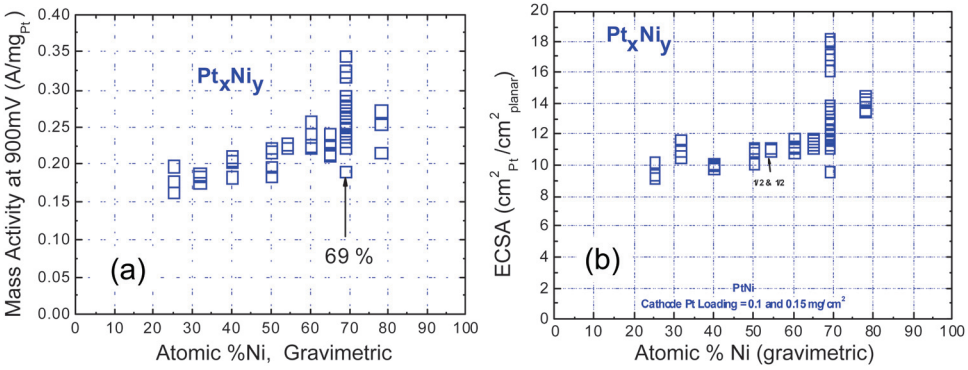


**Figure 3.** (Color online) $Pt_xNi_y$ mass activity determined at 900 mV at t = 1050 s (a), and electrochemical surface area (b), versus atomic percent Ni determined gravimetrically from calibrated sputter deposition rates.

For the $Pt_{1-x}Ni_x$ RDE measurements discussed in Fig. 12, the procedures for measuring electrochemical surface areas and ORR kinetic currents were the same as described in Ref. 17. All CVs were obtained at 50 mV/s, in 0.1 M $HClO_4$ at 22°C. RDE data were collected with Pine Instruments AFBCP bipotentiostats equipped with rotators operated at 900 rpm. The measurements were performed in 0.1 M $HClO_4$ electrolyte (triple distilled $HClO_4$ (GFS Chemicals) diluted with >18 MΩ deionised water) using a platinum wire counter electrode and a $Hg/HgSO_4$ reference electrode (nominal reference potential 630 mV vs. RHE). The potential of the reference electrode was calibrated against $H_2/H^+$ by bubbling $H_2$ through the electrolyte and then determining the potential at which the current reached zero when sweeping the potential above and below the nominal reference electrode potential. For $H_{upd}$ surface area measurements, the solution was purged with bubbling argon for 10 min. Eighteen cyclic voltammograms (CVs) were then collected at 50 mV/s between 1200 and 50 mV vs. RHE. For ORR activities, the solution was purged with oxygen for 10 min with the sample at 500 mV vs RHE before another three cyclic voltammograms were collected (50 mV/s between 1200 and 50 mV vs. RHE). The kinetic activity was then measured at 1000 mV.

## Results and Discussion

Figure 2a shows a summary plot of the absolute activity (900 mV, 1050 s) from an assortment of the revisited NSTF alloy catalysts as a function of the total atomic percent transition metal (Co + Ni), as measured gravimetrically through the catalyst deposition rate calibration. There is a general variability among the different lots and compositions but no significant consistent trend in the ORR activity for TM content between 20 atom % and about 65 atom % gravimetric. However, at nominally 69 ± 5% there appears to be a clear spike in the activity from $Pt_{1-x}Ni_x$. Figure 2b plots the absolute activity measured at t = 5 s versus t = 1050 s, as extracted from data such as in Fig. 1 for the various alloys, showing a generally good correlation between the clean surface and oxidized Pt surface activities. It also shows that the clean surface mass activity exceeds 0.8 A/mg-Pt for the best $Pt_{1-x}Ni_x$ compositions with 0.10 mg-Pt/cm$^2$ loadings.

Figure 3a shows the mass activity and Fig. 3b the Pt surface area for just the $Pt_{1-x}Ni_x$ series of the samples shown in Fig. 2. It is clear that both mass activity and surface area appear to be sharply increased near 69 atom % Ni as determined from the gravimetrically calibrated sputter deposition rates. The mass loading calibration procedure is accurate in an absolute sense, but the lack of precision better than ±5% at 0.1 mg/cm$^2$ makes it difficult to easily determine a finite peak width, which appears less than 5 atom %. That is, variability in sample to sample preparation at a given targeted composition could cause the exact composition of any sample to vary ±5 atom %. Some samples, produced with nominally identical compositions would then produce activities on the peak or sides of the peak. The extreme narrowness of the activity response peak of the NSTF $Pt_{1-x}Ni_x$ catalysts prompted us to investigate this high range of TM:Pt ratio more thoroughly, using both XRF and EMP to determine the values of x more precisely for the samples evaluated for ORR activity, even though the XRF and EMP measurements have to be independently calibrated against mass loadings in secondary measurements if absolute values of x are desired. The intent however was not to use XRF and EMP to determine the absolute position of the peak, but rather to be able to plot the ORR activity of the samples versus at% Ni with more resolution than provided by the gravimetrically determined Pt and Ni deposition rate values. This would hopefully reveal a finite peak width for this anomalous response of ORR activity on Pt:Ni ratio.

Figure 4 shows the mass activity versus the atomic % Ni for the same samples as in Fig. 3, but with the atomic % Ni determined by X-ray fluorescence (a) and electron microprobe analysis (b). These techniques are believed to have a measurement resolution of ±2 atom % in this application. The solid lines were added to help reveal what now appears to be a still very narrow peak but with finite width

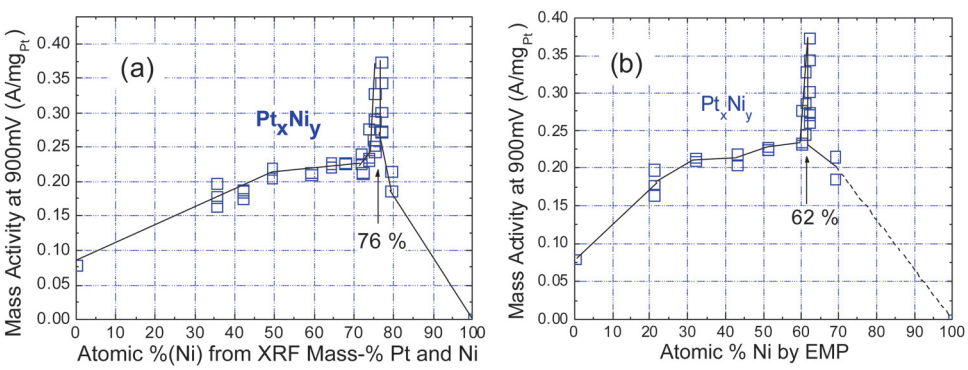


**Figure 4.** (Color online) Mass activity (1050 s) versus the atomic % Ni for the same samples as in Fig. 3, but with the atomic % Ni determined by X-ray fluorescence in (a), and electron microprobe analysis in (b).

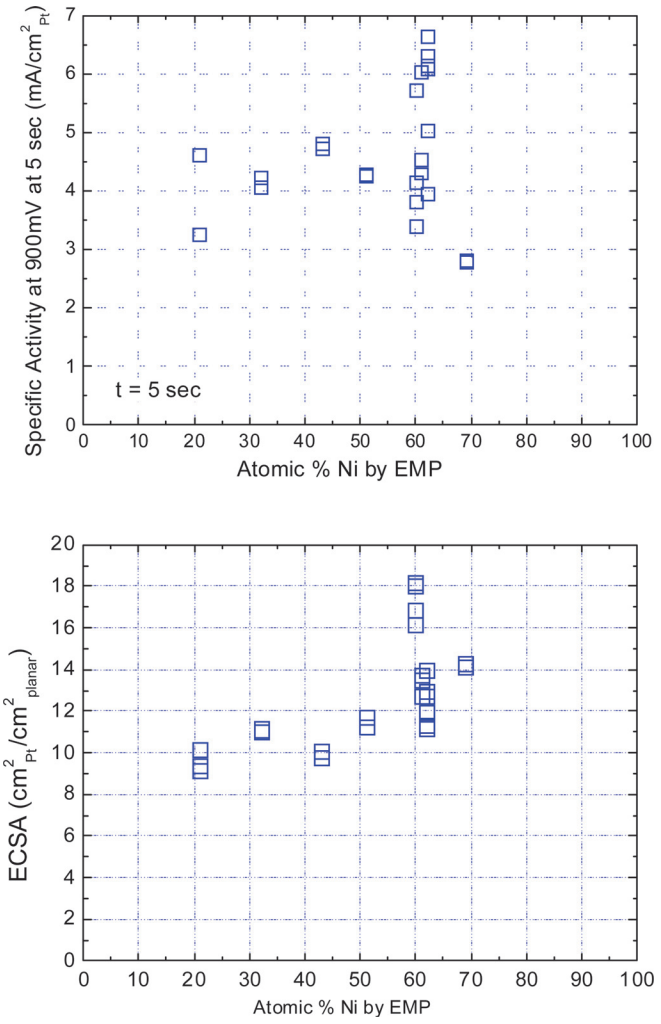


**Figure 5.** (Color online) (a) Specific activity at 900 mV determined from the ORR decay curves as illustrated in Fig. 1 at t = 5 s characteristic of the clean surface for comparison to RDE type measurements. (b) Surface enhancement factor for the same data set as in (a).

in both cases. However, the atomic percent Ni determined for the peak position is dependent on the calibration of the technique used for these non-planar and probably inhomogeneous samples, with XRF suggesting 76 atom % Ni and EMP 62 atom % Ni. These values straddle the gravimetric peak position of 69%, which is believed to be more accurate in the absolute sense discussed above. We take then the nominal composition of this peak composition to be $Pt_3Ni_7$.

Figure 5a shows the specific activity at 900 mV determined from the ORR decay curves as illustrated in Fig. 1 at t = 5 s, which is characteristic of the clean surface for comparison to RDE type measurements. Figure 5b shows the surface area enhancement factor for the same data set as in Fig. 5a. Both surface area and specific activity show about the same relative increase at the peak composition.

Figure 6 shows the mass activity and specific activity from the 50 $cm^2$ fuel cell measurements (t = 1050 s) of the $Pt_3Ni_7$ alloy (roll good process A) as function of cathode Pt loading, compared to the standard NSTF PtCoMn catalysts. It is clear in light of Figs. 3b and 6b that both surface area and specific activity are contributing to the ~50–60% increase in mass activity of the $Pt_3Ni_7$ over the PtCoMn as measured at t = 1050 s, characteristic of a partially oxidized surface, the same as shown in Fig. 5 for the clean surface.

Figure 7a shows an expanded view of the kinetic range of $H_2$/air galvanodynamic polarization curves from a subset of the $Pt_3Ni_7$ catalyst samples around the peak composition. It shows that the $H_2$/air kinetics do correlate with the $O_2$ ORR activity gains of the $Pt_3Ni_7$ over the more stable $Pt_3Ni_1$ or standard PtCoMn alloys. Even in this nominal kinetic range of low current densities however, there appears to be a reduction of the $Pt_3Ni_7$ samples' cell voltage gain as the current density increases. Figure 7b plots the $H_2$/air GDS polarization curve voltage at 20mA/$cm^2$ versus the ORR absolute activity at 900 mV (1050 s) for all the $Pt_{1-x}Ni_x$ catalyst samples. The curve fit shows a clear decrease in the slope (rate of $H_2$/air performance gain) as the ORR activity increases, suggesting some other factor is causing the full performance not to be realized under air that the ORR pure $O_2$ activity suggests should be seen.

Figure 8 shows the full current density range of many of the polarization curves shown in part in Fig. 7, revealing that the $Pt_3Ni_7$ alloys suffer from much reduced limiting current density compared to the PtCoMn and $Pt_3Ni_1$. In fact, we observe that the limiting current decreases as the amount of transition metal increases, and acid washing the catalyst before making the CCM increases the limiting current significantly. This is understood to be due to the significant amount of dealloying and dissolution of the excess Ni (above the stable $Pt_3Ni_1$ composition) into the membrane, similar to what was observed in acid soaked NSTF $Pt_{1-x}Ni_x$ alloys,[18] and NSTF Pt-TM ternaries.[19] Studies of the impact of various metal cations intentionally added to the membrane[20] allows us to conclude that the excess Ni cations in the membrane affects the net water transport across the membrane from anode to cathode, resulting in increased flooding of the NSTF cathodes and increased oxygen mass transfer overpotential. This is a fatal limitation of the highly active $Pt_3Ni_7$ alloys as they are currently made, and approaches to mitigate this undesirable effect are ongoing.

The dissolution of the excess Ni, whether in the membrane or by acid washing, does not cause any overt change in the appearance of the NSTF catalyst coated whiskers, as shown in Fig. 9, which compares SEM images of the $Pt_3Ni_7$ coated whiskers as-made (left) at the same magnification after the acid washing (right). Apparently

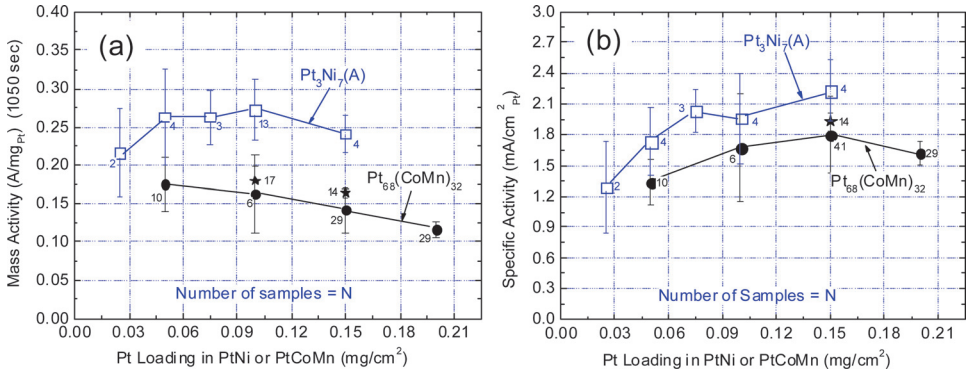


**Figure 6.** (Color online) Mass activity (1050 s) (a), and specific activity(1050 s) (b), as a function of Pt loading for the $Pt_3Ni_7$ alloy as made by process A, and the NSTF standard $Pt_{68}Co_{29}Mn_3$ alloy.

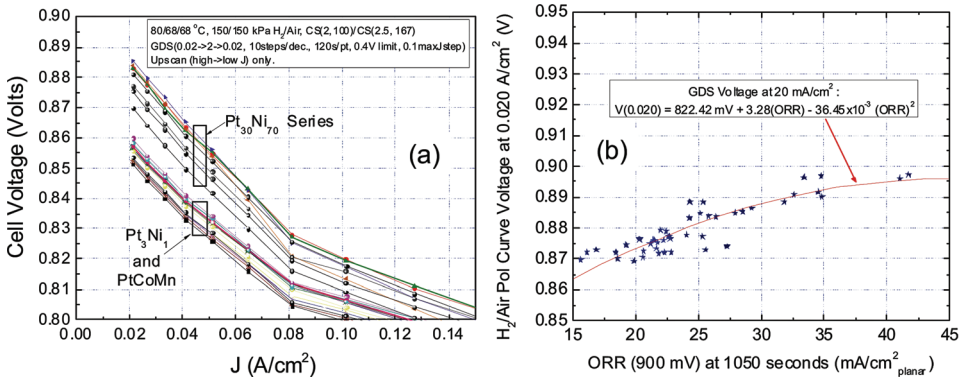


**Figure 7.** (Color online) (a) Hydrogen/air galvanodynamic polarization curves (GDS) in the kinetic region at the conditions shown in the inset for various NSTF $Pt_xNi_y$ compositions compared to $Pt_3Ni_1$ and the NSTF standard PtCoMn. (b) Plot of the $H_2$/air GDS cell voltage at 20 mA/cm$^2$ from data such as is plotted in (a) for a series of NSTF $Pt_xNi_y$ alloys as a function of ORR activity.

the structural changes due to the dealloying are occurring at a much smaller size scale.

The sharp dependence of ORR activity on at% Ni at the $Pt_3Ni_7$ composition begs explanation. We believe it is highly unexpected directly from any d-band density or oxygen binding energy calculations, DFT or lattice strain modeling, segregated surface structure or dealloyed Pt-skeleton, Pt-skin or core-shell structures studied to date.[21,22] One factor that does appear to be key is the fcc lattice parameter and perhaps the grain size at the peak composition. However, more likely we propose the effect may be the consequence of multiple competing effects as activity first increases as dealloying proceeds from Pt skin formation to nanoporous dealloying of several surface layers, and then decreases as ultimately the bulk core dealloys above a critical composition of $x = 0.62$ (by EMP) based on ex-situ dealloying experiments.

Figure 10a shows the Pt alloy lattice parameter for the different NSTF alloys shown in the inset and in Fig. 2. There is an essentially linear dependence of the lattice parameter contraction as the at% Ni and Co increases. (Similar XRD results were shown in an earlier study of transition metal dissolution from combinatorially sputtered $Pt_{1-x}Ni_x$ films ($0 < x < 1$) on NSTF supports[18]). A plot of the Pt fcc(111) grain size measured from the XRD data shows a similar linear increase as a function of at% Ni and Co. By combining the latter data set with that in Fig. 10a a correlation of lattice parameter with grain size appears as shown in Fig. 10b. From the EMP peak composition of 62% in Fig. 4b, Fig. 10 would imply that the key lattice parameter of the as-made catalyst is around 3.71 Å and key grain size around 7 nm.

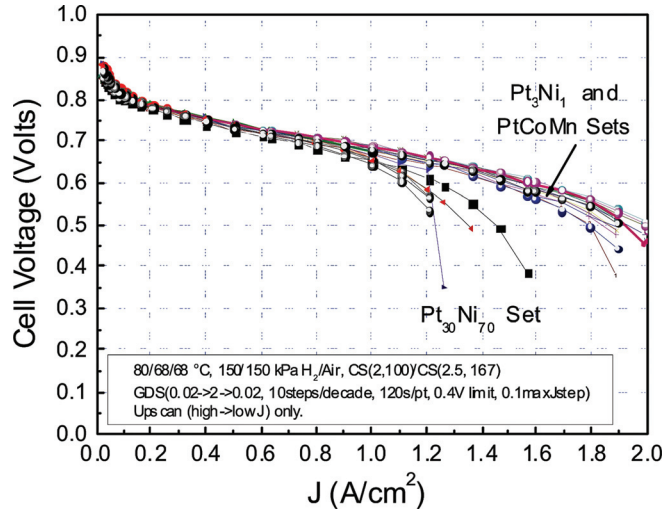


**Figure 8.** (Color online) $H_2$/air GDS polarization curves at the conditions shown in the inset for NSTF MEA's with the $Pt_3Ni_7$ composition versus the $Pt_3Ni_1$ and standard PtCoMn.

A set of twenty-four 50 cm$^2$ MEA's were fabricated with seven different lots and values of $Pt_{1-x}Ni_x$ alloy catalysts on the cathode. Figure 11 plots the surface area and mass activity for this set of MEA's as a function of the as-made catalyst fcc lattice parameter, revealing a sharp discontinuity at 3.708 Å. Despite the apparent dramatic increases, whether it is surface lattice strain or some other phenomenon causing the increases in ORR activity and surface area is difficult to conclude. This is in part because the XRD measurements are made on catalyst samples before they are applied to the PFSA membranes and tested in fuel cells, so the surface area and ORR activity are measured on a different catalyst composition and probably different structure than exists in the as-made catalyst. It is certain that with the standard thermal cycling and break-in conditioning used to bring the MEA's to full performance, much of the excess Ni rapidly dissolves into the membrane, partially dealloying the starting material as discussed further below.

Figure 12 shows the RDE current density at 1000 mV from a series of $Pt_{1-x}Ni_x$ alloys sputter deposited (process B) onto NSTF whisker coated glassy carbon disks. All disks have 0.1 $mg_{Pt}/cm^2$. Current density is measured from the up-sweep of a CV scan in 0.1 M $HClO_4$, at 900 rpm and 50 mV/s. The Ni composition was determined by EMP from catalyst deposited onto Si wafer witness substrates. Despite the scatter, there is a substantial peak in ORR activity seen around 78% Ni (from EMP), with most of the peak occurring for compositions having x in the range of $0.6 < x < 0.85$. These RDE measured values differ substantially in both the peak position and its compositional half-width range compared to the 50 cm$^2$ fuel cell activities shown in Fig. 4, viz. 62% Ni and x in the range of $\sim 0.58 < x < \sim 0.62$. Besides the difficulty of precisely calibrating the EMP values, the electrochemical environments and treatments of the samples in Figs. 12 and 4 were quite different and may be in part responsible for the differences. The degree of dealloying may be different between the two data sets in Figs. 4 and 12 due to the difference in electrolytes (solid PEM vs $HClO_4$), temperature of operation (ambient vs 80°C), voltage cycling history, and duration of operation.

Finally, Fig. 13 shows 50 cm$^2$ fuel cell mass activity measurements from MEA's fabricated at 3M with cathodes coated at Dalhousie University. The $Pt_{1-x}Co_x$ compositional spreads were deposited onto NSTF whisker substrates by process B, made into MEA's and tested at 3M. There is a clear suggestion of a peak in activity at the EMP-determined composition of ~62%, similar to what was seen for the EMP-determined $Pt_{1-x}Ni_x$ values in Fig. 4. However the peak amplitude or gain in activity over the standard PtCoMn is much smaller and the peak width broader ($0.58 < x < 0.68$) than was seen with $Pt_{1-x}Ni_x$.

## Discussion

Ni rich alloys of Pt with Ni have been investigated quite extensively recently for enhanced ORR activity in multiple structural forms. Relevant examples include single crystals and polycrystalline

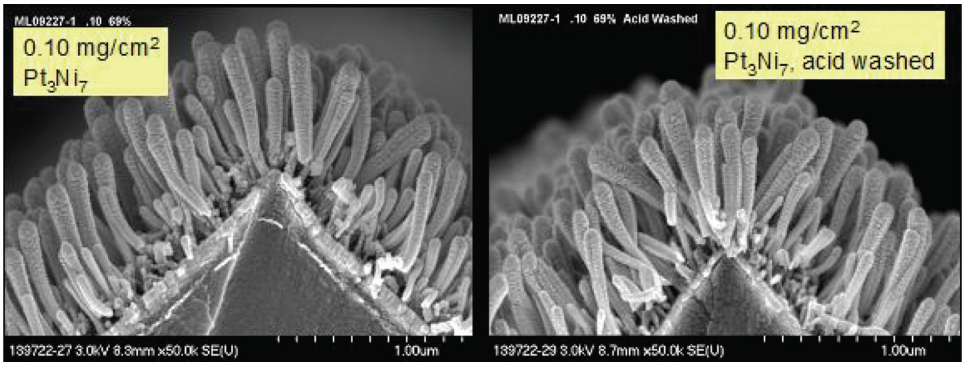


**Figure 9.** (Color online) SEM images at originally 50 kX, of the NSTF catalysts with $Pt_3Ni_7$ coatings as-made (left) and after acid washing (right).

bulk surfaces,[21,22] dealloyed bulk films,[23] sputter deposited thin films,[24,25] pulsed laser deposited films,[26] dealloyed Pt bimetallic nanoparticles,[27] dealloyed electrodeposited films,[28] and cover the compositional range for Ni from 0 to near 100%.

Toda et al. investigated the ORR activity of multiple compositions of PtM (M = Fe, Ni, Co) prepared as sputter deposited thin films.[24] They investigated six sputter deposited $Pt_{1-x}Ni_x$ alloy compositions over the x = 0.11–0.80 compositional range.[24] They report a similar Pt lattice spacing contraction as a function of the atomic percent Ni as shown here in Fig. 10a. However their alloys' kinetic activity shows a very broad dependence on composition that peaks at ~30 atom % Ni and shows essentially no activity at 70% Ni and above. Furthermore, they observe a significantly higher activity gain for PtFe than PtCo and PtNi. They discuss in detail the formation of a Pt skin several monolayers thick due to dealloying of the alloy surface that protects the interior from further corrosion, and the resultant modification of the skin's 5d valence band electronic structure due to that of the alloy sub-layers, even over distances of 10 Å or more. They suggest the effect must be reduced with increasing thickness of the Pt skin, and hence the extent of corrosion of the bulk TM elements.

Stamenkovic et al. have shown an increase in specific kinetic activity for ORR on the [111] facets of annealed $Pt_{1-x}Ni_x$ and $Pt_{1-x}Co_x$ extended surfaces (single and polycrystalline bulk surfaces with x = 0, 0.25 and 0.5), occurs for x = 0.33.[21,22] They compare Pt-skeleton vs Pt-skin vs Pt-poly surface structures to show that the Pt-skin are the most active for ORR, followed by Pt-skeleton and Pt-poly, the least active. It is the arrangement of M atoms in the surface and near-surface that is different which causes different amounts of shift in the d-band center relative to the Fermi level of the top layer of Pt atoms. This in turn affects the adsorption coverage of spectator species that interfere with ORR. They specifically exclude any contribution to the increased ORR activity from increases in surface area (roughening) due to dealloying.

Moffat et al. studied the kinetics of ORR on a series of electrodeposited $Pt_{1-x}Ni_x$ and $Pt_{1-x}Co_x$ alloy films and compared them to electrodeposited Pt and bulk polycrystalline Pt (28). RDE measurements gave $H_{upd}$ area-specific activities ~1.9–2.7 times larger for the alloys with $0.23 < x < 0.35$ compared to the electrodeposited pure Pt. The ORR enhancement factor was between 3 and 4.8 when as-deposited films with $x > 0.75$ were dealloyed. The maximum specific activity (2.5 $mA/cm^2_{Pt}$) was measured in Fig. 4 of Ref. 28 for a $Pt_{20}Ni_{80}$ (x = 0.80) film, while that of the next closest value of x measured (x = 0.65) corresponding to the adjacent minimum, gave a specific activity of 1.65 $mA/cm^2_{Pt}$. Although the data set in Ref. 28 is insufficiently dense to define a peak, if the x = 0.8 value were the peak, the ratio of the peak specific activity to the adjacent minimum would be about 1.5. In Fig. 5 our fuel cell measured NSTF $Pt_{1-x}Ni_x$ specific activities at the peak and adjacent minimum using the t = 5 s protocol are ~6.5 and 4.25 $mA/cm^2_{Pt}$ respectively, giving a similar ratio of 1.53. This could be interpreted to suggest that had the electrodeposited activities of Ref. 28 been measured with higher resolution of at% Ni, a similar peak shape and magnitude of specific activity may have been seen as we show in Fig. 5. Moffat et al. state in connection with CV curves in Fig. 5a of Ref. 28 that "The absence of a distinct increase in Hupd charge associated with the near-steady-state $Pt_{20}Ni_{80}$ voltammogram shown in Fig. 5a indicates that dealloying does not result in a significant increase in the electrode surface area of the specimen. . . .". This particular $Pt_{20}Ni_{80}$ electrodeposited film was formed by electrodeposition for only 1 min and was expected to be on the order of 20 nm thick, not too different from the thickness of the $Pt_3Ni_7$ films coated by vacuum deposition on the sides of the NSTF whiskers at the loadings used in this work. In contrast for the dealloyed NSTF PtNi films, Fig. 5 shows there are approximately equal contributions of specific activity and surface area gains that contribute to the mass activity, such as shown in Fig. 4. This difference may be associated with the quite different morphologies of the electrodeposited films of Ref. 28 and the sputter deposited films of this work, particularly due to the whiskerette morphology of the NSTF catalyst films coating the perylene red whisker cores.[29] It is important to note however that in thicker electrodeposited specimens, the NIST group reports that a significant

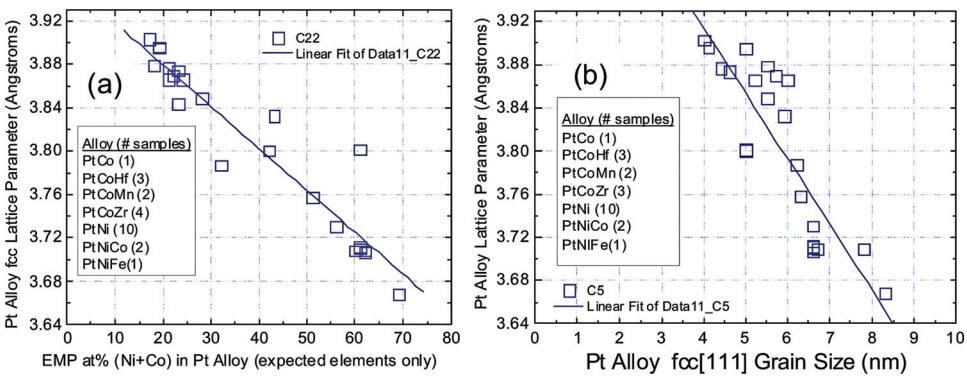


**Figure 10.** (Color online) (a) Pt alloy fcc lattice parameter as a function of the EMP determined atomic percent Ni, Co or Ni+Co for a series of different NSTF alloys. (b) Correlation of Pt alloy fcc lattice parameter with the fcc (111) grain size as derived from the data in (a) and a similar plot of NSTF fcc (111) grain size versus atomic percent (Ni+Co).

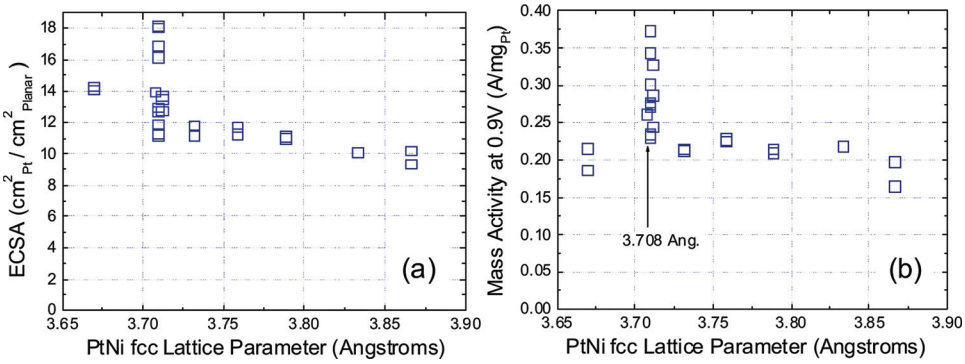


**Figure 11.** (Color online) Electrochemical surface area (a), and mass activity (b), as a function of the $Pt_xNi_y$ lattice parameter measured on the as-made catalyst prior to 50 $cm^2$ fuel cell testing at 3M.

portion of the six to seven fold enhancement of the ORR kinetics of $Pt_{20}Ni_{80}$ alloys over pure Pt is associated with surface area expansion that accompanies partial dealloying of Ni.[33]

Erlebacher and collaborators have studied the evolution of nanoporosity during electrochemical dealloying of $Pt_{1-x}Ni_x$ bulk alloys with high Ni content.[23,30–32] In Ref. 23 they studied dealloying of $Pt_{23}Ni_{77}$ metal foil precursors. Bulk composition analyses by EDS showed the average composition of the dealloyed region was $Pt_{70}Ni_{30}$ which overlays the original bulk composition as a Pt alloy-skin type structure.[23] The resulting pore structure is characterized by extremely small pores, ~2 nm in size, based on TEM imaging, that are orders of magnitude smaller than the grain size. Impregnating such bulk surfaces, dealloyed to varying depths, with hydrophobic protic ionic liquids with high $O_2$ solubility further increased the activity at 900 mV another factor of 2.5,[23] becoming equal to the kinetic current density at 0.9 V of annealed single crystal $Pt_3Ni(111)$ with the segregated surface structure.[22]

Mani et al. have recently reported on dealloyed binary $PtM_3$ (M = Cu, Co, Ni) and ternary $PtNi_3M$ (M = Cu, Co, Fe, Cr) nanoparticle electrocatalysts supported on carbon with as-made Pt/Ni ratios of 18/82 for binaries and 20/60 for the ternaries.[27] They utilize in-situ voltammetric dealloying followed by ex-situ ion exchange of the dealloyed cations from 10 $cm^2$ MEA's prior to fuel cell activity measurements under $H_2/O_2$. After dealloying, the bulk (ICP) composition Pt/Ni ratios changed to 82/18 and the surface composition (by XPS) to 77/23, reflecting both significant dissolution of the Ni and Pt enrichment of the surface. The resultant mass and specific activity gains at 900 mV were ~3x over standard pure Pt/C. Even further gains in mass activity, up to 0.472 A/mg at 0.9 V, were measured for the as-made nominal $Pt_{20}Ni_{60}Co_{20}$ composition ternary when dealloyed to a final bulk (ICP) composition of $Pt_{45}Ni_{49}Co_6$. In the binaries, the mass activity is primarily due to the gain in specific activity, while in the ternary both an increase in roughness factor and specific activity are seen. For both the binary and ternary compounds, 50–60 mV anodic shifts relative to pure Pt/C of the Pt-OH peaks in cyclic voltammograms were observed after dealloying and suggest at least one factor for the gains in activity.

Imbeault et al. reported on the ORR kinetics of $Pt_{1-x}Ni_x$ thin films prepared by crossed-beam pulsed laser deposition in 0.1 Torr He from pure Pt and Ni targets onto Si and amorphous graphite substrates for $0.0 \leq x \leq 0.73$.[26] Film composition was determined by energy-dispersive X-ray fluorescence. They observe Pt crystallite grain sizes in the range of 10–20 nm, and similar fcc lattice parameter contraction with increasing Ni as in Fig. 10a. They observe a uniform shift in the half-wave current potential for oxygen reduction as x increases due primarily to an increase in surface area from extensive de-alloying by CV cycling (0.05–1.05 V) in $H_2SO_4$, rather than

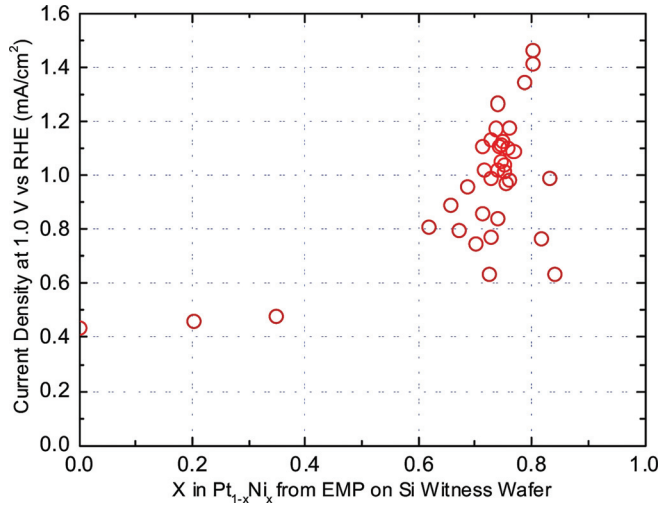


**Figure 12.** (Color online) RDE current density at 1000 mV from a series of $Pt_{1-x}Ni_x$ alloys sputter deposited onto the NSTF whisker coated glassy carbon disks. All disks have 0.1 $mgP_t/cm^2$. Current density is measured from the up-sweep, 0.1 M HClO4, 900 rpm, 50 mV/s. The Ni composition was determined by EMP from catalyst deposited onto Si wafer witness substrates.

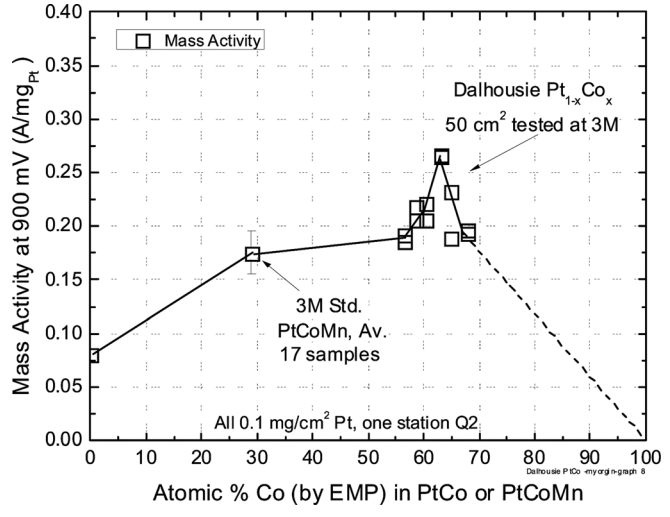


**Figure 13.** ORR mass activity measured in 50 $cm^2$ fuel cells at 3M versus atomic % Co for a series of catalyst compositions coated onto the NSTF whisker MCTS substrates in the Dalhousie sputtering chamber (process B). The average mass activity for 17, 50 $cm^2$ MEAs made with the 3M standard PtCoMn composition by the roll-to-roll process (process A) is shown for comparison. All Pt loadings were 0.1 $mg/cm^2$. The process B samples were acid washed prior to MEA fabrication.

an increase in specific kinetic activity. They conclude de-alloying is too extensive in their non-annealed films to form a Pt skin or modulated composition skin over alloy sub-layers, so essentially no modification of the electronic structure of the surface Pt occurs and no increase in kinetic activity was observed.

Liu et al. studied the oxygen reduction activity of five dealloyed $Pt_{1-x}Ni_x$ catalyst compositions deposited as thin films onto the NSTF supports that were grown on glassy carbon disks for RDE measurements.[25] The RDE measurement protocols were designed to follow changes in the catalyst surface area and specific activity properties during dealloying over a period of 9 h. $Pt_{25}Ni_{75}$ was seen to have a sizeable gain in activity/surface area over $Pt_{28}Ni_{72}$ and at least 3x higher surface area than pure Pt. The property changes observed were consistent with Ni dissolution starting with the surface and near-surface Ni atoms, resulting in a porous structure having increased surface area, up to 35 $m^2/g$ for the peak composition $Pt_{25}Ni_{75}$. As dealloying continued, a thicker Pt rich overlayer resulted, leading to reduced ORR activity, possibly from less compressive lattice strain at the surface. X-ray diffraction measurements indicated that over the limited time of the experiments with the voltage cycling protocol used, the Pt enriched outer layer shell also seemed to protect the Ni atoms from the deeper bulk regions of the catalyst.

The literature cited above shows that high mass activities of the $Pt_{1-x}Ni_x$ system with $x > 0.5$ are not unexpected. What is unexpected in the present work is the extraordinary sharpness of the dependence of ORR activity on the as-made composition of the NSTF electrocatalysts, which gravimetrically occurs around $x = 0.7$ and by EMP around $x = 0.62$. A possible explanation for this may come from the authors' previous work which focused on ex-situ dealloying of the NSTF catalysts via chemical dissolution.[18,19] Bonakdarpour et al., show convincingly that for $Pt_{1-x}Ni_x$ compositional spreads (with $0 < x < 1$) applied to NSTF support whiskers, ex-situ acid soaking will dealloy the as-made materials to a similar state as obtained in 50 $cm^2$ fuel cell after break-in and extensive testing. Indeed, similar behaviors were observed for both multiple PtM binaries (M = Fe, Ni) and PtMM' ternaries (M, M' = Co, Ni, Mn, Fe) as a result of the acid soaking. More specifically what was observed is that for $x < 0.62$ (by EMP), the near surface layers were significantly depleted of Ni, while for $x > 0.62$, the bulk also begins to dealloy as well and the lattice constant increases back towards that of richer Pt. Figure 14, reproduced from Ref. 18, shows how the composition of the catalyst coatings on the whiskers changed due to the acid soaking as a function of the as-made composition. For as-made catalysts with $x \sim 0.62$, the remaining average bulk composition in the acid soaked dealloyed NSTF $Pt_{1-x}Ni_x$ spreads were $\sim Pt_7Ni_3$ as determined by EMP. So it appears more than coincidental that the peak in fuel cell activity shown in Figs. 4b and 5 coincides with the as-made value of $x = 0.62$ (by EMP) in the ex-situ acid soaking measurements at which the bulk composition sharply begins to be dealloyed as well. This would suggest multiple competing effects as x moves from below 0.62 to above 0.62 that together give a sharply defined peak in activity. For $x < 0.62$ we view the polycrystalline NSTF thin film catalysts transitioning from the starting alloy to a progressively enriched Pt-skin type structure over the as-made alloy. Lattice strain and/or band structure effects due to a segregated surface skin would cause the activity to increase. As the value of x comes close to 0.62, the catalyst film coatings further dealloy to form a nanoporous Pt-skeleton type structure over the bulk that is now beginning to dealloy as well. The increase in surface area would further cause the mass activity to increase. Finally, for $x > 0.62$ the bulk starts to become increasingly and rapidly (as a function of x) dealloyed and there is now less and less lattice strain in the residual Pt surface layers and ORR activity starts to decrease from its peak. As x continues to increase above 0.62, there may be insufficient residual Pt to form a continuous skin, giving rise to smaller isolated Pt grains and therefore further loss of specific activity and surface area. These mechanisms or something similar could explain the sharpness of the ORR peak in activity we observe. This process may be uniquely dependent on the whiskerette structures that comprise the polycrystalline catalyst films on the NSTF whiskers.[29] For this structure, the key starting material parameters to optimize the effect would appear to be an fcc lattice parameter of 3.71 Å and a (111) grain size of ~7 nm. The peak effect is obtained when the dealloyed bulk mean composition is (by EMP) $Pt_7Ni_3$ and the lattice constant is in the range of ~3.84 Å.

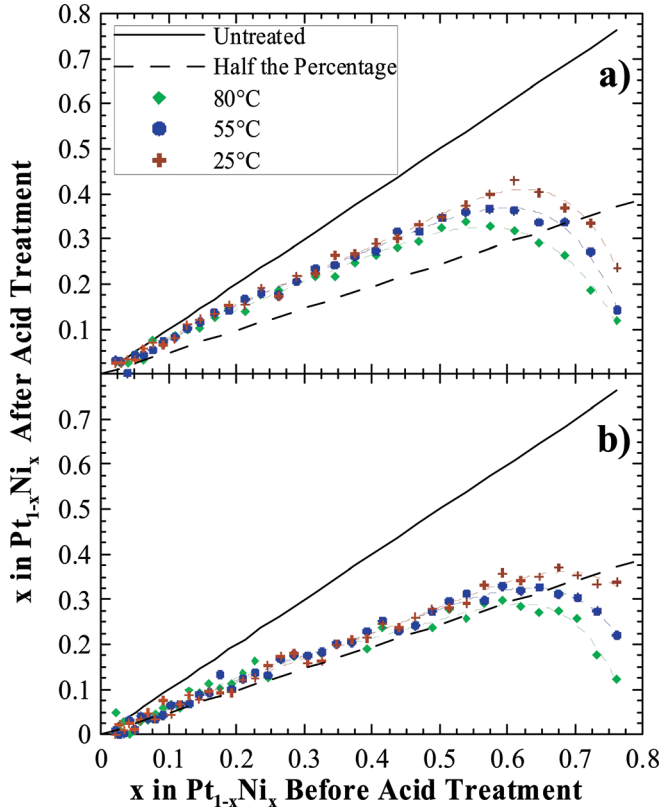


**Figure 14.** (Color online) Value of x in $Pt_{1-x}Ni_x$ before acid soaking versus x after acid soaking. Reprinted from Journal of Electrochemical Society with the kind permission of the Electrochemical Society.

It is notable that both RDE (Fig. 12) and fuel cell MEA measurements agree in showing a quite sharp dependence of ORR activity on composition for the NSTF $Pt_{1-x}Ni_x$ alloys. That Pt-Co also shows a similar, albeit lesser effect in Fig. 13 than the Pt-Ni alloys suggests a similar balance of competing effects resulting in a sharp peak in activity with composition, but reflecting perhaps the more facile Co dissolution versus Ni so that the overall gain in activity is not as large.

## Summary and Conclusions

We have investigated a large series of Pt-transition metal alloys covering a wide range of compositions up to high transition metal content of ~80% in some cases. All the catalysts were fabricated by vacuum sputter deposition onto NSTF catalyst support whiskers. They were all made into 50 $cm^2$ fuel cells and their ORR activity and surface areas measured. Ni was found to be unique in showing an extraordinarily sharp and large peak dependence of ORR mass activity at an as-made at% Ni content of ~69 ± 2 atom %, determined gravimetrically. The mass activity of the peak composition exceeds 0.35 $A/mg_{Pt}$ at 900 mV when measured in 50 $cm^2$ fuel cells from a partially oxidized surface. The alloy composition at the peak activity was determined gravimetrically and its narrow peak width validated by XRF and EMP. The gain in mass activity of the as-made $Pt_3Ni_7$ alloy is due to both increases in surface area and specific activity. The catalysts' lattice parameters and grain sizes were

characterized by XRD for a subset of the $Pt_{1-x}Ni_x$ as-made alloys. The peak in surface area and mass activity correlate to an as-made fcc lattice parameter of 3.71 Å and a fcc (111) grain size of 7 nm. The sharpness of the peak is proposed to result from competing factors that cause the activity to first rapidly increase and then decrease again as the as-made composition passes through the $Pt_{1-x}Ni_x$ value around $x \sim 0.62$ (EMP) at which the bulk is seen to quickly dealloy by ex-situ acid soaking. Due to significant dealloying of the excess Ni into the membrane and a consequential negative impact on the net water transport between the anode and cathode, the cathode is more susceptible to flooding and the high current density limiting current decreases with this unique alloy for cell voltages below ~0.7 V.

## Acknowledgments

The authors would like to thank Dr. Jason Bender of 3M Co. for the XRF data, and the Hydrogen, Fuel Cells and Infrastructure Technology Program [in the Office of Energy Efficiency and Renewable Energy] at the US Department of Energy for support under Grant DE-FG36-07GO17007.

## References

1. F. T. Wagner, B. Lakshmanan, and M. F. Mathias, *J. Phys. Chem. Lett.*, **1**, 2204 (2010).
2. M. K. Debe and R. J. Poirier, *J. Vac. Sci. Technol. A*, **12**, 2017 (1994).
3. M. K. Debe, in *Handbook of Fuel Cells—Fundamentals, Technology and Applications*, W. Vielstich, A. Lamm, and H. A. Gasteiger, Editors, Chap. 45, John Wiley & Sons, New York (2003).
4. D. Van der Vliet, D. Strmcnik, C. Wang, R. Atanasoski, M. Debe, N. Markovic, and V. Stamenkovic, 216th ECS Meeting, Vienna, Austria, Oct 4–9, 2009.
5. A. K. Schmoeckel, G. D. Vernstrom, A. J. Steinbach, S. M. Hendricks, R. T. Atanasoski, and M. K. Debe, 2006 Fuel Cell Seminar, Honolulu, Hawaii, Nov 13–17, 2006.
6. A. Bonakdarpour, K. Stevens, G. D. Vernstrom, R. Atanasoski, A. K. Schmoeckel, M. K. Debe, and J. R. Dahn, *Electrochim. Acta*, **53**, 688 (2007).
7. M. K. Debe, A. Schmoeckel, S. Hendricks, G. Vernstrom, G. Haugen, and R. Atanasoski, *ECS Trans.*, **1**(8), 51 (2006).
8. M. K. Debe, A. K. Schmoeckel, G. D. Vernstrom, and R. Atanasoski, *J. Power Sources*, **161**, 1002 (2006).
9. K. Noda, and M. K. Debe, *ECS Trans.* **3**(1), 835 (2006).
10. M. K. Debe, in *DOE Hydrogen Program Annual Merit Reviews, 2009 Presentation FC017, and 2010 presentation FC001*, http://www.hydrogen.energy.gov/pdfs/review10/fc017_debe_2009_o_web.pdf, http://www.hydrogen.energy.gov/pdfs/review10/fc001_debe_2010_o_web.pdf.
11. D. van der Vliet, D. Strmcnik, C. Wang, R. Atanasoski, M. Debe, N. Markovic, V. Stamenkovic, Abstract #841, 216th ECS meeting, Vienna, Austria, 2009.
12. Final Report for Cooperative Agreement DE-FC36-02AL67621, "Advanced MEA's for Enhanced Operating Conditions, Amenable to High Volume Manufacture," Sept 30, 2007.
13. M. K. Debe, A. E. Hester, G. D. Vernstrom, A. J. Steinbach, S. M. Hendricks, A. K. Schmoeckel, R. T. Atanasoski, D. J. McClure, and P. L. Turner, in *Proceedings of the 50th Annual Technical Conference of the Society of Vacuum Coaters*, Society of Vacuum Coaters, 2007.
14. J. R. Dahn, S. Trussler, T. D. Hatchard, A. Bonakdarpour, J. R. Mueller-Neuhaus, K. C. Hewitt, and M. Fleischauer, *Chem. Mater.*, **14**, 3519 (2002).
15. D. A. R. Barkhouse, A. Bonakdarpour, M. Fleischauer, T. D. Hatchard, and J. R. Dahn, *J. Magn. Magn. Mater.*, **261**, 399 (2003).
16. D. A. Stevens, S. Wang, R. J. Sanderson, G. C. K. Liu, G. D. Vernstrom, R. T. Atanasoski, M. K. Debe, and J. R. Dahn, *J. Electrochem. Soc.*, **158**, B899 (2011).
17. A. Bonakdarpour, K. Lake, K. Stevens, and J. R. Dahn, *J. Electrochem. Soc.*, **155** B108 (2008).
18. A. Bonakdarpour, J. Wenzel, D. A. Stevens, S. Sheng, T. L. Monchesky, R. Lobel, R. T. Atanasoski, A. K. Schmoeckel, G. D. Vernstrom, M. K. Debe, et al., *J. Electrochem. Soc.*, **152**, A61 (2005).
19. A. Bonakdarpour, R. Lobel, R. T. Atanasoski, G. D. Vernstrom, A. K. Schmoeckel, M. K. Debe, and J. R. Dahn, *J. Electrochem. Soc.*, **153**, A1835 (2006).
20. A. J. Steinbach, K. Alade-Lambo, H. Le, and M. K. Debe, Ext. Abstract GHT35a-22, Fuel Cell Seminar, Phoenix, AZ, Oct 27, 2008.
21. V. R. Stamenkovic, B. S. Mun, K. J. J. Mayrhofer, P. N. Ross, and N. M. Markovic, *J. Am. Chem. Soc.*, **128**, 8813 (2006).
22. V. R. Stamenkovic, B. Fowler, B. S. Mun, G. Wang, P. N. Ross, C. A. Lucas, and N. M. Markovic, *Science*, **315**, 493 (2007).
23. J. Snyder, T. Fujita, M. W. Chen, and J. Erlebacher, *Nature Materials* vol. **9**, (2005) 904.
24. T. Toda, H. Igarashi, H. Uchida, and M. Watanabe, *J. Electrochem. Soc.*, **146**, 3750 (1999).
25. G. C.-K. Liu, D. A. Stevens, J. C. Burns, R. J. Sanderson, G. Vernstrom, R. T. Atanasoski, M. K. Debe, and J. R. Dahn, *J. Electrochem. Soc.*, **158**, B919 (2011).
26. R. Imbeault, A. Pereira, S. Garbarino, and D. Guay, *J. Electrochem. Soc.*, **157** B1051 (2010).
27. P. Mani, R. Srivastava, and P. Strasser, *J. Power Sources*, **196**, 666 (2011).
28. T. P. Moffat, J. J. Mallett, and S.-M. Hwang, *J. Electrochem. Soc.*, **156**, B238 (2009).
29. L. Gancs, T. Kobayashi, M. K. Debe, R. Atanasoski, and A. Wieckowski, *Chem. Mater.*, 20, 2444 (2008).
30. J. Snyder, K. Live, and J. Erlebacher, *J. Electrochem. Soc.*, **155**, C464 (2008).
31. J. Erlebacher, M. Axix, A. Karma, and K. Sieradzki, *Nature (London)*, **410**, 450 (2001).
32. J. Erlebacher and R. Seshardi, *MRS Bull.*, 34, 561 (2009).
33. S.-M. Hwang, C. H. Lee, J. J. Kim, and T. P. Moffat, *Electrochim. Acta*, **55**, 8938 (2010).

# A New Paradigm for PEMFC Ultra-Thin Electrode Water Management at Low Temperatures

Andrew J. Steinbach, Mark K. Debe, Jimmy Wong, Michael J. Kurkowski, Andrew T. Haug, Daniel M. Peppin, Sandy K. Deppe, Susan M. Hendricks and Edward M. Fischer

*ECS Trans.* 2010, Volume 33, Issue 1, Pages 1179-1188.
doi: 10.1149/1.3484611

ECS Transactions, 33 (1) 1179-1188 (2010)
10.1149/1.3484611 ©The Electrochemical Society

# A New Paradigm for PEMFC Ultra-Thin Electrode Water Management at Low Temperatures

A. J. Steinbach, M. K. Debe, J. L. Wong, M. J. Kurkowski, A. T. Haug, D. M. Peppin, S. K. Deppe, S. M. Hendricks, E. M. Fischer

3M Company, Fuel Cell Components Program, 3M Center, St. Paul, MN 55144, USA

In this paper, we provide initial results of a novel method which dramatically improved the performance of ultra-thin electrode polymer electrolyte membrane fuel cells under highly water-condensing operating conditions, realized via modification of the anode gas diffusion layer and utilization of reduced anode reactant pressures, including sub-atmospheric pressure down to 20kPa. Measurements indicated that the sub-atmospheric anode reactant acted to greatly reduce the water flux exiting out the cathode, likely reducing cathode water flooding and oxygen transport limitations.

## INTRODUCTION

In addition to meeting cost, durability, and rated performance targets, polymer electrolyte membrane (PEM) fuel cell systems for automotive traction applications additionally need the capability to transiently attain relatively high current densities at low temperatures to provide drive-away power. Additionally, the system ideally would be robust towards atypical shutdown/restart events which may leave the fuel cell stack in a relatively flooded state.

Membrane electrode assemblies (MEAs) utilizing the ultra-thin (<1μm) 3M nanostructured thin film catalyst (NSTFC) technology have several demonstrated advantages compared to MEAs comprising conventional, relatively thick (~10μm) carbon-supported catalyst, such as increased durability towards start-stop(1) and voltage cycling(2), higher specific activity(3), and high specific rated power(3). However, the low temperature (0-50°C) steady state limiting current density of typical NSTFC MEAs under usual operating conditions is substantially lower than that of many conventional catalyst MEAs (0.2-0.4 v. >1A/cm$^2$ at 30°C, air cathode). This reduced low temperature performance can be attributed to the NSTFC's much higher water generation rate per unit catalyst volume and to an electrode pore structure that is more susceptible to water condensation.

We have recently validated a new strategy for low temperature water management for ultra-thin electrode MEAs which resulted in a several-fold increase in low temperature limiting current density with NSTFC MEAs, enabled by MEA product water removal predominantly via the anode. Increased product water removal out the anode decreased the cathode product water removal which reduced cathode flooding and oxygen mass transport limitations. Anode water removal was enhanced by reducing the anode hydrogen reactant pressure ($P_A$) from the typical atmospheric or higher to sub-

atmospheric as low as 20kPa. Further gains were realized through anode gas diffusion layer (GDL) optimizations, such as utilization of different backings.

## EXPERIMENTAL

### Baseline NSTFC MEA Preparation

NSTF PtCoMn ternary catalyst, containing either 0.05 or 0.10mg/cm$^2$ Pt, was prepared as a roll-good on continuous vacuum deposition equipment, as described previously (4). Catalyst coated membranes (CCMs) made with NSTFC were prepared by cutting 50cm$^2$ catalyst substrates from the uniform roll-good catalysts prepared above. The substrates were placed on either side of a 3M 850EW 20μm PEM and passed through a heated, pressurized laminator, after which the substrates were removed. The resultant anode/cathode loadings of the CCM were 0.05/0.10mg/cm$^2$ Pt. The anode GDL consisted of a bare carbon paper used as received with no microporous layer (MPL), and the cathode GDL consisted of a 3M proprietary design, utilizing MRC U105 carbon paper, carbon black, and hydrophobizing agents. Hardstop Teflon-coated fiberglass gaskets were selected to provide 10% compressive strain to the GDLs. CCMs, GDLs, and gaskets were assembled into a typical 50cm$^2$ electrode area quad serpentine test cell obtained from Fuel Cell Technologies.

### Test Equipment

The test stands consisted of thermal mass flow controllers for reactant control, an electronic load for cell polarization control, electronic temperature controllers, and either manually or electronically actuated back pressure controllers for reactant pressure control. Sub-atmospheric anode reactant pressure was enabled by modification of the test station to include a fixed Venturi vacuum source at the test station anode outlet, and a typical back pressure regulator was installed between the cell anode outlet and the vacuum source to control the cell anode reactant pressure. Cell temperature was controlled by placing a cold-plate (2°C) under the cell end-plates, coupled with cell heaters inserted into the end-plates which were controlled by an electronic temperature controller. Humidification was provided to the fuel cell by two LabAlliance HPLC pumps, one for each reactant stream. Each HPLC pump fed liquid water into a tee, into which the gaseous reactants were also fed; the wet reactant streams were then fed to the fuel cell. The humidification water was not heated prior to entering the cell, so the humidification water entered the cell primarily in the liquid phase. In our experience, this method of providing humidification works equivalently to sparge bottle humidifiers for small single cells. This humidification method also allowed for precisely controlling the mass flow rate of humidification water to the cell independently of the reactant pressures. The test stands were controlled by custom software, allowing for reproducible test operation.

### Evaluation Procedures

All MEAs were first conditioned using a process we refer to as “thermal cycling”, described here (5). After conditioning, low temperature water management MEA performance was evaluated using one or more of the following methods, Tests I-VI.

Test I: Cool Steady State Performance v. $P_A$. In this test, the MEA performance was evaluated as a function primarily of $P_A$. Operating conditions were 30±2°C cell temperature, 1800SCCM dry air at 150kPa cathode reactant, 800SCCM dry $H_2$ anode reactant at 20-200kPa, and the cell potential was held at 0.40V. The MEA was typically evaluated starting at the highest $P_A$ followed by stepwise decrease to the lowest $P_A$, and the MEA was held at each $P_A$ for 5-10 minutes which allowed steady performance to be achieved. Reported current densities (J) are those measured during the final 10% time of each $P_A$ step.

Test II: Cool Galvanodynamic Polarization Curves v. $P_A$. In this test, relatively slow polarization curves were taken to evaluate performance versus $P_A$. Operating conditions were 30°C cell temperature, constant stoichiometry 2.5 dry air at 150kPa cathode reactant, constant stoichiometry 2.0 dry $H_2$ anode reactant at 20-150kPa, and the cell current density was stepped from 0.10A/cm$^2$ to a maximum J in 0.05A/cm$^2$, 60s/pt steps. The maximum J was typically either 2.0A/cm$^2$ or the current density when a cell voltage of 0.40V was obtained. For J > 1.5A/cm$^2$, the test station's cooling capability was unable to maintain the cell at the 30°C setpoint, and the cell temperature increased to as much as 37°C at 2.0A/cm$^2$. Reported polarization curves were obtained by averaging the cell voltage and current density over the entirety of each step.

Test III: Cool Steady State Performance v. $P_A$, Cell Temperature. This test used the same experimental procedure as Test Type I, but the cell temperature was varied from 10-60°C.

Test IV: Water Effluent Flux Distribution v. $P_A$, Cell Temperature. In this test, the MEA performance and anode and cathode water effluent rates were evaluated as a function of cell temperature and $P_A$. Operating conditions were 23-50°C cell temperature, constant stoichiometry 2.0 dry air at 150kPa cathode reactant, constant stoichiometry 2.0 dry $H_2$ anode reactant at 20-200kPa, and the cell J was held at 1A/cm$^2$. Effluent flow rates were determined by condensing the water from the cathode and anode effluent streams in separate simple tube-in-tube heat exchangers cooled to 10°C, allowing the condensate to collect into PTFE containers for a period of time, and then massing the water collected over the time period. Typically three 20-30 minute collections were performed at each condition, and the collection efficiency was typically better than 90%. The water collection equipment did not allow for operation with $P_A$ < 1atm, so anode water flow rates for these conditions were estimated by subtracting the collection-efficiency-corrected cathode water flow rate from the water production rate.

Test V: Psuedo-Automotive Startup Transient v. $P_A$. The objective of this test was to evaluate the MEA performance in a pseudo-automotive startup procedure; see our previous publication (6) for further description and possible data analysis from this test. The MEA was first preconditioned to a relatively dry humidification state, cooled to the desired startup temperature with no reactant flow, and then the performance was evaluated immediately upon reintroduction of reactant gases. The MEAs were preconditioned at 80°C cell temperature, cathode reactant of 1657SCCM, 30% RH, 101kPa air, anode reactant of 696SCCM, 30% RH, 101kPa $H_2$, and fixed J of 0.05A/cm$^2$ for 5 minutes. The MEA was then cooled to the desired Startup Transient temperature of 30°C. For the Startup Transient, the conditions were set to cathode reactant of 1657SCCM, 0% RH, 101kPa air, anode reactant of 696SCCM, 0% RH, 30-150kPa $H_2$,

and the cell voltage was immediately set to 0.60V and held for 5 minutes, during which the J response was measured.

Test VI: Psuedo-Automotive Load Transient v. $P_A$. This test evaluated the MEA's ability to withstand a rapid increase in load from an idle state, as may be expected to occur in automotive traction applications, at various anode pressures. The MEA was first equilibrated at 50°C cell temperature, cathode reactant of 1657SCCM, 140% RH, 150kPa air, anode reactant of 696SCCM, 140% RH, 150kPa $H_2$, and fixed cell potential of 0.6V for approximately 5 minutes. Next, the load was decreased to 0.02A/cm$^2$ and held for 25s. The anode reactant was then quickly adjusted to the desired $P_A$ and held for 5 seconds. Finally, the Load Transient was conducted by rapid load increase to 1A/cm$^2$ in < 1s, and the cell was held under these conditions for 30s during which the cell voltage response was measured. Note that under this test, the anode humidification water mass flow rate was held fixed at the value required for 140% RH (inlet) at 150kPa, 50°C.

## RESULTS AND DISCUSSION

Impact of Anode Reactant Pressure on Performance Under Tests I-VI

As an introduction, Fig. 1 summarizes the results from several different water management experiments which demonstrate the dramatic impact of the decreased anode reactant pressure, all conducted with the Baseline NSTFC MEA. Details of the experimental procedures for these tests are provided in the Experimental section.

In Test I, two identical MEAs' performances were evaluated as a function of $P_A$ at fixed 30°C cell temperature and fixed reactant flow. The samples' current density at 0.40V was found to increase from 0.4 to over 1.2A/cm$^2$ as $P_A$ decreased from 200 to 25kPa, primarily in an exponential fashion. The two replicate samples showed excellent agreement.

Under Test II, constant stoichiometry polarization curves were taken as a function of $P_A$. As $P_A$ decreased from 150 to 100kPa, the limiting current density increased from approximately 0.4 to at least 2A/cm$^2$ (the test limit of the equipment), and further $P_A$ reduction resulted in increased cell voltage response for J between 0.3-1.7A/cm$^2$.

With Test III, the 0.4V J depended significantly on both $P_A$ (20-200kPa) and cell temperature (10-60°C). At 10°C, the measured J was relatively low at high $P_A$, and as $P_A$ decreased J was relatively unchanged until $P_A$ reached ~20kPa. As the cell temperature increased to 20°C, J at high $P_A$ was similar to that at 10°C, but as $P_A$ was decreased J increased at a faster rate than at 10°C and attained a higher maximum J. As the cell temperature increased further, J continued to increase at any given $P_A$ and the rate of J increase with decreasing $P_A$ also increased until an overall maximum J of ~ 1.45A/cm$^2$ was attained, nominally due to the limited cathode reactant flow rate (cathode stoichiometry was ~1.5 at 1.45A/cm$^2$ with the fixed 1800SCCM air flow).

In Test IV, the cell voltage at fixed J=1A/cm$^2$ was measured as a function of $P_A$ and cell temperature ranging from 23 to 50°C. At fixed T, the cell voltage increased in an apparent linear fashion as $P_A$ decreased. As T decreased at fixed $P_A$, the cell voltage decreased. Additionally, the sensitivity of V to $P_A$ also increased as T decreased.

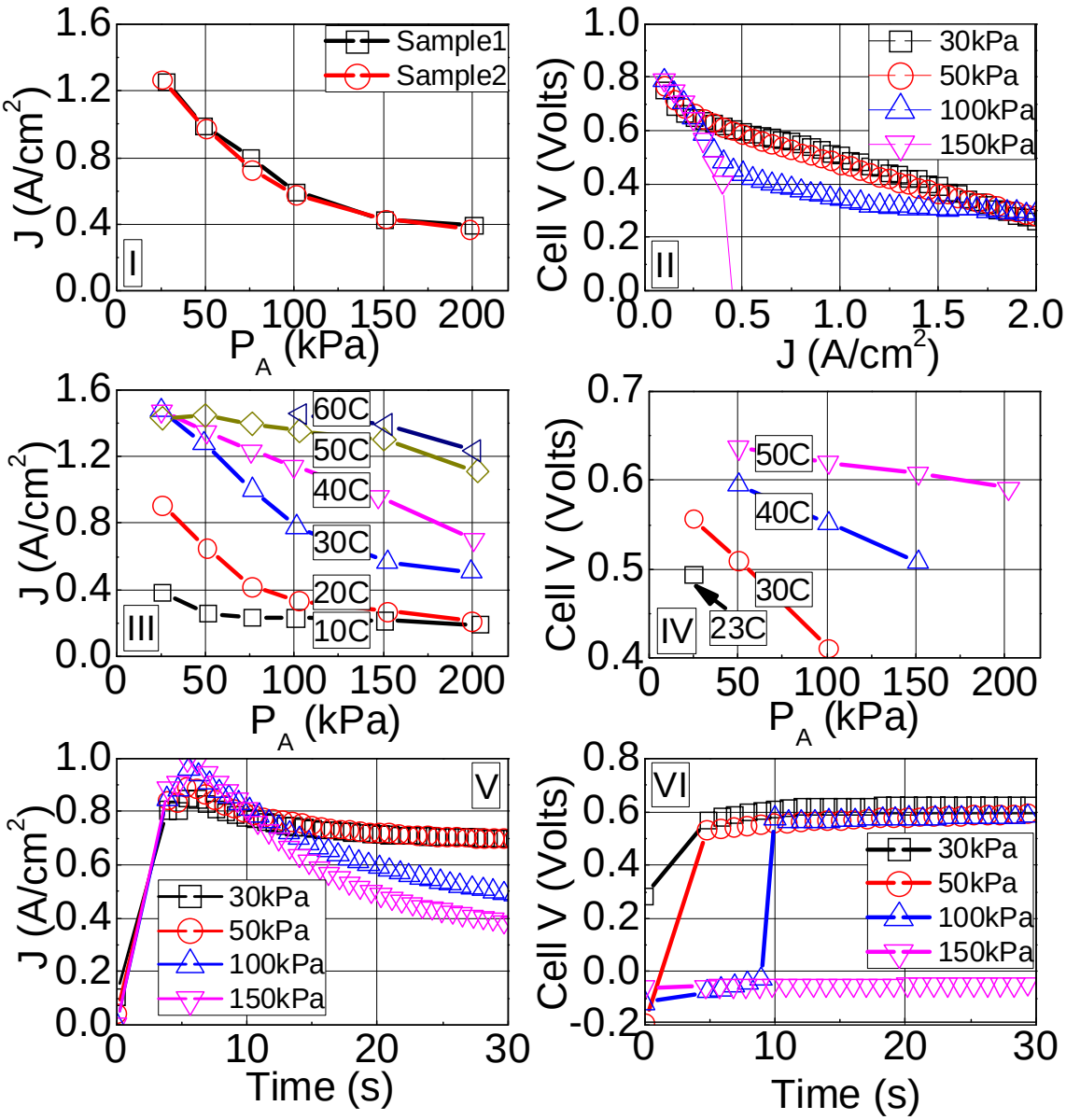


Figure 1. Evaluation of Baseline NSTFC MEA under Tests I-VI.

Test V evaluated the 0.6V current density performance under a pseudo-automotive startup procedure as a function of $P_A$. For all conditions, J increased rapidly from 0 to ~0.8-1.0A/cm$^2$, peaked within 7s, and then slowly decayed towards a steady state level. The decay in J after the peak is due to water accumulation in the MEA leading to oxygen mass transport restrictions. $P_A$ had only minimal effect on the peak J, but the ability to maintain high J after this peak period did increase as $P_A$ decreased.

Test VI evaluated the ability to maintain positive cell voltage during a fast load transient from 0.02 to 1.0A/cm$^2$, conducted with oversaturated gases of 140% RH. At 150kPa, the cell voltage remained at approximately -0.05V over the duration of the test, consistent with significant cathode oxygen mass transport limitations resulting in the evolution of $H_2$ gas being the dominant reaction rather than oxygen reduction. As the pressure was reduced to 100kPa, the initial cell voltage was negative but after 10s the cell spontaneously recovered and was able to produce a positive voltage. Further decreases in

$P_A$ resulted in shortening of the initial time with negative voltage, and at 30kPa the initial voltage was positive. The performance after 30s of operation was also found to improve significantly as $P_A$ was reduced.

Impact of Anode Pressure – Product Water Distribution, Phase Analysis

As observed in the multiple experiments of Fig. 1, reduction of the anode reactant pressure greatly increased the performance of the Baseline NSTFC MEA under relatively low temperature operation where significant water condensation can typically occur. In this section, we report experimental results and analysis which suggest that the improved performance with decreasing anode pressure is due to a reduction in the amount of product water removed out the cathode in the liquid phase.

At steady state, some fraction of the product water generated at the cathode electrode is transported through the cathode GDL and into the cathode flow field where it is removed from the cell, and the remainder is transported through the PEM, anode electrode and anode GDL into the anode flow field. Understanding the distribution of product water removal out the anode and cathode pathways can provide evidence towards the mechanism by which the reduced anode pressure causes increased performance at low temperature. In addition, the product water transported out the anode and cathode pathways is distributed among the liquid and vapor phases, and this phase distribution is also of considerable consequence for mechanistic understanding. The transport of liquid phase product water out the cathode pathway can lead to reduced performance since the presence of liquid water in the cathode electrode and GDL can restrict oxygen transport from the cathode flow field to the cathode electrode, leading to reduced oxygen concentration at the cathode electrode.

Fig. 2 shows the measured anode water effluent flow rate (top left), measured cathode water effluent flow rate (top right), and cell voltage (middle right) as a function of $P_A$ and cell temperature at fixed J of 1A/cm$^2$ under Test IV. Note that anode effluent flow rates were not measured for $P_A$ < 101kPa. These tests were conducted with dry inlet reactants, so the effluent water is the water produced from the fuel cell reaction. Several effects are apparent as $P_A$ was decreased at fixed cell temperature, namely the anode effluent water flow rate (WFR) increased, the cathode effluent WFR decreased, and the cell voltage increased. As the cell temperature decreased from 50 to 23°C, the cell voltage at a given $P_A$ decreased monotonically, but the water distribution out the anode and cathode was insensitive to cell temperature below 40°C.

Fig. 2 (middle left) shows the fraction of the total generated water removed out the anode, calculated by dividing the measured anode effluent flow rate (Fig. 2 top left) by the water generation rate of 0.280g/min for a 50cm$^2$ cell operating at 1A/cm$^2$. Since anode WFR measurements were not available when $P_A$ < 101kPa, the anode WFRs for said conditions were calculated by subtraction of the cathode WFR from the water generation rate and corrected by the average water collection error from this data set, 92.9 ± 1.4 %. For all T, the fraction of product water removed out the anode increased as $P_A$ decreased, reaching as high as 85% as $P_A$ decreased to 25kPa. As noted above, the fraction of water removed out the anode was insensitive to cell temperature between 23-40°C, and decreased when the cell temperature increased to 50°C. These results provide a qualitative rationale for the performance improvement with decreasing $P_A$, namely that

as the anode pressure was reduced, the amount of water leaving the cathode was also reduced and thereby the oxygen transport restrictions were reduced. However, this analysis alone does not provide insight into the strong dependence of cell voltage on temperature between 23-40°C where no change in anode-cathode product water distribution was observed.

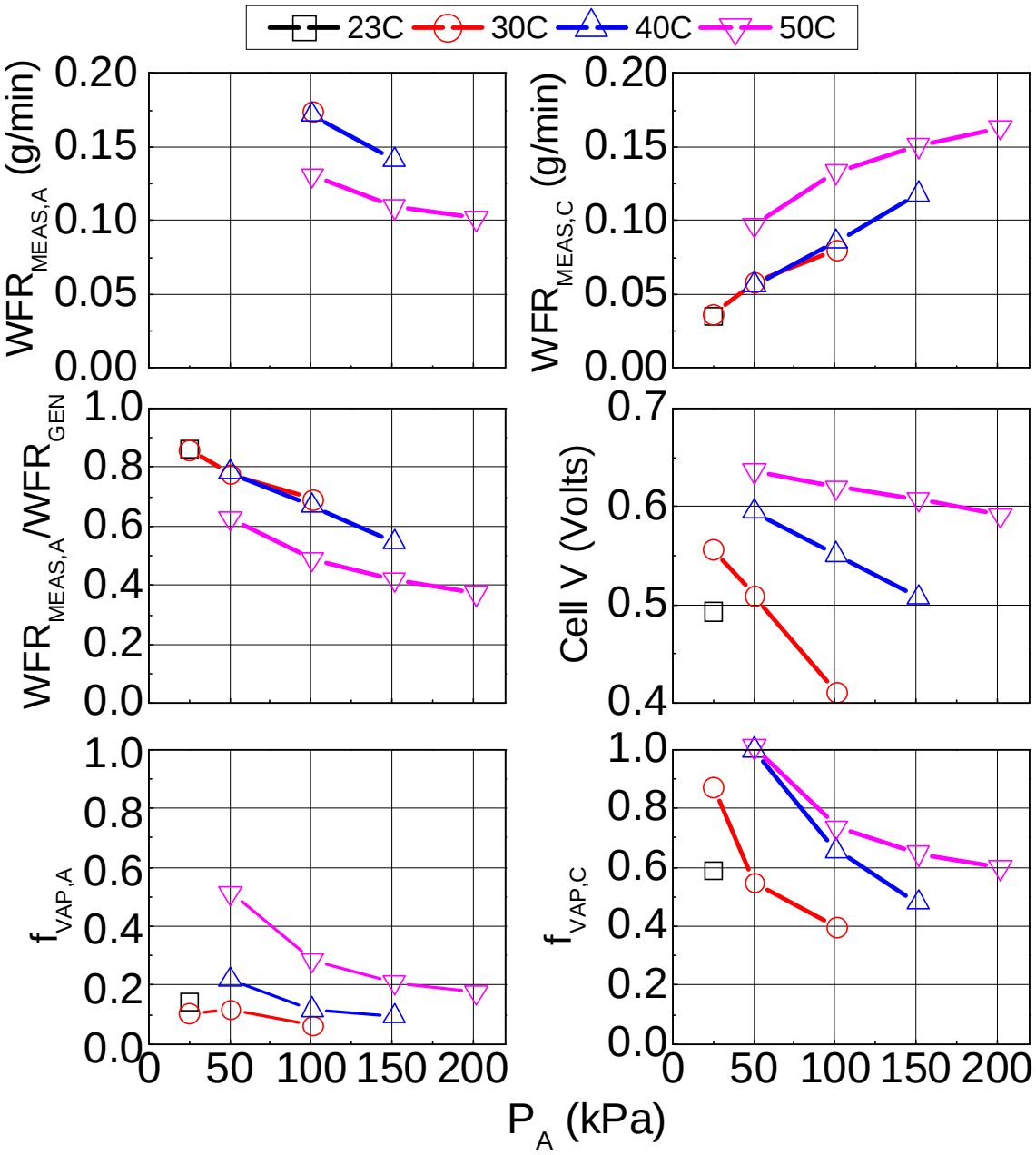


Figure 2. Test IV measured anode and cathode product water effluent rates and calculated vapor phase removal fractions with the Baseline NSTFC MEA.

Estimation of the phase of the water transported from the cathode electrode through the anode and cathode GDLs into the flow fields provides some insight into the performance dependence on cell temperature. The two figures in the bottom row of Fig. 2 show results of simple calculations which estimated the fraction of water removed out each electrode in the vapor phase for the anode (bottom left) and cathode (bottom right). The fractional vapor phase removal out each electrode was estimated by calculating the

water flow rate corresponding with vapor saturation of each electrode's reactant stream at the respective electrode's cell outlet boundary conditions, and dividing this calculated saturation water flow rate by the measured water flow rate exiting that electrode. While this simple calculation does not capture the complexity of PEM fuel cell two-phase water transport with the significant down-the-channel gradients of reactant concentration, current density, and water flux which are likely present in a working fuel cell, it does provide an initial basis for estimating overall tendency trends of vapor phase water removal from each electrode with changes in operating conditions. The saturation water flow rate at each electrode's cell outlet boundary conditions was calculated as follows. Eqn. 1 shows a version of Dalton's law of partial pressures, which states that the ratio of the saturated water vapor pressure to the total pressure ($p^*_{H20}/P_x$, x is anode or cathode) is equal to the ratio of the saturated vapor molar flow rate ($n^*_{VAP,x}$) to the total gas phase vapor and reactant molar flow rates ($n^*_{VAP,x}+n_{RCT,x}$). Each electrode's fractional vapor phase water removal rate ($f_{VAP,x}$) was calculated by Eqn. 2, which is a rearrangement of Eqn. 1 normalized to each electrode's measured total (liquid and vapor) molar water flow rate and calculated at each electrode's exit boundary conditions. Note that Eqn. 2 is valid only when the saturated water vapor pressure is less than the total pressure, which was the case for all conditions evaluated in this paper.

$$p^*_{H20}/P_x = n^*_{VAP,x}/(n^*_{VAP,x}+n_{RCT,x}) \quad [1]$$

$$f_{VAP,x} = n^*_{VAP,x} / n_{H2OMEAS,x} = n_{RCT,OUT,x}/(P_x/p^*_{H2O}-1) / n_{H2OMEAS,x} \quad [2]$$

The bottom row of Fig. 2 shows that for both electrodes, the fraction of water removed out each electrode in the vapor phase generally increased as $P_A$ decreased and as cell temperature increased. On the cathode, the fraction of vapor removal was generally higher than 40% for all cases, and at fixed cell temperature was found to increase substantially as $P_A$ decreased, due entirely to the decreasing absolute cathode effluent water flow rate with decreasing $P_{A,}$ since the cathode exit boundary conditions were fixed. On the anode, the fraction of water removed in the vapor phase was markedly smaller than that observed on the cathode under the same conditions, typically less than 30% for a majority of conditions, and was generally much less sensitive to changes in anode pressure than the cathode.

The analysis above reveals a qualitative correlation between fractional vapor phase water removal out the cathode and the measured cell voltage. As $f_{VAP,C}$ increased due to increasing cell temperature and decreasing anode pressure, the cell voltage also generally increased in similar trend. This can be rationalized by considering that as the fractional vapor phase removal out the cathode increases, the fractional *liquid* phase removal out the cathode decreases, thus lessening the water content of the cathode electrode and GDL and reducing oxygen transport restrictions from the cathode flow field to the cathode electrode.

Impact of MEA Components – Anode GDL Backing, Treatments

As discussed in the previous section, increasing the fraction of the total generated water removed via the anode correlates with significant performance improvement at relatively lower temperatures as the cell temperature and anode pressure were varied. As may be expected, one of the key MEA component variables found to be important in this

study was the anode GDL. Fig. 3 (left) compares the performance of Baseline NSTFC MEAs with several different anode GDL backings, used as received from the vendor with no MPL, and Fig. 3 (right) compares as-received backing "C" to a version with PTFE and MPL treatment. At 150-200kPa, little difference in performance was observed with the different anode GDLs, but the backing type had a strong influence on the rate and extent of J increase as $P_A$ was reduced, with backings "A" and "B" having approximately 3x the maximum J as type "E". Addition of MPL and PTFE treatment to backing "C" resulted in only a slight change compared to the untreated analogue.

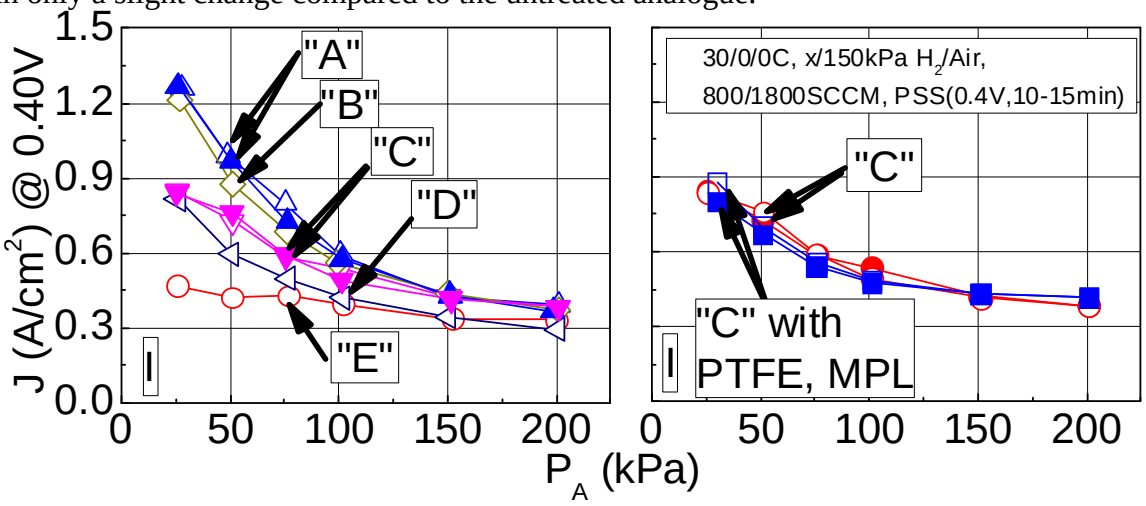


Figure 3. Baseline NSTFC MEA under Test I with different anode GDLs. Left: Various backings without PTFE or MPL. Right: Impact of PTFE and MPL with one backing.

While the relative distribution of product water removal out the anode and cathode and between liquid and vapor phases was considered a significant performance factor for temperature and $P_A$ variation, it does not necessarily explain the performance variation when the anode GDL was changed. Fig. 4 compares the performance and measured cathode effluent WFRs for MEAs with anode GDLs comprised of untreated backing "A" or type "C" which was treated with PTFE.

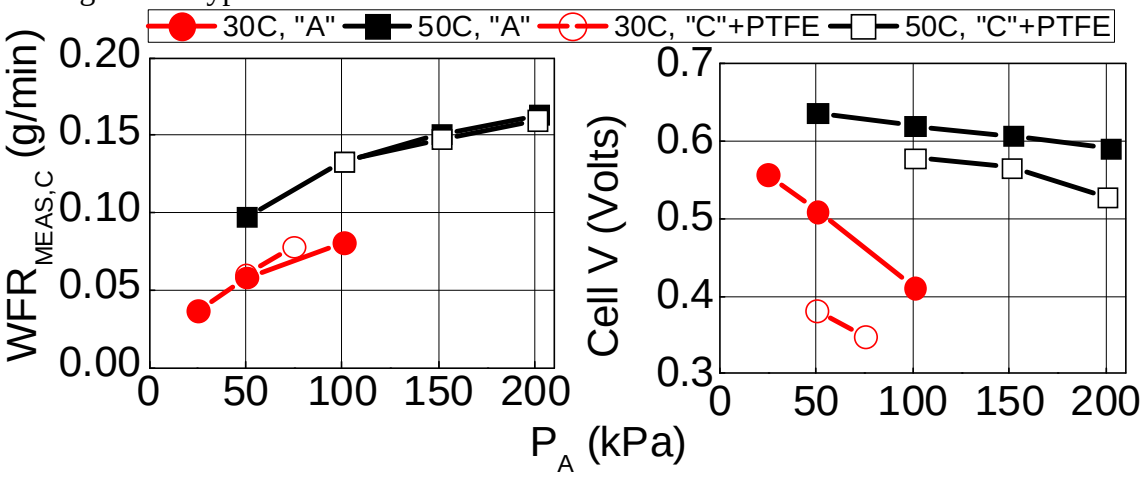


Figure 4. Baseline NSTFC MEA under Test IV with untreated type "A" or PTFE-treated type "C" anode backings, both without MPL.

While a significant and consistent performance difference was observed between the two anode GDLs at both 30 and 50°C, no significant difference in product water distribution out the anode and cathode was observed. As a result, there is also no

difference in the calculated distribution between vapor and liquid phase water removal. As such, while the reduction in liquid water removal out the cathode may explain the performance improvement as $P_A$ is reduced and cell temperature increases, it does not necessarily account for the performance difference caused by different anode GDLs; understanding the anode GDL material factors which influence low temperature performance is an active research topic in our laboratory.

## SUMMARY

In this paper, we reported a novel water management methodology for PEM fuel cells which utilize ultra-thin electrodes, such as the 3M Nanostructured Thin Film Catalyst. Under relatively low temperature conditions where significant water condensation occurs within the fuel cell, the limiting current density was found to increase by up to a factor of 4 when the anode hydrogen reactant operating pressure was reduced from 150kPa to 30kPa. This increased performance was found to have significant dependence on anode reactant pressure, cell temperature and variation of the anode gas diffusion layer. Product water distribution measurements suggest that the mechanism responsible for the improved low temperature performance observed with reduced anode reactant pressure was due to a reduction in product water removal out the cathode, likely reducing liquid water flooding and oxygen mass transport restriction. Simple water phase calculations suggest that the strong temperature dependence of performance is due to relative changes in the amount of water exiting the cathode in the liquid phase. The product water distribution and water phase analyses do not appear to explain the observed performance variation due to anode gas diffusion layer change, and is an active topic of research in our laboratory.

## ACKNOWLEDGEMENTS

We would like to acknowledge the US Department of Energy, which provided funding for this work under Grant DE-FG36-07GO17007.

## REFERENCES

1. A. J. Steinbach, K. Noda and M. K. Debe, ECS Trans., **3**(1) 835 (2006).
2. M. K. Debe, A. K. Schmoeckel, G. D. Vernstrom and R. Atanasoski, J. of Power Sources, **161** 1002 (2006).
3. M. K. Debe, in DOE Hydrogen Program Review, Presentation FC17, Washington DC (2009).
4. M. K. Debe, A.E. Hester, G. D. Vernstrom, A. J. Steinbach, S. M. Hendricks, A. K. Schmoeckel, R. T. Atanasoski, D. J. McClure, and P. L. Turner, "Nanostructured Thin Film Catalysts for PEM Fuel Cells by Vacuum Web Coating," in proceedings of the 50th Annual Technical Conference of the Society of Vaccum Coaters, Louisville, KY, May 1, 2007.
5. A. J. Steinbach, C.V. Hamilton, Jr., and M. K. Debe, ECS Trans., **11** (1) 889 (2007).
6. K. A. Lewinski, A. J. Steinbach, S. M. Hendricks, and D. R. Miller, ECS Trans., **16** (2) 831 (2008).

# Influence of Anode GDL on PEMFC Ultra-Thin Electrode Water Management at Low Temperatures

Andrew J. Steinbach, Mark K. Debe, Matthew J. Pejsa, Daniel M. Peppin, Andrew T. Haug, Mike J. Kurkowski and Susan M. Maier-Hendricks

*ECS Trans.* 2011, Volume 41, Issue 1, Pages 449-457.
doi: 10.1149/1.3635579

ECS Transactions, 41 (1) 449-457 (2011)
10.1149/1.3635579 ©The Electrochemical Society

# Influence of Anode GDL on PEMFC Ultra-Thin Electrode Water Management at Low Temperatures

A. J. Steinbach, M. K. Debe, M. J. Pejsa, D. M. Peppin, A. T. Haug, M. J. Kurkowski, S. M. Hendricks

3M Company, Fuel Cell Components Program, 3M Center, St. Paul, MN 55144, USA

In this paper, we provide results of new anode gas diffusion layer materials which dramatically improved the performance of ultra-thin electrode polymer electrolyte membrane fuel cells under highly water-condensing operating conditions, realized via optimization of the anode gas diffusion layer backing and microporous layer coatings.

## INTRODUCTION

In addition to meeting cost, durability, and rated performance targets, polymer electrolyte membrane (PEM) fuel cell systems for automotive traction applications additionally need the capability to transiently attain relatively high current densities at low temperatures to provide drive-away power. Additionally, the system ideally would be robust towards atypical shutdown/restart events which may leave the fuel cell stack in a relatively flooded state.

Membrane electrode assemblies (MEAs) utilizing the ultra-thin (<1μm) 3M nanostructured thin film catalyst (NSTFC) technology have several demonstrated advantages compared to MEAs comprising conventional, relatively thick (~10μm) carbon-supported catalyst, such as increased durability towards start-stop (1) and voltage cycling (2), higher specific activity (3), and high specific rated power(3). However, the low temperature (0-50°C) steady state limiting current density of typical NSTFC MEAs under usual operating conditions is substantially lower than that of many conventional catalyst MEAs (e.g. 0.2-0.4 v. >1A/cm$^2$ at 30°C, air cathode). This reduced low temperature performance can be attributed to the NSTFC's much higher water generation rate per unit catalyst volume and to an electrode pore structure that is more susceptible to water condensation.

We have previously reported a strategy for improved low temperature water management with ultra-thin electrodes which resulted in a several-fold increase in low temperature limiting current density with NSTFC MEAs, enabled by MEA product water removal predominantly via the anode and facilitated by reduction of the anode reactant pressure to sub-atmospheric pressures as low as 20kPa (4). Further work has revealed that choice of the anode gas diffusion layer (GDL) backing can also achieve several-fold gains in low temperature response even with atmospheric (101kPa) anode reactant pressure. Experiments consisted of MEA evaluation of several different anode GDL backings, with or without addition of various hydrophobic/hydrophilic treatments to the backing and with or without addition of either a typical microporous layer (MPL) or one modified to contain metal oxide nanoparticles. Low temperature performance variation

due to backing selection was found to be dominant; addition of hydrophobic/hydrophilic treatment to the backings and/or addition of microporous layers (MPLs) generally yielded much smaller effects.

## EXPERIMENTAL

### NSTFC MEA Preparation

NSTF PtCoMn ternary catalyst, containing 0.05, 0.10, or 0.15mg/cm$^2$ Pt, was prepared as a roll-good on continuous vacuum deposition equipment, as described previously (5). Catalyst coated membranes (CCMs) made with NSTFC were prepared by cutting 50cm$^2$ catalyst substrates from the uniform roll-good catalysts prepared above. The substrates were placed on either side of a PEM and passed through a heated, pressurized laminator, after which the substrates were removed. PEMs consisted of either a 3M 850EW 20-24μm unsupported PEM or a 3M 850EW ionomer incorporated into a thinner, supported PEM (6). The resultant anode/cathode loadings of the CCMs were either 0.05/0.10mg/cm$^2$ Pt or 0.05/0.15mg/cm$^2$ Pt. The anode GDL consisted of a variety of bare commercial and experimental carbon papers provided by several vendors, which were either used as received with no microporous layer (MPL) or with application of <10% PTFE to the bare backing and/or with application of MPLs consisting of several basis weights and two formulations (with or without metal oxide nanoparticles). Anode backings were obtained from Mitsubishi Rayon Corporation (MRC), Freudenberg FCCT (Freud), Hollingsworth and Vose (H+V), and Ballard Material Products. The cathode GDL was fixed and consisted of a 3M proprietary design, utilizing MRC U105 carbon paper, carbon black, and hydrophobizing agents. Hardstop Teflon-coated fiberglass gaskets were selected to provide 10% compressive strain to the GDLs. CCMs, GDLs, and gaskets were assembled into a typical 50cm$^2$ electrode area quad serpentine test cell obtained from Fuel Cell Technologies.

### Test Equipment

The test stands consisted of thermal mass flow controllers for reactant control, an electronic load for cell polarization control, electronic temperature controllers, and either manually or electronically actuated back pressure controllers for reactant pressure control. Cell temperature was controlled by a fan under the cell end-plates, coupled with cell heaters inserted into the end-plates which were controlled by an electronic temperature controller. Humidification was provided to the fuel cell by two LabAlliance HPLC pumps, one for each reactant stream. Each HPLC pump fed liquid water into a Swagelok tee, into which the gaseous reactants were also fed; the wet reactant streams were then fed to the fuel cell. The humidification water was not heated prior to entering the cell, so the humidification water entered the cell primarily in the liquid phase. In our experience, this method of providing humidification works equivalently to sparge bottle humidifiers for small single cells. The test stands were controlled by custom software, allowing for reproducible test operation.

Evaluation Procedures

All MEAs were first conditioned using a process we refer to as "thermal cycling", described in references (7). After conditioning, MEA water management performance was evaluated using one or more of the following methods, Tests I-IV.

Test I: High Current Test (HCT). In this test, the MEA performance was evaluated under a pseudo-automotive polarization curve at relatively high temperature. Operating conditions were 80°C cell temperature, cathode reactant stream of constant stoichiometry (2.5) 68°C dewpoint air at 150kPa total pressure, anode reactant stream of constant stoichiometry (2.0) 68°C dewpoint $H_2$ anode reactant at 150kPa total pressure, and the cell current density was scanned from 0.02A/cm$^2$ up to an upper limit of 2.0A/cm$^2$ in a mixed linear/log-stepping mode with 120s dwell time at each condition.

Test II: Psuedo-Automotive Startup Transient. The objective of this test was to evaluate the MEA performance in a pseudo-automotive startup procedure; see our previous publication (8) for further description and possible data analysis from this test. The MEA was first preconditioned to a relatively dry humidification state, cooled to the desired startup temperature with no reactant flow, and then the performance was evaluated immediately upon reintroduction of reactant gases. The MEAs were preconditioned at 80°C cell temperature, cathode reactant of 1657SCCM, 30% RH, 101kPa air, anode reactant of 696SCCM, 30% RH, 101kPa $H_2$, and fixed J of 0.05A/cm$^2$ for 5 minutes. The MEA was then cooled to the desired Startup Transient temperature of 30°C. For the Startup Transient, the conditions were set to cathode reactant of 1800SCCM, 0% RH, 150kPa air, anode reactant of 800SCCM, 0% RH, 101kPa $H_2$, and the cell voltage was immediately set to 0.40V and held for 10 minutes, during which the J response was measured.

Test III: Cool Steady State Performance v. Temperature, %RH. In this test, the MEA performance was evaluated as a function of cell temperature between 30 and 50°C and anode and cathode humidification of either 0 or 100% RH. Cathode reactant stream conditions were 1800SCCM fixed air flow at 150kPa total pressure and anode reactant stream conditions were 800SCCM fixed $H_2$ flow at 101kPa total pressure, and the cell potential was held at 0.40V for 10minutes at each condition; the cell current density over the final 1 minute was averaged and is reported here.

Test IV: Psuedo-Automotive Load Transient v. Temperature. This test evaluated the MEA's ability to withstand a rapid increase in load from an idle state, as may be expected to occur in automotive traction applications. The MEA was first equilibrated at the desired cell temperature, cathode reactant of 1657SCCM, 100% RH, 150kPa air, anode reactant of 696SCCM, 100% RH, 150kPa $H_2$, and fixed cell potential of 0.6V for approximately 5 minutes. Next, the load was decreased to 0.02A/cm$^2$ and held for 30s to emulate a system idle state. Finally, the Load Transient was conducted by rapid load increase to 1A/cm$^2$ in < 1s, and the cell was held under these conditions for 30s during which the cell voltage response was measured. Inability to attain a positive cell voltage within 5 seconds was considered a failure under this test.

## RESULTS AND DISCUSSION

Impact of Anode GDL Backing Under Tests I-IV

Fig. 1 shows the strong impact of anode GDL on performance under several tests which evaluate the MEA's ability to demonstrate high power (Test I), transient startup (Test II), steady state startup (Test III), and load transient (Test IV); details of the procedures for these tests are provided in the Experimental section. All anode GDLs consist of backings obtained from vendors to which similar backing hydrophobic treatments and MPLs were applied by 3M. MEAs consisted of 0.05/0.15mg-Pt/cm$^2$/NSTF on a supported PEM (6), with a fixed cathode GDL (MRC A), and all were evaluated on the same test station.

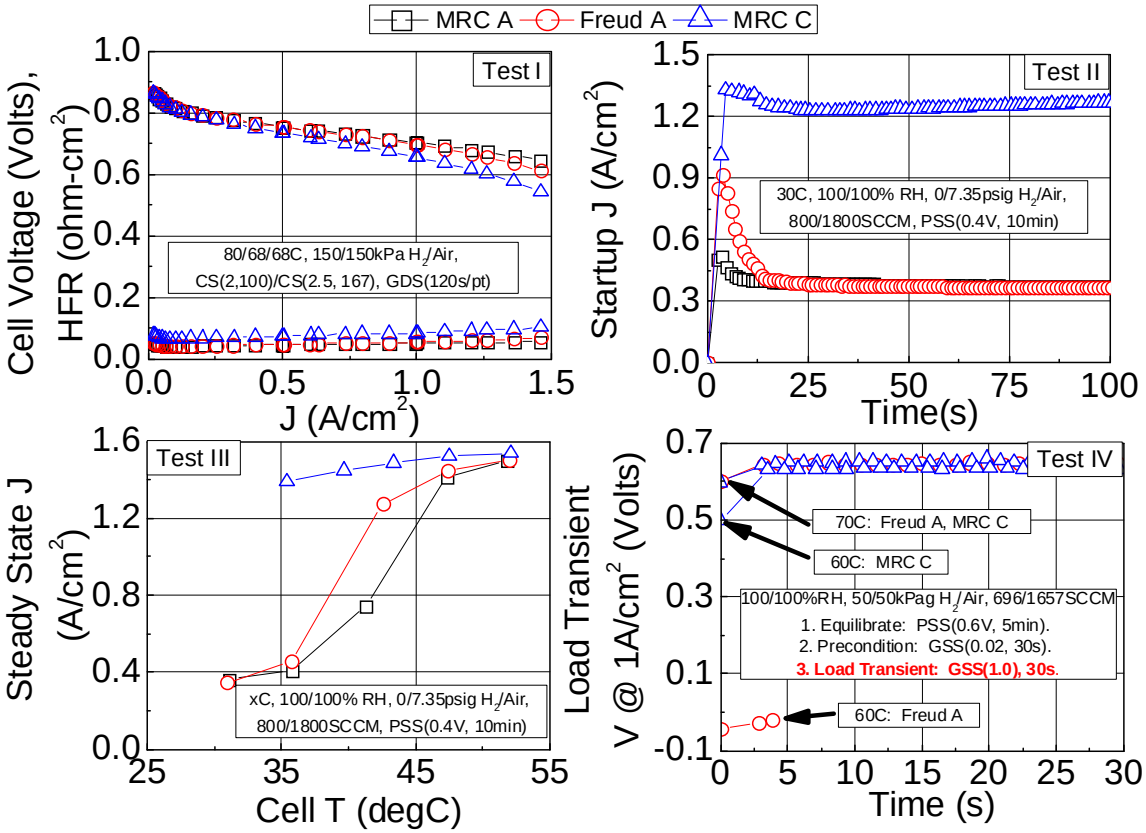


Figure 1. Variation in Test I-IV Performance v. Anode GDL. All anode GDLs comprised of vendor-supplied backing with 3M hydrophobic and MPL application.

Under Test I, the MEAs with GDLs MRC A and Freud A yielded similar performance whereas the MEA with MRC C had lower performance at high current density, due to higher HFR. Under Test II, a pseudo-system startup transient, Freud A GDL provided a short burst of higher performance than MRC A, but the current density dropped to the MRC A level within ~15s. MRC C, which had lower performance than the other GDLs under Test I, yielded transient current densities which were 50% higher than Freud A and a steady state current density approximately 3x than of the other two GDLs. Under Test III, MEAs with either MRC A or Freud A GDL had similarly low performances at 30°C. As the cell was heated, the performance with both GDLs improved, with Freud A having better performance at 40°C than MRC A. MRC C, which performed well under Test II, also performed well at low temperature steady state conditions. As the cell temperature exceeded 50°C, all three MEAs performed similarly.

Under Test IV, MEAs with either Freud A or MRC C performed similarly as the current density was stepped up from 0.02 to 1A/cm$^2$ when the cell temperature was 70°C, but at 60°C, Freud A was unable to provide a positive cell voltage at 1A/cm$^2$ whereas MRC C only showed a slight loss relative to 70°C.

Evaluation of Untreated Backing Type Under Tests I, III

Fig. 2 summarizes results which illustrate the influence of anode backing on both low and high temperature performance response under Tests III and I. Experiments were conducted with 3M NSTF MEAs comprising anode and cathode loadings of 0.05 and 0.10mg/cm$^2$ Pt with a 3M 20µm PEM. Anode GDLs comprised of the bare, untreated backings used as received from the vendors.

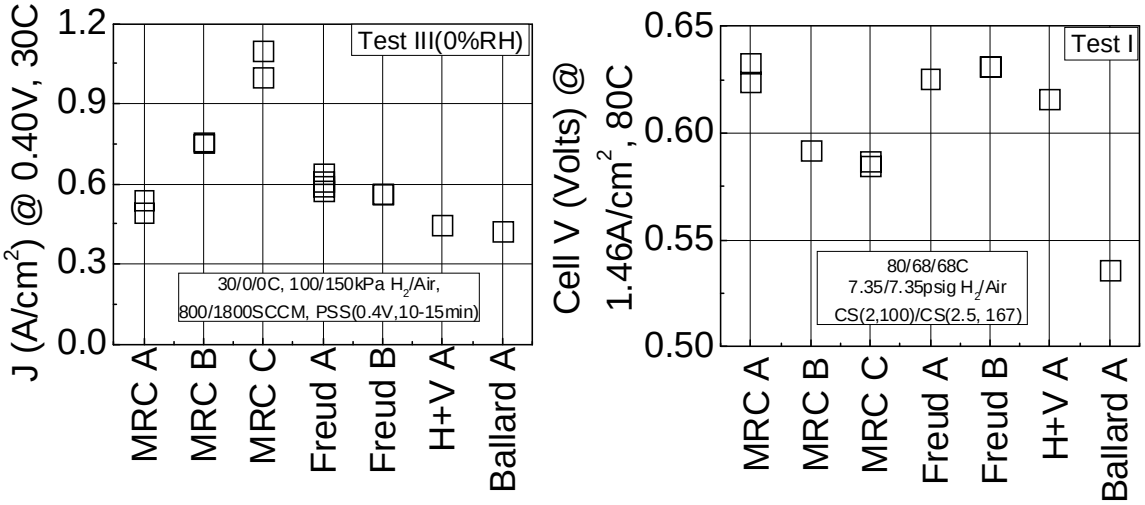


Figure 2. Impact of Anode GDL on Test III (left) and Test I (right).

Significant variation in response is observed with both low and high temperature response. At 30°C cell temperature, the current density varied more than a factor of 2 as the backing type varied. At 80°C cell temperature, the cell voltage change with anode backing was approximately 80mV, with MRC A, Freud A and Freud B giving the highest performances. A key observation is that the low temperature performance is not positively predictive of the high temperature response. MRC B and MRC C, which yielded the highest 30°C current density, also had 80°C performance which was ~ 30-40mV lower than MRC A. The primary factor for the reduced 80°C performance of MRC B and C is a higher measured in-cell resistance, as shown in Fig. 1 for MRC C.

Evaluation of Backing Thickness, Treatments Under Tests I, III

While product water removal out through the anode GDL is an effective means for improving low temperature performance in ultra-thin electrode MEAs(4), it is unclear if the anode GDL is an actual restriction for liquid water transport. In order to obtain a better mechanistic understanding of how the anode backing can so strongly influence low temperature performance, experiments were conducted to evaluate the impact of liquid water permeability and wettability. A summary of these results are shown in Fig. 3; the same CCM as Fig. 2 was used for Fig. 3 data.

Fig. 3 top shows an analogous experiment as shown in Fig. 2, but here either one or two untreated backings were installed, effectively doubling the GDL thickness and thereby doubling the bulk restriction towards liquid water flux. For either MRC A or Freudenberg A backings, no influence of GDL thickness was observed under Test III, the low temperature response. Under Test I, doubling the thickness of MRC A had no effect at 80°C, but doubling the thickness of Freud A appeared to be detrimental. Fig. 3 bottom summarizes the impact of the application of hydrophobic (PTFE) v. hydrophilic ($ZrO_2$) treatment to the Freudenberg A backing. Under Test III, application of PTFE resulted in a slight gain in output current density, whereas application of $ZrO_2$ resulted in a significant reduction in current density, with the output decreasing slightly as the wt% of the $ZrO_2$ in the treatment solution increased from 1 to 10 wt%. Under Test I at 80°C, only subtle effects were observed with the different backing treatments, other than at 10wt% $ZrO_2$ where the MEA's limiting current was reduced and was unable to attain 1.46A/cm$^2$. Test III results from Fig. 3 suggest that restriction of liquid water movement through the bulk of the anode GDL is not the primary performance limiting factor with either the MRC A or Freudenberg A.

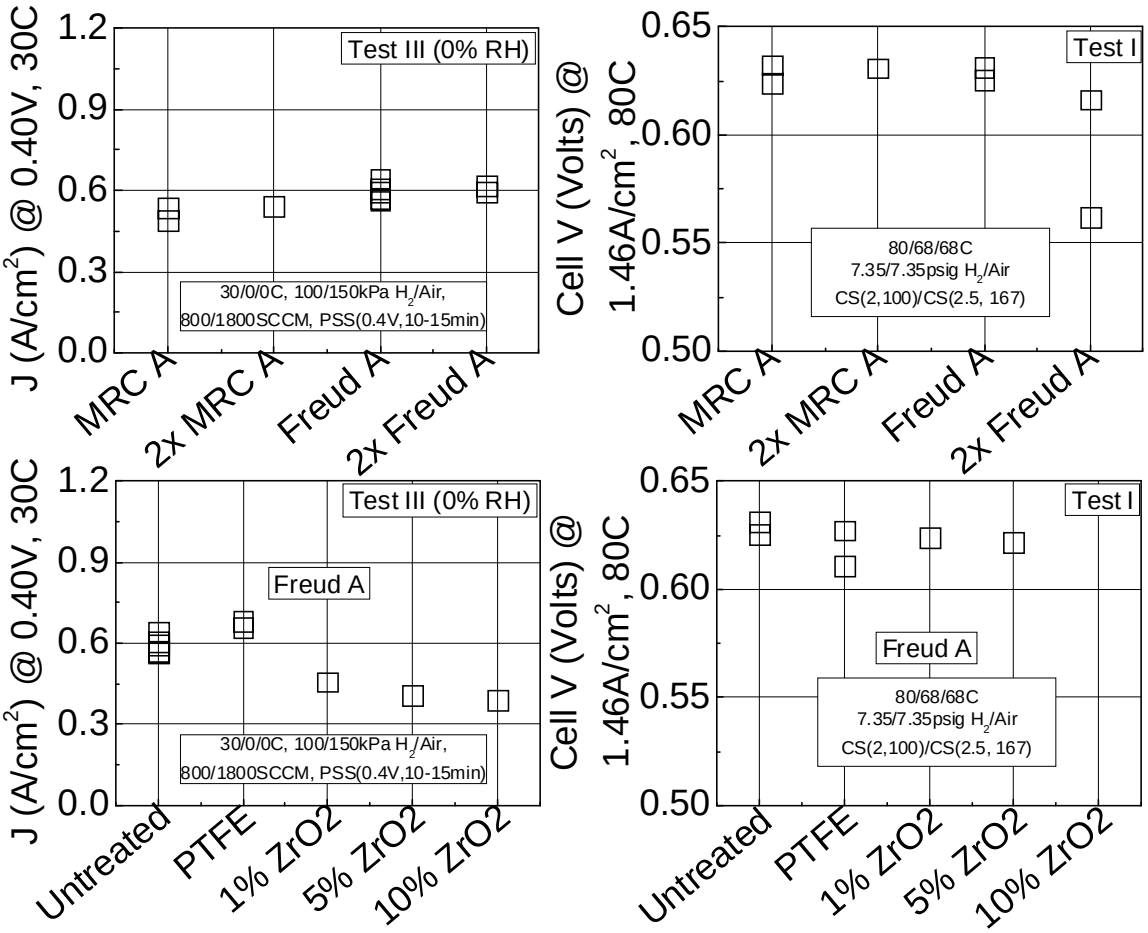


Figure 3. Impact of Anode GDL thickness with MRC A and Freudenberg A (top row) and Hydrophobic v. Hydrophilic Treatment of Freudenberg A (bottom row).

Evaluation of MPL Thickness, Composition Under Tests I, III

The impact of MPL on the low and high temperature performance was also examined. Fig. 4 summarizes experiments which evaluated the impact of MPL coating weight ("Basis weight") onto the Freud A and MRC C substrates. In this series of tests, the MPL consisted of a combination of hydrophobic polymers and carbon black. With Freud A under Test III, performance was found to decrease with increasing MPL coating weight, whereas at under Test I at 80°C a modest trend of increasing performance with increasing coating weight was observed. With MRC C under Test III, a slight reduction (<10%) was also observed with addition of MPL; under Test I, presence of MPL had no apparent affect on average.

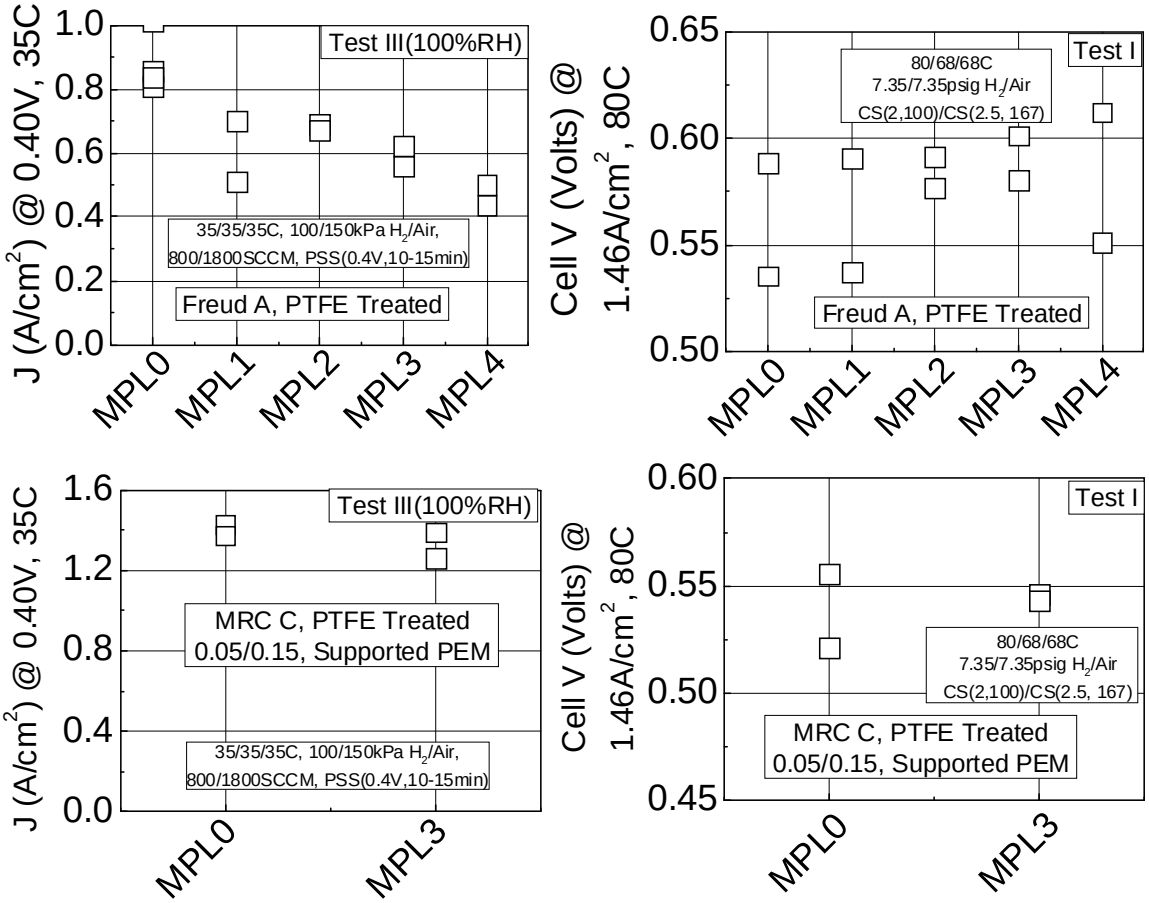


Figure 4. Impact of Standard MPL Basis Weight for Freud A (top) and MRC C (bottom) backing. Level 0 is no MPL; increasing numbers correlate with increasing MPL coating weight.

SEM micrographs were taken of a subset of the materials evaluated. Fig. 5 shows top-down views of MPL2 and MPL4 Freud A GDLs from Fig. 4. Edge view micrographs, not shown, suggest that the thickness increased from ~ 50 to ~75μm from MPL2 to MPL4. The top down view indicates relatively similar, homogenous MPL coatings for both anode GDLs with defects consisting of cracks on the order of hundreds of microns long and < 10 microns wide. Since the MPL composition and coating methodologies were the same for MPL2 and MPL4, a reasonable assessment is that the ~30% decrease in current output is due to the 50% increase in MPL thickness.

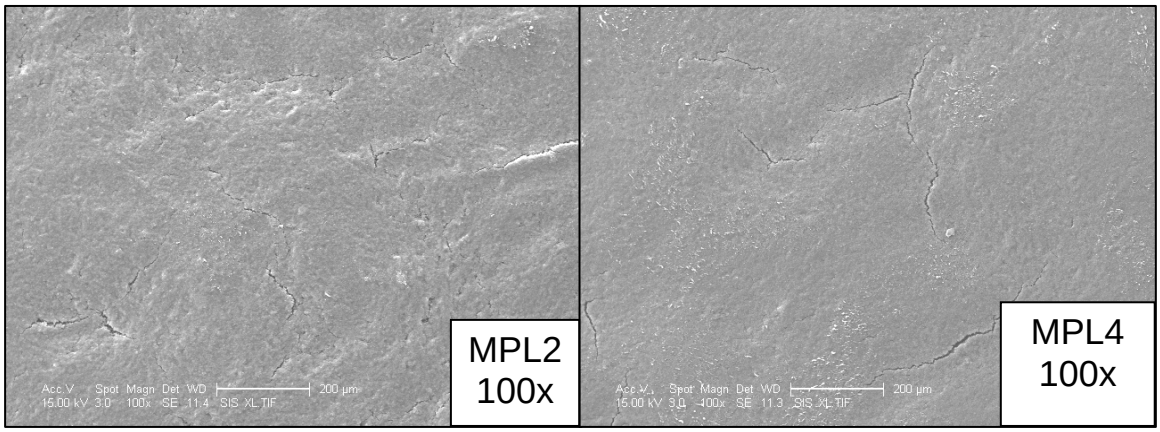


Figure 5. SEM Top-down views of MPLs 2 and 4 from Fig. 3. Scale bar is 200 microns; contrast and brightness increased to better show features.

In addition to MPL thickness, the impact of MPL composition was evaluated. Fig. 6 shows the results of a series of tests which examined the impact of total MPL basis weight with a standard MPL to which a stable metal oxide nanoparticle was added at approximately 10wt% of the carbon content. Metal oxide MPL basis weight increased ~45% from level 1 to 5. The CCM used for Fig. 5 was a 0.05/0.15mg-Pt/cm$^2$ on 3M 24u PEM. Subtle variations in the 35°C current density were observed as the metal oxide MPL basis weight increased, but not monotonically; on average, the metal oxide MPLs yielded slightly higher current output than the standard MPL. At 80°C, metal oxide MPLs 3, 4, and 5 had similar performances as standard MPL 3.

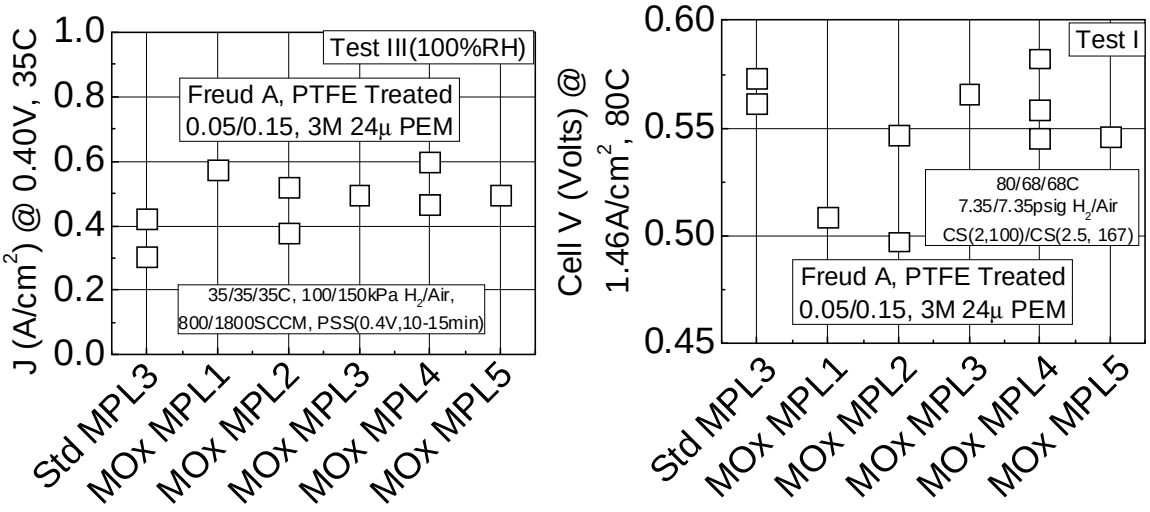


Figure 6. Impact of Metal Oxide-Containing MPL Total Basis Weight, all with PTFE treated Freud A backing. Increasing numbers correlate with increasing MPL coating weight. Std MPL3 has the same approximate basis weight as MOx MPL3.

## SUMMARY

In this paper, we reported the influences of anode GDL backing, backing treatments, and MPL thickness and composition on both the low temperature and high temperature response of MEAs with ultra-thin electrodes, such as the 3M Nanostructured Thin Film Catalyst. Anode backing was found to generally be the largest contributor to improved low temperature response; the best anode backing yielded an ~2x improvement in transient and an ~3x improvement in steady state 30°C performance over the baseline.

Exploratory studies on a subset of the backings were also conducted. Doubling the anode backing thickness had little effect on low temperature performance with two different backing types. Modification of one backing's wettability through application of either PTFE or $ZrO_2$ resulted in slight improvement with PTFE and modest to significant reduction with $ZrO_2$, dependent upon the level of $ZrO_2$ added.

Addition of a typical MPL to either of two backings resulted in slight to significant reduction in low temperature response relative to the untreated backings, dependent upon the amount of MPL added. Addition of a stable metal oxide nanoparticle to the MPL generally resulted in a slight increase in the low temperature performance with one backing compared to the same backing and MPL without metal oxide nanoparticles.

## ACKNOWLEDGEMENTS

We would like to acknowledge the US Department of Energy, which provided funding for this work under Grant DE-FG36-07GO17007.

## REFERENCES

1. A. J. Steinbach, K. Noda and M. K. Debe, ECS Trans., **3**(1) 835 (2006).
2. M. K. Debe, A. K. Schmoeckel, G. D. Vernstrom and R. Atanasoski, J. of Power Sources, **161** 1002 (2006).
3. M. K. Debe, in DOE Hydrogen Program Review, Presentation FC17, Washington DC (2009), http://www.hydrogen.energy.gov/pdfs/review09/fc_17_debe.pdf .
4. A.J. Steinbach, M.K. Debe et. al, ECS Trans., **33**(1) 1179 (2010).
5. M. K. Debe, A.E. Hester, G. D. Vernstrom, A. J. Steinbach, S. M. Hendricks, A. K. Schmoeckel, R. T. Atanasoski, D. J. McClure, and P. L. Turner, "Nanostructured Thin Film Catalysts for PEM Fuel Cells by Vacuum Web Coating," in proceedings of the 50th Annual Technical Conference of the Society of Vaccum Coaters, Louisville, KY, May 1, 2007.
6. GORE-SELECT® membrane prepared by Gore using 3M ionomer. GORE-SELECT and GORE and designs are trademarks of W.L. Gore and Associates, Inc. Further processing of the as-received membrane was done at 3M before converting the NSTF catalysts.
7. A. J. Steinbach, C.V. Hamilton, Jr., and M. K. Debe, ECS Trans., **11** (1) 889 (2007).
8. K. A. Lewinski, A. J. Steinbach, S. M. Hendricks, and D. R. Miller, ECS Trans., **16** (2) 831 (2008).

*Journal of The Electrochemical Society*, **159** (1) B54-B67 (2012)
0013-4651/2012/159(1)/B54/14/$28.00 © The Electrochemical Society

# Effect of Electrode Surface Area Distribution on High Current Density Performance of PEM Fuel Cells

**Mark K. Debe**[*,z]

*3M Fuel Cell Components Program, 3M Center, St. Paul, Minnesota 55144, USA*

Commercialization of automotive fuel cells requires current densities of 1.5 A/cm$^2$ above 650 mV with Pt loadings of 0.125 mg$_{Pt}$/cm$^2$ or less. Loss of high current density with cathode loadings below 0.2 mg$_{Pt}$/cm$^2$ in Pt/C electrodes is an issue that current kinetic/transport models are reported inadequate to explain. We show that this effect is much less at a given loading with the NSTF catalyst type electrodes and explain these differences using a model based on elementary kinetic gas theory and known molecule/surface interaction mechanisms that take place in the Knudsen regime. The result is an additional pre-exponential scaling factor $f(d_s)$ in the Butler-Volmer equation related to a distance metric $d_s$ describing the catalyst surface area distribution. We approximate this distance metric by the inverse of the surface area per unit volume of the electrode and define and test two possible functional forms for $f(d_s)$. The preferred form is able to predict the correct heat of enthalpy for $O_2$ physisorption and the observed ratio of current densities at V(iR-free) = 0.7 V for NSTF compared to Pt/C dispersed electrodes in the 0.05 to 0.15 mg$_{Pt}$/cm$^2$ range from published data for eleven different catalyst types and cathode loadings below 0.2 mg/cm$^2$.
 [DOI: 10.1149/2.032201jes] 

Manuscript submitted July 14, 2011; revised manuscript received October 3, 2011. Published December 8, 2011.

Automotive fuel cells are the ultimate solution for non polluting vehicles when powered by hydrogen from nationally secure and renewable energy sources. Performances of current generation vehicles are impressive but require significant improvements in performance and durability at the cost-driven amounts of precious metal catalysts equivalent to what are used in today's internal combustion engines.

The current platinum group metal (PGM) catalyst loading targeted for use in automotive fuel cells by the Dept. of Energy by 2015 is 0.125 g/cm$^2$ total per MEA.[1] This equates to about eight to ten grams per vehicle. If the required power densities of 0.125 g$_{PGM}$/kW$_{peak}$ are to ever be realized with 0.125 mg/cm$^2$ total of precious group metals, it is necessary to obtain at least 1 W/cm$^2$ at over 600 mV, preferably 650 mV for stack heat rejection requirements. Pt alloys offer an improvement in ORR activity over pure Pt catalysts, particularly PtNi and PtCo,[2] and indeed commercially available heat treated 30 wt% PtCo/C dispersed catalysts can reach or nearly reach the DOE targets for specific (0.72 mA/cm$^2_{Pt}$) and mass activity (0.44 A/mg$_{Pt}$), viz. 1.2 mA/cm$^2_{Pt}$ and 0.387 A/mg$_{Pt}$ in our laboratory measurements. In general, Pt alloys improve these fundamental characteristics by factors of 2 to 3 over pure Pt.[3] New "designer catalyst" approaches based on shape and size-controlled nanoparticles[4,5] recently introduced by ANL, core-shell nanoparticles[6,7] pioneered at Brookhaven National Labs, extended surface area catalysts like the NSTF catalysts discussed below, and dealloyed nanoporous surfaces[8,9] all utilize alloys for improved ORR activity and reduced precious metal usage. Key to their improved activity when properly made is the effect of a modulated surface composition that generates a Pt skin over varying alloy composition in the top few atomic layers which in turn affect the d-band structure of the surface Pt and delays the onset of adsorption of hydroxyls from blocking available Pt surface sites for $O_2$ adsorption.[10] But these improvements in oxygen reduction at 900 mV do not resolve the loss of high current density performance as loadings are reduced.

As traditional carbon supported catalysts are evaluated at lower and lower loadings on the cathode it has been shown that the high current density voltages decrease significantly more than expected based on 70 mV/decade Tafel slopes and currently understood sources of mass transport overpotential losses.[11–18] If low-loaded MEA's cannot maintain the power density of higher loaded MEA's, then more cells/stack are required which defeats the cost reduction of using lower Pt loading. In contrast to the nanoparticles dispersed onto carbon black support particles, NSTF catalysts comprise polycrystalline films of Pt or Pt alloys sputter coated onto non-corroding crystalline organic whiskers.[19] Fig. 1 shows a polarization curve from an NSTF catalyst based MEA with 0.1 mg/cm$^2$ of Pt in a PtCoMn alloy on the cathode, reproduced from reference 20. The ultra-thin NSTF electrodes show lower mass transport losses with catalyst loadings below 0.2 mg/cm$^2$ at higher current densities than thicker dispersed Pt/C electrodes.

Although discussed in the literature as early as 2003,[11,21,22] the assumption was that the unexpectedly faster fall-off of high current density performance at beginning of life with reduced loading was because of water flooding or non-optimized MEA electrode fabrication. Although these may be contributing factors, more recent state-of-the-art fuel cell models accounting for known and measured kinetic, mass, ionic and electronic transport losses still over-predict the cell voltage at high current densities, with increasing gaps as the loading drops below 0.2 mg/cm$^2$.[12,13] Greszler et al. conclude voltage dependent Tafel slopes are part of the issue, as the later transitions from 70 mV/decade seen at voltages above 0.8 V to 140 mV/decade below 0.7 V.[13,15] This Tafel slope transition is generally associated with decreased oxide coverage (Pt-OH) as the cell potential drops below 0.8 V. But it begs the question why this effect should worsen as loadings are reduced. Remaining discrepancies cannot be explained by increased values of bulk transport parameters in the electrodes and gas diffusion media and they propose that some other mechanism is restricting the current density very close to the Pt surface of each nanoparticle.[12,13] The discrepancy worsens at lower cell temperatures.[13] Sakai et al. of Nissan report that effective catalyst layer Knudsen diffusion coefficients, derived from Hg porosimitry, appear independent of the loading and some type of local transport resistance is found to increase rapidly with reduced loading.[14] They conclude the local transport resistances scale with catalyst layer thickness and the total roughness factor but no mechanism is proposed.[14] In a detailed study of the dependence of Pt utilization on relative humidity, Shinozaki et al. of Toyota measured Pt utilizations that doubled as the Pt wt% loading on the carbon doubled from 30 to 60 wt% with all other factors the same (their Fig. 13).[17] They suggest this might be related to the carbon support or ionomer structure in the vicinity of the catalyst particles, but offer no further explanation.

Nonoyama et al.[16] analyze oxygen transport diffusion resistances in the cathode layer as a function of loading and other parameters using an agglomerate model for the catalyst layer applied to limiting current data from a small cell under differential conditions. They model transport in the catalyst layer using an effective diffusion coefficient based on Knudsen diffusion, but do not model diffusion within the agglomerate particles, just between the agglomerates. They assume that at limiting current densities the oxygen concentration vanishes at the agglomerate particle surface adjacent an ideal ionomer film that completely encapsulates each agglomerate particle. They find that the total transport resistance increases as Pt loading is reduced from 0.2 to

* Electrochemical Society Active Member.
z E-mail: mkdebe1@mmm.com

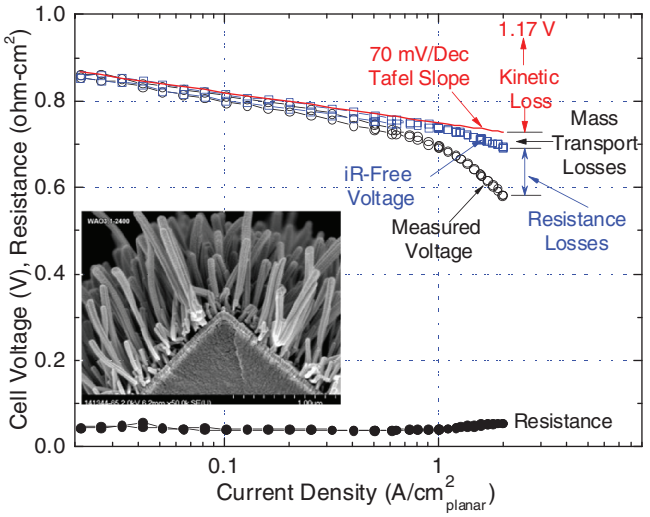


**Figure 1.** PEM fuel cell MEA polarization curve, with high frequency resistance and major loss contributions shown as a Tafel plot. Illustrated for an MEA having electrodes based on the NSTF PtCoMn catalyst (shown in the insert). Cell and test conditions: 50 $cm^2$ quad serpentine flow field; $H_2$/air stoichiometric flow rates = 2/2.5; $H_2$ and air pressure = 150 kPa; 2 minutes per point, both directions of scan; 850 equivalent weight, 24 μm thick PEM; anode catalyst: 0.05 mg-Pt/$cm^2$, NSTF PtCoMn; cathode catalyst: 0.10 $mg_{Pt}/cm^2$, NSTF PtCoMn; Gas diffusion media: MRC carbon paper with 3M microporous layers. Reproduced from slide 7 of reference 20.

0.15 to 0.1 mg/$cm^2$ and the layer thickness decreases from 13 to 10 to 6 microns respectively. They conclude that the increase is primarily due to ion transport in the ionomer layer surrounding each agglomerate particle, but are led to hypothesize an ionomer film "interfacial layer" that effectively increases the TEM observed ionomer layer thickness of 10 nm to 200 nm depending on the assumed catalyst utilization factors.

Similarly Yoon and Weber[18] explore the impact of mass-transport limitations at low Pt loadings in a systematic study of kinetic and transport phenomena using an agglomerate model. They account for transport of dissolved oxygen inside the particle using an effective diffusion coefficient for oxygen dissolved in water but like Nonoyama et al., invoke the effect of higher flux diffusion through the ionomer shell encapsulating the particles as leading to increased resistance with reduced loading. Their 1-D model indicates about a ± 5% change in current density at 0.5 V as the electrode thickness (and loading) are reduced from 15 to 5 microns for their nominal ionomer layer transport resistance (0.010 $m^2$ s bar/mole) and low versus high CL porosity.

Given the difficulty of the existing modeling approaches to explain the apparent fall-off of performance with loadings below 0.2 $mg_{Pt}/cm^2$, we have considered that part of the answer to the problem may lie with how the actual interaction of the $O_2$ molecules with the Pt surfaces is handled, specifically at the spatial scale of a mean free path. As Fig. 1 illustrates, the NSTF electrode structures demonstrate mass transport overpotential losses that begin to increase at lower values of catalyst loadings than are observed for thicker Pt/C type electrodes. This difference in performance behavior of the NSTF extended surface area catalyst and the dispersed nanoparticle catalyst types is equal to or larger than the loading effect seen within a given catalyst type. Understanding the source of this difference between these two catalyst types and how it depends on catalyst structure may shed light on why a loading dependence on mass transport occurs in the first place. In this paper we address that question of why the apparent loading dependent mass transport loss is dependent on the electrode structure. One key aspect to our approach is accepting that in the Knudsen transport regime, when the mean free path λ between gas phase molecular collisions is larger than the mean distance between solid surfaces bounding the gas, molecular transport is determined by molecule/surface collisions rather than gas phase molecular collisions. Above this spatial scale intermolecular gas phase collisions assure that translational momenta and velocities are equilibrated and randomized as in an ideal gas. Below that critical dimensional scale of approximately a mean free path the concept of a uniform pressure and hence uniform gas phase densities and velocity distributions can break down and they are not constrained to be equal to the gas phase averages if the nature of the wall surfaces and their spatial orientations or relative geometry can influence the transport rates and the collision frequencies with the walls and hence catalyst surface areas comprising those walls. That such surface collisions can influence the transport or velocity distributions of gases colliding with those surfaces within the dimensions of $\lambda^3$ is well known but may not have been considered before for fuel cell catalyst electrode structure effects. This refers to the fact as Knudsen showed theoretically and experimentally, and others since then, that a weakly interacting molecule rebounds from a solid wall according to the cosine law, and thermally accommodated (physisorbed) species always desorb with cosine law distributions.

A second key aspect of our approach is recognizing that models which assume the ORR currents derive simply from whether gaseous $O_2$ happens to hit a free and clean Pt surface site are unrealistic and over simplified at the operating conditions of a fuel cell. That is a good model for adsorption onto clean surfaces in ultra-high vacuum at submonolayer coverages, but not for surfaces covered with adsorbed hydroxyls, various anion impurities, double layer coverages of physisorbed water, all in a highly dynamic state of motion. Rather, oxygen reduction only occurs after oxygen chemisorption which occurs only after oxygen physisorption and any given oxygen molecule bouncing between catalyst surfaces which are on the order of λ or less apart, will make numerous solid surface collisions and physisorption attempts before ever successfully succumbing to reduction. The probability of chemisorption and hence current density, will be directly related to how many times it can be successfully physisorbed per unit time, and that rate is influenced by the first key aspect in the preceding paragraph specifically through the compactness of the catalyst surface area.

With these two key aspects we develop a model based on elementary kinetic gas theory that takes into account known mechanisms by which asymmetry of surface area distribution is able to influence the gas velocity distributions in the Knudsen regime and hence the surface sampling rate by physisorbing oxygen that takes place within approximately one mean free path of the catalyst surface. The result is an additional pre-exponential scaling factor $f(d_s)$ in the Butler-Volmer equation dependent on a distance metric $d_s$ describing the catalyst surface area distribution. We approximate this distance metric by $1/\rho_s$ ($cm^2_{Pt}/cm^3$), the inverse of the surface area per unit volume of the electrode and define and test two possible functional forms for $f(\rho_s)$. We use two criteria to judge whether the forms for $f(d_s)$ are correct. The preferred form is able to predict the correct heat of enthalpy $E_d$ for $O_2$ physisorption and the observed ratio of current densities at V(iR-free) = 0.7 V for NSTF compared to Pt/C dispersed electrodes in the 0.05 to 0.15 $mg_{Pt}/cm^2$ range from published data.

## Performance Falloff at High Current Densities – Impact of Catalyst Electrode Structure

Wagner et al.[12] and Greszler et al.[13] present the problem clearly for dispersed electrodes. With Pt/C loadings on the cathode of 0.4 mg/$cm^2$, cell voltages of at least 0.6 V at 1.5 A/$cm^2$ are achieved as required for cost effective heat rejection. But as the loading is reduced by one-half and then one-half again and so forth, the performance at high currents does not simply decrease by 20 mV per step expected from a Tafel slope of 70 mV/decade. They report that correcting for the known loss mechanisms due to electronic, ionic, and reactant transport impedances does not remove the discrepancy. The effect is worse for PtCo/C alloy catalysts investigated.

In Figure 2 we show polarization curves of iR-free cell voltage versus current density as a function of loading for Pt/C and PtCo/C as reproduced from reference 13. We also show polarization curves from NSTF-PtCoMn based MEA's measured at similar conditions, as

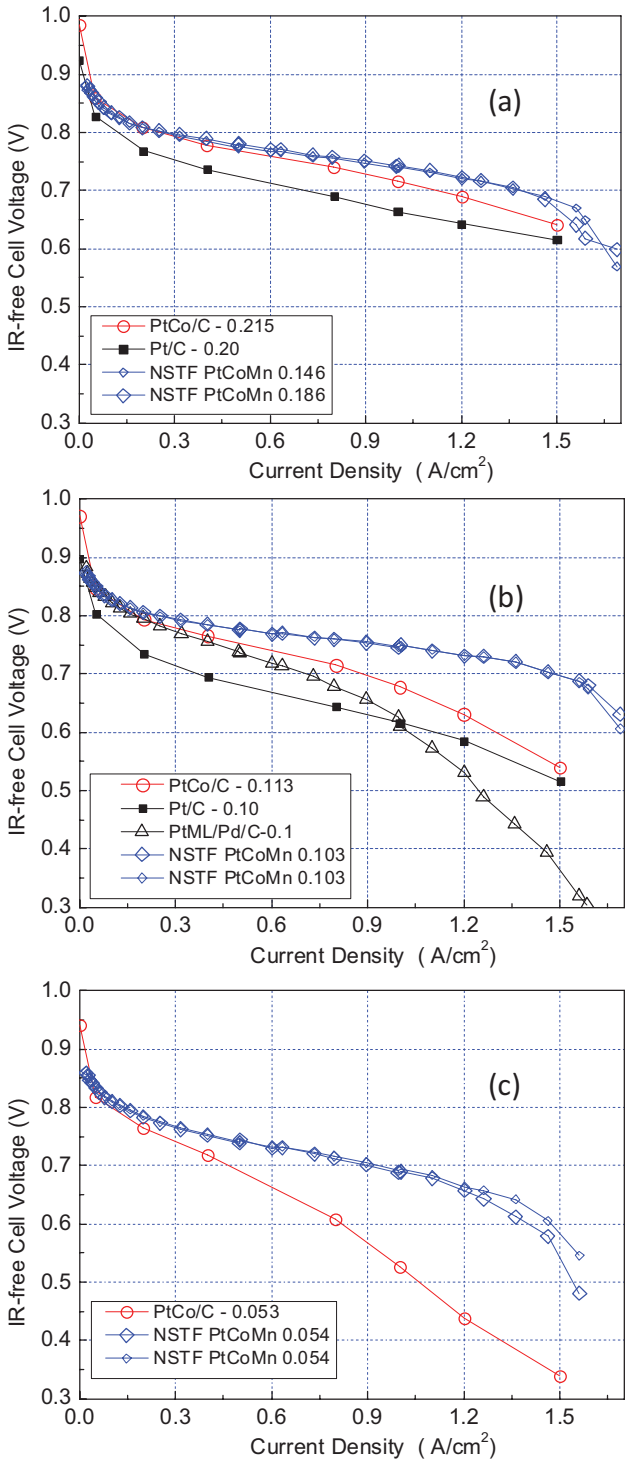


**Figure 2.** Galvanodynamic polarization curves of iR-free cell voltage versus planar current density from four basic catalyst types at different Pt loadings indicated in the legends. (a) NSTF, PtCo/C and Pt/C at Pt loadings from 0.146 to 0.215 mg/cm$^2$. (b) NSTF, PtCo/C, Pt/C, and PtML/Pd/C, all at ~0.10 mg/cm$^2$. (c) NSTF and PtCo/C at 0.054 mg/cm$^2$. All tests were in 50 cm$^2$ cells at 80°C, 150 kPa and subsaturated inlets. Further test conditions are given in the text. Plots were reproduced from references 13 and 23.

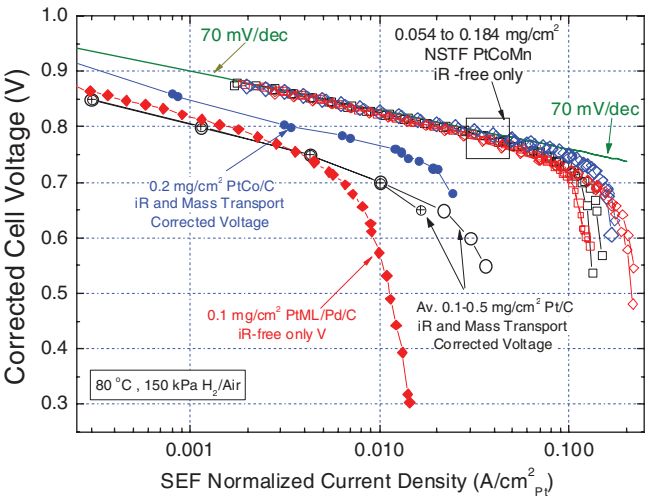


**Figure 3.** Hydrogen-air polarization Tafel curves of corrected cell voltage versus Pt surface area-normalized current density for several categories of catalyst types: open circles – Pt/C, GM data replotted from reference 12; solid circles – PtCo/C, GM data replotted from reference 13; solid diamonds – core shell PtML/Pd/C, 3M data, reference 24; open diamonds and squares – 3M data replotted from reference 23. GM data are both iR-free and model transport corrected cell voltages. 3M data are iR-free voltages only.

reproduced from reference 23. For both catalyst types, the iR-free cell voltage at 1.5 A/cm$^2$ gets progressively worse as loading decreases, but worsens more quickly for the thicker dispersed electrodes than for the ultra thin NSTF electrodes, which are some 10 to 20 times thinner. If it were a simple matter of cathode flooding due to water generation rates per unit volume of electrode, it would be expected to be much worse for the NSTF electrode. This strongly supports that the effect is not simply a water management issue. We also note that some fraction of the NSTF catalyst coated whisker surface area can be embedded into the PEM surface, either through direct penetration or squeezing of ionomer in between the whiskers during catalyst transfer. In most cases for low loadings, the whiskers maintain their parallel disposition but lay over so that their lengths are in close contact with the membrane. In either case, oxygen must diffuse through some amount of ionomer to reach that portion of surface in contact with ionomer.

Fig. 13(a) in reference 12 shows the iR and mass transport corrected polarization curves as a function of five cathode loadings of 50% Pt/Vulcan C in the range of 0.1 to 0.5 mg/cm$^2$. Fig. 13(b) of that reference shows that when the corrected voltages are plotted as surface area-normalized current density, A/cm$^2_{Pt}$, then all the five transport corrected curves collapse onto a common polarization curve. Slide 13 in reference 13 shows the same collapsed curves in a Tafel plot along with that from a high performing 30% PtCo/Vulcan C. In Fig. 3 we replot those curves from references 12 and 13, along with polarization curves taken at similar conditions from a series of MEA's having NSTF-PtCoMn cathodes at four loadings in the range 0.05 to 0.184 mgPt/cm$^2$ from reference 23, as shown in Fig. 2. The final curve in Fig. 3 is from a dispersed MEA with a Pt monolayer core-shell catalyst (Pd core), at a Pt loading of 0.1 mg$_{Pt}$/cm$^2$, similar to that discussed in reference 24 but taken at 150 kPa instead of 100 kPa in that reference. All curves in Fig. 3 were taken at 150 kPa $H_2$/air pressures, 80°C, have similar membrane thicknesses and equivalent weights, similar carbon paper based gas diffusion media and microporous layers, and 0.05 mg$_{Pt}$/cm$^2$ on the anode with the exception of the core-shell Pt/Pd/C MEA which had a 3M dispersed anode with 0.1 mg/cm$^2$. The anode/cathode stoichiometric flow rates were 1.5/2.0, 32% RH inlets for the GM data and 2/2.5 with 68°C inlet due points for the 3M data. Cell types are different but this is a small effect based on other comparisons of GM and 3M single cell measurements with identical MEA's. In Fig. 3 all the NSTF and PtML/Pd/C voltages are just iR-corrected for HFR, while the GM curves are iR and mass transport corrected based on the GM models.

All the catalyst types in Fig. 3 exhibit ~ 70 mV/dec Tafel slopes, but there is a large difference in the value of the (SEF = surface area

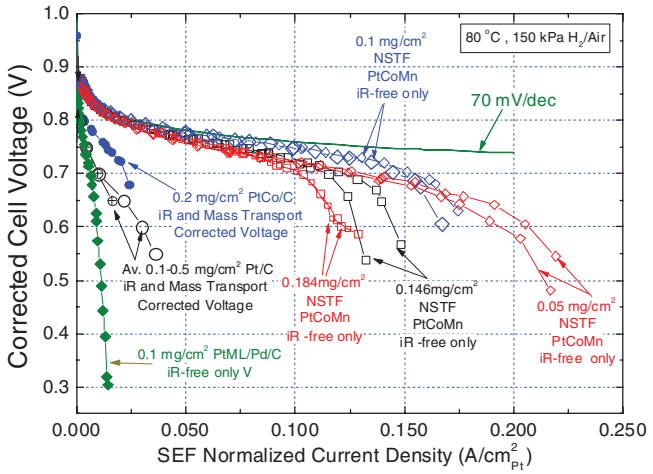


**Figure 4.** Linear current density plot of the graph in Figure 3.

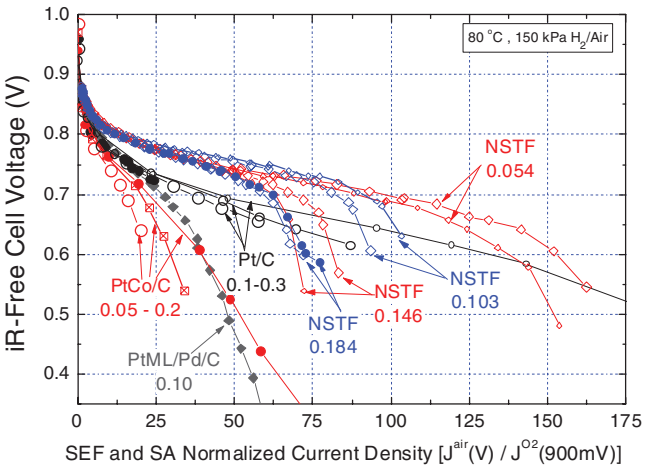


**Figure 5.** Corrected cell voltages from Figure 4 after further normalizing the axis to the ORR specific activity measured at 900 mV under oxygen. The iR and mass transport corrected GM cell voltage data from Fig. 4 were replaced with the measured iR-corrected-only cell voltages for the same catalysts from Fig. 2.

enhancement factor, $cm^2_{Pt}/cm^2_{planar}$) SEF-normalized current density where the iR corrected voltages start to deviate from that line or show a limiting value. Since the high current density values are the region of interest, it is more useful to plot the curves with a linear x-axis as in Fig. 4. It is readily apparent that the ultra-thin, low surface area NSTF electrodes are generating much high currents per unit of Pt surface area than the thicker, higher surface area Pt/C type electrodes. As seen in Fig. 3, at 0.8 Volts, the SEF normalized current density of the extended surface area NSTF electrodes is approximately 25 times those of the dispersed nanoparticle catalysts. Part of this can be expected to be due to the much higher specific activity of the NSTF extended surface area catalyst.[23,25–27] This suggests another level of current density normalization by specific activity to remove the effect of the kinetic activity so that we are left with just transport related differences of the comparative polarization curves.

Table I column 2 displays the ORR specific activity values at 900 mV for all the catalysts in Figs. 3 and 4. Using these values of area specific activity (SA) to normalize the already SEF-normalized current axis in Fig. 4 results in Fig. 5. (Note, the averaged Pt/C and PtCo/C curves in Fig. 4 were replaced with the specific loading curves in Fig. 2 for this phase of the analysis so all are just iR-free cell voltages. Spreadsheet data from reference 28 were utilized for this and Fig. 5 now shows three loadings of Pt/C and three of PtCo/C). Normalizing the current density by both the SEF and specific activity (SA) is equivalent to simply dividing the cell's total current at any given voltage under air by the total cell current at the conditions of the SA measurement, i.e. 900 mV under 100 kPa saturated oxygen (150 kPa total pressure). This generates a universal polarization curve that can be used to compare different catalyst types and structure, including non-PGM catalysts, specifically for the impact of Tafel slope or local transport losses at high current density. Compared to Fig. 4 this has now reduced the kinetic current density ratios of the NSTF and dispersed catalyst types from twenty-five to about three. These remnant differences in Fig. 5 among the different catalyst types is due to the combined effects of all mass transport losses, excluding cell resistance and specific activity. We will now use these universal polarization curves in Fig. 5 to develop a new transport related loss (or enhancement) factor deriving from the two key aspects defined at the end of the introduction and discussed more completely below.

**Table I. Catalyst activity and electrode parameters used to calculate the volumetric surface area density in Fig. 9.**

| Catalyst Type | Specific Activity $mA/cm^2_{Pt}$ at 900 mV, 100 kPa $O_2$ | SEF ($cm^2_{Pt}/cm^2_{planar}$) | Catalyst Layer Thickness (μm) | $\rho_s$ ($10^5$ $cm^2_{Pt}/cm^3$) |
|---|---|---|---|---|
| NSTF – 0.054 (2 curves) | 1.41, 1.35[a] | 7.21, 7.13[a] | 0.16 ± 0.018[e] | 4.51, 4.46 |
| NSTF – 0.103 (2 curves) | 1.69, 1.79[a] | 9.7, 10.1[a] | 0.32 ± 0.034[e] | 3.03, 3.16 |
| NSTF – 0.146 (2 curves) | 1.78, 1.83[a] | 11.4, 11.82[a] | 0.47 ± 0.048[e] | 2.42, 2.51 |
| NSTF – 0.186 (2 curves) | 1.72, 1.67[a] | 13.63, 13.14[a] | 0.61 ± 0.061[e] | 2.23, 2.15 |
| Pt/C – 0.10 | 0.278[b] | 47[d] | 3.45[d] | 1.36 |
| Pt/C – 0.20 | 0.219[b] | 96[d] | 5.4[d] | 1.76 |
| Pt/C – 0.30 | 0.186[b] | 145[d] | 7.8[d] | 1.87 |
| PtCo/C – 0.05 | 0.954[c] | 22[c] | 2.9 | 0.75 |
| PtCo/C – 0.10 | 0.94[c] | 47[c] | 5.8 | 0.82 |
| PtCo/C – 0.2 | 0.84[c] | 89[c] | 9 | 0.99 |
| PtMLPt/Pd/C – 0.1 | 0.11 | 111 | 5 | 2.22 |

[a] From slide 13 of reference 23.
[b] From slide 7 of reference 13.
[c] From reference 28.
[d] From slide 4 of reference 13.
[e] From Fig. 8.

### Relationship of ORR Rate Limiting Step to Physisorption and Kinetic Gas Theory

ORR is a multi-electron process usually considered to involve different reaction intermediates.[29] Based on mean-field transition state models, the Pt surface area normalized kinetic current density at a potential $E$ in RDE experiments has been proposed and occasionally modified[29–32] to be a function of the Gibbs energy of adsorption $\Delta G_{ad}$ of the reactive intermediates, temperature T, $O_2$ concentration $C_{O2}$ in the solution above the catalyst surface, and the surface coverage, $\Theta_{ad}$ of adsorbed spectator species (hydroxyl and anion impurities) as given in equation 1:

$$i = nFKc_{O_2}(1-\Theta_{ad})^x \exp\left(-\frac{\beta FE}{RT}\right)\exp\left(-\frac{\gamma\Delta G_{ad}}{RT}\right) \quad [1]$$

where $n$ is the number of electrons, $F$ is Faraday's constant, $K$ is the chemical rate constant, $\beta$ and $\gamma$ are symmetry factors often assumed to be equal to 1/2, and $R$ is the ideal gas constant.

A key assumption in the development of equation 1 is that the ORR rate limiting step is the 1st electron transfer step:

$$Pt(O_2)_{ad} + e^- \Rightarrow Pt(O_2^-)_{ad} \quad [2]$$

It assumes that oxygen adsorption is onto a surface primarily covered by hydroxyls rather than by reactive intermediates. This is a useful expression to understand the motivation for many of the promising electrocatalyst approaches under investigation to achieve or explain increased ORR activity. It suggests that anything done to the catalyst surface's atomic structure, electronic structure or composition that delays the onset of the adsorption of hydroxyls from blocking $O_2$ adsorption sites will have a positive impact on the specific activity since the pre-exponential $[1-\Theta_{ad}]$ term in 1 will be larger. Segregated surface structures, dealloyed surfaces, core-shell particles, shape controlled particles, extended surface area catalysts, alloy compositions to shift the d-band surface electronic density of states or contract the surface Pt lattice parameter are all approaches practiced to affect the pre-exponential factor in equation 1. It implicitly assumes by 2 that adsorption of oxygen into an activated chemisorbed state is the rate limiting step. However, as discussed earlier it is completely unphysical to think that the chemisorption occurs every time and only when an $O_2$ molecule happens to strike an exposed Pt surface atom(s). Physical adsorption of $O_2$ molecules into non-activated surface states, characterized by weak Van der Waals type forces, is a precursor for any activated chemisorption. It should be expected that a large fraction of $O_2$/catalyst surface interactions result in physisorption, and there is most likely substantial surface mobility of the physisorbed oxygen over the oxidized Pt surface and other ionic species that remain chemisorbed onto Pt at high potentials, by which the oxygen is able to probe the surface for open Pt sites. The lifetime of any physisorbed molecule is traditionally referred to as its sojourn time, $t_s$, on the surface.[33] The enthalpy of adsorption or desorption energy $E_d$ from the physisorbed state determines the sojourn time through the Arrhenius-type relation in 3,

$$t_s = t' \exp(E_d/RT) \quad [3]$$

where $t' \sim 10^{-13}$ to $10^{-12}$ seconds is the customary molecular period of oscillation of the molecule normal to the surface.

The incident flux rate of oxygen at the surface, molecules/cm$^2$-sec, is by definition proportional to the local pressure above the surface. But it does not account for the time spent by an $O_2$ molecule in a physisorbed state, which is the precursor adsorption state to chemisorption necessary for charge transfer. At one atmosphere pressure, the collision rate of gas molecules with a surface having $5\times10^{14}$ adsorption sites/cm$^2$-Pt is sufficient to form approximately $10^9$ monolayers per second if the sticking probability were one for all layers and there were no mass transport limitations. So if every one of the $O_2$ molecules that struck such a surface were reduced instantaneously, the current generated at 4 electrons/molecule would be 3.2 $\times$ $10^5$ A/cm$^2$-Pt. Since this is five orders of magnitude higher than what is observed under pure $O_2$ at any iR-free cell potential, chemisorption is a rare event relative to the number of attempts, N, per unit time made by an average $O_2$ molecule undergoing repetitive physisorption, desorption, and re-adsorption events. Another conceptually useful result derives from this collision frequency whereby each surface site is visited on average once every $10^{-9}$ seconds. For a typical physical adsorption heat of 5 kCal/mole, equation 3 gives $t_s$ $\sim 0.6 \times 10^{-9}$ s for $t' \sim 5 \times 10^{-13}$s. In other words the average interval of time between gas phase molecule collisions with a surface site is on the same order of time as a physisorbed molecule spends on the surface. There are not many more $O_2$ molecules striking a Pt atom per unit time than it can "process," rather the rates are similar.

### Relationship of Physisorption Surface Sampling Rates and Surface Area Distribution

So the $O_2$ sticking probability is far less than unity, few physisorbed molecules become chemisorbed before desorbing to "try again" to be reduced at another surface site. Anything that can increase the rate of these physisorption attempts by the average $O_2$ molecule will increase the observed current density assuming the same probability for chemisorption per physisorption event. It is obvious that increasing the number density of $O_2$ molecules in the gas phase (i.e. average pressure) will do this. But there two mechanisms by which the catalyst surface area distribution can conceivably impact this physisorption frequency and hence chemisorption frequency.

Fig. 6 is intended to help illustrate the following discussion of these mechanisms. First, not every $O_2$ surface collision is with a catalyst surface site since a substantial fraction of the electrode's pore wall material can be the support material, i.e. carbon for Pt/C. So all other factors being equal, if for one catalyst surface area distribution the average $O_2$ molecule makes N wall collisions per unit time and 50% are with C versus another catalyst distribution in which 75% of the collisions are with catalyst surface sites, then clearly the number of possible chemisorption events per unit time will be 1.5 times higher

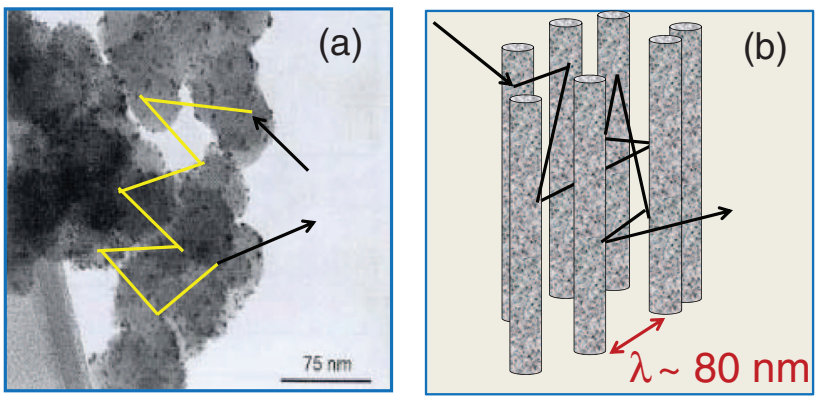


**Figure 6.** Illustration of hypothetical $O_2$ trajectories moving within electrodes comprised of either (a) dispersed nanoparticles supported on carbon, or (b) extended surface area NSTF catalysts separated on the order of a mean free path. The $O_2$ molecules spend their time either physisorbed or in transit between surfaces collisions with catalyst sites that are on the order of 1 $\lambda$ apart. The Pt surface sampling rate for the NSTF is intrinsically higher due to two effects, viz. the molecules in the Pt/C electrode have a higher probability of colliding with non-catalyst (carbon support) surface area, and the cosine law of desorption/surface scattering causes an asymmetry in the velocity vector distribution that increases the frequency of NSTF surface site collisions per unit time.

for the latter catalyst surface area distribution. An example of such catalyst structures would be ones with very different wt% Pt/C. Under such conditions the rate of Pt surface site sampling into physisorbed states will determine the rate of chemisorption into charge transfer states and thus be a rate determining step as much as are charge transfer and oxygen partial pressure. This mechanism is discussed in more detail below.

The second mechanism by which the catalyst surface area distribution can conceivably impact the rate of physisorption and hence chemisorption frequency, has its basis in the aforementioned fact that upon desorption from a surface from a physisorption state, the velocity vectors obey a cosine law with respect to the local surface normal. Furthermore, even if not fully accommodated, after multiple collisions, the velocity distribution approaches a cosine distribution. Knudsen showed theoretically and experimentally that a weakly interacting molecule rebounds from a solid wall according to the cosine law, i.e. the probability *du* that it's trajectory leaves the surface within a solid angle $d\omega$ that is at an angle $\theta$ with the surface normal is $du = (d\omega/\pi) \cos\theta$.[34] Further refinements of the cosine law by Maxwell assumes that a fraction $q$ of the impinging molecules leave according to the cosine law and 1-$q$ are specularly reflected. More complicated models have been proposed as well but do not change the basic premise and importance of the surface in affecting fluid flow in the Knudsen regime of sub-continuum flow and giving rise to the basic phenomena of thermal creep, thermal slip and viscous slip.[35] More recently Feres and Yablonsky[34,36] have developed a mathematical model of the gas-surface interactions for various surface roughness distributions and conclude that "Knudsen's cosine law is a stationary probability distribution of post-collision velocities. . . ." They conclude that even after one collision the cosine law can hold approximately depending on how "dispersing" the surface microgeometry is, and after multiple collisions the cosine law is approached asymptotically as the number of collisions increases, approaching faster the more dispersing the microgeometry. It is important to note that their model does not assume any interaction like physisorption that would cause the molecule to lose its memory of its incident trajectory completely. Finally we note that these effects are recognized as important for isotope separation approaches, devices for separating gases like $N_2$ and $CO_2$, coolant flow techniques and microscale electromechanical devices.

To see why this cosine law for desorption is important and can lead to more surface site sampling events per unit time, consider the following thought experiment of two planar surfaces separated by $z = \lambda$, the mean free path, that are much larger in the x,y directions. If there were no surface interactions except ideal conservation of momentum, and all $O_2$ molecules underwent purely specular reflection every time, then a snap shot of the velocity vector distributions of the gases between the plates at any instant of time would be identical to the bulk gas phase, with $v_z = v_x = v_y$ since it would be the same as though the surfaces weren't even there and the molecules had hit other gas molecules instead of the surfaces. But now suppose the surface does influence the gas velocities by changing them to be consistent with cosine law discussed above. For any gas molecule entering the space between the plates, after only a few wall collisions its velocity vector distributions coming off the surface will be cosine distributions and therefore have an asymmetric directionality imparted to them so that they tend to bounce around between the plates with higher probability of going in the z-direction than in the x or y directions. That means on average $v_z > v_x = v_y$. Hence every molecule will make on average more surface collisions per unit time than they would if there were no cosine law effect. In effect, the pressure vector normal to the surface has increased relative to those in the directions parallel to the planar surfaces. Clearly if the spacing of the planar surfaces was $z \gg \lambda$, then the effect of the wall collisions would be effectively eliminated as the gases intermixed and took on the normal homogeneous velocity vector distributions from intermolecular collisions. An example of this type of catalyst surface area distribution is the NSTF extended surface area catalysts, as shown in Fig. 1. For molecules deep within the uniformly oriented catalyst coated whiskers that are on the order of 80 nm (1 $\lambda$) apart, but much larger than $\lambda$ in the orthogonal directions, the effect will be similar to the ideal parallel plates and bias the $O_2$ molecules to have preferential velocity vectors normal to the whisker surfaces and therefore more collisions per unit time than they would if the catalyst surfaces were small randomly distributed dispersed cubo-octahedral or spherical nanoparticles. In effect the vertically oriented whiskers entrap the molecules forcing them to spend longer between them as illustrated in Fig. 6b. Furthermore, it should be clear that every collision with a surface is with a catalyst surface in this case as the extended surface area catalyst does not expose any of the interior support whisker. So the NSTF has the benefit of both of these mechanisms by which surface area distribution can influence the sampling rate for physisorption.

### Relating Rates of Physisorption, Surface Area Distribution and Kinetic Gas Theory

We now apply these concepts of surface site sampling rates, physisorbed dwell time, and gas/solid surface interaction influences to a physically intuitive model for $O_2$ molecular transport between catalyst sites based on simple kinetic gas theory. The current density in equation 1 is already normalized to active Pt surface area and is therefore not a useful starting point to investigate the impact of surface area distribution on current density. A useful form for the observable current density is given by equation 4:

$$J\left(A/cm^2_{planar}\right) = S\left(cm^2_{Pt}/cm^2_{planar}\right)\left[i_o(A/cm^2_{Pt})p^{\gamma}_{o_2}\left(1-\Theta_{ad}\right)^x \times \exp\left(-\frac{\beta F\eta}{RT}\right)\exp\left(-\frac{\gamma\Delta G_{ad}}{RT}\right)\right] \quad [4]$$

where $S$ is the surface area enhancement factor (SEF), $i_o$ the equilibrium exchange current density (per unit of Pt surface area), and $\eta = E_{iR-free} - E_{rev} + \eta_{tx}$ is the total iR-free overpotential. Models for mass transport losses $\eta_{tx}$ in equation 4 as in references 5–8 are generally based on mean field values for bulk and Knudsen diffusion. For MEA tests under air, oxygen concentration in the solution is replaced with its partial pressure $P^{\gamma}_{o_2}$. $E_{\text{rev}}$ is dependent on the conditions used for measuring $J$ and is given by

$$E_{rev} = 1.23 - 0.910^{-3}(T-298) + 2.303(RT/4F)\left(p^2_{H_2}p_{o_2}\right) \quad [5]$$

In the following we propose an additional pre-exponential factor $f$ in 4 to account for the effects of the surface sampling rate mechanisms we introduced above. It will be a function of the surface area distribution which we characterize by a single metric parameter $d_s$, as in 6:

$$J\left(A/cm^2_{planar}\right) = f(d_s)S\left(cm^2_{pt}/cm^2_{planar}\right)\left[i_o\left(A/cm^2_{Pt}\right)p^{\gamma}_{o_2}(1-\Theta_{ad})^x \times \exp\left(-\frac{\beta F\eta}{RT}\right)\exp\left(-\frac{\gamma\Delta G_{ad}}{RT}\right)\right]. \quad [6]$$

We will also require that the correct form for the pre-exponential scaling factor be able to satisfy two criteria. These Criteria are:

(1) the correct functional form must be able to predict a fundamental quantity, such as the desorption energy for physisorption, and
(2) it must be able to predict approximately correct ratios of observed current densities at a given iR-free cell voltage of the electrodes having different values of $d_s$.

We will propose and compare two functional forms for $f(d_s)$. From the kinetic theory of ideal gases the mean distance between $O_2$ molecules is given by L(cm) $\sim 4.6 \times 10^{-7}$ $(T/P)^{1/3}$ for P in units of Torr and T in Kelvin.[33] At 1.5 atmospheres (1140 Torr) and 80°C this gives L $\sim$ 3.1 nm which is in the range of the diameters of typical

Pt/C nanoparticles. The mean free path between ideal gas molecule collisions is $\lambda(\text{cm}) = 2.33 \times 10^{-20}\ T/(\xi^2 P)$ where $T$ is in Kelvin, $P$ is pressure in Torr and $\xi$ is the molecular diameter in cm. For air at 1.5 atmospheres at 80°C, $\lambda = 80$ nm. Molecular diffusion in pores of diameter $D$ applies when the Knudsen number $D/\lambda < 1$. That means the gas molecules collide with the pore walls more often than with other molecules. The average velocity in a Maxwell-Boltzmann velocity distribution for a molecule of molecular weight $M$ is $\upsilon_{av}$ (cm/sec) $= 1.45 \times 10^4 (T/M)^{1/2}$ for $T$ in Kelvin. For $O_2$ at 80°C, $\upsilon_{av} = 4.8 \times 10^4$ cm/sec, and it will take just $\tau \sim \lambda/\upsilon_{av} = 0.8 \times 10^{-10}$ sec on average for a molecule to travel one mean free path distance $\lambda = 80$ nm. Since in any time interval on this order the molecules that arrive at the surface and do manage to get reduced do so from a distance of one mean free path, this distance is a critical parameter. For a molecule that does not chemisorb, the average time it spends as a physically adsorbed molecule on the surface is given by the sojourn time in 3 above. The heat of physisorption is small, sufficient to stretch or bend bonds but not sufficient to break any. The enthalpy for physical adsorption reflects more the characteristics of the molecule than the surface it is visiting. Maximum observed enthalpy values for oxygen are summarized by Atkins at 21 kJ/mole or 5.02 kCal/mole.[37] For an enthalpy of adsorption or heat of desorption from a physisorbed state of approximately 5 kCal/mole at 80°C, $t_s = 1.3 \times 10^{-10}$ seconds which is very close to $\tau$. So for distances between catalyst sites less than about 80 nm, a physisorbed $O_2$ molecule will spend about as much time "sampling" the local surface for possible chemisorption sites, as traveling between surfaces of adjacent catalyst particles. If adjacent catalyst particle surfaces are further than $\lambda$ apart, then the oxygen molecules will spend more time in transit than adsorbed on a surface. Once a physisorbed $O_2$ molecule desorbs, it flies off the surface in a direction determined by a cosine distribution relative to the local surface normal. It can statistically travel at a mean speed $\upsilon_{av}$ a distance $\lambda$ before colliding with another $N_2$, oxygen or water vapor molecule and having its trajectory altered. It may get scattered in any direction, including back towards the particle it came from. But if it travels one mean free path, 80 nm, before having another chance to be backscattered towards the same catalyst particle surface again depends on how well distributed that catalyst surface is versus the catalyst support surface. Fig. 6 illustrates the concept by showing hypothetical paths for oxygen molecules moving between different types of catalyst surfaces separated by distances on the order of $\sim 1\ \lambda$. For a dispersed Pt/C electrode, Fig. 6a, the chances of the $O_2$ hitting the same nanoparticle surface again that it desorbed from is very small since the ~3 nm diameter Pt/C nanoparticle subtends such a small solid angle from a distance of $\lambda \sim 80$ nm above it. It is more likely that the desorbed $O_2$ molecule will next hit some non catalyst surface such as the carbon support. If on the other hand the catalyst surface from which it desorbed is an extended surface area catalyst, like NSTF, with lateral dimensions of microns, then that surface would subtend a large solid angle ($\sim 2\pi$) from a distance of 0.08 microns or less above it (1 $\lambda$). For those scattering events in which the particle was backscattered, the chances of it hitting such a surface again for another try at chemisorption would be near unity, and roughly within a time span of $\tau \sim 2\lambda/\upsilon_{av} \sim 1.6 \times 10^{-10}$ sec, again close to the sojourn time $t_s$ for a physisorbed molecule, suggesting that $\tau/t_s$ will be important for determining how many attempts to chemisorb the $O_2$ molecule is able to make per unit of time in its dwell-time near the catalyst surface. If the catalyst nanoparticles are sparsely distributed on the carbon particle, as in a low wt% Pt/C loading, the distance between such nanoparticles will be larger than on a high wt% loaded carbon catalyst. Similarly if the nanoparticles are inside a carbon pore and out of line of sight of other nanoparticles, they will not serve to be "visited" as frequently by the same molecules for multiple attempts at reduction, which may contribute to explaining why activities can be carbon dependent for the same wt% and particle diameters. On the other hand, for a porous, extended surface area catalyst electrode, with pore sizes of $\sim 1\ \lambda$ or less, the probability of the $O_2$ molecule hitting a catalytically active surface every time it collides with a surface will be near unity.

In summary the above molecular gas model suggests that a key property of the catalyst electrode is the geometric distribution of catalytically active sites per unit volume as well as how they are oriented as discussed in the section above titled Relationship of Physisorption Surface Sample Rates and Surface Area Distribution. For the case of the extended surface area NSTF catalysts, the catalyst coated whiskers are packed very closely together in the electrode and maintain substantial numbers of high aspect ratio pores between the whiskers that are on the order of tens of nm apart, i.e. on the order of $\lambda$, the mean free path between gas phase collisions. As explained previously, Knudsen's *cosine law* of desorption trajectories implies the $O_2$ molecules will have a higher number of catalyst surface collisions per unit time than if the NSTF catalyst coated whiskers were dispersed and spread out into a thicker electrode as isolated particles more than 1 $\lambda$ apart. This is consistent with experimentally observed lower performance for NSTF catalyst particles dispersed as an ink type electrode layer. If adjacent or opposing catalyst surfaces are spread apart by several mean free paths then the times between reduction attempts will be determined by rates of diffusion of $O_2$ through the nitrogen and water vapor majority gases from one surface to another, which will be slower than molecular speeds $v_{av}$, appropriate for transport over distances of $\leq 1\ \lambda$. If the collision cross-section a catalyst surface presents is a small fraction of the total material (support + catalyst) surface, then the number of chemisorption opportunities (physisorption attempts) per unit time will be smaller compared to a high fraction of catalyst surface area. So basically it comes down to: a) are the adjacent opposing catalyst surface sites spaced so far apart that the number of adsorption attempts per unit time is determined by diffusion speeds or are they sufficiently close that they are determined by average molecular velocity speeds (Knudsen flow), and b) is the surface area fraction that is catalytically active large or small and is it distributed asymmetrically? Both aspects relate to the compactness of the catalyst surface area which we take as a first order approximation to be embodied by the metric $d_s$ defined further below.

### Relation of SEF and SA Normalized Current Density to the Surface Area Distribution Metric

The above model for how the geometric distribution of catalyst surface area and kinetic gas parameters are related to the ORR rate limiting step can be applied to the data in Fig. 5 to account for some of the remaining transport overpotential losses of the different catalyst types.

As a measure of the remaining mass transport loss effects in Fig. 5, we take for each catalyst type the current density normalized by both SEF and Specific Activity at a fixed overpotential corresponding to the iR-free cell voltage of 0.7 V. For typical measured MEA resistances of $\sim 0.05$ ohm-cm$^2$, this corresponds to 625 mV of measured cell voltage at 1.5 A/cm$^2_{\text{planar}}$, typical of a desired peak power condition. For each catalyst type in Fig. 5 we also calculate the surface area volumetric density $\rho_s$ from the reported or measured SEF and electrode thickness values. The electrode thicknesses and SEF values for the 50 wt% Pt/C data are given in reference 13, which allows calculating the surface area density for each catalyst type. The 30 wt% PtCo/C thickness values were estimated to be 5/3 of the Pt/C due to the difference in wt% Pt loading on the carbon. The 30 wt% PtCo/C SEF values were obtained from reference 28. The $Pt_{ML}$/Pd/C electrode thickness was estimated to be $5 \pm 1$ microns thick by its fabricator based on experience with similar electrode coatings.[24]

For the NSTF sample electrodes, actual tested MEAs used to generate the data in Fig. 5 at each loading were measured for thickness by SEM. The CCM samples were potted and polished prior to SEM measurement. Fig. 7 shows example images at the different loadings. Thickness values were taken at between 12 and 20 positions along the electrodes shown in Fig. 7 and averaged to arrive at the values plotted versus loading in Fig. 8. For the thickness values, the linear regression fitted line in Fig. 8 was used to extract the NSTF electrode thickness for each loading. Table I gives the measured SEF values, Specific Activity (SA), thicknesses and calculated $\rho_s$ values for each catalyst type.

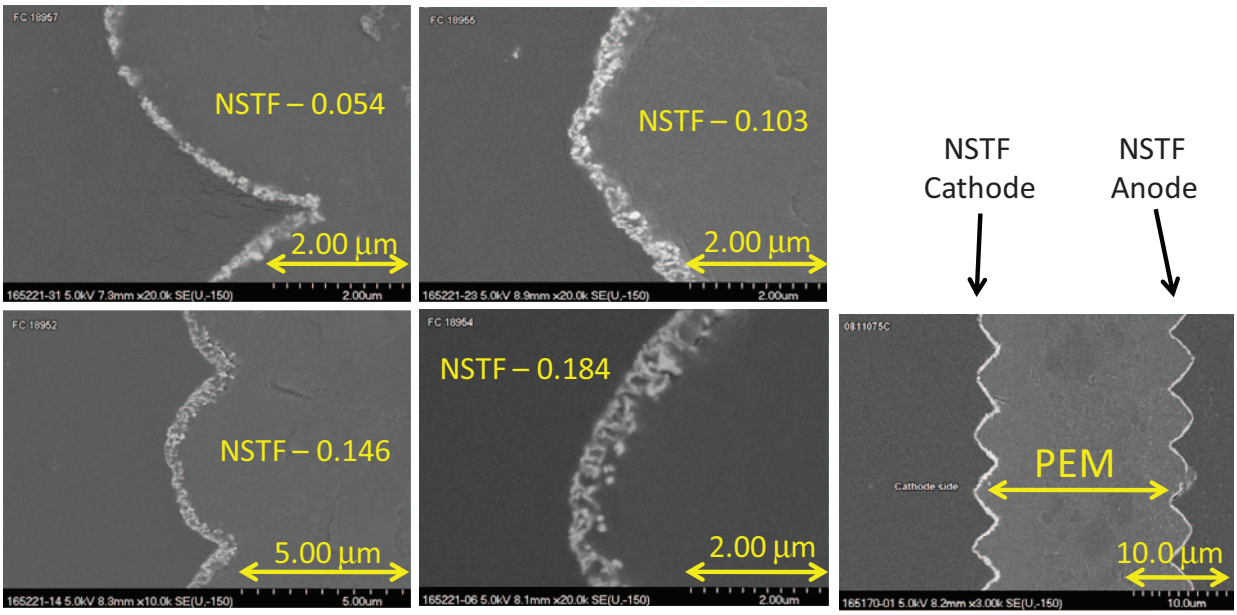


**Figure 7.** SEM cross-sectional images of NSTF PtCoMn catalyst coated membranes after they were tested to generate the data in Fig. 3. Samples were potted, polished and measured for thickness at 12 to 20 locations along each electrode shown.

Fig. 9 shows the SEF*SA-normalized current density at the iR-free cell voltage of 0.7 V from Fig. 5 plotted as a function of this surface area density, $\rho_s$. The apparent correlation of the SEF*SA normalized current with volumetric surface area density says that the amount of additional transport induced loss of observed planar current density at 650 mV (under 150 kPa $H_2$/air) compared to what the $O_2$ activity measurement at 900 mV (under 150 kPa saturated $O_2$) would project to 1.5 A/cm$^2$, is directly related to how compact the Pt surface area is within the electrode. This is a fundamental result because it is based on geometry and no amount of electrode formulating will improve this factor of the difference between thick, dispersed nanoparticle electrodes and thin extended surface area electrodes like NSTF. In this respect the carbon supports are a diluent. This effect is also consistent with the GM investigators' conclusions in 12 that the additional transport loss differences as a function of loading between their measured data and their modeled data must be occurring at or very close to the catalyst surfaces. Per the model above we would say this difference in transport overpotential is occurring on the order of one mean free path length from the surface. This simple application of kinetic gas theory would suggest the issue with loss of current density with more dispersed surface area is a boundary value problem with the appropriate scaling parameter being the ratio $\tau / t_s$, of the mean time between collisions with the bounding catalyst surfaces to the sojourn time in physisorption state on those surfaces. An alternative parameter might be the ratio, $d_s/\lambda$, i.e. a distance metric between opposing surfaces of adjacent catalyst nanoparticles, $d_s$, to the mean free path $\lambda$ between gas phase collisions. In the next section we use this ratio $\tau / t_s$ to define a first approximation for the scaling factor $f(d_s)$ in equation 6 and use it to determine a desorption energy, $E_d$ per Criterion 1 and the relative magnitudes of $f$ for the different catalyst types per Criterion 2 described below equation 6.

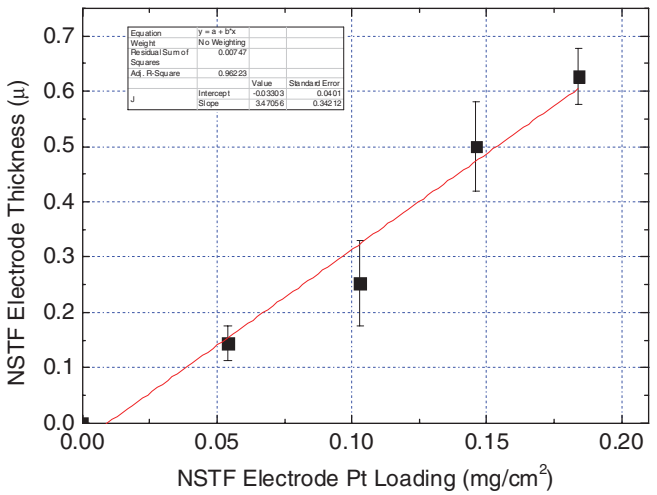


**Figure 8.** SEM determined electrode thickness versus Pt loading of NSTF PtCoMn catalyst coated membranes. from the images in Figure 7. The solid line least squares fit includes the origin. Error bars are based on thickness variations measured from 12 to 20 positions on any given SEM image.

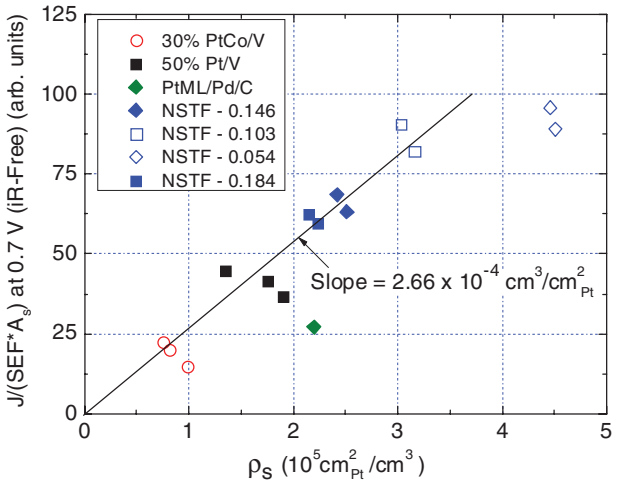


**Figure 9.** Surface area and specific activity normalized current density at 0.7 volts from Figure 5 plotted versus the volumetric surface area density, cm$^2$-Pt/cm$^3$ for the seven types of catalysts, derived from the electrode thickness and the measured or reported surface area enhancement factor values in Table I. The least squares fit shown excludes the PtML/Pd/Pt and NSTF-0.054 outliers since the thickness of the former is less accurately known and the iR-free cell voltage for the latter is decreasing due to other factors.

### Collision Frequency Scaling Factor – First Approach: $f(d_s) = \rho_s^{g-1}$

Figure 9 shows an essentially linear dependence of the ordinate on the volumetric surface area density. As the first approach to determine a functional form for the collision frequency scaling factor, $f(d_s)$ in 6 we will assume it has the simple form $\rho_s^{g-1}$. For an electrode of thickness $d$(cm) and volumetric surface area density $\rho_s(cm^2_{Pt}/cm^3) = S/d$, since $\rho_s^{g-1} S = d\rho_s^g$ we can rewrite 6 as the transfer current density:

$$J_{vol}(A/cm^3) = J\left(\frac{A}{cm^2}\right)\frac{1}{d} = \rho_s^g\left(cm^2_{Pt}/cm^3\right)p_{o_2}^{\gamma} \times \exp\left(-\frac{\beta F(E_{iR-free} - E_{rev} + \eta_{tx})}{RT}\right) \times \left[i_o\left(\frac{A}{cm^2_{Pt}}\right)C(\Theta_{ad}, \Delta G_{ad})\right] \quad [7]$$

We have introduced an exponent, $g$, in 7 to reflect an order parameter, analogous to $\gamma$ for $p_{o_2}^{\gamma}$ for how the volumetric current density depends on the magnitude of the volumetric surface area density, $\rho_s$. We next present a physical mechanism that will suggest a functional form for $g$. Then we will use that expression and apply equation 7 to the data in Fig. 9 to extract a value for the desorption energy for physical adsorption of oxygen molecules on the catalyst surface.

The mechanism proposed above for the dependence of the ORR current density on the compactness of the catalyst surface area at high current densities would suggest the pre-exponential factor in equation 7 must be able to account for the dependence of J on the geometric distribution of surface area as shown in Fig. 5. Each polarization curve in Fig. 4 was obtained by dividing the absolute current density $J(A/cm^2_{planar})$ measured under 150 kPa air at an arbitrary iR-free cell voltage $V \equiv E_{iR-free}$, by the measured surface area enhancement factor SEF $\equiv S(cm^2_{Pt}/cm^2_{planar})$. In Fig. 5 each of these corresponding curves was then divided by its catalyst's measured specific activity. This SA is identical to the SEF normalized absolute current density measured under 150 kPa pure oxygen saturated with 50 kPa partial pressure of water vapor at 900 mV. Hereafter we denote the 150 kPa $H_2$/air polarization curve conditions as *Condition 1* and the current density as $J_1$, and the 150 kPa $H_2/O_2$, 900 mV conditions as *Condition 2*, and that current density as $J_2$. Using equation 4 to represent the absolute current density $J_i(V)$ at *Condition* $i = 1$ or 2 this process is equivalent to the following expression:

$$\delta J_{1,2}(V) \equiv \frac{[J_1(V)]}{S}\Big/\frac{[J_2(0.9)]}{S} = \frac{[J_1(V)]}{d}\Big/\frac{[J_2(0.9)]}{d}, \quad [8]$$

which by equation 7 becomes:

$$\delta J_{1,2}(V) \equiv \frac{J_{1,vol}(V)}{J_{2,vol}(0.9)} = \rho_s^{(g_1-g_2)}\left[p^{\gamma}_{1,o_2}/p^{\gamma}_{2,o_2}\right] \times \exp\left(-\frac{\beta F(V-0.9) - (E_{1,rev} - E_{2,rev}) + (\eta_{1,tx} - \eta_{2,tx})}{RT}\right) \times (C_1/C_2). \quad [9]$$

From equation 9 we obtain:

$$log[\delta J_{1,2}(V)] = (g_1 - g_2)log(\rho_s) + B, \quad [10]$$

where

$$B = \log\left\{\left[p^{\gamma}_{1,O_2}/p^{\gamma}_{2,O_2}\right] \times \exp\left(-\frac{\beta F(V-0.9) - (E_{1,rev} - E_{2,rev}) + (\eta_{1,tx} - \eta_{2,tx})}{RT}\right)\left(C_1/C_2\right)\right\}. \quad [11]$$

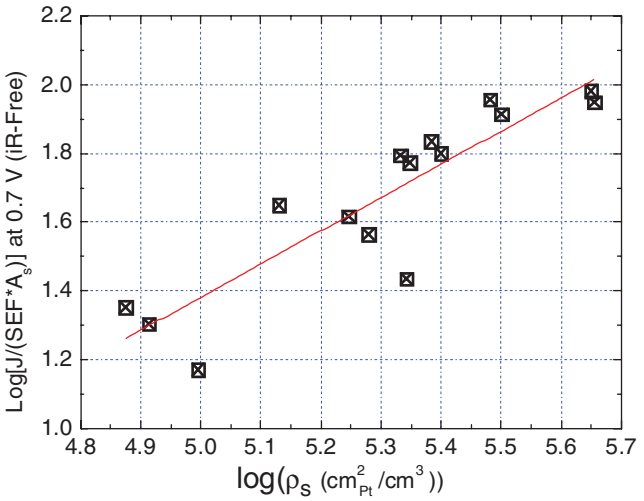


**Figure 10.** Surface area and specific activity normalized current density at 0.7 volts from figure 6 plotted versus the volumetric surface area density as a log-log plot.

Equation 10 has a form we can now apply to the data in Fig. 9. Fig. 10 shows the data in Fig. 9 replotted as a log-log plot to which the linear fit to all the catalyst types yields a slope of:

$$(g_1 - g_2) = 0.97 \pm 0.14 \quad [12]$$

We now use this result to test the physically intuitive model discussed in the section above titled Relation of SEF and SA Normalized Current Density to the Surface Area Distribution Metric by choosing a functional form for the exponent to predict a fundamental parameter, the desorption energy, $E_d$ from the physisorbed state. The mechanisms for how the high current density is enhanced for high values of volumetric surface area density due to increased collision frequencies led to a critical scaling parameter $\tau/t_S$. We define then

$$g \equiv 1 + \tau/t_S, \quad [13]$$

where $t_s$ is given in 3 and $\tau = \lambda/\upsilon_{av}$ is the ratio of the mean free path to the average molecular speed

$$\upsilon_{av} = 1.45 \times 10^4\sqrt{(T/M)}. \quad [14]$$

When $\tau << t_S$ then the transport time between physical adsorption events is much less important and the compactness of the surface area is irrelevant. If $\tau \geq t_S$ then the volumetric surface area density becomes important and increasingly so the shorter is $t_S$. Both the *Conditions* 1 and 2 are at 80°C so $\upsilon_{av}$ is the same for both and for oxygen, $\upsilon_{av} = 4.82 \times 10^4$cm/sec.

The slope of Fig. 10 is then given by

$$(g_1 - g_2) = (1/\upsilon_{av})(\lambda^{(1)} - \lambda^{(2)})/t_S = 0.97 \pm 0.14. \quad [15]$$

With the definition of $t_S$ in equation 3 we arrive finally at the dependence of $E_d$ on $\Delta\lambda = (\lambda^{(1)} - \lambda^{(2)})$as:

$$E_d(kCal/mole) = R_o T \ln[\upsilon_{av} t' \Delta g/\Delta\lambda\,(cm)] \quad [16]$$

The $O_2$ molecular mean free path length as a function of temperature $T$ and partial pressure $P$ are also well known from kinetic gas theory.[33] For a gas mixture of two gas types $i$ and $j$, the effective mean free path length for species $i$ moving through a majority species $j$ is:

$$\lambda_{i,j} = 4kT/[\pi(\xi_i + \xi_j)^2 P_j(1 + M_i/M_j)^{1/2}], \quad [17]$$

where $P$ is in Torr and $k = 1.035 \times 10^{-19}$ Torr-cm$^3$/°K. *Condition* 1 corresponds to $O_2$ moving in sub-saturated air at 150 kPa total pressure at 80°C. Letting $i$ correspond to $O_2$ and $j$ to $N_2$, ignoring the water vapor partial pressure, $P_{N_2} = 901$ Torr. Using standard values for the molecular diameters $\xi_{O_2} = 2.93 \times 10^{-8} cm$ and $\xi_{N_2} = 3.14 \times 10^{-8}$ cm, equation 17 yields $\lambda^{(1)}_{O_2,N_2} = 9.6 \times 10^{-6}$ cm for *Condition* 1.

For *Condition* 2, we have 100 kPa of pure oxygen moving through 50 kPa (380 Torr) of water vapor. In this case we take for $\xi_j = \xi_{H_2O} = 4.7 \times 10^{-8}$ cm,[38] and with $P_{H_2O} = 380$ Torr, equation 17 yields $\lambda^{(2)}_{O_2,N_2} = 1.26 \times 10^{-5}$cm for *Condition* 2. We have then $\Delta\lambda = \left(\lambda^{(1)} - \lambda^{(2)}\right) = 0.3 \times 10^{-5}$ cm. Finally, from equation 16, with $R_o = 1.986$ Cal/mole, T = 353°K, for $t' = 1$ to $5 \times 10^{-13}$ sec, we obtain respectively $E_d = 4.53$ to 3.4 kCal/mole. These are entirely reasonable values for the heat of oxygen physical adsorption since as noted above the maximum observed values for the enthalpy of oxygen physisorption are 5.02 kCal/mole.[37] This result based on the measured data in Fig. 9 and Table I would support the validity of the functional form for $g$ in 13 and its use as an exponent for the volumetric surface area density $\rho_s^g$ in the Butler-Volmer equation in 7. This meets *Criterion* 1.

For the *Criterion* 2, we can determine the value of $f(d_s) = \rho_s^{g-1}$ at the *Condition* 1 with the above values of $E_d$, $\lambda^{(1)}_{O_2,N_2} = 9.6 \times 10^{-6}$cm and equations 13 and 14. The result is $g_1 = 4.12$, so $f_1(d_s) = \rho_s^{3.12}$. From the values of $\rho_s$ in Table I for the various catalyst types, the scaling parameter $f_1(d_s)$ ranges from 0.41 to 0.969 for the PtCo/C electrodes, to 2.6 to 7.1 for the Pt/C electrodes, to 11.7 to 108 for the NSTF electrodes. This would represent a range of current density at a cell voltage of ~0.625 V (0.7 V, iR-free) under *Condition* 1 of over 200 between the lowest loading dispersed and NSTF electrodes. Since this is two orders of magnitude larger than what is seen in Fig. 2, this first functional form for $f(d_s)$ has failed *Criterion* 2. This leads to a second approach for the collision frequency scaling factor.

### Collision Frequency Scaling Factor – Second Approach: $f(d_s) = 1/(t_g + t_s)$

As a second approach we go back to the basic concept that the effect we are trying to explain is a sampling rate phenomenon: the more attempts per unit time the average oxygen molecule makes to become chemisorbed, the larger the observed ORR current density will be. Once a molecule finds an available site for chemisorption, the probability it will chemisorb is given by $e^{-\Delta G_{ad}/RT}$ and its potential residence time is enormous (years) due to the large value of $\Delta G_{ad}$ of activated desorption energy. The probability it will be reduced is given by the $\exp(-F\eta/RT)$ factor. So if chemisorbed it is essentially certain to be reduced so the more frequent the attempts at becoming chemisorbed the more frequently the average $O_2$ molecule will be reduced. This frequency factor $f$ for chemisorption attempts can be considered to be the inverse of an average cycle time between catalyst surface sampling events, $\tau_c = 1/f$. This average cycle time we define as the total time an average $O_2$ molecule (or a gas phase reaction intermediate) spends from one failed attempt at chemisorption, when it desorbs from a physisorption state, until the next such desorption. This sequence includes the average time it spends traveling in the gas phase from a desorption site to its next catalyst surface encounter, $t_g$, plus the average time it spends in a physisorption state on that next surface, $t_s$ or $\tau_c = t_g + t_s$.

Equation 3 gives the average time $t_s$ the oxygen molecule spends physisorbed. The time $t_g$that it spends in transit between sequential adsorption sites will obviously vary significantly depending on how far apart they are and if the molecule follows a path that includes collisions with non-catalyst surfaces along the way. From our thought experiment illustrated in Fig. 6, the shortest path would be one in which the desorbing molecule moves one mean free path away from a catalyst surface site and then is back scattered to the same surface vicinity again. This minimum time in the gas phase is $2\lambda/\upsilon_{av}$. If the adjacent or opposing catalyst surfaces are closer than one mean free path, then that time would be even shorter. In general this time interval can be captured as the average time for collisions with sequential catalyst surfaces separated by a mean distance metric $d_s$ or $d_s/v_{av}$. Determining an expression for such an average distance metric is difficult, as it might be expected to involve a product of pair-wise distribution functions of all possible catalyst adsorption sites spacings times some Gaussian or logarithmic weighting factor, averaged over some catalyst electrode volume, such as $\lambda^3$. We take a much simpler approach here and assume that the relevant distance metric is simply the inverse of the volumetric surface area density, $1/\rho_s$, which has the appropriate units of cm. With this assumption the average time in the gas phase between surface site collisions is in the range $2\lambda/\upsilon_{av} \le t_g \le 1/\rho_s v_{av}$. We assume further that the number of surface collision events with the minimum value of $t_g$ is roughly the same as those with the maximum value. This assumption is the simplest weighting function among different $t_g$ paths and allows us to take the average time in the gas phase to be simply the average of the minimum and maximum times in the gas phase, leading to the expression for the average time of $\tau_c$ in 18:

$$\tau_{c,av} = t_s + t_{g,av} = t' e^{\frac{E_d}{RT}} + [\lambda/\upsilon_{av} + 1/(2\rho_s \upsilon_{av})]. \quad [18]$$

The pre-exponential collision frequency factor to use in conjunction with $S\left(cm^2_{Pt}/cm^2_{planar}\right)$ in equation 6 must be dimensionless. For this we choose to normalize $\tau_{c,av}$ by the shortest assumed time interval between surface collisions $2\lambda/\upsilon_{av}$, giving as our final collision frequency scaling factor:

$$f = 2[1 + t'(\upsilon_{av}/2\lambda)e^{\frac{E_d}{RT}} + 1/(2\rho_s\lambda)]^{-1}, \quad [19]$$

which has the temperature and pressure dependence of the mean free path expression in 17.

Introducing $f$ into equation 6 yields,

$$J\left(A/cm^2_{planar}\right) = f(\lambda,\rho_s)S\left(\frac{cm^2_{Pt}}{cm^2_{planar}}\right)\left[i_o\left(\frac{A}{cm^2_{Pt}}\right)p^{\gamma}_{O_2}(1-\Theta_{ad})^x \times \exp\left(-\frac{\beta F\eta}{RT}\right)\exp\left(-\frac{\gamma\Delta G_{ad}}{RT}\right)\right] \quad [20]$$

We can now form the ratio of $J$ under *Conditions* 1 and 2 corresponding to the measured data in Fig. 5 similar to what was done in equation 8 with B defined in equation 11:

$$\delta J_{1,2}(V) \equiv \frac{J_{1,vol}(V)}{J_{2,vol}(0.9)} = ([f_1(\lambda,\rho_s/f_2(\lambda,\rho_s)]\exp(B). \quad [21]$$

Taking the derivative of $\delta J_{1,2}(V)$ with respect to $\rho_s$ and rearranging gives

$$\frac{\partial\delta J_{1,2}(V)}{\partial\rho_s}\{1/\delta J_{1,2}(V)\} = \left\{\frac{1}{f_1}\frac{\partial f_1}{\partial\rho_s} + f_2\frac{\partial(1/f_2)}{\partial\rho_s}\right\}. \quad [22]$$

The left side of 22 is a measurable quantity from Fig. 9 for each catalyst type at any voltage. We choose V(iR-free) = 0.7 volts. The right side can be expanded using the definitions of $f_1$ and $f_2$ from 19 with the dependence on conditions through $\lambda^{(1)}$ and $\lambda^{(2)}$ (simplifying $\lambda^{(m)}$ with $\lambda_m$) as:

$$\frac{1}{f_1}\frac{\partial f_1}{\partial\rho_s} + f_2\frac{\partial(1/f_2)}{\partial\rho_s} = \left(\frac{1}{4\rho_S^2}\right)\left[\frac{f_1}{\lambda_1} - \frac{f_2}{\lambda_2}\right] = \left(\frac{1}{4\rho_S^2}\right)\frac{2(\lambda_2-\lambda_1)}{\left(\lambda_1 + \frac{1}{2\rho_s} + X\right)\left(\lambda_2 + \frac{1}{2\rho_s} + X\right)}. \quad [23]$$

where

$$|X| = t'(\upsilon_{av}/2)(e^{\frac{E_d}{RT}} + 1) \quad [24]$$

Putting equation 23 into 22 and rearranging as a quadratic equation for X gives:

$$\rho_S^2 X^2 + \left[\rho_s + \rho_S^2(\lambda_2+\lambda_1)\right]X + \left[0.25 + \frac{\rho_s(\lambda_2+\lambda_1)}{2} + \rho_S^2\lambda_2\lambda_1 + \frac{\delta J_{1,2}(V)(\lambda_1-\lambda_2)}{2b(\rho_s)}\right] = 0, \quad [25]$$

where $b(\rho_s) = \partial\delta J_{1,2}(V)/\partial\rho_s$ is the slope of the linear fit through the data in Fig. 9. From equation 25 we can solve for X and from

**Table II. Input and output parameters for the second approach to calculating the collision frequency scaling factor in equation 19 for *Condition 1*.**

| Catalyst Type | $\rho_s$ ($\times 10^5$ $cm^2_{Pt}/cm^3$) | $\delta J_{1,2}$ ($V = 0.7$) | $E_d$ - sol'n 1 (kCal/mole) | $E_d$ - sol'n 2 (kCal/mole) | $f_1$ ($\lambda_1$, $\rho_s$) |
|---|---|---|---|---|---|
| NSTF – 0.054 | 4.46 | 95.8 | 4.72 | 4.97 | 0.926 |
| NSTF – 0.054 | 4.51 | 89.1 | 4.72 | 4.97 | 0.924 |
| NSTF – 0.103 | 3.03 | 90.5 | 4.71 | 5.02 | 0.904 |
| NSTF – 0.103 | 3.16 | 82.1 | 4.72 | 5.01 | 0.903 |
| NSTF – 0.146 | 2.42 | 68.6 | 4.73 | 5.05 | 0.877 |
| NSTF – 0.146 | 2.51 | 63.2 | 4.74 | 5.04 | 0.877 |
| NSTF – 0.184 | 2.15 | 62.3 | 4.74 | 5.07 | 0.863 |
| NSTF – 0.184 | 2.23 | 59.5 | 4.74 | 5.06 | 0.865 |
| Pt/C – 0.10 | 1.36 | 44.7 | 4.77 | 5.16 | 0.796 |
| Pt/C – 0.20 | 1.76 | 41.4 | 4.77 | 5.09 | 0.825 |
| Pt/C – 0.30 | 1.87 | 36.8 | 4.78 | 5.07 | 0.829 |
| PtCo/C – 0.05 | 0.75 | 22.6 | 4.89 | 5.30 | 0.660 |
| PtCo/C – 0.10 | 0.82 | 20.2 | 4.89 | 5.25 | 0.673 |
| PtCo/C – 0.2 | 0.99 | 14.8 | 4.89 | 5.18 | 0.697 |
| PtMLPt/Pd/C – 0.1 | 2.22 | 27.2 | 4.79 | 5.03 | 0.837 |

equation 24 calculate the values of $E_d$, the physical desorption heat:

$$X = \frac{-h \pm \sqrt{h^2 - 4AD}}{2A}, \quad A = \rho_s^2; h = [\rho_s + \rho_s^2(\lambda_1 + \lambda_2)] \text{ and}$$

$$D = 0.25 + \frac{\rho_s(\lambda_2 + \lambda_1)}{2} + \rho_S^2\lambda_2\lambda_1 + \frac{\delta J_{1,2}(V)(\lambda_1 - \lambda_2)}{2b(\rho_s)}. \quad [26]$$

For $E_d$ to be real we have taken the absolute value of the solutions of X from equation 25. The values of $\lambda_1$ and $\lambda_2$ are the same as used above for the *Conditions* 1 and 2 and we take $t' = 5 \times 10^{-13}$ sec. A linear fit of $\delta J_{1,2}(V)$ vs $\rho_s$ in Fig. 9, excluding the outliers (PtML/Pd/C and the two 0.05 NSTF), gives a slope of $b = 2.66 \times 10^{-4}$ $cm^3/cm^2_{Pt}$ with an adjusted $R^2$ of 0.98. The values of $\delta J_{1,2}(0.7V)$ at each catalyst's $\rho_s$ are those shown in Fig. 9 and Table II. With these input parameters we obtain finally the values for $E_d$ in Table II, for both quadratic solutions, and in the last column, the pre-exponential frequency scaling factor from equation 19 for *Condition* 1 (80°C, 150 kPa $H_2$/air).

The values of $E_d$ in the 4th column of Table II are slightly smaller than those in the 5th column derived from the second quadratic solution option from equation 25. The first solution average for the 15 samples is 4.77 ± 0.065 kCal/mole, which again is close to the maximum observed value for the enthalpy of oxygen physisorption given by Atkins as 5.02 kCal/mole.[37] The average desorption heat for the second solution is slightly larger at 5.08 ± 0.095 kCal/mole. For no other reason than this we assume the first solution of the quadratic equation 25 is the more correct one, and we used that average value of $E_d$ to calculate the collision frequency factor for *Condition* 1 for each catalyst type.

Fig. 11 shows the calculated pre-exponential frequency scaling factor $f$ as a function of the surface area volumetric density from the last column in Table II. A quadratic fit is shown for the dependence of $f$ on the $\rho_s$ that suggests the extended surface area catalyst NSTF with 0.05 mg/$cm^2$ PtCoMn will produce 40% more current density at 0.7 V (iR-free) than the PtCo/C at the 0.05 mg/$cm^2$ loading due to this effect under *Condition* 1 conditions. This is approximately consistent with the data in Fig. 2, and much more consistent with observation than the scaling factors derived in our first approach above based on $\rho_s^{(g_1 - g_2)}$, which predicted scaling factor ratios nearly two orders of magnitude larger. This second approach giving the pre-exponential frequency scaling factor $f$ defined as in 19 meets both *Criteria* 1 and 2 and is considered more correct. Fig. 11 suggests that electrode volumetric surface area density of at least $3 \times 10^5$ $cm^2_{Pt}/cm^3$ is necessary to minimize the effect.

The actual measured current densities ($A/cm^2_{planar}$) at 0.7 V (iR-free) can now be normalized by the pre-exponential frequency scaling factor $f_1$ for each catalyst type from Table II. The result is shown in Fig. 12. The current density of the NSTF samples with loading in the range of 0.184 to 0.103 mg/$cm^2$ and the PtCo/C samples at 0.20 mg/$cm^2$ now all have about the same current density values at 0.7 V (iR-free). The lower values for the other reduced loadings for these and the other catalyst types and loadings is presumably due to other differences in mass transport/Tafel slope loss factors between the catalyst types.

## Discussion

For electrodes with ultra-low loadings, the above analysis shows that using larger more closely packed particles in ultra-thin electrodes is beneficial to reach higher current densities. Using higher wt% catalyst coated supports (NSTF catalysts are ~ 95 wt%) and thinner layers should help for any catalyst type. This is most easily accomplished by eliminating the corrodible carbon in the layer, since it is not necessary for electronic conduction if that function can be handled by the catalyst coating, as in the submicron thick NSTF extended surface area catalysts. For such thin electrodes ionomer for proton conduction is also unnecessary when the catalyst is embedded in the PEM surface. Although this has been born out experimentally for years with the NSTF

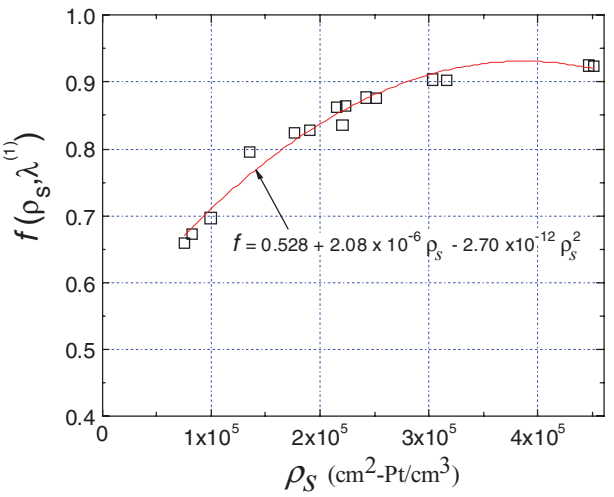


**Figure 11.** Pre-exponential collision frequency scaling factor as a function of the surface area volumetric density as obtained from Table II for *Condition* 1 (80°C, 150 kPa, $H_2$/air).

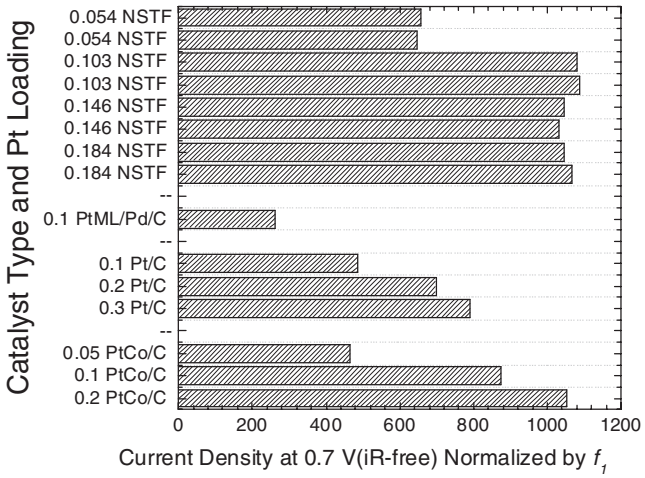


**Figure 12.** Measured current density at 0.70 Volts (iR-free) normalized by the pre-exponential frequency scaling factor from Table II for *Condition* 1 (80°C, 150 kPa, $H_2$/air). The 0.2 PtCo/C and NSTF PtCoMn between 0.184 and 0.103 mg/cm$^2$ now have similar performances. The remaining losses at lower loadings are presumed due to other mass transport and Tafel slope change affects.

type electrodes, a recent DFT analysis by Tripkovic et al. shows that the barriers to proton transport parallel to Pt(111) are small.[39] This compactness of highly oriented catalyst surfaces may also introduce other new physical mechanisms to enhance activity and durability as modeled recently by the Eikerling group.[40–42]

That the NSTF electrodes have catalyst surface area distributions better suited for more efficient oxygen reduction (capture and entrapment) has precedence with protein adsorption on similar structures.[43] In that work, Protein A, human IgG and Bovine serum albumin were adsorbed on four types of metal coated NSTF whiskers, Pt, Fe, CoCr, Cu, similar to those shown in Fig. 1. The NSTF coated whiskers were directly immersed in the protein solution. We reported that not only were the total amounts of viable protein adsorbable per unit area more than an order of magnitude higher than on planar surfaces, but surprisingly the rates of adsorption were much higher as well. This adsorption was of course from solution so only transport by Fickian diffusion applied. The only explanation was that the number of adsorption tries per unit time on the vertically oriented catalyst coated whiskers by the protein molecules deep within that NSTF structure was much higher, like the surface area, compared to the adsorption attempts on a planar surface from which a non-sticking protein could just as likely random walk away from the surface as diffuse back towards it.

Another Pt ORR related example of the importance of catalyst surface area compactness is given in the study by Bonakdarpour et al. of how peroxide production and release depends on the densities of NSTF whiskers on a glassy carbon disc in RRDE measurements.[44] A dramatic increase in $H_2O_2$ release was observed as the catalyst loading (number of catalyzed whiskers per unit area on the glassy carbon tip of RRDE) was decreased below 0.020 mg cm$^{-2}$. Those observations suggest that if the catalyst nanoparticles are sparsely distributed, the produced $H_2O_2$ cannot be efficiently reduced to $H_2O$ before it escapes, even though the rates are far lower than for typical Pt/C catalysts and scale with the higher RDE half-wave potentials.[44] For standard compact NSTF electrodes in MEA's this better ability to capture the peroxide intermediates may also be a significant part of the reason why $F^-$ ion release rates are measured to be two to three orders of magnitude lower than for dispersed electrodes on membranes with no free-radical scavenging chemical additives.[45]

Finally, another illustration of this fundamental particle entrapment/sampling rate phenomenon is observed any time a thin film metal is coated onto the as-fabricated oriented NSTF whiskers. Metal coated whiskers appear very black with reflectivity $< 1.5\%$ for $200 < \lambda < 800$ nm due to multiple scattering/absorption of the optical plane wave field between the oriented metallic whiskers.

Despite the assumptions in the proposed model and calculations to arrive at numerical values for the collision frequency scaling factor, it is perhaps surprising how well the second approach for determining a functional form for the collision frequency scaling factor *f* appears to have worked in the previous section. We have treated the electrode layers as consisting only of gas phase reactants, and ignored the effects on $O_2$ transport times of intervening material between adjacent Pt catalyst surfaces, such as ionomer or liquid water. However since the critical length is this model is the distance from the catalyst surface on the order of only a mean free path, or ~80 nm, this may not be too severe. Perhaps the more significant assumption is that we have gone beyond the concept of surface coverage of chemisorbed species being in equilibrium with a gas phase partial pressure above the surface (more appropriate for clean surfaces in ultra-high vacuum) to a concept of surface coverage of chemisorbed species in equilibrium with surface physisorbed species, and the dependence of the later on the spatial distribution of catalyst surface area and its effect on surface site collision rates in the Knudsen regime.

The scientific basis for consideration of any new idea or theory is whether it can match experiment, not whether if fits comfortably with our preconceived notions of intuition or common sense. The kinetic theory model and algebraic formulation we described are ultimately able to predict the observed differences in current density at 650 mV of the dispersed and NSTF polarization curves as shown in Fig. 12, as well as the heat of desorption from a physisorbed state, with only one adjustable parameter. This adjustable parameter is t', the customary period of molecular vibration ranging in the literature from $10^{-13}$ to $10^{-12}$ seconds. Even with this range, none of the model conclusions would be significantly changed from the results obtained with the value at the mid-point of $5 \times 10^{-13}$ s. Certainly a large approximation used is taking the volumetric surface area, $1/\rho_s$, as the distant metric for the mean time interval between surface collisions, $d_s/v_{av.}$ But this is a first order model approximation and not a fitting parameter. On a global basis, it seems adequate, but it would be very interesting to see measurements done with idealized catalyst surface structures, such as idealized lattice distributions of Pt nanoparticles or electrodes comprising Pt metal flakes with controlled spacings between them. Designed experiments with different wt% Pt/C but constant loading, identical catalyst particle sizes, carbon types and C/ionomer ratios would also be useful to explore the effects proposed. In this regard, the results in Fig. 13 of reference 17 showing that the Pt utilization of 30 wt% Pt/C is half that of 60 wt% Pt/C with the same carbon, C/ionomer ratio, at %RH values sufficiently low to exclude flooding are just what our model would predict. Note that changing $\rho_s$ by mixing in non-catalyzed carbon black with Pt/C would not be expected in this model to have an effect unless the mixing was complete on the scale of $\lambda^3$ or less.

Nothing in our approach would seem to exclude the long standing belief that observed Tafel slopes are related to some voltage dependent aspect of the adsorbed surface coverage of interfering species. It also of course does not replace the obvious dependence of ORR activity on Pt[hkl] facet sizes and distribution changes that may occur as loading is reduced with extended surface area catalyst like the NSTF (as seen in the 0.103 to 0.054 loading step.) So those affects contributing to the additional loss of high current density with reduced loading are in addition to the new collision frequency scaling factor *f* proposed in this work as a pre-exponential in the Butler-Volmer equation.

Despite the fact that the stimulus for developing this collision frequency scaling factor model was the observed excessive fall-off of high current density with reduced loading, it currently cannot explain that loss for any one catalyst type, such as the Pt/C, which has essentially the same surface area per unit volume, $\rho_s$, at all loadings. Hopefully it might provide an additional avenue for investigation, and a more sophisticated version of the model's key distance metric, $d_s$ might provide more insight. In this analysis we have taken the critical length dimension to be a mean free path, $l \sim \lambda$ below which

gaseous transport is Knudsen diffusion, and above which the diffusion is intermediate between Knudsen and viscous flow at $l \sim 111\ \lambda$.[33] But a more sophisticated treatment of the transition times $\tau_c$ in equation 18 might consider the transitional dimension to be that between $\lambda$ and the mid-point of the intermediate flow regime, $\lambda < l < 10\lambda$. At 10 $\lambda$, the critical dimension becomes ~800 nm and now within an order of magnitude of the Pt/C electrode thicknesses. This and the changing diffusion speed $v_{av}$ as diffusion goes from Knudsen to the edge of viscous may be the means by which the dependence on just $d_s = 1/\rho_s$ breaks down and the electrode thickness has an effect on collision frequency with the available surface area. Related to this is that there will be a gradient in $O_2$ concentration near the catalyst surface at the highest current densities extending over more of the electrode's thickness.

## Conclusions

We have developed a model to explain the significant difference in current density normalized by both surface area and specific activity, observed between low loaded catalyst electrodes having widely differing volumetric surface area densities, specifically dispersed Pt/C and NSTF electrodes. The model is based on the premises that the average time spent by oxygen molecules in physisorption states plus the mean time in transit between physisorption events determines a surface collision frequency factor that contributes directly to the rate of successful chemisorption and oxygen reduction, and also that the surface area distribution can impact this collision frequency. The rate of physisorption events is related to the gas phase molecular velocities in the Knudsen regime over distances of one mean free path, and a distance metric describing the spatial distance between catalyst surface area sites. Using kinetic gas theory and approximating the distance metric by the inverse volumetric surface area density, we tested two functional forms for a pre-exponential collision scaling factor introduced into the Butler-Volmer equation. The preferred scaling factor is able to satisfy two criteria: i) correct prediction of the desorption heat of 4.77 kCal/mole for $O_2$ from physisorbed states, and ii) prediction of the observed ratio of current densities at 0.7 V (iR-free) of published polarization curves from similar MEA's containing eleven Pt/C, PtCo/C and NSTF-PtCoMn cathodes with Pt loadings below 0.2 mg/cm$^2$. The scaling factor was found to have a quadratic dependence on volumetric surface area density and for the fuel cell data used to determine it, numerically ranged from a low of 0.66 to 0.93 for the catalysts having $\rho_s$in the range of $0.75 \times 10^5$ to $4.5 \times 10^5$ cm$^2{}_{Pt}$/cm$^3$. It suggests that electrode surface area densities of at least $3 \times 10^5$ cm$^2{}_{Pt}$/cm$^3$ are most desirable to minimize the effect. The enhanced current density for the extended surface area NSTF catalysts is intuitively consistent with the electrode structure's better ability to "entrap" adsorbing oxygen molecules due to the alignment, length to width ratios and spacing of the catalyst coated whiskers in conjunction with Knudsen's cosine law which serves to increase the molecule/surface collision rate per unit time. This concept may not have been considered previously for conventional electrodes and we suggest that a more sophisticated application of the model may be able to partially explain the excessive loss of high current density performance at low loadings seen with conventional Pt/C electrodes.

## Acknowledgments

The author thanks Thomas Greszler of the GM Global Research and Development Lab in Honeoye Falls, NY, for supplying spread sheet data and alloy activities for the polarization curves used from references 12 and 13. We also thank Michael Meyer of 3M Analytical for the NSTF SEM thickness measurements, and the 3M NSTF development team for the NSTF polarization curves used from reference 23. Finally, we acknowledge the support of the Dept. of Energy Office of Energy Efficiency and Renewable Energy for support under Grant DE-FG36-07GO17007.

## List of Symbols

### Acronyms

| | |
|---|---|
| *CCM* | Catalyst coated membrane |
| *MEA* | membrane electrode assembly |
| *NSTF* | Nanostructured thin film |
| *ORR* | Oxygen reduction reaction |
| *PGM* | Precious group metals |
| *SA* | Specific activity for ORR |
| *SEF* | Surface area enhancement factor |
| *PtML/Pd/C* | Pt monolayer on Pd on Carbon |

### Roman

| | |
|---|---|
| $E_d$ | Physical adsorption/desorption enthalpy/heat |
| $J$ | Current density, A/cm$^2{}_{Planar}$ |
| $g$ | exponent for first approach for collision scaling factor |
| $R$ | Ideal gas constant |
| $T$ | Temperature (K) |
| $F$ | Faraday's constant |
| $M_i$ | Molecular mass of species $i$ |
| $S$ | Pt surface area enhancement factor ($cm^2_{Pt}/cm^2_{planar}$) |
| $d$ | Electrode thickness |
| $d_s$ | Surface area distribution parameter or distance metric between catalyst particles |
| $f_i(d_s)$ | Pre-exponential collision frequency scaling factor for condition $i$ ($i = 1$ or 2) |
| $i_o$ | Equilibrium exchange current density |
| $t_s$ | Sojurn time of a physisorbed molecule |
| $t_g$ | Time in gas phase between successive catalyst surface site collisions on average |
| $t'$ | Molecular vibrational period of adsorbed molecules |
| $t_{g,av}$ | Average value of $t_g$ |
| $\upsilon_{av}$ | Average molecular speed in the gas phase |
| $E_{ir\text{-}Free}$ | Cell voltage corrected for internal resistances |
| $p_q$ | Partial pressure of gas species $q$ |
| $\delta J_{1,2}\,(V)$ | Ratio of $J_{1,vol}\,(V)\,over\,J_{2,vol}\,(0.9)$ |
| $J_{1,vol}\,(V)$ | Current density under conditions 1(80°C, 150 kPa $H_2$/air) at iR-free cell voltage V. |
| $J_{2,vol}\,(0.9)$ | Current density under conditions 2(80°C, 150 kPa $O_2$) at iR-free cell voltage of 900 mV. |

### Greek

| | |
|---|---|
| $\rho_s$ | Volumetric surface area density, cm$^2{}_{Pt}$/cm$^3$. |
| $\lambda^{(m)}$ *or* $\lambda_m$ | Gas phase mean free path under gas mixture, pressure, and temperature condition set $m$, cm |
| $\tau_{c,av}$ | Average cycle time for an $O_2$ molecule between sequential physisorption attempts |
| $\lambda_{i,j}$ | Effective mean free path of gas species $i$ moving through another species type $j$. |
| $\xi_i$ | Molecular diameter of species $i$. |
| $\Delta\lambda$ | Difference of mean free paths pertaining to operating Conditions 12, $\lambda^{(1)} - \lambda^{(2)}$ |

## References

1. DOE Website http://www.eere.energy.gov/hydrogenandfuelcells/mypp/pdfs/fuel_cells.pdf.
2. V. Stamenkovic, T. J. Schmidt, P. N. Ross, and N. M. Markovic, "Surface Composition Effects in Electrocatalysis: Kinetics of Oxygen Reduction on Well-Defined $Pt_3Ni$ and $Pt_3Co$ Alloy Surfaces," *Journal of Physical Chemistry B*, **106**, 11970–11979 (2002).
3. V. R. Stamenkovic et al., "Trends in Electrocatalysis on Extended and Nanoscale Pt-bimetallic Alloy Surfaces" *Nature Materials*, **6**, 241–247 (2007).
4. C. Wang, G. Wang, D. van der Vliet, K-C. Chang, N. M. Markovic, and V. R. Stamenkovic "Monodispersed $Pt_3Co$ nanoparticles as electrocatalyst: the effects of particle size and pretreatment on electrocatalytic reduction of oxygen," *Phys. Chem. Chem. Phys.*, **12**, 6933–6939 (2010).
5. J. B. Wu, J. L. Zhang, Z. M. Peng, S. C. Yang, F. T. Wagner, and H. Yang "Truncated Octahedral $Pt_3Ni$ ORR Electrocatalysts," *J. Am. Chem. Soc.*, **132**, 4984–4985 (2010).

6. M. Shao, K. Sasaki, N. S. Marinkivic, L. Zhang, and R. R. Adzic, "Synthesis and Characterization of Platinum Monolayer Oxygen-Reduction Electrocatalysts with Co-Pd Core-Shell Nanoparticle Supports," *Electrochem. Commun.*, **9**, 2848–2853 (2007).
7. R. R. Adzic, "Contiguous Platinum Monolayer Oxygen Reduction Electrocatalysts on High-Stability-Low-Cost Supports," 2010 DOE Hydrogen Program Annual Merit Review, presentation FC009, June 7–11, 2010, Washington, DC.
8. J. Erlebacher and J. Snyder, "Dealloyed Nanoporous Metals for PEM Fuel Cell Catalysis, *ECS Transactions*," **25**(1), 603–612 (2009).
9. S. Koh, N. Hahn, C. Yu, and P. Strasser, "Effects of Composition and Annealing Conditions on Catalytic Activities of Dealloyed Pt-Cu Nanoparticle Electrocatalysts for PEMFC," *J. Electrochem. Soc.*, **155**(12), B1281–B1288 (2008).
10. V. R. Stamenkovic et al., "Improved Oxygen Reduction Activity on $Pt_3Ni(111)$ via Increased Surface Site Availability," *Science*, **315**, 493–497 (2007).
11. H. Gasteiger, S. Kocha, B. Sompalli, and F. Wagner, "Activity benchmarks and requirements for Pt, Pt-alloy, and non-Pt oxygen reduction catalysts for PEMFC's," *Appl. Catal. B*, **56**, 9–35 (2005).
12. F. T. Wagner, B. Lakshmanan, and M. F. Mathias, "Electrochemistry and the Future of the Automobile," *J. of Physical Chemistry Lett.*, **1**, 2204–2219 (2010).
13. T. Greszler, S. Kumaraguru, N. Subramanian, B. Litteer, Z. Liu, and R. Makharia, "Hydrogen-Air Performance of Carbon –Supported Pt-alloy Catalyst Measured at High Current Density in Proton Exchange Membrane (PEM) Fuel Cells," 2008 Fuel Cell Seminar, Phoenix, AZ, Oct. 28, 2008. http://www.fuelcellseminar.com/assets/pdf/2008/wednesdayPM/GHT33-2_SKumaraguru.ppt.pd
14. K. Sakai, K. Sato, T. Mashio, A. Ohma, K. Yamaguchi, and K. Shinohara, "Analysis of Reactant Gas Transport in Catalyst Layers: Effect of Pt-Loadings," *ECS Transactions*, **25**(1), 1193–1201 (2009).
15. P. Y. Abel Chuang, "Fuel Cell Vehicle Commercial Applications and Challenges in Stack Research and Development," 2010 Fuel Cell Seminar and Exposition, San Antonio, TX, Oct. 19, 2010.
16. N. Nonoyama, S. Okazaki, A. Weber, Y. Ikogi and T. Yoshida, "Analysis of Oxygen-Transport Diffusion Resistance in Proton-Exchange-Membrane Fuel Cells," *J. Electrochem. Soc.*, **158**(4), B416–B423 (2011).
17. K. Shinozaki, H. Yamada, and Y. Morimoto, "Relative Humidity Dependence of Pt Utilization in Polymer Electrolyte Fuel Cell Electrodes: Effects of Electrode Thickness, Ionomer-to-Carbon Ratio, Ionomer Equivalent Weight, and Carbon Support," *J. Electrochem. Soc.*, **158**(5), B467–B475 (2011).
18. Wonseok Yoon and Adam Z. Weber, "Modeling Low-Platinum-Loading Effects in Fuel-Cell Catalyst Layers," *J. Electrochem. Soc.*, **158**(8), B1007–B1018 (2011).
19. M. K. Debe, in *Handbook of Fuel Cells – Fundamentals, Technology and Applications*, W. Vielstich, A. Lamm, H. A. Gasteiger, Editors, Ch. 45, John Wiley & Sons (2003).
20. M. K. Debe, DOE 2009 Hydrogen Program Annual Merit Review, Washington, DC. http://www.hydrogen.energy.gov/pdfs/review09/fc_17_debe.pdf
21. M. K. Debe, S. M. Hendricks, A. K. Schmoeckel, G. D. Vernstrom, R. T. Atanasoski, P. J. Kadera, and A. J. Steinbach, "Nanostructured Thin Film, Thin Layer Electrodes Optimized for PEM Fuel Cell Performance at High Current Density," 2004 Fuel Cell Seminar, San Antonio, TX, Nov. 1-5, 2004.
22. H. A. Gasteiger, et al., "Beginning-of-life MEA performance - Efficiency loss contributions," *Handbook of Fuel Cells – Fundamentals, Technology and Applications*, W. Vielstich, A. Lamm, H. A. Gasteiger, Editors, Ch. 46, John Wiley & Sons (2003), pp. 593–610.
23. M. K. Debe, DOE 2011 Hydrogen Program Annual Merit Review, Washington, DC. May 10, 2011, slides 12 and 13. http://www.hydrogen.energy.gov/pdfs/review11/fc001_debe_2011_o.pdf
24. Andrew Haug, Greg Haugen, Radoslav Atanasoski, Kotaro Sasaki, Yun Cai, and Radoslav Adzic, "Stability of a Pt-Pd Core-Shell Catalyst: A Comparative Fuel Cell and RDE Study," 218th ECS meeting, Las Vegas, NV, Oct.10-15, 2010, #743.
25. A. K. Schmoeckel, G. D. Vernstrom, A. J. Steinbach, S. M. Hendricks, R. T. Atanasoski, and M. K. Debe, "Nanostructured Thin Film Ternary Catalyst Activities for Oxygen Reduction," 2006 Fuel Cell Seminar, Honolulu, Hawaii, Nov. 13-17, 2006.
26. Dennis van der Vliet, Dusan Strmcnik, Chao Wang, Radoslav Atanasoski, Mark Debe, Nenad Markovic, and Vojislav Stamenkovic, "Multimetallic Catalysts for the Oxygen Reduction Reaction," 216th ECS meeting, Vienna, Austria, Oct. 2009.
27. Dennis van der Vliet, Chao Wang, Mark Debe, Radoslav Atanasoski, Nenad M. Markovic, and Vojislav R. Stamenkovic, "Platinum-alloy Nanostructured Thin Film Catalysts for the Oxygen Reduction Reaction," *Electrochimica Acta* **56**, 8695–8699 (2011).
28. Spreadsheet data provided by from Thomas Greszler, GM Global Research and Development Lab.
29. D. B. Sepa, M. V. Vojnovic, and A. Damjanovic, "Reaction Intermediates as a Controlling Factor in the Kinetics and Mechanism of Oxygen Reduction at Platinum Electrodes," *Electrochimica Acta*, **26**(6), 781–793 (1981).
30. V. Viswanathan, V. Rai, and H. Pitsch, "First-principles-based reaction kinetics model for Oxygen Reduction Reaction on $Pt_3Ni(111)$," *ECS Transactions*, **25**(1), 1353–1361 (2009).
31. N. M. Markovic and P. N. Ross, *Surf. Sci. Reports*, **45**, 117 (2002).
32. K. C. Nyerlin, W. Gu, J. Jorne, and H. G. Gasteiger, "Determination of Catalyst Unique Parameters for the Oxygen Reduction Reaction in a PEMFC," *J. Electrochem. Soc.*, **153**(10), A1955–A1963 (2006).
33. A. Roth, *Vacuum Technology*, North-Holland Publishing Co, New York, 1976.
34. R. Feres and G. Yablonsky, "Knudsen's cosine law and random billiards," *Chemical Engineering Science* **59**, 1541–1556 (2004).
35. E. H. Kinnard, *Kinetic Theory of Gases*, McGRaw-Hill, New York, 1938.
36. R. Feres and G. Yablonsky, "Probing surface structure via time-of-escape analysis of gas in Knudsen regime," *Chemical Engineering Science* **61**, 7864–7883 (2006).
37. P. W. Atkins, *Physical Chemistry*, Second Edition, W. H. Freeman and Co., San Francisco, 1982.
38. Saul Dushman, *Scientific Foundations of Vacuum Technique*, 2nd Edition, John Wiley & Sons, New York, 1962.
39. V. Tripkovic, E. Skulason, S. Siahrostami, J. K. Norskov, and J. Rosmeisl, "The oxygen reduction reaction mechanism on Pt(111) from density functional theory calculations," *Electrochimica Acta*, **55**, 7975–7981 (2010).
40. Karen Chan and Michael Eikerling, "A Pore-Scale Model of Oxygen Reduction in Ionomer-Free Catalyst Layers of PEFCs," *Journal of The Electrochemical Society*, **158**(1), B18–B28 (2011).
41. K. Chan, S. Vartak, A. Roudgar, K. Malek, and M. Eikerling, "Protons and Water in PEM Fuel Cells: Friend and Foe?" *2nd CARISMA International Conference on Progress in MEA Materials for Medium and High Temperature Polymer Electrolyte Fuel Cells*," La Grande Motte, France, Sept. 19–22, 2010.
42. Q. Wang, M. Eikerling, D. Song, and Z-S. Liu, "Modeling of Ultrathin Two-Phase Catalyst Layers in PEFC's," *J. Electrochem. Soc.*, **154**(6), F95–F101 (2007).
43. J. B. Stahl, M. K. Debe, and P. L. Coleman, "Enhanced bioadsorption characteristics of a uniquely nanostructured thin film," *J. Vac. Sci. Technol. A*, **14**(3), 1996, and US 5,709,943.
44. Arman Bonakdarpour, Tara R. Dahn, Radoslav Atanasoski, Mark K. Debe, and Jeff R. Dahn, "$H_2O_2$ Release During Oxygen Reduction Reaction on Pt Nano Particles," *Electrochemical and Solid-State Letters*, **11**, B208-B211, 2008.
45. Greg Haugen, Michael Emery, Steven Hamrock, Mike Hicks, Stephen Roscoe, Mark Schaberg, and Michael Yandrasits, *212th ECS Meeting* Washington, DC, October 10, 2007.

*Journal of The Electrochemical Society*, **159** (6) K165-K176 (2012)
0013-4651/2012/159(6)/K165/12/$28.00 © The Electrochemical Society


# Initial Performance and Durability of Ultra-Low Loaded NSTF Electrodes for PEM Electrolyzers

**M. K. Debe,[a,*,z] S. M. Hendricks,[a] G. D. Vernstrom,[a,*] M. Meyers,[a] M. Brostrom,[a] M. Stephens,[a] Q. Chan,[a] J. Willey,[b] M. Hamden,[b] C. K. Mittelsteadt,[b] C. B. Capuano,[c] K. E. Ayers,[c,*] and E. B. Anderson[c,*]**

[a] *3M Corporate Research, 3M Company, St. Paul, Minnesota 55144, USA*
[b] *Giner, Inc., Newton, Massachusetts 02466, USA*
[c] *Proton OnSite, Wallingford, Connecticut 06492, USA*

Water based electrolyzers offer a promising approach for generating hydrogen gas for renewable energy storage. 3M's nanostructured thin film (NSTF) catalyst technology platform has been shown to significantly reduce many of the performance, cost and durability barriers standing in the way of $H_2$/air PEM fuel cells for vehicles. In this paper we describe results from the first evaluations of low loaded NSTF catalysts in $H_2/O_2$ electrolyzers at Proton OnSite and Giner, Inc. Over two dozen membrane electrode assemblies comprising nine different NSTF catalyst types were tested in 11 short stack durability tests at Proton OnSite and 14 performance tests in 50 $cm^2$ single cells at Giner Electrochemical Systems. NSTF catalyst alloys of $Pt_{68}Co_{29}Mn_3$, $Pt_{50}Ir_{50}$ and $Pt_{50}Ir_{25}Ru_{25}$, with Pt loadings in the range of 0.1 to 0.2 mg/$cm^2$, were investigated for beginning-of-life performance and durability up to 4000 hours as both electrolyzer cathodes and anodes. Catalyst composition, deposition and process conditions were found to be important for meeting the performance of standard PGM blacks on electrolyzer anodes while using only 10% as much PGM catalyst. Analyses of MEA's after the durability tests by multiple techniques document changes in catalyst alloy composition, loading, crystallite structure and support stability.
 [DOI: 10.1149/2.065206jes] 

Manuscript submitted December 7, 2011; revised manuscript received February 28, 2012. Published April 4, 2012. This was Paper 694 presented at the Boston, Massachusetts, Meeting of the Society, October 9–14, 2011.

Pure pressurized hydrogen gas offers a convenient and predictable means for storing and transporting convertible energy from renewable or other energy sources for powering fuel cells for vehicle, portable and back-up power applications. Renewable energy sources such as wind and solar will require large, efficient and versatile energy storage means for load leveling over wide periods of time covering seconds to days for which electrochemical storage means offer many advantages. Regenerative fuel cells and $H_2/O_2$ electrolyzers used for energy storage are key examples. Water based electrolyzers with higher heating value voltage efficiencies of 75% are projected to be able to produce $H_2$ in the $3-$4/kg range, competitive with current gasoline prices, at reasonable electricity costs on the order of $0.05/kW-Hr.[1–4]

Proton exchange membrane (PEM) based water electrolyzers offer a promising pathway to efficient hydrogen production because of a small installation footprint, ease of handling the solid polymer electrolyte and ability to generate high pressure hydrogen with only deionized water and electricity as inputs. Commercial PEM electrolyzer costs based on current technology are excessive due both to low volume (batch) system assembly and high stack component material costs. However, the electrolyzer stacks and their internal components, viz. separator plates, PEM's and catalysts have cost factors that could benefit significantly from the technology improvements that PEM fuel cell development has enabled over the past decade or more. With respect to the electrocatalysts, current commercial PEM electrolyzers use 2 mg/$cm^2$ or more of precious group metals (PGM) on their anodes (oxygen evolution reaction, or OER) and cathodes (hydrogen evolution reaction, or HER). This paper addresses just such an example of using a promising advanced PEM fuel cell electrocatalyst for water electrolysis as well.

In the overall field of heterogeneous electrocatalysts, extended surface area catalysts demonstrate the highest overall specific activity for the oxygen reduction reaction (ORR) that is performance limiting on fuel cell cathodes. 3M's nanostructured thin film (NSTF) catalyst technology platform[5–9] is to date the only practical example of an extended surface area catalyst. The NSTF catalyst technology platform[7] has been shown to eliminate or significantly reduce many of the performance, cost and durability barriers standing in the way of cathodes and anodes for $H_2$/air PEM fuel cells for vehicles.[10,11] NSTF catalyst specific activities both by rotating disk electrode (RDE) methods[12–20] and in fuel cell membrane electrode assemblies (MEA's)[21,22] as well as durability[23–25] can be significantly higher than conventional carbon supported Pt catalysts, and mass activities are closely approaching the 2015 DOE targets of 0.44 A/mg at 900 mV.[13,14,20,26] More recent reports of oxygen evolution catalysts applied to the NSTF anodes and cathodes for fuel cell, cell reversal tolerance and electrolyzer applications are also starting to appear.[1,2,17,27–32]

The NSTF catalysts are formed by facile vacuum sputter-deposition of catalyst alloys onto a supported monolayer of oriented crystalline organic-pigment whiskers. The whisker support particles are crystalline whiskers, immune to corrosion thereby eliminating the high voltage corrosion plaguing carbon blacks. The NSTF support whisker is immune to chemical or electrochemical dissolution/corrosion because the perylene di-carboximide pigment it is made of is insoluble in typical acids, bases and solvents while its single crystalline nature endows it with a "band-gap" that does not support electrochemical corrosion currents, to well above 2 volts. This opens their potential use as electrodes for water electrolysis.[1–3] Besides the catalyst thin film nature, coating method and support characteristics, another dominant differentiator of the NSTF catalyst from dispersed carbon supported nanoparticles or PGM-blacks is the electrode thickness. The NSTF electrode is only 2 to 5% as thick as conventional electrodes. Whereas flooding of the ultrathin, hydrophilic NSTF electrodes under cool wet conditions can be an issue for cathode water management in PEM fuel cell applications, this appears to be an advantage for electrolyzer anodes where it is essential to deliver liquid water to the OER electrode. Fresh water flushing of the electrodes during electrolyzer operation is also thought to be an advantage for minimizing the effect of impurity adsorption on catalyst surfaces during long term operation.

In this paper we describe the results from an initial three year evaluation of low loaded NSTF catalysts in electrolyzers at Proton OnSite (Proton) and Giner, Inc. (Giner). NSTF PEM fuel cell catalysts with atomic composition $Pt_{68}Co_{29}Mn_3$ were first tested as both anodes and cathodes in single cell and short stack electrolyzers for performance and durability at Pt loadings of 0.10 to 0.15 mg/$cm^2$, less than one-tenth the platinum group metal (PGM) loadings of standard electrolyzer electrodes. These baseline results were followed by a series of NSTF oxygen evolution reaction (OER) capable electrodes

*Electrochemical Society Active Member.
[z] E-mail: mkdebe1@mmm.com

incorporating Ir and Ru at similar low loadings with various catalyst deposition process conditions.

The results to date are promising that NSTF electrodes will be able to meet or exceed the performance of standard PGM blacks on both the electrolyzer anode and cathode while using less than 10% of the traditional PGM loadings. At Giner performance tests of the baseline NSTF PtCoMn performed equivalent to or slightly better than the standard electrolyzer cathodes while for the anode studies we found compositions and applied surface energy treatments (SET) to NSTF–PtIr and NSTF-PtRuIr alloys that closely approached the performance of the standard electrolyzer anode PGM blacks but at loadings an order of magnitude lower. At Proton stability tests of the baseline NSTF $Pt_{68}Co_{29}Mn_3$ and Pt-Ir fuel cell catalysts performed stably as electrolyzer cathodes for up to 4000 hours until testing was stopped. On the electrolyzer anode the $Pt_{50}Ir_{50}$ (atomic%) alloys with 0.15 $mg_{Pt}/cm^2$ were stable at over 2.3 Volts for 2000 hours until testing was ended.

We carried out post-test characterization of both anode and cathode electrodes of a subset of the NSTF-catalyst coated MEA's using SEM, EDS, XRD, XRF and ICP after the durability testing at Proton had finished in order to measure changes in alloy Pt lattice constants, crystallite sizes, composition, catalyst particle morphology and whisker support stability. We discuss these and implications for obtaining further improved electrolyzer NSTF electrodes while maintaining the much lower loadings of PGM's.

## Experimental

*Catalyst and MEA preparation.*— The NSTF binary and ternary catalysts were formed by vacuum sputter-deposition of metal multilayers onto a supported monolayer of oriented crystalline organic-pigment whiskers.[7] The process for fabricating the crystalline whisker support film and subsequent over-coating with catalyst, is scaled-up as a roll-to-roll web coating process.[9] For all of the catalyst compositions studied in this work the NSTF whisker support films were fabricated on roll-to-roll production equipment. Except for the Pt-CoMn alloys, which were sputter deposited onto the whisker supports also using roll-to-roll production equipment, the Ir and Ru containing catalyst alloys were coated onto the whisker supports in a batch loaded vacuum chamber with multiple sputtering targets chosen for the desired alloy composition. For all these, the Pt and other metal alloy loadings were controlled by gravimetric calibration of the sputter deposition rates known to be accurate to ±5% both cross-web and down-web. Samples in the batch loaded chamber were attached to a rotating drum by which multiple layers of the Pt, Ir or Ru were applied in succession to give the overall loading and mole fraction of the desired composition.[33] For testing as electrolyzer cathodes we used the NSTF fuel cell $Pt_{68}Co_{29}Mn_3$ composition at Pt loadings of 0.15 $mg_{Pt}/cm^2$, and $Pt_{50}Ir_{50}$ at Pt loadings of 0.15 $mg_{Pt}/cm^2$. For testing as electrolyzer anodes we used $Pt_{50}Ir_{50}$ at loadings of 0.15 and 0.1 $mg_{Pt}/cm^2$, and $Pt_{50}Ir_{25}Ru_{25}$ at Pt loadings of 0.15 $mg_{Pt}/cm^2$. For some of the $Pt_{50}Ir_{50}$ and $Pt_{50}Ir_{25}Ru_{25}$ samples a proprietary surface energy treatment (SET) process that effectively produces many of the same characteristics as high temperature annealing was applied to the as-made catalysts.

These decal NSTF catalysts were then transferred using hot-roll lamination onto the surfaces of one side of specific membranes to make $\frac{1}{2}$-CCM's or one-sided catalyst coated membranes. The membranes used were Nafion 117 Membranes, or a thinner, lower equivalent weight 3M membrane (35 or 24μm, 850 EW). For the Nafion 117 membranes, the membranes that were cleaned first by washing in nitric acid and peroxide solutions were found to perform better. These $\frac{1}{2}$-CCM's were then provided to Giner and Proton who then combined them with their own $\frac{1}{2}$-CCM's or electrodes as shown in Figs. 1A and 1B to make the finished MEA. Depending on which electrode was being tested, the opposing electrode attached was either Pt-black (cathode) or for the anode, PtIr or another alloy black at loadings of greater than or equal to 2 $mg_{PGM}/cm^2$. In one instance a full CCM with 0.2 $mg/cm^2$ of NSTF-pure Pt on each electrode with Nafion 117 membrane was evaluated at Giner as well. All the post-durability tested MEA's that were characterized were of the type Fig. 1A.

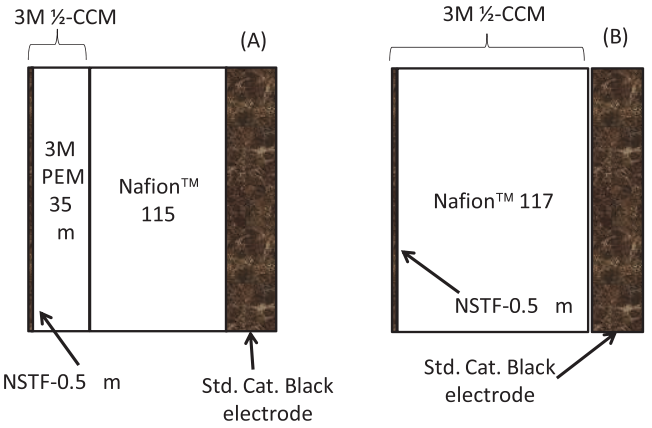


**Figure 1.** Illustration of the MEA constructions incorporating the NSTF electrodes: (A) The NSTF electrode is incorporated into a half catalyst coated membrane ($\frac{1}{2}$-CCM) at 3M which was then combined with a standard electrolyzer electrode $\frac{1}{2}$-CCM made by either Proton or Giner for testing. (B) The NSTF electrode is attached to a Nafion 117 membrane at 3M that then has a standard electrolyzer electrode attached at the testing site.

*Electrolyzer cell and testing conditions.*— At Giner, the MEA's were tested in 50 $cm^2$ single cell hardware obtained from Fuel Cell Technologies with serpentine flow fields, and a customized Pt-plated titanium anode end plate. The test stand supplied 18 MΩ water with a DI system in-line water flow rate of 300 mL/min. The test stand used an HP 6950L/T60, 320A/15 V power supply and an HP6050A electronic load for high frequency resistance (HFR) capability. The cell operating temperatures were between 80°C and 95°C, at pressures between ambient and 100 psig. Most of the MEA's tested at Giner were of the configuration shown in Fig. 1B. The cathode gas diffusion media were provided by Giner, and a proprietary Giner method for break-in conditioning was developed that achieved full performance in about four hours. Testing at Giner focused on beginning of life performance and stability testing up to 168 hours.

At Proton Onsite the test hardware used was their commercial stack hardware configured for multi-cell short stack testing and using a modified flow field for improved conductivity. The NSTF electrode active areas were provided as 10.8 cm × 10.8 cm squares, which in the Proton stack cells were reduced to circular shaped areas, 86 $cm^2$ in size. The operating temperatures used were 50 to 80°C. The hydrogen (cathode) pressures used ranged from 200 to 400 psi, and the oxygen (anode) sides were at ambient pressure. Most of the MEA's tested at Proton were of the configuration shown in Fig. 1A. Cathode gas diffusion layer (GDL) media were provided by both 3M and Proton but most results described here used Proton GDL media obtained commercially, and were not optimized with respect to the NSTF thin layer electrodes. Testing at Proton focused on long term durability testing rather than on optimized beginning of life performance. NSTF cathodes were tested up to times exceeding 4000 hours with stable performance, while anodes were operated for periods up to 2000 hours before tests were stopped without failure.

Table I summarizes the definitions of a subset of the MEA types that were tested at Proton and Giner the results of which are discussed below.

*Post-testing electrode characterization.*— After demonstrating adequate or better beginning of life performance with significantly reduced amounts of precious metal loadings, it was important to evaluate changes in the NSTF electrode portions of the MEA's listed in Table I after long term durability testing. For this purpose the half-CCM's from the MEA's tested for long periods in the Proton hardware were easily removed from the full MEA's for post-testing characteri-

**Table I. Definition of NSTF based MEA's tested at Giner and Proton sites.**

| MEA Type | Number Tested | Test Site | Cathode Catalyst | Cathode side 1/2-PEM | Anode side 1/2-PEM | Anode Catalyst | Number Hours Tested |
|---|---|---|---|---|---|---|---|
| A | 1 | Proton | NSTF $Pt_{68}Co_{29}Mn_3$, 0.15 mg-Pt/cm$^2$ with 60 Angsroms Ir on top. | 3M 800EW, 35 μm | Nafion 117 | Proton Std., >2 mg/cm$^2$ | 3600 |
| B | 1 | Proton | Proton Std., >2 mg/cm$^2$ | 3M 800EW, 35 μm | Nafion 117 | NSTF $Pt_{68}Co_{29}Mn_3$, 0.15 mgPt/cm$^2$ with 60 Angsroms Ir on top. | 1500 |
| C | 3 | Proton | NSTF $Pt_{68}Co_{29}Mn_3$, 0.15 mg-Pt/cm$^2$ | 3M 800EW, 35 μm | Nafion 117 | Proton Std., >2 mg/cm$^2$ | 4600, 3200, 2000 |
| D | 1 | Proton | NSTF $Pt_{50}Ir_{50}$, 0.15 mg-Pt/cm$^2$, 10 Å bi-layer, Pt final | 3M 800EW, 35 μm | Nafion 117 | Proton Std., >2 mg/cm$^2$ | 600 |
| E | 1 | Proton | Proton Std., >2 mg/cm$^2$ | 3M 800EW, 35 μm | Nafion 117 | NSTF $Pt_{50}Ir_{50}$, 0.15 mg-Pt/cm$^2$, 10 Å bi-layer, Pt final | 2000 |
| F | 1 | Proton | NSTF $Pt_{50}Ir_{50}$, 0.15 mg-Pt/cm$^2$, 16 Å bi-layer, Ir final | 3M 800EW, 35 μm | Nafion 117 | Proton Std., >2 mg/cm$^2$ | 3200 |
| G1 | 1 | Proton | Proton Std., >2 mg/cm$^2$ | 3M 800EW, 35 μm | Nafion 117 | NSTF $Pt_{50}Ir_{50}$, 0.10 mg-Pt/cm$^2$, 15 Å bi-layer, Ir final, + SET | 1500 |
| G2 | 1 | Proton | Proton Std., >2 mg/cm$^2$ | 3M 800EW, 35 μm | Nafion 117 | NSTF $Pt_{50}Ir_{50}$, 0.15 mg-Pt/cm$^2$, 15 Å bi-layer, Ir final, + SET | 1500 |
| H | 1 | Proton | Proton Std., >2 mg/cm$^2$ | 3M 800EW, 35 μm | Nafion 117 | NSTF $Pt_{50}Ir_{25}Ru_{250}$, 0.15 mg-Pt/cm$^2$, 10 Å tri-layer, Ir final | 275 |
| I | 1 | Proton | Proton Std., >2 mg/cm$^2$ | 3M 800EW, 24 μm | Nafion 117 | NSTF $Pt_{50}Ir_{25}Ru_{250}$, 0.15 mg-Pt/cm$^2$, 10 Å tri-layer, Process 2 | 275 |
| J | 2 | Proton | Proton Std., >2 mg/cm$^2$ | 3M 800EW, 24 μm | Nafion 117 | NSTF $Pt_{50}Ir_{25}Ru_{250}$, 0.15 mg-Pt/cm$^2$, 10 Å tri-layer, + SET | 483, 483 |
| K | 1 | Giner | NSTF P4-$Pt_{68}Co_{29}Mn_3$, 0.15 mg-Pt/cm$^2$ | Nafion 117 | | Giner 2 mg/cm$^2$ PtIr-black | |
| L | 1 | Giner | Giner 4 mg/cm$^2$ Pt-black | Nafion 117 | | NSTF $Pt_{50}Ir_{50}$, 0.15 mg-Pt/cm$^2$, 16 Å bi-layer, Ir final | |
| M | 1 | Giner | NSTF $Pt_{68}Co_{29}Mn_3$, 0.15 mg-Pt/cm$^2$ | Nafion 117 | | $Pt_{50}Ir_{50}$, 0.15 mg-Pt/cm$^2$, 16 Å bi-layer, Ir final | |
| N | 1 | Giner | NSTF $Pt_{68}Co_{29}Mn_3$, 0.20 mg-Pt/cm$^2$, P1-process | Nafion 117 | | NSTF $Pt_{68}Co_{29}Mn_3$, 0.20 mg-Pt/cm$^2$, P1-process | |
| O | 1 | Giner | Giner 4 mg/cm$^2$ Pt-black | 3M 800EW, 35 μm | 790 EW, 100 μm | NSTF $Pt_{50}Ir_{50}$, 0.15 mg-Pt/cm$^2$, 16 Å bi-layer, Ir final + SET | 168 |
| P | 1 | Giner | Giner 4 mg/cm$^2$ Pt-black | 3M 800EW, 35 μm | Nafion 115 | NSTF $Pt_{50}Ir_{25}Ru_{25}$ 0.15 mg-Pt/cm$^2$, 10 Å tri-layer, Ir final | |
| Q | 1 | Giner | Giner 4 mg/cm$^2$ Pt-black | 3M 800EW, 35 μm | 790 EW, 100 μm | NSTF $Pt_{50}Ir_{25}Ru_{25}$ 0.15 mg-Pt/cm$^2$, 10 Å tri-layer, Process 2 | 100 |
| R | 1 | Giner | Giner 4 mg/cm$^2$ Pt-black | 3M 800EW, 35 μm | 790 EW, 100 μm | NSTF $Pt_{50}Ir_{25}Ru_{25}$ 0.15 mg-Pt/cm$^2$, 10 Å tri-layer, + SET | 140 |

zation. Since all these NSTF containing electrodes were $\frac{1}{2}$-CCM's, their characterization was not directly affected by the opposing PGM-black catalyst electrode since it remained with the discarded $\frac{1}{2}$-CCM. However, catalyst elements that may have dissolved into the membrane and were transported over to the NSTF electrode under test, or which remained in the $\frac{1}{2}$-CCM membrane on the NSTF side would also be detectable by ICP and XRF. Multiple techniques described below were used to assess changes in the composition, loading, morphology and general distribution of the NSTF catalyst electrodes, as well as obtain evidence of elements crossing over the membrane between electrodes.

*X-ray diffraction (XRD).*—XRD was used to determine Pt alloy crystallite sizes in each fcc[hkl] direction, for evidence of crystallite growth or particle shape change over time, and Pt-Pt lattice constant shifts due to alloy composition changes over time. A portion of each sample was applied to a zero background specimen holder composed of single crystal quartz using double-coated tape. Reflection geometry data were collected in the form of a survey scan by use of a Philips (PANalytical, Natick, Massachusetts, USA) vertical diffractometer, copper $K_\alpha$ radiation, and proportional detector registry of the scattered radiation. The diffractometer was fitted with variable incident beam slits, fixed diffracted beam slits, and graphite diffracted beam monochromator. The survey scan was conducted from 30 to 95 degrees (2θ) using a 0.05 degree step size and 24 second dwell time. X-ray generator settings of 45 kV and 35 mA were employed.

The diffraction patterns were subjected to profile fitting using the analysis software: JADE, (version 9.0 Materials Data, Inc., Livermore, California, USA) to evaluate face-centered cubic (fcc) (111), (200), (220), (311), and (222) maxima width and angular positions. Apparent crystallite sizes were evaluated using fcc peak widths corrected for instrumental broadening and application of the Scherrer equation. Approximate lattice parameters were evaluated from fcc maxima angular positions using a least squares minimization procedure.

*Scanning electron microscopy (SEM).*—SEM analysis was used for obtaining visual evidence of changes in the electrodes' uniformity at the 1 kx and 10 kx magnification scales, and changes in the NSTF catalyst support whiskers and morphology of the catalyst coating on those whiskers at the highest magnification used, 50 kx. An Hitachi S-4700 field emission scanning electron microscope (FESEM) was used with the following imaging conditions: 2.0 kV, 20 kV, 8 mm and 12 mm WD, tilt: 0, SEI mode, condition 9; Magnifications: 300x, 1,000x, 2,000x, 3,000x, 4,000x, 10,000x, and 50,000x. The CCMs, decals and tested samples were all mounted onto an FESEM stub with carbon conductive tape, and then imaged using SEI (secondary electron imaging) for surface morphology information. Each sample was surveyed to take representative images of each sample in two different areas at several magnifications.

*X-ray fluorescence (XRF).*—XRF was utilized to deduce changes in the electrode loading and atomic composition over time, with depth resolution reflective of the whole electrode and the underlying PEM. It is detecting elements that have dissolved and gone into the membrane as well as those within the electrode boundary. Prior to data collection, each as-received sample was placed directly into a stainless steel XRF sample holder and secured into position using double coated tape. The prepared samples were subsequently analyzed for platinum, cobalt, manganese, Ir and Ru using a Rigaku ZSX-100e wavelength dispersive X-ray fluorescence spectrometer equipped with a rhodium X-ray source, a vacuum atmosphere, and a 20 mm diameter measurement area. Independent calibration curves for each element were utilized.

*Electron energy dispersive X-ray microanalysis (EDAX or EDS).*—In conjunction with the SEM imaging EDS was used for evaluation of the changes in atomic% compositions of the alloys within just the electrode boundaries. EDS can detect chemical elements higher than atomic number 6 (carbon) with detection limits possible for elements between 0.1 and 1.0 weight percent. It is useful in conjunction with XRF to show evidence for which components are more susceptible to dissolution into the membrane. The same Hitachi FESEM was used as for the SEM imaging above. Samples were analyzed using EDS analysis point and shoot mode and semi quantitative analysis at several different areas of the samples. EDS analysis was done at 20 kV accelerating voltage in a defined area in each SEM images. Magnifications used were 2,000x to 4,000x, with average compositions defined over a sample area of 54 microns × 33 microns.

*Inductively coupled plasma (ICP).*—ICP is a standard inorganic analysis method for quantitative measurement of the elemental loadings in the electrodes and the underlying PEM. It requires destruction of the sample. Samples were prepared in duplicate using the following fusion procedure: 1/8 of each CCM (with known total area) were put into zirconium crucibles. The samples were dried in an oven at 60°C and then cooled to room temperature. One gram of sodium peroxide was added to each crucible. Next the crucibles were gently heated on top of a Bunsen burner until the organic matters burned off. The crucibles were then moved closer to the flame so that the sodium peroxide started to melt. Crucibles were held on the flame for 5 minutes after the solid completely melted. Once the crucibles had cooled, 10 mL of hydrochloric acid solution (concentrated HCl:$H_2O$ = 1 : 1 by volume) was added drop by drop. The solutions were quantitatively transferred into 50 mL polypropylene centrifuge tubes, and diluted to 50 mL with 3% aqua regia (concentrated HCl : $HNO_3$ = 3: 1 by volume). An additional 20-fold dilution by volume with 3% aqua regia was performed in order to bring the signals within calibration range. The solutions were then analyzed by ICP-AES (atomic emission spectroscopy) for the determination of Co, Ir, Mn and Pt. The instrument used for elemental analysis was a Perkin Elmer Optima 4300DV ICP optical emission spectrophotometer. The samples were analyzed against external calibration curves generated using acid-matched solution standards containing 0, 0.2, 0.5, and 1 ppm of each analyte. A 0.5 ppm quality-control standard was used to monitor the accuracy of the calibration curves during the analysis. A 0.5 ppm solution of scandium was run in-line with the samples and standards to serve as an internal standard. The elements screened during this analysis were Co, Ir, Mn and Pt.

*CCM and decal controls.*—For each catalyst type, fresh 1/2-CCM controls were made using the same catalyst lots as were tested. The above analytical techniques were then applied to these CCM controls as well as the catalyst decals for comparison to the tested electrodes.

## Results and Discussion

Over a period of approximately three years, 14 NSTF based MEA's were tested for beginning of life performance and short term stability at Giner in their single cells, while 11 short stack builds at Proton evaluated the longer term durability of 9 different NSTF types of MEA's. In this section we begin with the beginning-of-life performances observed, then discuss examples of the long term durability tests of MEA's containing NSTF as either anodes or cathodes. This is followed by a summary of the post-durability test comparisons using SEM, XRD, EDS, XRF and ICP of the PtCoMn, PtIr and PtIrRu electrodes operated as both anodes and cathodes with comparisons of fresh catalyst decals or electrode/CCM control samples.

*Beginning-of-life performances.*— Fig. 2 shows SEM images at three magnifications of the catalyst decals and CCM control surfaces. Fig. 2A and 2B illustrate the typical appearance of the NSTF catalyst decals before transfer to the PEM. The microstructured substrate on which the catalyst coated whiskers are deposited is apparent in the SEM images in Fig. 2A. During the lamination transfer process of the catalyst from the decal to the membrane surface, the latter surface is automatically micro-replicated with the decal substrate's microstructure, as seen in Figs. 2C and 2E. The peak of one of the inverted ridges is further magnified in Fig. 2D, revealing the now inverted catalyst coated whiskers protruding from a CCM ridge peak.

Figs. 3A and 3B show polarization curves obtained at Proton and Giner respectively with MEA's having NSTF catalysts on the cathodes and standard PGM catalyst blacks on the anodes. Fig. 3A compares the polarization curves from MEA's C and D in Table I, in the Proton hardware for NSTF $Pt_{68}Co_{29}Mn_3$ and PtIr cathodes, each with Pt loadings of 0.15 $mg_{Pt}/cm^2$, to that from the baseline Proton MEA. The three MEA's have the same Proton anodes while the Proton baseline MEA cathode contains at least 2 $mg/cm^2$ of Pt. The Proton baseline MEA used Nafion 117 membrane while the equivalent thickness of the NSTF containing MEA's was over 0.02 mm (8 mils) thick. This could account for the increased apparent slope or MEA resistance of the NSTF containing MEA's in Fig. 3A.

Fig. 3B compares similar polarization curves from MEA K in Table I having an NSTF $Pt_{68}Co_{29}Mn_3$ cathode to a Giner baseline MEA. Both MEA's have the same Giner anode and both used Nafion 117 membrane. For the NSTF MEA K, the $Pt_{68}Co_{29}Mn_3$ cathode loading is 0.15 $mg_{Pt}/cm^2$ while for the Giner baseline MEA the cathode Pt-black loading is 4.0 $mg_{Pt}/cm^2$. The MEA with the NSTF cathode shows a uniform improvement in overpotential over the whole current range of approximately 20 mV, increasing as current density drops below 1 $A/cm^2$. Over this current density range, above 0.5 $A/cm^2$, the slope of the polarization curve is determined by the impedance, due primarily to the Nafion 117 membrane. Since the anodes and membranes were identical in Fig. 3B and the NSTF catalyst was used only on the cathode, the uniform improvement in overpotential over the whole range of current density in Fig. 3B is not inconsistent with a slightly improved HER kinetic activity of the NSTF anode with no attendant change in either total MEA impedance or mass transport overpotential. The fact they are so linear implies that there is

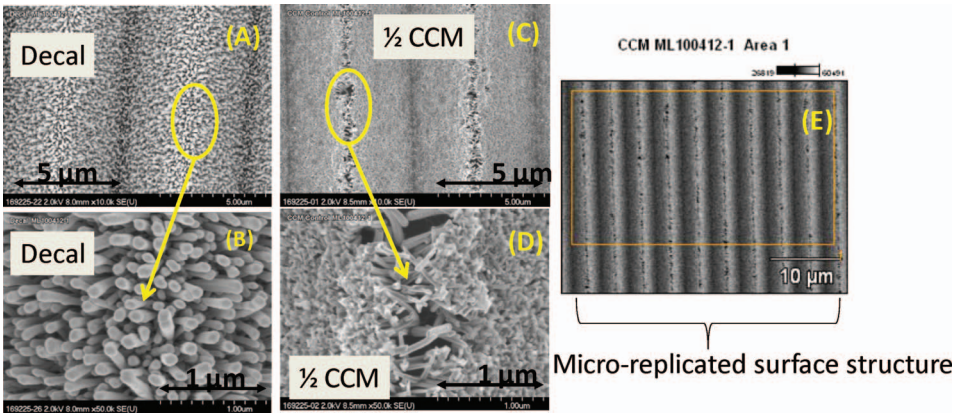


**Figure 2.** SEM images of the NSTF decals (A, B) and catalyst coated membrane surfaces (C, D, E) after catalyst transfer to the membranes at three levels of magnification.

negligible mass transport impedance for the evolved oxygen/water to get out/in from/to the anodes or the evolved hydrogen out of the cathodes. This would suggest the very thin NSTF $Pt_{68}Co_{29}Mn_3$ with 93% less Pt may have improved HER kinetics or wetting compared to the Pt black cathodes.

Fig. 4 (left) compares the beginning of life performance of various NSTF anode-containing MEA's with the Giner baseline standard MEA, with the latter containing 2 mg/cm$^2$ of PGM on the anode and 4 mg/cm$^2$ cathode on a Nafion 117 membrane. The solid black squares show the polarization curve from MEA N in Table I having a full NSTF-PtCoMn CCM, with 0.2 $mg_{Pt}$/cm$^2$ on each of its anode and

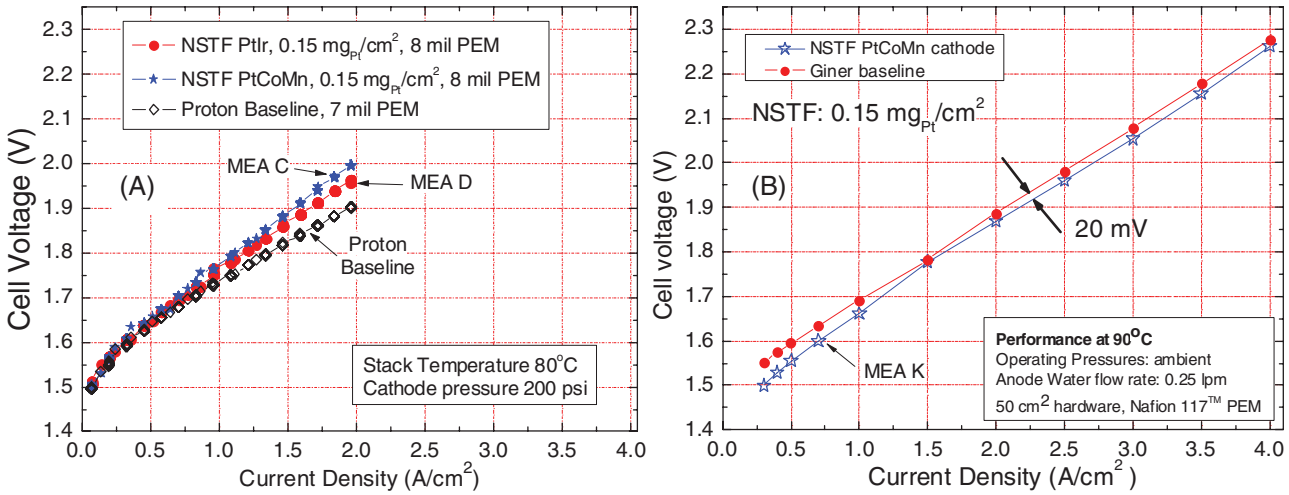


**Figure 3.** Polarization curves with NSTF catalysts as the cathodes at (A) Proton OnSite and (B) Giner, compared to their baseline MEA polarization curves.

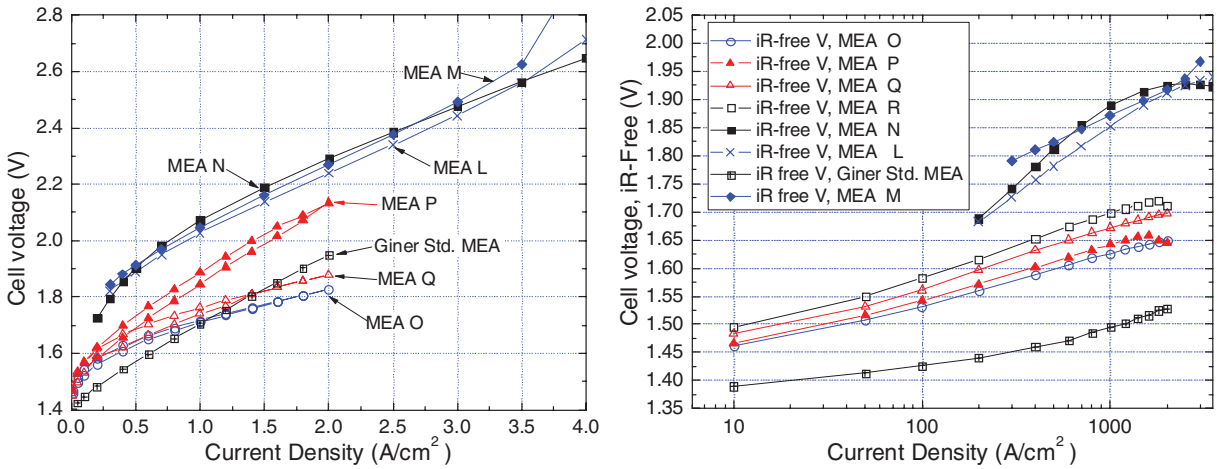


**Figure 4.** Comparison of polarization curves (Tafel plot on right) with a Giner standard MEA having 2 mg/cm$^2$ PtIr black on the anode, with various NSTF anodes containing MEA's having the indicated loadings and compositions and membranes in Table I. The Giner cathode, 4 mg/cm$^2$ Pt black, was used on all except for MEA's M and N. Cell temperatures were 80°C, with ambient pressures.

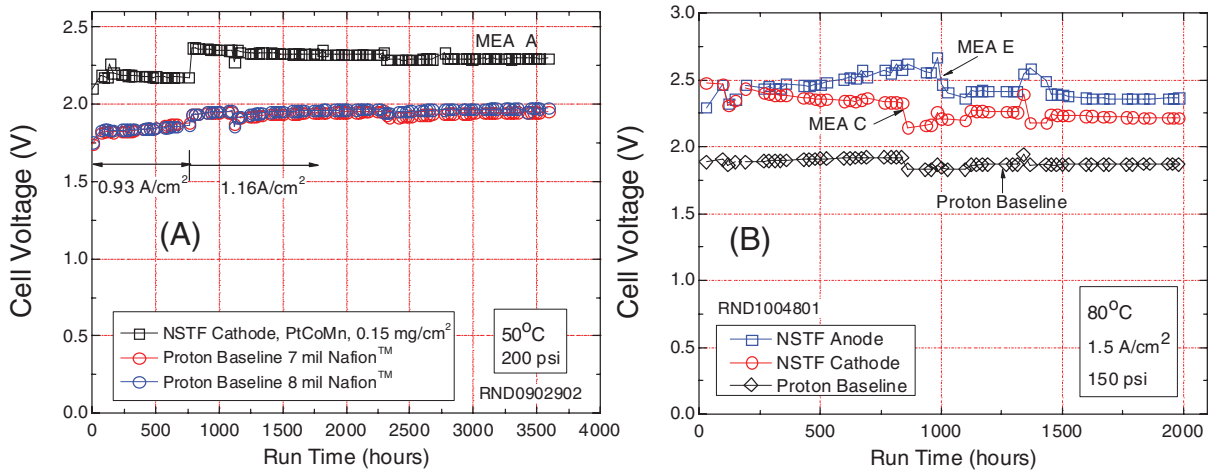


**Figure 5.** Cell voltage stability at constant current over time of three MEA's tested in a Proton short-stack. $\frac{1}{2}$-CCM's containing the NSTF PtCoMn catalyst used as a cathode (MEA A in Fig. 5A and MEA C in Fig. 5B, and NSTF PtIr (as-made) as an anode (MEA E in Fig. 5B), are compared to the Proton baseline CCM. Current densities, cell temperatures and cathode pressures are indicated on the figures.

cathode. The OER performance is substantially worse by 300 to 400 mV than the baseline over the whole 4 A/cm$^2$ current range. MEA's L and M show only a slight improvement obtained using NSTF $Pt_{50}Ir_{50}$ anodes (0.15 $mg_{Pt}/cm^2$) and either a 4 $mg_{Pt}/cm^2$ Giner cathode or a 0.15 $mg_{Pt}/cm^2$ PtCoMn cathode. In sharp contrast to MEA's L and M, MEA O shows a performance much closer to the Giner baseline, despite having substantially less PGM catalyst. MEA O in Table I contains an NSTF anode comprised of the same $Pt_{50}Ir_{50}$ catalyst as MEA's L and M, but it was surface energy treated (SET) before lamination. Similarly, MEA Q containing a $Pt_{50}Ir_{25}Ru_{25}$ anode with 0.15 $mg_{Pt}/cm^2$ shows similar close performance to the Giner baseline in the mid-current range, both initially and after 100 hours (not shown). MEA's O and Q were made from $\frac{1}{2}$-CCM's of NSTF anode attached to 3M 850 EW, 1 mil membrane, that were bonded to a Giner $\frac{1}{2}$ CCM consisting of a 4 mil, 792 EW membrane and their baseline cathode. MEA P on the other hand was made by bonding the 3M 800 EW based $\frac{1}{2}$-CCM to a Giner based Nafion 115 Membrane based $\frac{1}{2}$-CCM. Its polarization curve shows similar voltages at current densities below 0.5 A/cm$^2$ as MEA's, O and Q, but much higher impedance as indicated by the increased slope. This is believed due to the equivalent weight mismatch or bonding difficulties at the interface of the 3M 800 EW PEM and the 1100 EW of the Nafion 115 membrane. Fig. 4 (right) shows a Tafel plot of the iR-free cell voltages for the MEA polarization curves in Fig. 4 (left). IR-correcting the polarization curve of MEA P does bring it into congruence with MEA's O, Q, and R. The effects of the SET "annealing" of the NSTF PtIr (MEA O vs. MEA's L and M) or addition of Ru (MEA's P, Q and R vs. L, M and N), both appear to have made a dramatic improvement in the OER kinetics of the low loaded NSTF anodes. Fundamental study to determine how surface area and OER specific activity contribute to the high absolute activity of the low PGM-loaded NSTF alloys in MEA's O, P, Q and R is outside the scope of this initial experimental account. However based on much longer in-depth fuel cell studies of NSTF electrodes we might speculate that since the surface area for these catalysts will not likely be different from the ~8 m$^2$/g typically measured for NSTF PtCoMn by $H_{upd}$, that the specific activity for OER may be much larger than that of standard PGM black alloys, similar to the well documented 5x to 10x gain in ORR specific activity seen on these extended surface catalysts.[20,26,27] Certainly the biggest effect as just discussed above are the catalyst processing factors, e.g. the SET and "process 2" catalyst deposition processes, that enabled the performances of MEA types O through R to so dramatically improve over MEA types L and M. Tangents to the Tafel plots at lowest current densities in Fig. 4 suggest 30 mV/dec. for the Giner standard and 60 mV/dec. for the NSTF MEA types O through R. The equivalent performance in Fig. 4(A) above 1 A/cm$^2$ suggests the NSTF electrodes have lower impedance. Understanding the surface structural and compositional changes induced by these process factors in the PtIr and Pt(IrRu) alloys should be key to explaining the resulting large gain in absolute OER activity.

*Short stack durability testing.*— Fig. 5A shows cell voltage versus time for MEA A in Table I containing the first NSTF $Pt_{68}Co_{29}Mn_3$ cathode $\frac{1}{2}$-CCM tested for over 3500 hours in a short stack with two Proton baseline MEA's. Although the cell voltage is much higher than the baselines, the cell voltage is stable. The larger overpotential of the NSTF containing MEA A in 5A, compared to later tested MEA's C and D as shown in Figs. 3A and 7D, is believed to be due to different choices of gas diffusion media used for MEA's C and D versus A. Although it is not thought to be significant for cathode operation, the PtCoMn fuel cell catalyst used on the cathode in MEA A in Fig. 5A had a 60Å over-coating of Ir applied to the catalyst before transfer to the membrane as the cathode.

Cell voltage versus time at 80°C, 1.5 A/cm$^2$ and 150 psi of a second short stack build is shown in Fig. 5B, containing two NSTF containing MEA's, C and E in Table I, and one Proton baseline MEA. In this case a second MEA of type C with an NSTF $Pt_{68}Co_{29}Mn_3$ on its cathode and the standard Proton anode shows stable performance over the 2000 hours of test, similar to Fig. 5A. The other MEA in Fig. 5B, MEA E, has NSTF-PtIr (0.15 mg/cm$^2$, non-SET treated) on its anode and the standard Giner cathode. Performance of MEA E is also stable for the 2000 hours and not much different from the adjacent MEA C. Since MEA C with the standard Proton anode is only barely better than MEA E with the NSTF anode, and both are worse than the Proton baseline, this suggests that something other than the anode is responsible for much of the overpotential difference between these NSTF containing MEA's and the Proton baseline. One possible contributor is the higher impedance from membrane EW/bonding discontinuity discussed with Fig. 4. There are also possible GDL effects we have observed with the ultra-thin NSTF electrodes that may contribute as these components have not begun to be optimized for electrolysis operation. The important result from these tests is that the cell potentials were constant over the period of the test for both NSTF catalyst-electrode configurations. Notably the NSTF whisker support would appear to be stable at or above 2.3 volts on the anode for 2000 hours.

Fig. 6 shows cell performance versus time for three other MEA's containing NSTF catalysts operated as anodes at constant current, compared to the Proton baseline MEAs in the same short stack builds. In Fig. 6A MEA B used the same 60 Å of sputtered Ir

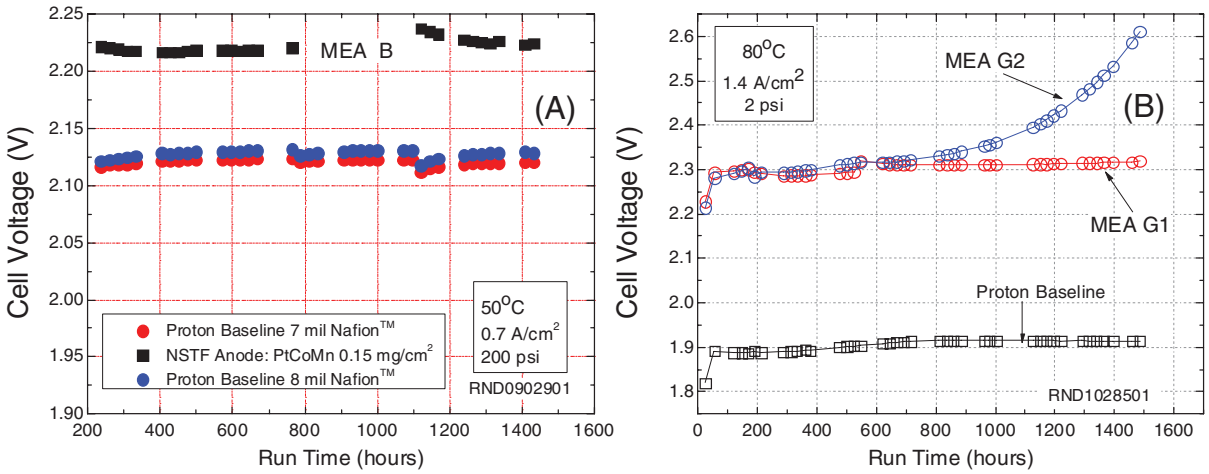


**Figure 6.** Cell voltage stability at constant current over time of three MEA's tested in a Proton short-stack. Proton baseline MEA's are compared to $\frac{1}{2}$-CCM's containing a third NSTF $Pt_{68}Co_{29}Mn_3$ catalyst used as an anode (MEA B in Fig. 6A), and two other NSTF PtIr (SET) catalysts as anodes (MEA's G1 and G2 in Fig. 6B). Current densities, cell temperatures and cathode pressures areas indicated and differ slightly from the conditions used in Fig. 5.

over-coating the NSTF $Pt_{68}Co_{29}Mn_3$ at the same loading as was used on the cathode in MEA A in Fig. 5A. Except for some unexplained midterm excursions, the cell voltage is again quite stable for 1500 hours in Fig. 6A. In Fig. 6B the two $Pt_{50}Ir_{50}$ anodes have loadings of 0.10 (MEA G1) and 0.15 (MEA G2) $mg_{Pt}/cm^2$, or approximately 0.2 and 0.3 $mg_{PGM}/cm^2$ total, and show very stable performance over the first 800 hours for the higher loaded case, and over the full 1500 hours of constant current operation for the lower loaded case. It is not known why one of the MEA's began to fail and the other did not. Again, there is a huge 400 mV difference in the cell voltage of the MEA's containing the NSTF anodes versus the Proton baseline, more than the 300 mV difference shown in the single cell tests of Fig. 4 at 1.4 $A/cm^2$ at similar pressures and temperatures. Furthermore, these PtIr anodes in Fig. 6B had been SET treated as had been MEA Q in the Fig. 4 that gave performance similar to the Giner baseline. This suggests something other than catalyst kinetics is limiting performance, i.e. impedance and mass transport. This difference is again believed due to effectively larger total membrane impedances resulting from the combination of two $\frac{1}{2}$-CCMs containing very different equivalent weight membranes in the MEA's in Fig. 6, as discussed above for MEA P in Fig. 4, as well as non-optimized GDL properties again.

*Post durability testing characterization.—SEM analyses.*— Fig. 7D shows another example of a Proton 3-cell stack operated for 3200 hours at constant current density of 1.86 $A/cm^2$ at 50°C and 200 psi cathode pressure. These MEA's also had the beginning-of-life performance shown in Fig. 3A. In these later sample tests, the NSTF containing MEA's have performances much closer to the baseline MEA's than in the initial tests discussed in Fig. 5, due to improvements learned from the earlier stack builds. Fig. 7A shows clear evidences of the impressions from the carbon fibers of the carbon paper gas diffusion layer used adjacent the cathode catalyst of MEA D. The original microstructure of the peaks, seen in Fig. 2E at about the same magnification, are no longer apparent, and the NSTF catalyst electrode layer itself appears broken (short, dark parallel stripes) in places as though the membrane had been stretched. In Fig. 7B at 10x higher magnification, and 7C at 50x higher magnification than 7A, the NSTF catalyst coated whiskers remain clearly apparent and little if any changed from their appearance in Fig. 2D or the way they generally appear in freshly made catalyst. Given the stable cell voltage, this level of electrode layer disruption appears not to be significant for cathode performance.

Fig. 8 shows SEM images at three magnifications of the NSTF electrode surface operated for 1500 hours as an anode on MEA G1 at the cell voltage versus time shown in Fig. 6B for the 0.1 $mg_{Pt}/cm^2$ PtIr case. Fig. 8A shows large metallic platelets covering a majority of the surface. Subsequent analyses suggest these platelets are Pt deposited from the order of magnitude higher loaded Pt-black cathode. In Fig. 8B at 10x higher magnification, the porous outer surface of the NSTF electrode structure is apparent between the larger platelets. In 8C at another 10X increase in page magnification, the catalyst coated whiskers are still apparent in the cracks between the platelets. The catalyst coating on the whiskers appears to have been affected, tending toward more agglomeration and clumping than the as-deposited catalyst. Although difficult to see convincingly at this magnification, the whisker support shapes do not appear to have been significantly changed. Similar affects were seen on the surface in MEA G2 of the PtIr sample that had the 0.15 $mg_{Pt}/cm^2$ loading, tested as in Fig. 6B.

*X-ray diffraction.*—Fig. 9 summarizes the XRD determined fcc(hkl) crystallite sizes and Fig. 10 the Pt lattice spacings for the decals, CCM controls and a) the NSTF PtCoMn cathodes in MEA C tested for 3200 hours as in Fig. 7D, b) the PtIr anodes in MEA's G1 and G2 tested for 1500 hours as in Figs. 6B and Fig. 8, c) the two PtIrRu samples, both type MEA J, tested as anodes for 483 hours at 1.4 $A/cm^2$, 50°C and 180 psi on the cathode. In the latter tests (not shown here), one of the MEA's increased from 2.3 V to 2.45 V in a single step but was otherwise stable over the 483 hour test period. The second MEA J with the PtIrRu anode increased continuously to 2.95 V at which time the test was ended. This determined the lifetime of that stack build. The 0-hour control was a fresh CCM made from the same material lots as used in the two tested samples.

Fig. 9 shows all the fcc(hkl) crystallite sizes exhibit similar trends regardless of alloy, anode or cathode and length of test. This suggests no preferred growth direction for the cases in which the crystallite sizes increase and that the crystallites have low aspect ratios, i.e. tend to be more spherical. The aged samples show very little change in crystallite size compared to the controls, with the exception of the 0.1 $mg/cm^2$ PtIr on the anode for 1500 hours. This sample, MEA G1, showed an ~40% increase in crystallite size. The crystallite sizes for the $Pt_{50}Ir_{25}Ru_{25}$ decreased slightly after just 483 hours in the short stack tests.

In Fig. 10 the fcc Pt lattice parameter of the $Pt_{68}Co_{29}Mn_3$ decreased slightly over the 3200 hours of cathode operation from 3.885 ± 0.005 to 3.882 ± 0.006 Å. However this is still within the difference and uncertainty of the measured values from the decal and fresh CCM, for which there should be no change. The Pt lattice spacing of the PtIr on the cathode for 3200 hours, MEA D, decreased from 3.895 ± 0.002 Å to 3.883 ± 0.006 Å implying that the catalyst has both increased its Ir content and improved the degree of alloying, This is because the lattice parameter is sensitive to the PtM atomic ratios (see Fig. 10 of reference 21). On the anode, the opposite effect is seen as the Pt-Pt lattice parameter increases for the PtIr (MEA

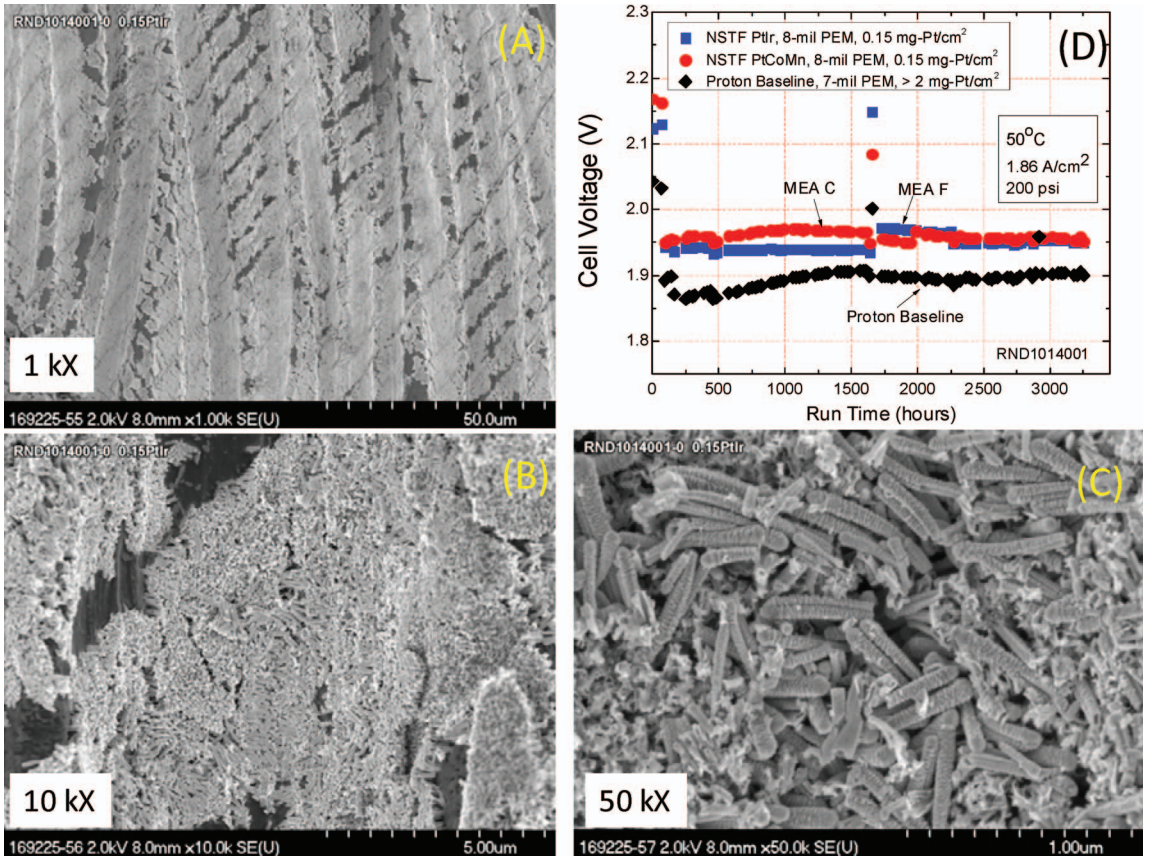


**Figure 7.** (A, B, C). SEM images at three magnifications of the NSTF electrode surface operated as a cathode in a $\frac{1}{2}$-CCM removed from MEA F after testing in a Proton stack for 3200 hours. (D) Cell voltage versus time of MEA's C and F compared with the baseline MEA at 1.86 A/cm$^2$, 50°C and 200 psi cathode pressure.

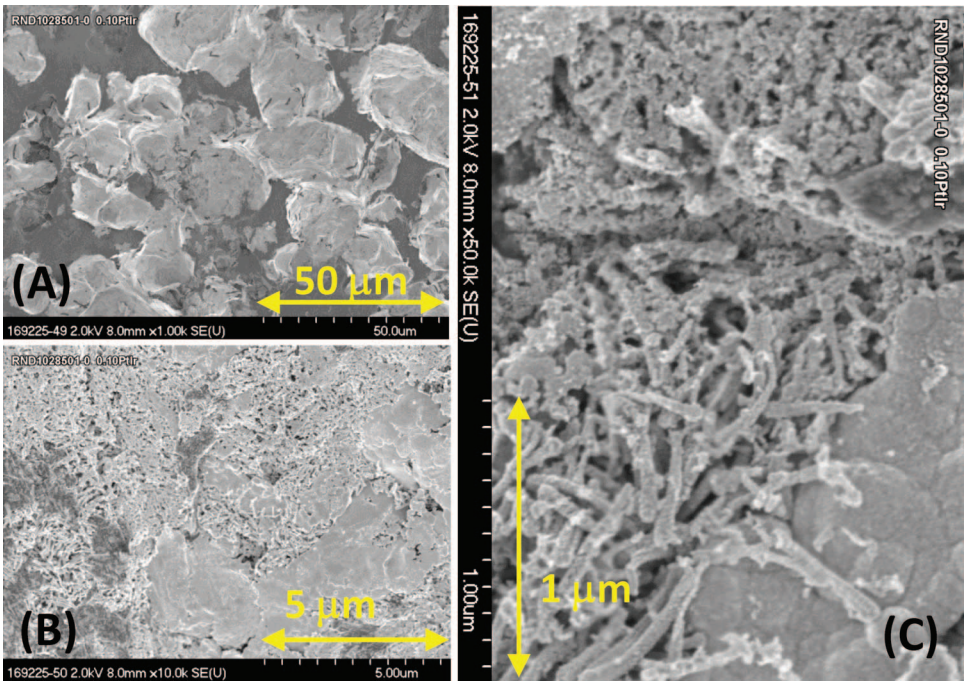


**Figure 8.** SEM images at three magnifications of the NSTF electrode surface operated as an anode in a $\frac{1}{2}$-CCM removed from MEA G1 tested in a Proton stack for 1500 hours with the cell voltage versus time shown in Fig. 6B for the 0.1 $mg_{Pt}/cm^2$ PtIr case (MEA G1).

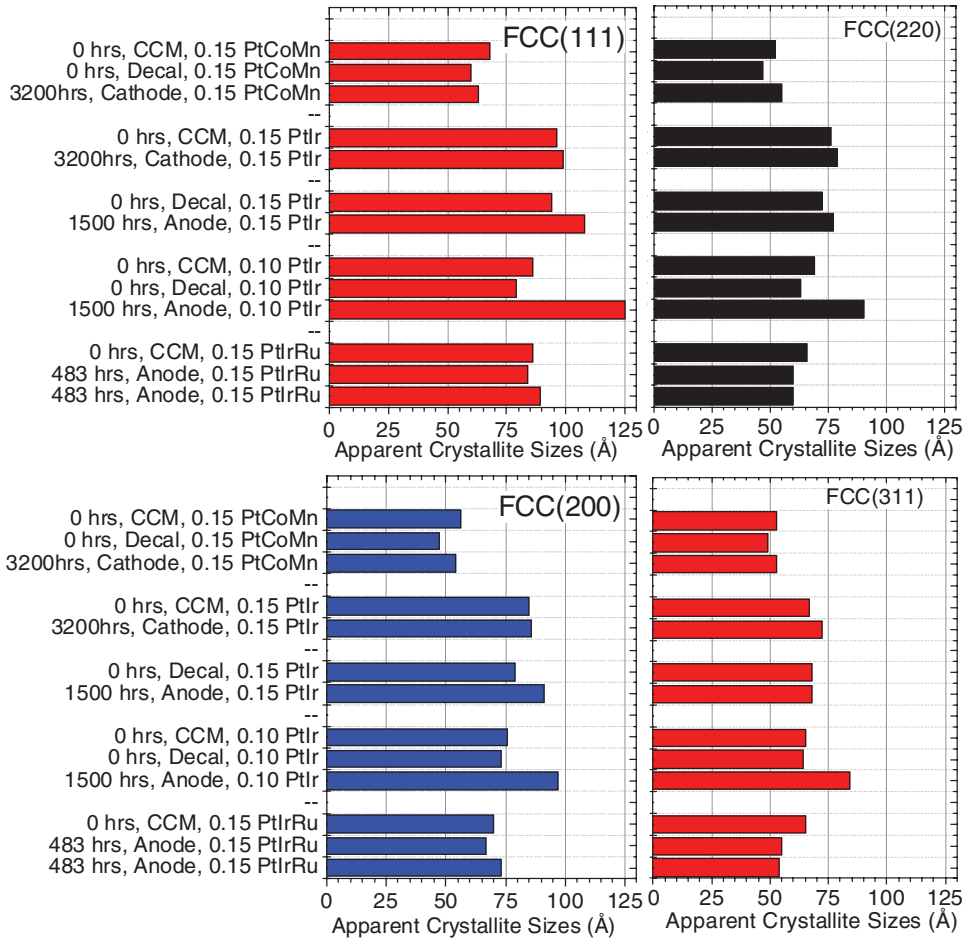


**Figure 9.** XRD determined fcc(hkl) crystallite sizes for the as-made decal catalysts (0 hours Decal), catalyst electrodes in the freshly made $\frac{1}{2}$-CCM's (0 hrs. CCM), and the durability aged PtCoMn electrodes from MEA C of Fig. 7D (3200 hrs., cathode), the aged PtIr anode electrodes (MEA's G1 and G2) from Figs. 6B and 8 (1500 hrs., Anode), and the two $Pt_{50}Ir_{25}Ru_{25}$ electrodes operated as anodes on the two type J MEA's for 483 hrs.

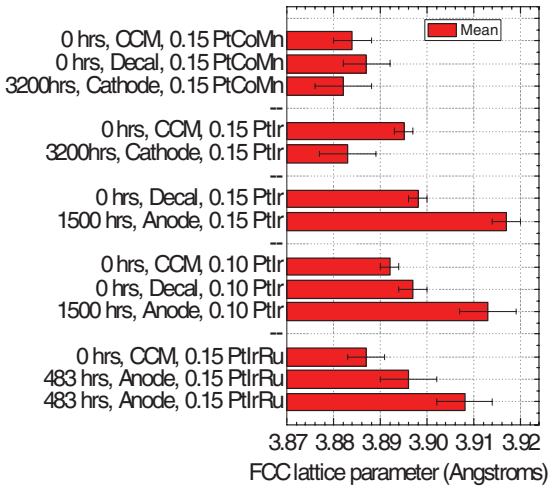


**Figure 10.** XRD determined fcc(hkl) lattice parameter for the as-made decal catalysts (0 hours Decal), catalyst electrodes in the freshly made $\frac{1}{2}$-CCM's (0 hrs. CCM), and the durability aged PtCoMn electrodes from MEA C of Fig. 7D (3200 hrs., cathode), the aged PtIr anode electrodes (MEA's G1 and G2) from Figs. 6B and Fig. 8 (1500 hrs., Anode), and the two $Pt_{50}Ir_{25}Ru_{25}$ electrodes operated as anodes on the two type J MEA's for 483 hrs.

G1 and G2) from 3.892 ± 0.002 Å to 3.913 ± 0.006 Å and 3.917 ± 0.003 Å respectively, and for the $Pt_{50}Ir_{25}Ru_{25}$ from 3.887 ± 0.004 Å to 3.902 ± 0.008 Å implying they are dealloying. They do not reach the 3.93 Å value for pure Pt so they retain some Ir or Ru, most likely just Ir.

*ICP characterization.*—Table II is a summary of ICP determined changes in catalyst loading of the PtCoMn and PtIr electrodes operated for 3200 hours on the cathode of MEA C and F as shown in Fig. 7D, and the PtIr electrodes operated for 1500 hours on the anode of MEA G1 and G2 as shown in Fig. 6B. ICP sample preparation recovers both the catalyst in the electrodes and whatever remained in the membrane that was part of the $\frac{1}{2}$-CCM sample removed for analysis. On the cathode, after 3200 hours, the NSTF PtCoMn sustained a Pt loading reduction of 42%, a Co loading reduction of 79% and a loss of essentially all the Mn which was expected. Surprisingly, a significant amount of Ir is detected although this PtCoMn catalyst did not have the additional 60 Å final deposition of Ir that earlier tested sample MEA A did. It is most likely that the detected Ir came to the cathode or its vicinity from the Proton Ir containing PGM-black catalyst used on their anode. After 3200 hours on the cathode, the PtIr $\frac{1}{2}$-CCM Pt loadings decreased 12% and the Ir loadings detected decreased 19%.

On the MEA G1 and G2 anodes after 1500 hours, the amount of Pt detected in the PtIr $\frac{1}{2}$-CCM electrode increased 90% on one sample and 98% on a second sample, and the Ir decreased 62% and 73% on the two samples respectively. These changes are consistent with the

**Table II. Summary of ICP determined changes in catalyst loading of the PtCoMn and PtIr electrodes operated for 3200 hours on the cathodes of MEA's C and F as shown in Fig. 7D, and the PtIr electrodes operated for 1500 hours on the anodes of MEA's G1 and G2 as shown in Fig. 6B. The asterisk indicates the initial values were assumed to be the as-made values.**

ICP: 3200 Hours on Cathode – $Pt_{68}Co_{29}Mn_3$

| μg/cm² | Pt | Co | Mn | Ir |
|---|---|---|---|---|
| Initial | 150 | 25.6 | 3.70 | 0 |
| After | 87.6 | 5.34 | 0.021 | 10.1 |
| % Change | −42 | 79 | −99.5 | $<\infty$ |

ICP: 3200 Hours on Cathode – $Pt_{50}Ir_{50}$

| μg/cm² | Pt\ \ Pt | Ir |
|---|---|---|
| Initial* | 150 | 157 |
| After | 132 | 127 |
| % Change | −12 | −19 |

ICP: 1500 Hours on Anode – $Pt_{50}Ir_{50}$, Two Samples

| μg/cm² | Pt | Ir | Pt | Ir |
|---|---|---|---|---|
| Initial | 150 | 157 | 100 | 104.5 |
| After | 285 | 59.4 | 198 | 28 |
| % Change | +90 | −62.2 | +98 | −73.2 |

ICP implied cathode changes that suggests Ir migrates away from the anode to the cathode, and the SEM images of Fig. 8 showing platelets of metal deposited onto the electrode surface, most likely Pt.

*EDS characterization.*—Fig. 11 shows a summary of the EDS determined atomic percentage changes of the PtCoMn and PtIr electrodes operated for 3200 hours on the cathode of MEA's C and F as G1 and G2 as shown in Fig. 6B. In Fig. 11B, only a slight indication of fluorine is seen in the EDS spectrum presumably through cracks in the electrode that exposes some of the perflurosulfonic acid membrane. In Fig. 11A, operating on the cathode for 3200 hours the PtIr electrode's atomic composition has not changed significantly, consistent with improved alloying and a reduction in the XRD lattice parameter. For the PtIr on the anode however, there has been a dramatic change in the composition indicated by the EDS, which no longer indicates any remaining Ir after the 1500 hours. This is consistent with the Ir losses indicated by ICP in Table II, and the XRD Pt-Pt lattice parameter increases in Fig. 10. The EDS is more surface sensitive than ICP or XRD, which may explain why it does not indicate any remaining Ir while the XRD and ICP both do.

For the PtCoMn electrode operated for 3200 hours on the cathode of MEA C, Fig. 11C indicates only a slight change in the Co/Pt ratio of atomic percentages, i.e. from 13/87 to 9/91. This change is consistent with the original $Pt_{68}Co_{29}Mn_3$ going to ~$Pt_3Co_1$, which is expected from fuel cell operation of these catalyst compositions as the Co dealloys in the acidic environment at low potentials and approaches the more stable $Pt_3M_1$ composition typical of several Pt-transition metal alloys. In this sample, more of the PFSA membrane is seen through cracks in the electrode, revealing more F as well as S.

*XRF characterization.*—Table III summarizes the changes in loading as determined by XRF for the same durability tested samples analyzed above with XRD, EDS and ICP. For the $Pt_{68}Co_{29}Mn_3$ electrode operated for 3200 hours on the cathode of MEA C, the top left section of Table III shows the Pt loading reduced by 12%, the Co by 36% and the manganese by 73%. This is also consistent with the $Pt_{68}Co_{29}Mn_3$ changing to something closer to $Pt_3Co_1$ as indicated by the EDS discussed above. Although no Ir was present initially in these samples, XRF indicates 3 μg/cm² in the control CCM, for which we have no explanation. However, a nearly 3-fold increase in Ir is detected in the long term durability tested electrode, consistent with the

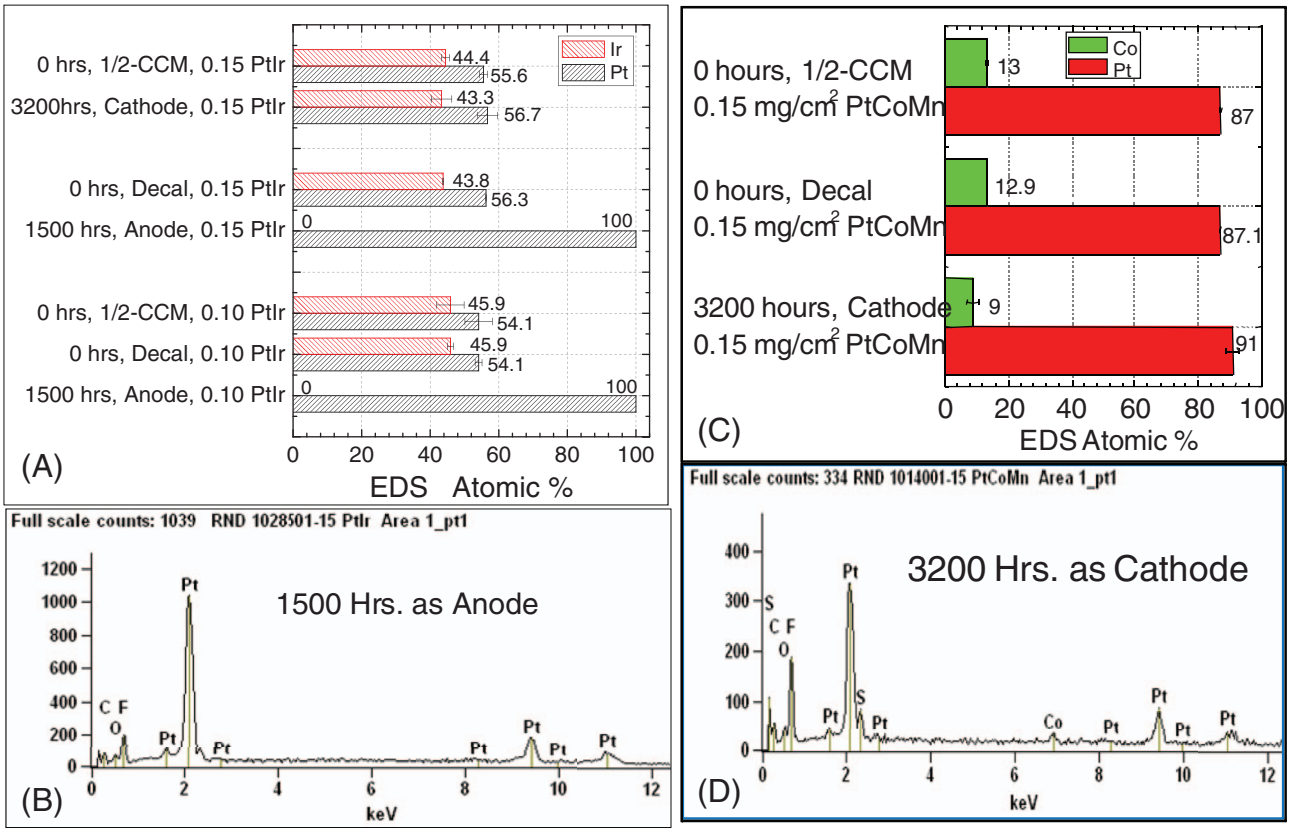


**Figure 11.** Summary of the EDS determined atomic percentages of the PtCoMn and PtIr catalysts in the decal and CCM controls, and the electrodes operated for 3200 hours on the cathode of MEA's C and F as in Fig. 7D, and the PtIr electrodes operated for 1500 hours on the anodes of MEA's G1 and G2 as shown in Fig. 6B.

**Table III. Summary of XRF determined changes in catalyst loading of the PtCoMn and PtIr electrodes operated for 3200 hours on the cathodes of MEA's C and F as shown in Fig. 7D, and the PtIr electrodes operated for 1500 hours on the anodes of MEA's G1 and G2 as shown in Fig. 6B.**

XRF: 3200 Hours on Cathode – $Pt_{68}Co_{29}Mn_3$

| $\mu g/cm^2$ | Pt | Co | Mn | Ir |
|---|---|---|---|---|
| Initial | 137 | 11 | 1.5 | 3 |
| After | 121 | 7 | 0.4 | 11 |
| % Change | −12 | −36 | −73 | +270 |

XRF: 3200 Hours on Cathode – $Pt_{50}Ir_{50}$

| $\mu g/cm^2$ | Pt | Ir |
|---|---|---|
| Initial | 139 | 96 |
| After | 136 | 126 |
| % Change | −2 | +31 |

XRF: 1500 Hours on Anode – $Pt_{50}Ir_{50}$, 2 Samples

| $\mu g/cm^2$ | Pt | Ir | Pt | Ir |
|---|---|---|---|---|
| Initial | 151 | 108 | 96 | 73 |
| After | 269 | 55 | 274 | 25 |
| % Change | +78 | −49 | +185 | −65 |

XRF: 483 Hours on Anode – $Pt_{50}Ir_{25}Ru_{25}$ Two Samples

| $\mu g/cm^2$ | Pt | Ir | Ru | Pt | Ir | Ru |
|---|---|---|---|---|---|---|
| Initial | 123 | 156 | 87 | 123 | 156 | 87 |
| After | 154 | 33 | 20 | 196 | 29 | 0 |
| % Change | +25 | −79 | −77 | +59 | −81 | −100 |

previous techniques' indications of significant Ir cross-over from the Ir-containing PGM-black anode. Also consistent with the prior characterization methods, the PtIr tested on the cathode for 3200 hours shows essentially no change in the amount of Pt but a 31% increase in the amount of Ir, again most probably from Ir cross-over (second section of Table III).

For the PtIr samples tested on the anode side for 1500 hours, (third section of Table III) the amount of Pt has increased by 78%, and the Ir has decreased by 49% for the 0.15 $mg_{Pt}/cm^2$ loaded sample, and +185% and −65% respectively for the 0.10 $mg_{Pt}/cm^2$ loaded sample. Both samples' trends are consistent with the ICP and EDS results above and the SEM visual evidence for the Pt platelets formed on the anode.

Note that the absolute amount of Ir lost from either loading of PtIr anode, ∼50 ± 2 $\mu g/cm^2$ suggests the amount of Ir cross-over from the anode to the cathode is independent of the anode loading. This may not be true for Pt on the anode. It may also be noteworthy that the apparent amount of Ir cross-over to the NSTF cathode from the Proton proprietary Ir-containing anode (∼10 $\mu g/cm^2$) appears to be less than the amount of Ir-lost from the NSTF anodes (∼50 $\mu g/cm^2$) shown in Table III. There could be several reasons for this including enhanced durability of the Proton PGM Ir containing anode catalyst, or an effect of the different $\frac{1}{2}$-membrane thicknesses. To see this latter possibility, suppose the same amount of Ir is lost to the membranes regardless of whether it comes from the low loaded NSTF PtIr or a higher loaded Ir containing PGM-black catalyst, and as stated before, the XRF is sensing the total material in the electrode and the $\frac{1}{2}$-PEM to which it is attached. Assume the Ir lost from the electrodes distributes uniformly across the membrane halves. In one case when the source is in the Nafion 117 membrane based $\frac{1}{2}$-CCM where Ir moves from the PGM source (anode) to the sink (NSTF cathode), the Ir gain in the NSTF $\frac{1}{2}$-PEM (35 microns thick for 3M side vs.178 microns for Nafion 117 membrane side) is only 35/178 or 20% of the amount left in the thicker Proton $\frac{1}{2}$-PEM side. In the reverse case, where the Ir source is the 3M NSTF PtIr $\frac{1}{2}$-CCM side, the NSTF $\frac{1}{2}$-CCM would appear to lose a larger fraction since the amount accounted by XRF in the thinner membrane would be smaller by the ratio 35/178 of what would be measurable in the other $\frac{1}{2}$-CCM had it been measured. In both cases then a ratio of about 5x for the apparent loss of Ir from the NSTF-PtIr electrode versus the apparent gain in Ir from the Ir-containing PGM-black electrode would be expected, very close to the 50/10 ratio observed.

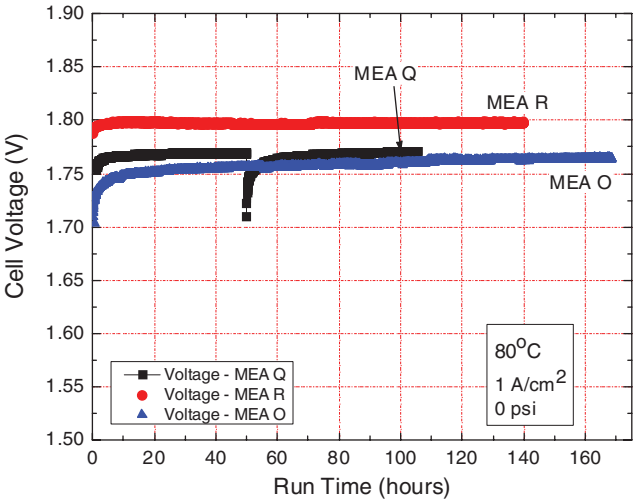


**Figure 12.** Single cell anode stability tests at Giner of the $Pt_{50}Ir_{25}Ru_{25}$ -SET catalyst (MEA R), the $Pt_{50}Ir_{25}Ru_{25}$ (non-SET) deposited with process 2 (MEA Q); and the $Pt_{50}Ir_{50}$-SET catalyst (MEA O).

Finally, for the $Pt_{50}Ir_{25}Ru_{25}$ anode of the J-type MEA's tested for 483 hours, (bottom section of Table III), the two samples consistently show Pt again increasing 25 to 59%, most likely due to cross-over from the Pt-black cathode. Again the Ir amount decreases by 80 ± 1%, as does the Ru, which appears depleted entirely in one sample and reduced by 77% in the second sample. This latter effect of the apparent instability of the $Pt_{50}Ir_{25}Ru_{25}$ in the short stack tests bears further inspection. This is because in the Giner single cell stability tests, the same catalysts appear to have very solid cell voltage stability on the anode for periods nearly as long as the short stack tests, or at least over times during which the stack cells were already decaying. This is shown in Fig. 12, which compares the cell voltage at 1 $A/cm^2$ for anodes containing the NSTF PtIr (0.15 $mg_{Pt}/cm^2$) that was SET treated (MEA O), and two of the three $Pt_{50}Ir_{25}Ru_{25}$ catalysts evaluated, one SET treated (MEA R), the other deposited with process 2 conditions (MEA Q). Only the PtIr anode curve (MEA O) shows a slight upward trend of cell voltage over time while the two $Pt_{50}Ir_{25}Ru_{25}$ (MEA's R and Q) curves are very stable over the 170 hours of test (A station shutdown and restart occurred for the MEA Q). This suggests that factors other than the catalyst compositions may be important for ensuring long term stability in the short stack, probably related to why the same anodes operated in the short stack began at cell voltages of 2.3 V (not shown) versus the <1.8 volts shown in Fig. 12.

## Conclusions

NSTF catalyst alloys with good ORR and HOR functionality as fuel cell cathodes and anodes respectively have been investigated for beginning-of-life performance and longer term durability as cathodes and anodes in $H_2/O_2$ electrolyzers, showing that they also have good OER and HER activities. Over two dozen samples comprising nine different NSTF catalyst types were tested in 11 short stack durability tests at Proton OnSite and 14 single 50 $cm^2$ cell tests at Giner Electrochemical Systems over a period of three years. The test objectives at Proton were primarily focused on obtaining the first NSTF catalyst durability measurements, while those at Giner focused on characterizing beginning of life performances. The 3M objectives were to obtain benchmark durability and performance data that could be correlated with catalyst composition, structure and processing conditions.

Beginning-of-life cathode performance of NSTF $Pt_{68}Co_{32}Mn_3$ and NSTF $Pt_{50}Ir_{50}$ catalysts were found to be equivalent to that of standard Pt-blacks having loadings an order of magnitude higher. Constant current short stack durability performances of MEA's having the NSTF $Pt_{68}Co_{29}Mn_3$ or PtIr catalysts on the cathodes and standard PtIr-blacks on the anodes were found to be stable for the duration of multiple such tests, some exceeding 4000 hours. Characterization of the NSTF electrodes with XRD, ICP, SEM/EDS and XRF after durability testing for up to 3200 hours were consistent in showing: a) stable Pt fcc(hkl) crystallite sizes and alloy composition's moving toward $Pt_3Co_1$, b) the $Pt_{50}Ir_{50}$ composition and absolute loadings were more stable than the $Pt_{68}Co_{29}Mn_3$ alloys, and c) Ir migration to the NSTF cathodes from the highly loaded standard PtIr-black anodes.

Beginning-of-life anode performances of SET treated NSTF-$Pt_{50}Ir_{50}$ and $Pt_{50}Ir_{25}Ru_{25}$ catalysts were found in single cell tests to be nearly equivalent to that of standard PtIr-blacks having loadings an order of magnitude higher. Short stack durability tests at constant current with these catalysts on the anodes and standard Pt-blacks on the cathodes were found to be stable for the duration of multiple such tests up to 2000 hours in length. Characterizations with XRD, ICP, SEM/EDS and XRF after durability testing were consistent in showing: a) NSTF whisker supports appear little affected after operation at 2.3 V for 1500 hours, b) an abundance of Pt platelets formed on the anodes with diameters on the order of 50 microns attributed to Pt cross-over from the Pt-black cathodes, c) slightly agglomerated catalyst morphology on the NSTF whisker support particles on the anodes, d) up to 40% increases in Pt crystallite sizes, e) over 50% loss of Ir from the as-made PtIr alloys, and f) much greater loss of Ru (and performance) than Ir in NSTF $Pt_{50}Ir_{25}Ru_{25}$ alloys tested on the anodes. Near equivalent beginning-of-life performances from NSTF alloy catalysts having only ~10% of the loadings of standard PGM blacks is promising that with further catalyst refinement, membrane and GDL optimization both overpotential and stability can be improved. NSTF-$Pt_{50}Ir_{50}$, at 0.10 or 0.15 $mg_{Pt}/cm^2$ that has been SET "annealed" appears to be a good first choice for both the cathode and anode for these membrane and GDL component refinements.

## Acknowledgments

Office of Transportation in the Office of Energy Efficiency and Renewable Energy at the US Department of Energy for its support under grant DE-FC36-07GO17007, grant DE-FG36-08GO18065, and grant DE-SC0004192.

## Acronyms

| | |
|---|---|
| CCM | Catalyst coated membrane |
| EDS | Electron energy dispersive X-ray microanalysis |
| HER | Hydrogen evolution reaction |
| HFR | High frequency resistance |
| HOR | Hydrogen oxidation reaction |
| ICP | Inductively coupled plasma |
| MEA | Membrane electrode assembly |
| NSTF | Nanostructured thin film |
| OER | Oxygen evolution reaction |
| ORR | Oxygen reduction reaction |
| PEM | Proton exchange membrane |
| PGM | Precious group metals |
| RDE | Rotating disk electrode |
| SEM | Scanning electron microscopy |
| SET | Surface energy treatment |
| XRD | X-ray diffraction |
| XRF | X-ray fluorescence |

## References


1. Katherine Ayers, 2011 *DOE Hydrogen Program Review*, PD071 May 11, Washington, D. C. http://www.hydrogen.energy.gov/pdfs/review11/pd071_ayers_2011_o.pdf.
2. Monjid Hamden, 2011 DOE Hydrogen Program Review, PD030 May 11, Washington, D. C. http://www.hydrogen.energy.gov/pdfs/review11/pd030_hamdan_2011_o.pdf.
3. K. E. Ayers, E. B. Anderson, C. B. Capuano, B. D. Carter, L. T. Dalton, and G. Hanlon, *ECS Trans.* **33**(1), 3 (2010).
4. K. E. Ayers, C. B. Capuano and E. B. Anderson, "Recent Advance in Cell Cost and Efficiency for PEM-Based Water Electrolysis," Abs. #283, *220 Th ECS Meeting*, Boston, MA, Oct., 2011.
5. M. K. Debe and A. R. Drube, *J. Vac. Sci. Tech. B*, **13**(3), 1236 (1995).
6. M. K. Debe and R. J. Poirier, *J. Vac. Sci. Tech. A*, **12**(4), 2017 (1994).
7. M. K. Debe, in *Handbook of Fuel Cells–Fundamentals, Technology and Applications*, W. Vielstich, A. Lamm, H. A. Gasteiger, Editors, Vol. 3, Part 3, Ch. 45, pp 576–589, John Wiley & Sons (2003).
8. Lajos Gancs, Takeshi Kobayashi, Mark K. Debe, Radoslav Atanasoski, and Andrzej Wieckowski, *Chemistry of Materials* **20**, 2444 (2008).
9. M. K. Debe, A. E. Hester, G. D. Vernstrom, A. J. Steinbach, S. M. Hendricks, A. K. Schmoeckel, R. T. Atanasoski, D. J. McClure, and P. L. Turner, "Nanostructured Thin Film Catalysts for PEM Fuel Cells by Vacuum Web Coating, in *Proceedings of the 50 th Annual Tech. Conference of the Society of Vacuum Coaters*, Louisville, KY, May 1, 2007, 175–185.
10. Mark K. Debe, *J. Electrochem. Soc.* **159**(1) B54–B67 (2012).
11. A. Kongkanand, Z. Liu, I. Dutta, and F. T. Wagner, *J. Electrochem. Soc.*, **158**(11), B1286 (2011).
12. Arman Bonakdarpour, Krystal Stevens, George D. Vernstrom, Radoslav Atanasoski, Alison K. Schmoeckel, Mark K. Debe, and Jeff R. Dahn, *Electrochim. Acta*, **53**, 688 (2007).
13. D. Van der Vliet, D. Strmcnik, C. Wang, R. Atanasoski, M. Debe, N. Markovic, and V. Stamenkovic, "Multimetallic Catalysts for Oxygen Reduction Reaction," *216 th ECS Meeting*, Vienna, Austria, Oct. 4–9, 2009.
14. K. J. J. Mayrhofer, D. Strmcnik, B. B. Blizanac, V. Stamenkovic, M. Arenz, and N. M. Markovic, *Electrochim. Acta*, **53**, 3181 (2008).
15. Arman Bonakdarpour, Tara R. Dahn, Radoslav Atanasoski, Mark K. Debe, and Jeff R. Dahn, *Electrochem. and Solid-State Letters*, **11**, B208 (2008).
16. D. A. Stevens, S. Wang, R. J. Sanderson, G. C. K. Liu, G. D. Vernstrom, R. T. Atanasoski, M. K. Debe, and J. R. Dahn, *J. Electrochem. Soc.*, **158**(8), B899 (2011).
17. G. C.-K. Liu, R. J. Sanderson, G. D. Vernstrom, D. A. Stevens, R. T. Atanasoski, M. K. Debe, and J. R. Dahn, *J. Electrochem. Soc.* **157**(2), B207 (2010).
18. Gary Chih-Kang, D. A. Stevens, J. C. Burns, R. J. Sanderson, G. D. Vernstrom, R. T. Atanasoski, M. K. Debe, and J. R. Dahn, *J. Electrochem. Soc.*, **158**(8), B919 (2011).
19. D. A. Stevens, R. Mehrotra, R. J. Sanderson, G. D. Vernstrom, R. T. Atanasoski, M. K. Debe, and J. R. Dahn, *J. Electrochem. Soc.*, **158**(8), B905 (2011).
20. Dennis van der Vliet, Chao Wang, Mark Debe, Radoslav Atanasoski, Nenad M. Markovic, and Vojislav R. Stamenkovic, *Electrochim. Acta*, **56**, 8695 (2011).
21. M. Debe, A. Steinbach, G. Vernstrom, S. M. Hendricks, M. J. Kurkowski, R. T. Atanasoski, P. Kadera, D. A. Stevens, R. J. Sanderson, E. Marvel, and J. R. Dahn, *J. Electrochem. Soc.*, **158**(8), B910 (2011).
22. A. Bonakdarpour, K. Stevens, G. D. Vernstrom, R. Atanasoski, A. K. Schmoeckel, M. K. Debe, and J. R. Dahn, *Electrochim. Acta*, **53**, 688 (2007).
23. M. K. Debe, A. Schmoeckel, S. Hendricks, G. Vernstrom, G. Haugen, and R. Atanasoski, *ECS Trans.* **1**(1), 51 (2006).
24. M. K. Debe, A. K. Schmoeckel, G. D. Vernstrom, and R. Atanasoski, *Journal of Power Sources*, **161**, 1002 (2006).
25. A. J. Steinbach, K. Noda, and M. K. Debe, *ECS Trans.* **3**(1), 835 (2006).
26. M. K. Debe, 2011 *DOE Hydrogen Program Review*, FC001, May 9-13, 2011, Washington D. C., http://www.hydrogen.energy.gov/pdfs/review11/fc001_debe_2011_o.pdf.
27. M. K. Debe, R. T. Atanasoski, and A. J. Steinbach, *ECS Trans.* **41**(1), 937 (2011).
28. G. D. Vernstrom, L. L. Atanasoska, G. M. Haugen and R. T. Atanasoski, "Catalyst durability for fuel cells under start-up and shutdown conditions: Evaluation of Ru and Ir sputter deposited on platinum in PEM environment," Abstract #1106, *220th ECS Meeting*, Boston, MA, Oct. 9–14, 2011.
29. T. D. Hatchard, J. E. Harlow, D. A. Stevens, Gary Chi-Kang Liu, R. J. Sanderson, N. van der Bosch, J. R. Dahn, G. M. Haugen, G. D. Vernstrom, and R. T. Atanasoski, *Electrochim. Acta* **56**(28), 10436–10442 (2011).
30. D. A. Stevens, R. J. Sanderson, T. D. Hatchard, T. C. Crowtz, J. R. Dahn, G. D. Vernstrom, G. M. Haugen, T. Watschke, L. L. Atanasoska, and R. T. Atanasoski, *ECS Trans.*, **33**(1), 419 (2010).
31. D. A. Cullen, K. L. More, K. S. Reeves, G. D. Vernstrom, L. L. Atanasoska, G. M. Haugen, and R. T. Atanasoski, *ECS Trans.*, **41**(1), 1099 (2011).
32. L. L. Atanasoska, G. D. Vernstrom, G. M. Haugen, and R. T. Atanasoski, *ECS Trans.*, **41**(1), 785 (2011).
33. Final Report for 3M/DOE Cooperative Agreement DE-FC36-02AL67621, "Advanced MEA's for Enhanced Operating Conditions, Amenable to High Volume Manufacture," Sept. 30, 2007.

REVIEW

doi:10.1038/nature11115

# Electrocatalyst approaches and challenges for automotive fuel cells

Mark K. Debe[1]

**Fuel cells powered by hydrogen from secure and renewable sources are the ideal solution for non-polluting vehicles, and extensive research and development on all aspects of this technology over the past fifteen years has delivered prototype cars with impressive performances. But taking the step towards successful commercialization requires oxygen reduction electrocatalysts—crucial components at the heart of fuel cells—that meet exacting performance targets. In addition, these catalyst systems will need to be highly durable, fault-tolerant and amenable to high-volume production with high yields and exceptional quality. Not all the catalyst approaches currently being pursued will meet those demands.**

The current performances of the small test fleets of vehicles powered by automotive fuel cells are impressive, reflecting 15 years of intense development of all aspects of proton exchange membrane (PEM) fuel cells that have brought the technology close to pre-commercial viability[1]. But to move towards a genuinely practical technology that can be mass-produced cost-effectively, important further improvements are needed. This calls for a critical look at how we need to develop key components determining fuel-cell performance, durability and cost. A pivotal component is the electrocatalyst system that underpins fuel-cell operation, and excellent reviews of progress made in Pt-based fuel-cell catalyst development for automotive applications have been written from both an academic perspective focused on fundamentals and from a perspective focused on the requirements of the automotive companies[2–6]. This review is provided from the perspective of a fuel-cell component supplier who needs to consider all factors that any electrocatalyst approach will need to meet if it is to be commercially successful. Following an overview of fuel cells and the challenges they need to meet for commercialization, I will consider the electrocatalyst system and the different approaches taken to ensure its performance meets automotive fuel-cell requirements. In my view, focusing only on catalytic activity targets will not be sufficient to meet the challenge posed by large-scale automotive fuel-cell commercialization, which requires the manufacture of catalyst electrodes at high rates, high quality and low costs.

## Fuel-cell components

An automotive fuel cell produces electricity from the electrochemical oxidation of hydrogen. It is manufactured as a stack of identical repeating unit cells comprising a membrane electrode assembly (MEA) in which hydrogen gas ($H_2$) is oxidized on the anode and oxygen gas ($O_2$) is reduced on the MEA cathode, all compressed by bi-polar plates that introduce gaseous reactants and coolants to the MEA and harvest the electric current (Fig. 1). The electrochemical reactions occur in the MEA electrodes, each attached to a solid polymer ion exchange membrane that conducts protons but not electrons. The cathode oxygen reduction reaction (ORR) and anode hydrogen oxidation reaction both occur on the surfaces of platinum (Pt)-based catalysts. Pure water and heat are the only byproducts. Porous gas diffusion layers transport reactants and product water between the flow fields and catalyst surfaces while exchanging electrons between them.

## The challenges for commercialization

Fuel-cell MEAs must meet three major criteria: cost, performance and durability. The cathode ORR is six or more orders of magnitude slower than the anode hydrogen oxidation reaction and thus limits performance, so almost all research and development focuses on improving the cathode catalysts and electrodes. Most MEA catalysts used today are based on Pt (in the form of nanoparticles dispersed on carbon black supports), with the high price of this scarce precious metal having a decisive impact on costs. Fuel-cell vehicles in the test fleets monitored by the United States Department of Energy (DOE) have used 0.4 mg of Pt per square centimetre (mg Pt $cm^{-2}$) or more on the cathode, and in these vehicles the catalyst/MEA stability has still been short of the 5,000-hour durability target[7]. How to reduce costs by reducing cathode loadings to $<0.1$ mg Pt $cm^{-2}$ without loss of performance or durability is the subject of most electrocatalyst research. Current US DOE 2017 targets[1] for electrocatalysts aim for a total (anode + cathode) platinum group metals (PGM) loading of 0.125 mg $cm^{-2}$ on MEAs able to produce rated stack

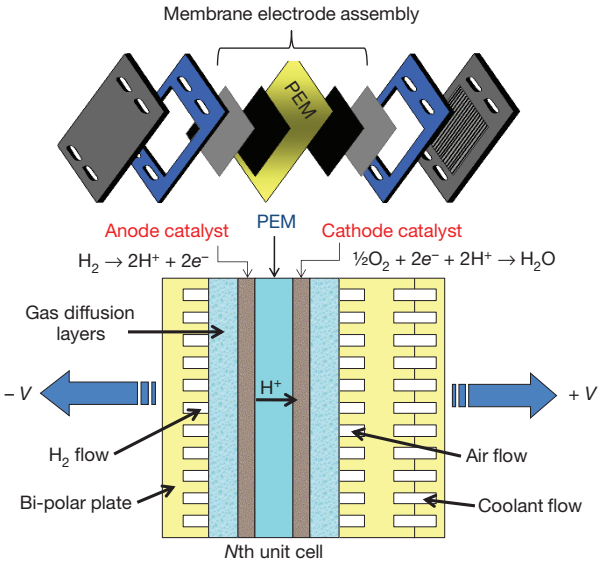


**Figure 1 | Fuel-cell components.** Unit cell cross-section of the *N*th unit cell in a fuel-cell stack, showing the components of an expanded MEA.

[1]3M Fuel Cell Components Program, 3M Center, St Paul, Minnesota 55144, USA.

**Table 1 | Development criteria for automotive fuel-cell electrocatalysts**

| | |
|---|---|
| Performance | • Must meet beginning-of-life performance targets at full and quarter power.<br>• Must meet end-of-life performance targets after 5,000 h or 10 years operation.<br>• Must meet performance, durability and cost targets and have less than 0.125 mg PGM per $cm^2$.<br>• Corrosion resistance of both Pt and the support must withstand tens of thousands of start-up/shut-down events.<br>• Must have low sensitivity to wide changes in relative humidity.<br>• Must withstand hundreds of thousands of load cycles.<br>• Must have adequate cool start, cold start and freeze tolerance.<br>• Must enable rapid break-in and conditioning (the period needed to achieve peak performance). |
| Materials | • Must have high robustness, meaning tolerance of off-nominal conditions and extreme-load transient events.<br>• Must produce minimal $H_2O_2$ production from incomplete ORR.<br>• Must have high tolerance to external and internal impurities (for example, $Cl^-$) and ability to fully recover.<br>• Must have statistically significant durability, meaning individual MEA lifetimes must enable over 99.9% of stacks to reach 5,000-hour lifetimes.<br>• Electrodes must be designed for cost-effective Pt recycling.<br>• Environmental impact of manufacturing should be minimal at hundreds of millions of square metres per year. |
| Process | • Environmental impact must be low over the total life-cycle of the MEAs.<br>• Manufacturing rates will need to approach several MEAs per second.<br>• MEA manufacturing quality must achieve over 99.9% failure-free stacks at beginning of life (one faulty MEA in 30,000 for just 1% stack failures).<br>• Proven high-volume manufacturing methods and infrastructure will be required.<br>• Catalyst-independent processes will be preferred, to enable easy insertion of new-generation materials. |

power densities of 8.0 kW $g^{-1}$ Pt. This gives 8 g of PGM per vehicle, similar to what is in an internal combustion engine today.

Vehicle operation imposes severe durability and performance constraints on the fuel-cell cathode electrocatalysts[1] beyond the fundamental requirement for high ORR activity. System integrators require that the MEA produce at least 0.6 V at 1.5–2 A $cm^{-2}$ owing to radiator size and related cooling constraints. Catalysts must survive hundreds of thousands of load cycles and tens of thousands of start-up and shut-down events over the 5,000-hour lifetime of the stack[1]. Although durability is beyond the scope of this review, serious degradation is associated with the tendency for the cathode to reach potentials above the onset of oxidation of carbon in contact with Pt, during even the short times when $H_2$/air waves move through the flow fields during start-up or shut-down[8]. Some of the countermeasures being developed are using more stable graphitized carbon, using catalyst supports that will not electrochemically corrode, and adding oxygen evolution catalysts to the mix to clamp the potentials at the start of water oxidation[9,10]. Table 1 summarizes these major catalyst requirements, along with secondary criteria and manufacturing considerations.

## Some fundamental electrochemical considerations

MEA performance is reflected in its polarization curve, a plot of cell voltage versus current density (Fig. 2). As current is drawn from a cell, its voltage decreases as a result of three primary sources of power loss: ORR kinetic losses of the cathode, current times resistance ($iR$) losses due to material and interface resistances, and mass transport overpotentials at high current densities when it is difficult for the catalyst to get enough oxygen from air. For the polarization curve conditions in Fig. 2, the theoretical open-circuit voltage (zero current) is 1.169 V; note that measured open-circuit voltages are lower than theoretical ones owing to imperfect separation of the gases by the membrane and its finite electronic resistance. Increases in load current cause the cell voltage to decrease logarithmically owing to kinetic losses (green line in Fig. 2), with the large cell-voltage loss of about 370 mV in going from open-circuit voltage to practical currents of just 0.1 A $cm^{-2}$ reflecting the sluggish ORR kinetics on Pt. The measured cell resistance multiplied by current density gives the $iR$ losses, which can be added to the measured polarization curve (blue symbols) to give the $iR$-free curve (red symbols). The remaining difference between the $iR$-free curve and the ideal kinetic line represents the sum of all mass transport losses. In the range of practical current densities, 0.1–2.5 A $cm^{-2}$, improvements in MEA resistance can have a much larger impact on actual cell voltage than improvements in kinetics. Cell resistances have therefore been researched, and have been reduced nearly as much as is possible using current membranes and gas diffusion media. Kinetic losses are more challenging because an order-of-magnitude improvement in ORR activity would gain only 60–70 mV, and progress in catalyst development so far has achieved only modest cell voltage gains of tens of millivolts. Reducing mass transport overpotentials by the same amount is less difficult.

Targeted catalyst development benefits from a detailed understanding of the metal-catalysed electrochemical reduction of oxygen to water, $O_2 + 4H^+ + 4e^- \rightarrow 2H_2O$, which is mechanistically complicated. It is usually thought to involve different reaction pathways such as direct $4e^-$ reduction of adsorbed oxygen to water; or a $2e^-$ reduction to adsorbed $H_2O_2$ that then either desorbs or undergoes a second $2e^-$ reduction to water[11]. Irrespective of mechanistic detail, the kinetic current density $i$, normalized by the surface area of the Pt electrode and generated at a potential $E$, has been proposed[12] to be a function of the Gibbs energy of adsorption $\Delta G_{ad}$

$$i = nFKc_{O_2}(1 - \Theta_{ad})^x \exp\left(-\frac{\beta FE}{RT}\right) \exp\left(-\frac{\gamma \Delta G_{ad}}{RT}\right) \quad (1)$$

where $n$, $F$, $K$, $x$, $\beta$, $\gamma$ and $R$ are constants, $c_{O_2}$ is the molecular oxygen concentration, and $\Theta_{ad}$ the fraction of electrode surface sites covered with adsorbates. A key assumption in the development of the $(1 - \Theta_{ad})$ pre-exponential factor is that the ORR rate-limiting step is the first electron transfer step, $Pt(O_2)_{ad} + e^- \rightarrow Pt(O_2^-)_{ad}$, with

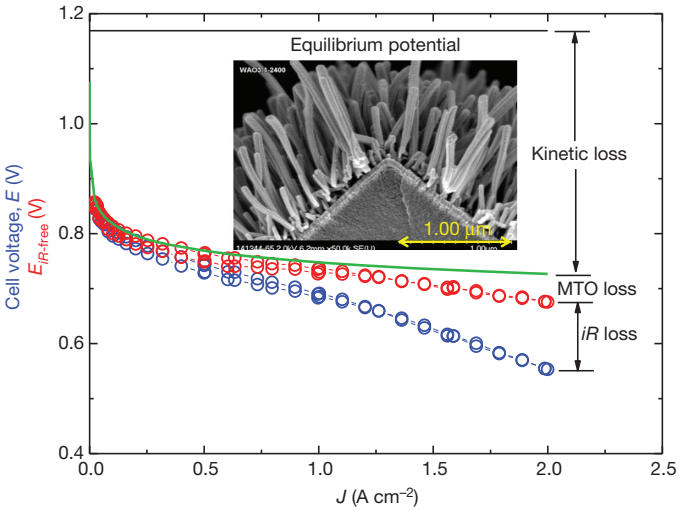


**Figure 2 | Fuel-cell polarization curve.** Measured PEM fuel-cell MEA polarization curve (blue) and $iR$-free (red) compared to a hypothetical curve for kinetic losses only (green). The difference gives the losses due to mass transport overpotentials (MTO). The polarization curve is from an MEA having electrodes based on the NSTF PtCoMn catalyst (inset) under 150 kPa $H_2$/air. Other conditions are given in ref. 23.

oxygen adsorption onto a surface primarily covered by impurities (hydroxyls) rather than reactive intermediates. This suggests that anything done to the surface's atomic or electronic structure that delays hydroxyls adsorbing and blocking $O_2$ adsorption sites will have a positive impact on the specific activity, because the $(1 - \Theta_{ad})$ term in equation (1) will be larger. This model underpins many approaches used to improve ORR electrocatalysts, although some recent model calculations and measurements are consistent with adsorbed oxygen or hydroxyl species playing a more active part as intermediates[6].

Electrocatalyst properties determining the observed current densities $J$ (in A per planar $cm^2$) in MEAs are the electrode's electrochemically active surface area $S$ (in $cm^2$ of Pt per planar $cm^2$), the kinetic current density $i$ as in equation (1) that reflects the catalyst's activity, and a recently proposed[13] collision frequency scaling factor $f(\lambda, \rho_S)$ that depends on the mean free path length $\lambda$ above the catalyst surface and on a spatial distribution function of surface area that to first order can be approximated by the catalyst surface area volumetric density $\rho_S$ (in $cm^2$ Pt per $cm^3$). Or, in brief, $J = f \cdot S \cdot i$. The value of $S$ is generally determined experimentally using cyclic voltammograms (see Box 1, which also provides catalyst activity definitions and DOE targets) and normalized by the electrode surface area to give the surface-area enhancement factor (in $cm^2$ of Pt per planar $cm^2$). Kinetic activity is measured *ex situ* in rotating disc electrode (RDE) apparatus[3,14,15] or *in situ* in fuel cells, with both methods requiring care to obtain reproducible results[3]. The two methods sample different surface states (that is, different amounts of hydroxyl or oxygen adsorption on platinum), so comparisons of RDE and fuel-cell activities are not always straightforward. The factor $f(\lambda,\rho_S)$, calculated from catalyst electrode physical properties, captures one way in which geometry has a differentiating role in comparing different electrocatalyst designs.

## The basic electrocatalyst designs

PEM fuel-cell electrocatalyst technology has relied almost exclusively on either Pt blacks (metal particles so tiny that they absorb light very well and appear black, having a high surface to volume ratio, ideal for catalysts) or Pt nanoparticles, 2–5 nm in size, dispersed onto larger carbon black particles. Neither will meet the DOE 2017 performance and durability targets at PGM loadings that meet the cost targets. But our fundamental understanding of what controls catalytic activity has dramatically improved in the last few years and is now guiding next-generation catalyst development. Most emerging approaches focus on controlling the surface structure and composition of catalytic nanoparticles to achieve higher ORR activity with less Pt, and new synthetic routes have delivered such 'designer nanoparticles' that meet or exceed the DOE 2017 targets for ORR activity. However, the newest approaches are barely out of the 'test-tube' stage: they have not yet been tested extensively in actual fuel-cell MEAs, and it remains to be seen which approaches can also meet the other practical MEA requirements (see Table 1).

The basic designs for platinum catalysts are summarized in Fig. 3, categorized by overall geometry of the catalyst and its support and then further subdivided according to structural morphology and composition. This approach illustrates that kinetic activity can change by nearly an order of magnitude when the catalyst is a discrete nanoparticle or a polycrystalline thin film, and that catalyst surface area per unit volume can affect the maximum achievable current density. Also, the volume occupied by the non-active support influences current density[13], while aspect ratios determine the packing of the catalyst supports and hence porosity and free-radical scavenging.

**BOX 1**

### Definitions and activity targets

- The surface-area enhancement factor is the Pt catalyst surface area $S$ measured by the charge generated from an under-potential deposited monolayer of hydrogen atoms on the Pt catalyst surface divided by the planar area of the sample ($cm^2$ Pt per planar $cm^2$).
- Pt loading is the number of mg of Pt per planar $cm^2$ in an MEA electrode layer.
- Absolute ORR kinetic activity is currently defined as the current density measured at 900 mV under one atmosphere of fully saturated pure oxygen, at 80 °C. For an MEA this means 150 kPa absolute pressure, due to 50 kPa of water vapour.
- The area-specific activity $A_s$ (A per $cm^2$ Pt) is determined by dividing the absolute activity by the surface-area enhancement factor.
- The mass activity $A_m$ (A per mg of Pt) is determined by dividing the absolute activity by the Pt loading.
- The DOE's 2017 target for $A_m$ is 0.44 A per mg Pt and its 2015 target for $A_s$ is 0.7 mA per $cm^2$ Pt (ref. 1).

## Extended surface area catalysts

Extended surface area (ESA) catalysts comprise large area surfaces extended in two dimensions like thin films. Their advantages over conventional Pt/C approaches are larger radii of curvature that make them more resistant to surface area loss via mechanisms such as Pt dissolution and redeposition, reduced mass transport losses, and in some cases the potential to eliminate corrosion of the catalyst support and simpler manufacturing. The area-specific ORR activities ($A_s$) of ESA catalysts are about ten times higher than nanoparticle-on-carbon catalysts, owing to electronic structure properties of thin films versus nanoparticles. Classic ESA examples are polycrystalline or single-crystalline bulk catalyst surfaces[16–20]; developed at Lawrence Berkeley and Argonne National Laboratory, these serve as valuable model systems that have shown the effect of structural aspects like single-crystal facet orientation, size, type and composition on activity. Some advanced ESA alloy catalysts exhibit a roughened 'Pt-skeleton' surface with Pt atoms covering the average bulk composition, or a highly coordinated pure 'Pt-skin' overlying a modulated surface structure in which the underlying three layers' composition oscillates towards the bulk composition[16,20]. Such a Pt-skin surface structure on $Pt_3Ni_1$ {111} was reported to have the world-record $A_s$ of 18 mA per $cm^2$ Pt (non-*iR* corrected), about 90 times higher than a standard commercial dispersed Pt/C in comparative RDE measurements[16]. The peculiar arrangement of Pt and Ni atoms in the top three layers of this system causes different amounts of shift in the *d*-band centre relative to the Fermi level of the topmost layer of Pt atoms, which is believed to affect the adsorption coverage of hydroxyl spectator species that interfere with ORR (see equation (1)). The quest is how to achieve this in a practical catalyst.

Nanostructured thin-film (NSTF) catalysts are the only practical ESA catalysts found so far[13,21–24]. The support is a thin monolayer of an oriented array of crystalline organic whiskers, less than 1 μm tall and 30 nm × 55 nm in cross-section. It is applied to a roll-good substrate (a material made by a roll-to-roll process) with a number density of 30–40 whiskers per square micrometre, and then magnetron sputter-coated with catalyst thin films of choice (Fig. 2, inset). The organic support whisker is non-conductive, does not support corrosion currents and its body-centred cubic crystalline nature influences the subsequent nucleation and growth of the catalyst thin films coating them[25]. NSTF electrocatalysts have documented basic advantages in $A_s$ of the catalyst[23,26], surface area utilization and stability[27,28], performance with ultralow PGM loadings[24], support corrosion resistance[29], high-volume manufacturability[30], and their release of $F^-$ ions from the ionomer (perfluorosulphonic acid) used in the membrane or electrode is up to three orders of magnitude lower[24,31]. (Incomplete oxygen reduction to water on Pt produces $H_2O_2$, which creates free radicals that attack the membrane ionomer. Membrane degradation rates are proportional to the $F^-$ ion release rates, with suppressed $F^-$ release showing that the unique geometry of NSTF catalysts facilitates scavenging of radicals before they reach the membrane.) The low-volume support makes NSTF electrodes 10 to 20 times thinner than equivalently loaded Pt/C dispersed electrodes, which means better access to all of the catalyst surface area at all current densities. It also means less volume for

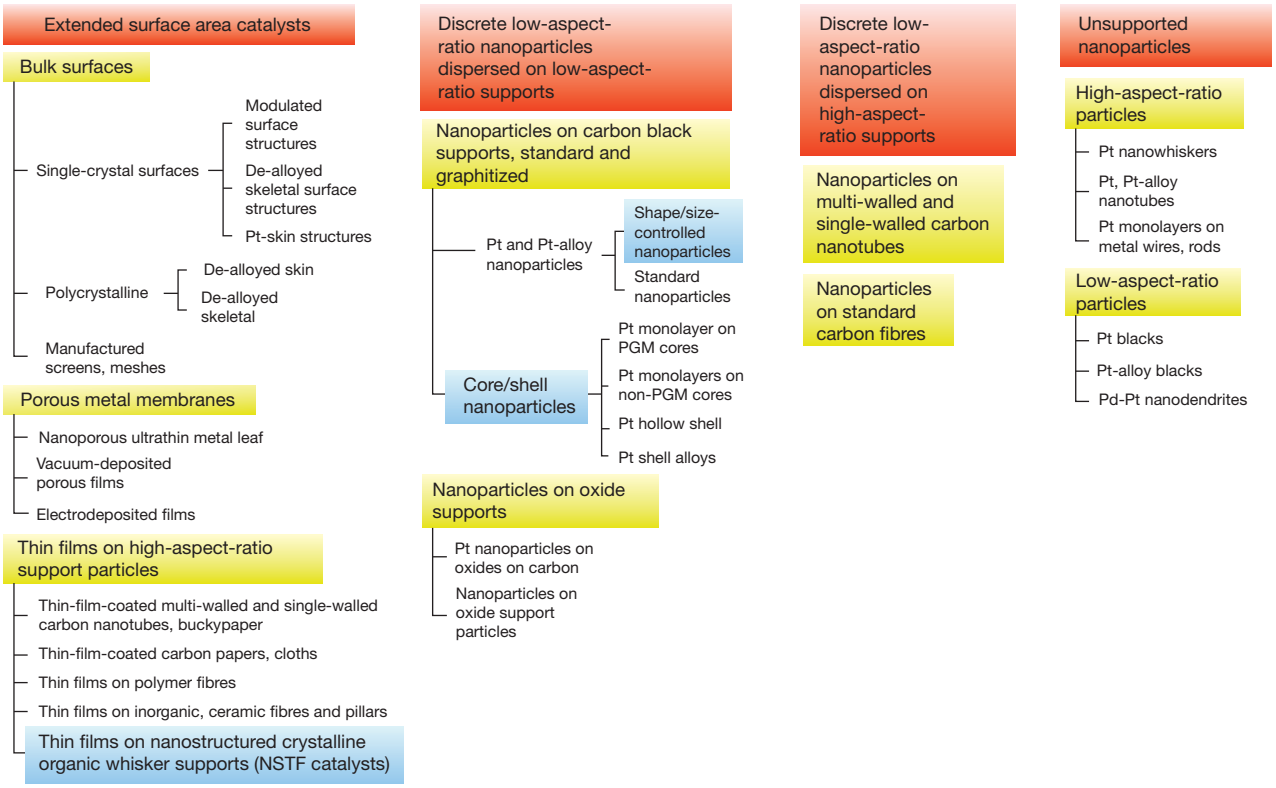


**Figure 3 | Basic platinum-based heterogeneous electrocatalyst approaches.** The four PEM fuel-cell electrocatalyst approaches (developed or under investigation) for the performance-limiting cathode ORR are shown, with Pt and Pt-alloy electrocatalysts listed according to the basic geometric structure of the catalyst particles and their supports. The main subcategories are highlighted in yellow. Catalyst approaches with the highest demonstrated activities are highlighted in blue.

storing any condensed product water that can lead to challenges in freeze-start, load transients (such as engine idling to full power as fast as possible) and cold operation, requiring different water-management strategies, anode gas diffusion layers, or modifications of operating protocols[32]. NSTF Pt alloys show the same activity gains over pure Pt as dispersed nanoparticles. De-alloying (see Box 2 for details) can endow the NSTF catalyst coating with core–shell properties as well, with sublayers affecting the lattice properties of the outermost Pt surface. The NSTF alloy catalyst with the largest production to date uses the $Pt_{68}Co_{29}Mn_3$ composition, which for loadings of 0.05–0.15 mg cm$^{-2}$ delivers $A_s$ values of 1.3–1.8 mA cm$^{-2}$ Pt, and mass activities ($A_m$) of 0.15–0.17 A cm$^{-2}$ Pt. Still under development are NSTF $Pt_{1-x}Ni_x$ alloy catalysts with an unusually sharply peaked gain in activity for $x = 0.7$ (ref. 33). They reach $A_s \approx 2.4$ mA cm$^{-2}$ Pt and $A_m$ from 0.24 to over 0.5 A mg$^{-1}$ Pt in 50-cm$^2$ fuel-cell measurements, with loadings below 0.15 mg Pt cm$^{-2}$ (refs 23, 24).

In related approaches, thin catalyst films are applied to single- or multi-wall carbon nanotubes[34,35] to achieve higher activity on a more durable support. These systems are more durable[35] than catalysts on high-surface-area carbons, but performances and activities have not improved significantly and the nanotubes will still ultimately corrode at high potentials.

Porous metal membranes[36–40], the third class of extended surface area catalysts, include nanoporous ultrathin metal leaves and vacuum-deposited, electrodeposited or laser-deposited porous films. They can be de-alloyed (see Box 2 for more details) to create nanoporosity, or to obtain specific modulated surface layer compositions similar to that of the $Pt_3Ni_1$ {111} system. These catalysts show high specific $A_s$ values similar to those of polycrystalline bulk surfaces but with higher surface area, and enable valuable studies of the de-alloying processes, but are mostly not amenable to high-volume manufacturing.

## Nanoparticles on low-aspect-ratio supports

This catalyst category is dominated by roughly spherical Pt or Pt alloy nanoparticles dispersed on standard or graphitized carbon black support particles, including conventional homogeneous Pt and Pt transition-metal alloy nanoparticles[3,19,41–43] and designer nanoparticles with size, shape and radial composition controlled to increase activity and reduce Pt.

### BOX 2

## De-alloying of Pt transition-metal alloys

The de-alloying of less-noble elements from Pt-alloys is a key strategy for creating Pt-based catalysts in all design categories. This means less stable elements initially alloyed with Pt (usually at a high atomic percentage of transition metal) are intentionally or unintentionally dissolved out to leave a nanoporous film, or skeletal surface or core–shell particle configuration[37,38,88] overlying a composition closer to a stable bulk alloy composition such as $Pt_3M_1$, where M is a transition metal. The process increases surface area, and creates in the outer few layers a modulated surface composition that leaves the surface Pt lattice contracted or its electronic structure favourably modified, as illustrated by lattice-strain control of the Pt shells formed around de-alloyed cores[94]. In the case of $Pt_{1-x}Ni_x$ bulk alloys with high Ni content, electrochemical de-alloying provide a means of studying[95–97] the evolution of nanoporosity. The resultant material, with average pore and ligament sizes of 3–5 nm and filled with hydrophobic protic liquids, displayed $S_m = 44$ m$^2$ per g Pt, and $A_m = 0.4$ A per mg Pt[95]. Strasser and colleagues have pioneered voltammetric de-alloying of electrode nanoparticles, composed of base-metal-rich bimetallic and trimetallic alloys[88,91,92,94], directly in the MEA and reported $A_s$ and $A_m$ values exceed the DOE 2017 and 2015 targets (Box 1). Although such *in situ* methods are not practical, understanding the de-alloying process is critical for optimizing the catalyst properties and *ex situ* de-alloying of these alloy systems is under investigation[93].

The state-of-the-art of conventional Pt and Pt-alloy/C electrocatalysts in dominant use today consist of Pt nanoparticles with diameters of 2–4 nm, dispersed onto larger high-surface-area carbon black support particles at Pt/C weight percentages of 20% to 60%. Commercial pure Pt/C catalysts have surface areas of 80–120 $m^2 g^{-1}$ Pt, specific activities of 0.15–0.2 mA $cm^{-2}$ Pt and mass activities of 0.1 to 0.12 A $mg^{-1}$ Pt measured in MEAs. Homogeneous Pt-alloy nanoparticles on carbon have historically been observed to increase ORR activity over pure Pt/C by about a factor of 2 to 2.5. The commercially available, heat-treated 30 weight per cent PtCo/C system routinely provides MEA measurement values of specific and mass activity in our 3M laboratory that are close to the DOE targets, for example, 1.2 mA $cm^{-2}$ Pt and 0.39 A $mg^{-1}$ Pt. For a wide range of carbon-based supports, initial Pt surface areas range from 20 to over 70 $m^2 g^{-1}$ Pt, but converge after stability testing to 20–30 $m^2 g^{-1}$ Pt (ref. 44).

Uniformly sized octahedra, cubes or other polyfaceted shapes identically terminated with {111} and {100} facets[45–48]can be produced, often using capping agents selectively to control facet growth rates. Truncated-octahedral $Pt_3Ni$ particles with predominantly {111} facets show $A_m$ values up to four times those of commercial Pt/C (ref. 46), and much higher than {100} bounded cubes[47]. Surface-specific activity strongly depends on the fraction of {111} surface exposed and is about a tenth that of bulk single-crystal $Pt_3Ni${111} surfaces, suggesting that larger shape-controlled particles with higher surface coordination (fewer surface defects where oxides preferentially form) or compositional gradients could improve activities[49]. In the case of monodispersed $Pt_3Co$ nanoparticles, these factors increase grain size and $A_s$ monotonically for particle sizes of 3–9 nm, while $A_m$ peaks at about 4.5 nm for optimum particle annealing at 500 °C (refs 45, 50). Monodispersed and homogeneous $Pt_{1-x}Ni_x$ nanoparticles with controlled Ni depletion from the outer surface layers exhibit a Pt-skeleton-type surface structure, with the improvement factor over Pt/C peaking at 4.5 nm for monodispersed PtNi (ref. 51). For similarly structured PtCoNi alloy particles, mass activities by RDE are reported to exceed 2.5 A $mg^{-1}$ Pt (ref. 52).

Core–shell nanoparticle electrocatalysts pioneered at Brookhaven National Laboratory constitute a highly promising subcategory of catalysts[52–64]. These systems exhibit higher mass activities because Pt is eliminated from the core of the catalyst particles, and higher specific activities because the core material influences the outer Pt monolayer and optimizes its surface electronic and structural properties. Examples include Pt monolayers on Pd and non-PGM cores, de-alloyed cores, 'Swiss-Pt' de-alloyed cores (full of pores), and hollow Pt or Pt-alloy shells[53,54,57–63]. The core material would ideally consist of non-PGM elements, though the successful Pt-monolayer core–shell catalysts so far have cores containing Pd, Au-Ni, Pd-Co, $Pd_3Co$, $Pd_3Fe$, Pd-Ir, Ir, Pd-Au, $AuNi_{0.5}Fe$, Pd-Nb, Pd-V, Pd-W and Ru monolayers on Pd cores. Fuel-cell MEA measurements with these novel catalysts at two industrial locations yield mass activities lower than the RDE values measured by the Brookhaven National Laboratory group[59,64], which may be due to non-optimized electrodes. Key development opportunities for this subcategory include development of scalable synthetic routes for generating 'pin-hole'-free Pt monolayers to protect the non-PGM core material from leaching; increasing specific activity while using less expensive core materials and optimizing electrode ink formulations; and further increased resistance to Pt dissolution due to repeated start-stop induced voltage cycling events.

Support corrosion is a problem for all these systems, pushing development towards dispersing the nanoparticle catalysts on graphitized, lower-surface-area carbons or single-wall or multi-wall carbon nanotubes (see below). Another strategy uses inherently more stable inorganic oxides as support. If these provide adequate conductivity, for example, where the oxide support is formed on carbon black, promising mass activities are obtained: 0.2 A $mg^{-1}$ Pt for Pt/C, 0.3 A $mg^{-1}$ Pt for Pt-$TaOPO_4$/C and 0.45 A $mg^{-1}$ Pt for heat-treated Pt-$TaOPO_4$/C (where C = Vulcan carbon)[65].

## Nanoparticles on high-aspect-ratio supports

This category includes Pt or Pt-alloy nanoparticles dispersed on standard carbon fibres as well as on single- or multi-walled carbon nanotubes[66]. As in the case of thin-film catalysts coated onto these types of supports, the objective is usually improved durability because the activity of the nanoparticles is not expected to change much with the aspect ratio of the support. In the case of carbon nanotube supports, their higher electrical conductivity is not really any advantage because electronic impedance of the electrodes is a very small contributor to the overall overpotential losses, but carbon nanotube supports can improve transport or water management[67]. However, concerns about the possible adverse health effects of carbon nanotubes without the counterweight of a significant functional performance or processing advantage may make them unattractive for high-volume electrode manufacturing.

## Unsupported nanoparticles

Unsupported nanoparticle catalysts include the traditional low-aspect-ratio particles of Pt and Pt alloy blacks[41], and new concepts that use Pt and Pt-alloys in the form of high-aspect-ratio structures such as nanotubes[68,69]and Pt monolayers on Pd nanowires and nanorods[70,71]. Although they are just at the initial-concept phase, the unsupported metal nanotube catalysts are claimed to improve $A_s$ values over bulk polycrystalline Pt by a factor of eight (ref. 69), and the monolayer systems are claimed to exhibit impressive mass activities of 0.4 A $mg^{-1}$ PGM[70,71](measured by RDE).

## Pt-free electrocatalysts

Owing to the scarcity and high cost of Pt, Pd-based catalysts (recently reviewed by Shao[72]) and Pd-based transition metal alloy catalysts (explored in the Myers group[73]) have been considered. But the best activities reported for Pd are barely equivalent to typical Pt/C, with the best use of Pd appearing to be in combination with Pt as in the core–shell configurations discussed above. In any case, replacement of most of the Pt by Pd may not significantly address the cost issue, owing to demand/price fluctuations[2].

Non-precious metal (NPM) catalysts eliminate PGMs completely to reduce costs, and have recently shown dramatic ORR activity improvements. Among the many approaches being explored[74–83], pyrolysis of cobalt- and iron-containing heteroatom polymer precursors (for example, porphyrins) has been the dominant route towards NPM catalysts. Active sites are believed to comprise metals coordinated to several nitrogen atoms, $MN_x$ (where M = Co, Fe). The Dodelet group's impregnation and pyrolysis process combining Fe precursors and a nitrogen precursor has led to the largest beginning-of-life activity increases[79,81]. The nature of the active site in these NPM catalysts is still debated, as is the question of whether Fe is associated with the active site or with the means of creating such a site. There is no way to measure area density of active sites as for Pt-based catalysts, so kinetic activity is reported as a volumetric current density. Kinetic activities measured at 0.8 V using pure $O_2$ have rapidly increased from 2.7 A $cm^{-3}$ in 2008 (ref. 82), to 99 A $cm^{-3}$ in 2009 (ref. 79), and 230 A $cm^{-3}$ in 2011 (ref. 81). The most recent increase was due to a large reduction in mass transport loss: the performance of a new NPM Fe-based cathode on Nafion 117 ionomer under 2-bar gauge $H_2$/air was 0.25 A $cm^{-2}$ at 0.5 V after 100 hours, about a tenth of the current density obtained with Pt-based cathodes. The key issues for NPM catalysts are mass transport losses and stability. A polyaniline FeCo-C catalyst with relatively high durability (700 hours) at 0.4 V in a $H_2$/air fuel cell and a peak power density of 0.55 W $cm^{-2}$ at 0.38 V under pressurized pure oxygen has been reported[83]. But NPM catalyst durability is worse at higher potentials—and for automotive purposes, performances at less than 0.6 V are largely irrelevant.

## Comparison of kinetic activities

As illustrated by the preceding discussion, a wide range of catalyst systems has been explored and Fig. 4 shows composite plots of $A_m$ versus

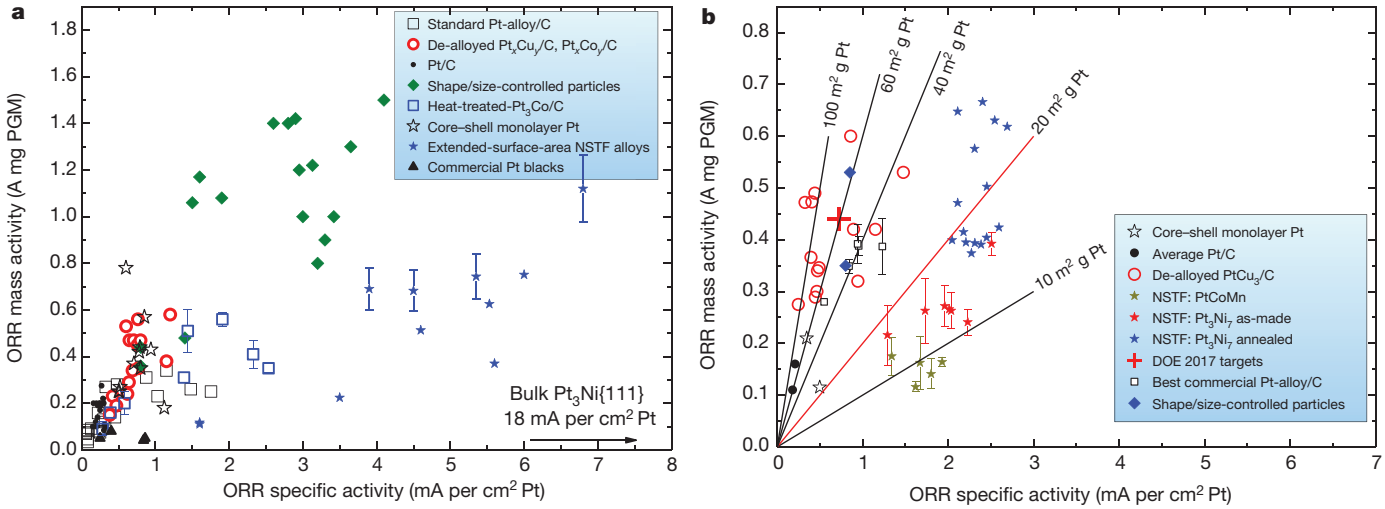


**Figure 4 | Kinetic activities of the main Pt-based electrocatalyst systems.** The ORR $A_m$ versus $A_s$ are shown for the major Pt-based electrocatalyst approaches listed in Fig. 3. **a**, Activities are measured by RDE at 900 mV for the following catalysts: standard Pt-alloys/C (refs 42, 43, 87), de-alloyed $PtM_3$/C (where M = Cu, Co) (refs 88–90), Pt/C (refs 3, 42, 44, 46–48, 50), shape- and size-controlled particles (refs 45, 47, 48, 50, 51), heat-treated $Pt_3Co$/C (ref. 42), core–shell monolayer Pt (refs 44, 56, 60, 62–64, 71), extended-surface-area NSTF alloys (refs 23,26) and commercial Pt blacks (refs 3, 48). **b**, Activities are measured in MEAs at 900 mV, 80 °C and 150 kPa saturated $O_2$ for the following catalysts: core–shell Pt monolayer (refs 49, 64), average Pt/C (refs 3, 91, 92), de-alloyed $PtCu_3$/C (refs 91–93), three extended-surface-area NSTF alloys (ref. 23), the DOE 2017 and 2015 targets, best commercial Pt-alloys/C (data from GM, 3M), and shape- and size-controlled particles (refs 46, 52). The scattering of activity values for any one type or reference represent different catalyst compositions, loadings or preparation and process treatments, not statistical variations in measurement.

$A_s$ measured by both RDE and in MEAs for the most promising ones. RDE values are generally larger than those measured in MEAs, reflecting not only the more complex environment of the catalyst in a working fuel cell but also the simple difference in protocol that allows RDE measurements on a clean surface while MEA values are obtained with oxidized surfaces. (Note that RDE measurements will also depend on temperature, voltage scan rate, *iR* and diffusion-correction factors.) For standard Pt/C or Pt alloy/C catalysts, only a few data points are given to represent generally accepted measured values. The figures show that several catalyst systems seem to be able to meet the DOE 2017 $A_m$ target of 0.44 A $mg^{-1}$ Pt; some systems come very close, including the best commercial Pt-alloy/C catalyst, for which durability is still an issue. The highest-performing systems in Fig. 4 are not yet practical, in that they are not able to simultaneously satisfy all the electrocatalyst requirements for high current density and durability at low loadings.

## Manufacturing and scalability

Manufacturability and quality control of MEAs produced at the rates ultimately required for true commercialization have not been an issue for the small fuel-cell vehicle fleets produced to date. But the lead time to get an MEA component qualified for insertion into a vehicle stack is about five years, and publicly announced future emergent fuel-cell vehicle volumes are tens to hundreds of thousands of vehicles per year by 2020. Clearly, the scalability of any new catalyst approach now has to be seriously considered from the outset. For many of the new catalyst approaches being evaluated at the 'test-tube' stage, it is not clear that the processes used to generate them would be scalable with the quality levels required. The DOE cost targets are based on 500,000 vehicles per year, and a particular MEA technology advanced to that emergent market level will not be easily discarded in favour of something totally new that may be better able to reach a more mature production level at say 10% of the world market in 2030 (or 15 million vehicles).

To illustrate the scales involved, consider that annual production of 15 million fuel-cell vehicles each with a stack containing 300 (versus the 400 required today) MEAs (each around 300 $cm^2$) would require 4.50 billion MEAs a year. With a production line at full capacity operating three shifts per day, 360 days per year, or about 8,000 hours per year with 80% average up-time to account for maintenance, repair and lot changes of input materials, the required production rate is about 11,700 MEAs per minute. To match car production at about one vehicle per minute per production line, or 300 MEAs per stack per minute, would require 20 full-capacity MEA production lines each producing 585 MEAs per minute or about 10 MEAs per second (with more production lines requiring more capital and operating costs). Individual piece part processing is out of the question.

Target loadings of about 0.1 mg Pt per $cm^2$ mean electrode thicknesses will be less than 2 μm, requiring precision coating methods with critical limits on debris and tolerances. High-volume roll-to-roll widths up to a metre in width should be possible, so even with ten MEAs across the web width, each measuring 10 cm × 30 cm, line speeds of 20 m $min^{-1}$ will be required. These MEAs have to be made with extraordinary quality control (one fatal MEA defect in 30,000 MEAs for 1% stack failures). The catalyst and catalyst/membrane integration manufacturing processes have to be simple, robust, few in number and have wide process parameter windows, given that the yields per step multiply. Just four sequential process steps with 90% yields would increase costs by 30% without recycling. Process steps for electrode formation that require hot bonding, annealing, solvent evaporation or drying steps lasting for minutes will require proportionately long manufacturing lines. Build-up of residues on the coaters, 8-hour shift lengths, ability to handle jumbo roll-goods, safety and catalyst batch-size limitations will be factors affecting batch sizes, throughputs and labour costs. At loading targets of even 0.125 mg $cm^{-2}$ on MEAs with 300 $cm^2$ active areas, the above line speeds require catalyst flow-through rates of 1.5 kg of Pt per hour—roughly US$2 million worth of Pt per day per manufacturing line, at a metal price of US$2,000 troy ounces. On-site recycling of scrap will probably be justified. Recycling of Pt, once it reaches the target stack loadings equivalent to the PGM amounts used in current internal combustion engines, will be justified by the same economic arguments currently used for recycling PGMs in catalytic converters. Ink mixing of dispersions for catalyst coating, if used, would have to keep pace and use chemistries compatible with coating line speeds and quality levels. Safety, environmental and cost control requirements will probably exclude coating processes using flammable solvents. I believe these requirements and the required production rates and levels of quality will ultimately result in catalyst layer coating by all-dry vacuum-coating methods, such as the method used to produce over 80% of the world's multi-layer optical-film-coated glass that is used in low-emissivity windows and produced at a

volume of 250 million square metres already in 2005 (ref. 84). All the above considerations regarding essential process requirements apply to catalyst-membrane integration and the fabrication and integration of other stack components as well.

## Perspective

Several catalyst systems have ORR kinetics adequate for automotive applications, including commercially available heat-treated PtCo/C. But at the required low PGM loadings, none are able yet to deliver in a fuel-cell environment the necessary high power, durability or robustness. Recent progress with 'designer' catalyst particles and ESA catalysts suggests that they will reach over the next few years their maximum kinetic performance, something close to the specific activity of 18 mA per $cm^2$ Pt measured by RDE on bulk crystals of $Pt_3Ni\{111\}$. The consistent difference between RDE and MEA values (see Fig. 4) implies that this ultimate performance maximum will be about 6–9 mA per square centimetre of Pt in a fuel-cell environment, well above the DOE 2017 target. But as the discussion of additional practical requirements and manufacturing issues has shown, impressive kinetic activity will not suffice to make a catalyst system attractive for large-scale automotive MEA production. I therefore consider that realizing target ORR activities may no longer be the most important goal, despite being the overwhelming focus of many researchers in the field. Instead, we should aim to achieve (at the required low PGM loadings) the durability and power targets using something that can be manufactured at high volumes with the requisite quality, throughput and yields. This poses a considerable challenge to the community, particularly when considering that for most catalyst systems durability, high power performance, quality and yield decrease as loadings decrease.

Grounds for optimism are the recent pace and diversity in the development of interesting new approaches to PEM fuel-cell electrocatalysts that optimize ORR kinetic activities without sacrificing durability or cost. A few material and design concepts are guiding these efforts, namely the use of extended-surface-area catalyst geometries; the use of alloys, particularly with Ni; the synthesis of catalysts with large, highly coordinated {111} facets; and the use of de-alloyed or annealed surface structures with increased surface area and a modulated composition that improves the activity of the topmost Pt layer. The ideal catalyst would embody all of these improvement characteristics[22].

These recent developments illustrate that the level and quality of fundamental research in the field need to continue unabated. Particularly beneficial would be a clear understanding of surface area and activity loss mechanisms, and insight into the causes of durability loss[85,86] associated with externally and internally generated impurities. I also hope for future electrocatalyst research exploring how membrane and microporous materials in contact with the catalyst and off-nominal operating events affect performance. We also need to know whether there are any fundamental processing rate limitations on high-volume manufacturability. These are the issues that will arise when the rubber meets the road, and will dictate the ultimate costs and customer acceptance of fuel-cell vehicles. It has been eighteen years since the first PtCo/C catalyst was investigated, but it is still not generally accepted for use in current fuel-cell vehicles; it may take even longer to implement any of the newer catalyst approaches into realistic electrodes.


1. The. US Department of Energy (DOE). *Energy Efficiency and Renewable Energy* http://www.eere.energy.gov/hydrogenandfuelcells/mypp/pdfs/fuel_cells.pdf and the *US DRIVE Fuel Cell Technical Team Technology Roadmap* (revised 25 January 2012) www.uscar.org/guest/teams/17/Fuel-Cell-Tech-Team.
**These websites define the most critical performance, durability and cost targets for the PEM fuel-cell MEA and each of its components, as well as stack and system requirements.**
2. Wagner, F. T., Lakshmanan, B. & Mathias, M. F. Electrochemistry and the future of the automobile. *J. Phys. Chem. Lett.* **1,** 2204–2219 (2010).
3. Gasteiger, H., Kocha, S., Sompalli, B. & Wagner, F. Activity benchmarks and requirements for Pt, Pt-alloy, and non-Pt oxygen reduction catalysts for PEMFCs. *Appl. Catal. B* **56,** 9–35 (2005).
**This paper first defined and explained the ORR activity targets and requirements for the PEM fuel-cell cathodes, particularly for fuel-cell vehicles.**
4. Markovic, N., Schmidt, T., Stamenkovic, V. & Ross, P. Oxygen reduction reaction on Pt and Pt bimetallic surfaces: a selective review. *Fuel Cells* **1,** 105–116 (2001).
5. Nørskov, J. K., Bligaard, T., Rossmeisl, J. & Christensen, C. H. Towards the computational design of solid catalysts. *Nature Chem.* **1,** 37–46 (2009).
6. Greeley, J. *et al.* Alloys of platinum and early transition metals as oxygen reduction electrocatalysts. *Nature Chem.* **1,** 552–556 (2009).
7. Wipke, K, *et al. Controlled Hydrogen Fleet and Infrastructure Analysis: 2011 DOE Hydrogen Program Annual Merit Review and Peer Evaluation Meeting* http://www.hydrogen.energy.gov/pdfs/review11/tv001_wipke_2011_o.pdf (National Renewable Energy Laboratory, 2011).
8. Reiser, C. A. *et al.* A reverse-current decay mechanism for fuel cells. *Electrochem. Solid-State Lett.* **8,** A273 (2005).
**This explains the basic mechanism by which fuel starvation or start-up and shut-down events in a PEM fuel cell can cause carbon corrosion on the cathode.**
9. Atanasoska, L. L., Vernstrom, G. D., Haugen, G. M. & Atanasoski, R. T. Catalyst durability for fuel cells under start-up and shutdown conditions: evaluation of Ru and Ir sputter-deposited films on platinum in PEM environment. *ECS Trans.* **41,** 785–795 (2011).
10. Halalay, I. C. *et al.* Anode materials for mitigating hydrogen starvation effects in PEM fuel cells. *J. Electrochem. Soc.* **158,** B313–B321 (2011).
11. Sepa, D. B., Vojnovic, M. V. & Damjanovic, A. Reaction intermediates as a controlling factor in the kinetics and mechanism of oxygen reduction at platinum electrodes. *Electrochim. Acta* **26,** 781–793 (1981).
12. Markovic, N. M. & Ross, P. N. Surface science studies of model fuel cell electrocatalysts. *Surf. Sci. Rep.* **45,** 117–229 (2002).
13. Debe, M. K. Effect of electrode surface area distribution on high current density performance of PEM fuel cells. *J. Electrochem. Soc.* **159,** B54–B67 (2012).
14. Mayrhofer, K. J. J. *et al.* Measurement of oxygen reduction activities via the rotating disc electrode method: from Pt model surfaces to carbon-supported high surface area catalysts. *Electrochim. Acta* **53,** 3181–3188 (2008).
15. Garsany, Y., Barurina, O. A., Swider-Lyons, K. E. & Kocha, S. S. Experimental methods for quantifying the activity of platinum electrocatalysts for the oxygen reduction reaction. *Anal. Chem.* **82,** 6321–6328 (2010).
16. Stamenkovic, V. R. *et al.* Improved oxygen reduction activity on $Pt_3Ni(111)$ via increased surface site availability. *Science* **315,** 493–497 (2007).
**This paper showed that the fundamental kinetic activity for oxygen reduction on bulk Pt–Ni alloy surfaces could be nearly two orders of magnitude higher than the standard dispersed Pt on carbon.**
17. Stamenkovic, V. R., Mun, B. S., Mayrhofer, K. J. J., Ross, P. N. & Markovic, N. M. Effect of surface composition on electronic structure, stability and electrocatalytic properties of Pt-transition metal alloys: Pt-skin versus Pt-skeleton surfaces. *J. Am. Chem. Soc.* **128,** 8813–8819 (2006).
**This paper demonstrates the sensitivity and specificity of ORR activity to the fundamental surface structure and composition of the top few layers of Pt transition metal alloys.**
18. Stamenkovic, V. R. *et al.* Trends in electrocatalysis on extended and nanoscale Pt-bimetallic alloy surfaces. *Nature Mater.* **6,** 241–247 (2007).
19. Paulus, U. A. *et al.* Oxygen reduction on high surface area Pt-based alloy catalysts in comparison to well defined smooth bulk alloy electrodes. *Electrochim. Acta* **47,** 3787–3798 (2002).
20. Stamenković, V., Schmidt, T. J., Ross, P. N. & Markovic, N. M. Surface composition effects in electrocatalysis: kinetics of oxygen reduction on well-defined $Pt_3Ni$ and $Pt_3Co$ alloy surfaces. *J. Phys. Chem. B* **106,** 11970–11979 (2002).
21. Debe, M. K. in *Handbook of Fuel Cells—Fundamentals, Technology and Applications* (eds Vielstich, W., Lamm, A. & Gasteiger, H. A.) Ch. 45 (John Wiley & Sons, 2003).
22. Debe, M. K., Atanasoski, R. T. & Steinbach, A. J. Nanostructured thin film electrocatalysts—current status and future potential. *ECS Trans.* **41,** 937–954 (2011).
23. Debe, M. K. *2009–2011 Annual Merit Reviews DOE Hydrogen and Fuel Cells and Vehicle Technologies Programs: Advanced Cathode Catalysts and Supports for PEM Fuel Cells* http://www.hydrogen.energy.gov/pdfs/review11/fc001_debe_2011_o.pdf (DOE, 2011).
24. Debe, M. K. Nanostructured thin film electrocatalysts for PEM fuel cells—a tutorial on the fundamental characteristics and practical properties of NSTF catalysts. *ECS Trans.* **45** (2), 47–68 (2012).
**This paper defines all the catalyst and MEA measured properties and published papers so far for the NSTF type catalyst electrodes.**
25. Gancs, L., Kobayashi, T., Debe, M. K., Atanasoski, R. & Wieckowski, A. Crystallographic characteristics of nanostructured thin film fuel cell electrocatalysts—a HRTEM study. *Chem. Mater.* **20,** 2444–2454 (2008).
26. van. der Vliet, D. *et al.* Platinum-alloy nanostructured thin film catalysts for the oxygen reduction reaction. *Electrochim. Acta* **56,** 8695–8699 (2011).
27. Debe, M. K., Schmoeckel, A. K., Vernstrom, G. D. & Atanasoski, R. High voltage stability of nanostructured thin film catalysts for PEM fuel cells. *J. Power Sources* **161,** 1002–1011 (2006).
28. Debe, M. K., Steinbach, A. J. & Noda, K. Stop-start and high-current durability testing of nanostructured thin film catalysts for PEM fuel cells. *ECS Trans.* **3,** 835–853 (2006).
29. Debe, M. K. *et al.* Durability aspects of nanostructured thin film catalysts for PEM fuel cells. *ECS Trans.* **1,** 51–56 (2006).
30. Debe, M. K. *et al.* in *Proc. 50th Annual Technical Conference of the Society of Vacuum Coaters* 175–185 (The Society of Vacuum Coaters, 2006).
31. Haugen, G., Barta, S., Emery, M., Hamrock, S. & Yandrasits, M. in *Fuel Cell Chemistry and Operation* (eds Herring, A. M., Zawodzinski Jr., T. A. & Hamrock, S. J.) 137 (ACS Symposium Series 1040, 2010).
32. Steinbach, A. *et al.* Influence of anode GDL on PEMFC ultra-thin electrode water management at low temperatures. *ECS Trans.* **41,** 449–457 (2011).

33. Debe, M. K. *et al.* Extraordinary oxygen reduction activity of $Pt_3Ni$. *J. Electrochem. Soc.* **158,** B910–B918 (2011).
34. Park, S. *et al.* Polarization losses under accelerated stress test using multiwalled carbon nanotube supported Pt catalyst in PEM fuel cells. *J. Electrochem. Soc.* **158,** B297–B302 (2011).
35. Wang, S., Jiang, S. P., White, T. J. & Wang, X. Synthesis of Pt and Pd nanosheaths on multi-walled carbon nanotubes as potential electrocatalysts of low temperature fuel cells. *Electrochim. Acta* **55,** 7652–7658 (2010).
36. Yang, R., Leisch, J., Strasser, P. & Toney, M. F. Structure of dealloyed $PtCu_3$ thin films and catalyst activity for oxygen reduction. *Chem. Mater.* **22,** 4712–4720 (2010).
37. Erlebacher, J. & Snyder, J. Dealloyed nanoporous metals for PEM fuel cell catalysis. *ECS Trans.* **25,** 603–612 (2009).
38. Erlebacher, J., Aziz, M., Karma, A., Dimitrov, N. & Sieradzki, K. Evolution of nanoporosity in dealloying. *Nature* **410,** 450–453 (2001).
39. Moffat, T. P., Mallett, J. J. & Hwang, S.-M. Oxygen reduction kinetics on electrodeposited $Pt_{100-x}Ni_x$, and $Pt_{100-x}Co_x$. *J. Electrochem. Soc.* **156,** B238–B251 (2009).
40. Imbeault, R., Antonio, P., Garbarino, S. & Guay, D. Oxygen reduction kinetics on $Pt_xNi_{100-x}$ thin films prepared by pulsed laser deposition. *J. Electrochem. Soc.* **157,** B1051–B1058 (2010).
41. Ralph, T. R. & Hogarth, M. P. Catalysis for low temperature fuel cells. *Platin. Met. Rev.* **46,** 3–14 (2002).
42. Schulenburg, H. *et al.* Heat-treated PtCo nanoparticles as oxygen reduction catalysts. *J. Phys. Chem. C* **113,** 4069–4077 (2009).
43. Thompsett, D. in *Handbook of Fuel Cells—Fundamentals, Technology and Applications* (eds Vielstich, W., Lamm, A. & Gasteiger, H. A.) Ch. 37 (John Wiley & Sons, 2003).
44. Wagner, F. T. Automotive Challenges and Opportunities for Oxygen Reduction Catalysts. In *First CARISMA Intl Conf.* (La Grande Motte, France, 23 September 2008).
45. Wang, C. *et al.* Monodisperse $Pt_3Co$ nanoparticles as electrocatalyst: the effects of particle size and pretreatment on electrocatalytic reduction of oxygen. *Phys. Chem. Chem. Phys.* **12,** 6933–6939 (2010).
46. Wu, J. B. *et al.* Truncated octahedral $Pt_3Ni$ ORR electrocatalysts. *J. Am. Chem. Soc.* **132,** 4984–4985 (2010).
47. Zhang, J., Yang, H., Fang, J. & Zou, S. Synthesis and oxygen reduction activity of shape-controlled $Pt_3Ni$ nanopolyhedra. *Nano Lett.* **10,** 638–644 (2010).
48. Lim, B. *et al.* Pd-Pt bimetallic nanodendrites with high activity for oxygen reduction. *Science* **324,** 1302–1305 (2009).
49. Gasteiger, H. A. & Markovic, N. M. Just a dream—or future reality? *Science* **324,** 48–49 (2009).
50. Wang, C. *et al.* Monodisperse $Pt_3Co$ nanoparticles as a catalyst for the oxygen reduction reaction: size-dependent activity. *J. Phys. Chem. C* **113,** 19365–19368 (2009).
51. Wang, C. *et al.* Correlation between surface chemistry and electrocatalytic properties of monodispersed $Pt_xNi_{1-x}$ nanoparticles. *Adv. Funct. Mater.* **21,** 147–152 (2011).
52. Markovic, N. Nanosegregated cathode catalysts with ultra-low platinum loading. In *2010 DOE Hydrogen Program Annual Merit Review* FC-006, http://www.hydrogen.energy.gov/pdfs/review10/fc008_markovic_2010_o_web.pdf (2011).
53. Shao, M., Sasaki, K., Marinkivic, N. S., Zhang, L. & Adzic, R. R. Synthesis and characterization of platinum monolayer oxygen-reduction electrocatalysts with Co-Pd core-shell nanoparticle supports. *Electrochem. Commun.* **9,** 2848–2853 (2007).
54. Bliznakov, S. T., Vukmirovic, M. B., Yang, L., Sutter, E. A. & Adzic, R. R. Pt monolayer on electrodeposited Pd nanostructures—advanced cathode catalysts for PEM fuel cells. *ECS Trans.* **41,** 1055 (2011).
55. Vukmirovic, M. B. *et al.* Platinum monolayer electrocatalysts for oxygen reduction. *Electrochim. Acta* **52,** 2257–2263 (2007).
56. Shao, M. H., Sasaki, K., Lui, P. & Adzic, R. R. $Pd_3Fe$ and Pt monolayer $Pd_3Fe$ electrocatalysts for oxygen reduction. *Z. Phys. Chem.* **221,** 1175–1190 (2007).
57. Zhang, J. *et al.* Platinum monolayer electrocatalysts for $O_2$ reduction: Pt monolayer on Pd(111) and on carbon-supported Pd nanoparticles. *J. Phys. Chem. B* **108,** 10955–10964 (2004).
58. Russell, A. E. *et al.* In situ XAS studies of core-shell PEM fuel cell catalysts: the opportunities and challenges. *ECS Trans.* **41,** 55–67 (2011).
59. Haug, A. *et al.* Stability of a Pt-Pd core-shell catalyst: a comparative fuel cell and RDE study. *218th ECS Meeting* abstr. 743 (The Electrochemical Society, 2010).
60. Knupp, S. L. *et al.* Platinum monolayer electrocatalysts for $O_2$ reduction: Pt monolayer on carbon-supported PdIr Nanoparticles. *Electrocatalysis* **1,** 213–223 (2010).
61. Xing, Y. *et al.* Enhancing oxygen reduction reaction activity via Pd-Au alloy sublayer mediation of Pt monolayer electrocatalysts. *J. Phys. Chem. Lett.* **1,** 3238–3242 (2010).
62. Wang, J. X. *et al.* Oxygen reduction on well-defined core-shell nanocatalysts: particle size, facet and Pt shell thickness effects. *J. Am. Chem. Soc.* **131,** 17298–17302 (2009).
**This is an exemplary paper in a long series by the Adzic group developing core–shell nanoparticle catalysts having Pt monolayer skins, controlled size and surface facets.**
63. Gong, K., Su, D. & Adzic, R. Platinum-monolayer shell on $AuNi_{0.5}Fe$ nanoparticle core electrocatalyst with high activity and stability for the oxygen reduction reaction. *J. Am. Chem. Soc.* **132,** 14364–14366 (2010).
64. Ball, S. *et al.* Structure and activity of novel Pt core-shell catalysts for the oxygen reduction reaction. *ECS Trans.* **25,** 1023–1036 (2009).
65. Korovina, A., Garsany, Y., Epshteyn, A., Swider-Lyons, K. E. & Ramaker, D. E. Insight into oxygen reduction on platinum-tantalum oxyphosphate electrocatalysts. *218th ECS Meeting* abstr. 687 (The Electrochemical Society, 2010).
66. Park, S. *et al.* Polarization losses under accelerated stress test using multiwalled carbon nanotube supported Pt catalyst in PEM fuel cells. *J. Electrochem. Soc.* **158,** B297–B302 (2011).
67. Wang, X., Waje, M. & Yan, Y. CNT-based electrodes with high efficiency for PEMFCs. *Electrochem. Solid-State Lett.* **8,** A42–A44 (2005).
68. Chen, Z., Waje, M., Li, W. & Yan, Y. Supportless Pt and PtPd nanotubes as electrocatalysts for oxygen-reduction reactions. *Angew. Chem. Int. Edn* **46,** 4060–4063 (2007).
69. van der Vliet, D. *et al.* Metallic nanotubes with tunable composition and structure as advanced electrocatalysts. *Nature Mater.* (submitted).
70. Zhou, H., Zhou, W.-P., Adzic, R. & Wong, S. S. Enhanced electrocatalytic performance of one-dimensional metal nanowires and arrays generated via an ambient surfactantless synthesis. *J. Phys. Chem. C* **113,** 5460–5466 (2009).
71. Adzic, R. Contiguous platinum monolayer oxygen reduction electrocatalysts on high-stability-low-cost supports. In *2011 DOE Hydrogen Program Annual Merit Review* FC-009, http://www.hydrogen.energy.gov/pdfs/review11/fc009_adzic_2011_o.pdf (2011).
72. Shao, M. Palladium-based electrocatalysts for hydrogen oxidation and oxygen reduction reactions. *J. Power Sources* **196,** 2433–2444 (2011).
73. Myers, D. Non-platinum bimetallic cathode electrocatalysts. In *2008–2010 DOE Hydrogen Program Annual Merit Reviews* http://www.hydrogen.energy.gov/pdfs/review10/fc004_myers_2010_o_web.pdf (2010).
74. Atanasoski, R. & Dodelet, J.-P. in *Encyclopedia of Electrochemical Power Sources* (eds Garche, J. *et al.*) Vol. 2 639–649 (Elsevier, 2009).
75. Lei, M., Li, P. G., Li, L. H. & Tang, W. H. A highly ordered Fe-N-C nanoarray as a non-precious oxygen-reduction catalyst for proton exchange membrane fuel cells. *J. Power Sources* **196,** 3548–3552 (2011).
76. Wang, S., Yu, D. & Dai, L. Polyelectrolyte functionalized carbon nanotubes as efficient metal-free electrocatalysts for oxygen reduction. *J. Am. Chem. Soc.* **133,** 5182–5185 (2011).
77. Zelenay, P. Advanced cathode catalysts. In *2010 DOE Hydrogen Program Annual Merit Review*, http://www.hydrogen.energy.gov/pdfs/review10/fc005_zelenay_2010_o_web.pdf (2010).
78. Ishihara, A., Ohgi, Y., Matsuzawa, K., Mitsushima, S. & Ota, K. Progress in non-precious metal oxide-based cathode for polymer electrolyte fuel cells. *Electrochim. Acta* **55,** 8005–8012 (2010).
79. Lefevre, M., Proietti, E., Jaouen, F. & Dodelet, J.-P. Iron-based catalysts with improved oxygen reduction activity in polymer electrolyte fuel cells. *Science* **324,** 71–74 (2009).
80. Bashyam, R. & Zelenay, P. A class of non-precious metal composite catalysts for fuel cells. *Nature* **443,** 63–66 (2006).
81. Proietti, E. *et al.* Iron-based cathode catalyst with enhanced power density in polymer electrolyte membrane fuel cells. *Nature Commun.* **2,** 416 (2011).
**This paper is the latest in a long series by these authors that show an amazing rate of improvement in non-precious metal catalysts' beginning-of-life performances under pure oxygen.**
82. Wood, T. E., Tan, Z., Schmoeckel, A. K., O'Neill, D. & Atanasoski, R. Non-precious metal oxygen reduction catalyst for PEM fuel cells based on nitroaniline precursor. *J. Power Sources* **178,** 510–516 (2008).
83. Wu, G., More, K. L., Johnston, C. M. & Zelenay, P. High-Performance electrocatalysts for oxygen reduction derived from polyaniline, iron and cobalt. *Science* **332,** 443–447 (2011).
84. Global *and China Low-E Glass Industry Report* http://pressexposure.com/Global_and_China_Low-E_Glass_Industry_Report,_2010_-_Published_by_ResearchInChina-205310.html (ResearchInChina, 2010).
85. Chen, S., Gasteiger, H. A., Hayakawa, K., Tada, T. & Shao-Horn, Y. Platinum-alloy cathode catalyst degradation in proton exchange membrane fuel cells: nanometer-scale compositional and morphological changes. *J. Electrochem. Soc.* **157,** A82–A97 (2010).
86. Kongkanand, A., Liu, Z., Dutta, I. & Wagner, F. T. Electrochemical and microstructural evaluation of aged nanostructured thin film fuel cell electrocatalyst. *J. Electrochem. Soc.* **158,** B1286–B1291 (2011).
87. Wagner, F. T. *et al.* Catalyst development needs and pathways for automotive PEM fuel cells. *ECS Trans.* **3,** 19 (2006).
88. Koh, S., Hahn, N., Yu, C. & Strasser, P. Effects of composition and annealing conditions on catalytic activities of dealloyed Pt-Cu nanoparticle electrocatalysts for PEMFC. *J. Electrochem. Soc.* **155,** B1281–B1288 (2008).
89. Oezaslan, M., Hasche, F. & Strasser, P. Structure-activity relationship of dealloyed $PtCo_3$ and $PtCu_3$ nanoparticle electrocatalyst for oxygen reduction reaction in PEMFC. *ECS Trans.* **33,** 333–341 (2010).
90. Strasser, P., Hahn, N. T. & Koh, S. Corrosion and ORR activity of Pt alloy electrocatalysts during voltammetric pretreatment. *ECS Trans.* **3,** 139–149 (2006).
91. Mani, P., Srivastava, R. & Strasser, P. Dealloyed binary $PtM_3$ (M = Cu, Co, Ni) and ternary $PtNi_3M$ (M = Cu, Co, Fe, Cr) electrocatalysts for the oxygen reduction reaction: performance in polymer electrolyte membrane fuel cells. *J. Power Sources* **196,** 666–673 (2011).
92. Neyerlin, K. C., Srivastava, R., Yu, C. & Strasser, P. Electrochemical activity and stability of dealloyed Pt-Cu and Pt-Cu-Co electrocatalysts for the oxygen reduction reaction (ORR). *J. Power Sources* **186,** 261–267 (2009).
93. Wagner, F. T. High-activity dealloyed catalysts. *2011 DOE Hydrogen Program Annual Merit Review* FC-087, http://www.hydrogen.energy.gov/pdfs/review11/fc087_wagner_2011_o.pdf (2011).

94. Strasser, P. *et al.* Lattice-strain control of the activity in dealloyed core-shell fuel cell catalysts. *Nature Chem.* **2,** 454–460 (2010).
95. Snyder, J., Fujita, T., Chen, M. W. & Erlebacher, J. Oxygen reduction in nanoporous metal-ionic liquid composite electrocatalysts. *Nature Mater.* **9,** 904–907 (2010).
**This paper shows that porosity on the nanometre scale can be controlled in Ni/Pt alloys, describes the spontaneous formation of core/shell catalysts during de-alloying and illustrates a new concept for enhancing the activity of solid surfaces in contact with ionic liquids.**
96. Erlebacher, J. & Seshardi, R. Hard materials with tunable porosity. *MRS Bull.* **34,** 561–568 (2009).
97. Snyder, J. & Erlebacher, J. The active surface area of nanoporous metals during oxygen reduction. *ECS Trans.* **41,** 1021–1030 (2011).

**Acknowledgements** I gratefully acknowledge support by the Fuel Cell Technologies Program in the Office of Energy Efficiency and Renewable Energy at the US Department of Energy, for grant DE-FG36-07GO17007.

**Author Information** Reprints and permissions information is available at www.nature.com/reprints. The author declares no competing financial interests. Readers are welcome to comment on the online version of this article at www.nature.com/nature. Correspondence and requests for materials should be addressed to the author (mkdebe1@mmm.com).

*Journal of The Electrochemical Society*, **158** (8) B919-B926 (2011)
0013-4651/2011/158(8)/B919/8/$28.00 © The Electrochemical Society


# Oxygen Reduction Activity of Dealloyed $Pt_{1-x}Ni_x$ Catalysts

**Gary Chih-Kang Liu,[a] D. A. Stevens,[a,*] J. C. Burns,[a,**] R. J. Sanderson,[a] George Vernstrom,[b,*] R. T. Atanasoski,[b,*] M. K. Debe,[b,*] and J. R. Dahn[a,*,z]**

[a]*Department of Physics and Atmospheric Science, Dalhousie University, Halifax, Nova Scotia, Canada B3H 3J5*
[b]*3M Fuel Cell Components Program, 3M Co., St. Paul, Minnesota 55144-1000*

Pt and intermixed $Pt_{1-x}Ni_x$ ($0.65 < x < 0.75$) catalysts were sputtered-deposited onto both bare and nanostructured thin film (NSTF)-coated glassy carbon disks. The oxygen reduction reaction (ORR) activities of the disks were determined from Rotating Disk Electrode (RDE) measurements. Experiments on the NTSF-coated disks examined both catalytic activities and the effects of high surface area supports in a single measurement. The RDE measurement protocols were designed to examine changes in catalyst properties and performance during de-alloying and thus did not include the typical "electrochemical cleaning" procedure at the beginning. Instead, a continuous CV-ORR measurement protocol was used to monitor the electrochemical performance indicators such as active surface area (SEF) and ORR kinetic current density of the catalysts over the course of 9 h. As an example, the SEF of $Pt_{25}Ni_{75}$ on the NSTF-support was initially 20 $cm^2_{Pt}/cm^2_{planar}$ and the SEF increased rapidly at the beginning of the experiment, then stabilized near ~50 $cm^2/cm^2$ as Ni de-alloyed. This is compared with sputtered Pt on NSTF support that showed SEF ~15 $cm^2/cm^2$. De-alloying is an effective way to create Pt-transition metal catalysts on NSTF with extremely high active surface area.
 [DOI: 10.1149/1.3595749] 

Manuscript submitted January 25, 2011; revised manuscript received March 17, 2011. Published June 8, 2011. This was Paper 690 presented at the Las Vegas, Nevada, Meeting of the Society, October 10–15, 2010.

The development of cost-effective electrocatalysts for the oxygen reduction reaction (ORR) with adequate activity and durability when integrated into proton exchange membrane fuel cell (PEMFC) membrane electrode assemblies for application in commercialized fuel cell vehicles after 2015 remains a key challenge.[1–3] Currently, Pt and Pt-alloys are catalysts of choice for the PEMFC cathode, where oxygen is reduced to water. Approaches used reduce catalyst cost and improve durability include: improving catalytic efficiency and lowering the overall Pt content by alloying Pt with other metals,[4,5] improving catalyst high voltage cycling resistance, impurity tolerance, and catalyst support corrosion tolerance. Until recently, studies of Pt-M alloys have typically focused on low M content alloys, such as $Pt_3Co$, $Pt_3Ni$, that showed improved ORR activities in the fuel cell environment,[6–9] Recent results for dealloyed, high M (e.g. M = Cu, Co) content catalysts have been very promising in terms of the activity gains seen or predicted.[10–13]

Dealloying refers to the partial, selective dissolution of less noble component(s) of a binary or ternary alloy precursor, resulting in a noble-enriched, porous structure that has high surface area.[14–16] Dealloyed Pt nanoparticle electrocatalysts have been reported by other groups to be highly active for ORR in acidic media.[10–13] When a high M content Pt-M (M = Cu, Co) alloy precursor is placed in a corrosive environment, the less noble element(s) from the surface and near-surface typically dissolves away, leaving behind a porous Pt-rich structure that has high surface area and high ORR catalytic activity. It has also been suggested that the high catalytic activity of dealloyed Pt-M catalysts results from a combination of both increased surface area and lattice strain between the Pt-rich shell and M-rich core.[12,17,18] Dealloyed Pt-Cu nanoparticles showed a core-shell structure after dealloying, with a Pt-rich shell and a Pt-Cu alloy core. The interatomic distance of Pt in the Pt-rich shell was found to be smaller than expected based on the chemical composition of the shell, suggesting the presence of a compressive strain that helped to enhance ORR activity.[12] Prior to dealloying, the PtM precursor would have had relatively low catalytic activity; as dealloying occurred, its electrochemical active surface area (ECSA) and specific ORR catalytic current density ($mA/cm^2_{catalyst}$) would have increased. This transient behavior can be monitored by electrochemical techniques such as testing of membrane electrode assemblies (MEAs) in fuel cells or testing of catalyst-coated disks with rotating disk electrode (RDE) techniques.

Traditionally, RDE measurements of sputtered thin Pt or Pt alloy films have been performed on mirror-polished glassy carbon (GC) disks.[19–21] In recent years, authors at Dalhousie University have been using a high surface area catalyst support grown on RDE disks,[22] namely 3M Company's nanostructured thin film (NSTF) support. NSTF substrates are self-assembled, organic, nano-structured "whisker" films produced by thermal vacuum deposition and subsequent annealing.[23–25] NSTF-supported catalysts are much less susceptible to support degradation even under transient, high potential excursions and allow for the use of low catalyst loadings while still maintaining high fuel cell current densities. Pt deposited onto NSTF support whiskers forms nanometer-sized whiskerettes and exhibits area-specific ORR kinetics very close to that of bulk polycrystalline Pt (Refs. 25–27) in a fuel cell MEA. In previous studies, the NSTF support was grown directly on the glassy carbon disk surface forming a support for sputter deposition of catalysts of interest. Post-RDE examination of the catalyst-support material by scanning electron microscope (SEM) showed the sputtered catalyst material remained intact on the NSTF whiskers after hours of RDE measurements. Electrochemical measurements of the catalyst supported on the NSTF-coated GC disks also demonstrated the impact of the NSTF surface roughening effect, and allowed for determination of the kinetic catalytic activity of different catalyst compositions.[22] NSTF-coated GC disks are a preferable alternative to mirror-polished GC disks because both the catalytic activity and the effects of the high surface area support can be examined in a single measurement. The material being measured has the same morphology, composition and surface structure as the material that would be used in a PEMFC, making NSTF-coated GC disks an ideal substrate for examining catalyst dealloying.

In this paper, Pt and $Pt_{1-x}Ni_x$ ($0.65 < x < 0.75$) were sputtered-deposited onto both bare and NSTF-coated GC disks. The $Pt_{1-x}Ni_x$ disks were produced by depositing intermixed Pt and Ni onto the substrate. On the mirror-polished disks, this produced relatively thick (on the order of 100–200 nm) intermixed $Pt_{1-x}Ni_x$ films. On NSTF-coated disks, the deposited layer thickness was lowered by a factor of 10–15 due to the large roughness factor introduced by the NSTF. The ORR activities of the disks were determined with RDE methods. The RDE measurement protocols were tailored to examine performance changes of the catalysts during dealloying and thus did not include an "electrochemical cleaning" procedure at the beginning of the experiment. Electrochemical cleaning in RDE experiments typically involves running multiple high rate potential cycles (typically 100–500 mV/s) in an inert gas saturated electrolyte. In this work it was important to avoid this electrochemical cleaning because the dealloying process may have commenced immediately

* Electrochemical Society Active Member.
** Electrochemical Society Student Member.
z E-mail: Jeff.Dahn@Dal.Ca

after the catalyst was exposed to acidic electrolyte in the RDE cell. Electrochemical cleaning would accelerate this process and prevent an accurate assessment of the impact of dealloying on performance. This cleaning step was therefore eliminated and cyclic voltammetry (CV) data in Ar saturated electrolyte (to determine the catalytic ECSA) and then ORR activity data in $O_2$ saturated electrolyte were collected as soon as the electrode tip was placed into the RDE cell. These CV/ORR tests were then repeated continuously for up to 9 h. The data from each CV-ORR test block were then analyzed and compared, in order to track the changes in ECSA and ORR current densities over the course of the experiment. This RDE protocol aimed to capture the catalytic performance of the $Pt_{1-x}Ni_x$ samples during dealloying. This paper discusses the trends in catalyst performance as a function of Ni content in $Pt_{1-x}Ni_x$ ($0.65 < x < 0.75$).

## Experimental

*Preparation of NSTF-coated GC disks.*—Details of NSTF whisker growth on arbitrary substrates can be found elsewhere.[25,26] GC disks, 5 mm in diameter (Tokai Carbon) were polished to produce a mirror-like surface before the NSTF support was grown on the polished and cleaned surface.[22]

*Sputtering of Pt-Ni catalysts.*—The catalysts were deposited on both mirror-polished and NSTF-coated GC disks with a Corona Vacuum Coaters V3T multi-target magnetron sputtering machine. Detailed information about this apparatus and its operation can be found elsewhere.[28,29] During deposition, the chamber pressure was kept at 0.85 mTorr with an argon flow rate of 3 sccm and substrates were mounted on a rotating table. The sputtering targets (Pt and Ni) were covered with different masks to control the deposition profiles. A "constant" mask was placed over the platinum target to deposit a constant amount (0.16 mg/cm$^2$) across the substrates mounted on the rotating substrate table. In order to deposit a high nickel content and to produce a linear gradient of $Pt_{1-x}Ni_x$ ($0.6 < x < 0.8$), two nickel targets were used. The first nickel target was covered with a "constant" mask in order to deposit a constant loading of 0.14 mg/cm$^2$ across each substrate. The second nickel target was covered with a "linear out" mask to deposit a linear gradient of nickel (0–0.04 mg/cm$^2$) across the sputtering track. Together, the two nickel targets were set to deposit a linear gradient of 0.14–0.18 mg/cm$^2$ nickel across the sputtered region. During deposition, the Pt and Ni targets were turned on at the same time. The substrate table rotated past each of the targets sequentially and this was repeated many times in order to ensure close to atomic level mixing of the deposited elements would occur on a flat substrate. On a rough substrate like NSTF, an even higher level of atomic mixing is achieved. The overall bulk composition ranged linearly from $Pt_{65}Ni_{35}$ to $Pt_{75}Ni_{25}$.

*Catalyst film composition.*—Figure 1 shows the composition of the sputtered catalyst film measured by different techniques. The mass of material deposited, shown in Fig. 1a, was determined by weighing preweighed aluminum disks placed along the sputtering track after deposition. Figure 1a shows mass data for two sputtered films; the first set of data was from the $Pt_{1-x}Ni_x$ intermix as described above, the second set of data was from a constant Pt film sputtered under identical conditions, resulting in a constant mass profile (0.16 mg/cm$^2$). The mass profile of $Pt_{1-x}Ni_x$ increased linearly (from 0.3 to 0.35 mg/cm$^2$) along the sputtered track due to increasing Ni content. The atomic fraction of Ni (x in $Pt_{1-x}Ni_x$) in the $Pt_{1-x}Ni_x$ composition spread calculated from each mass measurement is shown in Fig. 1b with a dashed line. Figure 1b compares the Ni ratio calculated from the mass data with measurements made by a JEOL 8200 electron microprobe. Figure 1b also shows the location of RDE disks positioned along the sputtering region as labeled circles. The Ni content increased from $x = 0.65$ (RDE disk number 1) to $x = 0.75$ (RDE disk number 5) along the sputtering track.

*Electrochemical measurements by RDE.*—All of the RDE measurements were performed using Pine electrochemical systems in a

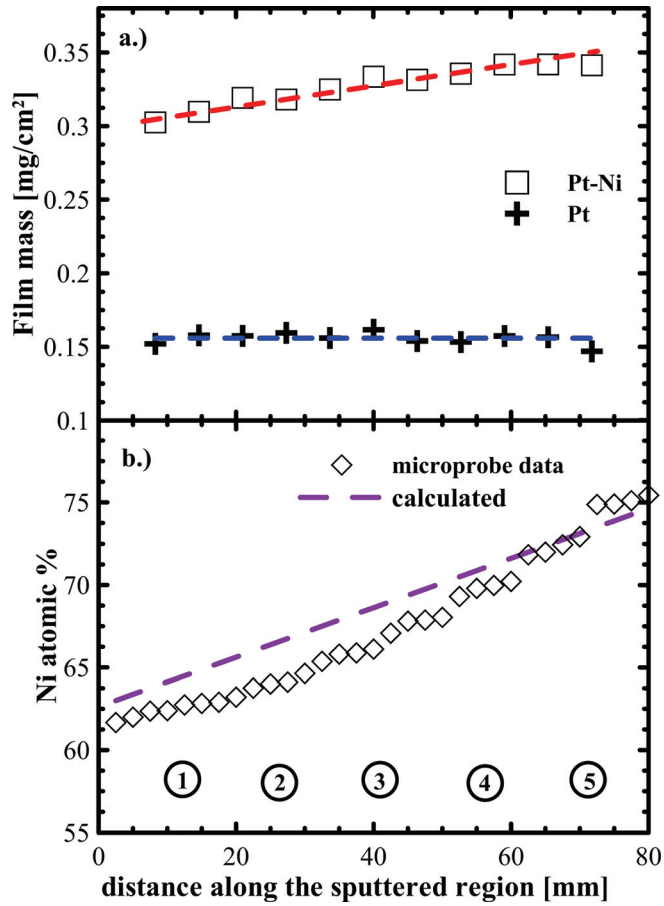


**Figure 1.** (Color online) Composition of sputtered Pt-Ni catalyst measured by mass (part a) and microprobe (part b), the circles at the bottom shows the locations of the RDE disks.

3-electrode solution cell. Details of the setup can be found elsewhere.[19,22] Pt wire was used for the counter electrode and a $Cl^-$ free Koslow mercury/mercurous sulfate electrode was used for the reference electrodes. These working, reference and counter electrodes were all placed in a 125 ml glass cell filled with 0.1 M $HClO_4$ electrolyte. The electrolyte was prepared from double distilled stock solution from GFS Chemical and 18 MΩ nano-pure water from a Barnstead NANOpure Diamond system. The potential of the $Hg/Hg_2SO_4$ reference electrode was calibrated for each catalyst material tested by determining the potential at which the current reached 0 mA/cm$^2$ in $H_2$-saturated electrolyte. All of the potentials quoted in this paper are values relative to the RHE calibration potentials measured. All measurements were carried out at ambient temperature. A homemade mounting device was used to facilitate mounting and alignment of the NSTF-coated disks into the RDE tip while minimizing damage to the catalyst-coated NSTF surface.[22] The device was fabricated from polyetherimide (Ultem 1000); it mounts and aligns the disk into the RDE tip in three steps. The first step latches the disk into the U-Cup, the second step secures the U-Cup (with disk inside) to the RDE tip and the third step aligns the disk and U-Cup with the RDE tip. In all three steps, the disk surface only makes contact with the device at the extreme outer rim; minimizing any damage to the sample.

*Large active surface area and IR-correction.*—The electrochemically active surface area (ECSA) of the samples was estimated by numerically integrating the charge in the $H^+_{des\ Ar-CV}$ region of the CVs taken under Ar-purged cell conditions and using the 210 $\mu$C/cm$^2$ conversion factor commonly used for the charge corresponding to a 1:1 coverage of polycrystalline Pt with adsorbed H atoms.[1] For each sample, the surface enhancement factor (SEF) is

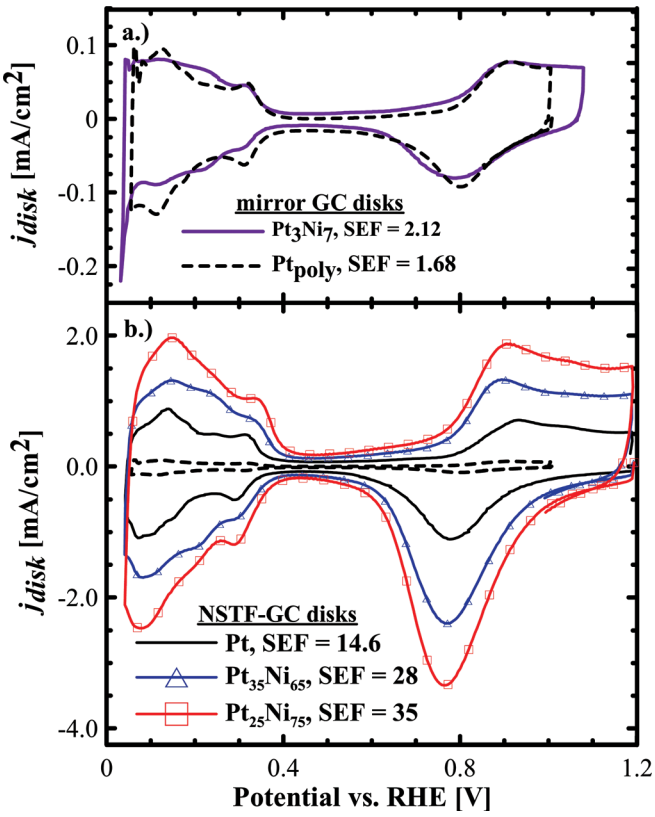


**Figure 2.** (Color online) CV of catalyst on planar GC disk surface (a) and NSTF-coated GC disk surface (b) in Argon saturated electrolyte.

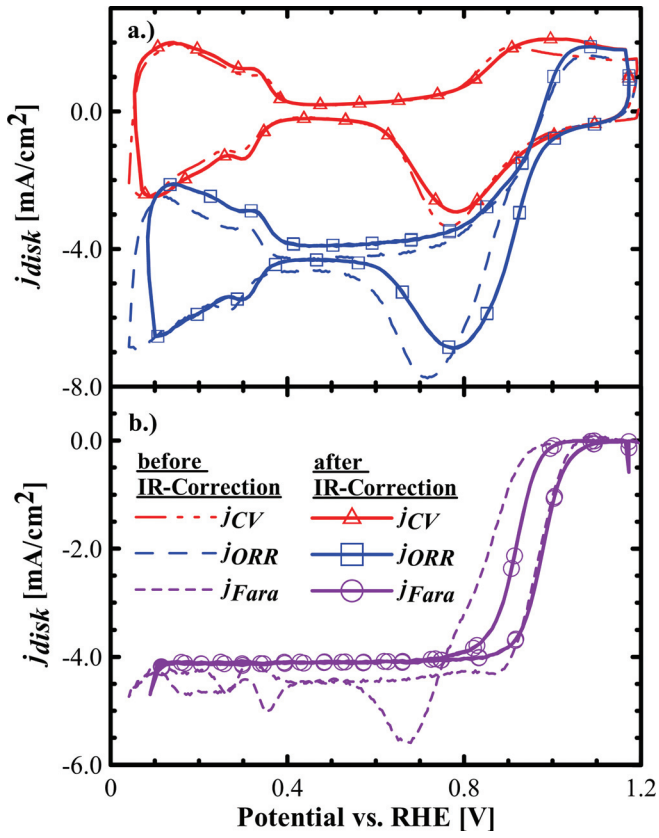


**Figure 3.** (Color online) Measured Ar CV and ORR curves before (dashed lines) and after (solid lines) IR correction shown in a). Faradaic current before (dashed lines) and after (solid lines) IR-correction shown in b).

the ratio of its ECSA to the planar surface area. CVs of selected samples are shown in Fig. 2a (mirror-polished disks) and Figure 2b (NSTF-coated disks). All of the samples were measured at 50 mV/s between 50 and 1200 $mV_{RHE}$ in Ar and $O_2$ saturated solutions. The SEF value determined for the polycrystalline Pt disk electrode was 1.68 $cm^2_{Pt}/cm^2_{planar}$ (shown by the dashed line in Fig. 2a) while the sputtered $Pt_3Ni_7$ film on a mirror-polished GC disk had a SEF value around 2.0 $cm^2_{Pt}/cm^2_{planar}$ (solid line). Figure 2b compares the CVs of the sputtered Pt and selected $Pt_{1-x}Ni_x$ samples on NSTF-coated GC disks. The SEF value of Pt sputtered on a NSTF-coated GC disk was 14.6 $cm^2_{Pt}/cm^2_{planar}$. This is consistent with previous data that showed the surface area on an NSTF substrate is about 14–15 times higher than the planar area.[25,26] Figure 2b also includes data for some of the $Pt_{1-x}Ni_x$ samples that showed much higher SEF values than sputtered Pt, with, for example, $Pt_{35}Ni_{65}$ showing ~28 $cm^2_{Pt}/cm^2_{planar}$ and $Pt_{25}Ni_{75}$ showing ~35 $cm^2_{Pt}/cm^2_{planar}$.

The measured current density (current per planar $cm^2$ of the electrode area) for an ORR experiment contains the ORR current density, $j_{ORR}$, a faradaic process, and both surface double layer charging and H-adsorption/desorption current densities, $j_{CV}$, which are non-faradaic processes. The faradaic current density of interest, $j_{fara}$, is therefore determined by subtracting the non-faradaic contribution (measured with Ar CVs) from the total current density.

$$j_{fara} = j_{ORR} - j_{CV} \quad [1]$$

Mass transport limitations in the RRDE experiment restrict the current density that can be measured. The impact of the boundary-layer diffusion-limited current density, $j_{diff}$, on the true kinetic ORR current measured per planar surface area, $j_{planar}$, can be removed through use of the Levich relation [1]

$$j_{planar} = (j_{fara} \times j_{diff}) / (j_{diff} - j_{fara}) \quad [2]$$

The mass transfer limited current density, $j_{diff}$, was read directly from the ORR ($j_{fara}$ vs. $V_{RHE}$) data for each corresponding rotation speed. The value of the current in the middle of the mass-transfer plateau was chosen as the mass-transfer limited current and was very close to the diffusion-limited current expected from a Koutecky-Levich analysis.[1] Finally, the kinetic current density, $j_{planar}$, was divided by the SEF to obtain the specific current density, $j_{specific}$

$$j_{specific} = j_{planar} / SEF \quad [3]$$

It is also important to take into account the resistance from the 0.1 M $HClO_4$ solution cell and its effect on the CV and ORR measurements.[30] The high current from NSTF-supported samples, together with the cell resistance, causes the potential of voltammetric features to shift during measurement. The potential shift is current dependent. IR correction of the measured data needs to be performed to ensure reliable determination of the faradaic ORR current density. Figure 3a shows the Ar CV and ORR data for $Pt_{35}Ni_{65}$ deposited on NSTF-coated GC disks before (dashed lines) and after (solid lines) IR-correction. Figure 3b shows the Faradaic current of the ORR measurement from the same material before (dashed line) and after (solid line) IR-correction. The impact of the ohmic contribution to the Faradaic current calculation is shown in Fig. 3b (dashed line). Instead of a flat, constant-current level, the diffusion-limited region of the Faradaic curve has multiple peaks. This is due to the misalignment of the potentials of the ORR and CV curves caused primarily by solution resistance in the RDE cell. IR-corrected Ar CV, ORR and Faradaic curves are shown in Fig. 3 as solid lines. After the IR-correction, there are small changes in the CV and ORR curves while the Faradaic curve shows a constant current level in the diffusion-limited region.

*Continuous CV-ORR measurement protocol.*—Traditionally, RDE measurements start with an electrochemical cleaning procedure

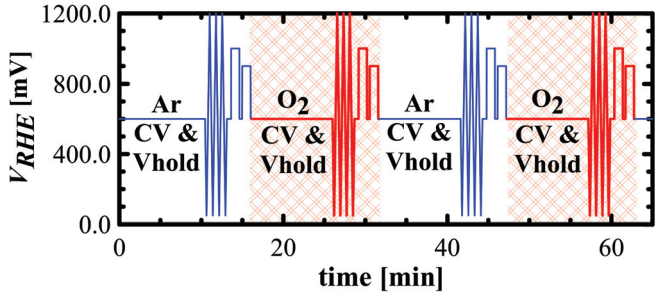


**Figure 4.** (Color online) Continuous RDE protocol has repeating Ar CV and ORR measurements with 10-min gas purges after switching gases.

that involves multiple cycles of fast (e.g. 500 mV/s) CVs over the same potential range of the measurements until a steady state voltammogram is obtained.[19–21] The data measured during the electrochemical cleaning procedures, if any, represents the transient behavior of the catalyst and are usually discarded. In this study, the authors are interested in the transient response of the sputtered catalysts to the Ar CV and ORR experiments prior to the steady state. In order to examine the transient behavior of the sputtered catalyst, the samples were examined through application of the continuous CV-ORR RDE protocol shown in Fig. 4. During an experiment, the catalyst supported on the NSTF-coated GC disks was mounted into the RDE tip and washed with warm nano-pure water before being placed in the RDE solution cell. Once in the cell, the electrode was first held at 600 $mV_{RHE}$ while Ar gas was continuously bubbling in the electrolyte for 10 min, as shown in Fig. 4. After the Ar purge, three 50 mV/s CV cycles were measured, followed by 1-min potential holds at 1000 and 900 $mV_{RHE}$ each. For each potential hold, the electrode was first held at 600 $mV_{RHE}$ for 10 s before stepping to the high potential for measurements. The purpose of a 600 $mV_{RHE}$ hold prior to the measurement is to electrochemically clean the catalyst surface. After the potential hold measurements in Ar-saturated electrolyte, the electrode potential was held at 600 $mV_{RHE}$ and the gas was changed to $O_2$ for a 10 min purge, shown in Fig. 4 by bold lines. After $O_2$ purging, the same CV and potential hold experiments were performed in the $O_2$-saturated cell, shown in Fig. 4 as bold lines and cross-hatched areas. After the $O_2$ measurements, the gas was changed back to argon and the "Ar purge-CV-Hold → $O_2$ purge-CV-Hold" test block was repeated many times. The data from this continuous CV-ORR testing protocol were then used to track SEF, $j_{planar}$, and $j_{specific}$ as a function of time for the catalyst materials of interest.

*XRD Characterisation.*—A Bruker D8 Discover diffractometer equipped with a Cu x-ray tube and an area detector was used to measure XRD data for a catalyst-coated NSTF-GC disk ex-situ during RDE testing. The electrode tip was removed from the electrolyte, dried for 5 min in a fan forced oven at 50°C and then installed upside down on the stage of the diffractometer. A low incident angle (6°) was used to irradiate about 1 $mm^2$ of the disk surface. Intensity vs. scattering angle data were collected between scattering angle of 30 and 55°, with the complete pattern recorded at 1 time. The detector counted for 900 s. After measurement, the electrode tip was returned to the RDE station for further CV-ORR cycling.

## Results and Discussions

Figure 5 shows selected CV and ORR curves for $Pt_{35}Ni_{65}$ sputtered onto a NSTF-coated GC disk. The figure also includes data for Pt sputtered on mirror-polished and NSTF-coated GC disks for comparison. The Pt control samples were measured with the same CV/ORR protocol described in the previous section. The data shown in Fig. 5 were corrected for RDE cell IR-drop as discussed earlier. Figure 5a shows that the CV curves for $Pt_{35}Ni_{65}$ had a larger hydrogen adsorption-desorption area than that of Pt on NSTF-coated GC disks (bold black line) at the beginning of the test protocol (test block #1,

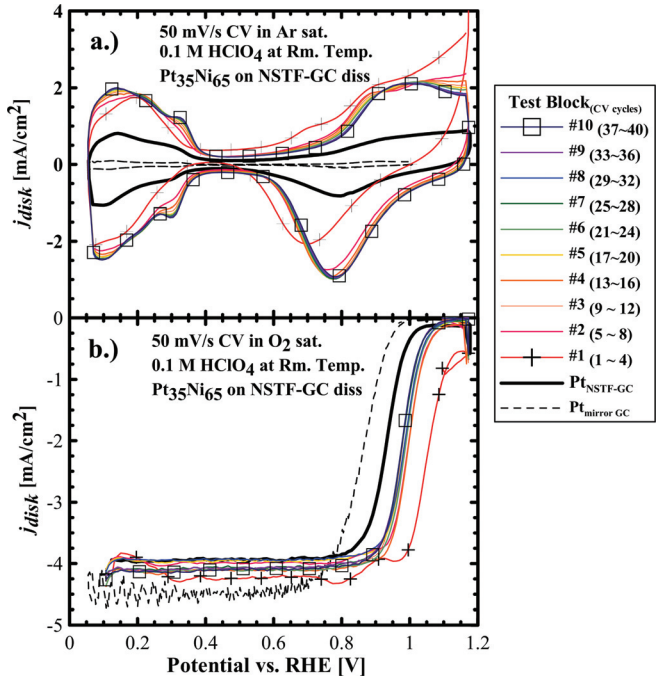


**Figure 5.** (Color online) Ar CV (a) and ORR (b) measurements from the continuous RDE protocol.

shown with crosses). As the experiment continued, the CV curves showed an apparent increase in the ECSA and voltammetric features appeared near 100 and 250 $mV_{RHE}$. Figure 5a also shows an apparent shift of the voltammetric onset associated with Pt-OH formation near 800 $mV_{RHE}$ during the anodic sweep. As the experiment progressed, the onset for Pt-$OH_{ads}$ formation shifted to a higher potential (see block 10 for example). This trend was apparent for all of the Pt-Ni samples measured by the continuous CV-ORR test protocol and will be discussed in more detail later.

Figure 5b shows selected ORR curves for $Pt_{35}Ni_{65}$ and Pt deposited on NSTF-coated GC disks. All ORR data were collected at 900 rpm with a sweep rate of 50 mV/s. All of the measurements shown reached the theoretical mass-transfer limited current which, according to the Levich equation, is ~4.5 mA/$cm^2$ for oxygen diffusion in 0.1 M $HClO_4$ electrolyte at room temperature and at 900 rpm. The onset potentials (the potential at which measurable current flow occurred) and half-wave potentials for catalysts from the same sputtering run deposited on flat surfaces were 50–100 mV lower than the onset and half-wave potentials of the catalysts sputtered onto NSTF-coated GC disks. The high onset and half-wave potentials measured for the NSTF-supported catalysts was in part caused by the high surface enhancement factor(SEF) of the NSTF substrate that was highlighted for Fig. 2. The Pt film sputtered on the mirror-polished disk had a SEF of ~1.8 $cm^2/cm^2$ and reached the diffusion-limited current level at ~0.75 $V_{RHE}$ while the NSTF-supported Pt had a SEF of ~14 $cm^2/cm^2$ and reached the diffusion-limited current level at ~0.85 $V_{RHE}$. Figure 5b also shows that $Pt_{35}Ni_{65}$ initially had a very high onset potential (in test block #1) and reached the diffusion-limited current level at ~1.0 $V_{RHE}$. The onset of the ORR curves shifted to a lower potential for the second test block and reached the diffusion-limited current level at ~0.95 $V_{RHE}$. The ORR half wave potential decreased slowly for the rest of the experiment (test block #3–#10).

The kinetic current densities of the Pt and $Pt_{35}Ni_{65}$ material supported on NSTF-coated GC disks shown in Fig. 5 were calculated and are plotted as Tafel-style graphs in Fig. 6. ORR activities of different catalysts in such Tafel plots are typically compared at potentials between 850 and 950 mV for thin film catalysts measured on flat surfaces as they have onset potentials near 900 mV and reached diffusion-limited currents near 800 mV. The NSTF-supported catalysts

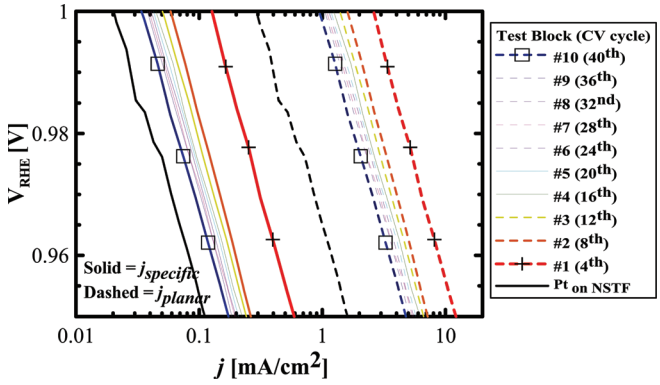


**Figure 6.** (Color online) Tafel plots of $Pt_3Ni_7$ catalyst compared with Pt on NSTF-coated GC disks. The dashed lines show planar current density data; the solid lines show the ORR performance per measured Pt area.

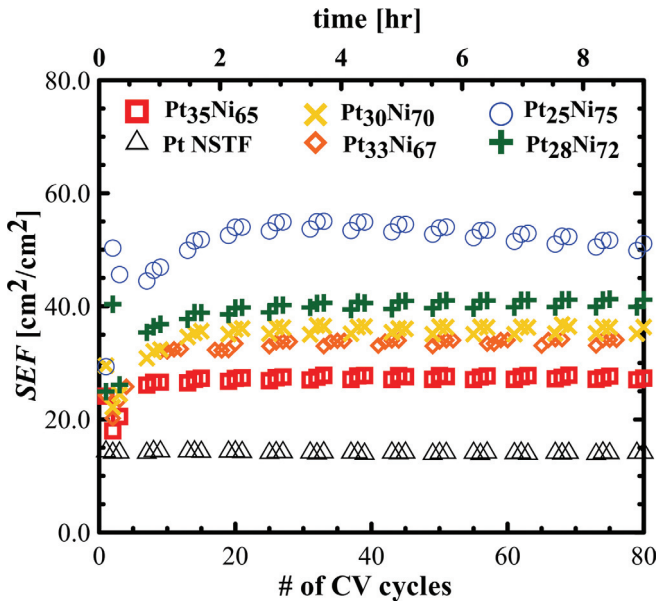


**Figure 7.** (Color online) SEF values of all Pt-Ni catalysts plotted as a function of CV cycle numbers. Data from sputtered Pt are also included for comparison.

described here have a higher onset potential (near 1000 mV) and reached the diffusion-limited currents near 900 mV. In order to minimize the error introduced by the diffusion correction, the catalytic activities of these catalysts need to be compared at higher potentials; between 950 and 1000 mV.

Figure 6 shows the Tafel-style plots in the kinetic region and presents the data in two formats: planar current density $j_{planar}$ (plotted with dashed lines) and specific current density $j_{specific}$ (current density normalized to the electrochemical surface area, plotted with solid lines). It is apparent that, on NSTF-coated disks, the $Pt_{35}Ni_{65}$ material has much higher planar current density than sputtered Pt. As shown in Fig. 6, $j_{planar}$ of $Pt_{35}Ni_{65}$ material reached $> 2$ mA/cm$^2$ at 1000 mV at the beginning (test block #1) before shifting to a lower current density level of $\sim 1.5$ mA/cm$^2$ at 1000 mV (test block #2) and gradually declined to $\sim 1$ mA/cm$^2$ at 1000 mV as the experiment progressed towards test block #10. The same Pt loading (with no Ni) deposited on NSTF-coated disks, on the other hand, shows $j_{planar}$ of only $\sim 0.2$ mA/cm$^2$. After normalizing the data by the active Pt surface area (SEF), it was found that $Pt_{35}Ni_{65}$ (at 0.15 mg Pt/cm$^2$) has higher $j_{specific}$ than sputtered Pt. As shown in Fig. 6, $j_{specific}$ of $Pt_{35}Ni_{65}$ reached $> 0.1$ mA/cm$^2_{Pt}$ at 1.0V at the beginning (test block #1), dropped to $\sim 0.06$ mA/cm$^2_{Pt}$ at 1.0 V (test block #2) and then continued to decrease, reaching $\sim 0.035$ mA/cm$^2_{Pt}$ for test block #10. The pure Pt disk exhibited $j_{specific}$ of $\sim 0.02$ mA/cm$^2_{Pt}$. Figure 6 also shows that the $Pt_{35}Ni_{65}$ catalyst material had the same Tafel slopes ($\sim$60 mV/decade) as sputtered Pt.

Figure 7 shows the SEF of different $Pt_{1-x}Ni_x$ compositions as functions of potential cycles. The data shown in Fig. 7 are grouped into test blocks, with three measurements of SEF per test block. Figure 7 also includes SEF data for Pt sputtered on a NSTF-coated GC disk for comparison. The continuous CV-ORR test protocol was performed on the sputtered Pt and $Pt_{1-x}Ni_x$ materials for 14 test blocks over 9 h. Conceptually, the CV-ORR test block could be repeated continuously for a very long period of time. However, as the experiment continues for more than couple of hours, atmospheric contamination of the liquid electrolyte of the RDE cell has a measurable impact on the catalyst performance. Therefore the continuous CV-ORR test protocol was used to examine the transient response of the catalyst only: from the initial point where the electrode is assembled, until the performance indicators reached a meaningful steady-state trend at the end of 14th test block.

Figure 7 shows a summary of SEF as a function of CV cycles for all $Pt_{1-x}Ni_x$ materials compared to sputtered Pt. The sputtered Pt had a SEF of $\sim 14$ cm$^2$/cm$^2$ and the SEF values showed a very subtle declining trend. The subtle decline in Pt SEF likely results from electrolyte contamination during the experiment. The Pt-Ni electrodes show a different trend: in general, all of the $Pt_{1-x}Ni_x$ electrodes had an initial SEF of $\sim 20$ cm$^2$/cm$^2$ (test block #1) which increased rapidly for the first few test blocks before reaching stable values. As the nickel content increased (x in $Pt_{1-x}Ni_x$ increased from 0.65 to 0.75), the maximum SEF value increased. $Pt_{35}Ni_{65}$ gave a maximum SEF of $\sim 28$ cm$^2$/cm$^2$ and the SEF for $Pt_{28}Ni_{72}$ reached a maximum value of $\sim 40$ cm$^2$/cm$^2$. The SEF of $Pt_{25}Ni_{75}$ material had the same trend and had an initial value of $\sim 20$ cm$^2$/cm$^2$, reaching a maximum of $\sim 55$ cm$^2$/cm$^2$ near test block #5–6. These rapid increases in surface area with increasing x are consistent with our observations in two accompanying reports[31,32] with de-alloyed $Pt_{1-x}Ni_x$ and $Pt_{1-x}Co_x$ coated NSTF whiskers. The peak value is dependent on the analytical method used to measure the at% Ni fraction, whether the measurement uses an MEA versus RDE sample, and to some extent the history of each sample.

These large increases in SEF relative to pure Pt are believed to be the result of Ni dealloying from the sputtered $Pt_{1-x}Ni_x$ catalysts during the CV cycling, the same as in Ref. 31. During the RDE experiments, the acidic electrolyte, together with the applied potential, created favorable conditions for the less-noble metal, Ni, in the $Pt_{1-x}Ni_x$ catalysts to dissolve. Dissolution of Ni from the catalyst surface and near-surface would likely lead to the formation of a porous, Pt-rich structure that has high surface area. It is not clear from these data whether bulk de-alloying occurred or whether the enriched Pt surface layers formed through surface de-alloying hindered Ni dissolution from the bulk. In order to investigate this further, an ex-situ XRD study was conducted. The XRD profile of one high Ni content disk was measured at various times throughout the CV-ORR protocol by removing the electrode from the electrolyte and transferring it to the diffractometer. After XRD data was collected, the electrode was returned to the solution cell for further testing.

Figure 8 shows the XRD data measured for a disk with $Pt_{0.28}Ni_{0.72}$ deposited on NSTF. The top dashed scan shows the pattern of the blank or bare (no catalyst coating) NSTF-coated disk; this background is present in all scans measured. This blank will contribute a background to the observed data. The scans for the $Pt_{0.28}Ni_{0.72}$ disk have been offset vertically for clarity. The total number of potential cycles completed during the CV-ORR protocol increases from the bottom to the top of the graph – the vertical offset for each scan has been set such that high angle intensity is located vertically according to the number of cycles completed. Three vertical dashed lines have been included on this figure; 39.8° showing where the (111) peak of FCC Pt would appear, $\sim$40.4° which corresponds to the (111) peak position expected for FCC $Pt_{0.75}Ni_{0.25}$ and 42.5°, the approximate

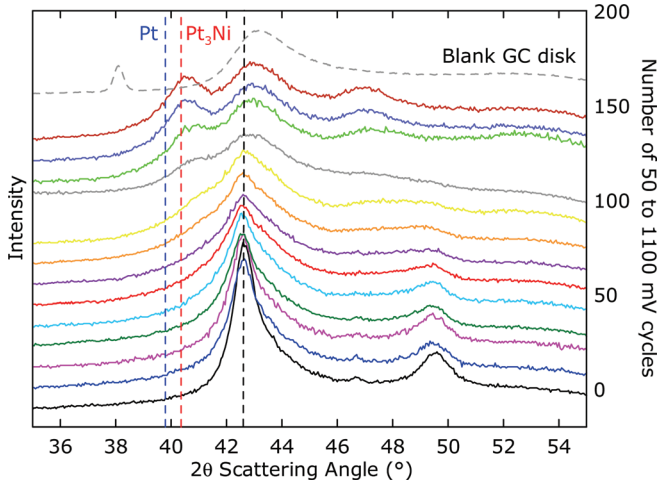


**Figure 8.** (Color online) XRD data for $Pt_{0.28}Ni_{0.72}$ on a NSTF-coated GC disk as a function of number of potential cycles. The scans have been offset vertically for clarity. The data measured on a blank disk is shown as the top scan in the figure. The number of potential cycles increases from the bottom to the top of the figure. The scattering angles expected for FCC Pt, $Pt_3Ni$ and the original sputtered material are shown as vertical dashed lines.

location of the initial (111) peak of the as-sputtered catalyst. At the start of the experiment, there are well resolved (111) and (200) peaks for a FCC lattice with a lattice constant of ~3.7 Å (significantly smaller than that expected for Pt—3.92 Å, but larger than that expected for Ni—3.52 Å). This is consistent with the deposited composition being a single phase. It could be characterized as either a contracted Ni-substituted FCC Pt lattice or as an expanded Pt-substituted FCC Ni lattice. As the catalyst was electrochemically cycled, the intensity of the (111) and (200) peaks in this scattering angle range decreased, suggesting loss of Ni. Even after 60 cycles, there is still some evidence that some of this phase remained, however there is also evidence for the emergence of a lower Ni content phase, with a lattice constant somewhat close to the $Pt_{0.75}Ni_{0.25}$ composition, although it is at a higher angle and thus likely contains more than 25% Ni. There is no evidence for any significant amounts of a pure Pt phase, thus the bulk of the catalyst still contains some Ni. With more CV-ORR cycles, most of the high Ni content phase has been lost, and the peaks from lower Ni phase are much stronger. This suggests that the bulk of the catalyst has lost much, but not all of the Ni. The time/potential cycle dependence of the emergence of the lower Ni content phase suggests that bulk de-alloying occurs only slowly during each potential cycle. This is therefore consistent with the idea that loss of surface Ni creates a Pt-rich surface layer that hinders subsequent diffusion of bulk Ni to the surface for dissolution.

Figure 9 shows $j_{planar}$ and $j_{specific}$ at 1.0 V $_{RHE}$ of sputtered Pt and $Pt_{1-x}Ni_x$ catalysts on NSTF plotted as a function of potential cycle number. The vertical scales of the figures were selected to best show the trends in the data of the entire experiment, therefore some of the data points from test block #1 are much higher than the scale and are not included in the figure. $j_{planar}$ of Pt sputtered on NSTF was ~0.3 mA/cm$^2$ at the beginning of the experiment and had a slight decline over the 14 test blocks (~9 h). All of the $Pt_{1-x}Ni_x$ catalysts showed higher $j_{planar}$ than that of sputtered Pt, however the current density for the first test block is high compared to the rest of the data collected. $Pt_{35}Ni_{65}$ showed an initial $j_{planar}$ of >5 mA/cm$^2$ in test block #1; this decreased to ~1.5 mA/cm$^2$ in the second test block. After test block #2, the current densities continued to decrease at a much lower rate, reaching ~0.8 mA/cm$^2$ at the end of the experiment (test block #14). Some of the $Pt_{1-x}Ni_x$ catalysts showed $j_{planar}$ of >10 mA/cm$^2$ (off-scale) in the first test block. The high ORR current density in the first test block is also shown in the RDE measurements in Fig. 5. When comparing trends in planar current density, $j_{planar}$, for different catalysts, it is apparent that an

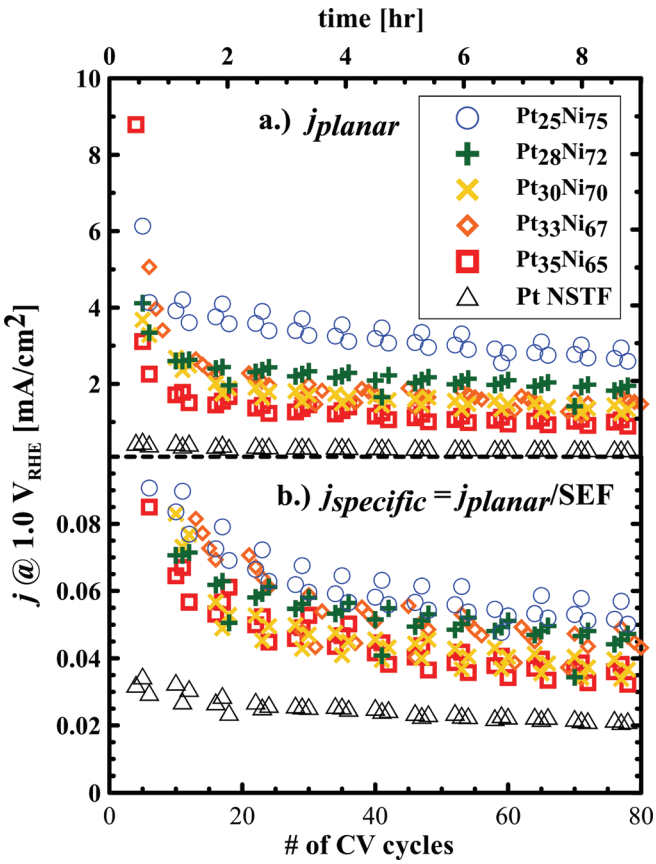


**Figure 9.** (Color online) $j_{planar}$ and $j_{specific}$ of all Pt-Ni catalyst plotted as a function of CV cycle numbers. Data from sputtered Pt are also included for comparison.

increase in Ni content (x in $Pt_{1-x}Ni_x$) results in a higher $j_{planar}$ level, with $Pt_{25}Ni_{75}$ having the highest current densities.

Figure 9b shows the area specific current densities, $j_{specific}$, of all the $Pt_{1-x}Ni_x$ catalysts as a function of number of the potential cycles. The trends observed in $j_{specific}$ are similar to those seen for $j_{planar}$, with an initial large current density drop between the first and the second test block, and then slow loss in specific activity to the end of the experiment. Figure 9b also shows that the catalyst with highest Ni content, $Pt_{25}Ni_{75}$, has the highest $j_{specific}$, i.e. highest catalytic activity per Pt site. The loss in activity for both $j_{planar}$ and $j_{specific}$ is likely the combined result of Ni de-alloying, surface structure rearrangement and some contribution from electrolyte contamination. During the RDE measurements, Ar or $O_2$ were continuously bubbled through the electrolyte solution and vented into the ambient environment. Although the experiment apparatus and glassware were cleaned to the highest standards, and Ar or $O_2$ were continuously bubbled through the electrolyte, creating a small positive pressure in the solution cell, the cell was still open to the atmosphere. It is possible that trace atmospheric contaminants could enter the cells and dissolve into the electrolyte, potentially poisoning the catalyst surfaces to some extent.

Recent investigations on Pt-Cu dealloyed catalysts by Strasser et al. suggested that the area-specific activity gains seen for such catalysts result from both an increase in ECSA and, to a larger extent, the presence of compressive strain in the catalyst surface layers.[12] The compressive strain is thought to arise from the different lattice parameters between the Pt-rich shell and the Pt-Cu alloy core of the de-alloyed material. It is possible that core-shell like catalysts were formed from the $Pt_{1-x}Ni_x$ catalysts deposited on NSTF that have been described in this paper. At the beginning of the experiments reported here, only a small amount of surface and near-surface Ni has been lost (as shown from the XRD data), resulting a

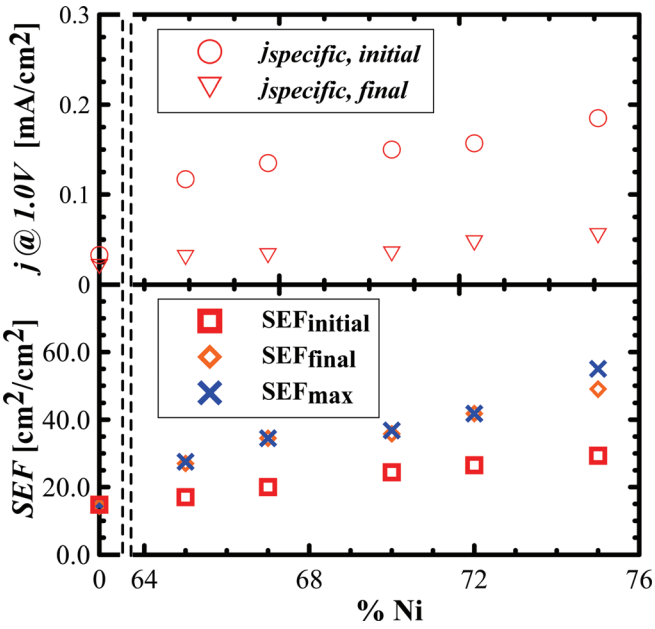


**Figure 10.** (Color online) Summary of ORR performance indicators of Pt-Ni catalysts plotted as a function of Ni content. The maximum SEF and $j_{specific}$ of the samples are from test block 4–6 for different $Pt_{1-x}Ni_x$ compositions.

thin layer of Pt-rich shell (maybe exhibiting high strain). This material had the highest ORR activity. As de-alloying continued, more Ni dissolved, resulting in a thicker shell and hence possibly less lattice strain at the surface. This resulted in a decrease in ORR activity. A similar scenario has been proposed to explain the very sharp peak in activity of $Pt_3Ni_7$ seen in MEA fuel cell measurements discussed in Ref. 31.

The SEF and $j_{specific}$ measured by the continuous CV-ORR RDE protocol, are plotted as a function of Ni content in Fig. 10. The Pt-area specific current densities, $j_{specific}$, of all the $Pt_{1-x}Ni_x$ catalysts compositions tested were higher than that of sputtered Pt. As discussed earlier, the initial $j_{specific}$ of $Pt_{1-x}Ni_x$ catalysts measured in the first test block were nearly an order of magnitude higher than that of Pt in some cases. As the experiment progressed, the combined impact of further de-alloying, and possible contamination of the electrolyte lowered the ORR activity. The final $j_{specific}$ from test block #4, shown by triangles in Fig. 10, indicates that the ORR activities of $Pt_{1-x}Ni_x$ were still higher than sputtered Pt even after significant dealloying and some possible electrolyte contamination had occurred. Figure 10 also shows that $Pt_{25}Ni_{75}$ has the highest $j_{specific}$ after 14 test blocks. The SEFs of the $Pt_{1-x}Ni_x$ catalysts show the same trend, with $Pt_{25}Ni_{75}$ showing a SEF of ~25 $cm^2/cm^2$ at the beginning of the experiment, reaching a maximum of ~55 $cm^2/cm^2$ before declining to 50 $cm^2/cm^2$ at the end of the testing period. In Ref. 31 (one of the current three-part submissions) we show that both specific activity and surface area contribute to a sharply peaked dependence of mass activity on Ni content (at x = 70 atom % Ni measured gravimetrically, 62 atom % Ni by EMP) in MEA fuel cell measurements.

## Conclusions

Intermixed $Pt_{1-x}Ni_x$ ($0.65 < x < 0.75$) materials were sputter-deposited onto NSTF-coated GC disks and studied for ORR activity by RDE techniques via a continuous CV-ORR protocol that tracked the performance indicators (SEF, $j_{planar}$, $j_{specific}$) of the catalyst materials over 9-h. The use of NSTF-coated GC disks in RDE measurements was proven to be a viable method for screening catalysts because both the catalytic activity and the effects of a high surface area support can be examined in a single experiment. The purpose of using a continuous CV-ORR test protocol was to examine the transient behavior of the catalyst and shed insight on the de-alloying process of the material.

All of the $Pt_{1-x}Ni_x$ catalyst materials showed an initial SEF of ~20 $cm^2/cm^2$. While the SEF for sputtered Pt showed a steady level around 14 $cm^2/cm^2$ throughout the experiment, the SEF of $Pt_{1-x}Ni_x$ material showed a rapid increase for the first few test blocks before plateauing. Catalysts with higher Ni content showed higher SEF plateau values, with $Pt_{25}Ni_{75}$ being the highest, showing a SEF of ~50 $cm^2/cm^2$ at the end of 14th test block. The area-specific ORR activity, $j_{specific}$ at 1000 $mV_{RHE}$, was shown to be as high as ~0.15 mA/$cm^2$ for $Pt_{1-x}Ni_x$ catalysts at the beginning of the test sequence. This dropped towards ~0.05 mA/$cm^2$ as the tests continued for 9 h. Sputtered Pt, for comparison, reached 0.03 mA/$cm^2$ at the beginning of the test sequence; this activity had dropped to ~0.02 mA/$cm^2$ after multiple CV-ORR blocks. The trends in SEF and $j_{specific}$ of the $Pt_{1-x}Ni_x$ material agreed with the current understanding of dealloying process and its impact on catalytic performance. In a corrosive environment, the less noble metal of the $Pt_{1-x}Ni_x$ alloy should dissolve easily. The dissolution of Ni probably started with surface and near-surface Ni atoms, forming a porous structure that has high surface area, increasing SEF. The dissolution of Ni likely created a thin Pt-rich outer layer with a different lattice constant than the Ni-rich core. This structure was shown to have high ORR activity. As dealloying continued, the Pt-rich outer layers may increase somewhat in thickness, leading to decline in area specific current density. However, their thickness must be less than 2 nm, because no evidence for pure Pt was observed in XRD experiments. The Pt-enriched outer layer shell also seems to protect Ni atoms from the deeper bulk regions of the catalyst from dissolution by limiting diffusion of Ni to the surface. This was demonstrated by XRD measurements which showed bulk de-alloying occurred at a relatively slow rate with multiple potential cycles.

## Acknowledgment

The authors thank Simon Trussler for fabrication of devices and the US DOE for funding under 3M grant DE-FG36-07GO17007. Dalhousie University also assisted in meeting the publication costs of this article.

## References

1. H. A. Gasteiger, S. S. Kocha, B. Sompalli, and F. T. Wagner, *Appl. Catal. B*, **56**, 9 (2005).
2. F. T. Wagner, B. Lakshmanan, and M. F. Mathias, *J. Phys. Chem. Lett.*, **14**, 2204 (2010).
3. F. T. Wagner, H. A. Gasteiger, R. Makharia, K. C. Neyerlin, E. L. Thompson, and S. G. Yan, *ECS Trans.*, **3**(1), 19 (2006).
4. A. B. Anderson, N. M. Neshev, R. A. Sidik, and P. Shiller, *Electrochim. Acta*, **47**, 2999 (2002).
5. A. Bonakdarpour, K. Lake, K. Stevens, and J. R. Dahn, *J. Electrochem. Soc.*, **155**, B108 (2008).
6. T. J. Schmidt, V. Stamenkovic, M. Arenz, N. M. Markovic, and P. N. Ross, *Electrochim. Acta*, **47**, 3765 (2002).
7. V. Stamenkovic, T. J. Schmidt, P. N. Ross, and N. M. Markovic, *J. Electroanal. Chem.*, **554**, 191 (2003).
8. B. Fowler, C. A. Lucas, A. Omer, G. Wang, V. R. Stamenkovic, and N. M. Markovic, *Electrochim. Acta*, **53**, 6076 (2008).
9. S. Koh, M. F. Toney, and P. Strasser, *Electrochim. Acta*, **52**, 2765 (2007).
10. R. Srivastava, P. Mani, and P. Strasser, *J. Power Sources*, **190**, 40 (2009).
11. K. C. Neyerlin, R. Srivastava, C. Yu, and P. Strasser, *J. Power Sources*, **186**, 261 (2009).
12. P. Strasser, S. Koh, T. Anniyev, J. Greeley, K. More, C. Yu, Z. Liu, S. Kaya, D. Nordlund, H. Ogasawara et al., *Nat. Chem.*, **2**, 454 (2010).
13. P. Mani, R. Srivastava, and P. Strasser, *J. Power Sources*, **196**, 666 (2011).
14. H. W. Pickering, *Corros. Sci.*, **23**, 1107 (1983).
15. J. Erlebacher, M. J. Aziz, A. Karma, N. Dimitrov, and K. Sieradzki, *Nature (London)*, **410**, 450 (2001).
16. K. Sieradzki, *J. Electrochem. Soc.*, **140**, 2868 (2003).
17. M. Lischka, C. Mosch, and A. Gross, *Electrochim. Acta*, **52**, 2219 (2007).
18. J. K. Norskov, J. Rossmeisl, A. Logadottir, J. R. Kitchin, T. Bligaard, H. Jonsson, and L. Lindqvist, *J. Phys. Chem. B*, **108**, 17886 (2004).
19. X. Li, S. Park, and B. N. Popov, *J. Power Sources*, **195**, 445 (2010).
20. A. Bonakdarpour, R. Lobel, S. Sheng, T. L. Monchesky, and J. R. Dahn, *J. Electrochem. Soc.*, **153**, A2304 (2006).
21. C. J. Clarke, G. J. Browning, and S. W. Donne, *Electrochim. Acta*, **51**, 5773 (2006).

22. G. C. K. Liu, R. J. Sanderson, G. Vernstrom, D. A. Stevens, R. T. Atanasoski, M. K. Debe, and J. R. Dahn, *J. Electrochem. Soc.*, **157**, B207 (2010).
23. M. K. Debe and R. J. Poirier, *J. Vac. Sci. Technol. A*, **12**, 2017 (1994).
24. M. K. Debe and A. R. Drube, *J. Vac. Sci. Technol. B*, **13**, 1236 (1995).
25. M. K. Debe, in *Handbook of Fuel Cells—Fundamentals, Technology and Applications*, Vol. 3, W. Vielstich, A. Lamm, and H. A. Gasteiger, Editors, p. 576, John Wiley & Sons, Chichester (2003).
26. M. K. Debe, A. K. Schmoeckel, G. D. Vernstrom, and R. Atanasoski, *J. Power Sources*, **161**, 1002 (2006).
27. L. Gancs, T. Kobayashi, M. K. Debe, R. Atanasoski, and A. Wieckowski, *Chem. Mater.*, **20**, 2444 (2008).
28. J. R. Dahn, S. Trussler, T. D. Hatchard, A. Bonakdarpour, J. R. Mueller-Neuhaus, K. C. Hewitt, and M. Fleischauer, *Chem. Mater.*, **14**, 3519 (2002).
29. V. Chevrier and J. R. Dahn, *Meas. Sci. Technol.*, **17**, 1399 (2006).
30. D. van der Vliet, D. S. Strmcnik, C. Wang, V. R. Stamenkovic, N. M. Markovic, and M. T. M. Koper, *J. Electrocatal. Chem.*, **647**, 29 (2010)
31. D. A. Stevens, S. Wang, R. J. Sanderson, G. C. K. Liu, G. D. Vernstrom, R. T. Atanasoski, M. K. Debe, and J. R. Dahn, *J. Electrochem. Soc.*, **158**, B899 (2011).
32. M. K. Debe, A. J. Steinbach, G. D. Vernstrom, S. M. Hendricks, M. J. Kurkowski, R. T. Atanasoski, P. Kadera, D. A. Stevens, R. J. Sanderson, E. Marvel et al., *J. Electrochem. Soc.*, **158**, B910 (2011).

# Alternative Catalyst Supports Deposited on Nanostructured Thin Films for Proton Exchange Membrane Fuel Cells

Arnd Garsuch, D. A. Stevens, R. J. Sanderson, S. Wang, R. T. Atanasoski, S. Hendricks, M. K. Debe and J. R. Dahn

*J. Electrochem. Soc.* 2010, Volume 157, Issue 2, Pages B187-B194.
doi: 10.1149/1.3261855

*Journal of The Electrochemical Society*, **157** (2) B187-B194 (2010)
0013-4651/2009/157(2)/B187/8/$28.00 © The Electrochemical Society



# Alternative Catalyst Supports Deposited on Nanostructured Thin Films for Proton Exchange Membrane Fuel Cells

**Arnd Garsuch,[a] D. A. Stevens,[a] R. J. Sanderson,[a] S. Wang,[a] R. T. Atanasoski,[b] S. Hendricks,[b] M. K. Debe,[b,*] and J. R. Dahn[a,*,z]**

[a]*Department of Physics and Atmospheric Science, Dalhousie University, Halifax, Nova Scotia B3H 3J5, Canada*
[b]*3M Center, 3M Fuel Cell Components Program, St. Paul, Minnesota 55144, USA*

A series of platinum-coated underlayer materials, alumina, gold, titanium carbide, and titanium disilicide, deposited by a high throughput magnetron sputtering method have been investigated as cathode catalyst supports in fuel cells. Orthogonal thickness gradients of the underlayer materials (0–100 nm planar equivalent) and the platinum top layer (0–75 nm planar equivalent) made up the 76 × 76 mm libraries. The resulting catalyst films were characterized by surface profilometry, X-ray diffraction, scanning electron microscopy, and X-ray photoelectron spectroscopy. The electrochemical properties of the catalyst composition spreads were investigated simultaneously in 64-electrode proton exchange membrane fuel cells with emphasis placed on the determination of the electrochemical surface area (ECSA) as a function of underlayer thickness and chemistry. The present study shows that gold and titanium disilicide used as underlayers on 3M's nanostructured thin film supports lead to a loss of ECSA during operation. Migration and surface accumulation were observed when gold was used as underlayer material. For titanium disilicide, alloying and the generation of platinum silicide phases occurred. Alumina and titanium carbide were found to be potentially acceptable underlayer materials as well as alternative support materials on the basis of their influence on the catalyst surface area.
 [DOI: 10.1149/1.3261855] 

Manuscript submitted July 13, 2009; revised manuscript received October 15, 2009. Published December 7, 2009.

Polymer electrolyte membrane fuel cells (PEMFCs) are promising power sources for automotive applications in the future.[1] The main environmental advantage of using PEMFCs in vehicles is the reduction of carbon dioxide emissions, pollutants, and consumption of fossil fuels.[2]

To fully commercialize PEMFCs for automotive vehicles, their high production cost needs to be reduced while improving performance and durability. The core of a PEMFC, the membrane electrode assembly (MEA), consists of two electrocatalyst electrodes (anode and cathode) with gas diffusion layers (GDLs) on either side of the proton-conducting ion-exchange membrane. Each of these MEA components contributes to the overall performance, stability durability, robustness, and cost of a PEMFC, and thus research efforts have been focused on the improvement of the electrocatalyst and membrane properties.[3]

Platinum or platinum alloys are commonly used as the catalyst on the anode side for the hydrogen oxidation reaction (HOR) and on the cathode side for the oxygen reduction reaction (ORR) in a PEMFC. These catalysts may consist of highly dispersed platinum particles (2–3 nm) supported on carbon blacks, activated carbon, or carbon nanotubes. A range of factors[4] are known to contribute to the significant performance degradation of PEMFCs that can occur during long-term operation or as a result of adverse operating conditions (e.g., fuel starvation on the anode side during start-up and shutdown[5]). These include Pt-catalyzed corrosion of the carbon support,[6] oxidation and decomposition of the GDL,[7] dissolution or poisoning of the Pt catalysts on the cathode and anode side,[8] and degradation of the ion-exchange membrane through attack by hydrogen peroxide derived free radicals.[9]

Research work on cathode electrocatalysts has focused on the fundamental understanding of the mechanism of the ORR and the multiple surface area loss mechanisms of Pt that lead to fuel cell performance degradation.[10-13] A significant loss of electrochemical surface area (ECSA) can occur over time during fuel cell operation as a result of electrochemically driven dissolution of Pt metal at high potentials ($Pt \rightarrow Pt^{z+} + ze^-$). Pt dissolution is most significant in the cathode of the PEMFC and results in the agglomeration and growth of Pt nanoparticles on the carbonaceous support material forced by the Ostwald ripening process.[14] In addition dissolved Pt ions diffuse into the ion-exchange membrane and subsequently precipitate inside the ionomer phase or at the interface of the cathode and membrane according to the reaction with permeating hydrogen ($H_2 + Pt^{2+} \rightarrow 2H^+ + Pt$).[15]

3M's nanostructured thin film (NSTF) catalyst and support system overcomes many of these limitations.[16] The 3M NSTF catalyst support consists of oriented, nanometer-sized crystalline organic whiskers, which are synthesized by sublimation and subsequent annealing of an organic pigment material based on a perylene dicarboximide compound. This pigment material gives a monolayer of oriented crystalline whiskers with number densities greater than 3 billion/cm$^2$. The whiskers have a rectangular cross section of around 30 × 50 nm and an average length of 0.5–1 μm. To be used in a fuel cell MEA, the whiskers are coated with Pt-based catalysts by physical vapor deposition methods such as sputter deposition, giving thin catalyst films that encapsulate the whisker structures. Earlier work by Debe et al. demonstrated the higher stability and durability of NSTF catalysts in comparison to conventional carbon-supported dispersed Pt catalysts.[17] Furthermore, the organic crystalline whisker support also epitaxially affects the subsequent nucleation and growth of Pt whiskerettes on whisker sides, maximizing the amount of Pt[111] surface facets.[18] In addition to being an excellent catalyst support on its own, the NSTF support is an excellent substrate for the rapid screening of a wide range of potential underlayer materials for fuel cell applications. Underlayer materials that show promise could feasibly be used on NSTF to modify the dimensions and morphology of the catalyst support whisker or on their own as particulate catalysts supports to replace conventional high surface area carbon supports. The NSTF technology is useful for studying underlayer materials because a wide range of elements and compounds can be prepared through sputter depositions and because their high aspect ratio and surface area allow for the subsequent preparation of high surface area platinum-based catalysts for realistic fuel cell testing under realistic conditions.

In the present study we have investigated NSTF supports coated first with an underlayer material (gold, alumina, titanium carbide, or titanium disilicide), and then with a platinum overlayer. This work was used to ascertain how different underlayer materials influence the ECSA of the platinum overlayer.

## Experimental

*Catalyst preparation.*— Composition spreads of platinum deposited on the different underlayer materials were prepared using a Corona Vacuum Coaters V3T magnetron sputtering system. Further details about the equipment used are given in Ref. 19. Two inch

* Electrochemical Society Active Member.
z E-mail: jeff.dahn@dal.ca

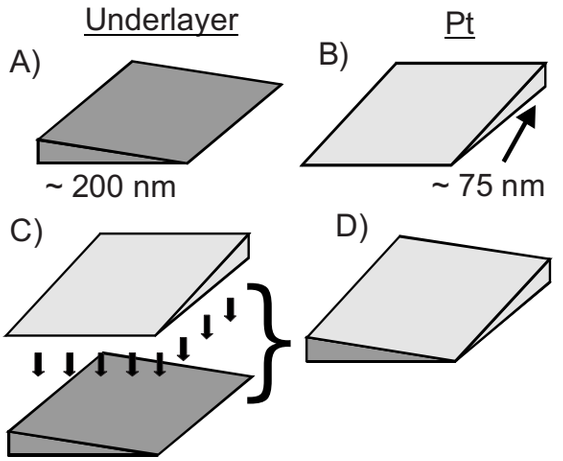


**Figure 1.** Composition spread sputtering approach to study the impact of underlayer materials on the ECSA and durability of Pt. Films were deposited on a range of substrates for property and performance measurements.

diameter sputtering targets (99.99% purity) of the underlayer materials Au, $Al_2O_3$, TiC, and $TiSi_2$ as well as Pt were used to prepare the different catalyst composition spreads. Au and Pt were sputtered using MDX-1K DC (Advanced Energy) power supplies at a power of 30 and 50 W, respectively. TiC and $TiSi_2$ were sputtered at 100 W using an RFX 600A (Advanced Energy) radio frequency (rf) power supply. $Al_2O_3$ was sputtered at 200 W using the rf power supply. The chamber pressure was between 0.4 and 0.6 mTorr during sputtering. Ultrapure Ar (99.999%) was used, which was supplied at constant flow rate during the sputtering run.

Specially designed masks were positioned in front of each target to produce films with linearly varying thickness with position as shown in Fig. 1 and as explained in Ref. 19. Figure 1A shows the 76 × 76 mm film of the underlayer materials, which were approximately 200 nm thick (planar equivalent) at the thickest point. Figure 1B shows the Pt "wedge", which was about 75 nm thick (planar equivalent) at the thickest point. The target power and deposition time of the underlayer materials were set according to previous calibration runs. The platinum overlayer was deposited so that the maximum platinum loading was approximately 0.15 mg/cm$^2$ (75 nm) at the thick end of the Pt gradient. Figure 1C shows that the Pt wedge was deposited on top of the underlayer wedge to create the layered structure in Fig. 1D. The underlayer wedge was orthogonal to the Pt wedge, which ensures that a wide range of underlayer/Pt thickness combinations are present in the sample depicted by Fig. 1D.

Some samples were made where only the underlayer film was sputtered, as in Fig. 1A, or only the Pt film, as in Fig. 1B. These films were coated on Si wafer strips coated with strips of tape for profilometry experiments, on NSTF support whiskers for X-ray diffraction (XRD) experiments to determine grain size, and on a set of preweighed Al foil disks for mass per unit area determinations. Some Pt-only wedges were also coated on NSTF support whiskers for 64-electrode fuel cell testing as described below.

A set of different 76 × 76 mm substrates was arranged on the sputtering table for each sputtering experiment to receive the underlayer/Pt film shown in Fig. 1D. Silicon wafer pieces were used to determine the thickness of the deposited films vs position with a profilometer. A 76 × 76 mm piece of NSTF whisker coated substrate film was coated with a catalyst and then used to collect XRD patterns for structure analysis. Two 100 × 100 mm pieces of NSTF support substrate film were coated with centered 76 × 76 mm films as in Fig. 1D. In this case, the coating was applied through a shadow mask which had an 8 × 8 array of 5 mm diameter holes, so that 64 discrete catalyst electrodes were prepared. The method is described in Ref. 20 and 21. These 64-electrode catalyst films were then transferred to proton exchange membranes by heat lamination.

Glassy carbon (GC) disks were used as substrates for the films used in X-ray photoelectron spectroscopy (XPS) measurements. The GC disks were mounted onto the substrate table, where they were equally spaced over the 76 mm wide range of the sputtering track. In these experiments, a constant thickness of Pt was coated on top of a linear gradient of the underlayer.

*Characterization.— Film thickness.*— The thickness vs position measurements of the underlayer wedges (Fig. 1A), Pt wedges (Fig. 1B), and underlayer/Pt films (Fig. 1D) deposited on Si wafers were performed using a Dektak 8 Advanced Development Profilometer (Veeco Instruments Inc.). The thickness profile of a platinum wedge (Fig. 1B) was also calculated from gravimetric measurements on preweighed aluminum disks, which were placed on the substrate table during a preliminary calibration run. The mass gain was determined using a Cahn 29 microbalance and the film thickness was calculated assuming the bulk density for platinum. The power and deposition time of platinum were set according to the calibration run (Fig. 1A) for the final catalyst preparation runs (Fig. 1D).

*Scanning electron microscopy.*— To observe the microscopic features of the NSTF whisker film coated with the different underlayer materials, Au, $Al_2O_3$, TiC, and $TiSi_2$, high resolution images were taken using a cold field emission Hitachi S-4700 scanning electron microscope (SEM). Images were acquired at 10 kV accelerating voltage with the secondary electron imaging technique.

*XRD.*— The crystal structure of the different underlayer materials deposited on NSTF whisker film strips was determined as a function of film thickness from XRD measurements using the sputter depositions as shown in Fig. 1A. Pt grain size (from the 111 peak) was calculated as a function of Pt thickness as well as underlayer material thickness using films as in Fig. 1D deposited on NSTF support whiskers. The X-ray system was equipped with an *x*-*y* translation stage, a Cu target X-ray tube, an incident beam monochromator to select Cu Kα radiation, and a position-sensitive Inel CPS-120 detector. XRD patterns were collected every 5 mm on the underlayer materials deposited on NSTF support strips (underlayer materials only, Fig. 1A) and every 5 mm in both the *x* and *y* directions on the 76 × 76 mm underlayer/Pt films on NSTF support film pieces (Pt and underlayer materials, Fig. 1D). Grain sizes were calculated using the Scherrer equation by fitting Lorentzian shaped profiles to the measured data. Instrumental resolution was determined using an NIST corundum standard, and calculated grain sizes were corrected accordingly.

*XPS.*— Surface composition and depth profile measurements of two selected underlayer/Pt samples were made using a VG Microtech Multilab XPS system (Thermo Electron Corporation) equipped with a CLAM-4 hemispherical analyzer. The analyzer was operated in constant pass energy mode (50.0 eV) with a Mg Kα radiation (1253.6 eV, 15 kV, and 20 mA) source. The acquisition parameters were as follows: 0.1 eV energy step size, 5 mm analyzer slit, and 200 ms dwell time. The operating pressure during data acquisition was maintained $<5 \times 10^{-9}$ bar. The measurements were performed on the Pt on TiC and on the Pt on $TiSi_2$ samples deposited on conductive GC disks. The C 1s spectra of the samples (adventitious carbon, 284.5 eV) were used as reference for correction due to charging effects, if present.

*Fuel cell testing.*— The 64-electrode PEMFC infrastructure developed at Dalhousie University was used to investigate the ECSAs of the catalyst composition spreads. A detailed description of the 64-electrode PEMFCs and associated test stations is given elsewhere in literature.[20,21] Briefly, the fuel cell consisted of a segmented electrode (64 electrodes) and a continuous counter electrode. A serpentine flow field plate made from POCO Graphite (grade AXF-5Q) was used as the counter electrode. The segmented electrode was made from Ultem 1000 (polyetherimide) with 64 embedded POCO Graphite rods (grade AXF-5Q). A serpentine flow field was ma-

chined through the embedded rods in the Ultem block to have gas flow to all 64 electrodes. The segmented electrode was covered with 64 GDL disks (one per channel) and a gasket material with 64 holes (8 mm in diameter). The gasket was used to hold the discrete GDL disks in place and control the extent of GDL compression. The GDL material was a carbon paper with a teflonized microporous layer supplied by 3M Company. The catalyst-coated NSTF support film was decal transferred to a proton exchange membrane. Preparation of the final catalyst-coated membrane was carried out by an in-house hot-roll lamination process at 3M Center, St. Paul, MN. The fully laminated membrane consisted of 64 discrete electrodes on the cathode side and a continuous layer of Pt-coated NSTF covering the anode side (entire area) of the membrane. The catalyst-containing membrane was placed in the fuel cell so that the 64 catalyst electrodes were in contact with the corresponding 64 GDL disks. Another piece of gasket holding a GDL square was added to form the anode-side counter electrode. The graphite flow field plate was placed over the MEA, and the entire cell was sandwiched between aluminum end plates.

The test station used to simultaneously measure the response of all 64 catalyst electrodes has been described in Ref. 20 and 21. The 64-electrode fuel cell was installed inside a mechanical convection oven. Ultrahigh purity gases were humidified with nanopure water and supplied to the flow field plates at controlled gas flow rates.

At first, cyclic voltammograms (CVs) were recorded on all 64 electrodes at a scan rate of 20 mV/s at room temperature. During the collection of the CV's, 5% hydrogen in argon (500 sccm, oversaturated) and argon (500 sccm, oversaturated) were supplied to the counter and working electrodes, respectively. The ECSA ($cm^2_{CV}/cm^2_{planar}$) was determined by integrating the charge in the hydrogen desorption region of the CVs obtained, using a conversion factor of 210 $\mu C/cm^2_{Pt}$. The ECSA determined from these initial CVs is called "initial" in the figures displaying fuel cell results. The gas supply of the 64-electrode fuel cell was then switched to hydrogen (anode) and air (cathode), with both gases flowing at 500 sccm and 100% relative humidity (at 75°C), and the temperature of the fuel cell was increased to 75°C. The 64-electrode fuel cell was then electrochemically cycled between 0.9 and 0.3 V. The cell potential was changed in 50 mV steps and it was held constant for 10 s at each potential step. After each cycle the cell potential was held constant at 0.4 V for 5 min. Approximately 80 of the described cycles were carried out before the gases were switched back to 5% hydrogen in argon (anode side) and argon (cathode side). The 64-electrode fuel cell was allowed to cool down to room temperature and, after cooling, a second set of CVs were recorded as detailed above. The ECSA for this second set of CVs is called "final" in the figures displaying fuel cell results.

## Results

*Film thickness*.— To characterize the platinum overlayer, a Pt wedge as in Fig. 1B was deposited on a silicon wafer as well as on preweighed aluminum disks in a preliminary calibration run. Figure 2 shows the Pt film thickness vs position measured by the Dektak profilometer. The film thickness increases linearly across the sputtering track. Figure 2 also shows the film thickness calculated from the mass gain of the preweighed aluminum disks assuming a bulk density of 21.09 $g/cm^3$ for platinum. The thicknesses measured by a Dektak profilometer and determined from weigh disk experiments are in good agreement. The fit equation shown in Fig. 2 was used to determine the planar equivalent platinum thickness vs position for all the subsequent samples (as in Fig. 1D) prepared using the same sputtering conditions for Pt. The film thickness variation with position of the various underlayer materials (Fig. 1A) was also investigated in several calibration runs before the preparation of the underlayer/Pt films (Fig. 1D). Figure 3 shows the film thicknesses vs position of the different underlayer materials measured with a Dektak profilometer. A linearly increasing deposition of the underlayer materials along the range of the sputtering track was observed in all

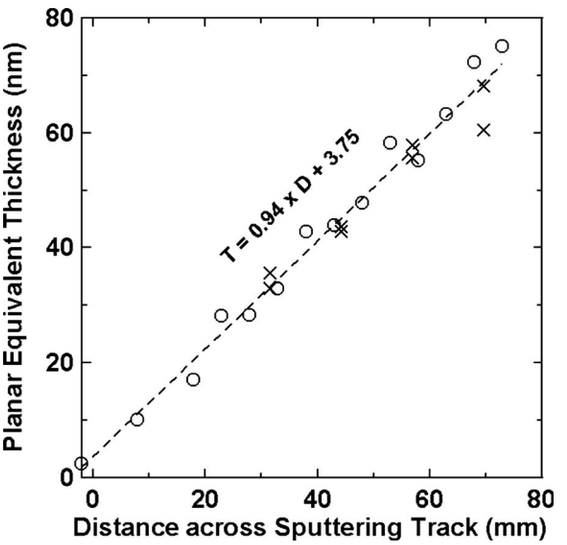


**Figure 2.** Thickness of a linear gradient of platinum with distance across the sputtering track. The thicknesses were measured with a Dektak profilometer (circles) and calculated from masses deposited onto aluminum foil disk weights (crosses). Both sets of data were combined to give the fit equation shown.

cases. Based on the results of the underlayer calibration runs, the deposition time and target powers were adjusted according to the desired film thicknesses of each underlayer material and overlaying Pt. For the preparation of the underlayer/Pt samples as shown in Fig. 1D, an underlayer thickness of 100 nm at the thickest point and a Pt coating thickness of 75 nm at the thickest point was targeted.

Figure 4 shows the measured film thickness plotted vs the calculated film thickness for all the underlayer/Pt films prepared. For each sample, 64 positions on an 8 × 8 array were measured. If the underlayer material deposits as a smooth layer and does not influence

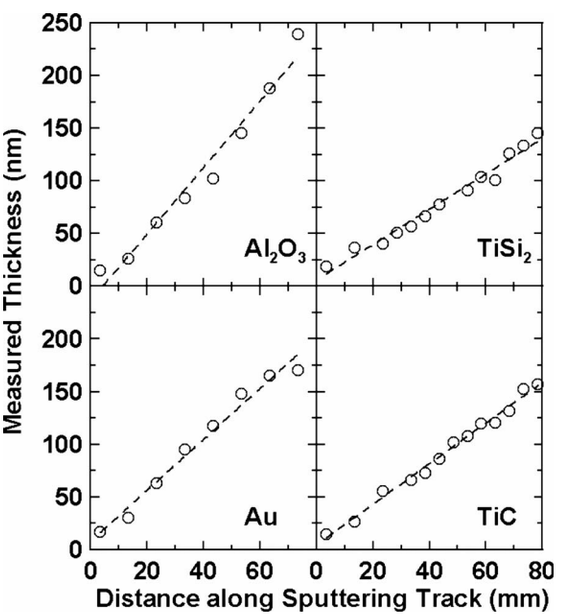


**Figure 3.** Thicknesses of nominally linear gradients of $Al_2O_3$, Au, $TiSi_2$, and TiC as a function of distance across the sputtering track. The thicknesses were measured with a Dektak profilometer. Each panel also includes a least-squares regression fit to the data obtained.

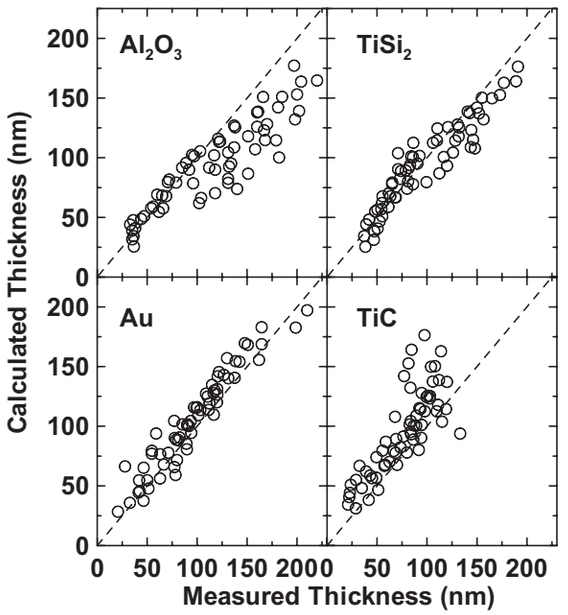


**Figure 4.** Total planar equivalent thickness (underlayer + overlayer) measured with a Dektak profilometer plotted against thickness expected from two orthogonal linear gradients of an underlayer material with a platinum overlayer. The underlayer present is indicated on each panel.

the morphology of the subsequent platinum overlayer deposition, then the measured data (open circles) should fall on the dashed line with slope = 1 for all catalyst compositions prepared. The composition spreads made with gold and titanium disilicide underlayers follow the trend, and maximum film thicknesses between 175 and 200 nm were obtained. Somewhat more scatter was observed in the measured data for the alumina underlayer material. The sputter-deposited alumina may be porous, resulting in a rough surface leading to the observed scatter. The composition spread made with a titanium carbide underlayer gave a total thickness of around 130 nm in the thick TiC and Pt corner of the film. The thicknesses in this region of the film are significantly lower than expected for a linear combination of deposited film thicknesses. The thicknesses measured along the thin Pt end of the sample followed the linear profile expected for a region containing mostly the TiC gradient. This suggests that TiC may be depositing with a rough morphology. Much of the Pt overlayer deposit may then fill in the roughness in the TiC deposit and thus cause the total deposited thickness to increase less than would be expected.

*Scanning electron microscopy*.— SEM images were taken of all investigated underlayer materials (Fig. 1A) deposited on NSTF support film. Figure 5 shows some of the scanning electron micrographs. The SEM images were taken for a 100 nm planar equivalent coating of each of the underlayer materials. The alumina, titanium carbide, and titanium disilicide underlayer materials had a similar morphology, comprising small particles coating the NSTF whiskers. In addition, a preferred deposition at the top of the whiskers can be seen, creating a "baseball-bat-like shape" for the coated NSTF whiskers. A slightly different morphology was observed for the Au-coated whisker film. The Au coating formed larger particles with poorly defined edges. The gold deposited preferentially on the top of the whiskers, sometimes forming aggregates connecting numerous whiskers.

*XRD*.— The impact of the different underlayer materials on the phases present and the extent of crystallinity of the subsequent Pt overlayer was investigated by XRD measurements. Figure 6 shows XRD patterns for the four different underlayer materials coated on

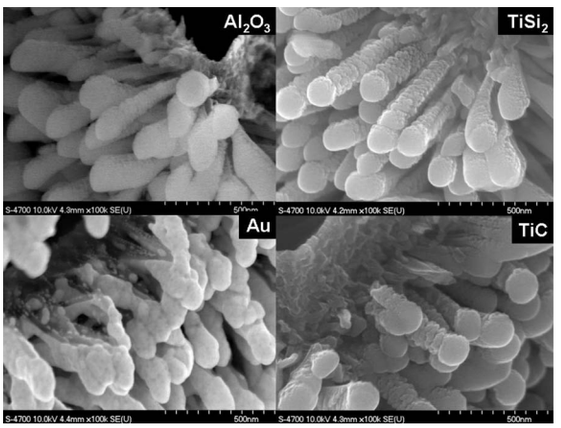


**Figure 5.** Representative SEM images of ~100 nm planar equivalent coating of each of the underlayer materials on NSTF. The scale bar on each panel represents 500 nm. The material present is indicated in the top right corner of each image.

NSTF whiskers. Each panel shows a series of scans, collected at different underlayer thicknesses. In each panel, the underlayer thickness increases from the bottom scan to the top scan, and the scans have been offset vertically for clarity. Figure 6 shows that gold is the only material that deposits as a crystalline layer on the NSTF whiskers. The characteristic diffraction peaks of gold located at 37.9 and 44.0° were assigned to the (111) and (200) Bragg planes of the face-centered cubic (fcc) Au structure. The diffraction peaks at higher angles are not shown here. No diffraction peaks, apart from those of the NSTF support, were observed in the XRD patterns of alumina, titanium carbide, and titanium disilicide. This suggests that these three underlayer materials deposit as amorphous or highly nanocrystalline coatings. The small diffraction peak at around 44.2° in the patterns of $Al_2O_3$, TiC, and $TiSi_2$ comes from the NSTF support substrate. The XRD patterns of all the underlayer materials coated with Pt (as in Fig. 1D) are shown in Fig. 7. In addition, the

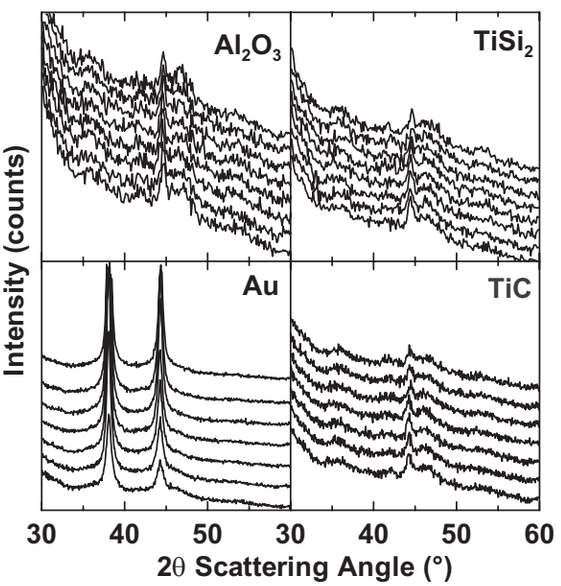


**Figure 6.** XRD spectra for the different underlayer materials deposited on NSTF. The material present is indicated on each panel. Each panel contains multiple scan, with each scan collected at a different underlayer thickness. The scans have been vertically offset for clarity. The underlayer thickness increases from the bottom scan to the top scan.

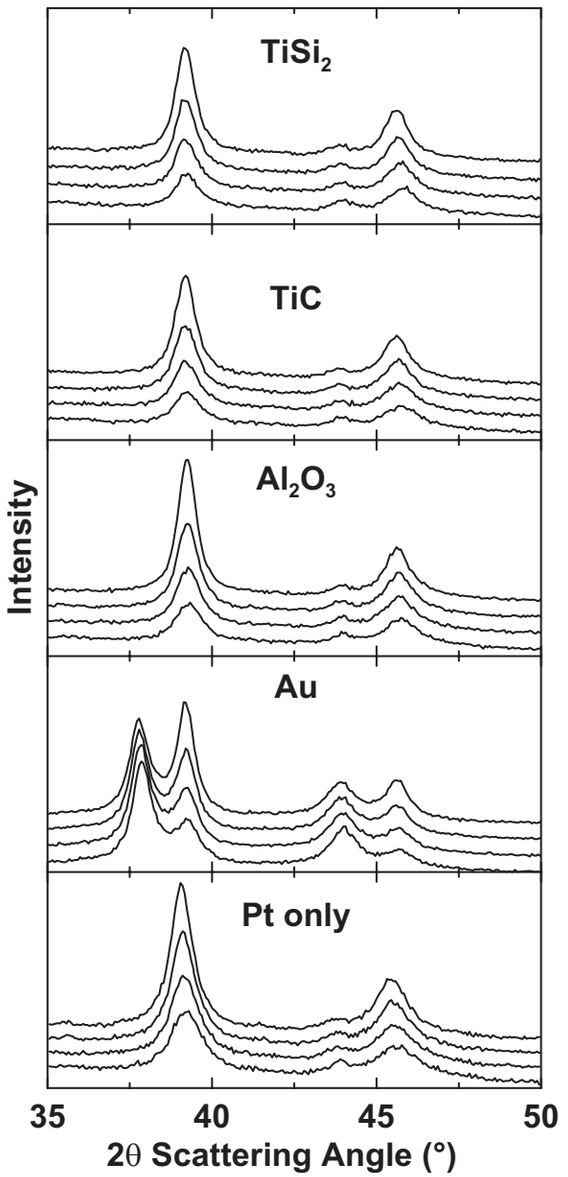


**Figure 7.** Selected XRD spectra for thick underlayer samples (~70 nm planar equivalent) with increasing Pt overlayer thicknesses (out to ~75 nm planar equivalent). The spectra have been offset vertically for clarity. For a given underlayer material (indicated on each panel) the platinum thickness increases from the lowest to the highest spectrum.

X-ray pattern of Pt directly deposited on an NSTF whisker (as in Fig. 1B) is given. All patterns show the typical diffraction peaks for crystalline fcc platinum, which are located at 39.3° [Pt(111)] and 45.7° [Pt(200)]. Additional diffraction peaks seen were only seen when Au was present as an underlayer. The lattice constants for Au and Pt differ enough that two distinguishable sets of diffraction peaks are present in the XRD pattern of Au coated with Pt. The Pt (111) and (200) peak intensities increase with increasing Pt thickness simply because more Pt is present.

Figure 8 shows calculated Pt grain sizes plotted against the thickness of platinum for the various underlayer materials. The grain sizes have been calculated for the Pt(111) peaks using the Scherrer equation. The filled circles show the grain sizes as a function of the planar equivalent platinum thickness. Each panel contains calculated Pt grain sizes for different underlayer thicknesses, so the spread in the data at given Pt thickness is a measure of the dependence of Pt

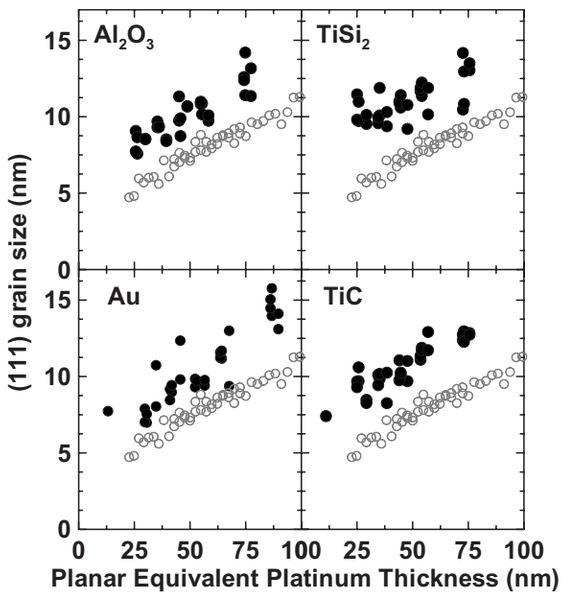


**Figure 8.** Grain sizes for the (111) peak position of Pt calculated from XRD measurements. Filled circles show the grain sizes as a function of planar equivalent platinum thickness. Empty circles show grain sizes for a separate composition spread of platinum only. The underlayer material present is indicated in each panel.

grain size on underlayer thickness. The empty circles in each panel represent grain sizes only for platinum (as in Fig. 1B) directly deposited on an NSTF whisker. The Pt grain sizes were found to vary between 6 and 13 nm for the alumina, titanium carbide, and titanium disilicide coated NSTF whisker materials. The values calculated for Pt on these three underlayer materials were not strongly correlated with the underlayer thickness as the extent of spread for a given deposited Pt thickness is relatively small. They are higher than those measured on an NSTF coated with Pt only for the same Pt loading, possibly because the surface roughness generated by the underlayer material provides nucleation and growth sites for larger Pt particles.

*ECSA measurements*.— ECSA values were calculated from the amount of charge passed during proton adsorption/desorption in CV measurements, after correcting for the double layer capacitance. Figure 9a and b shows ECSA data for Pt directly deposited on NSTF as a function of Pt loading for a cell straight after assembly (Fig. 9a) and after the electrochemical cleaning process described in the Experimental section (Fig. 9b). The ESCA has significantly increased

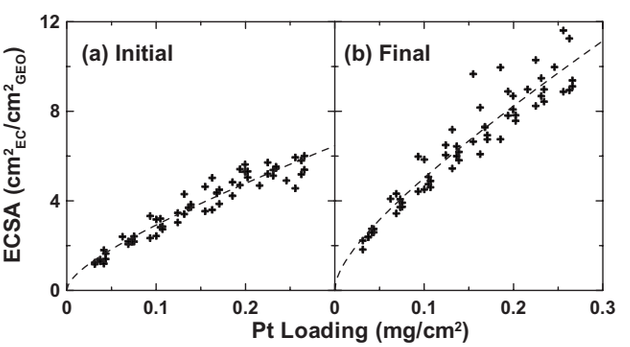


**Figure 9.** Specific ECSAs calculated from the H-desorption region of the CVs for a linear gradient of platinum directly deposited on the NSTF support. (a) shows ECSA values for the electrodes in the cell as-assembled. (b) shows ECSA data for electrodes after electrochemical cleaning.

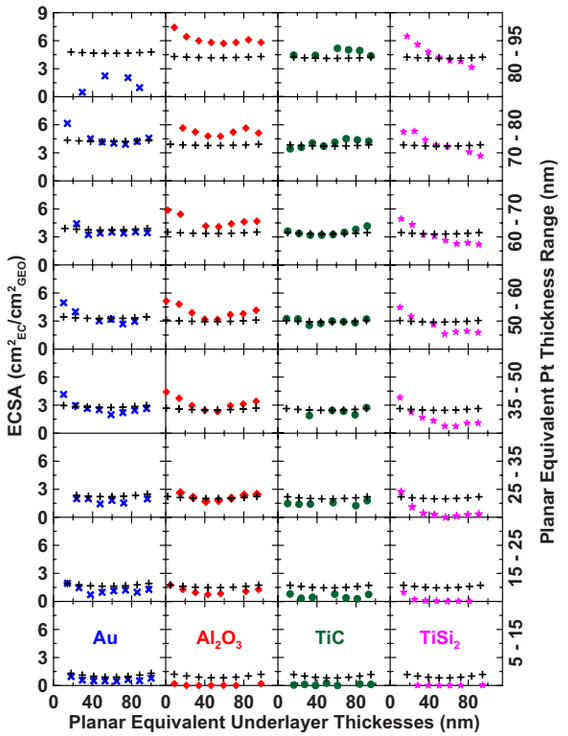


**Figure 10.** (Color online) Specific ECSAs calculated from the H-desorption region of the CVs for the different underlayers with linear platinum overlayer gradients. The data were collected straight after cell assembly. Each column shows the data for one underlayer, with underlayer thickness increasing from left to right. The platinum overlayer thickness increases from the bottom panel to the top panel, with the approximate thickness range indicated on the right-hand axes. X—Au, diamond—$Al_2O_3$, circle—TiC, star—$TiSi_2$, and cross (black)—without underlayer.

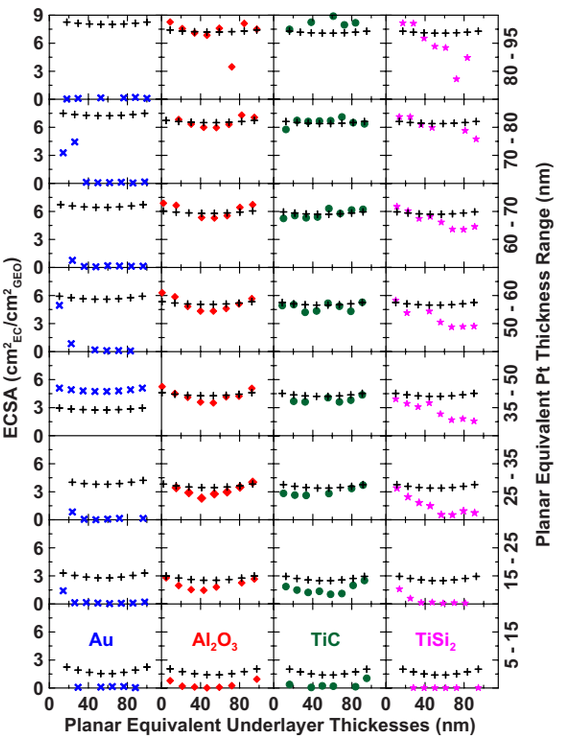


**Figure 11.** (Color online) Specific ECSAs calculated from the H-desorption region of the CVs for the different underlayers with linear platinum overlayer gradients. The data were collected straight after electrochemical cleaning of the cell. Each column shows the data for one underlayer, with underlayer thickness increasing from left to right. The platinum overlayer thickness increases from the bottom panel to the top panel, with the approximate thickness range indicated on the right-hand axes. X—Au, diamond—$Al_2O_3$, circle—TiC, star—$TiSi_2$, and cross (black)—without underlayer.

by the end of the cleaning process, most likely primarily because surface impurities have been removed. In Fig. 9a and b it is clear that, for platinum coated on bare NSTF whiskers, the ECSA increases as the platinum loading increases. As the platinum loading increases, the primary platinum [111] grain size on the NSTF whiskers also increases, as shown in Fig. 8.

To fully understand the relationship between loading and surface area, there is a need to know the shape of the primary platinum particles. Platinum typically deposits as small whiskerettes on the side of the NSTF samples.[18] In one model these whiskerettes can be represented by cylinders to determine an approximate relationship between surface area and loading. The dashed lines in Fig. 9 show the fits obtained using this model. The fit parameters obtained from these fits were used to determine the ECSA expected for a given platinum loading deposited on an underlayer material. To determine whether the underlayer has an impact on the ECSA of the platinum overlayer, it is useful to compare the measured ECSA for a given underlayer/Pt overlayer combination to the ECSA expected for the amount of platinum deposited on the underlayer. This information is presented in Fig. 10 and 11, which show measured and predicted ECSA values, respectively. Figure 10 shows the values measured after cell assembly. Figure 11 shows the values measured after the electrochemical cleaning process. Each column of panels summarizes the data for one underlayer material. The underlayer present is indicated in the bottom panel of each column. For each panel, the underlayer thickness increases from left to right. Each panel shows data for a small range of platinum thicknesses. The approximate Pt thickness ranges present are indicated on the right-hand axes. The Pt thickness ranges present increase from the bottom panel to the top panel. The crosses on each panel show the values expected for a Pt-only sample of the same platinum loading.

The Au and TiC underlayers show similar behavior in the as-assembled state. The ECSA values measured were typically close to those expected for the amount of platinum deposited onto the underlayer, except at very low platinum loadings, suggesting that these underlayers have minimal impact on the surface area of deposited platinum. The presence of an alumina underlayer seems to cause the platinum surface to increase especially for the electrodes with high platinum loading. This suggests that an alumina underlayer may influence the morphology of a sputtered Pt overlayer. The samples with a $TiSi_2$ underlayer were the only ones to suffer a loss in ECSA as the underlayer thickness increased relative to the ECSA expected for the amount of platinum present. A cause of this behavior is proposed in the next section.

The electrochemical cleaning process changed the ECSA values of the materials prepared. It is likely that the surface after electrochemical cleaning is more representative of the surface that would be present in an operating fuel cell. After this cleaning process, all except the gold underlayer composition spreads showed increased ECSA values when no or only a thin layer of underlayer material was present. The removal of surface impurities together with surface rearrangement of the Pt is assumed to be responsible for the observed gain in specific ECSA. Although all fuel cell catalysts and MEAs need to be "broken-in" through a cleaning process before full performance is obtained, the lower absolute surface area and the higher specific activity for ORR of the thin layer NSTF catalysts make them more sensitive to this effect. Ongoing research at 3M has

established the importance of the membrane properties and processing, the catalyst composition, and the break-in protocol for minimizing the cleaning time in operating fuel cells.

Figure 11 shows a dramatic loss of ECSA for the Pt on Au underlayer as the Au thickness increases compared to Fig. 10. With only a small underlayer thickness (20–25 nm planar equivalent) of gold, it was difficult to see any H adsorption/desorption in the CVs and hence the ECSA values were close to 0. It is very likely that the underlying gold segregates and migrates to the surface of the platinum grains causing this extreme reduction of active surface area.[22] The present results are in good agreement with the experimental work of Tsong et al., who investigated surface segregation trends in Pt–Au alloys by applying atom-probe field ion microscopy.[23] Hörnström et al. also reported a strong surface segregation of gold in three different Pt–Au alloys containing between 2 and 90 wt % gold. The alloys were studied using Auger electron spectroscopy.[24] The results obtained unambiguously showed the detrimental impact of gold on the electrocatalytic activity of platinum. Hence, gold is a poor choice as a support material for platinum to be used as a cathode catalyst in a PEMFC. In earlier work we showed that the HOR overpotential for a Pt–Au binary composition was also significantly increased when intermediate levels of gold were present.[20] As a result the HOR capability significantly degraded.

For the composition spread made with alumina, the specific ECSA values after electrochemical cleaning were very close to those expected for the platinum loading present, except at very low platinum loadings. Alumina is an electrical insulator and thus the CV signal comes from the platinum overlayer. It is possible that at low platinum loadings the platinum forms discrete particles separated from each other and thus there is a lack of conductivity, leading to low ECSAs. The composition spread having titanium carbide as an underlayer material showed essentially the same behavior as the alumina underlayer. The ECSA values are similar to the data obtained for platinum directly deposited on an NSTF whisker (as in Fig. 1B) suggesting that, from an electrochemical perspective, TiC and alumina are promising support materials for ORR catalysts in PEMFC.

Figure 11 shows that the specific ECSA values for the $TiSi_2$ underlayer samples still decrease as the $TiSi_2$ underlayer thickness increases after electrochemical cycling. At low underlayer thicknesses, the ECSA values were close to those expected for Pt only. $TiSi_2$, like Au, does not appear to be an appropriate underlayer or support material for platinum-based ORR catalysts in PEMFC. It is possible that the presence of silicon (in $TiSi_2$) leads to the formation of a binary or ternary silicide phase (Pt–Si or Pt–Ti–Si) at the interface between the underlayer and Pt. This silicide phase would consume Pt and presumably have a negative impact on the electrochemical behavior of the prepared composition spread because the effective ECSA is significantly reduced. XPS measurements and depth-profile analysis were completed to look for more compelling evidence of the formation of a silicide phase.

*XPS.*— The formation of the Pt-silicide phase was investigated by performing depth-profile analysis. Figures 12 and 13 show the Pt 4f and the Ti 2p spectra of the electrocatalyst samples prepared with TiC and $TiSi_2$ as underlayers, respectively. The XPS spectra were recorded on Pt-coated titanium carbide and Pt-coated titanium disilicide samples deposited on GC disks as a function of sputter etch depth. XPS spectra were recorded at each etch level. The films were etched between spectral acquisitions using an argon ion beam having a spot diameter of 600 μm.

For platinum deposited on titanium carbide, the Pt $4f_{7/2}$ and Pt $4f_{5/2}$ lines were observed at binding energies of 71.0 and 74.3 eV, respectively. The observed Pt $4f_{7/2}$ peak position corresponds to the value of platinum in the metallic state.[25] Figure 12 shows that the Pt 4f peak positions do not change significantly for the Pt–TiC composition during depth-profile analysis. The observed peak positions varied throughout between 71.0 and 71.15 eV. When platinum is deposited on titanium disilicide, the Pt $4f_{7/2}$ and Pt $4f_{5/2}$ lines of the first layer were also observed at binding energy values of 71.0 and 74.3 eV. As the platinum was gradually etched away by the argon plasma, both platinum peak positions shifted to higher values. Figure 13 shows the position of the Pt $4f_{7/2}$ peak as a function of etching level for both the Pt/TiC and Pt/$TiSi_2$ samples. The shift of the peak is obvious for the Pt/$TiSi_2$ sample. Binding energy values of 71.65 and 74.9 eV were recorded for the Pt $4f_{7/2}$ and Pt $4f_{5/2}$ lines after etching of the top layer(s) of the Pt/$TiSi_2$ sample. We attribute these findings to the formation of platinum silicide phases at the interface between Pt and $TiSi_2$. Similar observations were reported by Solina et al., who investigated the interface structure of ultrathin platinum films deposited on 100 silicon.[26] The authors used electron-beam evaporation and dc-magnetron sputtering for their film deposition. Solina et al. reported that the resultant XPS data unambiguously confirmed the existence of platinum silicide between the platinum and silicon.[26]

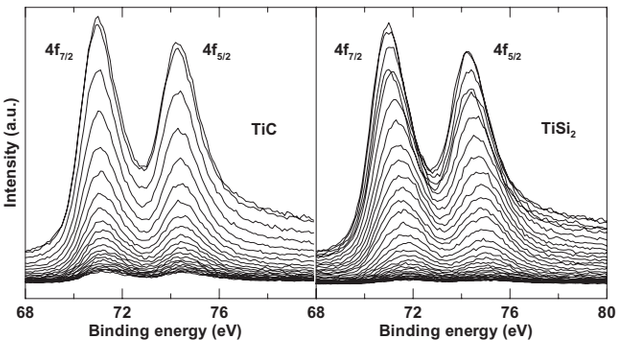


**Figure 12.** Platinum 4f XPS spectra of the electrocatalyst samples with TiC and $TiSi_2$ underlayer materials. The XPS spectra were recorded on Pt–TiC and Pt–$TiSi_2$ sputter deposited on GC disks. The XPS spectra at each etch level are shown.

As the etching of the Pt/$TiSi_2$ and Pt/TiC catalyst layers proceeded, the intensity of the Pt $4f_{7/2}$ and Pt $4f_{5/2}$ lines of both catalyst compositions gradually decreased. Figure 13 shows that for the platinum deposited on titanium disilicide, the Pt peaks do not shift further at an intermediate etch level and the Pt $4f_{7/2}$ peak position remains at 71.65 eV, suggesting that the Pt–Si phase is found at the bottom of the Pt layer.

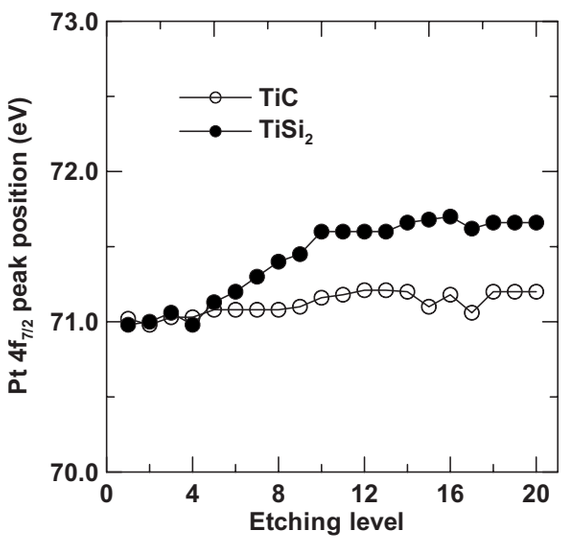


**Figure 13.** Peak position of the Pt $4f_{7/2}$ peak as a function of etching level for both the Pt/TiC and Pt/$TiSi_2$ samples.

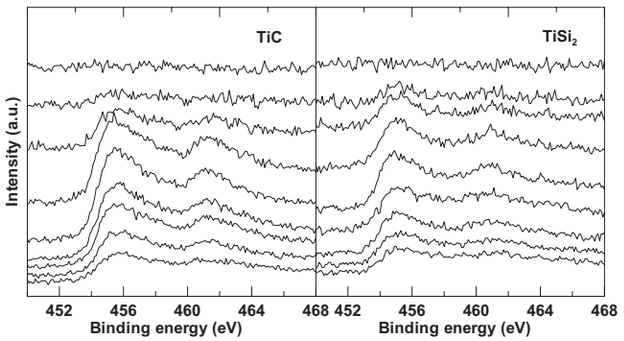


**Figure 14.** Titanium 2p XPS spectra of the electrocatalyst samples with TiC and $TiSi_2$ underlayer materials. The XPS spectra were recorded on Pt–TiC and Pt–$TiSi_2$ sputter deposited on GC disks. The XPS spectra at every second etch level are shown.

The Ti 2p spectra obtained (Fig. 14) indicate that no titanium is present on the top surface of the deposited catalyst layers. The Ti 2p spectra at every second etch level are shown here. After a few layers of platinum have been etched away, distinguishable peaks could be observed in the Ti 2p XPS spectra. For the Pt/TiC sample, peaks are located at 455.5 and 461.1 eV, respectively. Similar binding energy values are given in the literature[27-29] for Ti in TiC. Teghil et al. and Jelinek et al. reported peak positions of 455.0 and 460.6 eV, which they assigned to Ti species bonded to C in the metal carbide. Nevertheless, it is also possible that other components such as $Ti^{3+}$ or $Ti^{4+}$ (from $Ti_2O_3$ or $TiO_2$) exist in both catalyst compositions prepared. Similar peak positions have been reported for Ti(IV) oxide (456.0 and 461.6 eV) and for Ti species with intermediate oxidation states (TiO 455.1 eV).[27,28,30] Oxygen may have been introduced during the deposition runs due to residual oxygen in the sputtering chamber. The presence of oxygen could also arise from exposure to air during storage before the acquisition of XPS spectra. The Ti 2p peaks of both compositions show maximum intensities at intermediate etch levels. Continuing etching leads to a steady decrease of Ti 2p peak intensity due to the removal of the catalyst film.

## Conclusion

A series of these platinum-coated underlayer materials was deposited by a high throughput magnetron sputtering method on 3M's NSTF support whiskers for fuel cell testing. Surface profile measurements showed that the resulting composition spreads consisted of 0–100 nm of the underlayer materials and 0–75 nm of the platinum top layer. Electrochemical testing showed that gold and titanium disilicide underlayers and supports caused loss of Pt ECSA during operation with hydrogen and air. Migration and surface accumulation were observed when gold was used as an underlayer material. In the case of titanium disilicide, alloying and the generation of platinum silicide phases occurred, which could be confirmed by XPS measurements and subsequent depth-profile analysis. Electrocatalysts need to satisfy many different criteria to be acceptable for fuel cell use. This study has shown that alumina and titanium carbide are promising underlayer materials on the NSTF whiskers as well as alternative support materials in their own right because the Pt ECSA is not lost through normal fuel cell operation. Further testing would be required to assess surface area stability under more aggressive "abnormal" process conditions.

## Acknowledgments

We acknowledge the support of the Canada Foundation for Innovation, the Atlantic Innovation Fund, and other partners which fund the Facilities for Materials Characterization, managed by the Institute for Research in Materials, and the U.S. Department of Energy for its support of the 3M NSTF catalyst development.

*Dalhousie University assisted in meeting the publication costs of this article.*

## References

1. www1.eere.energy.gov/hydrogenandfuelcells, last accessed November 16, 2009.
2. J. O'M. Bockris and A. K. N. Reddy, *Modern Electrochemistry*, 2nd ed., Kluwer-Plenum, New York (2000).
3. DOE Hydrogen and Fuel Cell Program, Annual Merit Review, DOE, Washington, DC (2009).
4. R. Brodup, J. Meyers, B. Pivovar, Y. Seung Kim, R. Mukundan, N. Garland, D. Meyers, M. Wilson, F. Garzon, D. Wood, et al., *Chem. Rev. (Washington, D.C.)*, **107**, 3904 (2007).
5. C. A. Reiser, L. Bregoli, T. W. Patterson, J. S. Yi, D. Yang, M. L. Perry, and T. D. Jarvi, *Electrochem. Solid-State Lett.*, **8**, A273 (2005).
6. K. Kinoshita and J. Bett, *Carbon*, **11**, 237 (1973).
7. D. Wood, J. Davey, F. Garzon, P. Atanassov, and R. Borup, *Proceedings of the Fuel Cell Seminar*, Los Alamos National Laboratory (2005).
8. K. Kinoshita, J. T. Lundquist, and P. Stonehart, *J. Electroanal. Chem. Interfacial Electrochem.*, **48**, 157 (1973).
9. J. Roziere and D. J. Jones, *Annu. Rev. Mater. Res.*, **33**, 503 (2003).
10. U. A. Paulus, A. Wokaun, G. G. Scherer, T. J. Schmidt, V. Stamenkovic, N. M. Markovic, and P. N. Ross, *Electrochim. Acta*, **47**, 3787 (2002).
11. H. T. Duong, M. A. Rigsby, W. P. Zhou, and A. Wieckowski, *J. Phys. Chem. C*, **111**, 13460 (2007).
12. K. J. J. Mayrhofer, D. Strmcnik, B. B. Blizanac, V. Stamenkovic, M. Arenz, and N. M. Markovic, *Electrochim. Acta*, **53**, 3181 (2008).
13. V. Komanicky, K. C. Chang, A. Menzel, N. M. Markovic, H. You, X. Wang, and D. Myers, *J. Electrochem. Soc.*, **153**, B446 (2006).
14. P. J. Ferreira, G. J. la O', Y. Shao-Horn, D. Morgan, R. Makharia, S. Kocha, and H. A. Gasteiger, *J. Electrochem. Soc.*, **152**, A2256 (2005).
15. J. Zhang, B. A. Litteer, W. Gu, H. Liu, and H. A. Gasteiger, *J. Electrochem. Soc.*, **154**, B1006 (2007).
16. M. K. Debe, Presentation FC 17, DOE Hydrogen Program Review, DOE, Washington, DC (2009).
17. M. K. Debe, A. K. Schmoeckel, G. D. Vernstrom, and R. Atanasoski, *J. Power Sources*, **161**, 1002 (2006).
18. L. Gancs, T. Kobayashi, M. K. Debe, R. Atanasoski, and A. Wieckowski, *Chem. Mater.*, **20**, 2444 (2008).
19. J. R. Dahn, S. Trussler, T. D. Hatchard, A. Bonakdarpour, J. R. Mueller-Neuhaus, K. C. Hewitt, and M. Fleischauer, *Chem. Mater.*, **14**, 3519 (2002).
20. D. A. Stevens, J. M. Rouleau, R. E. Mar, A. Bonakdarpour, R. T. Anasoski, A. K. Schmoeckel, M. K. Debe, and J. R. Dahn, *J. Electrochem. Soc.*, **154**, B566 (2007).
21. D. A. Stevens, J. M. Rouleau, R. E. Mar, R. T. Atanasoski, A. K. Schmoeckel, M. K. Debe, and J. R. Dahn, *J. Electrochem. Soc.*, **154**, B1211 (2007).
22. Y. Ma and P. B. Balbuena, *Surf. Sci.*, **602**, 107 (2008).
23. T. T. Tsong, Y. S. Ng, and S. B. McLane, Jr., *J. Chem. Phys.*, **73**, 1464 (1980).
24. S. E. Hörnström, L. I. Johansson, and A. Flodström, *Appl. Surf. Sci.*, **26**, 27 (1986).
25. A. Kakanakova-Georgieva, Ts. Marinova, O. Noblanc, C. Arnodo, S. Cassette, and C. Brylinski, *Appl. Surf. Sci.*, **121**, 208 (1997).
26. D. M. Solina, R. W. Cheary, P. D. Swift, S. Dligatch, G. M. McCredie, B. Gong, and P. Lynch, *Thin Solid Films*, **372**, 94 (2000).
27. R. Teghil, L. D'Alessio, A. De Bonis, A. Galasso, P. Villani, and A. Santagata, *Thin Solid Films*, **515**, 1411 (2006).
28. F. Santerre, M. A. El Khakani, M. Chaker, and J. P. Dodelet, *Appl. Surf. Sci.*, **148**, 24 (1999).
29. M. Jelinek, T. Kocourek, J. Kadlec, V. Vorlicek, M. Cernansky, V. Studnicka, A. Santoni, P. Bohac, and F. Uherek, *Thin Solid Films*, **506**, 101 (2006).
30. D. Simon, C. Perrin, and J. Bardolle, *J. Microsc. Spectrosc. Electron.*, **1**, 175 (1976).

*Electrochemical and Solid-State Letters*, **11** (11) B208-B211 (2008)
1099-0062/2008/11(11)/B208/4/$23.00 © The Electrochemical Society

# $H_2O_2$ Release during Oxygen Reduction Reaction on Pt Nanoparticles

**Arman Bonakdarpour,[a,z] Tara R. Dahn,[a] R. T. Atanasoski,[b,*] M. K. Debe,[b,*] and J. R. Dahn[a,*]**

[a]*Department of Physics and Atmospheric Science, Dalhousie University, Halifax, Nova Scotia B3H 3J5, Canada*
[b]*3M, Fuel Cell Components Program, St. Paul, Minnesota 55144, USA*

The impact of 3M's nanostructured thin film electrocatalyst loading on rotating ring-disk electrode (RRDE) experiments for the oxygen reduction reaction (ORR) in a 0.1 M $HClO_4$ solution has been studied. The electrocatalysts were prepared by sputtering Pt onto support whiskers and have been reported to exhibit one of the best specific activities of any ORR catalyst thus far. However, a dramatic increase in $H_2O_2$ release was observed as the catalyst loading (number of catalyzed whiskers per unit area) on the glassy carbon tip of RRDE was decreased below 20 $\mu g\ cm^{-2}$, confirming some earlier observations reported by our group and other research groups with some other types of catalysts. These observations suggest that oxygen reduction occurs through a $H_2O_2$ intermediate, and if the catalyst nanoparticles are sparsely distributed, the produced $H_2O_2$ cannot be efficiently reduced to $H_2O$ before it escapes. Similar observations have been made for Se/Ru/C and Fe–N–C catalysts.
 [DOI: 10.1149/1.2978090] 

Manuscript submitted May 8, 2008; revised manuscript received July 10, 2008. Published September 12, 2008.

The best catalyst for the reduction of oxygen, which is the cathodic reaction of proton exchange membrane fuel cells (PEMFCs), is still Pt or an alloy of Pt.[1] Nonetheless, from both fundamental and applied points of view, the oxygen reduction reaction (ORR) continues to be an active research field with experimental and theoretical approaches focused on understanding the limiting factors and the possible failure modes that could be plaguing the ORR electrocatalysis.[2-8]

The desired route of oxygen reduction is the $4e^-$ pathway leading to $H_2O$; however, a partial $2e^-$ reduction to $H_2O_2$ is also possible. Besides involving fewer electrons per $O_2$ molecule, the $H_2O_2$ becomes highly corrosive when it breaks down into free radicals like OH• and OOH•. The radicals, which can form in the presence of metals, have a detrimental impact on the Nafion polymer used in the PEMFCs.[9,10] The radicals are known to initiate a chain oxidation reaction by attacking the carboxylic end groups of the polymer.[11,12] Minimizing the release of $H_2O_2$ is thus of great importance in the design of ORR electrocatalysts. ORR on Pt surfaces is known to be generally a $4e^-$ reaction.[13] Rotating ring-disk electrode (RRDE) experiments on single crystals of Pt, polycrystalline Pt, and even supported Pt have shown no detectable $H_2O_2$ above 0.6 V.[13,14] The $H_2O_2$ is observed only at low potentials corresponding to the hydrogen adsorption region where Pt sites get covered with $H_{upd}$. The $H_2O_2$ release also increases in the presence of strongly adsorbed anions like $Cl^-$ or $Br^-$.[15,16] Se- or S-covered Pt surfaces or the presence of decomposition products from residual solvents used in the membrane casting process in the electrolyte have also shown increased levels of released $H_2O_2$.[17] All these observations indicate that site availability, which would be severely compromised in the presence of impurities, is critical in the release of $H_2O_2$.

We present evidence here that in the case of nanoparticles, the amount of detected $H_2O_2$ also depends on the catalyst loading (mass per $cm^2$) on the RRDE tips. The first such observation was perhaps made by Inaba and co-workers.[18] They reported that for carbon-supported Pt (Pt/C) the fraction of $H_2O_2$ increased when loading of catalyst on the tip of the RRDE decreased. In two earlier publications we reported the impact of the loading of non-Pt-based ORR electrocatalysts on the fraction of $H_2O_2$ release.[19,20] For Fe–N–C type catalysts,[19] prepared by solid-state reaction of carbon and Fe precursors in the presence of ammonia, and Se/Ru/C catalysts,[20] prepared by the chemical reduction of metal salts in an aqueous environment, increased fractions of $H_2O_2$ release were detected when the catalyst loading was lowered on the RRDE tip.

The samples studied here were nanostructured Pt thin films supported on crystalline organic pigment support whiskers developed at 3M Company. The desired catalysts (Pt or Pt alloy) can be deposited by a common physical vapor deposition technique like magnetron sputtering. These support structures consist of a single layer of self-assembled crystalline whiskers that grow by a screw-dislocation mechanism when a vacuum-deposited organic pigment (CAS no. PR149) film is annealed at 250–270°C.[21] Typical individual whiskers are about 1000 nm in length and about 50 nm in diameter, with an areal number density of 3–4 billion per $cm^2$.[21] Production and characterization of these nanostructured thin film (NSTF) catalyst films and early fuel cell results are described by Debe et al.[21-23] More recent results on the electrochemical stability and applications of Pt-alloys/NSTF are described elsewhere.[24-27] In a fuel cell environment, in addition to a lower required Pt loading, Pt/NSTF catalysts have shown a remarkable electrochemical stability which is manifested when the catalysts are subjected to high potential cycling tests.[24] The stability and high activity of these catalysts is attributed to their larger grain size (10–15 nm) and preponderance of (111) facets.[28] Conventional and commercial Pt/C catalysts have shown poor stability when exposed to high potential cycling.[24] A recent report by Ahluwalia and Wang shows that the U.S. Department of Energy's catalyst goals for 2010 can be achieved using 3M's NSTF technology.[29]

## Experimental

*Preparation of sputtered Pt on nanostructured thin-film support.*— The preparation of NSTF support is explained in more detail by Debe,[21-23] as are procedures for forming catalyst-coated membranes for fuel cell testing. Here, Pt electrocatalyst was deposited onto a NSTF support film using a magnetron sputtering system. The depositions produced catalyst-coated whisker films for this study with a planar loading equivalent of 0.15 mg Pt $cm^{-2}$. In order to evaluate the catalyst using RRDE, the catalyst-coated NSTF whiskers were carefully brushed off of the original substrate web using a solder brush and collected as a powder for subsequent dispersion. Precautions were taken to avoid any contamination of the catalyst with impurities. The bare NSTF supports have no activity toward oxygen reduction and are electrochemically inactive.

*Electrochemical measurements.*— We used a Pine Instruments RRDE system, a Pt-wire counter electrode, and 0.1 M $HClO_4$ as the electrolyte. A $Cl^-$-free Koslow $Hg/Hg_2SO_4$ (MMS) reference electrode was used. All measurements were performed at room tempera-

* Electrochemical Society Active Member.
z E-mail: arman@chml.ubc.ca

ture (21°C). Extreme care was taken to ensure the cleanliness of the glassware, cell parts, and the samples during handling. Potentials mentioned in this article are referenced to the reversible hydrogen electrode (RHE), and currents are all normalized by the geometric area of the disk electrode.

The RHE scale for the MMS reference electrode was established by bubbling $H_2$ in the solution and measuring the open-circuit voltage (OCV) of the cell using both disk (when the Pt/NSTF sample was used) and the ring electrodes. The OCV values of the disk (when the Pt/NSTF sample was used) and the ring, always within 5 mV or less, were averaged and used as the RHE scale for the measurements. This reference calibration was performed for each individual disk assembly.

For the Pt/NSTF samples, slurries were prepared using only nanopure water and the Pt/NSTF powder. No Nafion was used. The slurry concentrations applied to the RRDE tip were adjusted to provide catalyst mass loadings of 1.25, 2.5, 5, 10, 20, 40, 60, 80, and 100 $\mu g\ cm^{-2}$ when a 15 $\mu L$ drop was placed on a glassy carbon (GC) disk. These mass loadings refer to the mass of Pt placed on the GC electrode tip and do not include the mass of whisker supports (less than 10%). The 0.15 mg Pt $cm^{-2}$ loading mentioned earlier refers to the mass of Pt sputter deposited on the NSTF whisker support and should not be confused with the loadings on the GC electrode tip. The deposited catalyst slurry was dried under air. For all measurements the adhesion of the electrocatalyst to the GC disk was excellent and no loss of electrocatalyst occurred during the measurements as evidenced by an unchanged hydrogen underpotential deposition cyclic voltammogram (CV) before and after ORR testing.

Details of RRDE experiments for Pt/NSTF are explained elsewhere.[27] Briefly, we maintained a strict standard of cell setup and cleaning procedures to achieve state-of-the-art values for the ORR activity of standard Pt. Cyclic voltammetry in Ar-saturated cells and oxygen reduction polarizations in oxygen saturated cells were performed. The sweep rate was 50 mV $s^{-1}$ for all the measurements. Enough CVs under argon up to OCV (1.05 V vs RHE) were performed until steady-state voltammograms were obtained. Only then were measurements in oxygen made.

The collection efficiencies of the Pt ring (7.5 and 8.5 mm inside and outside diameters, respectively) electrode were obtained by the method explained in Ref. 30. These measurements were performed for different mass loadings. In general, the collection efficiency was in the range of 15–20%. The percentage of $H_2O_2$ was calculated by

$$\%H_2O_2 = \frac{200 \times I_{ring}}{(N \times I_{disk}) + I_{ring}} \quad [1]$$

where $N$ is the collection efficiency, measured experimentally for each electrode. The ring electrode was held at 1.2 V vs RHE during the ORR measurements. The RRDE rotation rate was 900 rpm. A linear dependence of the limiting current on the square root of the rotation rate was observed for the high Pt leadings (40–80 $\mu g\ cm^{-2}$) in the range of 400–2500 rpm.

## Results and Discussion

Detailed characterization of Pt/NSTF and Pt-alloy/NSTF catalysts is provided in earlier publications.[27,31,32] Electrochemical measurements like cyclic voltammetry of these electrocatalysts can also be found elsewhere.[27] The electrochemical active surface area, determined from $H_{upd}$, varies linearly as a function of the catalyst loading on the GC disk electrode.[27]

Figures 1a and b show the oxygen reduction currents and the percentage of $O_2$ molecules which are reduced and released as $H_2O_2$ in the electrolyte for different catalyst loadings, respectively. There is a gradual and monotonic increase in the percentage of $H_2O_2$ detected by the ring electrode as the loading of catalysts is lowered. The disk and ring current densities of a Pt film sputtered on a GC disk are also shown for comparison. The increased percentage of $H_2O_2$ is not due to the bare GC electrode. As a reminder, there is

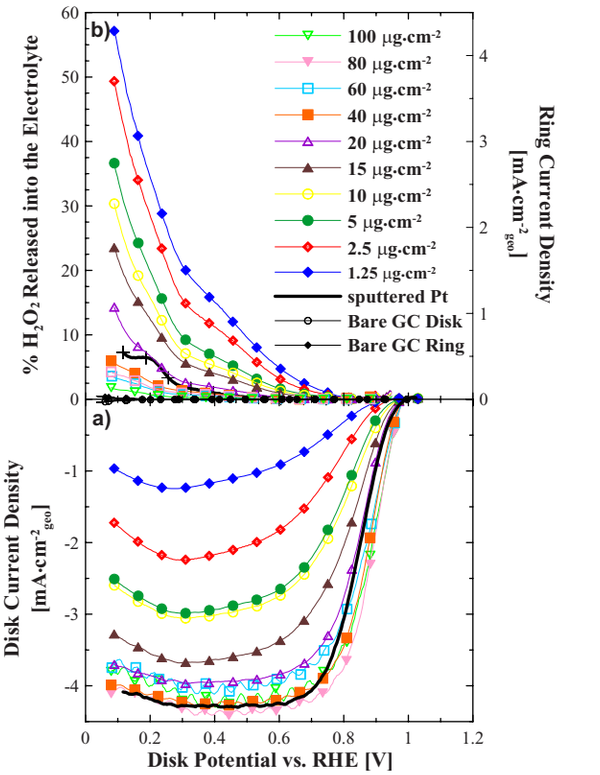


**Figure 1.** (Color online) Oxygen reduction measurements (a) and percentage of $H_2O_2$ released (b) for Pt/NSTF shown for different catalyst loadings on the RRDE tip. Bare GC disk current density (a) and the corresponding ring current density (b) are also shown.

also no carbon support in these catalysts. At 0.6 V the $H_2O_2$ released into the electrolyte increases from about 1 to about 10% when the catalyst loading decreases from 15 to 1.3 $\mu g\ cm^{-2}$. Even at 0.6 V, or the minimum operating potential of PEMFCs, the $H_2O_2$ release of Pt/NSTF is still below 1% even for a loading of 20 $\mu g\ cm^{-2}$, which can still be considered ultralow compared to the loadings targeted for use in PEMFC vehicles. In general, in operating fuel cells, the measured fluoride ion release rates, which presumably directly correlate to the $H_2O_2$ production, are found to be orders of magnitude lower for NSTF catalysts than conventional Pt/carbon-based electrodes.[33,34]

As already mentioned, there is also a monotonic change in the reduction curves (disk currents) as the catalyst content is lowered. This is partly due to an increased fraction of $2e^-$ reduction. However the shape of the curves also changes from a sigmoidal wave to a more linear shape. The "upturn" in the disk reduction currents, which commences at around 0.25 V, coincides with an increased yield of $H_2O_2$ vs potential. This increase in the slope of $\%H_2O_2$ vs potential is due to the $H_{upd}$ on the Pt grains. More detailed RRDE studies of Pt/NSTF kinetics can be found elsewhere.[27,35] In short, the Pt/NSTF shows a specific activity which is similar to bulk Pt surfaces and is about 10× higher than Pt/C.[25]

Figure 2a shows the derivative plots of the ORR curves shown in Fig. 1a. The "half-wave potentials" estimated from the maxima of the curves in Fig. 2a are shown in Fig. 2b. The half-wave potential, as originated from polarography studies, refers to a potential where half the value of diffusion-limited current is reached.[36] If the current–potential ($I$-$V$) curve is an ideal sigmoid, the derivative would be a bell-shaped curve and a maximum would occur at the half-wave potential. The trend in the oxygen reduction currents vs loading is also similar among Pt/C, Fe–N–C, and Se/Ru/C types of catalysts. Within a given window of mass catalyst loadings, the oxy-

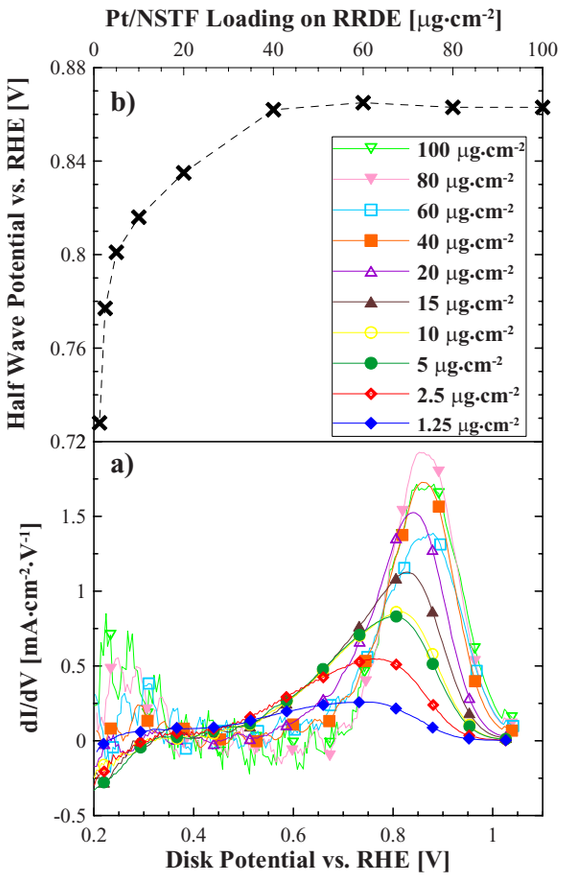


**Figure 2.** (Color online) (a) Derivatives of the ORR data shown in Fig. 2a and b and the half-wave potentials obtained from (a).

gen reduction curves reach the diffusion-limited current. Increasing the mass density beyond this level could lead to currents which are higher than the Levich's diffusion-limited current because of an increase in the surface roughness. For Pt/C, Pt/NSTF, Se/Ru/C, and Fe–N–C this "optimum" deposition is about 15, 40, 100, and 800 μg $cm^{-2}$, respectively. The catalyst loading in fuel cell membrane electrode assemblies (MEAs) are generally much higher, and the loading here in RDE experiments should not be confused with the loadings of fuel cell MEAs. At lower loadings the shape of the *I-V* curves deviates from a sigmoid and the derivative shows asymmetry. Under these conditions the "half-wave potential" is not well defined. We have provided Fig. 2, nonetheless, to show the impact of catalyst loading on the sensitive derivative plots and the "half-wave potential." In a recent publication, Mayrhofer et al. reported very similar observations for the impact of Pt/NSTF catalyst loading on the oxygen reduction currents in RDE experiments.[37] They also report an optimum Pt/NSTF loading of about 40 μg $cm^{-2}$, where the diffusion-limited current is reached using nearly identical experimental conditions. This higher loading, as (compared to Pt/C) required to yield a diffusion-limited current, is attributed to the lower specific area of the Pt/NSTF catalysts.[37]

Figure 3 shows the $\%H_2O_2$ vs loading of the catalyst on RDE tips at 0.3 and 0.6 V vs RHE. When the catalyst loading on the RDE tip is greater than 20 μg $cm^{-2}$, the peroxide release is independent of the loading. Below 20 μg $cm^{-2}$, however, there is a dramatic increase in the released peroxide when loading on the GC tips decreases. The observed trend is very similar at both potentials. In the case of non-noble metal catalysts, the $\%H_2O_2$ released at a given potential showed an almost linear dependence on the logarithm of the loading.[19] Measurements of peroxide were performed at different rotation speeds for all loadings, and no dependence on the rotation speed of RDE was observed. The inset in Fig. 3 shows the percentage of $H_2O_2$ released into the electrolyte for different rotation speeds when a loading of 5 μg $cm^{-2}$ was used.

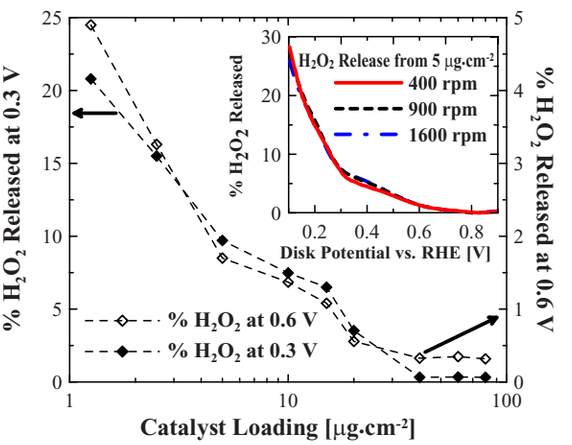


**Figure 3.** (Color online) Variation of $H_2O_2$ released at 0.3 and 0.6 V vs RHE for different loadings of Pt/NSTF on the RDE tip. The inset shows the release of $H_2O_2$ at different rotation speeds for a catalyst loading of 5 μg $cm^{-2}$.

The increase in the percentage of $H_2O_2$ released as the loading decreases reported here for Pt/NSTF is also similar to Pt/C, Fe–N–C, and Se/Ru/C.[18,38] In these three classes of ORR catalysts, at a given potential there is a monotonic increase in the percentage of detected $H_2O_2$ as the loading decreases. This $H_2O_2$ detected by the ring can be considered "free" and does not further reduce to $H_2O$. We speculate that on all these catalysts the $O_2$ molecules first reduce to $H_2O_2$ and then disproportionate to $H_2O$. When the loading of the catalysts is lowered and active sites become sparsely distributed on the RRDE tips there is a smaller probability that $H_2O_2$ molecules get further reduced to $H_2O$; thus, the fraction of "free" $H_2O_2$ is increased.

## Conclusions

The loading of catalyzed whiskers on GC disks has a direct impact on the fraction of $H_2O_2$ that is released in the electrolyte. As loading of catalyst decreases on the tip of the RDE, the level of $H_2O_2$, as detected by the ring electrode, increases. When the real density (or thickness) of the catalyst layer is higher, $O_2$ molecules are more efficiently reduced to water. These observations are in agreement with similar studies on Pt/C and non-Pt catalysts such as Fe–N–C and Se/Ru/C recently reported in the literature. All these observations suggest that the reduction of at least a significant fraction of $O_2$ molecules to $H_2O$ occurs through an $H_2O_2$ intermediate. Researchers should be aware of this loading dependence regardless of their choice of ORR catalyst.

## Acknowledgments

The Dalhousie authors acknowledge the financial support of National Sciences and Engineering Research Council of Canada and 3M for this work. A.B. acknowledges the Killam and Summer Foundations for scholarship support. The work reported here was partially supported by The Hydrogen, Fuel Cells and Infrastructure Technology Program in the Office of Energy Efficiency and Renewable Energy at the U.S. Department of Energy under cooperative agreement DE-FC36-02AL67621.

*Dalhousie University assisted in meeting the publication costs of this article.*

## References

1. H. A. Gasteiger, S. S. Kocha, B. Sompalli, and F. T. Wagner, *Appl. Catal., B*, **56**,

9 (2005).
2. J. K. Norskov, J. Rossmeisl, A. Logadottir, L. Lindqvist, J. R. Kitchin, T. Bligaard, and H. Jonsson, *J. Phys. Chem. B*, **108**, 17886 (2004).
3. V. R. Stamenkovic, B. Fowler, B. S. Mun, G. Wang, P. N. Ross, C. A. Lucas, and N. M. Markovic, *Science*, **315**, 493 (2007).
4. V. R. Stamenkovic, B. S. Mun, M. Arenz, K. J. J. Mayrhofer, C. A. Lucas, G. F. Wang, P. N. Ross, and N. M. Markovic, *Nat. Mater.*, **6**, 241 (2007).
5. J. Zhang, K. Sasaki, E. Sutter, and R. R. Adzic, *Science*, **315**, 220 (2007).
6. K. C. Neyerlin, W. B. Gu, J. Jorne, and H. A. Gasteiger, *J. Electrochem. Soc.*, **153**, A1955 (2006).
7. R. Srivastava, P. Mani, N. Hahn, and P. Strasser, *Angew. Chem., Int. Ed.*, **46**, 8988 (2007).
8. J. Greeley, J. Rossmeisl, A. Hellman, and J. K. Nørskov, *Z. Phys. Chem.*, **221**, 1209 (2007).
9. J. Healy, C. Hayden, T. Xie, K. Olson, R. Waldo, A. Brundage, H. Gasteiger, and J. Abbott, *Fuel Cells*, **5**, 302 (2005).
10. C. Zhou, M. A. Guerra, Z. M. Qiu, T. A. Zawodzinski, and D. A. Schiraldi, *Macromolecules*, **40**, 8695 (2007).
11. S. J. Hamrock and M. A. Yandrasits, *Polym. Rev.*, **46**, 219 (2006).
12. D. A. Schiraldi, *Polym. Rev.*, **46**, 315 (2006).
13. N. M. Markovic and P. N. Ross, *Surf. Sci. Rep.*, **45**, 121 (2002).
14. U. A. Paulus, T. J. Schmidt, H. A. Gasteiger, and R. J. Behm, *J. Electroanal. Chem.*, **495**, 134 (2001).
15. T. J. Schmidt, U. A. Paulus, H. A. Gasteiger, and R. J. Behm, *J. Electroanal. Chem.*, **508**, 41 (2001).
16. N. M. Markovic, H. A. Gasteiger, B. N. Grgur, and P. N. Ross, *J. Electroanal. Chem.*, **467**, 157 (1999).
17. Y. B. Mo and D. A. Scherson, *J. Electrochem. Soc.*, **150**, E39 (2003).
18. M. Inaba, H. Yamada, J. Tokunaga, and A. Tasaka, *Electrochem. Solid-State Lett.*, **7**, A474 (2004).
19. A. Bonakdarpour, M. Lefevre, R. Z. Yang, F. Jaouen, T. Dahn, J. P. Dodelet, and J. R. Dahn, *Electrochem. Solid-State Lett.*, **11**, B105 (2008).
20. A. Bonakdarpour, C. Delacote, R. Yang, A. Wieckowski, and J. R. Dahn, *Electrochem. Commun.*, **10**, 611 (2008).
21. M. K. Debe, in *Handbook of Fuel Cells: Fundamentals, Technology and Applications*, 1st ed., W. Vielstich, A. Lamm, and H. A. Gasteiger, Editors, p. 576, John Wiley & Sons, Chichester, England (2003).
22. M. K. Debe and A. R. Drube, *J. Vac. Sci. Technol. B*, **13**, 1236 (1995).
23. M. K. Debe and R. J. Poirier, *J. Vac. Sci. Technol. A*, **12**, 2017 (1994).
24. M. K. Debe, A. K. Schmoeckel, G. D. Vernstrom, and R. T. Atanasoski, *J. Power Sources*, **161**, 1002 (2006).
25. M. K. Debe, in *The 3rd International Hydrogen and Fuel Cell Expo Proceedings*, Session FC-8, p. 1, Tokyo, Japan (2007).
26. A. Bonakdarpour, R. Lobel, S. Sheng, T. L. Monchesky, and J. R. Dahn, *J. Electrochem. Soc.*, **153**, A2304 (2006).
27. A. Bonakdarpour, K. Stevens, G. D. Vernstrom, R. Atanasoski, A. K. Schmoeckel, M. K. Debe, and J. R. Dahn, *Electrochim. Acta*, **53**, 688 (2007).
28. L. Gancs, T. Kobayashi, M. K. Debe, R. Atanasoski, and A. Wieckowski, *Chem. Mater.*, **20**, 2444 (2008).
29. R. K. Ahluwalia and X. Wang, *J. Power Sources*, **177**, 167 (2008).
30. T. J. Schmidt and H. A. Gasteiger, in *Handbook of Fuel Cells: Fundamentals, Technology and Applications*, 1st ed., W. Vielstich, A. Lamm, and H. A. Gasteiger, Editors, p. 316, John Wiley & Sons, Chichester (2003).
31. A. Bonakdarpour, R. Lobel, R. T. Atanasoski, G. D. Vernstrom, A. K. Schmoeckel, M. K. Debe, and J. R. Dahn, *J. Electrochem. Soc.*, **153**, A1835 (2006).
32. A. Bonakdarpour, J. Wenzel, D. A. Stevens, S. Sheng, T. L. Monchesky, R. Lobel, R. T. Atanasoski, A. K. Schmoeckel, G. D. Vernstrom, M. K. Debe, and J. R. Dahn, *J. Electrochem. Soc.*, **152**, A61 (2005).
33. M. K. Debe, A. K. Schmoeckel, S. M. Hendricks, G. D. Vernstrom, G. M. Haugen, and R. T. Atanasoski, *ECS Trans.*, **1**(8), 51 (2006).
34. G. Haugen, M. Emery, S. M. Hamrock, M. Hicks, S. Roscoe, M. Schaberg, and M. Yandrasits, Paper 533 presented at The Electrochemical Society Meeting, Washington, DC, Oct 7-12, 2007.
35. K. J. J. Mayrhofer, B. B. Blizanac, M. Arenz, V. R. Stamenkovic, P. N. Ross, and N. M. Markovic, *J. Phys. Chem. B*, **109**, 14433 (2005).
36. P. M. S. Monk, *Fundamentals of Electro-Analytical Chemistry*, p. 384, John Wiley & Sons, Chichester (2001).
37. K. J. J. Mayrhofer, D. Strmcnik, B. B. Blizanac, V. Stamenkovic, M. Arenz, and N. M. Markovic, *Electrochim. Acta*, **53**, 3181 (2008).
38. A. Bonakdarpour, M. Lefevre, R. Yang, F. Jaouen, T. Dahn, J.-P. Dodelet, and J. R. Dahn, *Electrochem. Solid-State Lett.*, **11**, B105 (2008).

*Journal of The Electrochemical Society*, **158** (8) B905-B909 (2011)
0013-4651/2011/158(8)/B905/5/$28.00 © The Electrochemical Society


# Dissolution of Ni from High Ni Content $Pt_{1-x}Ni_x$ Alloys

**D. A. Stevens,[a,*] R. Mehrotra,[a] R. J. Sanderson,[a] G. D. Vernstrom,[b,*] R. T. Atanasoski,[b,*] M. K. Debe,[b,*] and J. R. Dahn[a,*,z]**

[a]*Departments of Physics and Chemistry, Dalhousie University, Halifax, Nova Scotia, Canada B3H 3J5*
[b]*3M Co., 3M Center, St. Paul, Minnesota 55144-1000*

Three $Pt_{1-x}Ni_x$ catalyst compositions, with high Ni content, were sputter deposited onto 3M Company's Nano-Structured Thin Film catalyst support to determine whether the high oxygen reduction reaction (ORR) activities recently reported are a surface phenomenon or require bulk Ni dissolution. The electrodes with $Pt_{0.27}Ni_{0.73}$ throughout had the highest mass specific ORR activity of the samples tested. When some of the $Pt_{0.27}Ni_{0.73}$ was replaced with either Pt or $Pt_{0.75}Ni_{0.25}$, the mass activity dropped. These results confirmed that continuous high Ni content is required to obtain high mass activity.
 [DOI: 10.1149/1.3595747] 

Manuscript submitted January 25, 2011; revised manuscript received May 9, 2011. Published June 8, 2011.

Platinum-transition metal alloy catalysts such as Pt-Co, Pt-Cu, Pt-Ni etc. have been shown to exhibit higher oxygen reduction reaction (ORR) activity than platinum for Proton Exchange Membrane Fuel Cells.[1] Recent results for $Pt_{1-x}Ni_x$ sputter deposited on 3M Company's Nano-Structured Thin Film (NSTF) catalyst support[2,3] showed a significant increase in ORR activity over a small composition range ($\sim 75 \pm 2\%$ Ni, as measured by electron microprobe - EMP) in both fuel cell and Rotating Disk Electrode (RDE) measurements.

The reasons for this peak in ORR activity are not as yet well understood. Pt-skeleton and Pt-skin structures have recently been proposed[4–6] to explain high activities seen for polycrystalline bulk $Pt_{0.75}M_{0.25}$ alloys. A core-shell model has been advanced[7–9] to explain high activity for $Pt_{1-x}Cu_x$ alloys deposited on carbon supports. The Pt-skeleton model envisages loss of surface transition metal atoms. This results in a roughened surface and some enhancement of ORR activity as a result of electronic contributions from the underlying bulk $Pt_{0.75}M_{0.25}$ composition. The Pt-skin model proposes segregation of Pt atoms to the surface. This creates Pt-deficient sub-surface layers that enhance the activity of the Pt surface layer. The core shell model envisages extensive de-alloying of the Pt surface creating a Pt-rich shell over a transition metal rich core. Experimental results strongly suggest the metal rich core introduces a compressive strain in the Pt surface layer caused by lattice mismatch between the two "phases."[10]

These models all envisage a structure where most of the alloying element remains. Ex-situ X-Ray Diffraction (XRD) assessment during RDE testing of a glassy carbon disk coated with $Pt_{0.28}Ni_{0.72}$ sputter-deposited on NSTF whiskers showed that these catalysts lose much of the Ni during electrochemical testing.[11,12] The models described above do not really describe the resultant catalyst produced by this sort of process. Further work is therefore required to understand what is happening with these catalysts. In our recent publications on the $Pt_{1-x}Ni_x$ system,[11,12] it was clearly shown that high Ni content catalysts have higher ORR activity than lower Ni content catalysts. This was confirmed in both RDE and fuel cell testing. It was also shown that this activity reached a peak somewhere around the $Pt_{0.3}Ni_{0.7}$ composition. Much of the Ni originally present was lost through dissolution. The activity enhancement resulted from a combination of higher Pt surface area (likely because a porous film was created by Ni dissolution) and increased area specific activity ($mA/cm^2_{Pt}$) of the low Ni content catalyst that remained. It was not clear from the data presented how far into the bulk of the catalyst Ni dissolution needs to proceed in order to reach peak ORR activity. This increase in activity for the $Pt_{1-x}Ni_x$ system has also been reported by other researchers[13,14] and is thus a material of interest to the fuel cell community. The data presented in this paper answers the question of how far into the catalyst Ni dissolution needs to occur.

The NSTF catalyst support is grown from an organic pigment, commonly known as perylene red, N,N-di(3,5-xylyl)perylene-3,4: 9,10 bis(dicarboximide).[15] It is deposited as a smooth film via vapour deposition on a surface and then vacuum annealed to form a high density array of closely packed whiskers which are crystalline and have a rectangular cross-section of ~53 by 27 nm and lengths around 500–1000 nm. Pt or Pt-alloys sputter deposited onto these whiskers conformally coat the whisker surface but also form small "whiskerettes" on the sides of the whiskers with ~8 nm diameter cross-sections.[10] NSTF-based Pt catalysts exhibit ORR specific activities ($mA/cm^2_{EC}$, where the electrochemical area is calculated from integration of the charge in the $H_{ads}$-$H_{des}$ region of standard cyclic voltammograms) very close to that of bulk-polycrystalline Pt. This is significantly different from catalysts applied as small particles on a carbon surface that are typically used in PEM fuel cells. Such catalysts typically have electrochemical area specific ORR activities approximately 10 times lower than bulk polycrystalline Pt.

During sputter deposition, the catalyst typically forms a relatively smooth coating over the whisker surfaces. As the deposited amount increases, the whiskerettes start to form and appear to extend in length. In addition, the thickness of the deposited layer and length of the whiskerettes decreases from the top to the bottom of the whisker, presumably due to shadowing effects, see for example Fig. 2 in Ref. 16. It appears that the whiskerettes are essentially single grains and the primary particles from a catalytic surface area standpoint. For the samples reported in this paper, the elements (Pt and Ni) were deposited in a manner that would encourage intimate mixing of the elements at the atomic level. This paper answers the question of how important it is that the as-deposited composition be uniform or have high nickel content throughout (i.e. are the activity gains seen the result of predominantly modification of the catalyst whiskerette surface or is Ni dissolution from the bulk of the whiskerette required).

## Experimental

Four $Pt_{1-x}Ni_x$ catalyst compositions were prepared through sputter deposition from Pt and Ni targets. The methods used have been described in detail elsewhere[17,18] and are described briefly below. Two of these compositions were prepared as "two-layer" catalysts. All catalysts contained 0.1 mg $Pt/cm^2$; the two-layer catalysts differed in the amount of Ni present in each layer. Figure 1 shows a pictorial representation of three of the compositions prepared. This figure shows schematically how the films would appear when deposited on flat substrates. The catalyst present on NSTF would certainly have a predominantly two-layer structure similar to that illustrated in Fig. 1, however shadowing effects may change the relative thicknesses of these layers at different locations along the length of the whiskers and on different sides of the whiskerettes. Detailed

* Electrochemical Society Active Member.
z E-mail: jeff.dahn@dal.ca

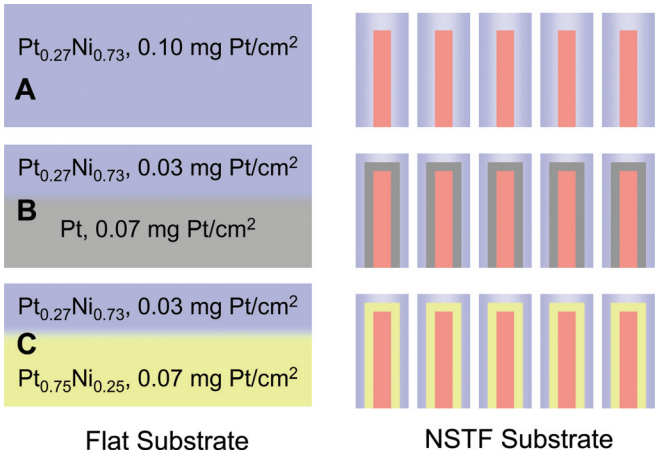


**Figure 1.** (Color online) Schematic illustration of the compositions prepared and tested.

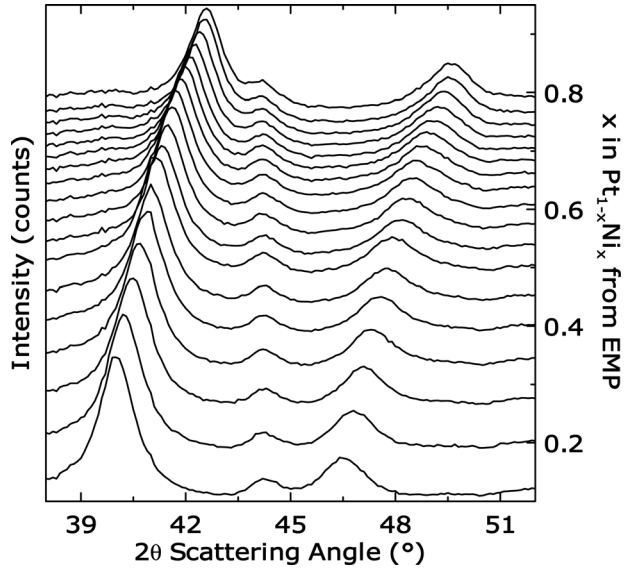


**Figure 2.** XRD data for composition D, fully intermixed $Pt_{1-x}Ni_x$. The scans have been offset vertically for clarity. The magnitude of the offset is directly proportional to the atomic fraction of Ni determined from EMP measurements of the same film deposited on a Si wafer. The composition for a given scan can therefore be determined by seeing where it intersects with the right hand vertical axis.

investigation of the catalyst morphology on NSTF is beyond the scope of this short communication.

Composition A had a constant $Pt_{0.27}Ni_{0.73}$ composition. This composition was shown to have much higher ORR activity than pure Pt.[9,10] This composition was prepared to give an indication of baseline performance. Composition B had a small amount of the high ORR activity (Composition A) catalyst deposited over a Pt base layer as-sputtered. If the high activity was caused by dissolution of Ni only from the top few surface layers of the catalyst then this composition would be expected to perform as well as composition A. Composition C had a small amount of composition A deposited over a $Pt_{0.75}Ni_{0.25}$ base layer. A pure Pt sputtering run was also completed for reference to allow for comparison of ORR activities of the different compositions prepared to that of Pt. Finally, sample D was prepared as a binary $Pt_{1-x}Ni_x$ spread, with the atomic fraction of Ni varying between $x = 0.12$ and $x = 0.8$. This composition spread was used primarily to determine the relationship between lattice constant and Ni content for catalysts deposited on NSTF.

The composition spreads were deposited on a series of substrates mounted on a rotating substrate table that was attached to the inside of the door of the sputtering chamber. The substrates used included pre-weigh aluminum disks for gravimetric determination of the sputtered catalyst loading, NSTF whisker substrate film and from 3M, a Si wafer for x-ray diffraction assessment and NSTF whisker-coated graphite disks (pyrolytically treated grade AXF-5Q from Poco Graphite) for RDE testing. These disks were whisker coated at 3M prior to sputtering. The Si wafer was also used for electron microprobe characterisation of composition. The centers of the substrates and disk holders were located at the same distance from the centre of the sputtering chamber as the Pt and Ni sputtering targets. Each target was covered with a mask that limited the deposition to a constant loading across a 75 mm sputtering track. During sputter deposition, the substrate table rotated past each target sequentially, receiving less than a monolayer planar equivalent of either Pt or Ni on average with each pass. For the two-layer depositions, the Ni target power was increased part way through the run in order to change the amount of Ni being deposited with each pass.

XRD measurements were collected with a two different machines. A Bruker D8 discover x-ray system equipped with a x-y-z translation stage, a Cu target x-ray tube, an incident beam monochromator to select Cu Kα radiation and an area detector was used for some samples. The detector was set in a position that allowed for collection of data over a scattering angle range of 30–57° simultaneously. The incident beam was set at 6° in order to sample a relatively large area of the thin film to improve counting statistics. XRD spectra were measured at a series of points across the composition spreads for the catalyst deposited on a Si wafer and also on the NSTF whisker coated substrate, counting for 1800 s for each scan. After mechanical failure occurred with the Bruker diffractometer, another diffractometer was used. This diffractometer uses an INEL CPS120 curved, position sensitive detector coupled to an X-ray generator that is equipped with a Cu target X-ray tube.

RDE data were collected with Pine Instruments AFBCP bipotentiostat. The measurements were performed in 0.1 M $HClO_4$ electrolyte (triple distilled $HClO_4$ diluted with >18 MΩ deionised water) using a platinum wire counter electrode and a $Hg/HgSO_4$ reference electrode (nominal reference potential 630 mV vs. RHE) and a rotation rate of 900 rpm. The potential of the reference electrode was calibrated against $H_2/H^+$ by bubbling $H_2$ through the electrolyte and then determining the potential at which the current reached zero when stepping the potential above and below the nominal reference electrode potential. The disks were installed in the rotator shaft, rinsed with deionised water and electrolyte then lowered into the electrolyte. The solution was purged with bubbling argon for 10 min while held at 500 mV vs. RHE. Eighteen cyclic voltammograms (CVs) were then collected at 50 mV/s between 1100 and 30 mV vs. RHE. The solution was then purged with oxygen for 10 min, again while held at 500 mV vs. RHE before another three cyclic voltammograms were collected (50 mV/s between 1100 and 30 mV vs. RHE). This argon/oxygen CV protocol was repeated at least 8 times to assess how catalyst surface area and ORR activity changed with time.

## Results and Discussion

It is useful to examine the XRD data for Sample D, the fully intermixed composition spread with a large variation in Ni content (12–80 atom %) deposited on NSTF. Previous measurements have shown that intermixes of the two elements form solid-solution FCC lattices,[9] with the lattice constant decreasing as the Ni content increases. Figure 2 shows the XRD data measured for sample D deposited on NSTF whiskers, together with the Ni content measured by EMP for the same material deposited on a Si wafer. The scans have been offset vertically for clarity. The magnitude of the offset used was directly proportional to the Ni content measured with EMP and thus the composition of a given scan can be determined by looking at where that scan intersects the composition axis.

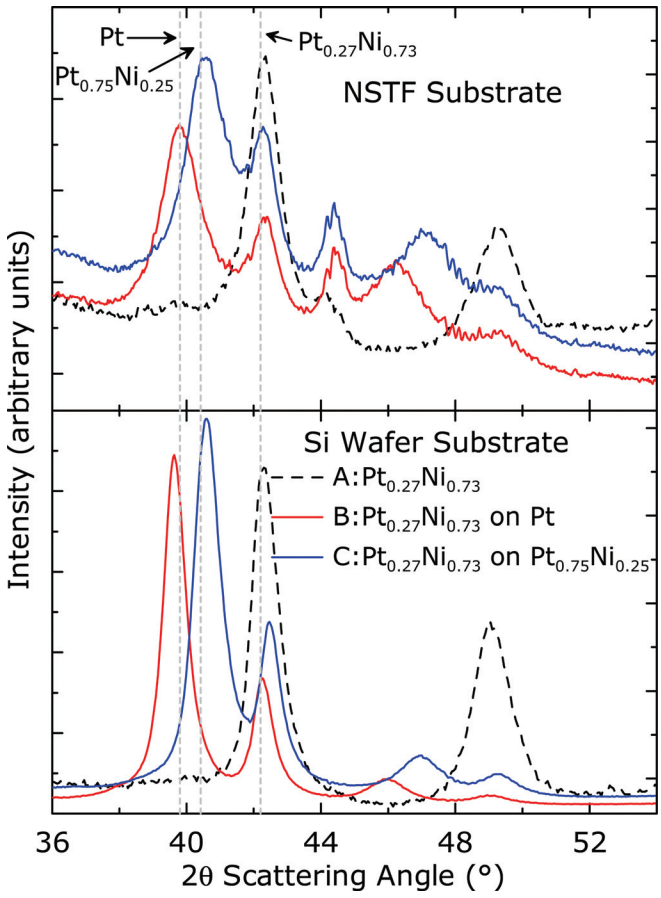


**Figure 3.** (Color online) XRD data recorded on samples from the $Pt_{1-x}Ni_x$ sputtering runs. The bottom panel presents the data collected for the deposits on Si wafer. The top panel shows the data collected for the catalysts deposited on NSTF whiskers. The peak positions expected for specific compositions based on the data in Fig. 2 are shown as dashed grey lines in this figure.

This figure shows that the positions of the (111; ~40–42°) and (200; ~47–50°) peaks shift with increasing Ni content, as expected. The peak around 44° comes from the NSTF substrate and thus does not shift with changing composition. The peak positions that would be expected for the other three compositions can be determined from the data in Fig. 2.

Figure 3 shows the XRD data collected for the films deposited on both a Si wafer (a planar surface – bottom panel) and on NSTF whiskers (a rough surface – top panel). Pt and Ni both exist in FCC lattices. The peak positions expected for the three compositions targeted (Pt, $Pt_{0.27}Ni_{0.73}$, and $Pt_{0.75}Ni_{0.25}$) are also indicated on this figure. These positions were extracted from the data presented in Fig. 2. The XRD scan for the constant composition sample, Composition A, ($Pt_{0.27}Ni_{0.73}$) on the Si wafer shows 2 peaks [(111) and (200)] consistent with a high Ni content FCC lattice. On NSTF whiskers, the same peaks are present. The peaks are present at scattering angles close to those predicted from Fig. 2. Additional peaks can be seen around 35 and 44°; these come from the NSTF substrate and can thus be ignored in all the NSTF data.

Composition B ($Pt_{0.27}Ni_{0.73}$ deposited on Pt) exhibits two relatively strong intensity peaks at 39.7 and 42.3° for the Si wafer spectrum. The first peak comes from the Pt base layer (Pt has a lattice constant that would give a peak at 39.8°). The second peak comes from the $Pt_{0.27}Ni_{0.73}$ as it occurs at the same scattering angle seen for the (111) peak of compositon A. The second peak has a lower area than the first peak, as would be expected as it contains only 30% of the deposited platinum. There are also two peaks at higher angles; these correspond to the (200) peaks of the Pt and $Pt_{0.27}Ni_{0.73}$

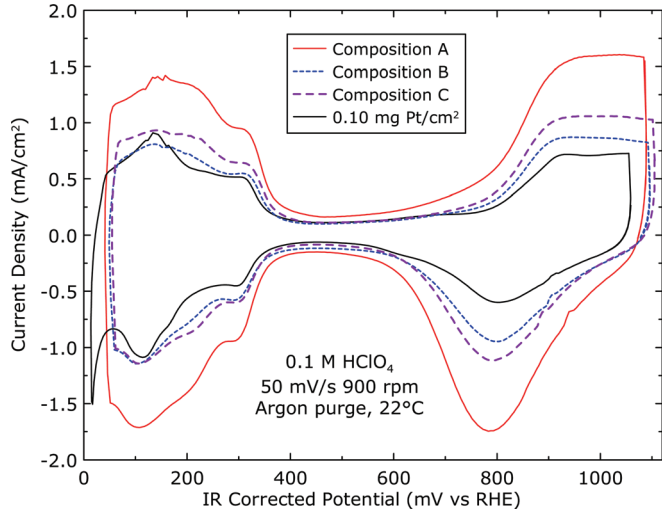


**Figure 4.** (Color online) Representative cyclic voltammograms for the samples prepared in this study. The voltammograms were collected at 50 mV/s in argon saturated 0.1 M $HClO_4$ electrolyte, with a rotation rate of 900 rpm.

layers. The samples deposited on NSTF also showed the same combination of peaks. Thus it is clear that the catalyst is present on NSTF as a bilayer deposit, with discrete low and high nickel content layers. The (111) peak positions are located at scattering angles very close to those predicted for Pt and $Pt_{0.27}Ni_{0.73}$ from Fig. 2. It is therefore clear that the bilayer structure is preserved, even for the catalyst deposited on the rough NSTF substrate.

The XRD data for Composition C ($Pt_{0.27}Ni_{0.73}$ deposited on $Pt_{0.75}Ni_{0.25}$) deposited on a Si wafer also shows two well-defined peaks in the 37–43° range, consistent with a bi-layer system. The first peak occurs around 40.6°, indicating a slightly contracted FCC Pt lattice and consistent with a composition close to the position expected for a composition around $Pt_{0.75}Ni_{0.25}$. The second peak occurs around 42.5°. This comes from the $Pt_{0.27}Ni_{0.73}$ top layer as it occurs at the same scattering angle as the (111) peak for composition A. The peak appears to be shifted to a somewhat higher angle, however this shift in part results from the tail in the intensity of the first (111) peak for this sample. It may also result from a slight vertical offset of the sample in the diffractometer which would create an off-axis shift. Overall these XRD data clearly show that the catalysts deposit as discrete layers on both flat Si wafers and rough NSTF substrates during sputtering.

Figure 4 shows cyclic voltammograms (CVs) for the three compositions tested, together with data for constant Pt (at the same Pt loading) for comparison. These cyclic voltammograms were measured approximately 1 h after the electrode was first immersed in the electrolyte. Before these CVs were collected therefore, the electrode was cycled between 1100 and 30 mV vs. RHE 58 times; 52 times with argon purge and 6 times with oxygen purge in the electrolyte. It is clear that the electrode with high Ni content throughout (composition A) has a much higher electrochemical surface area than the other samples. Composition B has a CV that is quite close to that for Pt, and the CV for composition C is closer to that for composition B than for composition A. All the electrodes with Ni (as-sputtered) do however have a more pronounced peak around 200 mV than the Pt baseline electrode. This suggest that the presence of (or loss of) Ni may change the relative amounts of different facets or modify the number and/or nature of the step-edges present on the electrode surface.

Repeated CV-ORR measurements were completed on these electrodes to study how the electrode surface structure and catalytic activity changed with potential cycling. Figure 5 shows how the surface enhancement factor (SEF) data calculated from the $H_{des}$ branches of the CVs changes for the different electrode

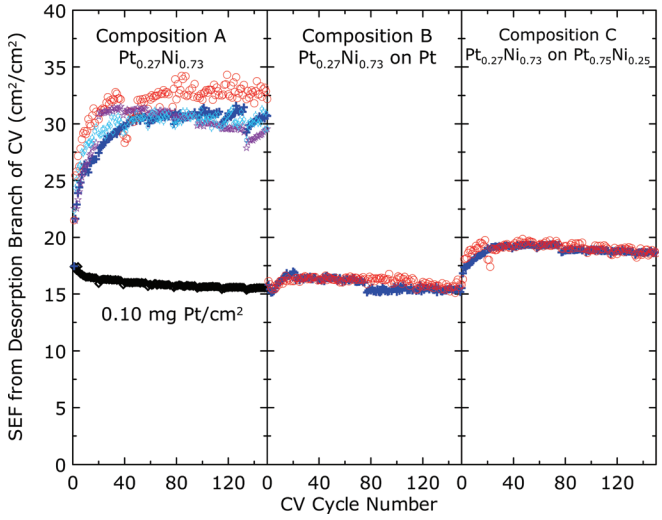


**Figure 5.** (Color online) Surface enhancement factor (SEF) from RDE measurements on disks from the different sputtering runs over multiple potential sweeps in argon and oxygen. The SEF was determined from the integrated charge during H-desorption.

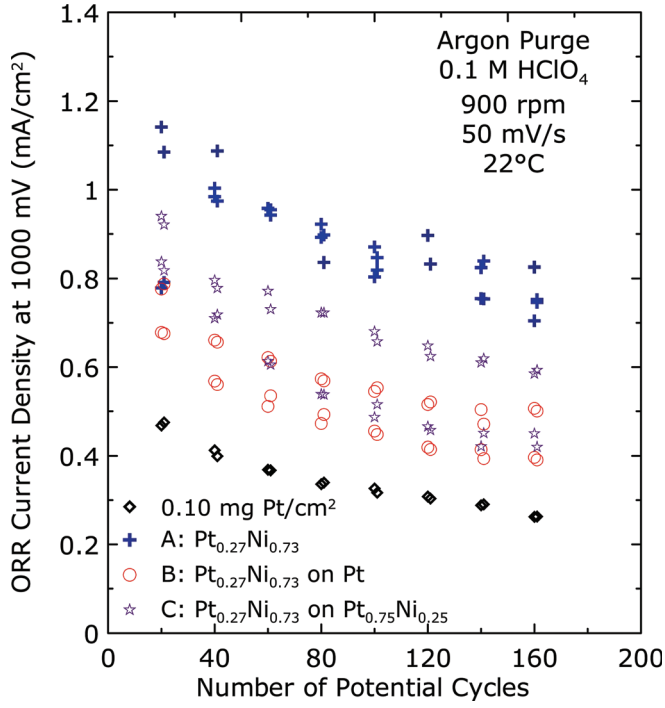


**Figure 6.** (Color online) ORR current density from the up sweep measured at 1000 mV vs. RHE. The ORR curves were measured in oxygen-saturated 0.1 M $HClO_4$ electrolyte at 50 mV/s with a rotation rate of 900 rpm. Multiple ORR measurements were performed to assess stability with repeated potential cycling.

compositions, where SEF is defined as the measured Pt electrochemical surface area divided by the geometric area of the electrode. It is clear from these data that only composition A, with high Ni content throughout, exhibited SEF values significantly larger than that measured on Pt only (at the same Pt loading). It takes a few cycles for this surface area to evolve, consistent with a time/potential dependent rate of dissolution of Ni from the bulk. Composition B also showed a very small increase in SEF for the first few cycles. This likely resulted from loss of Ni from the top layer. This process would have left behind a porous/roughened Pt surface. The surface area increase observed was, however, very small. Composition C also showed an increase in SEF for the first few cycles reaching an SEF value a little higher than the SEF of Pt only. This may have resulted from some loss of Ni from the $Pt_{0.27}Ni_{0.73}$ top layer. Again, however, the SEF gain seen was small compared to that seen for composition A. From these results it is clear that bulk Ni dissolution from a continuous high Ni content deposit is required in order to see significant changes in catalyst surface area.

It is more important for fuel cell applications to know whether such increases in surface area translate to enhanced ORR activity for a given Pt loading. In order to determine this, the ORR RDE curves were analyzed to determine the current density at 1000 mV vs. RHE as a function of the number of potential cycles completed. A potential of 1000 mV was selected as these high Ni catalysts typically reach the diffusion limited current density by 900 mV and can have half-wave potentials around 950–975 mV. In order to ensure that the data are reliable, it is important the current densities be significantly lower than the diffusion limited current densities. Figure 6 shows the current density at 1000 mV vs. RHE as a function of the number of potential cycles completed. These current densities were determined from the up-sweep after iR correction. The up-sweep was selected to ensure the surface was relatively clean, thereby minimizing the impact of surface –OH groups on ORR activity.

All samples, including Pt, showed a loss in ORR activity with repeated potential cycling. This has been seen by us before and may result from a combination of contamination of the electrolyte with atmospheric impurities,[9] poisoning of the catalyst surface with $SO_4^{2-}$ from the reference electrode or decomposition products from $ClO_4^-$ in the electrolyte. This contamination occurs because the electrolyte is very pure initially (and is prepared fresh for each run) and thus will readily take up impurities, and the tests take many hours to complete. Recent work at Dalhousie University has allowed us to develop protocols to minimize the performance loss associated with these processes and thus we expect this to be less of an issue for future catalyst studies. It is important to note that all samples showed essentially the same slope in performance loss and thus appear to suffer from contamination issues at the same rate.

The Pt baseline showed an initial ORR activity around 0.5 mA/cm$^2$. This had decreased to 0.3 mA/cm$^2$ by the end of the experiment. Composition A showed a much higher ORR activity initially of 1.2 mA/cm$^2$; this had decreased to ~0.8 mA/cm$^2$ by the end of the experiment. The other compositions showed ORR activities between that seen for Pt and that seen for Composition A. Composition B seems to exhibit lower activity than Composition C. This is somewhat consistent with the SEF data in Fig. 4, although the ORR activity gain relative to Pt was much larger than the change in SEF. This implies that the intrinsic activity per active platinum site is higher in Compositions B and C than for pure Pt. It is not clear from the figures whether this is the case for Composition A. To assess this, it is useful to determine the specific activity (ORR current density at 1000 mV divided by the SEF). The values obtained for data at the start of the experiment are: Pt—29 $\mu A/cm^2_{Pt}$, Composition A—37 $\mu A/cm^2_{Pt}$, Composition B—46 $\mu A/cm^2_{Pt}$, Composition C—46 $\mu A/cm^2_{Pt}$. These data show that all the catalysts prepared have active sites that are more active than pure Pt, with compositions B and C possibly being more active than composition A. However, for a fuel cell application where cost and efficiency are key issues, the activity per mg of Pt is a more relevant measure of performance. All the samples measured here have the same Pt loading and thus the absolute measured current density is a direct measure of mass activity. It is therefore clear that Composition A outperforms Compositions B and C from a practical stand-point as its absolute current density (mA/cm$^2$) was the highest. The fact that the specific activity for Composition A was lower than that for Compositions B and C but its absolute current density was higher just means that the gain in surface area for Composition A was larger than the loss in specific activity. From these results we conclude that $Pt_{1-x}Ni_x$, when deposited on NSTF whiskers, needs to initially have high Ni content

throughout in order to maximize mass specific activity. A highly porous Pt-skin model (where Ni has been lost deep into the whiskerettes) may therefore be a better model for explaining the high activity seen in these materials. The porous nature of the resultant deposit would create the high observed surface area and the residual Ni may help to somewhat increase the intrinsic activity of the catalytic sites that are present relative to that observed for Pt by modifying the catalytic surface electronic structure. A similar model was advanced in our previous paper to explain the extraordinarily sharp dependence of mass activity measured in 50 $cm^2$ fuel cells around $Pt_3Ni_7$.[2,13,14] Finally we note that a similar effect of going from a single layer of composition A to a bi-layer composition B was observed in 50 $cm^2$ MEA fuel cell measurements. In Fig. 3b of Refs. 2 and 10, the pair of sample data points marked $^1/_2$ & $^1/_2$ were made specifically with a pure Pt underlayer and a top layer of $Pt_3Ni_7$, the composition of the surface area peak. The resultant surface areas and activity of the samples when tested, however, were equivalent to having been made with the average Pt/Ni ratio, implying intermixing of the Pt and $Pt_3Ni_7$ alloy layers to form a single layer of $\sim$ PtNi composition.

## Summary and Conclusions

Single layer and Bi-layer catalysts were deposited on NSTF and assessed for the impact of the composition of the base layer on the measured ORR activity and catalyst surface area. X-ray diffraction data showed that the catalysts deposited as discrete layers during sputtering on both flat Si wafer and rough NSTF substrates. The highest mass activity was seen for Composition A (constant $Pt_{0.27}Ni_{0.73}$ throughout). When some of the high Ni content material was replaced by either pure Pt (Composition B, $Pt_{0.27}Ni_{0.73}$ on Pt) or $Pt_{0.75}Ni_{0.25}$ (Composition C, $Pt_{0.27}Ni_{0.73}$ on $Pt_{0.75}Ni_{0.25}$), the mass activity decreased, suggesting Ni needs to dissolve from the bulk of the whiskerettes on NSTF in order to maximize mass activity. In order for this to occur, the Ni content has to be high throughout to ensure that the Ni percolation threshold is exceeded. Somewhat higher intrinsic catalytic site activities were observed for the bi-layer samples, however this benefit was lost from a practical standpoint by the lower active surface area that was created as a result of incomplete Ni dissolution from low Ni regions.

From these results a highly porous Pt-skin type model is proposed to explain the high activity recently reported for high Ni content catalysts deposited on NSTF. For this model it is proposed that bulk Ni dissolution occurs throughout the deposited film creating a high catalytic surface area. Not all of the Ni is however lost. The results obtained suggest that the remaining Ni modifies the electronic properties of the Pt surface to increase the activity of the catalytic sites relative to Pt.

## Acknowledgments

The authors would like to acknowledge financial support from the US DOE under 3M Grant DE-FG36-07GO17007.

## References

1. F. T. Wagner, B. Lakshmanan, and M. F. Mathias, *J. Phys. Chem. Lett.*, **1**, 2204 (2010).
2. M. K. Debe, A. J. Steinbach, G. D. Vernstrom, S. K. Hendricks, M. J. Kurkowski, R. T. Atanasoski, P. Kadera, D. A. Stevens, E. Marvel, and J. R. Dahn, *ECS Trans.*, **33**(1), 143 (2010).
3. D. A. Stevens, T. D. Hatchard, R. J. Sanderson, R. T. Atanasoski, M. K. Debe, and J. R. Dahn, *ECS Trans.*, **33**(1), 37 (2010).
4. K. J. J. Mayrhofer, D. Strmcnik, B. B. Blizanac, V. Stamenkovic, M. Arenz, and N. M. Markovic, *Electrochim. Acta*, **53**, 3181 (2008).
5. V. R. Stamenkovic, B. S. Mun, M. Arenz, K. J. J. Mayrhofer, C. A. Lucas, G. F. Wang, P. N. Ross, and N. M. Markovic, *Nature Mater.*, **6**, 241 (2007).
6. V. R. Stamenkovic, B. Fowler, B. S. Mun, G. F. Wang, P. N. Ross, C. A. Lucas, and N. M. Markovic, *Science*, **315**, 493 (2007).
7. S. Koh and P. Strasser, *J. Am. Chem. Soc.*, **129**, 12624 (2007).
8. P. Mani, R. Srivastava, and P. Strasser, *J. Phys. Chem. C*, **112**, 2770 (2008).
9. P. Strasser, *Rev. Chem. Eng.*, **25**, 255 (2009).
10. P. Strasser, S. Koh, T. Anniyev, J. Greeley, K. More, C. F. Yu, Z. C. Liu, S. Kaya, D. Nordlund, H. Ogasawara, et al., *Nat. Chem.*, **2**, 454 (2010).
11. G. C. K. Liu, D. A. Stevens, J. C. Burns, R. J. Sanderson, G. D. Vernstrom, R. Atanasoski, M. K. Debe, and J. R. Dahn, *J. Electrochem. Soc.*, **158**, B919 (2011).
12. M. K. Debe, A. J. Steinbach, G. D. Vernstrom, S. K. Hendricks, M. J. Kurkowski, R. T. Atanasoski, P. Kadera, D. A. Stevens, R. J. Sanderson, E. J. Marvel, et al., *J. Electrochem. Soc.*, **158**, B910 (2011).
13. C. Wang, M. F. Chi, G. F. Wang, D. van der Vliet, D. G. Li, K. More, H. H. Wang, J. A. Schlueter, N. M. Markovic, and V. R. Stamenkovic, *Adv. Funct. Mater.*, **21**, 147 (2011).
14. T. P. Moffat, J. J. Mallett, and S.-M. Hwang, *J. Electrochem. Soc.*, **156**, B238 (2009).
15. M. K. Debe, in *Handbook of Fuel Cells—Fundamentals, Technology and Applications*, W. Vielstich, A. Lamm and H. A. Gasteiger, Editors, p. 576, John Wiley & Sons, Chichester (2003).
16. L. Gancs, T. Kobayashi, M. K. Debe, R. Atanasoski, and A. Wieckowski, *Chem. Mater.*, **20**, 2444 (2008).
17. J. R. Dahn, S. Trussler, T. D. Hatchard, A. Bonakdarpour, J. R. Mueller-Neuhaus, K. C. Hewitt, and M. Fleischauer, *Chem. Mater.*, **14**, 3519 (2002).
18. D. A. R. Barkhouse, A. Bonakdarpour, M. Fleischauer, T. D. Hatchard, and J. R. Dahn, *J. Magn. Magn. Mater.*, **261**, 399 (2003).

Electrochimica Acta 56 (2011) 8695–8699

Contents lists available at ScienceDirect

Electrochimica Acta

journal homepage: www.elsevier.com/locate/electacta

# Platinum-alloy nanostructured thin film catalysts for the oxygen reduction reaction

Dennis van der Vliet[a], Chao Wang[a], Mark Debe[b], Radoslav Atanasoski[b], Nenad M. Markovic[a], Vojislav R. Stamenkovic[a,*]

[a] Materials Science Division, Argonne National Lab., 9700 S. Cass Ave, LeMont, IL 60439, USA
[b] 3M Fuel Cell Components Program, 3M Center, St. Paul, MN 55144, USA

ARTICLE INFO

*Article history:*
Received 1 July 2011
Received in revised form 16 July 2011
Accepted 16 July 2011
Available online 23 July 2011

*Keywords:*
Oxygen reduction reaction
Rotating disk electrode
Nanostructured thin film
Fuel cells

ABSTRACT

In an effort to study advanced catalytic materials for the oxygen reduction reaction (ORR), a number of metallic alloy nanostructured thin film (NSTF) catalysts have been characterized by rotating disk electrode (RDE). Optimal loadings for the ORR and activity enhancement compared to conventional carbon supported nanoparticles (Pt/C) were established. The most efficient catalyst was found to be PtNi alloy with 55 wt% of Pt. The enhancement in specific activity is more than one order of magnitude, while the improvement factor in mass activity is 2.5 compared to Pt/C. Further lowering of the platinum to nickel ratio in NSTF catalysts did not lead to increased mass activity values.



## 1. Introduction

The need for clean and efficient use of energy rather than burning fuel in internal combustion engines instigated many companies to pursue fuel cell operated devices and vehicles available to the general public [1]. A major challenge lies in optimizing the oxygen reduction reaction [2–6], especially to make fuel cells operable in large-scale automotive applications. This challenge sparked a concentrated effort to improve fuel cell catalysts [2,3,7–17] to meet the U.S. Department of Energy targets [18,19].

One of the busiest fields currently is the development of high surface area catalysts. These catalysts are usually carbon-supported, which is accompanied by many problems, such as contact resistance between metallic particles and the carbon matrix, particle dissolution [20–22] and agglomeration [21,23] and carbon support corrosion [21,24,25]. It has been shown that the nanostructured thin film catalysts [23,26,27], which have no carbon support, are much more stable in a membrane electrode assembly (MEA) than any supported nanoscale catalyst [18]. For this reason, the activities for the ORR of a range of PtNi and PtCo based binary and ternary NSTF catalysts have been established by RDE, both at room temperature and at 333 K – a temperature close to the operating temperature of a polymer electrolyte fuel cell [5]. The proper loading of the catalysts was determined in detail, and activities are reported.

The most active system found in this work is the PtNi binary NSTF with mass activities exceeding those of carbon supported high surface area catalysts. The PtCo NSTF catalysts were significantly less active than their nickel-containing counterparts. Several ternary catalysts were tested as well, and the activity of those did not approach the level of the PtNi, with the exception of the PtNiFe NSTF. Finally, the content of Pt in the PtNi NSTF was further reduced in an effort to lower the total Pt loading, which did not lead to increased kinetic activities, and hence also did not yield increased mass activities. It should be noted that these NSTF PtNi alloys did not include the more recently developed 3M $Pt_3Ni_7$ alloys reported recently [28].

## 2. Experimental

The metallic NSTF catalysts were prepared by 3M as reported previously [23,26,28–30]. In brief, the desired metals were sputtered consecutively on a substrate web coated with perylene red whiskers. This creates the so-called nanostructured thin film catalyst. In order to facilitate measurements in RDE, the individual whiskers were brushed off the web and stored as a powder. The Pt/C catalyst used in this work is a state-of-the-art 5 nanometer sized Pt catalyst from Tanaka (TKK, Tokyo), supported on vulcan.

The suspension needed for electrode preparation for the thin film RDE method [31] was made in, a glass vial with Milli-Q

* Corresponding author. Tel.: +1 630 252 5181.
*E-mail address:* vrstamenkovic@anl.gov (V.R. Stamenkovic).

0013-4686/$ – see front matter © 2011 Elsevier Ltd. All rights reserved.
doi:10.1016/j.electacta.2011.07.063

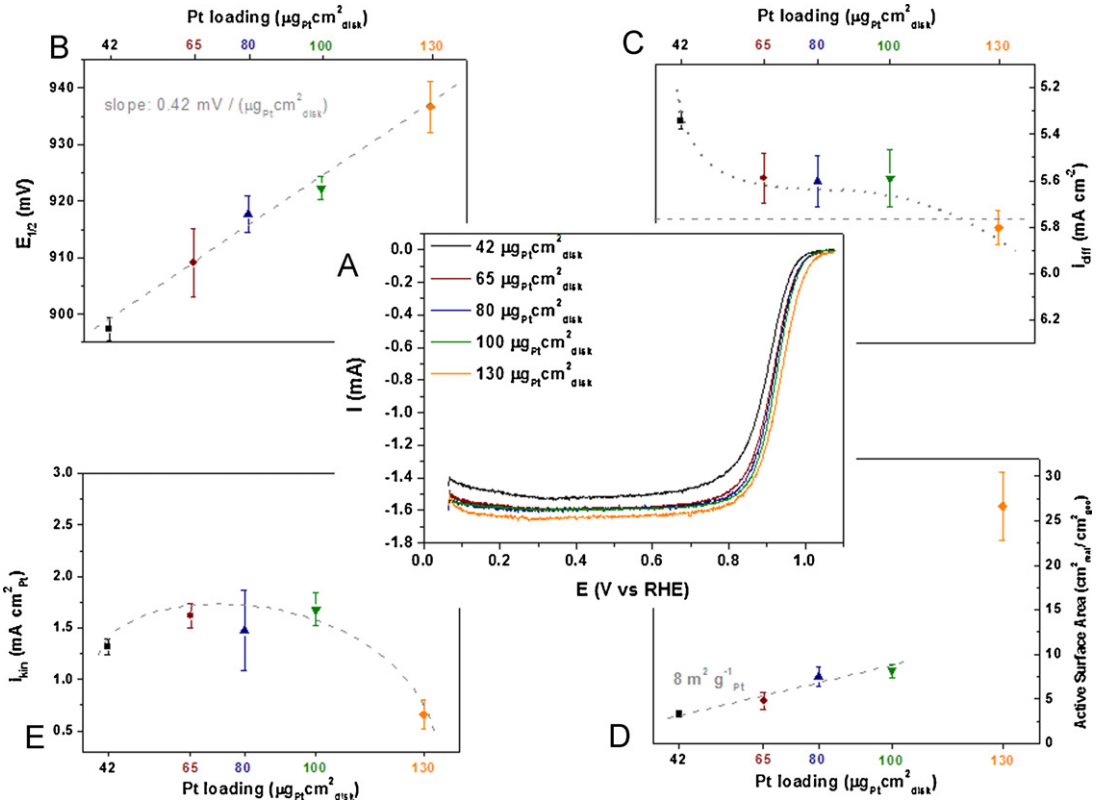


**Fig. 1.** Effect of the loading of NSTF catalyst on the glassy carbon substrate. (A) Family of the ORR polarization curves, measured at 293 K with a rotation of 1600 rpm and a scan rate of 20 mV $s^{-1}$ in 0.1 M $HClO_4$. (B) The effect of the loading on the half-wave potential. (C) Diffusion limiting currents for the ORR. (D) Active surface areas as estimated from $H_{upd}$. (E) Kinetic current density for the ORR at 0.9 V versus RHE. Standard deviations determined from four independent measurements are shown by error bars.

$H_2O$ (18.2 MΩ resistivity). About 2 mg of NSTF catalyst powder was weighed and 2 ml Milli-Q water added. Next, the suspension was sonicated until desirable homogeneity was obtained. A pre-polished Glassy Carbon (GC) disc of 6 mm in diameter was used as a substrate. A measured volume of the sonicated catalyst suspension was then pipetted onto the GC disc. After the electrode had dried in inert atmosphere, the electrode was rinsed with Milli-Q water to protect the catalyst from contamination and exposure to atmospheric gases. The electrolyte was in all cases 0.1 M $HClO_4$, prepared by diluting concentrated 70% concentrated perchloric acid.

A standard 3-electrode cell with a heating jacket was used in all measurements. An Ag/AgCl electrode in equilibrium with the electrolyte separated from the cell by a salt bridge was used as the reference electrode. The Luggin–Haber capillary was positioned as close to the electrode as possible without disturbing the flow by rotation, generally at about 10 mm distance from the surface of the disk. Any residual Ohmic losses [32] were compensated for by positive feedback in the potentiostat. The reference electrode was calibrated with a reversible hydrogen electrode (RHE), and all potentials reported here are with respect to the RHE. The counter electrode was a Pt mesh.

## 3. Results and discussion

### 3.1. Determination of proper platinum loading

Before activity measurements could be commenced, the proper loading of particles on the glassy carbon needed to be determined. Mayrhofer et al. [33] determined this to be 42 $\mu g_{Pt}$ $cm^{-2}{}_{disk}$, while 3M Company uses a loading of 0.1 $mg_{Pt}$ $cm^{-2}$ on the fuel cell cathode [23]. Our determination of the optimal loading is shown in Fig. 1. Insert A of the figure shows the full ORR polarization curves in 0.1 M perchloric acid with a rotation of 1600 rpm. The curves compare well to those reported before [33,34], and the influence of the loading is illustrated in this graph. First, the potential at half the diffusion limiting current, the so-called half-wave potential ($E_{1/2}$) increases linearly with loading from 42 to 130 $\mu g_{Pt}$ $cm^{-2}{}_{disk}$, shown in detail in Fig. 1B. The increasing value for $E_{1/2}$ with increasing loading makes the traditional measure of activity (overpotential at half-wave) difficult to apply for this catalyst, unless the loading is kept constant. Also, high loading decreases the potential window of the kinetic region (at currents lower than half the diffusion limiting current) and can introduce larger errors from reading the current at the steep part of the curve [31].

Secondly, the diffusion limiting current ($I_{diff}$) increases with increasing loading, with a stable region from 60 to 100 $\mu g_{Pt}$ $cm^{-2}{}_{disk}$, as shown in Fig. 1C. This is in agreement with our previous experiments [33], *i.e.* the lower diffusion limiting currents exhibit the same kinetic current densities when properly corrected for the diffusion contribution, however, a proper diffusion limiting current is recommended. The diffusion limiting current observed in the experiment is also a measure of NSTF distribution on the glassy carbon substrate. Even at higher loadings $I_{diff}$ will occasionally be lower than theoretically expected. This is indicative of a poor catalyst distribution on the GC disk, with part of the glassy carbon surface uncovered, while other spots on the disk are too thickly coated by the NSTF. When the loading is increased above 100 $\mu g_{Pt}$ $cm^{-2}{}_{disk}$, $I_{diff}$ is getting higher than expected, since the catalyst layer becomes too thick and multilayered. As a consequence the mass-transport of reactant molecules cannot be approximated with the case of flat rotating electrode [35,36].

Furthermore, the active surface area (SA) increases with increasing loading. The SA was determined by both integrating the $H_{upd}$, as well as determining the charge of CO stripping to reduce uncer-

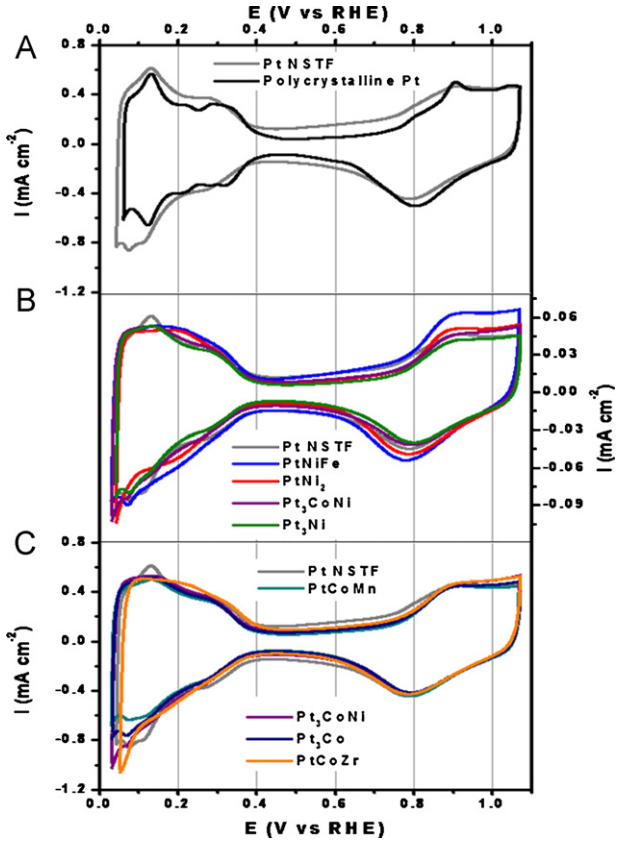


**Fig. 2.** Cyclic voltammetries for the various NSTF catalysts at 293 K in 0.1 M $HClO_4$ with a scan rate of 50 mV $s^{-1}$. (A) The comparison between monometallic Pt NSTF and polycrystalline bulk platinum. (B and C) Binary and ternary NSTFs.

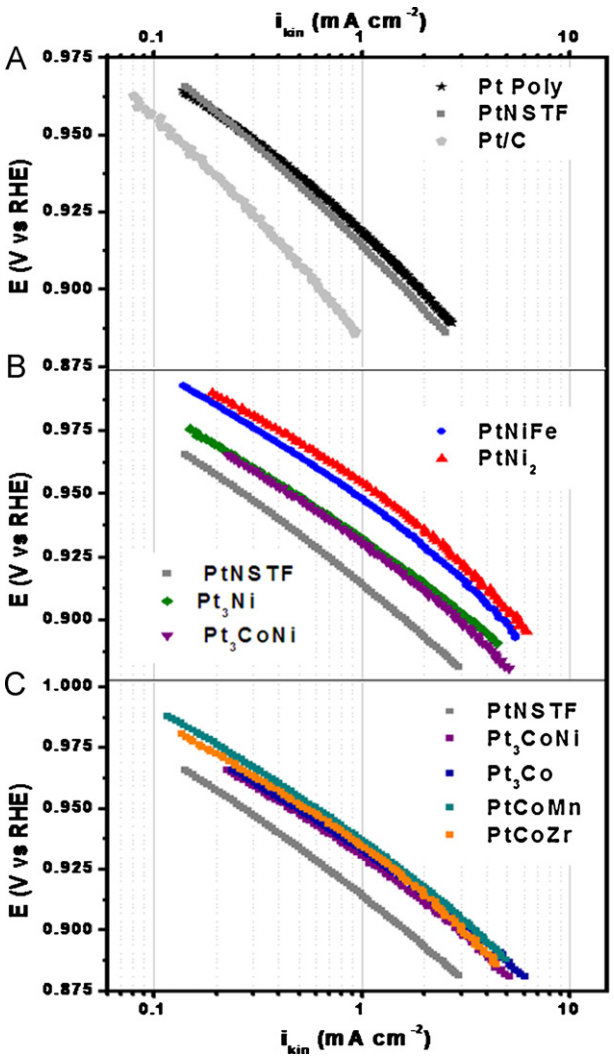


**Fig. 3.** ORR on NSTF catalysts, compared to polycrystalline Pt. (A) Tafel plots for the monometallic Pt sample, compared to Pt poly and state of the art Pt/C catalyst. (B and C) Tafel plots for the PtNi and Pt–Co based alloys.

tainty, and similar values for the SA were obtained with both methods. As can be seen in Fig. 1D, this is a linear trend until about 100 $\mu g_{Pt}\ cm^{-2}{}_{disk}$, with a surface area of ~8 $m^2$ per gram of Pt. This coincides with the appearance of the higher diffusion limiting current as mentioned before, and is indicative of a multi-layer of NSTF on the GC disk, which causes the SA per gram of Pt to increase. However, as mentioned in the previous paragraph, the specific activity is reduced significantly due to mass transport issues in multi-layer NSTF, therefore the mass activity is negatively affected as well.

Additionally the kinetic current at 0.9 V versus RHE, is shown in Fig. 1E. Clearly, lower and higher loadings have affected measured activity for the ORR. At low loadings, the amount of catalyst is not enough to ensure complete coverage of glassy carbon support, which causes lower $I_{diff}$ and underestimation of specific activity. In order to avoid issues with loading, we determined the most optimal value in these experiments to be 65 $\mu g_{Pt}\ cm^{-2}{}_{disk}$. This is low enough to avoid problems due to the increased $I_{diff}$, yet high enough to prevent undesirable distribution of the NSTF. All data reported here were measured with 65 $\mu g_{Pt}\ cm^{-2}{}_{disk}$.

### 3.2. Cyclic voltammetry

The following Pt-alloy and monometallic Pt NSTF catalysts were considered in this research. $Pt_3Co$, $Pt_3Ni$, $PtNi_2$, $Pt_{0.32}Ni_{0.61}Fe_{0.07}$ alloy, a $Pt_{0.67}Co_{0.30}Mn_{0.03}$ alloy, a $Pt_{0.4}Co_{0.5}Zr_{0.1}$ alloy, and a $Pt_3CoNi$ alloy.

For the ease of comparison, the cyclic voltammograms (CVs) of the catalysts are divided into two categories: one group containing platinum nickel alloys (PtNi of various compositions and PtNiFe ternary alloy) and the other group containing platinum cobalt alloys (PtCo, PtCoMn and PtCoZr). The PtCoNi ternary alloy, falls into both categories, while Pt NSTF was used as a benchmark system.

Blank CVs are shown in Fig. 2, with the PtNi and PtCo alloys in insert B and C respectively. To make an obvious comparison between nanostructured catalysts and bulk polycrystalline Pt the cyclic voltammertries are compared in Fig. 2A. The underpotentially deposited hydrogen ($H_{upd}$) region at potentials lower than 0.4 V exhibits broader features for the NSTF catalyst. This is a first indication that on the thin film catalyst a plethora of lower coordinated Pt atoms are on the surface and the size of crystalline facets are smaller than on poly Pt. It is clear that the differences in cyclic voltammetry between the alloy catalysts are subtle. $Pt_3Ni$ and PtCoNi exhibit similar CVs, both closely resembling the blank CV of Pt NSTF, while the capacity of the double layer is independent of the electrochemically active surface area ($H_{upd}$ region). There is even less difference between the various cobalt containing catalysts, where only PtCoZr exhibits the broader $H_{upd}$ region seen with PtNiFe and $PtNi_2$.

### 3.3. Oxygen reduction reaction

The results for the ORR are shown in Figs. 3–5. Tafel plots are shown in Fig. 3 in order to compare the activity for the NSTF cata-

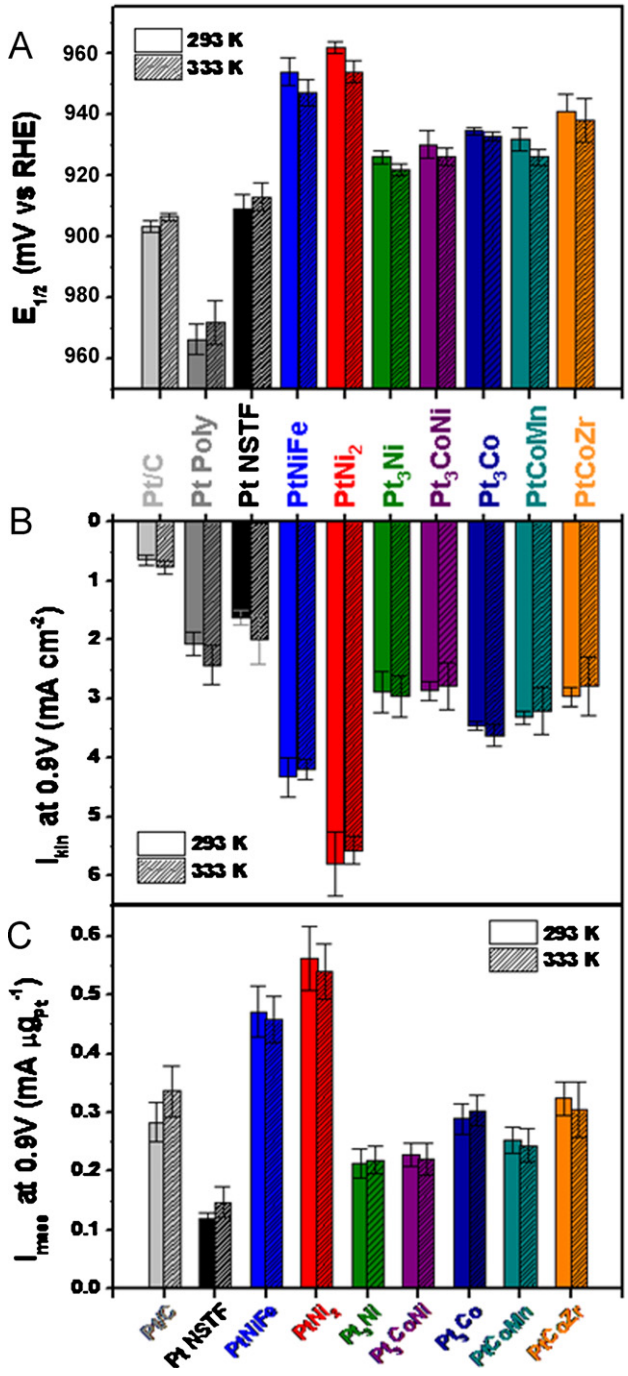


**Fig. 4.** Bar graphs of the ORR on NSTF catalysts, compared to polycrystalline Pt. (A) Half-wave potential ($E_{1/2}$). (B and C) Specific and mass activities at 0.9 V. The single-color bars represent the value at 293 K, and the accented bars represent 333 K. (For interpretation of the references to color in this figure legend, the reader is referred to the web version of the article.)

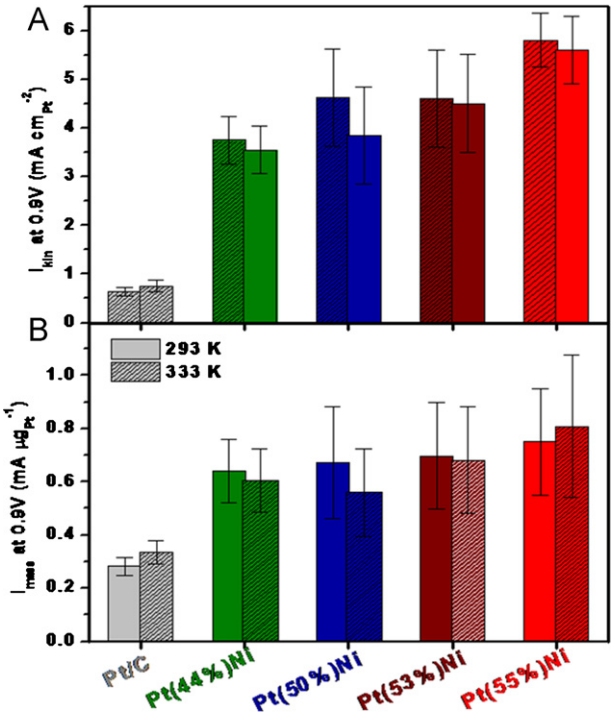


**Fig. 5.** Bar graphs of the ORR on PtNi catalysts with different Pt content. Light grey bars show the Pt/C catalyst as a reference. (A) Specific and (B) mass activities at 0.9 V. The single-color bars represent the value at 293 K, and the accented bars represent 333 K. (For interpretation of the references to color in this figure legend, the reader is referred to the web version of the article.)

lysts over the potential range from 0.85 to 0.95 V. Based on Fig. 3A, it is clear that the Pt NSTF catalyst by itself offers a substantial improvement over carbon supported Pt/C catalyst. Obvious from Fig. 3B is the high activity for the ORR for the low-Pt content PtNi catalysts, PtNiFe and $PtNi_2$, an order of magnitude higher than the Pt/C catalyst, and 3 times more active than the monometallic Pt NSTF. The other PtNi and PtCo based catalysts are very similar in activity, as can be seen in Fig. 3C. The specific activity is better illustrated in Fig. 4, in which the half-wave potential, insert (A), and kinetic current at 0.9 V, insert (B), are compared. Again, the obvious conclusion from this graph is that the two catalysts with high nickel content; *i.e.* PtNiFe and $PtNi_2$ are superior in activity to the other NSTFs and the Pt/C catalyst. This conclusion is true even when we consider the mass activities at 0.9 V shown in Fig. 4C. Carbon supported nanoparticles have high mass activities, due to their high surface area per gram of catalyst, which is almost an order of magnitude higher than the average value for the NSTF catalysts ($\sim 10\,m^2/g_{NSTF}$). However, the specific activity enhancement of the PtNi alloy NSTF catalysts is substantial, so that they actually have a higher mass activity than the carbon supported Pt nanoparticles.

A further observation in this graph is that the activity of alloy catalysts reduces upon an increase of the temperature, whereas the activity of monometallic Pt increases upon the same temperature increase. This temperature effect is fully reversible, *i.e.* the activity of the alloy NSTF is restored to the initial value when the temperature is brought back down to 293 K, dismissing any permanent alteration of our catalyst by dissolution of the non-Pt alloy metals. The exact cause of this temperature effect requires careful consideration, and is likely to have its origins in the increased affinity for surface oxides at higher temperatures.

Finally, the PtNi alloy with lower Pt content was characterized as well, in order to increase mass activity even further. Our previous results [37] showed that the optimal catalyst composition was with lower Pt content than $Pt_3Ni$. Fig. 5 shows the results for the ORR activity at 0.9 V, both in specific and mass activity. The decrease in specific activity is obvious when the platinum content is lowered, but the expected increase in mass activity is not observed. Based on that, the PtNi alloy with about 55 wt% platinum is found to be the most efficient catalyst.

## 4. Conclusion

A range of multimetallic carbon free platinum-based nanostructured thin film catalysts have been characterized by the rotating

disk electrode. The optimal loading for RDE measurements of NSTF catalysts was determined to be 65 $\mu g_{Pt}\,cm^{-2}{}_{disk}$. Of all catalysts measured, the PtNi alloys show more promising activities for the ORR than the Pt–Co based alloys. The PtNi and PtNiFe alloys exhibit superior specific and mass activities compared to monometallic Pt NSTF and Pt/C catalyst. The most active catalyst is determined to be the PtNi alloy with 55 wt% of platinum. These results reaffirm that the NSTF catalysts present a very promising system as cathode material in PEM fuel cells.

## Acknowledgement

This work was supported by the contract (DE-AC02-06CH11357) between the University of Chicago and Argonne, LLC, and the US Department of Energy. 3M Cells and Infrastructure Technology Program [in the Office of Energy Efficiency and Renewable Energy] at the US Department of Energy, specifically for grant DE-FG36-07GO17007.

## References

[1] B. Johnston, M.C. Mayo, A. Khare, Technovation 25 (2005) 569.
[2] H.A. Gasteiger, S.S. Kocha, B. Sompalli, F.T. Wagner, Appl. Catal. B: Environ. 56 (2005) 9.
[3] H.A. Gasteiger, J.E. Panels, S.G. Yan, J. Power Sources 127 (2004) 162.
[4] M.C. Tucker, J. Power Sources 195 (2010) 4570.
[5] H.A. Gasteiger, M.F. Mathias, Fundamental research and development challenges in polymer electrolyte fuel cell technology, in: M. Myrthy, T.F. Fuller, J.W. Van Zee, S. Gottesfeld (Eds.), Proton Conducting Membrane Fuel Cells III: Proceedings of the Electrochemical Society, vol. 2002-31, The Electrochemical Society Inc., Pennington, NJ, 2005, p. 1.
[6] F.T. Wagner, B. Lakshmanan, M.F. Mathias, J. Phys. Chem. Lett. 1 (2010) 2204.
[7] K.J.J. Mayrhofer, B.B. Blizanac, M. Arenz, V.R. Stamenkovic, P.N. Ross, N.M. Markovic, J. Phys. Chem. B 109 (2005) 14433.
[8] J.X. Wang, N.M. Markovic, R.R. Adzic, J. Phys. Chem. B 108 (2004) 4127.
[9] L. Xiao, L. Zhuang, Y. Liu, J.T. Lu, H.D. Abruna, J. Am. Chem. Soc. 131 (2009) 602.
[10] J. Hernandez, J. Solla-Gullon, E. Herrero, A. Aldaz, J.M. Feliu, J. Phys. Chem. C 111 (2007) 14078.
[11] L.G.R.A. Santos, K.S. Freitas, E.A. Ticianelli, Electrochim. Acta 54 (2009) 5246.
[12] A.S. Arico, P. Bruce, B. Scrosati, J.M. Tarascon, W. Van Schalkwijk, Nat. Mater. 4 (2005) 366–377.
[13] A. Atkinson, S. Barnett, R.J. Gorte, J.T.S. Irvine, A.J. Mcevoy, M. Mogensen, S.C. Singhal, J. Vohs, Nat. Mater. 3 (2004) 17.
[14] P. Strasser, S. Koh, T. Anniyev, J. Greeley, K. More, C.F. Yu, Z.C. Liu, S. Kaya, D. Nordlund, H. Ogasawara, M.F. Toney, A. Nilsson, Nat. Chem. 2 (2010) 454.
[15] K.J.J. Mayrhofer, M. Arenz, Nat. Chem. 1 (2009) 518.
[16] J. Greeley, I.E.L. Stephens, A.S. Bondarenko, T.P. Johansson, H.A. Hansen, T.F. Jaramillo, J. Rossmeisl, I. Chorkendorff, J.K. Norskov, Nat. Chem. 1 (2009) 552.
[17] D. Strmcnik, K. Kodama, D. van der Vliet, J. Greeley, V.R. Stamenkovic, N.M. Markovic, Nat. Chem. 1 (2009) 466.
[18] K. Epping Martin, P. Kopasz John, W. McMurphy Kevin, Status of fuel cells and the challenges facing fuel cell technology today Fuel Cell Chemistry and Operation, vol. 1040, American Chemical Society, 2010, pp. 1–13.
[19] Multi-Year Research, Development and Demonstration Plan: Technical Plan – Fuel Cells, Multi-Year Research, Development and Demonstration Plan: Planned Program Activities for 2005–2015, 2007.
[20] K. Kinoshita, J.T. Lundquist, P. Stonehart, J. Electroanal. Chem. Interfacial Electrochem. 48 (1973) 157.
[21] S. Zhang, X.-Z. Yuan, J.N.C. Hin, H. Wang, K.A. Friedrich, M. Schulze, J. Power Sources 194 (2009) 588.
[22] K.J.J. Mayrhofer, S.J. Ashton, J.C. Meier, G.K.H. Wiberg, M. Hanzlik, M. Arenz, J. Power Sources 185 (2008) 734.
[23] M.K. Debe, A.K. Schmoeckel, G.D. Vernstrorn, R. Atanasoski, J. Power Sources 161 (2006) 1002.
[24] V. Komanicky, K.C. Chang, A. Menzel, N.M. Markovic, H. You, X. Wang, D. Myers, J. Electrochem. Soc. 153 (2006) B446.
[25] Y. Shao, J. Wang, R. Kou, M. Engelhard, J. Liu, Y. Wang, Y. Lin, Electrochim. Acta 54 (2009) 3109.
[26] M.K. Debe, A.K. Schmoeckel, S.M. Hendricks, G.D. Vernstrom, G.M. Haugen, R.T. Atanasoski, ECS Trans. 1 (2006) 51.
[27] A.J. Steinbach, K. Noda, M.K. Debe, ECS Trans. 3 (2006) 835.
[28] M.K. Debe, A.J. Steinbach, G.D. Vernstrom, S.M. Hendricks, M.J. Kurkowski, R.T. Atanasoski, P. Kadera, D.A. Stevens, R.J. Sanderson, E. Marvel, J.R. Dahn, J. Electrochem. Soc. 1 (2011) B910.
[29] M.K. Debe, A.R. Drube, J. Vacuum Sci. Technol. B 13 (1995) 1236.
[30] M.K. Debe, R.J. Poirier, J. Vacuum Sci. Technol. A: Vacuum Surf. Films 12 (1994) 2017.
[31] T.J. Schmidt, H.A. Gasteiger, G.D. Stab, P.M. Urban, D.M. Kolb, R.J. Behm, J. Electrochem. Soc. 145 (1998) 2354.
[32] D. van der Vliet, D.S. Strmcnik, C. Wang, V.R. Stamenkovic, N.M. Markovic, M.T.M. Koper, J. Electroanal. Chem. 647 (2010) 29.
[33] K.J.J. Mayrhofer, D. Strmcnik, B.B. Blizanac, V. Stamenkovic, M. Arenz, N.M. Markovic, Electrochim. Acta 53 (2008) 3181.
[34] A. Bonakdarpour, K. Stevens, G.D. Vernstrom, R. Atanasoski, A.K. Schmoeckel, M.K. Debe, J.R. Dahn, Electrochim. Acta 53 (2007) 688.
[35] F. Gloaguen, P. Convert, S. Gamburzev, O.A. Velev, S. Srinivasan, Electrochim. Acta 43 (1998) 3767.
[36] J. Perez, E.R. Gonzalez, E.A. Ticianelli, Electrochim. Acta 44 (1998) 1329.
[37] C. Wang, M.F. Chi, G.F. Wang, D. van der Vliet, D.G. Li, K. More, H.H. Wang, J.A. Schlueter, N.M. Markovic, V.R. Stamenkovic, Adv. Funct. Mater. 21 (2011) 147.


(This is a sample cover image for this issue. The actual cover is not yet available at this time.)

Journal of Power Sources 215 (2012) 77–88

Contents lists available at SciVerse ScienceDirect

Journal of Power Sources

journal homepage: www.elsevier.com/locate/jpowsour

# Kinetics of oxygen reduction reaction on nanostructured thin-film platinum alloy catalyst

R.K. Ahluwalia [a,*], X. Wang [a], A. Lajunen [b], A.J. Steinbach [c], S.M. Hendricks [c], M.J. Kurkowski [c], M.K. Debe [c]

[a] Argonne National Laboratory, Argonne, IL 60439, USA
[b] Aalto University, School of Engineering, Aalto, Finland
[c] 3M Fuel Cell Components Program, St. Paul, MN, USA

## HIGHLIGHTS

- Nanostructured thin-film ternary PtCoMn cathode catalyst.
- Pressure and relative humidity dependence of oxygen–reduction reaction kinetics.
- 39.5 kJ $mol^{-1}$ activation energy for ORR kinetics.
- 0.13–0.25 A $mg_{Pt}^{-1}$ mass activity at 0.9 V, 1 atm $H_2$ and $O_2$, 80 °C and 100% RH.
- 1.7–2.0 mA $cm_{Pt}^{-2}$ specific activity at 0.9 V, 1 atm $H_2$ and $O_2$, 80 °C and 100% RH.

## ARTICLE INFO

*Article history:*
Received 6 February 2012
Received in revised form
24 April 2012
Accepted 26 April 2012
Available online 4 May 2012

*Keywords:*
Polymer electrolyte fuel cells
Alloy catalysts
Oxygen reduction reaction kinetics
Mass activity
Specific activity

## ABSTRACT

The kinetics of the oxygen reduction reaction (ORR) on nanostructured thin-film (NSTF) ternary PtCoMn catalyst was investigated in 50 $cm^2$ proton-exchange membrane single cell fixtures. The investigation covered a wide range of oxygen partial pressures (0.2–0.5 atm), temperatures (30–90 °C), relative humidities (25–100%), and Pt loadings (0.05–0.2 mg $cm^{-2}$) in the cathode catalyst. The kinetic data were derived from cell polarization curves measured during Galvanodynamic scans from near open-circuit to a high current density and back to near open-circuit. The kinetic data were correlated with a single Tafel equation and a transfer coefficient that is a function of the relative humidity (RH). The correlation indicates a 0.36 order for the $O_2$ partial pressure, 39.5 kJ $mol^{-1}$ activation energy for the temperature dependence, and an additional 0.9 order for RH dependence. The calculated mass activities and specific activities at 0.9 V Ohmic resistance corrected cell voltage, 1 atm $H_2$ and $O_2$ partial pressures, 80 °C and 100% RH agree well with the measured values of 0.13–0.25 A $mg_{Pt}^{-1}$ and 1.7–2.0 mA $cm_{Pt}^{-2}$ for the cells with different Pt loading.

Published by Elsevier B.V.

## 1. Introduction

Nanostructured thin film electrocatalysts have shown promise in addressing the performance, cost and durability barriers that must be overcome for mass commercialization of automotive fuel cells. Several studies by Debe and associates [1–3] have demonstrated that the NSTF catalysts can have significantly higher specific activity and durability than the conventional carbon supported highly dispersed Pt catalysts. The NSTF catalysts are formed by vacuum sputter-deposition of catalyst alloys onto a supported monolayer of highly oriented crystalline organic-pigment whiskers [1]. The support whiskers have a high aspect ratio (20–50), 0.6–2 μm length, rectangular lath-like morphology, 55 ± 12 nm width and 27 ± 7 nm thickness, and 3–5 × $10^9$ $cm^{-2}$ a real number density [1]. The whiskers have been coated with pure Pt as well as binary and ternary Pt alloys [2,3]. The PtCoMn ternary alloy (nominal 68:29–30:2–3 atomic ratio) is of particular interest as it has been evaluated extensively for performance and durability under potential cycling conditions (cyclic voltammetry with $H_2$/$N_2$), long holds at 1.5 V and higher potentials (support stability), and startups and shutdowns in $H_2$/air [4,5].

The purpose of this work is to characterize the activity of the ternary $Pt_{0.68}Co_{0.3}Mn_{0.02}$ NSTF catalyst for the oxygen reduction reaction (ORR) in $H_2$/air fuel cells. The intent is to determine the ORR activity as a function of the oxygen partial pressure, temperature, relative humidity and Pt loading. Previous studies on the ORR activities of Pt and PtCoMn catalysts on NSTF whiskers have used the rotating ring-disk electrode (RRDE) method in 0.1 M $HClO_4$ at

* Corresponding author. Tel.: +1 630 252 5979; fax: +1 630 252 3296.
*E-mail address:* walia@anl.gov (R.K. Ahluwalia).

0378-7753/$ – see front matter Published by Elsevier B.V.
doi:10.1016/j.jpowsour.2012.04.077

room temperature to 60 °C [6]. These studies have shown that the area specific activity of Pt/NSTF is similar to that of bulk Pt and that the activity of the ternary PtCoMn catalyst is about twice the activity of Pt/NSTF. The observed enhancement in the ORR activity in the RRDE measurements is similar to the results obtained in 50 $cm^2$ $H_2$/air fuel cells [6–10].

Our approach to determine the ORR kinetics for PtCoMn/NSTF from the polarization curves for $H_2$/air fuel cells benefits greatly from similar work described in literature on dispersed Pt/C electrodes. The past work has relied on holding the cell at a constant potential for 10 min or longer to ensure that the catalyst reaches the corresponding equilibrium Pt oxide coverage [11]. The advantage of using long hold times is that the data are quite reproducible; the disadvantage is that the data cannot be directly used to analyze the polarization curves that are generally obtained at faster scan rates. We used a slightly different approach of holding for 2 min at each data point and averaging the potentials measured during downscans from 0.02 to 2 A $cm^{-2}$ and reverse upscans from 2 to 0.02 A $cm^{-2}$ (10 points per decade) to estimate cell voltages at conditions approaching the equilibrium oxide coverages. Future work will explicitly determine the oxide coverage in the ternary catalyst as a function of the cathode potentials, the effect of the oxide coverage on the ORR activity, and the dynamics of Pt oxidation and Pt oxide reduction.

## 2. Experimental

Eight 50 $cm^2$ active area single cells were assembled with a 24 μm membrane (850 equivalent weight), the ternary NSTF catalyst, and 3 M gas diffusion layers (GDL) into a Fuel Cell Technologies test cell containing quad serpentine flow fields. The GDL consisted of a backing paper to which was applied a hydrophobic treatment and an MPL (micro-porous layer). All cells had a Pt loading of 0.05 mg $cm^{-2}$ in the anode. Two of the eight cells had a Pt loading of 0.103 mg $cm^{-2}$ in the cathode. The Pt loading in the cathode in the other cells (two each) was 0.054, 0.146 and 0.186 mg $cm^{-2}$. All cells were first conditioned using a "thermal cycling" process, described in detail in Steinbach et al. [12], which consisted of repeated temperature and voltage cycles over a period of 2–3 days until stable performance was reached. Next, oxygen reduction activity of the cathode catalyst, short resistance and $H_2$ crossover, and electrochemically active surface area (ECSA) of cathode catalyst were measured, after which a series of tests were conducted, as described below.

Table 1 lists the baseline Pt loading in the electrodes and the operating conditions. One of the cells with 0.103 mg $cm^{-2}$ Pt loading in the cathode was considered as the reference. The reference operating conditions were 80 °C cell temperature, 1.5 atm $H_2$ and air inlet pressures, 65 °C inlet dew point temperatures, and $H_2$ and $O_2$ stoichiometries (SR) of 2.

Table 2 summarizes the test matrix with eight series of tests. Series 1 tests varied the cell temperature from 75 °C to 90 °C ($P$ = 1.5 atm, $SR_c$ = 2, $SR_a$ = 2) with the inlet dew points predetermined as a function of pressure, temperature and anode/cathode stoichiometry to maintain 100% relative humidity (RH) at cell exit. In all tests, humidification water was injected directly into the anode and cathode feed streams to reach the set dew points. Also, the outlet RH was not measured but was estimated from the cell operating conditions.

**Table 1**
Reference Pt loading in electrodes and cell operating conditions. The outlet RH is 100% at all reference operating conditions.

| $L_{Pt}$ (c) mg.$cm^{-2}$ | $L_{Pt}$ (a) mg.$cm^{-2}$ | T°C | $T_{DP}$(c)°C | $T_{DP}$ (a)°C | P atm | SR(c) | SR(a) |
|---|---|---|---|---|---|---|---|
| 0.1 | 0.05 | 80 | 65 | 65 | 1.5 | 2 | 2 |

The backpressure regulator was used to vary the cell inlet pressure in Series 2 tests from 1 to 2.5 atm ($T$ = 80 °C, $SR_c$ = 2, $SR_a$ = 2). As explained later, the target inlet pressure could not be reached under some conditions even with the backpressure valve completely open to the ambient. As in Series 1 tests, the inlet dew points were also adjusted to maintain 100% RH at cell exit.

Series 3 tests varied the inlet dew points from dry (no water addition) to 80 °C ($P$ = 1.5 atm, $T$ = 80 °C, $SR_c$ = 2, $SR_a$ = 2). Series 5 tests varied the $O_2$ stoichiometery from 1.5 to 5 with the inlet dew points adjusted to maintain 100% RH at cell exit ($P$ = 1.5 atm, $T$ = 80 °C, $SR_a$ = 2). Series 6 tests varied the $H_2$ stoichiometry from 1.2 to 5 with the dew points held at the reference value of 65 °C ($P$ = 1.5 atm, $T$ = 80 °C, $SR_c$ = 2). Series 7 tests were designed to investigate the cell operation during warm-up at 30, 45 and 60 °C with dry feeds ($P$ = 1.5 atm, $SR_c$ = 2, $SR_a$ = 2). Similarly, Series 8 tests were designed to investigate cell operation during idling at low pressures and high $O_2$ stoichiometries.

Series 4 tests were conducted on cells with different Pt loadings in the cathode. These cells were only operated at the reference conditions.

To check for cell-to-cell variability, all tests were repeated on the companion cells with identical Pt loadings in the cathode.

Fig. 1a–h present the polarization curves for the eight series of tests. These were obtained during Galvanodynamic scans (GDS) at cell current densities varying from 0.02 to 2 A $cm^{-2}$. Only the data up to 1 A $cm^{-2}$ are plotted in Fig. 1 since significant mass transfer effects are present at higher current densities. Our procedure was to start the measurements near the open circuit at 0.02 A $cm^{-2}$, then increase the current density in steps until either 2 A $cm^{-2}$ was reached or the cell voltage decreased to 0.40 V, followed by an upscan back to 0.02 A $cm^{-2}$. The cell voltages were measured at ten current steps per decade but the maximum step size was limited to 0.1 A $cm^{-2}$. The cell was held for 120 s at each current step and the cell voltage was recorded every 5 s. Also, the cell resistance was determined every 5 s by on-line AC impedance measurements between 10 and 1 kHz, from which the high frequency resistance (HFR) was estimated by fitting to a Randle's cell model. The cell voltages presented in Fig. 1 are the measured values averaged over the last 30 s at the set current densities.

Prior to the start of the experiments, the electrochemical surface areas were determined by cyclic voltammetry (CV) between 0.085 and 0.65 V (vs. RHE) at 100 mV $s^{-1}$ scan rate, with $H_2/N_2$ at 70 °C, 70 °C dew points and ambient pressure. ECSA values were determined by averaging the oxidative and reductive $H_{UPD}$ peak areas from 100 CVs and assuming a 210 μC $cm_{Pt}^{-2}$ charge-to-area conversion factor. The measured ECSA values, listed in Table 3, decrease from 12.4 $m^2$ $g^{-1}$ at 0.054 mg $cm^{-2}$ Pt loading to ~7 $m^2$ $g^{-1}$ at 0.186 mg $cm^{-2}$ Pt loading, and are five to ten times smaller than the ECSA of highly dispersed Pt/C (55–70 $m^2$ $g^{-1}$ for Pt/C with 0.4 mg $cm^{-2}$ Pt loading).

Table 3 includes the surface enhancement factors (SEF) obtained by multiplying the measured ECSA by the Pt loading. The SEF ($cm_{Pt}^2.cm^{-2}$) grows with increase in Pt loadings at a rate that is less than linear. Also included in Table 3 are the thicknesses of the catalyst layers as measured from SEM cross-sectional images of the NSTF catalyst-coated membranes [10]. These NSTF catalyst layers are only about one-tenth as thick as the conventional Pt/C catalysts with similar Pt loadings.

Hydrogen crossover current density and cell short resistance were determined by measuring the plateau currents between 0.4 and 0.6 V cell potentials with saturated $H_2/N_2$ at 1.5 atm total pressure and 80 °C cell temperature. Table 2 shows that the $H_2$

**Table 2**
Pt loading and cell operating conditions for test series 1–8.

| | | | | | | | | |
|---|---|---|---|---|---|---|---|---|
| *Test Series 1: Effect of temperature* | | | | | | | | |
| Pt loading: 0.1(c), 0.05(a) mg.cm$^{-2}$; Pressure:1.5 atm; SR: 2(c), 2(a) | | | | | | | | |
| | Run 1.1 | Run 1.2 | Run 1.3 | Run 1.4 | Run 1.5 | | | |
| Temperature,°C | 75 | 80 | 85 | 90 | 95 | | | |
| Dew point T(c),°C | 55 | 65 | 74 | 82 | 89 | | | |
| Dew point T(a),°C | 55 | 65 | 74 | 82 | 89 | | | |
| *Test Series 2: Effect of pressure* | | | | | | | | |
| Pt loading: 0.1(c), 0.05(a) mg.cm$^{-2}$; Temperature: 80 °C; 1.5 atm; SR: 2(c), 2(a) | | | | | | | | |
| | Run 2.1 | Run 2.2 | Run 2.3 | Run 2.4 | Run 2.5 | | | |
| Dew point T(c),°C | 73 | 70 | 65 | 56 | 40 | | | |
| Dew point T(a),°C | 73 | 70 | 65 | 56 | 40 | | | |
| Pressure, atm | 1 | 1.25 | 1.5 | 2 | 2.5 | | | |
| *Test Series 3: Effect of relative humidity* | | | | | | | | |
| Pt loading: 0.1(c), 0.05(a) mg.cm$^{-2}$; Temperature: 80 °C; Pressure:1.5 atm; SR: 2(c), 2(a) | | | | | | | | |
| | Run 3.1 | Run 3.2 | Run 3.3 | Run 3.4 | Run 3.5 | Run 3.6 | Run 3.7 | Run 3.8 |
| Dew point T(c),°C | 0 | 50 | 55 | 60 | 65 | 70 | 75 | 80 |
| Dew point T(a),°C | 0 | 50 | 55 | 60 | 65 | 70 | 75 | 80 |
| *Test Series 4: Effect of platinum loading* | | | | | | | | |
| Temperature: 80 °C; Dew point: 65 °C(c), 65 °C(a); Pressure:1.5 atm; SR: 2(c), 2(a) | | | | | | | | |
| | Run 4.1 | Run 4.2 | Run 4.3 | Run 4.4 | | | | |
| Pt loading(c), mg.cm$^{-2}$ | 0.05 | 0.1 | 0.15 | 0.2 | | | | |
| Pt loading(a), mg.cm$^{-2}$ | 0.05 | 0.05 | 0.05 | 0.05 | | | | |
| *Test Series 5: Effect of cathode stoichiometry* | | | | | | | | |
| Pt loading: 0.1(c), 0.05(a) mg.cm$^{-2}$; Temperature: 80 °C; Pressure:1.5 atm; | | | | | | | | |
| | Run 5.1 | Run 5.2 | Run 5.3 | Run 5.4 | | | | |
| Dew point T(c),°C | 60 | 65 | 68 | 75 | | | | |
| Dew point T(a),°C | 60 | 65 | 68 | 75 | | | | |
| SR(c) | 1.5 | 2 | 2.5 | 5 | | | | |
| SR(a) | 2 | 2 | 2 | 2 | | | | |
| *Test Series 6: Effect of anode stoichiometry* | | | | | | | | |
| Pt loading: 0.1(c), 0.05(a) mg.cm$^{-2}$; Temperature: 80 °C; Dew point: 65 °C(c), 65 °C(a); Pressure:1.5 atm; | | | | | | | | |
| | Run 6.1 | Run 6.2 | Run 6.3 | Run 6.4 | Run 6.5 | | | |
| SR(c) | 2 | 2 | 2 | 2 | 2 | | | |
| SR(a) | 1.2 | 1.5 | 2 | 2.5 | 5 | | | |
| *Test Series 7: Cold temperatures* | | | | | | | | |
| Pt loading: 0.1(c), 0.05(a) mg.cm$^{-2}$; Pressure:1.5 atm; SR: 2(c), 2(a) | | | | | | | | |
| | Run 7.1 | Run 7.2 | Run 7.3 | | | | | |
| Temperature,°C | 30 | 45 | 60 | | | | | |
| Dew point T(c),°C | 0 | 0 | 0 | | | | | |
| Dew point T(a),°C | 0 | 0 | 0 | | | | | |
| *Test Series 8: Idle operation* | | | | | | | | |
| Pt loading: 0.1(c), 0.05(a) mg.cm$^{-2}$; Temperature: 80 °C; Dew point: 80 °C(c), 80 °C(a); | | | | | | | | |
| | Run 8.1 | Run 8.2 | Run 8.3 | Run 8.4 | | | | |
| Pressure, atm | 1.05 | 1.1 | 1.2 | 1.3 | | | | |
| SR(c) | 10 | 5 | 2.5 | 1.75 | | | | |
| SR(a) | 2 | 2 | 2 | 2 | | | | |

crossover current density of the membrane at these pressure and temperature conditions was about 2.4–3.5 mA cm$^{-2}$ and the short resistance of the eight cells varied between 182 and 933 Ω cm$^2$.

Table 3 lists the mass activities of Pt in each cell measured in $H_2$/$O_2$ at 80 °C, 1 atm reactant $H_2$ and $O_2$ pressures and 100% RH. The mass activity measurement was made by first reducing the cathode with a 15 min hold under $H_2/N_2$ at ~0.10 V, after which the cathode was switched to $O_2$ and the cathode potential was then immediately held at 0.90 V for 20 min. The listed mass activity values are the current densities, adjusted for $H_2$ crossover and shorting currents, at a cell voltage of 0.9 V after 17.5 min. The measured mass activity is 0.18 A.mg$_{Pt}^{-1}$ for the reference cell with 0.103 mg cm$^{-2}$ Pt loading and is somewhat higher in cells with lower Pt loading. This value may be compared with the 0.13 A mg$_{Pt}^{-1}$ mass activity of 47% Pt/C (TKK) reported by Neyerlin et al. [11] and 0.1 A mg$_{Pt}^{-1}$ mass activity of TKK PtCo dispersed on corrosion resistant (CR) carbon as reported by Wagner et al. [13]. Thus, as noted in earlier publications, the mass activity of ternary PtCoMn/NSTF is 40% higher than Pt/C in spite of the much lower ECSA and 80% higher than PtCo/CR-carbon [6,7]. The reason for this result is the much higher specific activity of PtCoMn/NSTF. Table 3 shows that the ternary NSTF catalyst has a specific activity between 1.7 and 2 mA.cm$_{Pt}^{-2}$, which is 6–8 times the reported values of 0.25 mA cm$_{Pt}^{-2}$ for Pt/C and 0.3 mA cm$_{Pt}^{-2}$ for PtCo/CR-carbon [13].

## 3. Kinetics of oxygen reduction reaction

We investigated the ORR kinetics by analyzing the polarization data for low current densities, $i < 0.5$ A cm$^{-2}$, where the mass transfer effects are negligible. We averaged the cell potentials measured during the upscans and downscans in order to remove any non-equilibrium effects caused by the finite Pt oxidation kinetics. We assessed the effect of the finite kinetics of Pt oxidation and PtO reduction near the open-circuit potentials by running polarization tests at the reference conditions with 10 min hold at each data point. The data showed only small and random differences between the cell voltages measured with 2 min and 10 min hold times. We excluded $i < 0.1$ A cm$^{-2}$ polarization data while determining the ORR rate constants for three reasons. First, our analysis procedure involved normalizing the error (difference in the modeled and measured current densities) by the measured current density, which skewed the results by placing a large weight on the small current density data. Second, the flow rates of feed gases are held at threshold values for $i < 0.1$ A cm$^{-2}$, so that that the

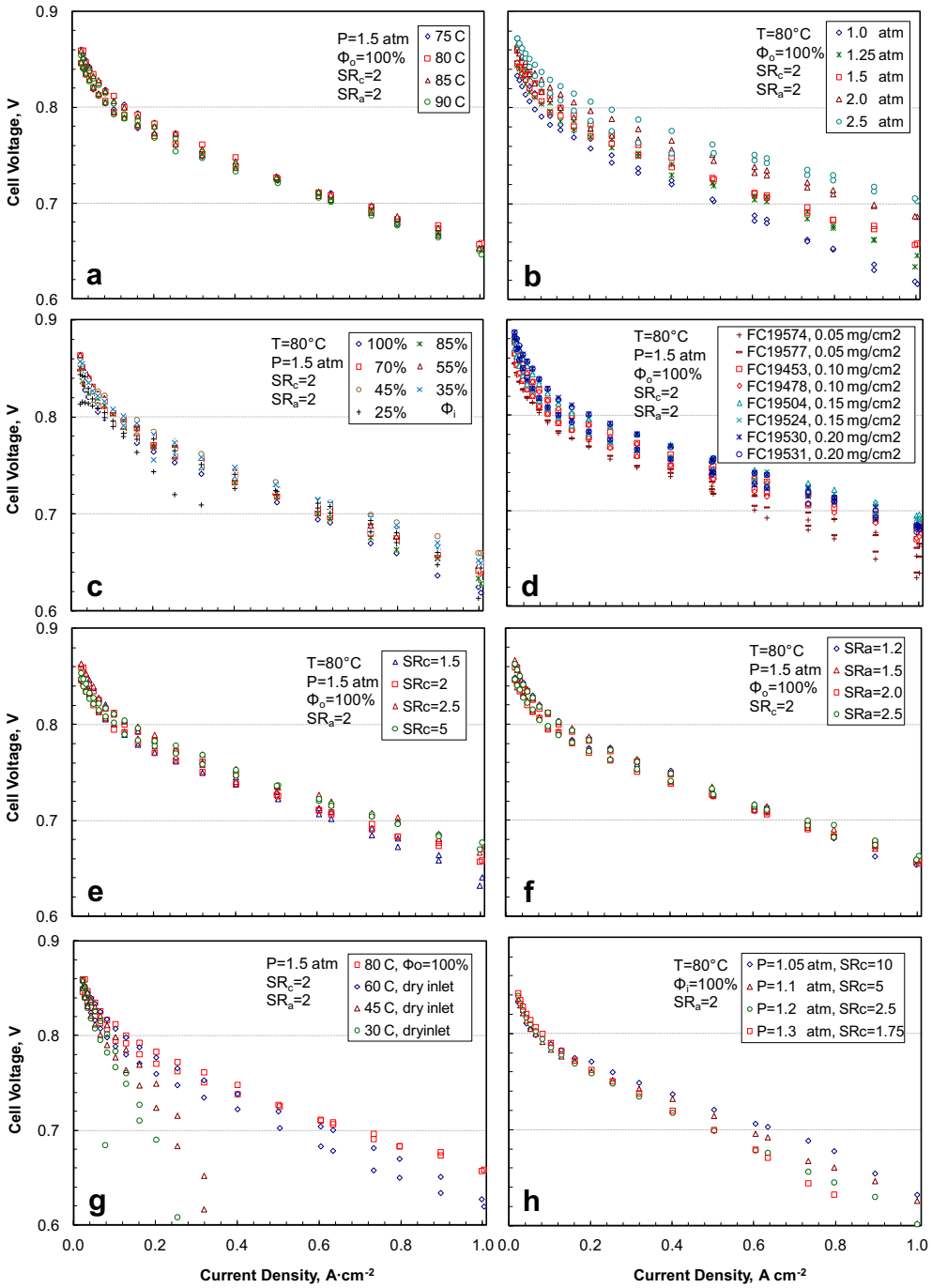


**Fig. 1.** GDS polarization curves with 2-min hold at each data point. Excluding Fig. 1d, all data taken on the reference cell with 0.103 mg $cm^{-2}$ Pt loading in the cathode. Data for both upscans and downscans included.

**Table 3**
Cell characterization and performance data, all activities measured at 0.9 V IR-corrected cell voltage, 80 °C and 100% RH.

| Cell Designation | 19,574 | 19,577 | 19,453 | 19,478 | 19,504 | 19,524 | 19530 | 19531 |
|---|---|---|---|---|---|---|---|---|
| Pt Loading, mg $cm^{-2}$ | 0.054 | 0.054 | 0.103 | 0.103 | 0.146 | 0.146 | 0.186 | 0.186 |
| ECSA, $m^2_{Pt}.g^{-1}$ | 12.4 | 12.6 | 9.8 | 9.8 | 9.2 | 8.4 | 7.2 | 7.0 |
| SEF, $cm^2_{Pt}cm^{-2}$ | 6.7 | 6.8 | 10.1 | 10.1 | 13.4 | 12.2 | 13.4 | 13 |
| Catalyst Layer Thickness, mm | 0.16 ± 0.018 | | 0.32 ± 0.034 | | 0.47 ± 0.048 | | 0.61 ± 0.061 | |
| $H_2$ Crossover, mA $cm^{-2}$ | 3.2 | 3.1 | 2.8 | 2.9 | 3.0 | 2.4 | 3.5 | 3.1 |
| Short Resistance, Ω $cm^2$ | 588 | 267 | 933 | 664 | 182 | 216 | 340 | 379 |
| Absolute Activity, mA $cm^{-2}$ | 11.3 | 13.5 | 17.6 | 18.8 | 23.5 | 23.3 | 25.5 | 24.1 |
| Mass Activity, A $mg^{-1}_{Pt}$ | 0.21 | 0.25 | 0.17 | 0.18 | 0.16 | 0.16 | 0.14 | 0.13 |
| Specific Activity, mA $cm^{-2}_{Pt}$ | 1.69 | 1.99 | 1.74 | 1.86 | 1.75 | 1.91 | 1.90 | 1.85 |

anode/cathode stoichiometries and exit dew points are different from those for $i > 0.1$ A cm$^{-2}$. Finally, the crossover current ($i_x$) can be a significant fraction of the total current for $i < 0.05$ A cm$^{-2}$ but we did not specifically measure the RH dependence of $i_x$. We emphasize, however, that whereas the $i < 0.1$ A cm$^{-2}$ data were not included in determining the ORR rate constants, they were considered in the subsequent evaluation of the kinetic model.

We represented the cell voltage ($E$) at the measured current density ($i$) in terms of the Nernst potential ($E_N$) calculated at the cell temperature ($T$) and the partial pressures ($P$) of $H_2$ and $O_2$, the cathode overpotential for ORR ($\eta$), and the Ohmic drop due to HFR ($R_\Omega$).

$$E = E_N - iR_\Omega - \eta \quad [1]$$

$$E_N = E_0 + \frac{RT}{nF}\ln\left(\frac{P_{H_2}P_{O_2}^{1/2}}{\Phi}\right) \quad [2]$$

where $E_0$ is the standard potential for the fuel cell reaction assuming that the product water is liquid, $\Phi$ is the relative humidity (1 for 100% RH), and $n$ equals 2.

$$E_0 = 1.23 + 0.000833(T - 298) \quad [3]$$

We neglect the small anode overpotential for the facile hydrogen oxidation reaction [10] and assume that the sluggish oxygen reduction reaction on cathode follows the Tafel equation with a single Tafel slope over the cathode potential range of interest.

$$i + i_x = i_0 A_{Pt} L_{Pt} P_{O_2}^{\gamma} \Phi^{\beta} \exp\left(\frac{\alpha n F}{RT}\eta\right) \quad [4]$$

where $i_x$ is the hydrogen crossover current density, $i_0$ is the exchange current density (A.cm$^{-2}_{Pt}$), $A_{Pt}$ is the electrochemically active surface area (ECSA, cm$^2_{Pt}$.mg$^{-1}$), $L_{Pt}$ is the Pt loading (mg cm$^{-2}$), $\gamma$ is the order with respect to $O_2$ partial pressure, $\Phi$ is the relative humidity, $\beta$ is the order with respect to $\Phi$, and $\alpha$ is the transfer coefficient. It is assumed that $H_2$ that crosses over undergoes $H_2 = 2H^+ + 2e^-$ half–cell reaction on the cathode catalyst, produces a mixed cathode potential, and leads to an internal cathodic current density ($i_x$).

### 3.1. Cell-averaged kinetics

We investigated the cell ORR kinetics by using the average $H_2$ and $O_2$ partial pressures across the cell (see Appendix 1). We found that the ORR overpotentials correlated better with the RH at cell exit rather than the inlet or average RH values. We formulated a stepwise procedure for determining $\gamma$, $i_0$, $\alpha$, and $\beta$. We first determined $\gamma$ by using the average polarization data in Series 2 at 80 °C, 50% $H_2$ and $O_2$ utilizations, and 100% RH at cell exit. For these conditions, Fig. 2a presents the ORR overpotential as a function of the current density for different air inlet pressures in the Series 2 tests. Fig. 2b indicates that the data in Fig. 2a are well correlated if the current density is scaled by $P_{O_2}^{-\gamma}$ with a $\gamma$ of 0.36. Here, $P_{O_2}^{\gamma}$ represents the average partial pressure of $O_2$ in the channel, and is calculated by accounting for the pressure drop ($\Delta P$) in the flow field and the $O_2$ consumption. The following correlation, developed from the measured inlet pressure in tests in which the exit pressure was 1 atm, was used to estimate $\Delta P$ (kPa) in terms of the gas volumetric flow rate ($\dot{V}$ in m$^3$ s$^{-1}$, superscripts a and c denote anode and cathode, respectively).

$$\Delta P^a = 1.6 + 1.3 \times 10^5 \dot{V} + 1.2 \times 10^9 \dot{V}^2$$

$$\Delta P^c = 1.8 + 2.3 \times 10^5 \dot{V} + 5.9 \times 10^9 \dot{V}^2 \quad [5]$$

In the second step, we investigated the temperature dependence of $i_0$ by analyzing the Series 1 data at 75, 80, 85 and 90 °C, with 50% $H_2$ and $O_2$ utilizations and 100% RH at cell exit, see Fig. 3a. We included the Series 2 data for 1, 1.25, 2 and 2.5 atm inlet pressures by using the $\gamma$ values determined in the first step. We correlated the data, plotted as semi-logs in Fig. 3b, with straight lines and estimated $\alpha$ from the slope and $i_0$ from the intercept as per the following equation ($\Phi = 1$).

$$\eta = \frac{RT}{\alpha nF}\ln\left[(i + i_x)P_{O_2}^{-\gamma}\right] - \frac{RT}{\alpha nF}\ln\left(i_0 A_{Pt} L_{Pt} \Phi^{\beta}\right) \quad [6]$$

Fig. 3b presents the estimated $i_0$ as a function of 1/T and leads to the following Arrhenius correlation with an activation energy ($E_{O_2}$) of 57.7 kJ mol$^{-1}$ for the ORR.

$$i_0 = i_{or}\exp\left[-\frac{E_{O_2}}{R}\left(\frac{1}{T} - \frac{1}{T_r}\right)\right] \quad [7]$$

where $i_{or}$ is the exchange current density at the reference temperature ($T_r = 353$ K).

The third step consisted of investigating the RH dependence of the ORR. Fig. 4a presents the ORR overpotentials in the Series 3 tests for different exit RH at 80 °C and in the Series 2 tests for 1, 1.25, 2 and 2.5 atm inlet pressures. As per Eq. (6), we fitted the data with straight lines on semi-log axes and used the slopes to determine $\alpha$ as a function of $\Phi$, see Fig. 4b.

$$\alpha = \frac{0.4665}{1 + 0.0926\Phi} \quad [8]$$

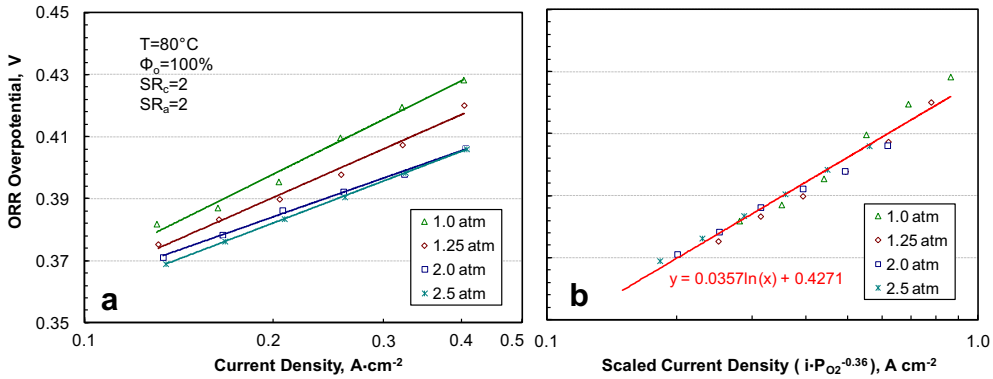


**Fig. 2.** Derived cell-averaged ORR overpotentials in series 2 data (a) and determination of the order with respect to $P_{O_2}$ (b).

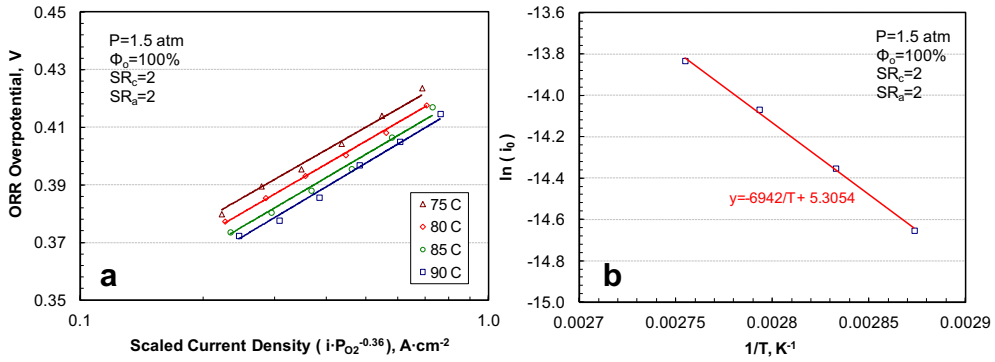


**Fig. 3.** Derived cell-averaged ORR overpotentials in series 1 data (a) and determination of the activation energy $E_{O_2}$ for temperature dependence (b)

We used the intercepts in Fig. 4a to determine $i_0\Phi^{\beta}$ and these are presented in Fig. 4c. The power law fit in Fig. 4c leads to the following estimates for $i_{or}$ (A.cm$_{Pt}^{-2}$) and $\beta$.

$$i_{0r} = 5.7 \times 10^{-7}, \quad \beta = 1.3. \qquad [9]$$

### 3.2. Local ORR kinetics

Whereas the above correlation for the average ORR kinetic rate is useful for characterizing the cell performance, it is desirable to have the ability to estimate the ORR overpotentials for the local values of $i$, $T$, $P_{O_2}$, and $\Phi$. For this purpose, we developed a simple one-dimensional model to estimate the local values of $i$,$P_{O_2}$, $P_{H_2}$ and $\Phi$ from the measured cell polarization curves. The model solves the following set of equations for anode and cathode pressures and for molar flow rates ($\dot{N}$) of $H_2$, $O_2$ and $H_2O$ (subscript w) in the anode (superscript a) and cathode (superscript c) channels considering the source terms for the electrochemical reactions and water transport flux ($J_w^m$) across the membrane (superscript m) by electro-osmotic drag and diffusion (normal direction y).

$$\frac{dP^c}{dx} = -\frac{\Delta P^c}{L} \qquad [10]$$

$$\frac{dP^a}{dx} = -\frac{\Delta P^a}{L} \qquad [11]$$

$$\frac{d\dot{N}^c_{O_2}}{dx} = \left(\frac{i+i_x}{4F}\right)W_m \qquad [12]$$

$$\frac{d\dot{N}^c_{w}}{dx} = -\left(\frac{i+i_x}{2F} + J^m_w\right)W_m \qquad [13]$$

$$\frac{d\dot{N}^a_{H_2}}{dx} = -\left(\frac{i+i_x}{2F}\right)W_m \qquad [14]$$

$$\frac{d\dot{N}^a_{w}}{dx} = -J^m_w W_m \qquad [15]$$

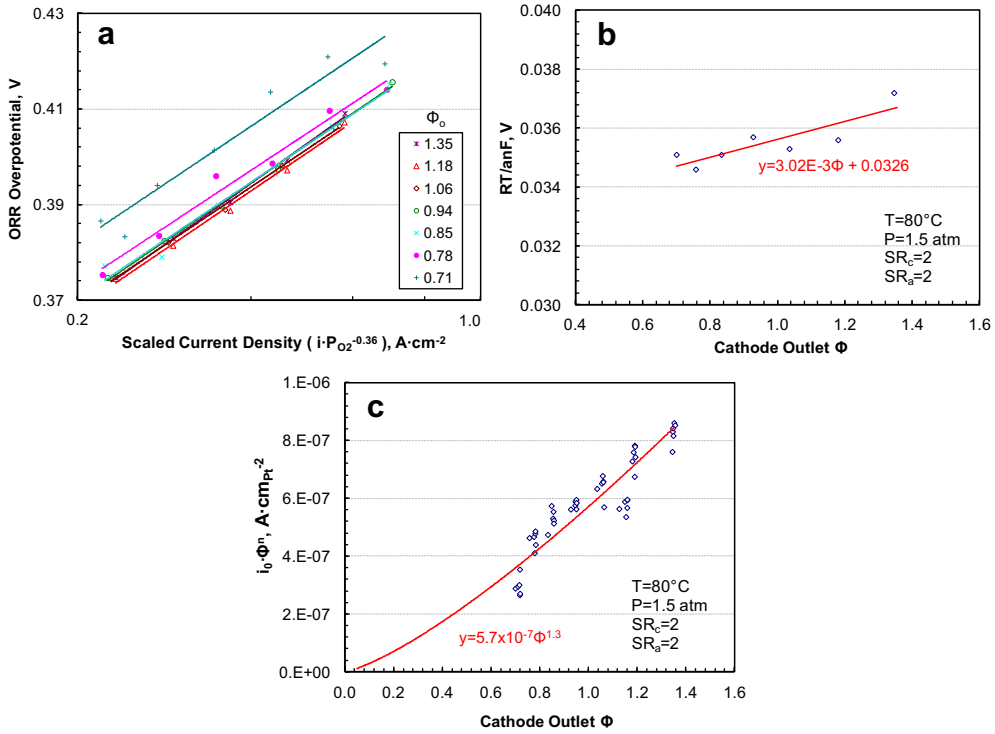


**Fig. 4.** Derived cell-averaged ORR overpotentials in series 3 data (a) and determination of the transfer coefficient, $\alpha$ (b) and the order with respect to RH, $\beta$ (c).

The following auxiliary equations define $J_w^m$ and relate $P_{O_2}$, $P_{H_2}$ and $\Phi$ to the molar flow rates. Also, the current density $i$ is given by Eq. (4).

$$J_w^m = \beta_\lambda \left(\frac{i}{F}\right) - \left(\frac{\rho_m}{EW}\right) D_\lambda \frac{\partial \lambda}{\partial y} \quad [16]$$

$$\dot{N}_{ws}^c = \frac{P_s}{P_c - P_s} \sum_{i \neq w} \dot{N}_i^c \quad [17]$$

$$\dot{N}_{ws}^a = \frac{P_s}{P_a - P_s} \sum_{i \neq w} \dot{N}_i^a \quad [18]$$

$$\Phi^c = \frac{\dot{N}_w^c}{\dot{N}_{ws}^c} = \frac{P_w^c}{P_s} \quad [19]$$

$$\Phi^a = \frac{\dot{N}_w^a}{\dot{N}_{ws}^a} = \frac{P_w^a}{P_s} \quad [20]$$

$$P_{H_2} = \frac{\dot{N}_{H_2}^a}{\sum \dot{N}_i^a} P^a \quad [21]$$

$$P_{O_2} = \frac{\dot{N}_{O_2}^c}{\sum \dot{N}_i^c} P^c \quad [22]$$

The following equation is used to calculate $\lambda$ ($\lambda^c$ or $\lambda^a$) as a function of $\Phi$ ($\Phi^c$ of $\Phi^a$).

$$\lambda = \begin{cases} 23.82\Phi^4 - 28.53\Phi^3 + 8.36\Phi^2 + 5.92\Phi + 0.1 & (\Phi \leq 1) \\ 9.67 + 2.8(\Phi - 1) & (\Phi \leq 3) \\ 15.27 & (\Phi > 3) \end{cases} \quad [23]$$

In the above equations, $H_2$ flows in the anode channel along the $x$ direction (L is the total length) whereas air flows in the cathode channel along the −x direction, superscript s represents saturation, $\lambda$ is the water uptake in the membrane, $\rho_m$ (2000 kg m$^{-3}$) and EW (850) are the membrane density and equivalent weight, and $W_m$ is the membrane width. Note that $P_s$ is the saturation pressure of water vapor and is a function of temperature only. Similarly, $\dot{N}_{ws}^c$ and $\dot{N}_{ws}^a$ are the molar flow rates of saturated water vapor and are related to $P_s$ through Eqs. (17) and (18).

For expediency, we assumed that the electro-osmotic drag coefficient ($\beta_\lambda = 1$) and the water diffusion coefficient ($D_\lambda = 1.5 \times 10^{-6}$ cm$^2$ s$^{-1}$) are constant, so that Eq. (16) can be integrated analytically to obtain the $\lambda$ profile and hence the water transport flux $J_w^m$ across the membrane.

$$J_w^m = \beta_\lambda \left(\frac{i}{F}\right) - \left(\frac{\rho_m}{EW}\right)\left(\frac{D_\lambda}{\delta_m}\right)(\lambda^c - \lambda^a) \quad [24]$$

where $\delta_m$ is the membrane thickness.

A simple first-order finite-difference scheme was used to integrate Eqs. (10)–(15) simultaneously. We marched from anode inlet ($x = 0$) to anode outlet, i.e., the equations were integrated in the forward flow direction for the anode stream and in the backward flow direction for the cathode stream. The required boundary conditions for the anode stream were determined from the known molar flow rates of $H_2$ and $H_2O$ in the anode feed gas. The required boundary conditions for the cathode stream are unknown and had to be determined iteratively. Our approach was to use a hybrid method, combining steepest descent with quasi-Newton update technique, to determine $\dot{N}_{O_2}^c$ and $\dot{N}_w^c$ at $x = 0$ such that $\dot{N}_{O_2}^c$ and $\dot{N}_w^c$ calculated by solving Eqs. (10)–(15) at cathode inlet match the experimental values (control variables).

We used an optimizer to determine the combination of $i_{or}$, $E_{O_2}$, and $\beta$ that minimizes the root mean square difference between the measured and modeled current densities normalized by the measured current density in Series 1-3 data. The parameters were allowed to vary over a wide range: $5 \times 10^{-8}$–5 x $10^{-6}$ A cm$_{Pt}^{-2}$ for $i_{or}$, 20–80 kJ mol$^{-1}$ for $E_{O_2}$, and 0.25–2.5 for $\beta$. Attempts to vary $\alpha$ proved unsuccessful because of convergence problems arising from the extreme sensitivity of the calculated overpotentials to $\alpha$. It was also not possible to vary $\gamma$ because, over the range of pressures for which the data were available, the calculated overpotentials were far less sensitive to $\gamma$ than to other parameters. For these reasons, we retained Eq. (8) for $\alpha$ and kept $\gamma$ at 0.36. We used a sequential quadratic programming technique for solving nonlinear constrained optimization problems. The following were the initial values of the various parameters appearing in Eq. (4) as determined by the optimizer: $i_{or} = 6.8 \times 10^{-7}$ A cm$_{Pt}^{-2}$, $E_{O_2} = 39.5$ kJ mol$^{-1}$, and $\beta = 0.9$. In a follow-on attempt, $\beta$ was allowed to vary linearly with $\Phi$ since subsequent analysis suggested a stronger dependence of ORR kinetics on RH under dry conditions than can be explained with a constant $\beta$. The optimized value of $\beta$ is given by the following linear function.

$$\beta = \begin{cases} 0.9 + 1.5(0.65 - \Phi) & \Phi < 0.65 \\ 0.9 & \Phi \geq 0.65 \end{cases} \quad [25]$$

For illustrative purposes, Appendix 2 shows the calculated profiles of $i$, $P_{O_2}$, $P_{H_2}$ and $\Phi$ in Run 1.2 at 0.4 A cm$^{-2}$.

Fig. 5 compares the measured and modeled cell current density with the above parameters. It includes data from the tests in Series 1, 2 and 3 with different T, P and RH. All these tests were run with 50% $H_2$ and $O_2$ utilizations and a Pt loading of 0.103 mg cm$^{-2}$ in the cathode and 0.05 mg cm$^{-2}$ in the anode. For the data included in Fig. 5, the standard deviation ($s$) between the modeled ($i_m$) and measured ($i_d$) current densities is 22.1 mA cm$^{-2}$ and the correlation coefficient ($R^2$) is 0.993.

Even though a direct comparison between the ORR kinetic parameters derived here for the ternary PtCoMn/NSTF with those reported in the literature for Pt/C is not meaningful because of the different catalysts (alloy vs. monometallic, polycrystalline thin-film

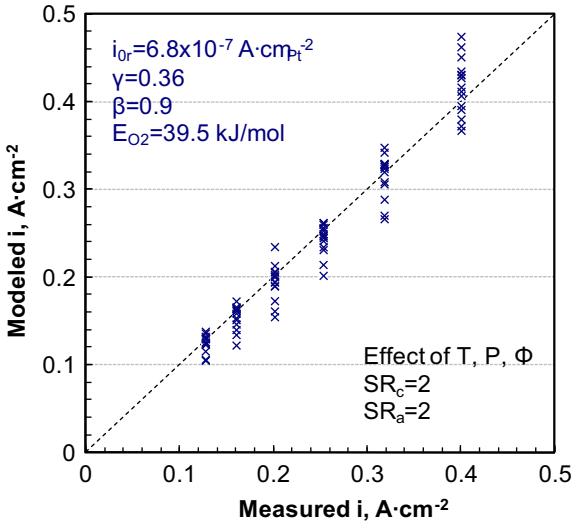


**Fig. 5.** Test of the local ORR kinetic correlation against data from series 1, 2 and 3.

vs. crystalline nanoparticles, nm vs. μm curvature, etc) and supports (organic vs. carbon, whiskers vs. particles, etc), it may be useful to discuss the associated trends. The PtCoMn/NSTF system shows a small RH dependence of the Tafel slope ($2.303RT/\alpha nF$) that at 80 °C decreases from 82 mV/decade for 100% RH to 78.5 mV/decade for 50% RH. The Pt/C system has a constant Tafel slope, 65 ± 2 mV/decade [11,14], although dependence of $\alpha$ on RH has been observed at 120 °C [15]. The pre-exponential term in Eq. (4), however, varies as $\Phi^{0.9}$ for PtCoMn/NSTF, whereas Pt/C shows no dependence on RH for $\Phi > 0.75$ but significant reduction for $\Phi < 50$–60% [16] possibly due to its effect on the $H^+$ concentration in the ionomer under very dry conditions ($\lambda < 2$–4). The PtCoMn/NSTF system has no ionomer in the catalyst layer other than the membrane material that partially fills the voids between the catalyst-coated whiskers when the CCM is formed. Also, the ORR kinetics on PtCoMn/NSTF shows smaller dependence on $P_{O_2}$ ($\gamma$ of 0.36 vs. 0.54) and temperature (activation energy of 39.5 kJ/mol vs. 67 kJ/mol) than Pt/C [17,18], possibly implying different rate-controlling steps in the overall mechanism [10].

The graphs in Fig. 6 show the validity of the kinetic parameters with respect to single variables, i.e., temperature (and RH) in Fig. 6a (Series 1 data), pressure (and RH) in Fig. 6b (Series 2 data), and RH in Fig. 6c (Series 3 data). Fig. 6 shows reasonable match between the model and data if $i_{or}$ is slightly adjusted (by −4% to 6%) to account for variations in measured polarizations in the different series of tests (see Fig. 11). The standard deviation and $R^2$ are 13.1 mA cm$^{-2}$ and 0.9977 for data with varying temperatures, 22.5 mA cm$^{-2}$ and 0.9928 for data with varying pressures, and 22 mA cm$^{-2}$ and 0.996 for data with varying relative humidities.

Fig. 7 tests the applicability of the model parameters in capturing the effects of cathode and anode stoichiometry. It includes data from the tests in Series 5 and 6, which were not used in determining the optimum choice of the ORR kinetic parameters. We found that $i_{or}$ has to be increased by ~15% at $SR_c = 5$ and ~40% at $SR_c = 10$ (Fig. 8b) in order to get a good match between the model and the data ($s = 34$ mA cm$^{-2}$, $R^2 = 0.9836$). This increase in $i_{or}$ at high $SR_c$ may be related to the resultant high pressure drop that enhances air flow under the lands in the serpentine flow field. It has been suggested that this enhanced air flow assists in removing the liquid water from the GDL under the land, relieves liquid saturation in the cathode catalyst layer, and thereby improves the catalyst activity [19]. We determined an empirical factor ($f$) that describes the enhancement in $i_{or}$ as a function of the cell cathode stoichiometry and the local current density.

$$f = 1 + (f_1(SR) - 1) f_2(i)$$

$$f_1(SR) = \begin{cases} 1.4 & SR_c > 10 \\ 1.0 + 0.0033(SR_c - 2)^2 + 0.0233(SR_c - 2) & SR_c > 1.75 \end{cases}$$

$$f_2(i) = \begin{cases} 1 & i > 0.125 \\ \dfrac{i}{0.125} & i \le 0.125 \end{cases} \qquad [26]$$

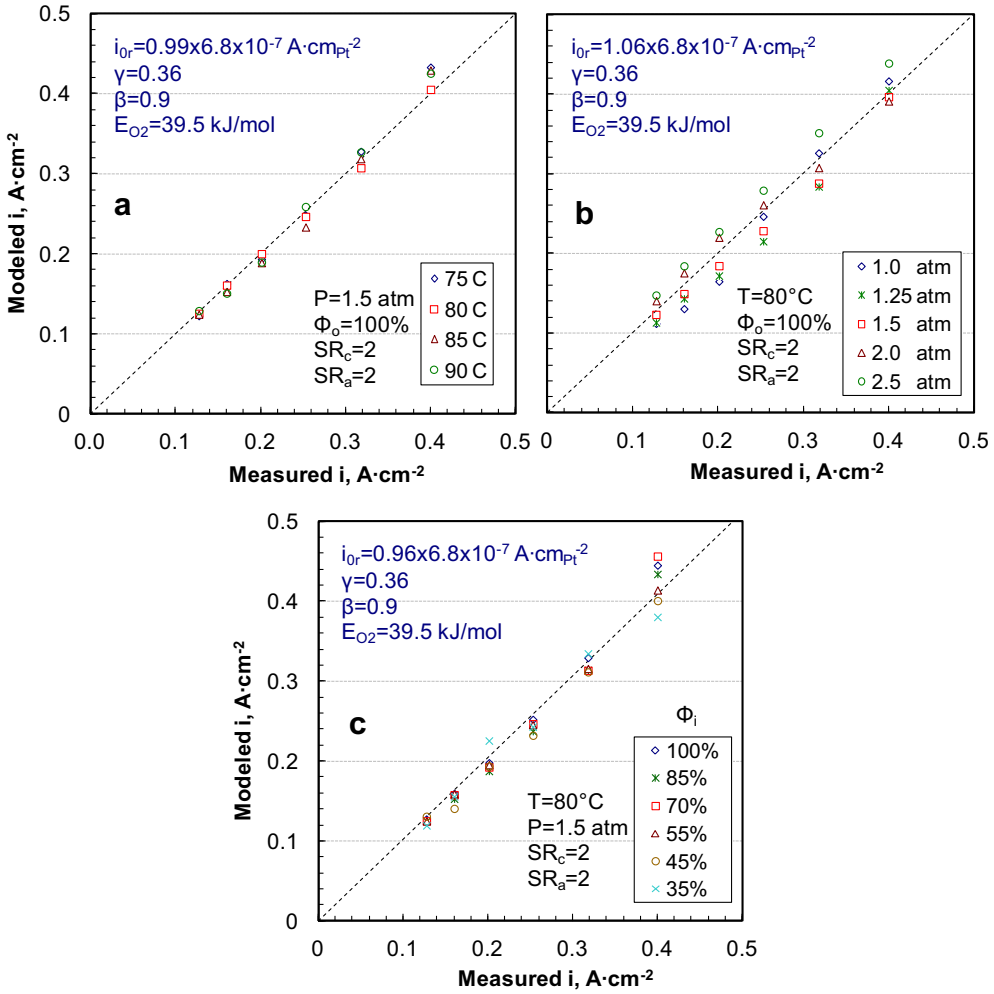


**Fig. 6.** Test of the local ORR kinetic correlation against series 1 data with varying temperature (a), series 2 data with varying pressure (b) and series 3 data with varying RH (c).

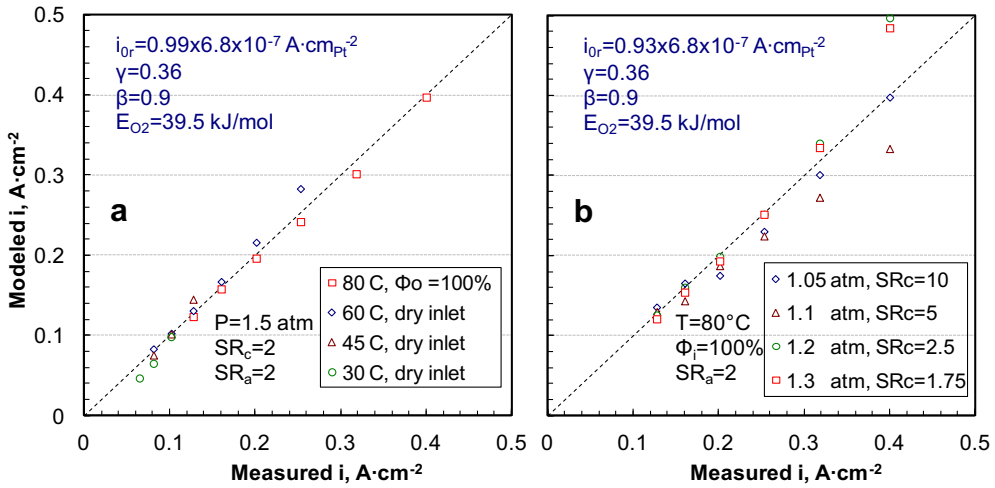


**Fig. 7.** Test of the local ORR kinetic correlation against series 5 data with varying cathode stoichiometry (a), and series 6 data with varying anode stoichiometry (b).

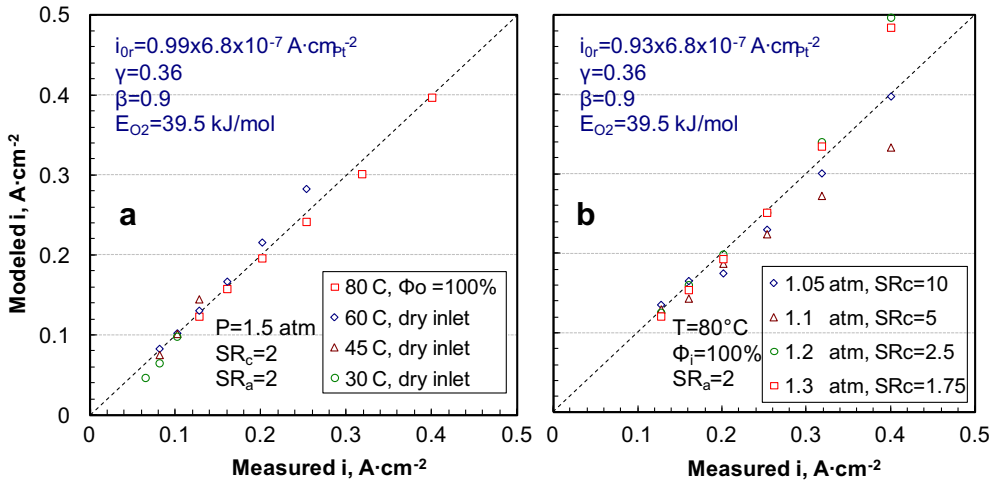


**Fig. 8.** Test of the local ORR kinetic correlation against series 7 data for low cell temperatures (a), and series 8 data for low pressures (b).

In our interpretation, whereas the kinetic parameters $\alpha$, $\beta$, $\gamma$, $i_{or}$ and $E_{O_2}$ are unique to the PtCoMn/NSTF catalyst, the factor $f$ is specific to the flow field and is likely to change with a different cell design.

As expected, the match between the model and data is better in Fig. 7b ($s = 9$ mA cm$^{-2}$, $R^2 = 0.9989$) than in Fig. 7a since the anode stoichiometry influences the ORR kinetics only indirectly, i.e., through water balance.

Fig. 8a provides a test of the applicability of the ORR kinetic parameters at low temperatures that the cell may experience during startup (Series 7 data) with dry feeds. The comparison is restricted to 0.1 A.cm$^{-2}$ at 30 °C, 0.15 A.cm$^{-2}$ at 45 °C, and 0.25

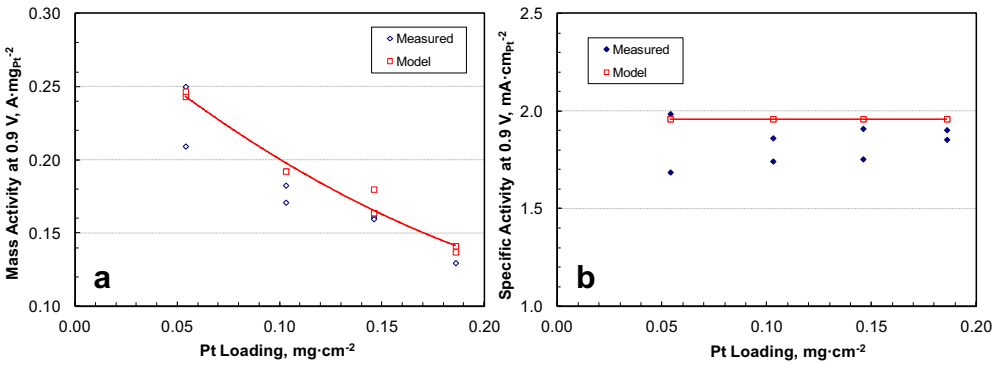


**Fig. 9.** Model validation against measured mass activities and specific activities for the cells with different Pt loadings.

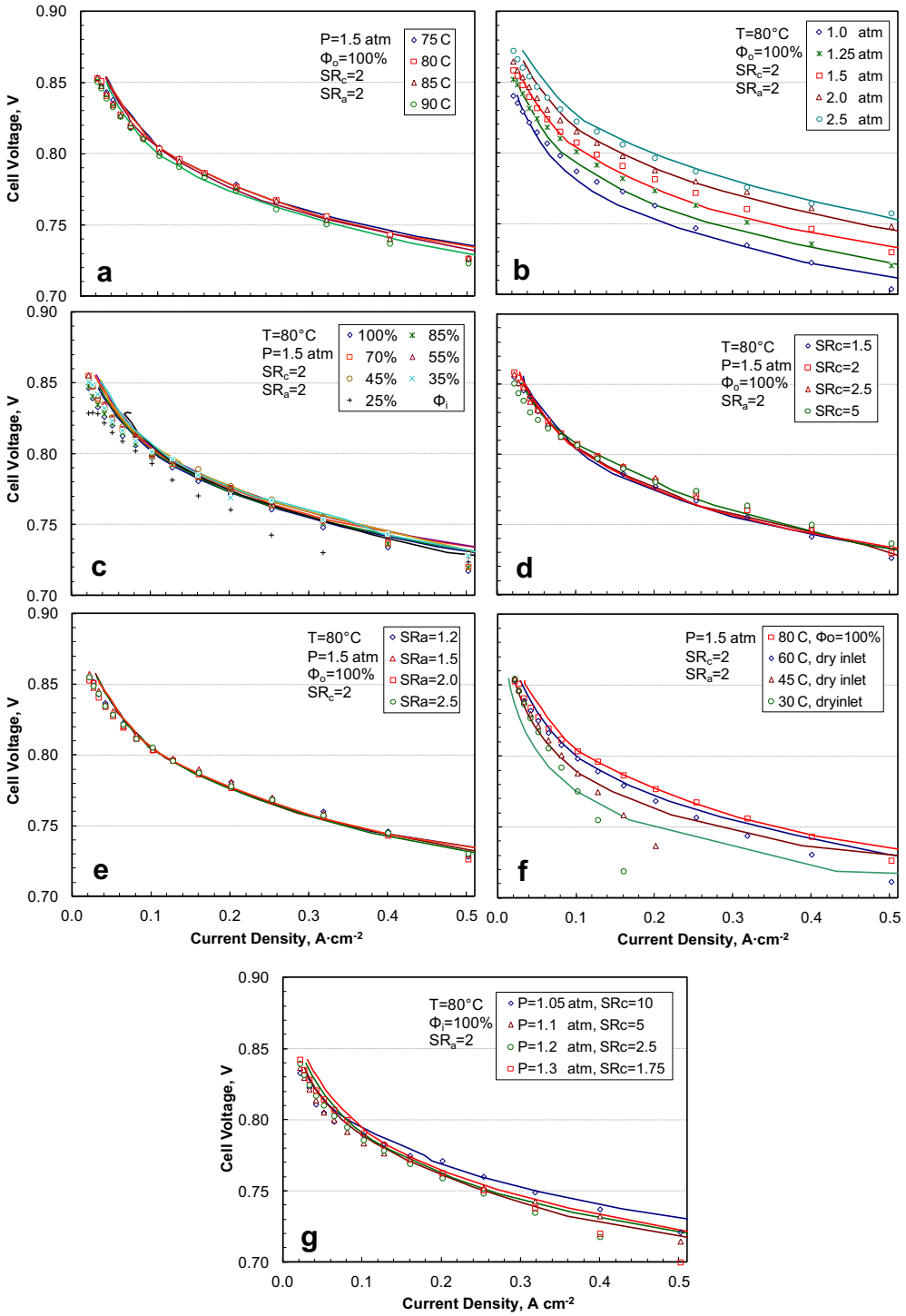


**Fig. 10.** Model validation against polarization data on the reference cell for different T (a), P (b), RH (c), $SR_c$ (d), $SR_a$(e), cold temperatures (f), and low pressures and high $SR_c$ (g).

A.cm$^{-2}$ at 60 °C since the mass transfer effects are evident at higher current densities at these temperatures. The data in Fig. 8a suggest that an activation energy of 39.5 kJ mol$^{-1}$ adequately reflects the effect of temperature on ORR kinetics over the range of 30–90 °C ($s = 2.3$ mA cm$^{-2}$, $R^2 = 0.9959$).

Fig. 8b measures the "goodness" of the correlation for low pressure and high-SR data (Series 8 for idling conditions, 100% inlet RH). We see that the empirically derived $f$ function adequately describes the enhancement in $i_{or}$ at high stoichiometries.

### 3.3. Discussion of the results

Fig. 9a compares the mass activities measured during Series 4 tests with the current densities calculated from our model for 0.9 V IR-corrected cell voltage, $P_{O_2} = 1$ atm, and $\Phi = 1$. As stated earlier, the measured mass activities correspond to current densities measured 20 min after holding the cell at 0.9 V. Fig. 9b gives a similar comparison between the modeled and measured specific current densities. Fig. 9a and b include data from cells (pairs) with

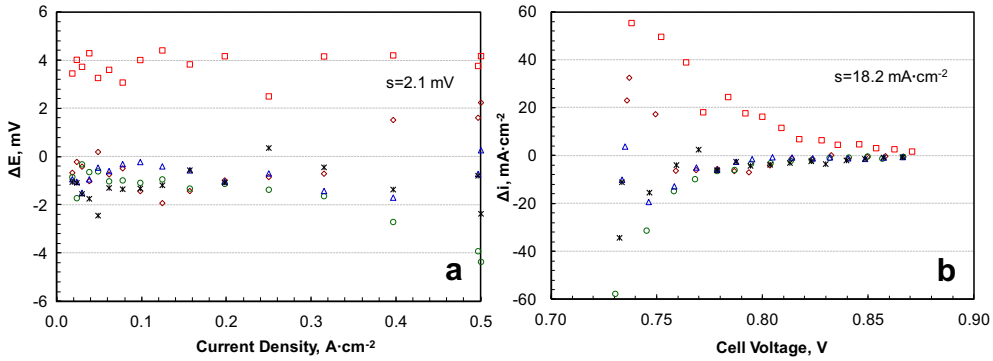


**Fig. 11.** Variability in data from six repeats of tests in series 1, 2, 3, 4, 5 and 6 at reference conditions. All data from the reference cell with 0.103 mg $cm^{-2}$ Pt in the cathode.

different Pt loadings. The favorable comparisons suggest that the ORR kinetic parameters ($\alpha$, $\beta$ and $\gamma$) can be used for PtCoMn/NSTF cathode catalysts with different Pt loadings if the variation in ECSA with Pt loading is taken into account.

Fig. 10 compares the modeled and measured polarization curves for the seven series of tests conducted on the reference cell. There is generally a good agreement between the modeled and measured cell voltages for current densities between 0.1 and 0.4 A.$cm^{-2}$ except under very dry conditions, such as at 25% RH in Series 3 data, where there is additional voltage loss due to membrane dry-out. The discrepancy at higher current densities is attributed to mass transfer effects that will be analyzed in a follow-on paper. The mass transfer effects (possible catalyst layer flooding) are evident even at 0.1 A.$cm^{-2}$ for cell temperatures below 45 °C (Series 7 data). The model correctly calculates the ordering of cell voltages with temperature ($E$(75 °C) > $E$(80–85 °C) > $E$(90 °C)) in Series 2 data. The model also calculates the increase in cell voltage with increase in $SR_c$ for current densities between 0.1 and 0.4 A $cm^{-2}$, as measured in Series 5 data, and the observed reordering in cell voltages with respect to $SR_c$ at lower current densities.

It is worth mentioning that the inlet pressure is the control variable except at low pressures (1–1.05 atm data) and high current densities or high cathode stoichiometries. In these instances, the outlet pressure is 1 atm and the inlet pressure is raised to produce the specified flow rate, see Eq. (5). Thus, the cell inlet pressure for the Series 8 data identified as 1.05 atm and $SR_c = 10$ can be higher than for the 1.2 and 1.3 atm, lower $SR_c$ data, and may show higher cell voltages at current densities >0.1 A.$cm^{-2}$.

The cell voltages calculated from our correlation are within 5–10 mV of the measured values for current densities lower than 0.1 A $cm^{-2}$. In taking the polarization data at current densities between 0.02 and 0.1 A $cm^{-2}$, the $H_2$ and air flow rates were held at the set threshold values, 100 slpm for $H_2$ and 185 slpm for air. Cell operation at high air stoichiometry results in the relative humidity staying close to the inlet value, which can be as low as 40% in the Series 2 test at 75 °C and the Series 5 test at 1.5 nominal $SR_c$ (see Table 2). We found much better agreement between the model and low-RH data for <0.1 A.$cm^{-2}$ current densities if $\beta$, the order with respect to RH, is allowed to increase for $\Phi < 0.65$, as in Eq. (25).

The polarization data for the reference conditions in Table 1 were taken at different times in Series 1, 2, 3, 5 and 6 tests. We have used these data to establish the variability in our measurements. Fig. 11a indicates that the measured cell voltages at the reference conditions are reproducible within ±5 mV and have a standard deviation of 2.1 mV over the current density range of 0.02–0.5 A $cm^{-2}$. Fig. 11b presents the corresponding variation in the current density estimated by using a Tafel slope of 82 mV/decade in Eq. (4). The standard deviation for the estimated current densities is 18.2 mA $cm^{-2}$ over a range of 0.73–0.87 V IR-corrected cell voltages. Our kinetic correlation has a comparable standard deviation of 9–22.5 mA $cm^{-2}$ for all the data taken in Series 1, 2, 3, 5 and 6 tests along with ±6% variation in $i_{or}$. Thus, the "goodness" of the ORR correlation is consistent with the accuracy and reproducibility of the polarization data.

Further work is required to verify and improve the kinetic model. The model reliability will improve with more accurate and reproducible data (see Fig. 11). Additional data are needed to test the RH dependence of ORR kinetics ($\alpha$ and $\beta$) and the effect of high $SR_c$ on $i_o$.

## 4. Summary and conclusions

The kinetics of the oxygen reduction reaction (ORR) on PtCoMn/NSTF can be correlated with the following simple Tafel equation with a single value of the transfer coefficient ($\alpha$).

$$i + i_x = i_0 A_{Pt} L_{Pt} P_{O_2}^{\gamma} \Phi^{\beta} \exp\left(\frac{\alpha n F}{RT}\eta\right)$$

$$i_0 = i_{or} f(SR_c) \exp\left[-\frac{E_{O_2}}{R}\left(\frac{1}{T}-\frac{1}{T_r}\right)\right],$$

$$i_{0r} = 6.8x10^{-7} A.cm_{Pt}^{-2},\quad E_{O_2} = 39.5 kJ.mol^{-1},\quad T_r = 353K$$

$$\gamma = 0.36$$

$$\beta = \begin{cases} 0.9 + 1.5(0.65 - \Phi) & \Phi < 0.65 \\ 0.9 & \Phi \geq 0.65 \end{cases}$$

$$\alpha = \frac{0.4665}{1 + 0.0926\Phi}$$

$$f = 1. + (f_1(SR) - 1) f_2(i)$$

$$f_1(SR) = \begin{cases} 1.4 & SR_c > 10 \\ 1.0 + 0.0033(SR_c - 2)^2 + 0.0233(SR_c - 2) & SR_c > 1.75 \end{cases}$$

$$f_2(i) = \begin{cases} 1 & i > 0.125 \\ \dfrac{i}{0.125} & i \leq 0.125 \end{cases}$$

We regard the kinetic parameters $i_{or}$, $\alpha$, $\beta$, $\gamma$ and $E_{O_2}$ as specific to the PtCoMn/NSTF catalyst tested and the factor $f$ that accounts for the increase in catalyst activity at high stoichiometries as an attribute

of the flowfield design. The ECSA ($A_{Pt}$) is a function of the Pt loading in the cathode catalyst, decreasing from 12.5 ± 0.1 $m^2\ g^{-1}$ for 0.054 mg $cm^{-2}$ Pt loading to 7.11 ± 0.1 $m^2\ g^{-1}$ for 0.186 mg $cm^{-2}$ Pt loading. The order ($\beta$) for RH dependence increases sharply for $\Phi$ below 0.65. The above choice of the kinetic parameters is consistent with the cell polarization data at 30–90 °C, 0.1–0.5 atm $P_{O_2}$, 35–100% RH ($\Phi$) and 0.054–0.186 mg $cm^{-2}$ Pt loading ($L_{Pt}$) and also with the mass activity and specific activity measurements in $H_2/O_2$ at 0.9 V IR-corrected cell voltage, 80 °C, 1 atm $P_{H_2}$ and $P_{O_2}$, and 100% RH.

## Acknowledgments

This work was supported by the Fuel Cell Technologies Program of the U.S. Department of Energy's Office of Energy Efficiency and Renewable Energy. Dr. Nancy Garland and Mr. Jason Marcinkoski are the DOE's program managers for this work. The authors thank Dr. Romesh Kumar for many helpful discussions.

## Appendix 1. Average $H_2$ and $O_2$ pressures in the Cell

$$P_{O_2} = \frac{P^c_{in}}{2}\left[X^c_{O_2,in} + \left(1 - \frac{\Delta P^c}{P^c_{in}}\right)X^c_{O_2,o}\right]$$

$$\dot{N}^c_{O_2,o} = \dot{N}^c_{O_2,in}(1 - 1/SR_c)$$

$$X^c_{O_2} = \frac{\dot{N}^c_{O_2}}{\sum \dot{N}^c_i}$$

$$P_{H_2} = \frac{P^a_{in}}{2}\left[X^a_{H_2,in} + \left(1 - \frac{\Delta P^a}{P^a_{in}}\right)X^a_{H_2,o}\right]$$

$$\dot{N}^a_{H_2,o} = \dot{N}^a_{H_2,in}(1 - 1/SR_a)$$

$$X^a_{H_2} = \frac{\dot{N}^a_{H_2}}{\sum \dot{N}^a_i}$$

where $X$ is the mole fraction and the subscripts *in* and *o* denote the cell inlet and outlet, respectively.

## Appendix 2. Representative axial profiles

Fig. 12 presents a sample of the calculated axial profiles of $i, P_{O_2}$, $P_{H_2}$ and $\Phi$ for Run 1.2 at 0.4 A.$cm^{-2}$. The anode $H_2$ stream in Fig. 12 flows from left to right while the cathode air stream flows from right to left.

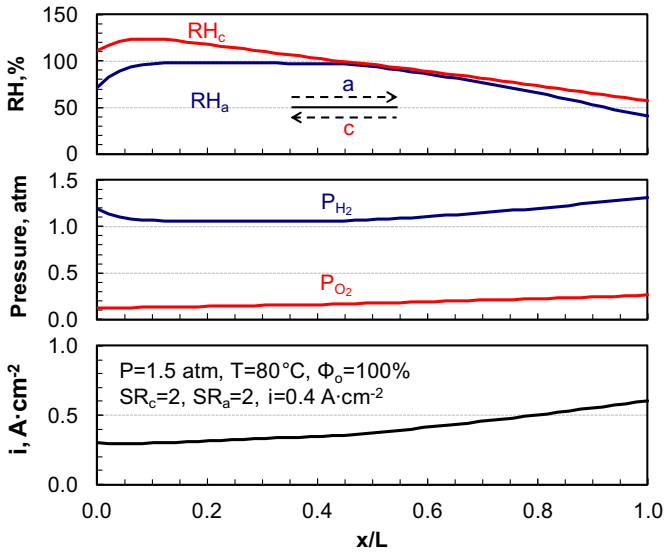


**Fig. 12.** Sample axial profiles of $i, P_{O_2}$, $P_{H_2}$ and Φ in run 1.2 at 0.4 A $cm^{-2}$.

## References

[1] M.K. Debe, in: W. Vielstich, A. Lamm, H.A. Gasteiger (Eds.), Handbook of fuel cells: Fundamentals, Technology and Applications, vol. 3, John Wiley & Sons, Chichester, England, 2003.
[2] M.K. Debe, A.K. Schmoeckel, R.T. Atanasoski, G.D. Vernstrom, Paper 64 Presented at the fuel cell Seminar, Palm Springs, CA, 14–18 Nov. 2005.
[3] M.K. Debe, A.K. Schmoeckel, S.M. Hendricks, G.D. Vernstrom, G.M. Haugen, R.T. Atanasoski, ECS Trans. 1 (8) (2006) 51.
[4] M.K. Debe, A.K. Schmoeckel, G.D. Vernstrom, R. Atanasoski, J. Power Sources 161 (2006) 1002–1011.
[5] A.J. Steinbach, K. Noda, M.K. Debe, ECS Trans. 3 (1) (2006) 835–853.
[6] A. Bonakadarpour, K. Stevens, G.D. Vernstrom, R. Atanasoski, A.K. Schmoeckel, M.K. Debe, J.R. Dahn, Electrochim. Acta 53 (2007) 688–694.
[7] M.K. Debe, A.K. Schmoeckel, R.T. Atanasoski, G.D. Vernstrom, Paper 583 Presented at the fuel cell Seminar, Honolulu, HI, 13–17 Nov. 2006.
[8] D. van der Vliet, C. Wang, M. Debe, R. Atanasoski, N. Markovic, V. Stamenkovic, Electrochim. Acta 56 (2011) 8695–8699.
[9] D. van der Vliet, D. Strmcnik, C. Wang, R. Atanasoski, M. Debe, N. Markovic, V. Stamenkovic, Multimetallic catalysts for the oxygen reduction reaction, 216th ECS Meeting, Vienna, Oct. 2009.
[10] M.K. Debe, J. Electrochem. Soc. 159 (1) (2012) B54–B67.
[11] K.C. Neyerlin, W. Gu, J. Jorne, H.A. Gasteiger, J. Electrochem. Soc. 153 (2007) A1955–A1963.
[12] A.J. Steinbach, C.V. Hamilton, M.K. Debe, ECS Trans. 11 (1) (2007) 889–897.
[13] F.T. Wagner, H.A. Gasteiger, R. Makharia, K.C. Neyerlin, E.L. Thompson, S.G. Yan, ECS Trans. 3 (1) (2006) 19.
[14] K.C. Neyerlin, W. Gu, J. Jorne, H.A. Gasteiger, J. Electrochem. Soc. 154 (2007) B631–B635.
[15] H. Xu, Y. Song, H.R. Kunz, J.M. Fenton, J. Electrochem. Soc. 152 (2005) A1828–A1836.
[16] K.C. Neyerlin, H.A. Gasteiger, C.K. Mittelsteadt, J. Jorne, W. Gu, J. Electrochem. Soc. 152 (2005) A1073–A1080.
[17] K.C. Neyerlin, W. Gu, J. Jorne, H.A. Gasteiger, J. Electrochem. Soc. 154 (2007) B279–B287.
[18] H.A. Gasteiger, J.E. Panels, S.G. Yan, J. Power Sources 154 (2007) 162–171.
[19] H. Yamada, T. Hatanaka, H. Murata, Y. Morimoto, J. Electrochem. Soc. 153 (2006) A1748–A1754.

# Mesostructured Thin Films as Electrocatalysts with Tunable Composition and Surface Morphology

Dennis F. van der Vliet[1,+], Chao Wang[1,+], Dusan Tripkovic[1], Dusan Strmcnik[1], Xiao Feng Zhang[2], Mark K. Debe[3], Radoslav T. Atanasoski[3], Nenad M. Markovic[1] and Vojislav R. Stamenkovic[1*]

[1] Materials Science Division, Argonne National Laboratory, Argonne, IL, 60439, USA

[2] Hitachi High Technologies America Inc., Pleasanton, CA 94588, USA

[3] Fuel Cell Components Program, 3M Co., St. Paul, MN, 55144, USA

**Amongst the most challenging issues in technologies for electrochemical energy conversion are the insufficient activity of the catalysts for the oxygen reduction reaction (ORR), catalyst degradation, and carbon support corrosion. In an effort to address these barriers, we aimed towards carbon-free multi/bi-metallic materials in the form of mesostructured thin films with tailored physical properties. We present here a new class of metallic materials with tunable near-surface composition, morphology and structure that have led to greatly improved affinity for the electrochemical reduction of oxygen. The level of activity for the ORR established on mesostructured thin film catalysts exceeds the highest value reported for bulk polycrystalline Pt bimetallic alloys, and is 20-fold more active than the current state-of-the-art Pt/C nanoscale catalyst.**

Over the last decades, extensive research has been devoted to develop technologies that can effectively convert energy and become economically viable for use by the general public. Great expectations are held for technologies such as fuel cells and lithium-air batteries that rely on electrochemical processes. In both cases, satisfactory energy density can be attained; however, a major challenge lies in the insufficient activity and durability of materials that are currently employed as cathode catalysts for electrochemical

[+] The authors that have equally contributed to the accomplished work

[*] Corresponding Author: vrstamenkovic@anl.gov

reduction of oxygen. These limitations inevitably lead to a lower operating efficiency of the devices, which highlights the need for development of more active and durable oxygen reduction reaction (ORR) catalysts. [1-12] In the case of fuel cells, most of the research centers on platinum, the best monometallic catalyst for the ORR. At the present state of development, an approximately fivefold reduction in Pt content is necessary to meet cost requirements for large scale automotive applications. [5] Pt-based alloys have already made an impact in fuel cell catalyst design by decreasing the amount of platinum while improving activity and durability [12-18], which places these materials at the focus of intensive fundamental and applied research on both extended (bulk)[17-25] and nanoscale systems. [7,14-16,26-34] The main challenge in that effort is linked to the possibility of achieving the unique structural and compositional profile of the $Pt_3Ni(111)$ alloy, which was established from single crystal studies. [12,17] Such a profile was obtained on extended surfaces by thermal annealing that facilitates thermodynamically driven segregation of Pt to form a pure ordered surface layer, denoted as Pt(111)-Skin. The electronic structure of Pt(111)-Skin is altered by the subsurface layer of PtNi (in 1:1 ratio) and is responsible for the extreme ORR activity, which is nearly two orders of magnitude higher than the state-of-the-art Pt/C catalyst. Consequently, the ability to mimic the compositional profile and structure of Pt-Skin in high surface area catalysts would bring unprecedented benefits to technologies that rely on the ORR. However, despite numerous attempts, this goal has not been achieved yet for practical catalysts.

Here we present a new class of catalysts based on mesostructured multimetallic thin films with adjustable structure and composition, which have been tailored to emulate the distinctive properties of the Pt(111)-Skin, to be employed in electrochemical devices. The design of these materials relied on our previous work related to well-defined extended and nanoscale surfaces in the form of PtM alloys (M = Ni, Co, Fe, V, Ti). [17-20] We aimed towards catalysts that can bridge the world of extended surfaces with superior activity and nanoscale systems with high specific surface area, in order to harvest maximal utilization of precious metals. Such synergy is foreseen to be present at the mesoscale, which does not only imply a specific length scale, but rather a principle of operating “in between” different physical regimes that exhibit

distinct functional behavior. [35] Considering that mesoscale materials chemistry is still in its infancy, it is expected that this field will open novel pathways in materials design that arise from the rational control of physicochemical properties and functionality of mesostructured systems. In particular, for electrocatalytic systems most prior work has emphasized either achievement of high surface area through small particle size, or the attainment of better understanding of fundamental properties through the use of extended surfaces. From such studies, it is well known that there are substantial differences in catalytic properties between nanoscale and bulk materials. The benefits of targeting "mesoscale" architectures between these extremes have scarcely been explored, especially in the sense of transferring superior characteristics from extended surfaces to practical materials. In view of that, instead of using discrete nanoparticles (3-5 nm) supported on high surface area carbon [26-28,32-34,36], we deployed continuous Pt and Pt-alloy nanostructured thin films (NSTF) [29,37-41] over an oriented array of molecular solid whiskers by physical vapor deposition. Specifically, planar magnetron sputter deposition was used to deposit thin metal films of Pt alloys with a wide range in composition. Such NSTF catalysts provide good surface area utilization and eliminate issues related to carbon support corrosion and contact resistance at the carbon-metal interface that would lead to poor utilization and degradation of the catalyst. [14] The capability to control the deposition rate, as well as the combination and order of constituents signifies sputter deposition as an effective tool to form thin films with desirable thickness, composition profile and surface roughness. However, the surface structure of a thin film, an important catalytic parameter, [33,42-44] cannot be altered by this method to match those established on single crystalline systems. For that reason, we attempted a thorough examination of thin film properties on extended, flat, non-crystalline and chemically inert substrates such as a mirror polished glassy carbon surface. This approach brings an additional level of control in terms of defined geometric surface area and surface roughness factor that is unattainable in the case of nanoscale substrates. Consequently, our efforts have been directed toward exploring structural transitions in polycrystalline thin films.

The first step comprised the deposition of a pure Pt thin film onto an ultra-high vacuum (UHV) cleaned glassy carbon substrate, which was followed by thermal annealing in reductive atmosphere (see

Methodology). The morphology of the Pt film was validated by scanning tunneling microscopy (STM) as shown in Figure 1A and B. The difference between as-deposited versus annealed Pt films indicates substantial change in thin film surface morphology due to rearrangement of the Pt topmost atoms towards the (111) structure with minimum surface energy. The as-deposited Pt film has corrugated nanostructured three dimensional surface morphology with an average grain size of ~5 nm, while morphology of the annealed thin film has been transformed into a smooth two dimensional surface with large 20x100 nm (111) facets. In accordance with STM results, the characteristic surface features are also confirmed by electrochemical cyclic voltammetry (CV). Figure 1A reveals that the CV of the as-deposited thin film surface matches the one established for bulk polycrystalline Pt. On the other hand, Figure 1B shows that the CV of the annealed Pt thin film underwent extensive transformation from typical polycrystalline into Pt(111)-like with characteristic fingerprint features between 0.5 and 0.9 V; the so called butterfly region that corresponds to adsorption/desorption processes of $OH_{ad}$ on Pt(111) facets (see Supplemental Information). Therefore, it is evident from both STM and CV that the annealed extended thin film consists of predominantly (111) facets encompassing the entire surface. In fact, the degree of resemblance in electrochemical signature between the annealed thin film surface and single crystal Pt confirms that the (111) facets are both large and interconnected. The synergy between the surface structure, domain size and functionality, defines that the thin film surface has a distinct mesostructred morphology. These findings clearly demonstrate the feasibility of controlling surface ordering of extended Pt thin films deposited over a non-crystalline substrate, i.e., without use of templates for epitaxial growth. Instead of building the crystal lattice from a seed or underlying crystalline substrate, individual randomly oriented nanoscale grains coalesce and form large well-ordered (111) facets. All of that greatly expands the potential for utilization of thin film materials and introduces thermal annealing in controlled atmosphere as a compelling tool in the fine tuning of a thin film's structure and hence electrocatalytic properties.

In the following steps we proceed towards a bimetallic PtNi thin film with the same thickness in order to mimic the composition profile of the $Pt_3Ni(111)$ system and to replicate its unique catalytic

properties. The results from electrochemical measurements in Figure 1C and D confirm that similar to monometallic Pt, the polycrystalline nature of the as-deposited alloy thin film is predominantly transformed into a Pt(111)-Skin like surface. This is obvious from both the cyclic voltammetry of the annealed alloy thin film that resembles the one obtained on $Pt_3Ni(111)$ and its superior catalytic activity for the ORR, which was up to now obtained exclusively on the $Pt_3Ni(111)$-Skin surface. [17,45] The combination of Pt(111)-Skin like voltammetry and dramatic increase in the ORR activity proves that surface ordering from randomly oriented towards (111) is indeed feasible for bimetallic thin films, and demonstrates that the catalytic improvement obeys the same mechanism as previously reported for Pt-bimetallic single crystal surfaces, i.e., electronic modification of the topmost Pt layer leads to extreme catalytic enhancement solely for (111) orientation. [19] Therefore, the ORR specific activity which equals 70% of the value established for the most active catalyst, $Pt_3Ni(111)$-Skin, serves as a descriptor that (111)-Skin facets are dominating on the annealed thin film surface. Together this demonstrates the two-fold power of annealing in facilitating the formation of the mesostructured alloy thin film morphology, characterized by both an energetically more favorable surface state rich in (111) facets, and the desired compositional profile.

It is these results that provide the driving force for ashift towards corresponding thin-film based high surface area materials. A Pt-alloy NSTF catalyst is deposited by magnetron sputtering over an array of molecular solid whiskers, composed of an organic pigment N,N-di(3,5-xylyl)perylene-3,4:9,10 bis(dicarboximide); hereafter denoted as perylene red. [29,37-39,46] Figure 2 illustrates the step by step deposition process of the thin metal films onto the perylene red support, as well as high resolution- scanning electron microscopy (HRSEM) and transmission electron microscopy (TEM) micrographs of the NSTF whiskers. These images reveal a detailed insight into critical parameters of the NSTF such as metallic film thickness, length, shape, and surface morphology. A single whisker measures on average about 800 nm in length, while the film thickness is 5-20 nm. In Figure 2, it is clearly visible that on the sides of a single whisker, smaller metal alloy whiskerettes are formed with a diameter of ~5 nm (Figure 2C), while a close up of a broken whisker (Figure 2B) illustrates the metallic film/shell that surrounds the perylene red substrate.

Surface specific HRSEM in Figure 2B and D unveils that the side walls along the whisker have a very rough surface morphology, consisting mainly of whiskerette tips bonded closely to each other to produce densely packed corncob-like features, providing the validity of terming this material a nanostructured thin film. It is important to emphasize that the highly grained texture of the NSTF side walls made of closely packed whiskerettes is also confirmed in the TEM micrograph in Figure 2E. Such structural parameters greatly affect the functional properties of the NSTF, and therefore the ability to control and tune them along with the near-surface compositional profile can lead towards substantial gain in catalytic performance.

In what follows, we apply an experimental approach combined with the knowledge related to highly active well-defined single crystalline and extended thin film surfaces in order to develop mesostructured thin film electrocatalysts with advanced properties. In-situ high resolution- SEM and TEM are simultaneously employed during NSTF annealing in controlled atmosphere. This allows us to visualize real-time structural changes at atomic level and to follow rearrangements of the surface and sub-surface morphology of thin film materials. Such insight is invaluable in the fine tuning of the materials' properties. Figure 3 depicts in-situ results obtained during thermal annealing of a single PtNi-NSTF whisker. The NSTF catalyst is mounted onto the HRTEM heating stage and introduced to a reductive atmosphere of argon and hydrogen gasses. As the specimen is gradually heated, no change in surface morphology is observed as depicted in Figure 3A-A', which reveals the initial stage and a close up of the grained highly corrugated whisker side wall and its surface. Once the temperature reaches 300$^{o}$C, we start to follow real-time restructuring of the thin film's morphology. Figure 3B-B' captures the onset of the surface transformation, which appears as a smoothening of the near surface regions. The steady state structure is achieved after 30 minutes and is shown in Figure 3C-C'. These images illustrate that the densely packed organization with the initial three dimensional surface morphology is being transformed into a more homogeneous, flat and ordered two dimensional thin film material with clearly observable crystalline features in its walls. This thermodynamically driven transition releases stress and strain of the as-deposited thin film and leads towards the state with minimum surface energy without compromising the overall shape and dimension of

the whisker. Similarly to Pt thin films on glassy carbon, the initial nanostructured surface morphology that originated from the closely bonded whiskerettes' tips is transformed into a smooth continuous film with large crystalline domains (20-40 nm). Specifically, randomly oriented nanoscale grains coalesce and give rise to a mesostructured thin film with unique physicochemical properties, therefore, the materials after this treatment will be referred to as mesostructured thin films (Meso-TF). Close inspection of HRTEM micrographs after applied thermal treatment (see Supplemental Information) confirms that emerged facets with (111) structure prevail on the surface while undercoordinated sites are diminished, which also has important implications towards improved stability. As a side-effect, the perylene red substrate is removed during this procedure (details can be found in the Supplemental Information). In addition to HRTEM/SEM studies, X-ray diffraction measurements are presented in the SI, which show enhanced alloying and an increase of (111) oriented domains on the Meso-TF.

The final step in the characterization is to obtain the electrochemical signature and compare adsorption and catalytic properties between different classes of thin film materials and state-of-the-art Pt/C catalyst by rotating disk electrode (RDE), see Methods section. Expectedly, from the cyclic voltammetry depicted in Figure 4 we find that the smooth morphology of the Meso-TF slightly lowers the electrochemically active surface area (ECSA), from ~11 $m^2/g$ for the NSTF to ~9 $m^2\ g_{Pt}^{-1}$ for the Meso-TF. This implies that most of the inner portion of the whiskers, which has been vacated by the perylene red, is not electrochemically active, presumably due to lack of penetration of the electrolyte into the hollow of the whisker (see closed whisker end in Figure 3). As shown in Figure 4A, the CV of PtNi NSTF whiskers exhibits similar behavior to monometallic Pt NSTF with clearly visible polycrystalline Pt-poly features due to the adsorption-desorption processes of underpotentially desposited hydrogen ($H_{upd}$). However, the $H_{upd}$ region of PtNi Meso-TF is significantly different with a characteristic flat plateau (Figure 4A), which confirms that the surface has a relatively large contribution of (111) facets compared to the highly corrugated sputtered thin film that is rich in low-coordinated Pt sites. This is also in good agreement with HRTEM and XRD results . Moreover, the onset of surface oxide formation is shifted positively in the following order: Pt-NSTF < PtNi-

NSTF < PtNi Meso-TF. Accordingly, the ORR polarization curves, shown in Figure 4B, follow the same trend in activity. Figure 4C and D summarize kinetic current densities (specific activities per electrochemically active surface area of Pt) as Tafel plots and bar graph, respectively. Since specific activity is a fundamental property of a material that reflects its intrinsic catalytic performance, as opposed to mass activity which emphasizes the optimized dispersion of a material, our focus has been placed on boosting specific activity. This approach leads to a higher turnover frequency (the measure of activity per active site), which may result in better utilization of Pt, culminating in higher mass activity. Considering the large increase in specific activity, we report values measured at 0.95 V to avoid diffusion-induced errors in kinetic current densities. The order of specific activity becomes apparent, with Pt/C being the least active, followed by Pt-NSTF and polycrystalline Pt. One can observe a significant increase in activity for PtNi Meso-TF, accompanied by a decrease in Tafel slope from ~70 mV/dec for monometallic Pt to ~40 mV/dec. This value is considerably lower than those commonly reported for Pt based catalysts in the literature [19,47], but it is in line with the value obtained on $Pt_3Ni(111)$-Skin. [47] The activity of PtNi Meso-TF exhibits an improvement factor of over 8 versus Pt-poly and Pt-NSTF. Additionally, when compared to the state-of-the-art conventional Pt/C catalyst, the specific activity of the PtNi Meso-TF achieves an unprecedented 20-fold enhancement. Even though optimal film thickness, alloy composition and total Pt loading will be extensively studied in the future, the measured improvement expressed in $A/mg_{Pt}$ corresponds to a mass activity that is already three times higher than the U. S. Department of Energy technical target. [12] Together the flat voltammetric curves, the trend in specific activity, the low Tafel slope, and the structural characterizations strongly suggest that the annealed PtNi Meso-TF has a Pt-Skin type near-surface structure.

In order to review findings on thin film based mesostructured catalysts and to merge them into the same chart with nanoscale systems and bulk materials, we present in Figure 5 the ORR activity map for different classes of Pt alloys, *i.e.*, from nanoparticles dispersed on high surface area carbon, to polycrystalline bulk materials and to single crystalline alloys of $Pt_3Ni(hkl)$ surfaces. [19] This map shows a huge span in intrinsic specific activities among materials of the same bulk elemental composition which differ in form and

surface structure. It also demonstrates the importance of controlling fundamental properties that determine catalytic performance; specifically that the ability to alter physical parameters such as particle size, near-surface composition profile, morphology and surface structure can lead to great improvements in functional properties of real catalysts. Notably, we have explored a number of nanostructured thin film catalysts with different composition as summarized in Figure 5; however, for the sake of brevity in this report we have presented only the results for the PtNi in detail. The activity values are given for Pt alloys with different transition metals associated with the atomic number (*Z*). The main features in Figure 5 are designated activity regions for different classes of materials. Metallic nanoparticles (NP) of Pt and Pt alloys dispersed on a high surface area carbon support exhibit profoundly lower activities compared to their polycrystalline bulk counterparts. The assigned region which reflects the activity range of metallic NPs is based on the literature data reported for Pt-alloys obtained by conventional impregnation methods. The next level in activity is reserved for extended bulk polycrystalline systems, where the specific activity of $Pt_3M$-alloys can be improved by a factor of three versus Pt-poly. As mentioned above, the capability to control the surface structure leads to an additional boost in activity, and hence the highest ORR activity ever measured was obtained for the $Pt_3Ni(111)$-Skin surface. Based on the values depicted in Figure 5, the nanostructured thin film catalysts can successfully mimic catalytic behavior of polycrystalline bulk materials, while Pt-alloy mesostructured thin films exceed the range designated for polycrystalline systems. This is the first practical catalyst to approach the levels of activity previously reserved only for bulk single crystalline surfaces, due to the formation of a surface and near-surface structure similar to that of ideal $Pt_3Ni(111)$-Skin. These bimetallic Meso-TF materials preserve sufficiently high specific surface area, which enables better utilization of precious metals. Moreover, Pt-based catalysts with mesoscale features additionally avoid the activity losses that are caused by the higher fraction of low-coordinated surface atoms that are present in nanoscale catalysts. [14] Consequently, thin film electrocatalysts are neither hampered by the stability issues that accompany the use of high surface area carbon support, nor by the loss of active surface area due to particle agglomeration. The mesostructured thin films, therefore, unite the beneficial properties of both the

nanoscale and the extended bulk systems, and lead to new design rules for producing highly active and durable electrocatalysts. These findings provide a proof of concept that the ability to tailor composition, morphology and structure of the thin-film based materials at mesoscale allows the harvesting of maximal performance from employed constituents. This is a seeding study on mesoscale ordering in electrocatalysts where further advancement towards an increased presence of (111) facets and optimization of the thin film thickness may lead to additional improvements in specific and mass activities.

In summary, we report on a new class of mesostructured catalysts based on thin films with adjustable composition profile and surface morphology. These materials are in the form of metallic thin films with properties that have been tailored to improve activity for the oxygen reduction reaction. The obtained ORR activity is the highest ever measured on non-bulk catalysts owing to the beneficial near-surface compositional profile and its highly crystalline surface morphology. The exceptional properties of this Meso-TF are comparable to extended single crystalline surfaces and improvement factors in kinetic activity of 8 versus polycrystalline Pt and 20 versus Pt/C are observed. The substantial advances in catalytic performance are obtained through structural mesoscale ordering of the thin film induced by thermal annealing in reductive atmosphere. The approach as developed can be applied to generate a wide range of (electro)catalysts with tailored structure/composition, ultra-low precious metal content and superior functional properties such as activity and durability.

# Methods

**THIN FILM DEPOSITION**

Thin metal films were deposited by planar magnetron sputter deposition method on the UHV cleaned surface of a mirror polished glassy carbon substrate with 6 mm in diameter (base vacuum $1\times10^{-10}$ Torr). The deposition rate was set to (0.3 Å/sec) by quartz crystal microbalance and an exposure of 7 s was calibrated for the nominal thickness of 2.2 ~ 2.3 Å for a monolayer of Pt. The film thickness was derived from the exposure time of computer

controlled shutters during deposition. The thickness of all thin films in this study was 20 nm. In the case of nanostructured thin film catalysts consecutive layers of platinum and metal of choice were deposited onto the NSTF layer of oriented organic pigment (*N*,*N*-di(3,5-xylyl)perylene-3,4:9,10bis(dicarboximide), perylene red) whiskers also by planar magnetron sputter deposition method in vacuum. [48] The deposition process covered each of the perylene red whiskers with a thin metallic film. Both the monometallic Pt and the Pt-alloy catalyst were obtained by this method. The Meso-TF were obtained by thermal annealing of NSTF at 400$^{o}$C in a hydrogen rich atmosphere. The temperature was increased in 20$^{o}$C/5 min increments and the whole process lasted two hours.

**ELECTROCHEMICAL MEASUREMENTS**

Autolab PGSTAT 30 with FI20, ECD, ADC and SCAN GEN modules was used for the electrochemical measurements. Perchloric acid diluted with MilliQ water to 0.1M was in all cases the electrolyte. Used gases were research grade (5N5+) argon and oxygen. In all experiments, a silver-silver chloride was reference electrode. However, all potentials referred to in this paper are converted to the pH independent reversible hydrogen electrode scale. We repeated all experiments 8 times to confirm reproducibility, and to improve accuracy in the determination of kinetic activities. Kinetic current densities were obtained from the measured ORR polarization curves in accordance to the Koutecky-Levich equation: $I_{ORR}^{-1} = I_{kinetic}^{-1} + I_{diffusion}^{-1}$. The electrochemically active surface area of the nanocatalysts was determined by integrating both the $H_{upd}$ part of the CV, and polarization curve obtained by oxidation of a monolayer of adsorbed carbon monoxide in order to avoid underestimation of the surface area due to altered hydrogen adsorption properties. All catalysts were deposited on RDE made of glassy carbon and the loading of the nanoscale thin film catalysts was adjusted to be 60 $\mu g_{Pt}/cm^2_{disk}$, while the loading for Pt/C obtained from TKK was 12 $\mu g_{Pt}/cm^2_{disk}$. Kinetic current densities as reported are in all cases normalized by electrochemically active surface area.

**MICROSCOPY**

A Hitachi H-9500 environmental transmission electron microscope operated at 300 kV was used to perform microstructural characterization and in situ heating TEM study. Powder samples were attached to the heating zone of a Hitachi gas injection-heating holder. Images of nanoparticles were first recorded at room temperature, followed by heating of the specimen inside the microscope chamber with a vacuum level of about $10^{-4}$ Pa. A CCD (charged-couple device) camera was used to monitor the microstructural evolution and record images and videos. Each heating temperature was held for at least 10 minutes for detailed structural characterization, including morphology and atomic structure. A Hitachi SU70 high resolution field-emission SEM was used for routine nanoparticle sample inspection. For the detailed surface morphology study at nanometer scale, a Hitachi S-5500 ultrahigh resolution cold field-emission SEM delivered a much higher resolution power (0.4 nm secondary electron image resolution at 30 kV) than normal SEM because of the specially designed objective lens. On both SU70 and S-5500, secondary electron images were taken at 15 kV or 30 kV to reveal the surface morphology of both the as-deposited, as well as the annealed nanoparticles.

**REFERENCES**


1 Borup, R. *et al.* Scientific aspects of polymer electrolyte fuel cell durability and degradation. *Chem. Rev.* **107**, 3904-3951 (2007).

2 Wagner, F. T., Lakshmanan, B. & Mathias, M. F. Electrochemistry and the Future of the Automobile. *J. Phys. Chem. Lett.* **1**, 2204-2219 (2010).

3 Adzic, R. R. *et al.* Platinum monolayer fuel cell electrocatalysts. *Top. Catal.* **46**, 249-262 (2007).

4 Bruce, P. G., Freunberger, S. A., Hardwick, L. J. & Tarascon, J. M. Li-O-2 and Li-S batteries with high energy storage. *Nat. Mater.* **11**, 19-29 (2012).

5 Gasteiger, H. A., Kocha, S. S., Sompalli, B. & Wagner, F. T. Activity benchmarks and requirements for Pt, Pt-alloy, and non-Pt oxygen reduction catalysts for PEMFCs. *Applied Catalysis B-Environmental* **56**, 9-35 (2005).

6 Arico, A. S., Bruce, P., Scrosati, B., Tarascon, J. M. & Van Schalkwijk, W. Nanostructured materials for advanced energy conversion and storage devices. *Nat. Mater.* **4**, 366-377 (2005).

7 Strasser, P. *et al.* Lattice-strain control of the activity in dealloyed core-shell fuel cell catalysts. *Nature Chem.* **2**, 454-460 (2010).

8 Greeley, J. *et al.* Alloys of platinum and early transition metals as oxygen reduction electrocatalysts. *Nature Chem.* **1**, 552-556 (2009).

9 Zhang, J., Sasaki, K., Sutter, E. & Adzic, R. R. Stabilization of platinum oxygen-reduction electrocatalysts using gold clusters. *Science* **315**, 220-222 (2007).

10 Nilekar, A. *et al.* Bimetallic and Ternary Alloys for Improved Oxygen Reduction Catalysis. *Top. Catal.* **46**, 276-284 (2007).
11 Gorlin, Y. & Jaramillo, T. F. A Bifunctional Nonprecious Metal Catalyst for Oxygen Reduction and Water Oxidation. *J. Am. Chem. Soc.* **132**, 13612-13614 (2010).
12 Debe, M. K. Electrocatalyst approaches and challenges for automotive fuel cells. *Nature* **486**, 43-51 (2012).
13 Snyder, J., Fujita, T., Chen, M. W. & Erlebacher, J. Oxygen reduction in nanoporous metal-ionic liquid composite electrocatalysts. *Nat. Mater.* **9**, 904-907 (2010).
14 Wang, C. *et al.* Design and Synthesis of Bimetallic Electrocatalyst with Multilayered Pt-Skin Surfaces. *J. Am. Chem. Soc.* **133**, 14396-14403 (2011).
15 Wang, C. *et al.* Multimetallic Au/$FePt_3$ Nanoparticles as Highly Durable Electrocatalyst. *Nano Lett.* **11**, 919-926 (2010).
16 Ferreira, P. J. *et al.* Instability of Pt/C electrocatalysts in proton exchange membrane fuel cells - A mechanistic investigation. *J. Electrochem. Soc.* **152**, A2256-A2271 (2005).
17 Stamenkovic, V. R. *et al.* Improved oxygen reduction activity on $Pt_3Ni(111)$ via increased surface site availability. *Science* **315**, 493-497 (2007).
18 Stamenkovic, V. R. *et al.* Trends in electrocatalysis on extended and nanoscale Pt-bimetallic alloy surfaces. *Nat. Mater.* **6**, 241-247 (2007).
19 Stamenkovic, V., Schmidt, T. J., Ross, P. N. & Markovic, N. M. Surface composition effects in electrocatalysis: Kinetics of oxygen reduction on well-defined $Pt_3Ni$ and $Pt_3Co$ alloy surfaces. *J. Phys. Chem. B* **106**, 11970-11979 (2002).
20 Stamenkovic, V. R., Mun, B. S., Mayrhofer, K. J. J., Ross, P. N. & Markovic, N. M. Effect of surface composition on electronic structure, stability, and electrocatalytic properties of Pt-transition metal alloys: Pt-skin versus Pt-skeleton surfaces. *J. Am. Chem. Soc.* **128**, 8813-8819 (2006).
21 Koh, S. & Strasser, P. Electrocatalysis on bimetallic surfaces: Modifying catalytic reactivity for oxygen reduction by voltammetric surface dealloying. *J. Am. Chem. Soc.* **129**, 12624-12625 (2007).
22 Zhang, J. L., Vukmirovic, M. B., Xu, Y., Mavrikakis, M. & Adzic, R. R. Controlling the catalytic activity of platinum-monolayer electrocatalysts for oxygen reduction with different substrates. *Angew Chem Int Edit* **44**, 2132-2135 (2005).
23 Mukerjee, S. & Srinivasan, S. Enhanced Electrocatalysis of Oxygen Reduction on Platinum Alloys in Proton-Exchange Membrane Fuel-Cells. *J. Electroanal. Chem.* **357**, 201-224 (1993).
24 Toda, T., Igarashi, H., Uchida, H. & Watanabe, M. Enhancement of the electroreduction of oxygen on Pt alloys with Fe, Ni, and Co. *J. Electrochem. Soc.* **146**, 3750-3756 (1999).
25 Mavrikakis, M. Computational methods: A search engine for catalysts. *Nat. Mater.* **5**, 847-848 (2006).
26 Mani, P., Srivastava, R. & Strasser, P. Dealloyed Pt-Cu core-shell nanoparticle electrocatalysts for use in PEM fuel cell cathodes. *J. Phys. Chem. C* **112**, 2770-2778 (2008).
27 Wang, C. *et al.* Monodisperse $Pt_3Co$ Nanoparticles as a Catalyst for the Oxygen Reduction Reaction: Size-Dependent Activity. *J. Phys. Chem. C* **113**, 19365-19368 (2009).
28 Wang, C. *et al.* Monodisperse $Pt_3Co$ nanoparticles as electrocatalyst: the effects of particle size and pretreatment on electrocatalytic reduction of oxygen. *Phys. Chem. Chem. Phys.* **12**, 6933-6939 (2010).
29 van der Vliet, D. *et al.* Platinum-alloy nanostructured thin film catalysts for the oxygen reduction reaction. *Electrochim. Acta* **56**, 8695-8699 (2011).
30 Zeis, R., Mathur, A., Fritz, G., Lee, J. & Erlebacher, J. Platinum-plated nanoporous gold: An efficient, low Pt loading electrocatalyst for PEM fuel cells. *J. Power Sources* **165**, 65-72 (2007).

31 Habas, S. E., Lee, H., Radmilovic, V., Somorjai, G. A. & Yang, P. Shaping binary metal nanocrystals through epitaxial seeded growth. *Nat. Mater.* **6**, 692-697 (2007).
32 Tao, F. *et al.* Reaction-Driven Restructuring of Rh-Pd and Pt-Pd Core-Shell Nanoparticles. *Science* **322**, 932-934 (2008).
33 Inaba, M. *et al.* Controlled growth and shape formation of platinum nanoparticles and their electrochemical properties. *Electrochim. Acta* **52**, 1632-1638 (2006).
34 Paulus, U. A. *et al.* Oxygen reduction on carbon-supported Pt-Ni and Pt-Co alloy catalysts. *J. Phys. Chem. B* **106**, 4181-4191 (2002).
35 Antonietti, M. & Ozin, G. A. Promises and problems of mesoscale materials chemistry or why meso? *Chem. Eur. J.* **10**, 28-41 (2004).
36 Mukerjee, S., Srinivasan, S., Soriaga, M. P. & Mcbreen, J. Role of Structural and Electronic-Properties of Pt and Pt Alloys on Electrocatalysis of Oxygen Reduction - an in-Situ Xanes and Exafs Investigation. *J. Electrochem. Soc.* **142**, 1409-1422 (1995).
37 Debe, M. K. & Drube, A. R. Structural Characteristics of a Uniquely Nanostructured Organic Thin-Film. *Journal of Vacuum Science & Technology B* **13**, 1236-1241 (1995).
38 Debe, M. K. & Poirier, R. J. Postdeposition Growth of a Uniquely Nanostructured Organic Film by Vacuum Annealing. *Journal of Vacuum Science & Technology a-Vacuum Surfaces and Films* **12**, 2017-2022 (1994).
39 Debe, M. K., Schmoeckel, A. K., Vernstrom, G. D. & Atanasoski, R. High voltage stability of nanostructured thin film catalysts for PEM fuel cells. *J. Power Sources* **161**, 1002-1011 (2006).
40 Debe, M. K. in *Handbook of Fuel Cells – Fundamentals, Technology and Applications* (eds W. Vielstich, A. Lamm, & H. A. Gasteiger) Ch. 45, (John Wiley & Sons, 2003).
41 Debe, M. K. *et al.* Extraordinary Oxygen Reduction Activity of $Pt_3Ni_7$. *J. Electrochem. Soc.* **158**, B910-B918 (2011).
42 Somorjai, G. A. Surface Science and Catalysis. *Science* **227**, 902-908 (1985).
43 Tao, A. R., Habas, S. & Yang, P. D. Shape control of colloidal metal nanocrystals. *Small* **4**, 310-325 (2008).
44 Lai, S. C. S. & Koper, M. T. M. The Influence of Surface Structure on Selectivity in the Ethanol Electro-oxidation Reaction on Platinum. *J. Phys. Chem. Lett.* **1**, 1122-1125 (2010).
45 Wadayama, T. *et al.* Oxygen reduction reaction activities of Ni/Pt(111) model catalysts fabricated by molecular beam epitaxy. *Electrochem. Commun.* **12**, 1112-1115 (2010).
46 Gancs, L., Kobayashi, T., Debe, M. K., Atanasoski, R. & Wieckowski, A. Crystallographic characteristics of nanostructured thin-film fuel cell electrocatalysts: A HRTEM study. *Chem. Mater.* **20**, 2444-2454 (2008).
47 Subbaraman, R., Strmcnik, D., Paulikas, A. P., Stamenkovic, V. R. & Markovic, N. M. Oxygen Reduction Reaction at Three-Phase Interfaces. *ChemPhysChem* **11**, 2825-2833 (2010).
48 Debe, M. K. *et al. Nanostructured Thin Film Catalysts for PEM Fuel Cells by Vacuum Web Coating*. (Society of Vacuum Coaters - 50th Annual Technical Conference Proceedings, 2007).

## Acknowledgements

*This work was supported by the U.S. Department of Energy, Office of Science, Office of Basic Energy Sciences, Materials Sciences and Engineering Division, and by the Office of Energy Efficiency and Renewable Energy, Fuel Cell Technologies Program. Argonne National Laboratory is a U.S. Department of Energy Office of Science Laboratory operated by UChicago Argonne, LLC under contract no. DE-AC02-06CH11357*

## Author Contributions

D.F.V., C.W. and V.R.S. designed the experiments. C.W., D.F.V., D.T., D.S., X.F.Z., R.T.A., M.K.D. and V.R.S. carried out the experimental work. D.F.V., C.W., M.K.D., N.M.M. and V.R.S. discussed the results and V.R.S. wrote the manuscript.

## Additional Information

The authors declare no competing financial interests.

# Figure Captions

**Figure 1. Cyclic voltammetry and STM images of Pt and Pt alloy 20 nm thin films deposited on a glassy carbon substrate: (A) as-deposited Pt thin film (solid line) and Pt(111) (dashed line), (B) annealed Pt thin film (solid line) and Pt(111) (dashed line), (C) cyclic voltammetry of as-deposited (blue line), annealed PtNi thin film (red line) and $Pt_3Ni$(111)-Skin (dashed line), (D) specific activities measured by RDE in 0.1 M $HClO_4$ with 1600 rpm, 20 mV/s at 0.95 V with corresponding improvements factors *vs.* polycrystalline Pt.**

**Figure 2. High resolution SEM and TEM micrographs of the NSTF whiskers: (A) HRSEM snapshot of a group of whiskers that indicates their length, shape and alignment after thin film deposition; (B) HRSEM close up of an intentionally broken single whisker that demonstrates the thickness of the metallic film over perylene red substrate; Schematic illustration of the vacuum protocol that has been used for the growth of aligned perylene red substrate, which is then coated by metallic thin film with adjustable thickness and composition profile; (C) HRTEM close up of a single whisker side, which reveals growth of whiskerettes along the whisker; (D) HRSEM insight into the whisker's surface shows a closed packed formation of whiskerette tips with ~5nm in diameter that facilitates highly corrugated morphology. (E) TEM micrograph of a whisker side that confirms the grained texture of the sputtered thin film and the average diameter of the whiskerettes.**

**Figure 3. In-situ transformation from nanostructured into mesostructured thin film during annealing: (A)-(C) HRTEM images of progressive annealing between room temperature and 400$^{o}$C on a single whisker that capture the ordering from randomly oriented to a homogeneous structure with visible crystalline domains; (A')-(C') HRTEM close up of the transformation for the same near surface region during annealing: from highly corrugated into a flat and smooth surface morphology. (1-3$^{o}$) Schematic illustration of the mesoscale ordering during annealing and formation of the mesostructured thin film catalyst, associated with corresponding HRSEM insets.**

**Figure 4. Cyclic voltammetry on the Pt-based thin film catalysts: (A) Cyclic voltammograms of Pt-NSTF, PtNi-NSTF and PtNi-Meso-TF; (B) the ORR polarization curves; and (C) corresponding Tafel plots (Tafel slopes are determined at potentials higher than the half-wave potential ($E_{1/2}$; potential at which I = ½ $I_{diff}$), to avoid diffusion and solution resistance induced errors ). (D) Specific activities measured at 0.95 V and improvement factor versus Pt-Poly (and Pt-NSTF).**

**Figure 5. Activity map for the ORR obtained for different classes of Pt-based materials. Improvement factors are given based on activities compared to the values for polycrystalline Pt and state of the art Pt/C catalyst established by RDE measurements in 0.1 M $HClO_4$ at 0.95 V.**

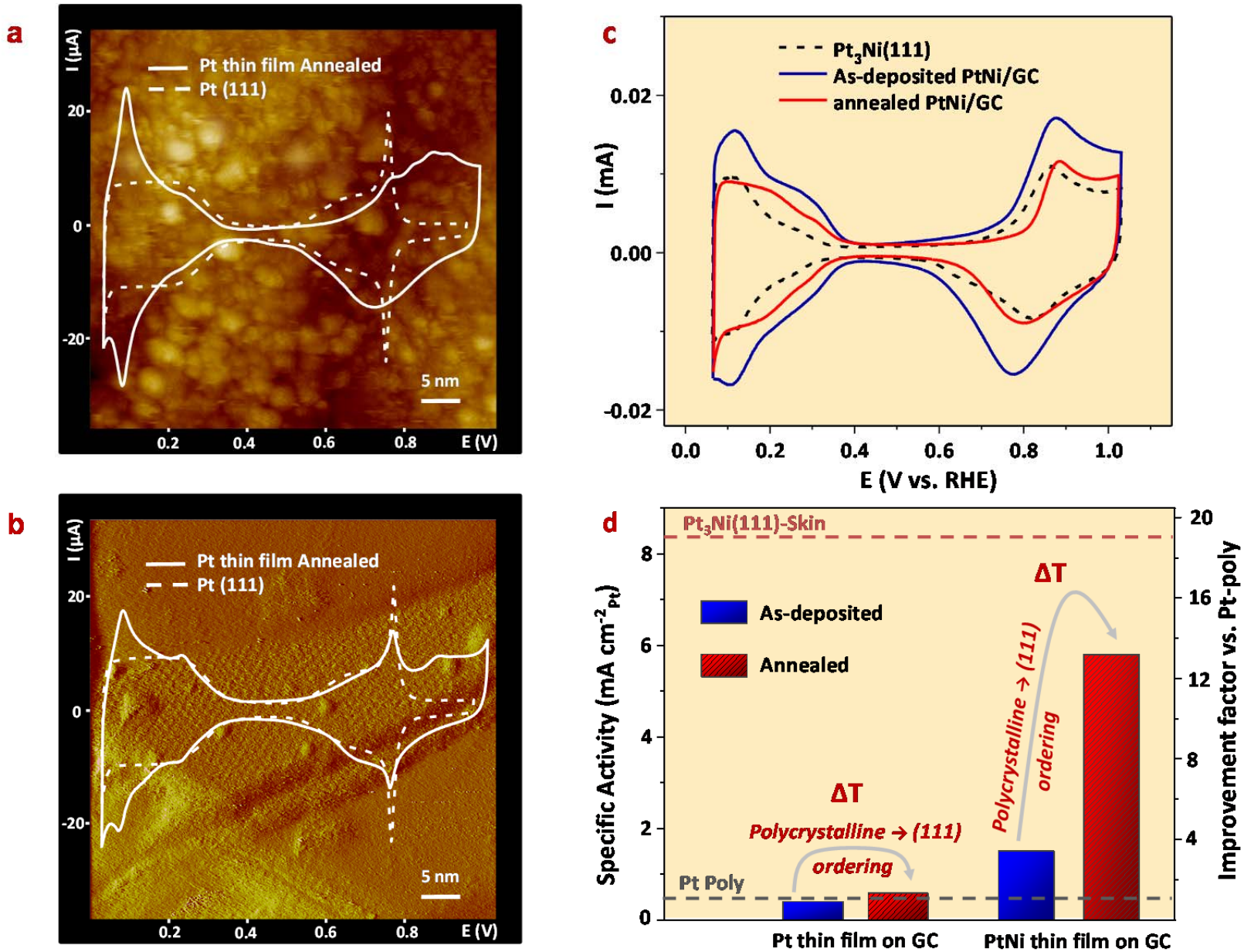


Figure 1. NM12020356

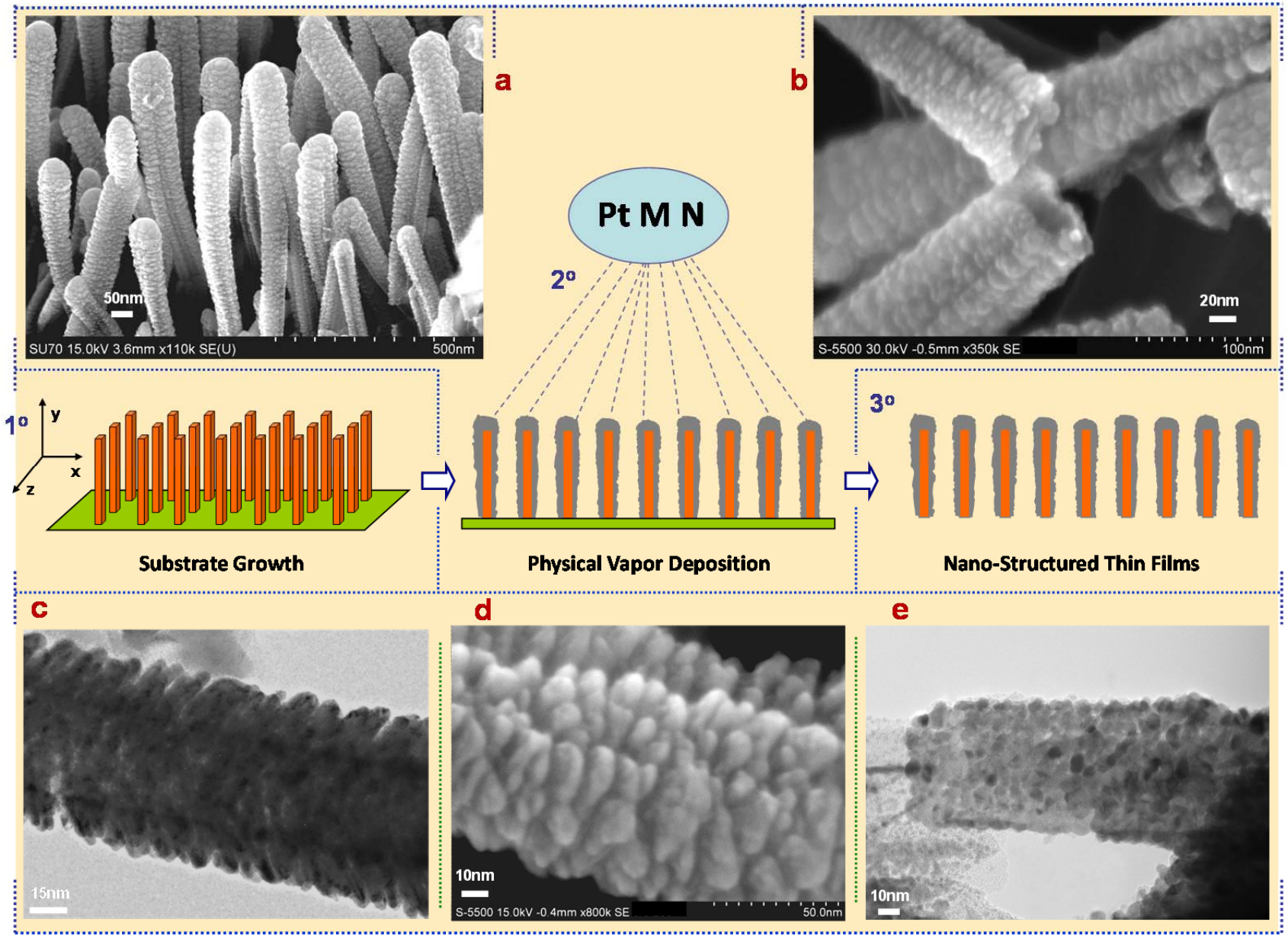


Figure 2. NM12020356

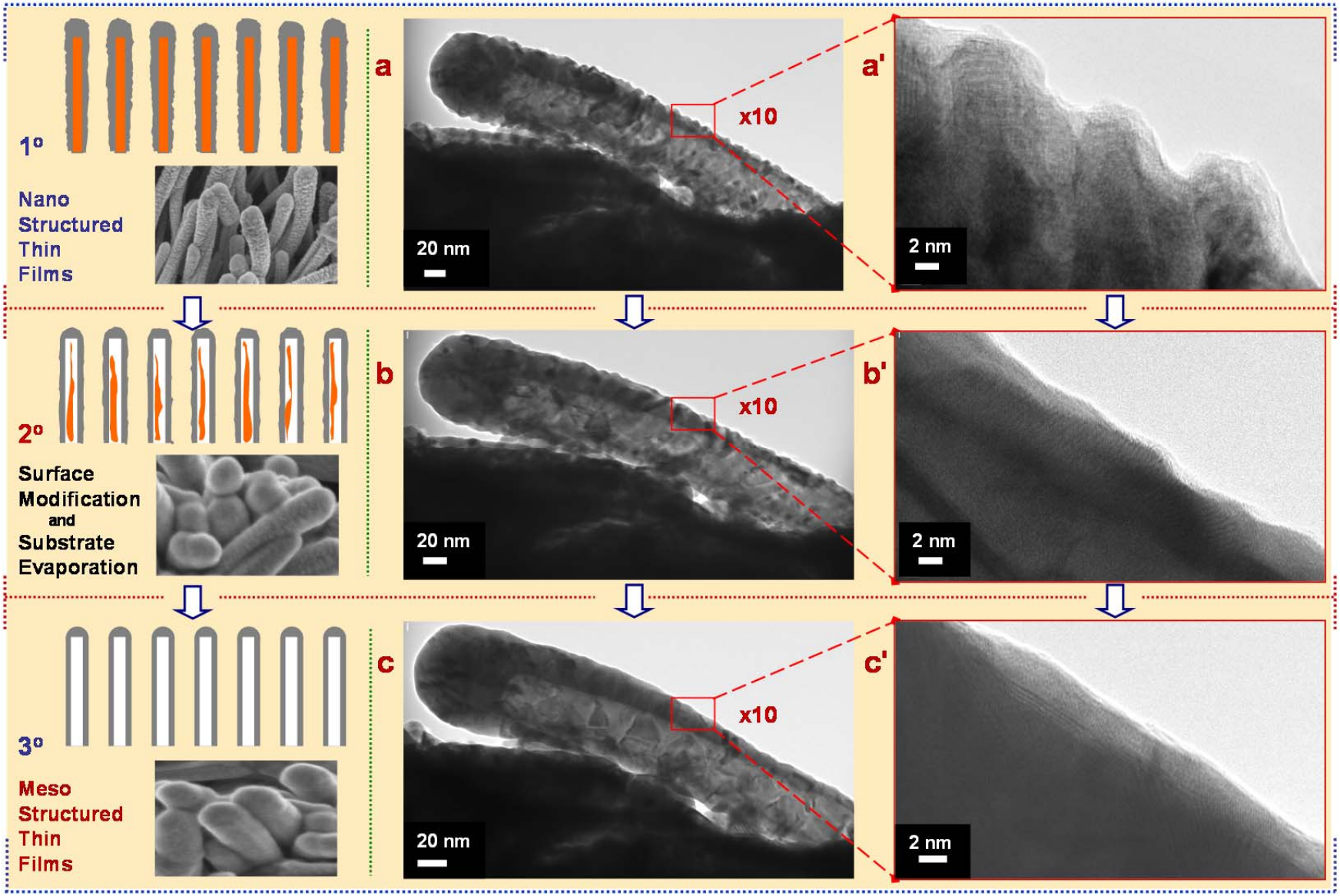


Figure 3. NM12020356

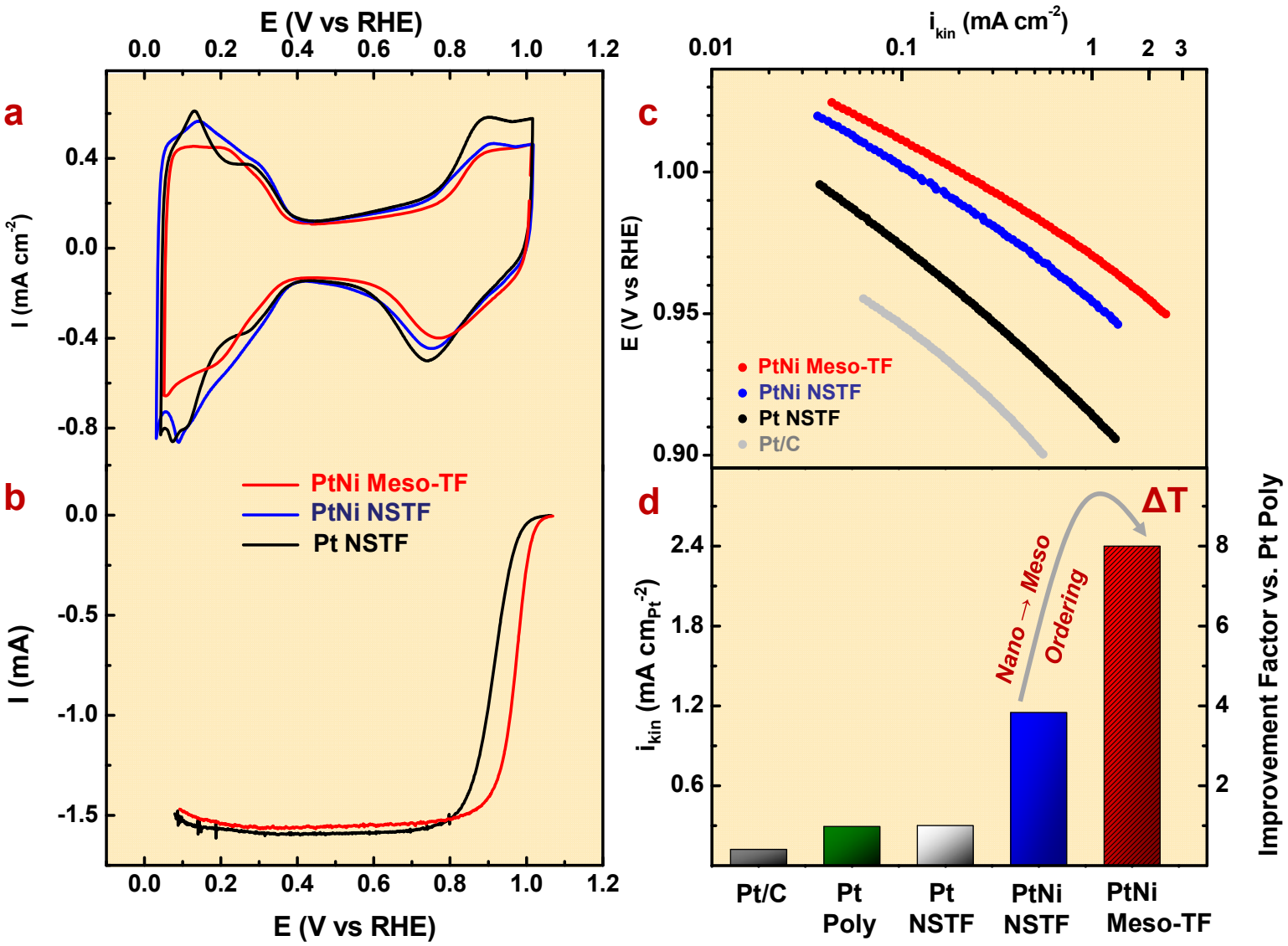


Figure 4. NM12020356

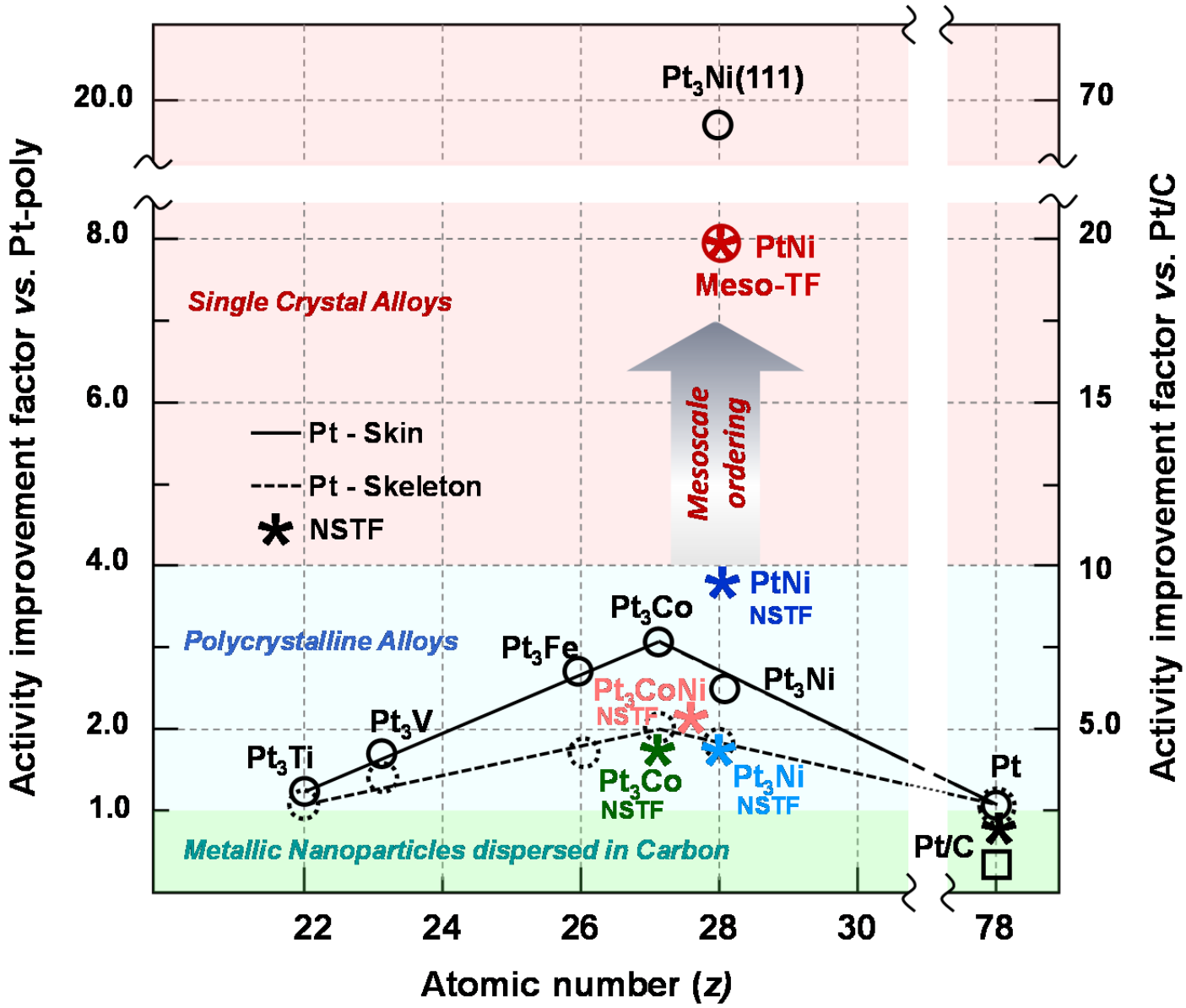


Figure 5. NM12020356

# Mesostructured Thin Films as Electrocatalysts with Tunable Composition and Surface Morphology

Dennis F. van der Vliet[1,+], Chao Wang[1,+], Dusan Tripkovic[1], Dusan Strmcnik[1], Xiao Feng Zhang[2], Mark K. Debe[3], Radoslav T. Atanasoski[3], Nenad M. Markovic[1] and Vojislav R. Stamenkovic[1*]

[1] Materials Science Division, Argonne National Laboratory, Argonne, IL, 60439, USA

[2] Hitachi High Technologies America Inc., Pleasanton, CA 94588, USA

[3] Fuel Cell Components Program, 3M Co., St. Paul, MN, 55144, USA

## Supplemental information

[+] The authors that have equally contributed to the accomplished work

[*] Corresponding Author: vrstamenkovic@anl.gov

## Electrochemical characterization of thin films

In addition to measurements in 0.1 M perchloric acid electrolyte, we evaluated the morphology of thin metal Pt-film on glassy carbon substrate in 0.05 M sulfuric acid electrolyte. Due to the presence of sulfates and their specific adsorption exclusively on Pt(111) facets, the cyclic voltammetries measured before and after annealing represent strong proof of surface restructuring, from highly polycrystalline into (111)-like. The CV of as-deposited film suggests polycrystalline arrangement of the topmost Pt atoms with two sharp $H_{upd}$ peaks that originate from (110) and (100) facets (Fig. S1A) and it completely overlaps with the CV measured on Pt-poly. Even though annealed surface still has typical, yet substantially suppressed, $H_{upd}$ peaks from (110) and (100) facets, the appearance of the characteristic reversible butterfly peak confirms that (111) facets are dominant after annealing (Fig. S1B).

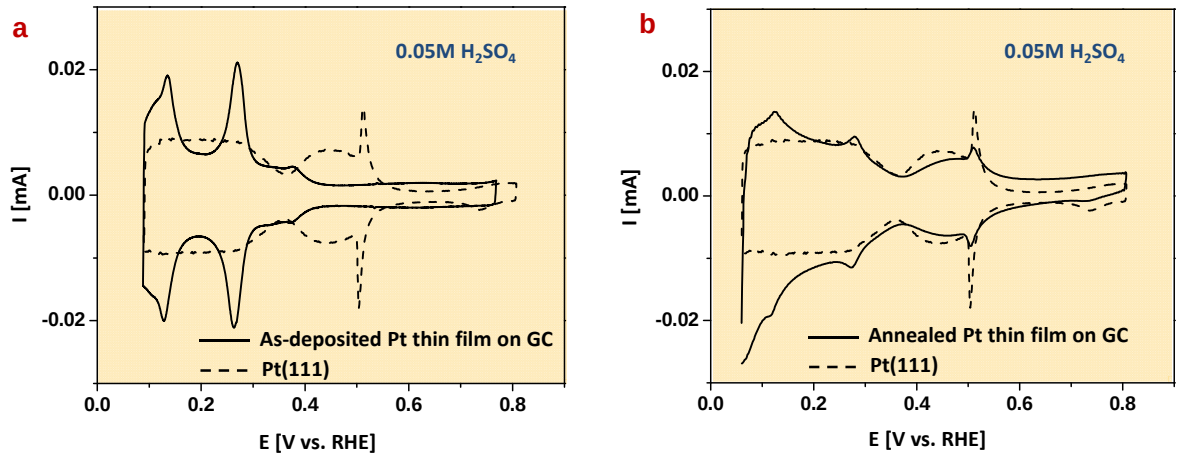


**Figure S1. Cyclic voltammetries of Pt thin film deposited on mirror polishes glassy carbon substrate in 0.05 M $H_2SO_4$ electrolyte purged with argon gas recorded with 50 mV/s sweep rate at 20°C: (A) as deposited 20 nm Pt thin film is overlapped with Pt-poly (solid line) and Pt(111) bulk single crystal (dashed line) and (B) annealed 20 nm Pt thin film (solid line) and Pt(111) bulk single crystal (dashed line)**

## X-Ray diffraction of thin film catalysts

XRD experiments (shown in Figure S2) show that during annealing there is a small angle shift due to the lowered lattice constant, which points to further alloying of the catalyst with Pt atoms being replaced by Ni in the crystal lattice. Furthermore, the grain size of the (111) facets increase as is evident from the increased sharpness of the (111) peak in the XRD pattern. Finally the ratio between the (111) and (200) orientations

has substantially increased, reinforcing the conclusion that annealing induces the phase transition into (111) preferred structure on the Meso-TF.

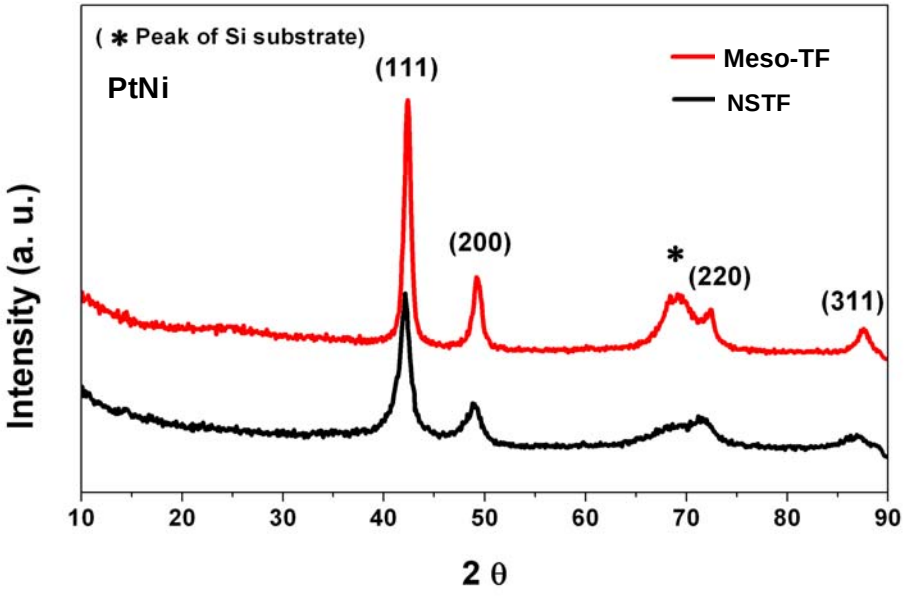


**Figure S2. XRD analysis of PtNi Meso-TF compared to its NSTF precursor.**

## Infrared spectra of perylene red removal

The annealing protocol of NSTFC was performed in quartz tube and reductive hydrogen rich atmosphere. This was accomplished by custom design of a quartz tube furnace that was sealed to prevent leaking of hydrogen and inlet of oxygen from the atmosphere. During a two hours temperature treatment we could follow the appearance of a red residue on the walls of the quartz tube in the direction of the hydrogen flow. That was in line with the observation during in-situ HRTEM studies and corresponded to the removal of the perylene red substrate from the NSTFC. In order to confirm this we performed careful infrared analyses of perylene red and residue after annealing. In Figure S2, infrared spectra of perylene red and residue after annealing are shown for comparison.

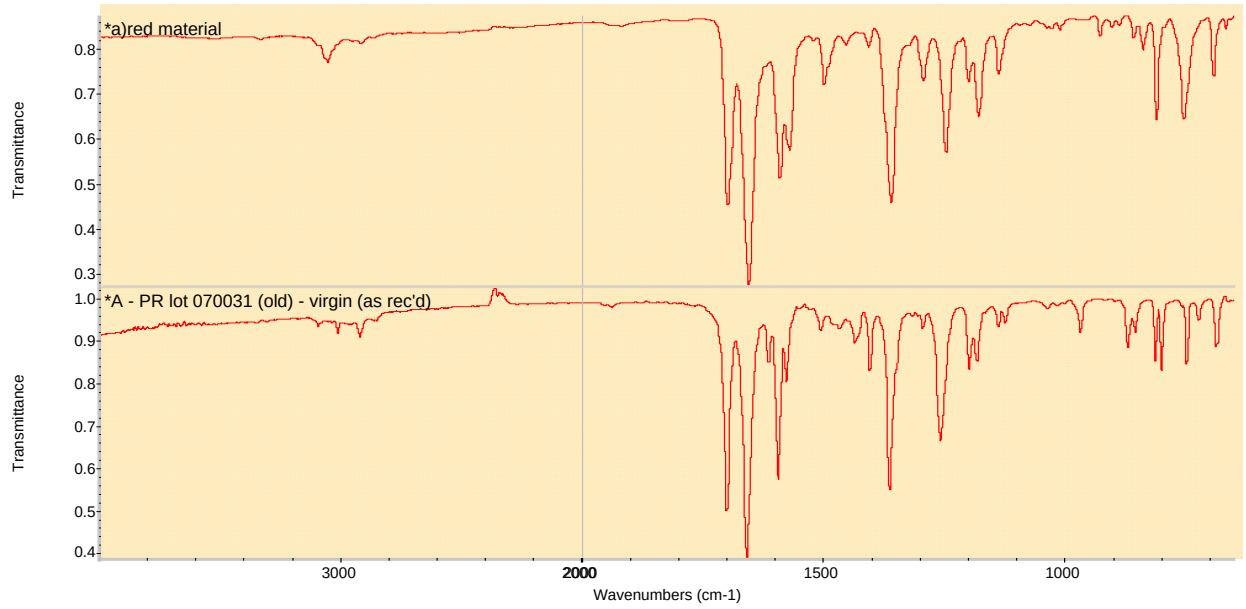


**Figure S3. Infrared spectra recorded on the Bruker Hyperion 2000 FT-IR microscope equipped with the Tensor 27 FT-IR spectrometer. The isolated materials were placed on a micro KBr plate and spectra were recorded in transmission mode: Top spectrum – red material removed from quartz glass (the specimen was viewed under a stereomicroscope and a surgical scalpel blade was used to isolate the red material from quartz glass substrate); Bottom spectrum – reference spectrum of perylene red**

Two infrared spectra show characteristic fingerprint similarity, indicating the existence of same/similar molecular species in both cases. Based on infrared band assignments (Table I in J. Vac. Sci. Technol., Vol.

21(1) 74-79 (1982)), it seems clear that the biggest change in the sublimed material is removal of the phenyl groups from the perylene red compound. The key bands are at 720, 800 and 970 $cm^{-1}$ (phenyl C-H bending modes); 1474, 1488 and 1618 $cm^{-1}$ (phenyl ring stretch modes). There are also shifts in the imide bands that could be a result of the removed xylyl groups attached to the imide. Hence, the material of the glass is partially decomposed perylene red, which is plausible considering the applied annealing conditions. All of this leads to the conclusion that perylene red was removed from the inner portion of the whiskers. In order to get an idea of the mass change we performed thermogravimetric (TGA) analysis (results not shown here) and it was possible to match actual mass losses with the initial ratio of perylene red in whiskers, which is ~6%. Cleanliness of the remaining material and absence of any indication in cyclic voltammetry that would correspond to the residual organic molecules was strong proof that perylene red was entirely removed from the NSTF whiskers. Further characterization of the structure and morphology has led to the conclusion that induced structural changes along with the perylene red removal produced material with distinctive structure and morphology.

## In-situ TEM characterization

In situ annealing of NSTF whiskers was performed in HRTEM described in Methodology section. In Figure S4 additional micrographs that reveal surface restructuring of the thin metal film are shown.

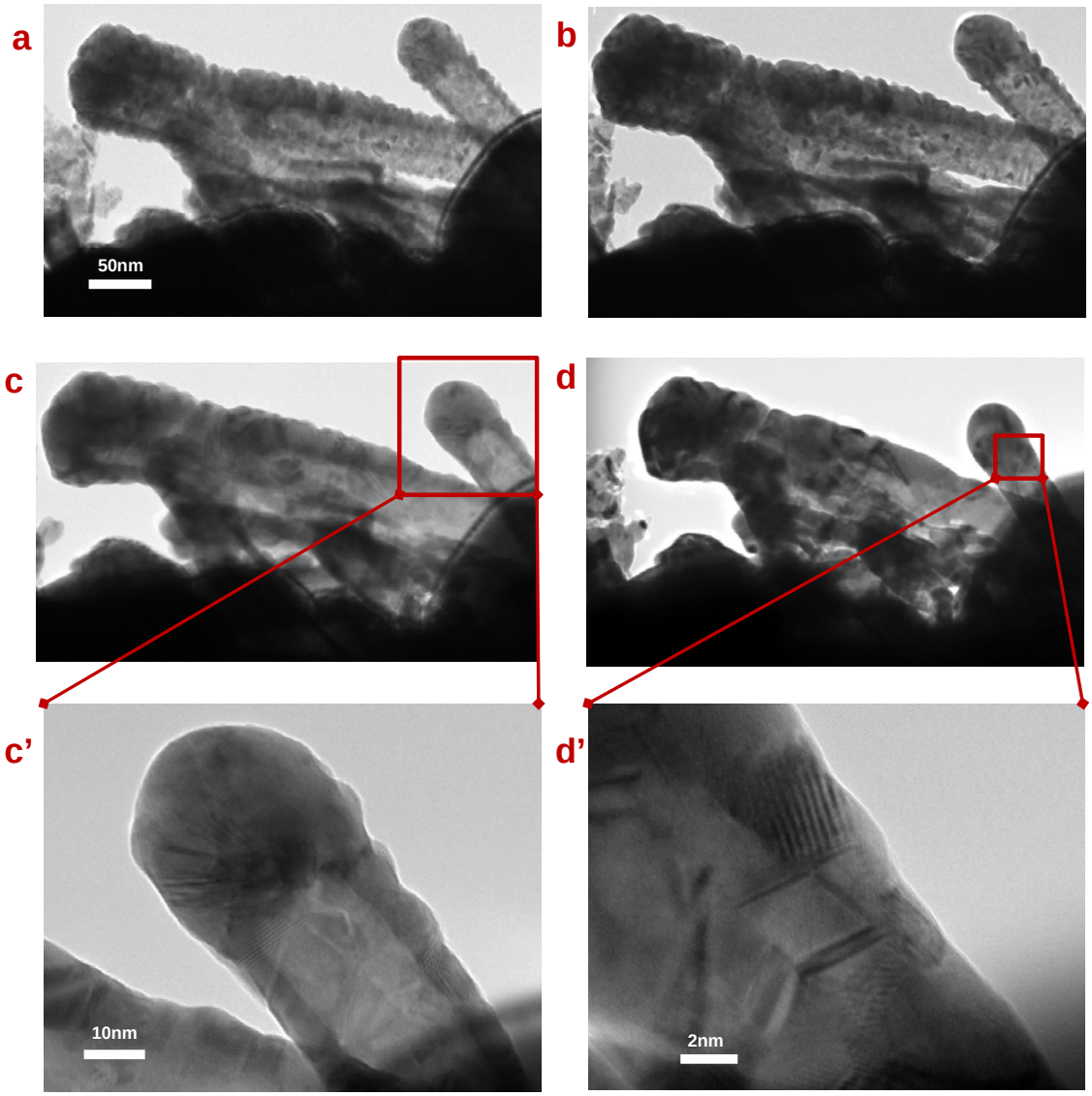


**Figure S4. In-situ transformation of thin films based catalyst from nanostructured into mesostructured morphology during annealing at 400°C: (A)-(D) HRTEM images of progressive annealing on a group of whiskers that capture the surface restructuring of the thin film: from highly grained to a homogeneous wall structure with large crystalline domains; (C')-(D') HRTEM close up of the near surface region transformed: from highly corrugated into a flat and smooth surface morphology with visible single crystalline facets.**